

WORLD METEOROLOGICAL ORGANIZATION

COMPENDIUM OF METEOROLOGY

For use by
CLASS I AND CLASS II METEOROLOGICAL PERSONNEL

Editor
Aksel Wiin-Nielsen

VOLUME II
PART 4 – TROPICAL METEOROLOGY

Prepared by
Professor T. N. Krishnamurti



WMO - No. 364

Secretariat of the World Meteorological Organization - Geneva - Switzerland
1979

© 1979, World Meteorological Organization

NOTE

The designations employed and the presentation of material in this publication do not imply the expression of any opinion whatsoever on the part of the Secretariat of the World Meteorological Organization concerning the legal status of any country, territory, city or area, or of its authorities, or concerning the delimitation of its frontiers or boundaries.

CONTENTS

	<u>Page</u>
Foreword	XI
Preface	XIII
Introduction	XV
 Chapter 1 - THE ZONALLY AVERAGED TROPICAL CIRCULATION	
1.1 Introduction	1
1.2 Zonal velocity	1
1.3 Mean meridional circulation	2
1.4 Temperature field	5
1.5 Moisture field	5
1.6 Meridional transports by the zonally symmetric circulations	5
 Chapter 2 - ZONALLY ASYMMETRIC FEATURES OF THE TROPICS	
2.1 Introduction	11
2.2 Gradient level winds (Atkinson, 1970)	11
2.3 The motion field in the upper troposphere	14
2.4 The temperature field	16
2.5 East/west circulations in the tropics	18
2.6 The moisture field	21
2.7 Sea-level pressure	24
2.8 Other parameters	24
 Chapter 3 - A SURVEY OF TROPICAL DISTURBANCES	
3.1 Introduction	27
3.2 Some selected disturbances	28

	<u>Page</u>
3.3 Westward motion of the tropical disturbances	33
3.4 Composite tropical disturbances	34
3.5 Western Pacific Ocean cloud clusters	35
3.6 The Reed and Recker composite wave	38
3.7 A composite West African wave	38
 Chapter 4 - RADIATIVE PROCESSES IN THE TROPICS	
4.1 Introduction	43
4.2 Numerical calculations of radiative processes	43
4.3 Short-wave radiation	44
4.4 Long-wave radiation	48
4.4.1 The specification of cloudiness	50
4.5 Heat balance of the Earth's surface	52
4.6 Radiative heat balance at the top of the atmosphere	58
4.7 Radiation measurements with instrumented aircraft	62
4.8 Radiation measurements from balloon-borne radiometers	64
4.9 Surface-based radiation instruments	65
4.10 Radiation climatology of the tropics	67
 Chapter 5 - THE TROPICAL BOUNDARY LAYER	
5.1 Empirical concepts	70
5.2 Observational aspects of the boundary layer	73
5.3 Recent observational findings	74
5.4 A simple model of the tropical boundary layer	82
5.5 Scale analysis of the large-scale tropical boundary layer	83
5.6 Cross-equatorial flows and planetary boundary layer dynamics	85
 Chapter 6 - TROPICAL CUMULUS CONVECTION	
6.1 Introduction	89
6.2 Parcel and slice methods	89
6.3 A simple cloud model	92
6.4 Budget studies	98
6.4.1 Moist static energy ($Q = E$)	102

	<u>Page</u>
6.4.2	Vorticity 102
6.4.3	Western Pacific Marshall area budget studies 102
6.4.4	Basic budget equations 102
6.5	Parameterization theories 115
6.5.1	Introduction 115
6.5.2	Kuo's parameterization procedure 116
6.5.3	Moist convective adjustment 118
6.5.4	Arakawa-Schubert theory 121
 Chapter 7 - SEA BREEZE AND DIURNAL CHANGES IN THE TROPICS	
7.1	Introduction 126
7.2	Sea-breeze models 126
7.3	Some observational aspects of diurnal changes 133
7.4	Diurnal variation in the monsoon belt 137
7.4.1	Diurnal variation in rainfall over India 140
7.5	Final remarks 140
 Chapter 8 - ATLANTIC DISTURBANCES	
8.1	Introduction 143
8.2	Waves in the trade-wind belt 143
8.3	Inverted V cloud formations 152
8.4	Squall lines over the Atlantic 152
8.5	Surges in the trades 152
8.6	The ITCZ (Intertropical Convergence Zone) in the Atlantic 155
8.6.1	Theories of the ITCZ 155
8.7	Subtropical cyclones 158
8.8	Other Atlantic disturbances 158
 Chapter 9 - PACIFIC DISTURBANCES	
9.1	Variations of sea-surface temperature (SST) over the Pacific Ocean and large-scale teleconnections 159
9.2	Transient disturbances in the lower troposphere 163
9.3	Formation of near-equatorial anticyclonic eddies 165
9.4	The eastern Pacific Ocean 167

	<u>Page</u>
Chapter 10 - INDIAN OCEAN DISTURBANCES DURING THE NORTHERN WINTER SEASON	
10.1	180
10.2	180
10.3	185
Chapter 11 - HURRICANES	
11.1	186
11.2	188
11.3	194
11.3.1	194
11.3.2	196
11.4	197
11.5	200
11.5.1	200
11.5.2	200
Chapter 12 - THE TRADE-WIND INVERSION	
12.1	204
12.2	210
12.3	214
12.4	219
12.5	223
Chapter 13 - WEATHER SYSTEMS OVER ASIA	
13.1	224
13.2	224
13.3	226
13.4	229
13.5	230
13.6	231
13.7	237
13.8	238
13.9	244
13.10	247

	<u>Page</u>
13.11 Monsoon disturbances	247
13.12 Mid-tropospheric cyclones of the southwest monsoons	255
13.13 Final remarks	260
 Chapter 14 - AFRICAN WEATHER SYSTEMS	
14.1 Introduction	261
14.2 Rainfall distribution	261
14.3 The time-averaged motion field over Africa during the winter and summer months	264
14.4 The time-averaged temperature field over Africa during the winter and summer months	268
14.5 Surface-flow patterns over Africa	268
14.5.1 Vertical slope of the pressure system	273
14.6 Some climatological aspects of the Sahara Desert	273
14.7 Heat lows over the African deserts	273
14.8 West African wave disturbances	278
14.9 West African disturbance lines	279
14.9.1 Squall lines "An Integral Part of the African Wave"	279
14.9.2 Other squall line models	279
14.10 Central Africa	284
14.11 Cross-equatorial flow near the east African coast	292
 Chapter 15 - SOUTH AMERICAN NEAR-EQUATORIAL RAINBELTS AND DRY ZONES	
15.1 Rainfall and lower tropospheric flow fields	293
15.2 The low-level easterly wind maximum during February	293
15.3 Northeast Brazil	293
15.4 Synoptic maps during the rainy season	299
 Chapter 16 - TROPICAL CLOUD COVER, RAINFALL AND SATELLITE METEOROLOGY	
16.1 Introduction	304
16.2 Tropical rainfall climatological aspects	310
16.3 Mapping of rainfall rates from satellite brightness data	316
16.4 Rainfall maps from microwave radiometer data	319

	<u>Page</u>
Chapter 17 - TROPICAL UPPER-TROPOSPHERIC PHENOMENA	
17.1	The subtropical jet stream of winter 323
17.2	Barotropic instability of the tropical upper-level jets 327
17.3	The northward seasonal march of the Tibetan high 331
17.4	Tropical oceanic upper-level cold lows 331
17.4.1	The maintenance of the cold low 335
17.5	A review of tropical upper-tropospheric energetics during the northern summer 344
17.5.1	Normal versus anomalous years 348
17.6	On the quasi-stationarity of the upper-tropospheric climatology 348
Chapter 18 - THE TROPICAL LOWER STRATOSPHERE	
18.1	The quasi-biennial oscillation (QBO) 351
18.2	Spectral analysis in the tropical lower stratosphere 356
18.3	The large quasi-stationary gyres 358
Chapter 19 - MISCELLANEOUS PHENOMENA AND PROBLEMS IN THE TROPICS	
19.1	Diurnal changes in near-equatorial continental regions away from the coast 359
19.2	Diurnal changes over the open oceans 359
19.3	Diurnal change of the monsoon trough 364
19.4	Wave CISK 366
19.5	Sea-surface temperature anomalies over the tropics and tropical weather 366
Chapter 20 - FIELD EXPERIMENTS OVER THE TROPICS AND FUTURE TROPICAL OBSERVING SYSTEMS	
20.1	Introduction 367
Chapter 21 - NUMERICAL WEATHER PREDICTION OVER THE TROPICS	
21.1	Filtered barotropic model 378
21.2	The basic dynamics of the barotropic model 378
21.3	Some properties of the barotropic flows 380
21.3.1	Parcel invariants 380

	<u>Page</u>
21.3.2	Domain invariants 380
21.3.3	Energy exchanges of the barotropic model 381
21.4	Numerical prediction techniques 382
21.4.1	The advective term for filtered models 382
21.4.2	Time-differencing scheme 383
21.4.3	Boundary conditions 384
21.5	One-level primitive equation model 384
21.5.1	Invariants of the shallow-water equations 386
21.5.2	Numerical prediction techniques 386
21.5.3	The problem of geopotential height in low latitudes 387
21.5.4	Single-level initialization 387
21.5.5	Static initialization 387
21.5.6	Numerical prediction techniques 388
21.5.7	Semi-Lagrangian advection 389
21.5.8	On the treatment of the pressure-gradient force and divergence in the mass-continuity equation 390
21.5.9	Boundary conditions for single-level dynamical initialization 390
21.5.10	Single-level dynamic initialization 390
21.5.11	Multi-level dynamical initialization 391
21.5.12	One-level primitive equation model with bottom topography 392
21.6	Multi-level primitive equation prediction model 392

LIST OF APPENDICES

(i)	Moist and dry static energy equations 396
(ii)	Conditional instability of the first kind 398
(iii)	Arakawa's identity relating saturation specific humidity to the moist static energy 400
(iv)	Necessary conditions for the existence of barotropic instability 400
(v)	Finite difference methods for studying barotropic instability in the tropics 402
(vi)	Combined barotropic/baroclinic instability 404
(vii)	Kinematic vertical velocity for a triangular array 407

	<u>Page</u>
(viii) The Ekman vertical velocity	408
(ix) Explanation of terms in the energy equations.....	409
REFERENCES.....	411

FOREWORD

The need for teaching aids, particularly compendia of lecture notes, for the training of the higher categories of meteorological personnel has been expressed on many occasions by the various constituent bodies of the Organization. The WMO Executive Committee and its Panel of Experts on Education and Training agreed that the Organization should take the necessary steps to prepare a series of compendia of lecture notes in different branches of meteorology for use by Class I and Class II meteorological personnel. The series now consists of two Volumes each comprising several Parts.

Volume I consists of three Parts dealing with dynamic meteorology (published in 1973), physical meteorology (published in 1973) and synoptic meteorology (published in 1978) respectively. Volume II, which covers the lecture notes in the applied meteorological fields, is now being prepared. Three Parts have already been published, namely, general hydrology (1977), aeronautical meteorology (1978) and marine meteorology (1979).

This present text constitutes Part 4 of Volume II; it deals with tropical meteorology and has been prepared by Professor T.N. Krishnamurti to whom I wish to express my sincere appreciation for the excellent work he has carried out.

I feel confident that the material contained in this publication will be an invaluable training aid to students and instructors alike.

D. A. Davies.

(D. A. Davies)
Secretary-General

Geneva, December 1979

PREFACE

The lecture notes on Tropical Meteorology are prepared for the needs of Class I and Class II meteorological personnel. The 21 chapters cover a wide range of topics from the sea breeze to the planetary scale. The lecture notes are based on my lecture course on tropical meteorology at Florida State University. A number of ideas have come from my own research group over a 10-year period. I am indebted to Drs. Gene Bierly, Richard Greenfield and Jay Fein for their support. A word of thanks also goes to Dr. H. Taba and Professor G. O. P. Obasi for the support of this effort through WMO sponsorship. Finally, thanks also go to Professors R. P. Pearce, A. Wiin-Nielsen and Dr. Y. Ramanathan for a careful review of the manuscript.

Tallahassee
May 1, 1979

T. N. Krishnamurti

INTRODUCTION

The first chapter considers the zonally averaged tropical circulation, but in doing so, presents an over-simplified view of the tropics. We ask: What does a typical meridional cross section of time and zonally averaged wind, temperature, moisture or any other property look like? This kind of a view generally appeals to climate modellers who wish to parameterize the overall circulation pattern (Gestalt). The recent essay on the General Circulation of the Atmosphere by Lorenz (1967) includes a large number of excellent diagrams which illustrate the meridional variation of zonally averaged atmospheric properties. It is of interest to note that this famous essay on the general circulation of the atmosphere does not broach the question of maintenance of any of the individual zonally asymmetric elements - the so-called Gestalt - of the general circulation. The general atmospheric circulation means different things to different people. To some, the understanding of prominent time-averaged gyres such as the Icelandic low, the Aleutian low, the Subtropical highs, the Siberian high, the Tibetan high and prominent convergence zones such as the ITCZ, the monsoon troughs, etc. is essential to an understanding of the general circulation of the atmosphere. In this text, we shall consider all such time-averaged properties (zonally averaged or not) in our definition of the general circulation.

The first two chapters of this text deal respectively with the zonally symmetric and zonally asymmetric aspects of time-averaged tropical flows. The zonally symmetric aspect has many limitations. Some of these will become more apparent as we go into the following chapters. It is easy to see that the zonal averaging does not permit us to distinguish between, for example, places such as the equatorial Amazon belt, equatorial east Africa and equatorial Indonesia. These three regions possess quite different properties. If we were to describe the tropics of a planetary atmosphere, some 10 million miles away via remote sensing, then perhaps we would be satisfied by an over-simplified zonally symmetric description based on a few numbers. The tropical Gestalt usually included elements such as subtropical highs, trade wind belts, trade wind inversions, trade wind clouds, oceanic and land area convergence zones (ITCZ), monsoon lows, heat lows, equatorial waves, easterly waves, tropical depressions, tropical jet streams, cross-equatorial impulses, upper cold lows, quasi-stationary disturbances, hurricanes, typhoons, monsoon westerlies, monsoon surges, floods, droughts, tropical squall lines over land and oceanic areas, dust storms, sea breezes and so on. The question therefore arises as to whether such phenomena are an over-exaggeration of the Gestalt which could perhaps be described more simply. Possibly this latter view emerges from the idea that quasi-geostrophic physics is capable of providing an adequate description for much of what goes on in the middle and high latitudes. It is, however, becoming quite clear that even in the middle and high latitudes, there exists a vast degree of complexity in the components of the motion systems, and they are in fact not adequately handled in day-to-day numerical weather prediction. The problems in low, as well as high, latitudes are all far more complex than they might seemingly appear. The tropical systems depend crucially on convection which is sensitive to a number of factors such as sea-surface temperature, the heat balance of the land areas, the mountains and scale-interactions.

The tropical phenomena presented above have very varied structures. The problems of maintenance, as far as we understand them at present, also seem to vary considerably from one phenomenon to the other. In some cases, subsidence and shallow convection play a dominant role while in others, large scale vertical motions and deep convection is crucial. Somewhat different physical processes usually take precedence in one region as compared to another, and thus the Gestalt that emerges provides a fairly complex tropical general circulation. This does make one wonder if a satisfactory theory of the general circulation can yet be presented taking into account the role played by the Gestalt. The state of the art has not gone far enough to permit any such unified theory of the tropical general circulation.

A number of tropical field experiments have taken place in recent years. The focus has been towards understanding convection, air-sea interaction, the structure of hurricane rain areas, atmospheric radiation, the tropical boundary layer and monsoonal circulations. We shall see later that even a seemingly simple problem such as an understanding of the westward propagation of a non-deepening tropical wave disturbance is not a simple matter. We shall find that the large scale disturbances whose scale is of the order of a few thousand km coexist with embedded cumulus and cumulonimbus clouds. Their seemingly innocuous westward motion is tied to a large number of subtle balances of mass, moisture, momentum, heat and kinetic energy. These balances are achieved by the large scale as well as by the embedded cumulus scale motions. Large-scale field experiments have been designed to provide answers to some of the questions raised in preliminary studies. Many more such field experiments are needed however to obtain further understanding of tropical motion systems.

Frequently, a student of tropical meteorology wishes to study an episode of intense rainfall or floods or droughts in his or her country. It soon becomes evident that what seemed to be a simple episode is, in fact, a complex story of scale interactions. The experience can, at times, become somewhat frustrating. There are those who feel that a few simple and salient principles describing the episode should be extracted. There is no question that in the maze of complex interactions such an approach is desirable. This, of course, requires good intuition and a knowledge of the problem. The ultimate understanding of the governing physical processes of a phenomenon would enable one to provide a description via a physical model. This in turn should be valuable in predicting similar phenomena. Unfortunately, understanding and prediction do not seem to go hand in hand. Even, if one knew the simplified picture of the salient dynamical and thermodynamical processes for, say, an African wave disturbance, one might still be far from having the ability to predict whether or not it would rain over northern Nigeria 24 to 36 hours ahead. The prediction problem is an entirely different one and entails more than a knowledge of the physical processes - e.g. computational procedures, initial data and adequate computer storage. It is also subject to the inherent limitations of predictability.

In Chapter 3, we present an overview of some typical large-scale tropical disturbances. Here the student should try to contrast their structures with those of extra-tropical weather systems.

In the following three chapters (4, 5 and 6) we present some background of the relevant radiative processes, boundary layer processes and convective processes that are important for understanding the details of tropical weather systems. In

Chapter 7 we present the sea breeze problem and the diurnal changes over the tropics and introduce concepts of tropical dynamics in a simple form.

Oceanic disturbances of the Atlantic, Pacific and Indian oceans are discussed in Chapters 8, 9 and 10. Chapter 11 is devoted to the typhoon problem, going into the question of formation, motion and structure as well as the current status of the modification efforts by man. The trade wind inversion which is ever present over tropical oceans is separately discussed in Chapter 12. The continents of Asia, Africa and South/Central America are reviewed in Chapters 13, 14 and 15. Here more details on rain-producing weather systems of the monsoon-affected regions of the world and tropical rainforests are examined. A discussion of tropical cloud cover, rainfall and satellite meteorology is presented in Chapter 16. Phenomena of the tropical upper troposphere and of the lower stratosphere are examined in Chapters 17 and 18. A miscellany of other tropical phenomena not highlighted above are reviewed in Chapter 19. The descriptions are more sketchy and illustrate a host of unsolved problems deserving further study. In many instances these are perhaps the very problems that students from tropical countries wish to study but about which, unfortunately, very little is known at present.

As stated earlier the general lack of meteorological observations has led to a number of field experiments over the tropics in recent years. Chapter 20 presents a review of these from the point of view of modern observing systems and illustrates the kinds of problems they seek to solve.

The final Chapter 21 of these notes is on numerical weather prediction techniques for the tropics. The outline here is designed to provide the background for some simple forecast models on relatively small electronic computers.

An appendix provides useful mathematical frameworks for the studies of tropical weather systems.

Chapter 1

THE ZONALLY AVERAGED TROPICAL CIRCULATION

1.1 Introduction

A long term averaging (over a season or a month) is usually carried out to portray the zonally symmetric distributions of the atmospheric variables. We shall use the notation:

$$[Q] = \oint Q dx / \oint dx \quad (1.1)$$

to denote a zonal average of Q around a latitude circle, and the notation:

$$\bar{Q} = \int_0^{\tau} Q dt / \tau \quad (1.2)$$

to denote a time average of Q over a period τ .

$[\bar{Q}]$ is a function of y, p , i.e. it varies in the meridional vertical plane.

In this section we shall first examine the geometry of the isopleths of the following quantities in this vertical plane.

- (a) zonal velocity $[\bar{U}]$
- (b) mean meridional circulation $[\bar{\Psi}]$
- (c) temperature $[\bar{T}]$
- (d) moisture $[\bar{q}]$

One of the main purposes of this depiction is to take a quick look at the vertical structure of the tropical atmosphere as a function of latitude. In the next section we shall examine the important question of the zonal asymmetry of the tropical atmosphere. References may be made to Newell *et al.*, (1972) and Oort and Rasmussen (1971) for the diagrams in the following sections.

1.2 Zonal velocity

The easterly-westerly distribution of the zonal velocity $[\bar{U}]$ for the four seasons is illustrated in Figure 1.1. Over the Equator, easterlies prevail from the surface up to 100 mb. The climatological westerly jet, strongest near 200 mb during winter, should be noted. The latitude of strongest westerlies shifts from roughly 30°N during winter to roughly 45°N during the summer season. Other interesting aspects of these flows are the vertical shear distributions. During summer over the belt 0 to 20°N, easterlies increase with height. In this belt, during the northern winter, easterlies increase in intensity between the surface and 850 mb and decrease with

altitude above that level. The easterly, westerly shears at different latitudes have important dynamical implications. During the autumn, the tropical easterlies are strongest near the 300 mb surface whilst during spring this level is in the lower troposphere near the 700 mb surface.

1.3 Mean meridional circulation

This is usually depicted via the use of a streamfunction $\overline{\Psi}$.

The mass continuity equation for these zonally symmetric motions can be written as:

$$\frac{\partial \overline{V}}{\alpha \partial \phi} - \frac{\overline{V} \tan \phi}{\alpha} + \frac{\partial \overline{\Omega}}{\partial p} = 0 \quad (1.3)$$

or

$$\frac{\partial \overline{V}}{\alpha \partial \phi} \cos \phi + \frac{\partial \overline{\Omega}}{\partial p} \cos \phi = 0 \quad (1.4)$$

It is convenient to define the streamfunction for the mean meridional circulation by the relations:

$$\frac{\partial \overline{\Psi}}{\alpha \partial \phi} = - \overline{\Omega} \frac{2\pi \alpha \cos \phi}{g} \quad (1.5)$$

$$\frac{\partial \overline{\Psi}}{\partial p} = \overline{V} \frac{2\pi \alpha \cos \phi}{g} \quad (1.6)$$

Note that $\overline{\Omega}$ and \overline{V} satisfy the continuity equation and $\overline{\Psi}$ has the dimensions kg s^{-1} .

What is generally available are the wind observations which are used first to construct the field of the meridional wind \overline{V} . Next the vertical motion $\overline{\Omega}$ is constructed from the continuity equation (1.3). Instead of looking at the fields of \overline{V} and $\overline{\Omega}$ we shall merely look at the field of the streamfunction $\overline{\Psi}$. Its geometry, via equations (1.5) and (1.6) tells us the fields of the meridional and vertical velocities.

Figure 1.2 shows the seasonal values of the mean meridional circulation. The interval between adjacent isopleths of $\overline{\Psi}$ denotes the amount of mass (10^9 kg s^{-1}) circulating in these channels.

It should be noted that these are the diagrams that one uses to illustrate the so-called Hadley, Ferrel and Polar cells, the three cells of the mean meridional circulation. From the point of view of the tropics, the Hadley cell is the one of most interest and we shall examine that in Figure 1.2. The ascending and the descending branches of the cell are easy to identify here. The winter and summer Hadley cells are more intense than those during the other two seasons. This diagram is based on studies of Newell *et al.*, (1972). There is an interesting seasonal shift of the latitude of the ascending branch of the Hadley cell, near 10°N during N summer, near 5°S during N winter and near the Equator during spring. In the ascending branch of the Hadley cell, the intensity of rising motion is of the order of 0.4 cm s^{-1} , while the north-south component attains a magnitude of the order of 1 to 3 m s^{-1} . We shall note from the distribution of temperature \overline{T} that these Hadley circulations are thermally

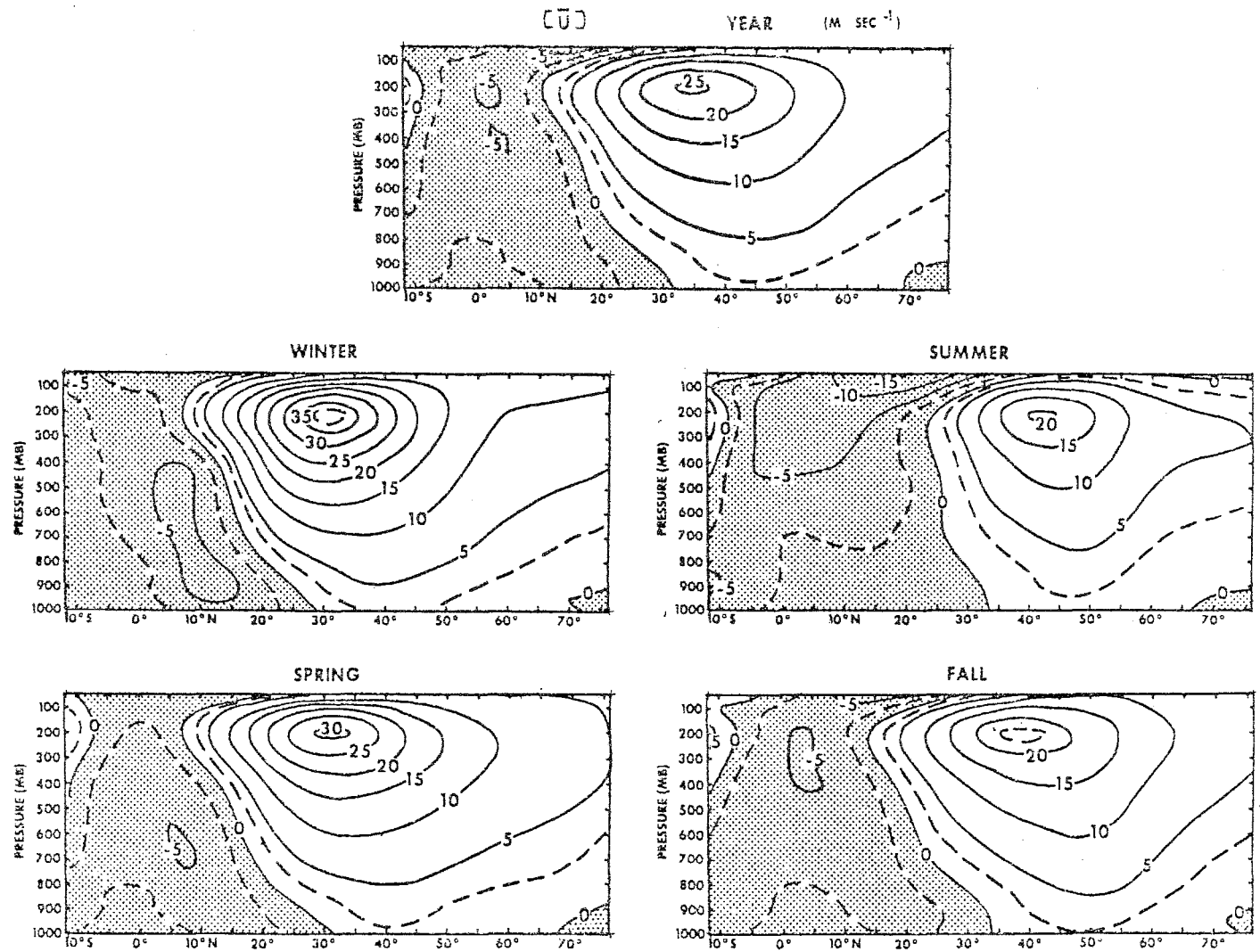


Figure 1.1 - Mean zonal wind component [u] for year and seasons. (Units in m s⁻¹)

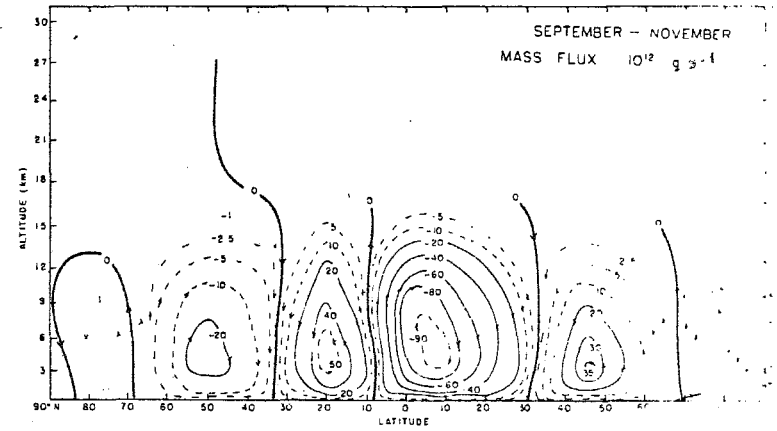
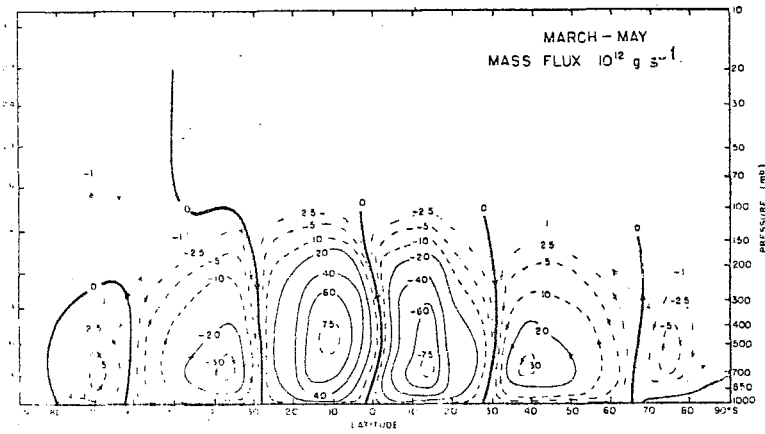
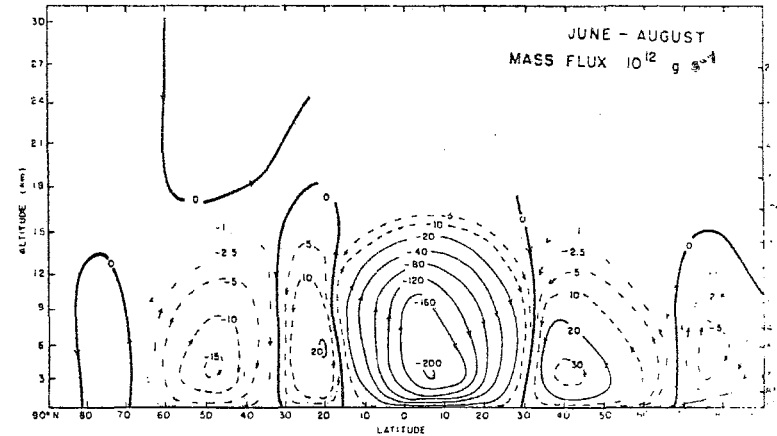
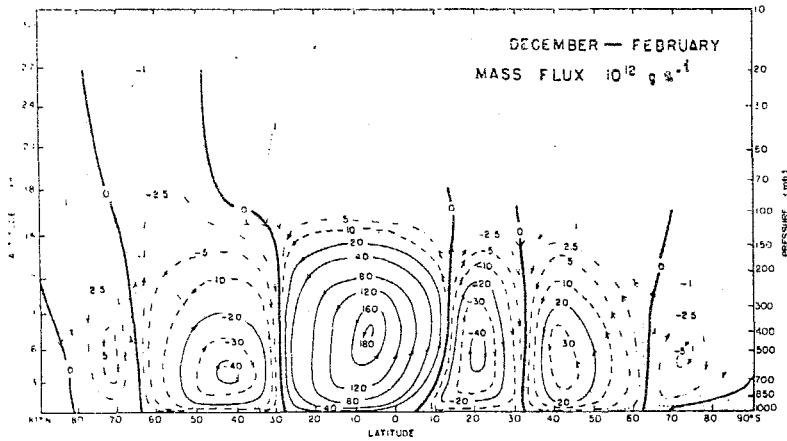


Figure 1.2 - Mean meridional motions

direct i.e. the rising branch is at a slightly warmer temperature compared to the descending branch which is at a relatively colder temperature (at the same pressure level). This has important implications for the generation of zonal kinetic energy from the zonally available potential energy.

1.4 Temperature field

The field of zonally averaged temperature $[\bar{T}]$ (seasonal mean) is presented in Figure 1.3. The thermal field illustrates the strong meridional gradient in the middle latitudes, and the lack of it over the tropics. Other features such as the annual cold tropical tropopause and warm subtropical lower tropospheric temperatures during the northern summer are worth noting. It should be noted too that the zonal average smooths out the land-ocean contrasts, since it does not represent either land or ocean. This is especially significant during the northern summer, where the zonal asymmetries are quite large, and the symmetric component, such as shown in Figure 1.3, is not very representative of the meridional variation, except perhaps in the context of the generation of zonal kinetic energy by the Hadley cell.

1.5 Moisture field

The field of specific humidity $[\bar{q}]$ is illustrated in Figure 1.4. Largest values around 18 g kg^{-1} are found near the Equator. These should be compared with values of about 6 g kg^{-1} in the middle latitudes near 45°N . An interesting consequence of such large magnitudes of moisture in low latitudes is the so-called virtual temperature correction. For a surface temperature of 20°C the corresponding correction is of the order of 3°C which is substantial in thermodynamical calculations. The meridional gradient of moisture in the tropics is large (see Figure 1.4) and gives rise to a considerable meridional gradient of the virtual temperature, although the meridional gradient of temperature (Figure 1.3) is smaller.

The zonally symmetric component of moisture is again quite smooth and the land-ocean contrasts are not represented.

1.6 Meridional transports by the zonally symmetric circulations

It is well known that the Hadley cell plays an important role in poleward fluxes and we shall illustrate this here. In this context, using the notation of Lorenz (1967), we consider a variable Q .

$$\text{Let } Q = \bar{Q} + Q'$$

where \bar{Q} is a time average, and Q' a departure from a time average. We may also write:

$$Q = [Q] + Q^*$$

where $[Q]$ is a zonal average and Q^* is a departure from a zonal average. Using the above two relations the total meridional transport of Q can be written in the form:

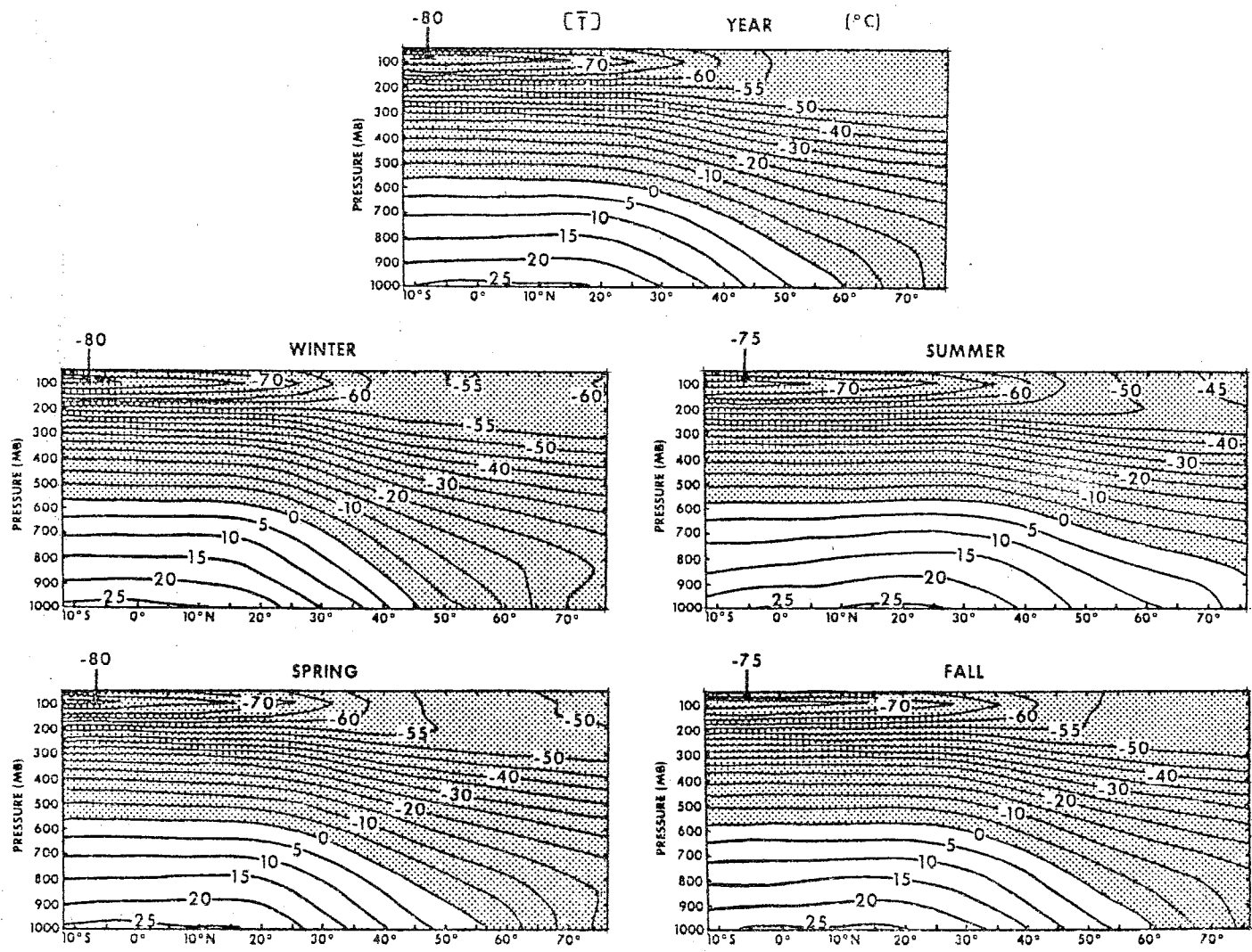


Figure 1.3 - Mean temperature $[\bar{T}]$ for year and seasons (Units in $^{\circ}\text{C}$)

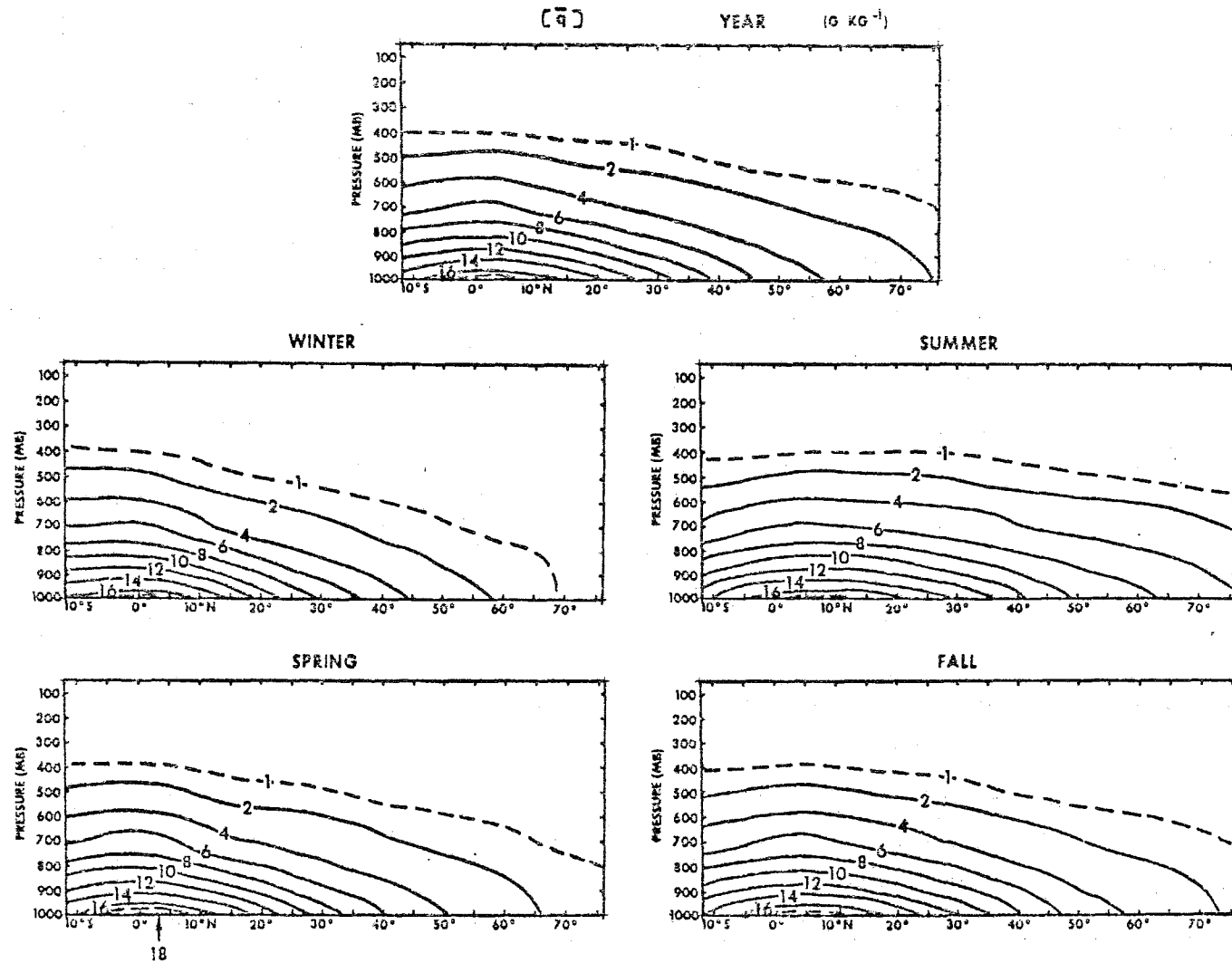


Figure 1.4 - Mean specific humidity $[\bar{q}]$ for year and seasons (Units in grams of water vapour per kilogram of air)

$$[\overline{QV}] = [\overline{Q}] [\overline{V}] + \overline{[Q] \cdot [V]} + \overline{[Q^*V^*]}$$

TOTAL TRANSPORT = TRANSPORT BY MEAN MERIDIONAL CIRCULATION + TRANSPORT BY TRANSIENT EDDIES + TRANSPORT BY STANDING EDDIES

In Tables 1.1 through 1.5 we show the following meridional transports for January and July, from Oort and Rasmussen (1971):

- (i) momentum
- (ii) sensible heat
- (iii) potential energy
- (iv) latent heat, and
- (v) kinetic energy.

The transports by the three processes are identified by the following letters:

- TE Transient eddies
- SE Standing eddies, and
- MMC Mean meridional circulation.

The calculations here are only for the northern hemisphere. Of interest for the tropical atmosphere are the entries at the Equator, 15°N and 30°N. During the northern winter the mean meridional circulation is fairly intense between the Equator and 30°N. We note that at the Equator and 15°N a large proportion of the transport is carried out by the mean meridional circulations. This is especially large for the sensible heat, potential energy and latent heat. As regards fluxes of momentum and kinetic energy, the transports by transient eddies begin to become large at 15°N and polewards. During the summer season the Hadley cell between the Equator and 30°N is considerably weaker and transports by the mean meridional circulations dominate only at the Equator in these tables.

TABLE 1.1 - Meridional transport of momentum*
(units in m²s⁻²)

Month	Eq.	15°N	30°N	45°N	60°N
January					
TE	-0.1	3.4	13.3	11.2	2.8
SE	-0.7	0.1	4.6	0.9	-11.8
MMC	-0.8	4.9	-1.7	-2.3	0.5
July					
TE	1.4	1.1	4.4	7.2	-0.4
SE	0.7	2.5	3.1	0.3	-0.4
MMC	2.4	-0.2	-0.0	-0.9	-0.1

*Numbers represent averages for the layer between 1012.5 mb and 75 mb. For conversion to angular momentum transfer, multiply by $(2\pi a^2 \cos^2 \phi) (p_o - p_r) g^{-1}$

TABLE 1.2 - Meridional transport of sensible heat*
(units in $^{\circ}\text{C m s}^{-1}$)

Month	Eq.	15°N	30°N	45°N	60°N
January					
TE	-0.4	-0.8	4.7	6.9	8.6
SE	-0.0	0.0	2.2	10.3	7.8
MMC	-27.0	-23.0	4.0	7.0	-3.0
July					
TE	0.1	-0.3	0.3	4.1	4.8
SE	0.1	0.1	0.2	0.7	-0.6
MMC	26.0	-1.0	2.0	4.0	1.0

*Numbers represent averages for the layer between 1012.5 mb and 75 mb. For conversion to units of energy transfer, multiply by $(2\pi a \cos \phi) c_p (p_o - p_r) g^{-1}$

TABLE 1.3 - Meridional transport of potential energy*
(units in $10^2 \text{ gpm m s}^{-1}$)

Month	Eq.	15°N	30°N	45°N	60°N
January					
TE	-0.0	-0.1	-0.2	-0.4	0.2
SE	-0.0	-0.0	-0.1	0.1	0.2
MMC	40.0	37.0	-6.0	-14.0	6.0
July					
TE	0.0	-0.0	-0.0	-0.2	-0.0
SE	0.0	-0.1	-0.0	0.0	0.1
MMC	-40.0	2.0	-4.0	-7.0	-1.0

*Numbers represent averages for the layer between 1012.5 mb and 75 mb. For conversion to units of energy transfer, multiply by $(2\pi a \cos \phi)(p_o - p_r) g^{-1}$, (1 gpm = $10 \text{ m}^2 \text{ s}^{-1}$)

TABLE 1.4 - Meridional transport of latent heat*
(units in $\text{g kg}^{-1} \text{ m s}^{-1}$)

Month	Eq.	15°N	30°N	45°N	60°N
January					
TE	0.3	0.8	2.1	1.5	0.9
SE	-0.0	0.2	0.4	0.7	0.2
MMC	-3.8	-3.5	0.1	0.5	-0.1
July					
TE	-0.1	0.3	0.5	1.6	1.3
SE	0.0	0.4	1.3	-0.0	-0.0
MMC	5.0	0.1	0.1	0.6	0.2

*Numbers represent averages for the layer between 1012.5 mb and 75 mb. For conversion to units of energy transfer, multiply by $(2\pi a \cos \phi) L \times (p_o - p_r) g^{-1}$

TABLE 1.5 - Meridional transport of kinetic energy*
(units in $\text{m}^3 \text{ s}^{-1}$)

Month	Eq.	15°N	30°N	45°N	60°N
January					
TE	20	30	360	170	100
SE	-0	-10	180	80	20
MMC	30	50	-50	-50	10
July					
TE	-30	-10	10	70	-0
SE	-10	-10	0	-0	0
MMC	-30	0	-0	-20	-0

*Numbers represent averages for the layer between 1012.5 mb and 75 mb. For conversion to units of energy transfer, multiply by $(2\pi a \cos \phi) \times (p_o - p_r) g^{-1}$

Chapter 2

ZONALLY ASYMMETRIC FEATURES OF THE TROPICS

2.1 Introduction

Seasonal or monthly mean weather maps are particularly important in the tropics. The following example illustrates this point. Over the North American continent, the January mean sea level isobar map (i.e. $\bar{p}_s(x,y)$) consists of a large continental anticyclone extending southwards from the Arctic and Canada towards the southern United States. This monthly mean pattern does not reveal any of the migrating polar front cyclones that cause much of the weather there during the winter season. The reason for this is that climatological charts in middle latitudes do not display the transient disturbances. A similar exercise carried out over the global tropical belt shows that daily as well as monthly mean charts both carry much the same information. The subtropical highs, the equatorial troughs, the monsoon troughs, the trades of the two hemispheres are common in both the daily and the mean charts. Another way of expressing this is that climatological means carry much of the variance of the total motion field in the tropics. Thus an understanding of the maintenance of the time averaged zonally asymmetric feature of the tropics is important. A student of tropical meteorology should know tropical climatology well.

A detailed description of the time-averaged zonally asymmetric feature of the tropics entails knowledge of a number of variables, such as the motion, temperature, pressure and moisture, at a large number of levels in the atmosphere. Much of the information on the time-averaged state of the tropical atmosphere is still not properly documented. It is a voluminous task to describe 5 or 6 variables around the global tropics at some 10 levels of the atmosphere for 4 different seasons. Instead of presenting 240 such maps we shall present some salient features of the zonal asymmetries of the tropics. A number of atlases of the tropical mean state providing this kind of information are listed in Table 2.1.

2.2 Gradient level winds (Atkinson, 1970)

One of the best sources of reference for time averaged low level flows over the tropics is the atlas by Atkinson (1970). It represents the flow field near the 1 km level. This atlas contains the monthly mean flows over the global tropics for the entire year. The observations include many decades of wind data. In this section, we present two of these charts, Figures 2.1 and 2.2. It is quite clear from these charts that the tropical flows are quite asymmetric in the zonal and meridional directions. The principal asymmetric features are:

- (i) The subtropical highs
- (ii) The tropical convergence zones

TABLE 2.1 - A list of some tropical atlases

AUTHOR	YEAR PUBLISHED	PARAMETER	PERIOD COVERED	INSTITUTION
T. N. Krishnamurti E. B. Rodgers	1970	200 mb winds daily maps global tropics	June 1 to August 31, 1967	Florida State University
T. N. Krishnamurti E. Astling	1975	200 mb winds daily maps global tropics	June 1 to August 31, 1972	Florida State University
P. C. Chin M. H. Lai	1974	Mean maps of winds, temperature, all levels	All months	Royal Observatory, Hong Kong
G. Atkinson	1970	Mean winds, gra- dient level, 3000 feet	All months	Air Weather Service Scott, III
J. Sadler	1972	Mean winds, eastern Pacific 200, 250, 300 mb	All months	Navy Postgraduate School Monterey, Calif.
J. Sadler B. Harris	1970	Mean winds, all levels, S.E. Asia	All months	University of Hawaii
C. V. Ramage C.R.V. Raman	1972	Mean streamlines, Indian Ocean	All months	National Science Found., Wash.
C. Aspliden G. Dean H. Landers	1966	Streamlines, iso- bars SFC, 200 mb Atlantic Ocean	Summer, 1963 Daily maps	Florida State University
G. Dean	1971	Mean streamlines, isotherms, all levels Africa	All months	Florida State University
G. Dean	1974	Mean streamlines, isotherms, all levels Africa	All months	Florida State University

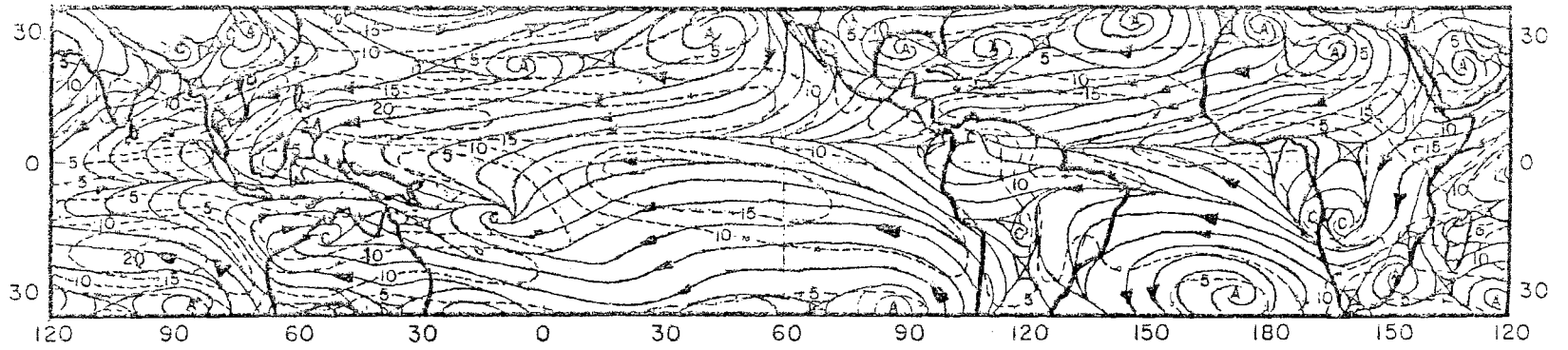


Figure 2.1 - Resultant gradient-level wind for January (from AWSTR 215 |45|)

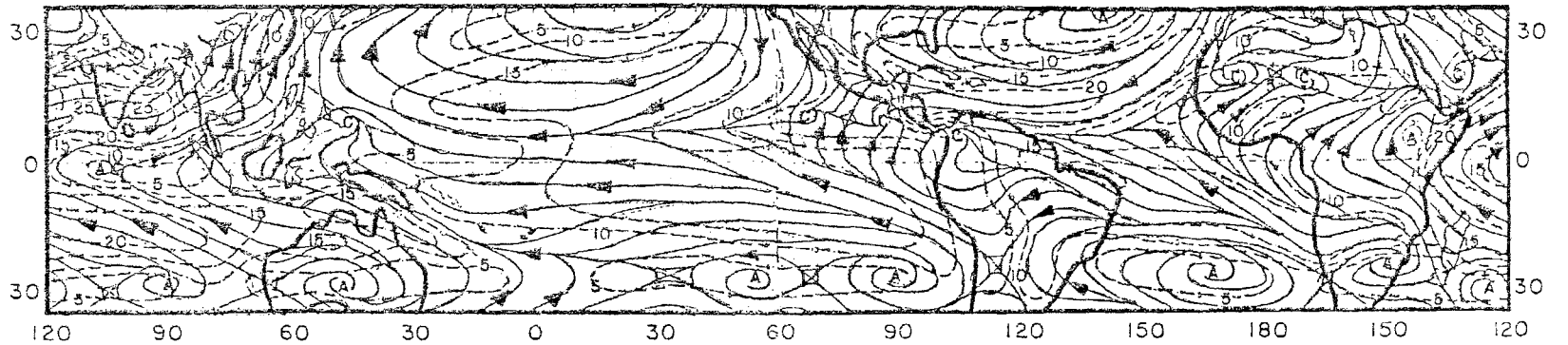


Figure 2.2 - Resultant gradient-level wind for July (from AWSTR 215 |45|)

- (iii) The southeast and northeast trade wind systems
- (iv) The Asian monsoon flows of the summer and winter seasons
- (v) The monsoon trough of the summer season
- (vi) The heat lows over the deserts
- (vii) The cross-equatorial flow over the Indian Ocean - Arabian Sea during northern summer. The intensity of this flow attains values close to 35 knots in the mean
- (viii) The slightly stronger intensity of the trades over the winter hemisphere (Krishnamurti *et al.*, 1975)
- (ix) A strong zonal asymmetry in the location of the vortices and stream-line convergence zones (near the ITCZ) over the oceanic and land areas. This is quite pronounced during the northern summer. During the northern winter this zone remains north of the Equator over the Atlantic and the eastern Pacific Ocean; elsewhere it is located south of the Equator. During the northern summer this zone is north of the Equator everywhere reaching as far as 25°N over northern India.

All of these features exhibit seasonal changes. The various atlases mentioned in Table 2.1 provide more complete information.

2.3 The motion field in the upper troposphere

The depiction of the mean motion field at 200 mb has received far more attention in recent years because of the availability of high level cloud motion vectors and commercial aircraft wind reports.

Figures 2.3 and 2.4 illustrate two typical winter and summer maps respectively over the global tropical belt. The salient features of the winter season (Krishnamurti, 1961; Sadler, 1965) are summarized in the following paragraphs.

The subtropical westerly jet stream exhibits a quasi-stationary 3-wave pattern with maximum velocity off the southeastern United States, the Mediterranean Sea and the coast of Japan. The strongest winds are found in the latter region. The quasi-stationary geometry of the wind-speed field is an unexplained phenomenon. Although there is some evidence of its relation to intense convection over three continental regions of the equatorial tropics, i.e. the northwestern part of South America, central Africa and the Indonesia/ Borneo area, these relationships have not been adequately exploited. The latitude of the subtropical jet streams during the northern winter is roughly 27°N (Krishnamurti, 1961). During this period the flows over the southern tropical oceans, at 200 mb, exhibit mid-oceanic troughs in the motion field. These troughs are found in the middle of the Atlantic and in the Indian and the Pacific Oceans (Krishnamurti *et al.*, 1973). These are quasi-stationary troughs and their analogous counterparts are found over the northern tropical oceans during the northern summer, see Figure 2.4. The zonal asymmetry of the 200 mb flows during the northern summer has been discussed at some length in the literature (Krishnamurti, 1971a, 1971b, Krishnamurti *et al.*, 1973, 1974). The salient climatological features of these flows are: The Tibetan and West African high pressure areas, the mid-Pacific trough, the mid-Atlantic trough, the tropical easterly jet over Asia and equatorial Africa, and the Mexican high. We shall discuss some dynamical aspects of these features in another section.

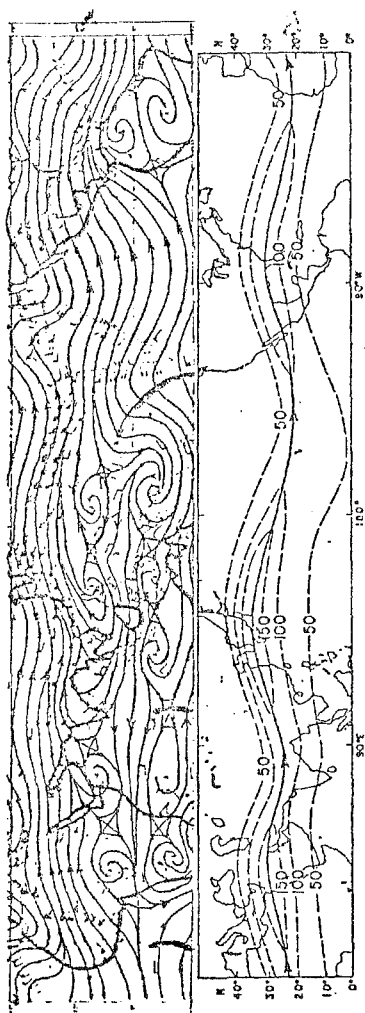


Figure 2.3 - (top) An example of 200 mb daily chart streamlines. Northern winter. (bottom) Winter mean isotachs, 200 mb

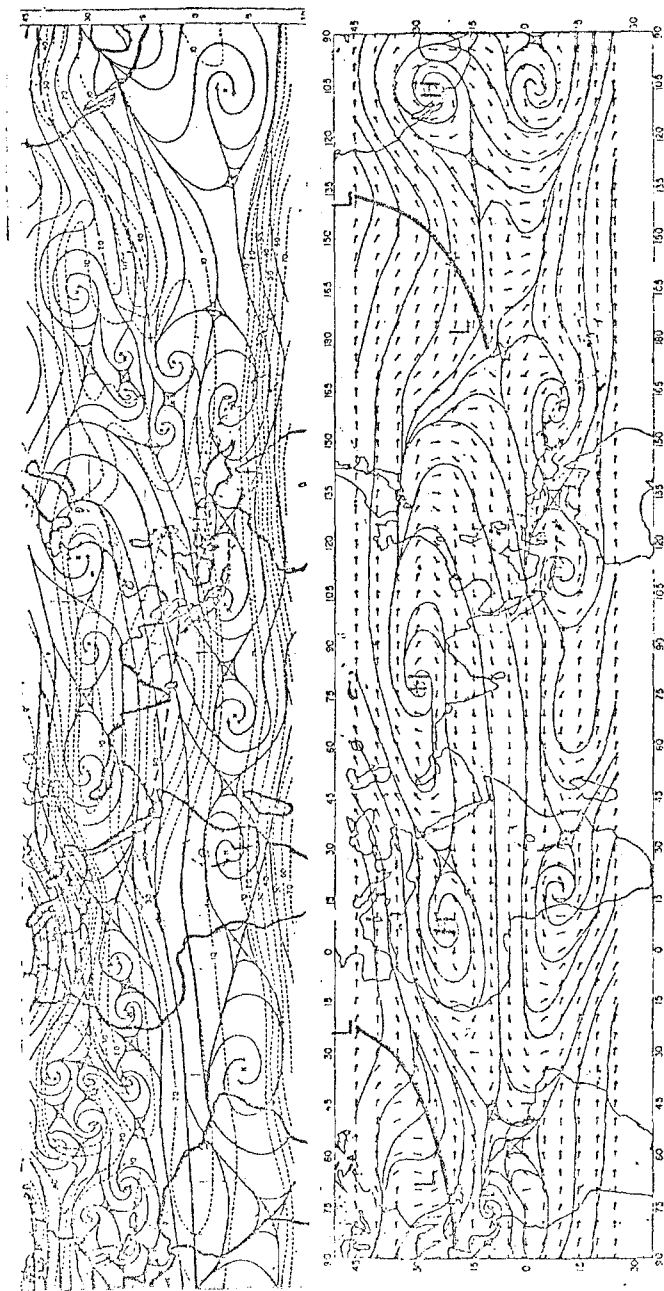


Figure 2.4 - (top) An example of 200 mb chart. Northern summer. (bottom) Summer mean flows, 200 mb

These large amplitude features of the time-averaged motion field carry about 50 per cent of the total variance of the total horizontal motion field. Thus one would see most of the above-mentioned features on daily upper-level maps during the northern summer (Krishnamurti *et al.*, 1970, 1975). As stated earlier, it is important to appreciate and obtain a good understanding of the time-averaged large-scale zonal asymmetry of the flows.

2.4 The temperature field

The most conspicuous aspect of the thermal field is the zonal asymmetry evidently related to the land-ocean distributions. Over the summer hemisphere the air over the land areas is much warmer than that over the oceanic tropics, the converse being the case over the winter hemisphere. The most pronounced zonal asymmetry is found near the Earth's surface and near the 300 mb surface. The former is related to the sensible heat flux from the land areas and the latter to deep convective and subsidence warming. Because of the large heat capacity of the oceans, the seasonal change of temperature over the oceans is small whereas the seasonal change in the temperature of the Earth's surface is very large. This is reflected strongly in the air temperature. Reference should be made to Table 2.1 for regional and global details of the thermal field. Figures 2.5 and 2.6 show the temperature distribution at 300 mb for the winter and summer seasons. The most pronounced zonal asymmetry occurs during the northern summer (Figure 2.6) and is due primarily to the influence of the elevated Asian land mass. The highest temperatures are found over the Tibetan Plateau. The 200 mb anticyclones (Figure 2.4) over Tibet, West Africa and Mexico are warm while the mid-oceanic troughs are cold. During the northern winter, the thermal field at 300 mb shows relatively smaller temperatures over the land areas of the northern hemisphere (Figure 2.5) while the oceanic areas are somewhat warmer. During this period the middle oceanic troughs (Figure 2.3) over the southern oceans are colder and the anticyclonic circulations near the land areas of the southern hemisphere are relatively warm. It should be noted that the amplitude of the zonal asymmetry decreases rapidly with height and that the phase reverses above the tropical tropopause, the troughs becoming warm and the ridges becoming cold in the lower stratosphere. An interesting illustration of the zonal asymmetry of the thermal field was presented by Flohn (1968). This is illustrated here in Figure 2.7. This diagram shows a vertical structure of the temperature anomaly field at 32°N where the zonal average is removed from the temperature distribution at each pressure level. The high temperature region over the Tibetan Plateau and relatively colder regions over the oceanic tropics are clearly evident. These time-averaged zonal asymmetries should be viewed along with the geometry of the divergent east-west circulation (presented in the next section) since they have important dynamical implications. The temperature observations over the global tropical belt are still far from what is desirable to describe large-scale weather systems. During 1978-79 we expect to see the first global tropical data collection during the First GARP Global Experiment (FGGE).

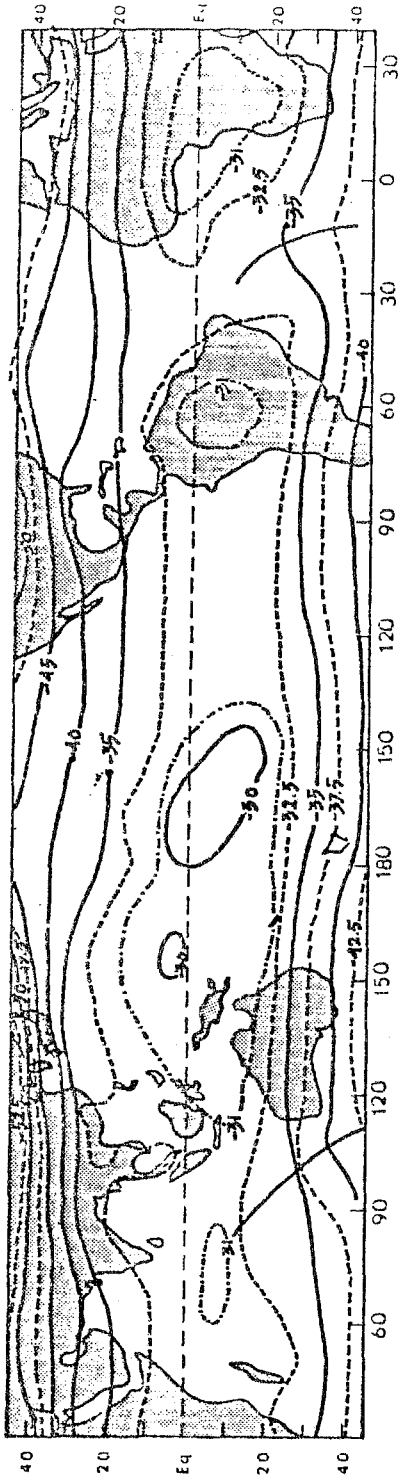


Figure 2.5 - Mean temperature at 300 mb, Dec., Jan., Feb.

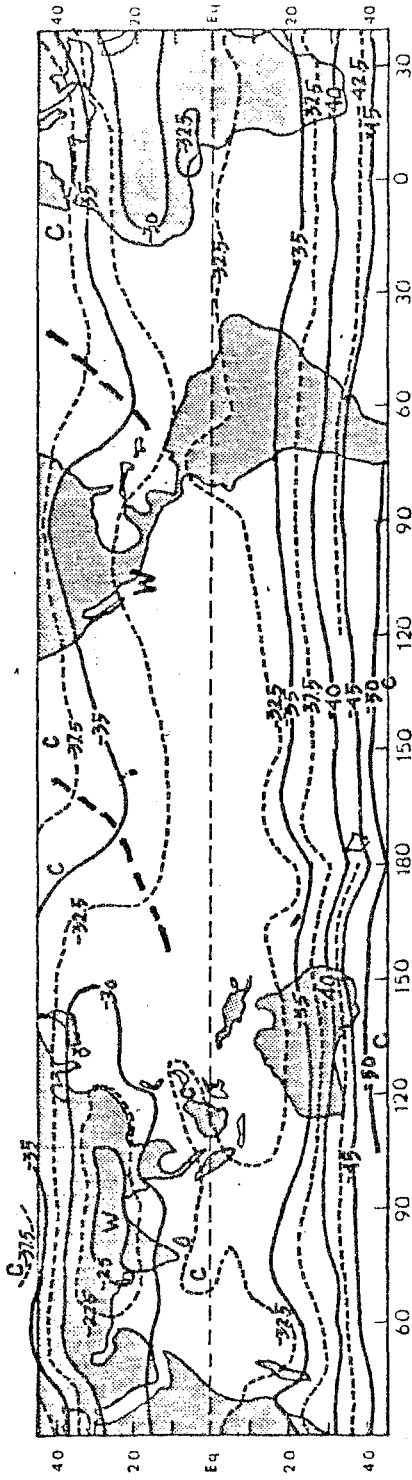


Figure 2.6 - Mean temperature at 300 mb, June, July, August

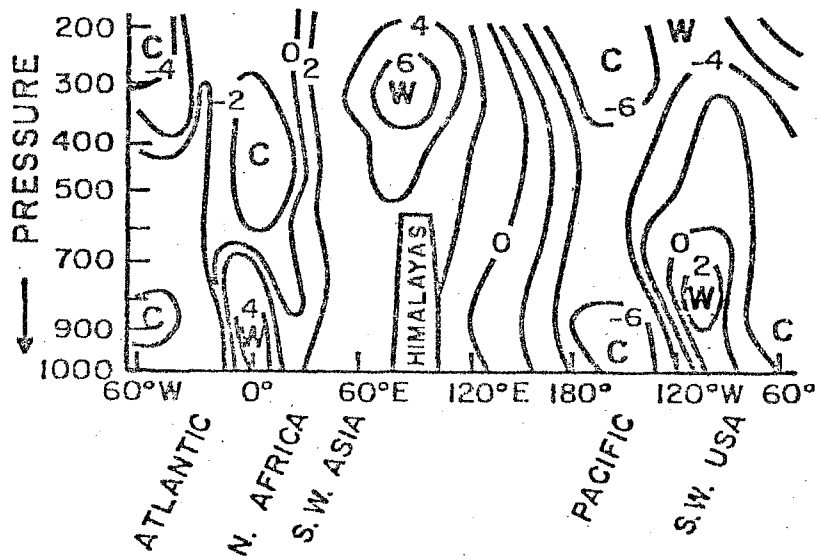


Figure 2.7 – July temperature anomalies along 32°N (Flohn)

Positive anomalies in the upper troposphere between 30°E and 130°E; monsoon region.
 Positive temperature anomalies (>0°C) over Tibet near 300 mb.
 Low-level positive anomalies over Africa and western North America.
 Oceanic negative anomaly centres.

2.5 East/west circulations in the tropics

The time-averaged east/west circulations are essentially divergent motions and are quite analogous to the Hadley type vertical overturnings described in Chapter 1.

Here we decompose a horizontal velocity vector \vec{V} into the rotational part \vec{V}_Ψ and a divergent part \vec{V}_χ i.e.:

$$\vec{V} = \vec{V}_\Psi + \vec{V}_\chi \tag{2.1}$$

A time mean velocity potential $\bar{\chi}$ is defined by:

$$\vec{V}_\chi = - \nabla \bar{\chi} \tag{2.2}$$

We define the intensity of the Hadley and east/west circulations by the respective relations:

$$I_H = -\frac{1}{L} \oint \frac{\partial \bar{\chi}}{\partial y} dx \quad (2.3)$$

$$I_E = -\frac{1}{(y_2 - y_1)} \int_{y_1}^{y_2} \frac{\partial \bar{\chi}}{\partial x} dy \quad (2.4)$$

where L is the length of a latitude circle and y_1 and y_2 are the southern and northern limits of a tropical channel of interest. Note that I_H varies along y , while I_E varies along x . A proper geometrical depiction of the Hadley cell can be presented on a meridional vertical plane while that for the east/west cell would be a zonal plane. The velocity potential χ for a seasonal mean is obtained from a solution of the equation:

$$\nabla^2 \bar{\chi} = -\nabla \cdot \vec{V} \quad (2.5)$$

where \vec{V} is a seasonal mean horizontal velocity vector and is assumed to be known. In this study there are no east/west boundaries as the latitude band of interest encompasses the globe, and $\bar{\chi}$ is set to zero at the north and south boundaries.

It is important to recognize that most of the variance (about 80 per cent) of the motion field is described by the rotational part (Krishnamurti, 1971a). However all circulations in vertical planes such as the Hadley and east/west type circulations are divergent circulations and are not explicitly described by the rotational part of the wind. These divergent circulations are extremely important for the understanding of the time-averaged motion field. In the following section we present a framework of dynamical equations that may be useful for studies of the time-averaged motions.

The geometry of the velocity potential $\bar{\chi}$ and typical streamlines of the divergent part of the motion field are illustrated in Figures 2.8 and 2.9 for the summer and winter seasons, respectively. These are based on 3-month averages for a particular year at the 200 mb surface. As stated earlier, one could portray such fields at many vertical levels and for many different seasons. Furthermore, one could examine the interannual variability of the functions. It is quite clear from Figures 2.8, 2.9 that the divergent circulations are present in the zonal as well as the meridional planes. The major centre of the east/west circulations during the northern summer is found on the northern part of the Bay of Bengal. This centre shifts towards Indonesia-Borneo during the northern winter season. The streamlines of the divergent part of the flows converge to the mid-oceanic troughs in these two examples for the summer and winter seasons. During the northern summer the divergent outflow regions are the region of the Asian summer monsoons and the Pacific coast of southern Mexico, while for the northern winter season there are three such regions; the northwestern part of South America, central Africa and Indonesia. These three regions of high-level divergent outflow coincide roughly with the three intense rainfall belts during the northern winter. This geometry may have some important bearing on the three waves of

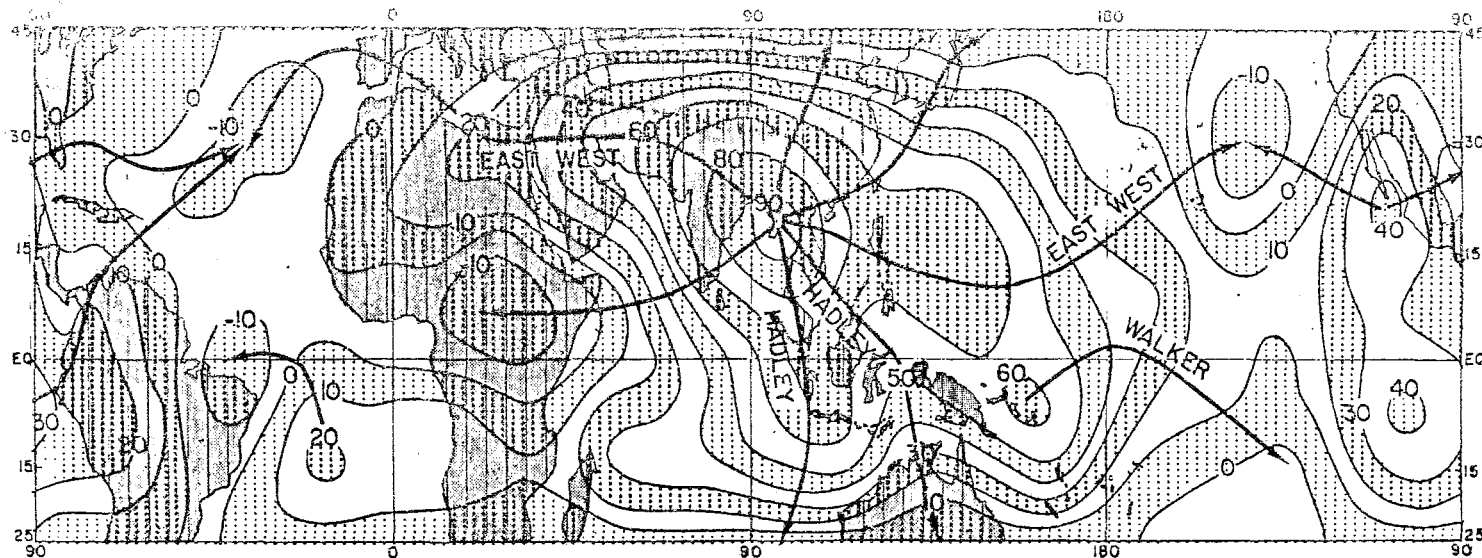


Figure 2.8 - Isopleths of velocity potential $\times 10^5 \text{ m s}^{-1}$ and streamlines of the divergent part of the wind. Northern summer, June, July, August 1967

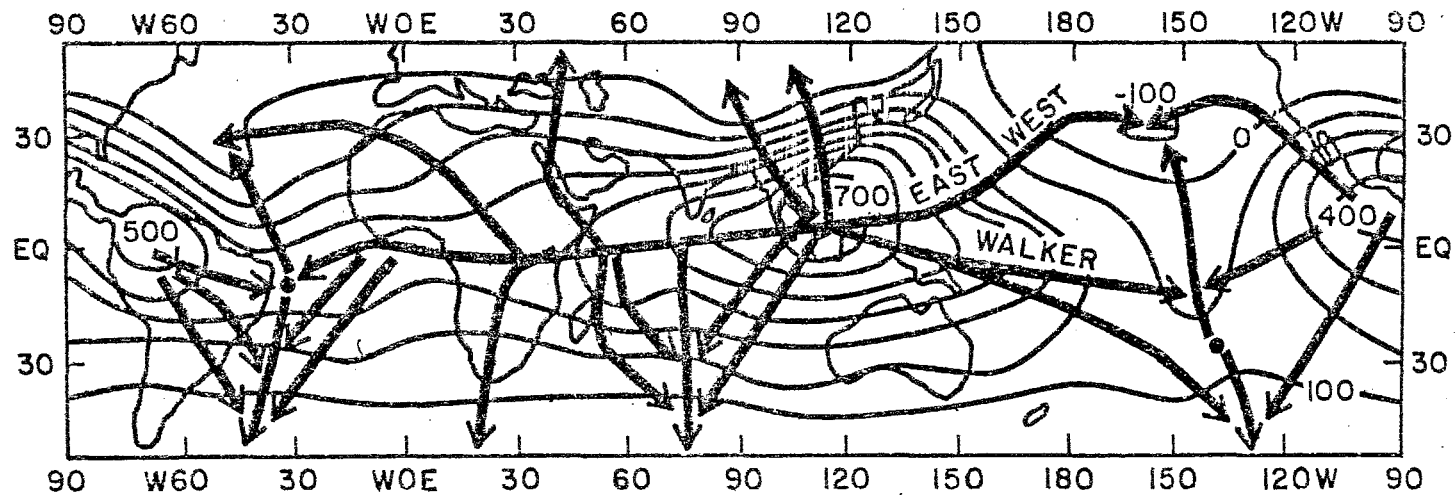


Figure 2.9 - Isopleths of velocity potential $\times 10^4 \text{ m s}^{-1}$ and streamlines of the divergent part of the wind. Northern winter, January, February, March 1969

the quasi-stationary subtropical jet stream of winter, discussed earlier. A proper numerical simulation of the subtropical jet streams during winter should take into consideration these rainfall belts, the southern ocean troughs and the geometry of the east/west and Hadley type vertical overturnings. We shall discuss this aspect further in our discussions of the dynamics of these jet streams. Figure 2.10 shows a schematic vertical section of these vertical circulations for the summer and the winter seasons. The vertical cells are time-averaged east-west circulations, somewhat analogous to the geometry of the Hadley, Ferrel and Polar cells frequently portrayed to depict the circulations in north/south planes. Furthermore, it should be noted that these are thermally direct circulations (see Figure 2.7 from Flohn's study of the thermal field). As a consequence, these vertical circulations are capable of generating eddy kinetic energy on the scales of these circulations. It is felt that tropical planetary scale quasi-stationary waves acquire kinetic energy by this process.

2.6 The moisture field

This is by far the most important scalar field in the tropics. The distribution of the moisture, although to a large extent dynamically controlled, still determines the evolution of many smaller scale disturbances. The presence of desert and oceanic areas makes this field zonally asymmetric. The climatology of the moisture field is very important for the general circulation of the atmosphere. Observational inadequacies make it difficult to obtain any very reliable sources of references in this area. The data sources that will become available during 1979 from the First GARP Global Experiment are expected to be the most reliable for a description of the global moisture field. Scientists have asked how important the definition of the detailed moisture field is. Some feel that a simple zonally-symmetric geometry of the moisture field would adjust to a reasonable geometry in a matter of a few days of numerical integration in global general circulation models. This was, in fact, demonstrated by Mintz in some early runs with a two-level general circulation model. It seems from these studies that the spatial distribution of the time-averaged planetary scale moisture distribution can be explained from simple formulations of sources and sinks and a reasonable simulation of the advection. However, the assumption that the moisture variable is passive and its details somewhat dynamically redundant, could be a disastrous one for studying the short range evolution of tropical weather systems. We shall discuss this further in later sections. It is felt that the climatology of the global moisture is an important study and hence we present here, in Figures 2.11 and 2.12, two moisture fields for January and July at 850 mb, i.e. the isopleths of specific humidity (g kg^{-1} units). During the northern winter, three regions of large specific humidity (12 g kg^{-1}) over the northwestern part of South America, equatorial Africa and over Indonesia may be noted. These regions were earlier emphasized in the discussion of the northern winter east/west circulation and tropical rainfall belts. During the northern summer the regions of high moisture are found over the monsoon belts near the foothills of the Himalayas (14 g kg^{-1}) and over the equatorial eastern Pacific, again closely related to the location of the divergent out-flows shown in Figure 2.9. Large zonal asymmetries are found during the northern summer near 20°N . Because of the dynamical influences of the motion systems, the specific humidity distribution over the tropical oceans is not uniform. Gradients in the east/west and north/south directions over the oceans are primarily associated with weather systems with ascending and descending motions. The seasonal

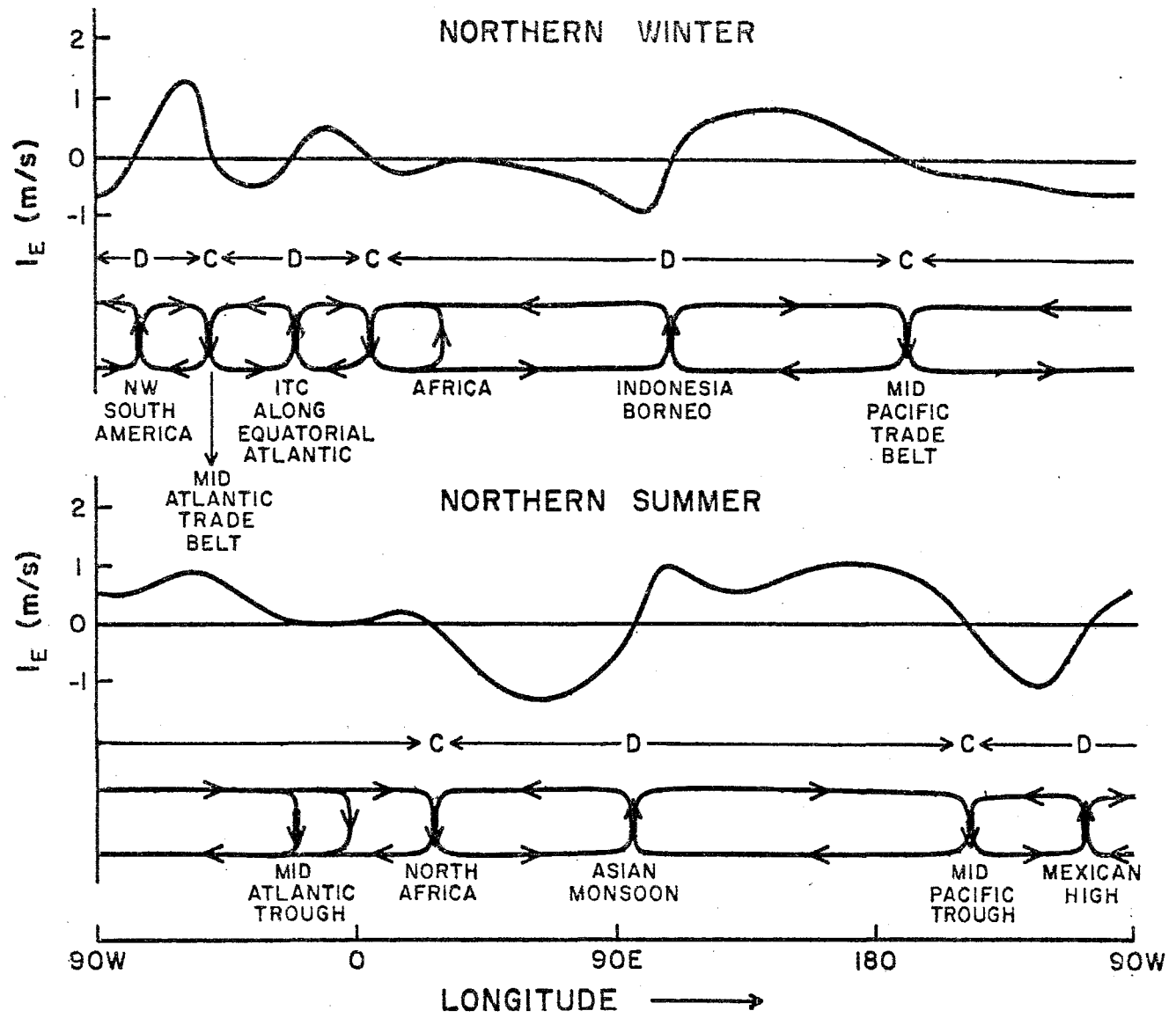


Figure 2.10 - Intensity I_E of the east/west circulation during the northern winter and northern summer, and a schematic outline of the vertical circulation cells in the east/west vertical plane

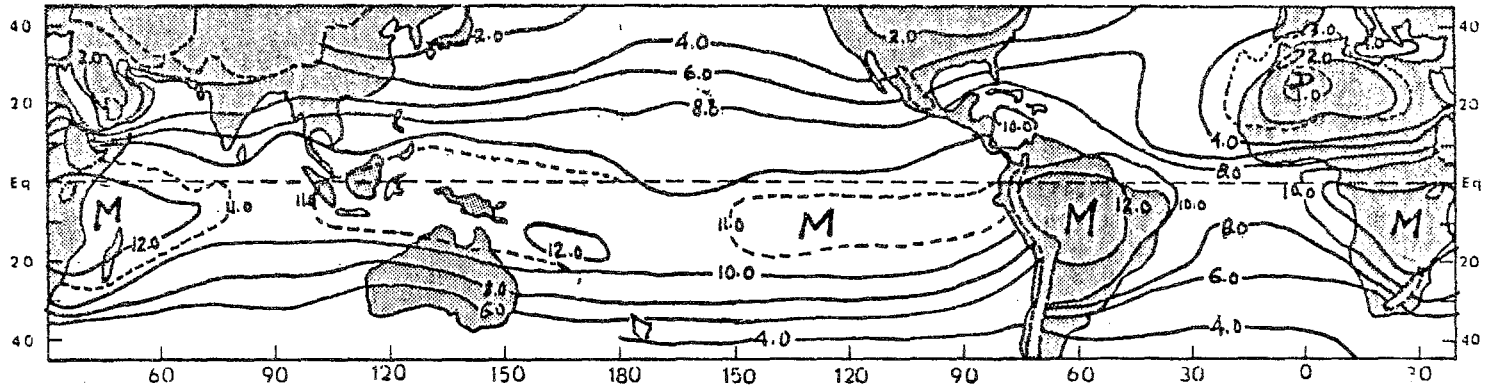


Figure 2.11 - Specific humidity at 850 mb (g kg^{-1}) January

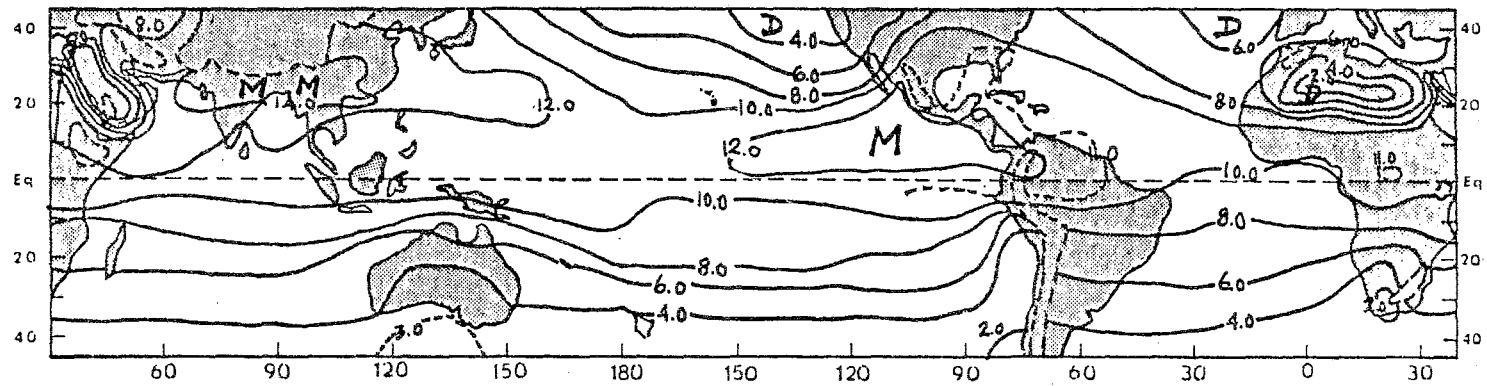


Figure 2.12 - Specific humidity at 850 mb (g kg^{-1}) July

changes in the distribution of specific humidity are large. The largest values of specific humidity are found over the land areas and not over the oceanic tropics. This is related to larger temperatures of land areas which can hold large amounts of moisture prior to saturation, the monsoon belts being the moistest in this sense.

2.7 Sea-level pressure

Here we shall present sea-level isobars for January and July (see Figures 2.13, 2.14 from the Atlas of Crutcher and Davies, 1969). The January features are dominated by the strong pressure gradient near 100°W over Asia, i.e. south of the Siberian surface anticyclone. The subtropical highs are better organized over the northern oceans during the northern summer and less so during the northern winter. The descending branch of the Hadley Cell is more intense near 30°N during northern winter compared to the northern summer (Figure 1.2). The subtropical highs have intense descending motion towards the eastern part of the anticyclonic circulations. The descent is in part contributed by the east/west circulations of the northern summer (Figures 2.8 and 2.9), which would account for the intensity of the subtropical high during the northern summer. The equatorial trough (low pressure belt near the Equator) is found as far as 20°N during the summer monsoon season over the Asiatic land mass. The pressure field has frequently been described in meteorological literature. It should, of course, be said that the various references show some differences in the distribution of pressure for the same month for different years. The zonal asymmetries of the pressure field are consistent with the asymmetries of the other time-averaged fields discussed in the previous sections.

2.8 Other parameters

The tropical climatologist should have a ready source of reference on the zonal asymmetries of several other observed and derived variables that cannot be easily presented in this kind of text. Among these, one of the most important fields is that of sea-surface temperature. One of the best sources of reference on this is a new data set compiled by the Rand Corporation in Santa Monica, California (Alexander and Mobley, 1974). This compilation contains a global ocean temperature distribution for a one degree latitude by one degree longitude mesh of grid points. Values of monthly averages for all twelve months are available.

The following is a list of some other useful parameters:

- (i) Height of base and of the top of the trade wind inversion (Riehl, 1945, Neiburger and Chien, 1957)
- (ii) Monthly mean cloud amounts (Sadler, 1970)
- (iii) Satellite digital cloud brightness charts (Taylor and Winston, 1968)
- (iv) Orography, mountain heights (Gates, 1973)
- (v) Albedo of the Earth's surface (Katayama, 1967a)
- (vi) Tropical monthly rainfall (Wernstedt, 1972)
- (vii) Monthly mean total solar radiation reaching the Earth's surface (Katayama, 1966, 1967a, b)

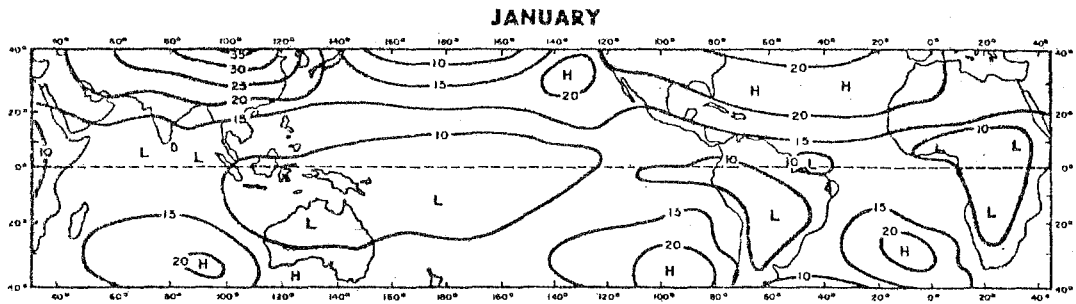


Figure 2.13 - Mean sea-level pressure in millibars (after Crutcher and Davis)

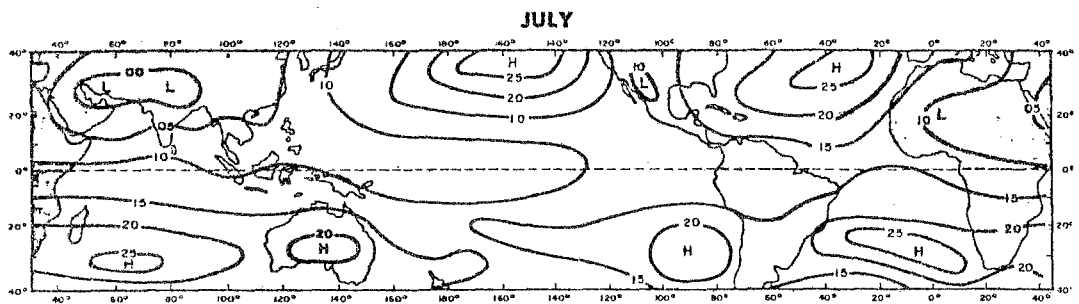


Figure 2.14 - Mean sea-level pressure in millibars (after Crutcher and Davis)

- (viii) Net outgoing longwave radiation (Winston, 1967)
- (ix) Monthly mean net solar radiation absorbed by the troposphere (Katayama, 1966, 1967a,b).

There are, furthermore, charts of dynamical parameters such as energy, momentum and moisture transports and fields of convergence of fluxes, etc.; these again exhibit large zonal asymmetries in the tropical atmosphere. We shall refer to these in the discussions of transient motions of the atmosphere.

Chapter 3

A SURVEY OF TROPICAL DISTURBANCES

3.1 Introduction

In the previous two chapters we have considered the time-averaged climatology of the tropics. The transient motions in the tropics occur on a wide range of scales from cumulus clouds and sea-breeze phenomena to planetary waves and transient Hadley cells. There have been two approaches to the study of tropical transient disturbances. The first of these consists of the classical synoptic analysis techniques developed by Palmer, Sadler and others. In these, one portrays the two-dimensional analysis of scalar and vector fields for several map times and at several vertical levels of the atmosphere. Aids such as vertical cross-sections, time sections, satellite photographs, past history and dynamic redundancy usually play an important role in such analyses. The second approach uses a space-time filter to isolate dominant disturbances, e.g., up to 1000 km and 3 to 5 day time scales.

Streamline-isotach analysis is a very useful aid in the identification of tropical disturbances. The analysis of the temperature field is not always an easy task, but it should be carried out whenever possible. The thermal amplitude of synoptic scale disturbances is generally large ($> 1^{\circ}\text{C}$) over land-area tropics, and in the upper troposphere over most of the tropics. Sea-level pressure is also a desirable field to analyse and this should also be attempted, especially for land-area disturbances. The field of relative humidity is important for defining the moisture distribution in synoptic scale disturbances. This should be analysed first at the surface and then at 850 and 700 mb. The use of microwave radiometric information from polar orbiting satellites can be useful in providing a vertical constraint on such analyses, i.e., the field of total precipitable water. However, its availability in operational time is virtually non-existent in most developing countries.

The tropical analyst should also have access to the monthly mean climatology for his region. This should include detailed maps of most of the fields discussed above.

Far more important than any of the above are satellite images. In order to follow the life cycle and passage of tropical disturbances effectively, a ground station with picture receiving capability is essential. Pictures from satellites, with day and night imagery (visible and infra-red) are received by a number of developing countries.

Other analysis aids include construction of time sections and vertical cross-sections. The availability of information from radar sets at airports and at weather services is also extremely useful for tropical analysis. Many disturbance lines are essentially meso-scale and it is not always possible to locate these in operational practice without the aid of radar imagery.

The disturbances of the so-called "synoptic scale"⁰ have their maximum intensity in the lower, middle or upper troposphere. A variety of tropical disturbances is usually found in different parts of the world. Figure 3.1 lists some salient tropical transient phenomena of the lower troposphere. In this list there are a number of westward propagating wave disturbances whose vertical structure is not quite the same in different regions. This category includes the near equatorial ITCZ waves which can be seen over the entire tropical oceanic belt. There are tropical oceanic depressions, monsoon depressions, easterly waves, equatorial waves, African waves, and monsoon cyclones among the major disturbances. There are also some other phenomena such as the low level jet and trade inversions. These latter are very important. A separate discussion of hurricanes and typhoons is presented later.

3.2 Some selected disturbances

We shall next review some observational aspects of certain wave type disturbances. Figure 3.2 shows the structure of the surrounding (environmental) zonal wind where such disturbances have been observed. The season is northern summer and the latitudinal belt is between 5°N and 25°N. In the Caribbean, there are low level easterlies and high level westerlies (during the early summer season). The depth of the monsoon westerlies increases from Africa to India and decreases east of that. In most of this part of the global belt, easterlies increase with height in the upper troposphere. Farther to the east over the central Pacific, the lower tropospheric monsoon westerlies are absent and easterlies increase somewhat with height in the middle troposphere.

Figure 3.3 illustrates the vertical structure of some typical disturbances that are found in these five regions. The abscissa in these drawings is a west/east co-ordinate. These are based on synoptic studies of Baumhefner (1968), Pedgley and Krishnamurti (1976), Krishnamurti et al., (1975) and Reed and Recker (1971). The last two are based on composite methods. In these, the approximate horizontal scales of the disturbances are as follows:

Caribbean Easterly Wave	1000 km
African Monsoon Cyclone	2000 km
Monsoon Depression	2000 km
Western Pacific ITCZ Wave	2000 km
Central Pacific ITCZ Wave	2000 km

It should be noted that a wide range of scales can be found in observations and the true appreciation of these can be obtained by examination of daily weather maps at different regional meteorological forecast centres. All of these disturbances are known to propagate westward at a speed of roughly 5° to 7° longitude per day. We shall comment further on this later.

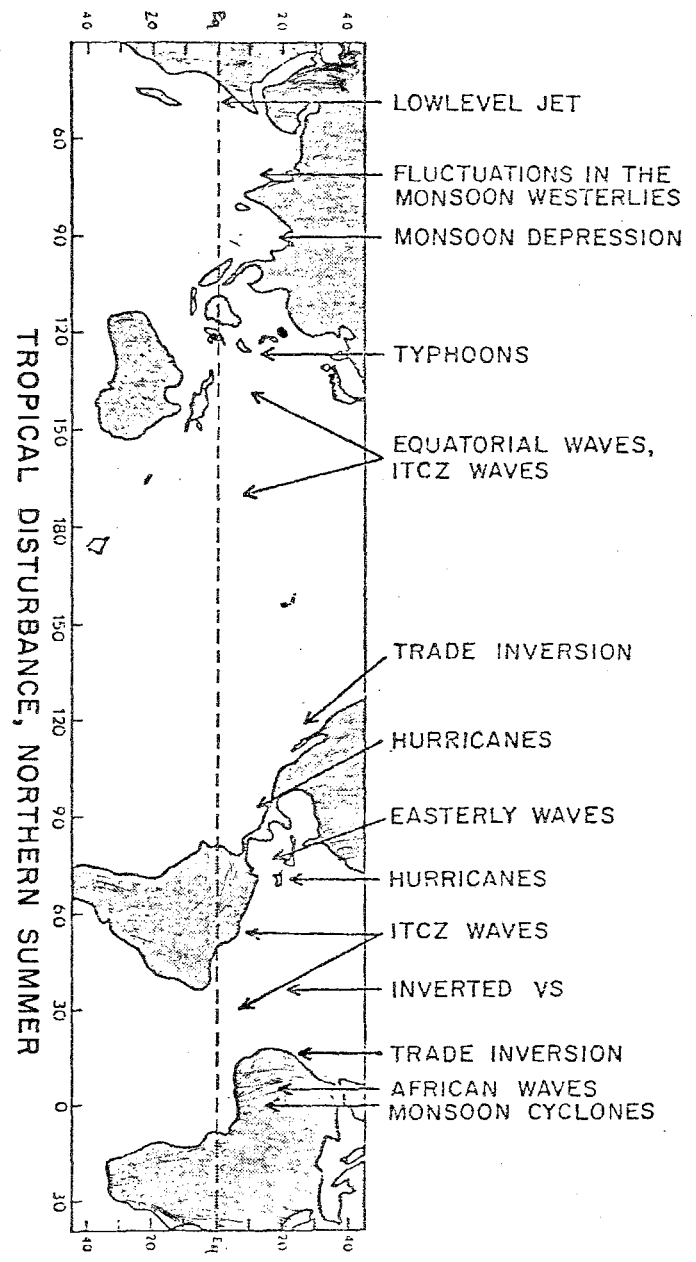


Figure 3.1

ENVIRONMENTAL ZONAL WIND AS A FUNCTION OF HEIGHT

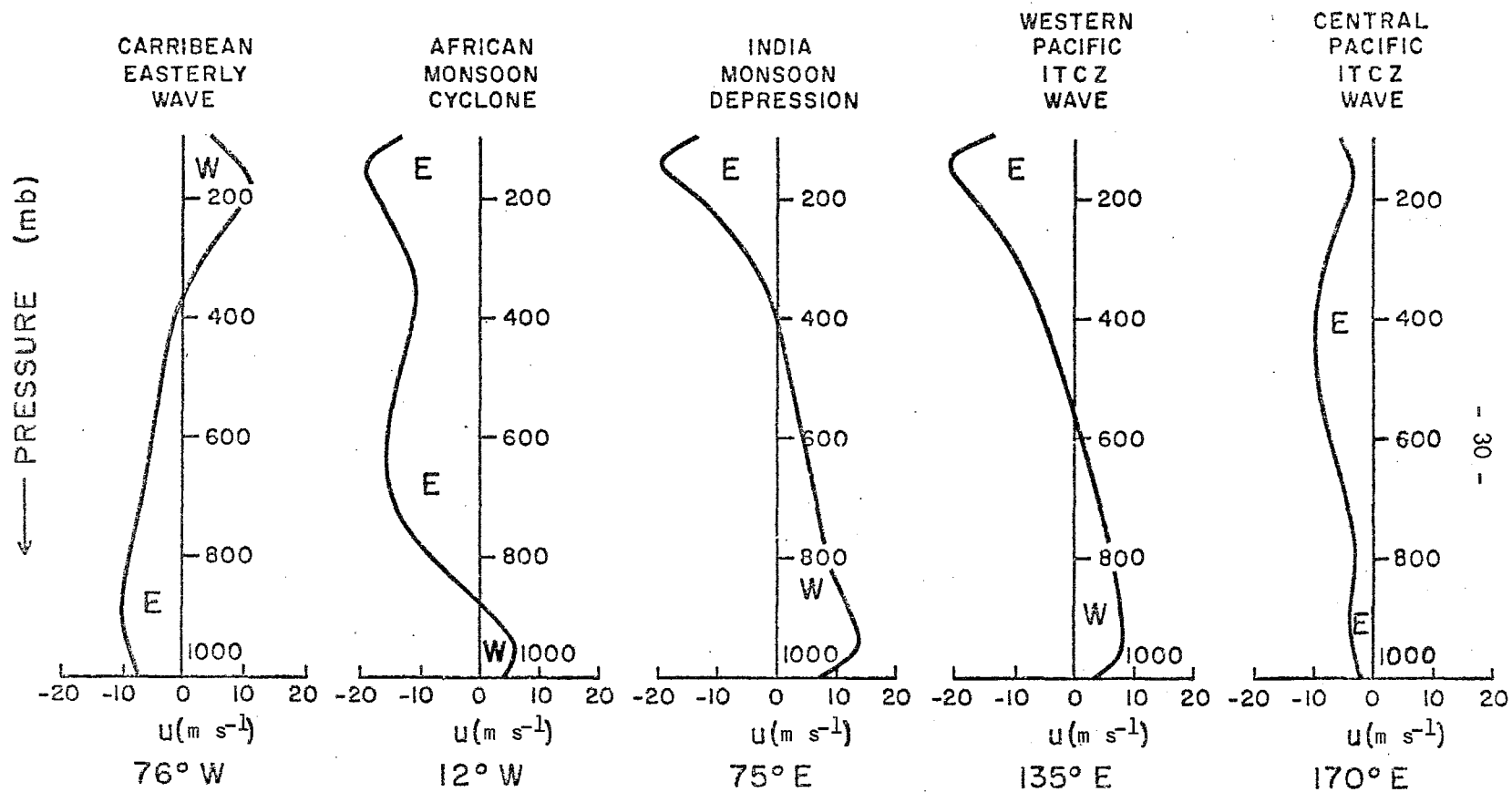


Figure 3.2

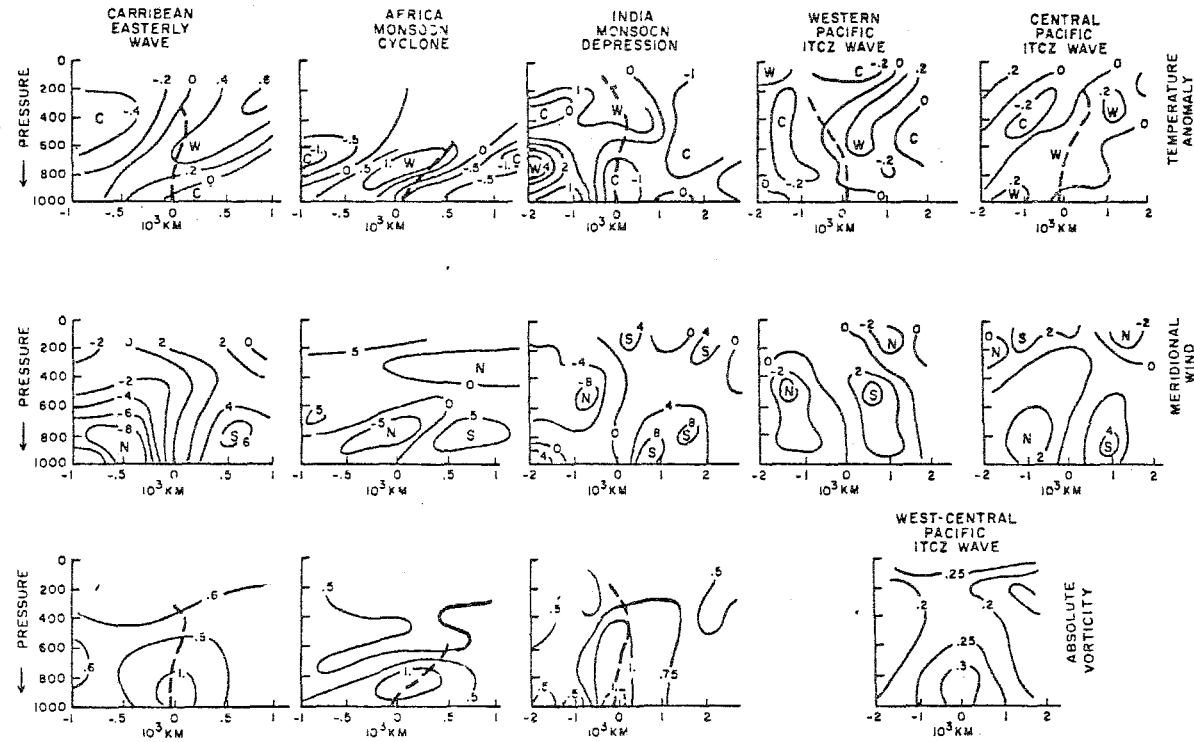


Figure 3.3 - Vertical structure of selected tropical disturbances. Top: Temperature anomaly ($^{\circ}\text{C}$); Middle: Meridional wind (m s^{-1}); Bottom: Absolute vorticity (10^{-4} s^{-1})

The three panels in the vertical (Figure 3.3) show respectively the following:

Top: Temperature anomaly ($^{\circ}\text{C}$)
Middle: Meridional wind (m s^{-1})
Bottom: Absolute vorticity (10^{-4} s^{-1})

We note significant differences in the structure of these disturbances. The thermal amplitude of the oceanic disturbances is small (about 1°C) compared to the land area monsoon disturbances (2° to 3°C). The West African monsoon cyclone is a shallow disturbance and above 500 mb the thermal field does not seem to have much definition. The Indian monsoon depression does seem to have a well-defined cold core in the lower troposphere and a warm core in the upper troposphere. The thermal structure of the oceanic disturbance shows a very weak cold core near the sea surface in the sub-cloud layer below 900 mb. The meridional wind structure is usually quite variable in these disturbances, and the amplitude in most instances lies between 4 and 8 m s^{-1} . Except for the West African monsoon cyclone, the wave structure of most of these disturbances seems to extend up to 400 mb. The vorticity isopleths of the lower panel show a gradual decrease of cyclonic vorticity with height for the Caribbean easterly wave. The West African monsoon cyclone has negligible cyclonic vorticity above 600 mb. The Indian monsoon depression extends all the way up to 300 mb, and the west central Pacific composite ITCZ waves have an anticyclonic circulation in the upper troposphere. However, the magnitudes are extremely small in the Pacific ITCZ waves. This may be a consequence of the compositing procedure of many individual waves. The intensity of these five disturbances can also be viewed from the point of rainfall rates. In these examples the observed rainfall rates were as follows:

Caribbean waves	2.5 cm day^{-1}
West African monsoon cyclone	2 cm day^{-1}
Indian monsoon depression	20 cm day^{-1}
Pacific ITCZ waves	2 cm day^{-1}

The land area monsoon depressions (and also oceanic tropical depressions) are the more vigorous disturbances. They come next in class to hurricanes and typhoons in their rainfall intensities. The structure of the oceanic tropical depression is not illustrated here. They usually form in the tropical oceans from waves and vortices in shearing currents in the region of the intertropical convergence zone.

The life cycle of these disturbances is roughly 3 to 6 days. Wind observations suggest that the frequency of the disturbances is roughly one in about five days, except for the land area monsoon depressions, which are found to occur one in roughly two weeks during the monsoon months.

The dynamics of these disturbances are not too well understood. Selected case studies suggest the following barotropic energy exchanges:

Caribbean region	Barotropically stable, energy exchange primarily from eddies to zonal (Krishnamurti <i>et al.</i> , 1973, Tripoli and Krishnamurti, 1975)
------------------	---

West Africa	Barotropically unstable (Tripoli and Krishnamurti, 1975, Burpee, 1972, Reed <u>et al.</u> , 1977)
Monsoon depression	Weakly barotropically unstable (Krishnamurti <u>et al.</u> , 1975)
Western Pacific	Barotropically unstable (Nitta and Yanai, 1969).

The information presented above is based on a number of regional studies utilizing the lower tropospheric data. Not much information is available on the generation of eddy kinetic energy from eddy available potential energy. There is, however, reason to believe that cumulus convection would generate substantial amounts of eddy available potential energy in these rain producing systems and hence might be an important source of eddy kinetic energy. In order to carry out detailed observational energetics experiments one would need observations on the mesoscale where the rain producing disturbances may have large energy conversions. Except for a few field experiments, such as BOMEX, GATE and ATEX, such observations are simply not available. Much of these data sets remain to be analysed in this context. Next we shall make some remarks on the westward motion of these disturbances.

3.3 Westward motion of the tropical disturbances

As stated earlier, tropical disturbances all seem to propagate westward with a speed of roughly 5° to 7° longitude per day. As shown in Figure 3.1, the basic zonal current in the lower troposphere is quite asymmetric in the zonal direction. It turns out that this is an important feature for some aspects of the dynamics of these systems.

Studies of the Caribbean easterly waves suggest that their westward motion may be primarily dominated by barotropic dynamics, i.e. to the west of the trough line $\frac{\partial \zeta}{\partial t} > 0$ because of the beta effect and the advection of cyclonic relative vorticity. The divergence term of the vorticity equation has the opposite effect since convergence and upward motion are found east of the trough line in this case.

In the case of West African disturbances, their westward motion may be described by quasi-geostrophic physics. In this situation advection of the warm dry desert air gives rise to substantial ascent and convergence west of the trough line. The westward motion is found to be, in some cases, primarily due to the beta effect and the convergence term. The relative vorticity advection at low levels tends to be negative west of the trough line and it has an opposite effect.

The westward motion of the monsoon depression is a complex problem. The depression moves westwards in a broadscale southwesterly current. Some recent studies on the westward motion of a depression suggest that the barotropic and quasi-geostrophic dynamics are found to be inadequate to describe its westward motion. We shall discuss this in some detail in the section on monsoon disturbances. We note here that the influence of mountains and the convergence associated with the monsoon cloud clusters all have a significant influence on the westward motion of the disturbance. The student of synoptic meteorology should recall the following equations for the phase speed of Rossby waves and divergent waves respectively:

$$C = U - \frac{\beta L^2}{4\pi^2} \tag{3.1}$$

$$C = U - \frac{\frac{\beta L^2}{4\pi^2} + \eta_1 + \eta_2 \frac{\partial D}{\partial x}}{1 + \eta_3 + \eta_4 \frac{\partial D}{\partial x}}$$

The latter formula is due to Petterssen (1956) where η_1 , η_2 , η_3 , and η_4 are functions of the zonal velocity, the width of the current, the curvature of flow and the latitude. In a westerly trough $\eta_2 > 0$, and the effect of convergence (D stands for divergence) ahead of the trough is to speed up the motion of the trough. This formula is useful for investigating the influence of convergence and divergence on the phase speed of wave disturbances. In the tropics westward propagating disturbances would speed up if low level convergence occurs ahead of (i.e. west of) the trough line. In this situation

$$U < 0, \quad -\frac{\beta L^2}{4\pi^2} < 0, \quad \eta_2 \frac{\partial D}{\partial x} < 0$$

The denominator is positive since η_3 and η_4 are positive and $\ll 1$. Hence $c < 0$ and the divergence term $\eta_2 \frac{\partial D}{\partial x}$ contributes to a faster westward propagation. One should ask in a given situation which factors contribute to the magnitude of divergence D. Many factors such as quasi-geostrophic physics, mountains, and convection need to be examined to determine their influence on the divergence distributions. Tropical disturbances usually tend to set off local east/west overturnings on the scale of the disturbance. This overturning is accompanied by lower tropospheric convergence and divergence distributions. These in turn may at times give a sizeable magnitude for $\frac{\partial D}{\partial x}$ and thus the local east/west overturnings have an influence on the speed of propagation of the disturbance. A word of caution is necessary here with regard to this review of some salient disturbances. The variability of the structure of disturbances is quite large from one case to another. As a result, a blind application of the ideas expressed above may prove to be disastrous in some situations. Each event should first be examined in detail in its own light, and diagnostic models can be extremely useful in revealing the mechanics of each. Only by examining a vast number of disturbances can one learn about the atmosphere. One simple reason for this high degree of variability is that there are several scales of motion present "simultaneously" along with the disturbances one is interested in. The physics that govern the different scales is quite different, and scale interactions make it an extremely hard problem.

3.4 Composite tropical disturbances

This introduction would not be complete without a reference to some recent attempts to obtain composite structures of tropical disturbances. In this area prominent contributions were made by Williams (1970), Reed and Recker (1971), Yanai et al., (1973), Reed et al., (1977), and many others.

This approach is primarily necessitated by the lack of observations over the tropics. It goes well beyond the determination of a structure of the mass, motion, thermal and moisture variables of the composite storms. It is, in fact, designed to ask questions regarding the parameterization of cumulus scale motions which are not

easily obtainable from observations on the synoptic scale. Being truly diagnostic approaches, they assume that the time tendency terms of the large scale are known and the cumulus scale properties are unknown. In particular, such approaches are designed to provide information regarding the vertical mass flux by an ensemble of cloud populations, the vertical distribution of cumulus-scale heating and the distributions of fluxes of momentum, vorticity and moisture. The preparation of a composite of observations over many days, which provides the fields of large scale variables and the mean speed of propagation of the disturbance, is not an easy proposition. Many assumptions that "border on details of cloud physics" need to be made in order to close these systems. Several of these assumptions are not fully justified at the present state of the art.

3.5 Western Pacific Ocean cloud clusters

Williams and Gray (1973) placed a rectangular mesh of grid points (4 degree squares) on satellite photographs of cloud clusters classified into various different categories. The upper air network of weather stations is located in these composite coordinate squares, the (0, 0) square being at the centre of a cloud cluster. Some results of their compositing for a so-called "composite cloud cluster" are illustrated in Figure 3.4. The major message is that the conservative cluster over the western Pacific carries a cyclonic relative vorticity of the order of $0.7 \times 10^{-5} \text{ s}^{-1}$ in the troposphere below 400 mb, and it is capped by an anticyclonic vorticity centre in the upper troposphere. The corresponding divergence profile shows that there is a deep layer of convergence which extends all the way to 400 mb with divergence prevailing in the upper troposphere. The magnitude of convergence is about $0.4 \times 10^{-5} \text{ s}^{-1}$. This is a very weak disturbance. The upward large-scale vertical motion is of the order of 150 mb day^{-1} (or roughly 1 to 2 cm day^{-1}). The new information is the rather high level of non-divergence and the middle tropospheric convergence. In the past, much emphasis had been placed on boundary layer convergence and high level divergence in tropical disturbances. The middle tropospheric convergence is considered to be a feature of the cluster-dynamics. Its full implications are not quite clear as yet. This study of Williams and Gray (1973) and an earlier study by Riehl and Malkus (1961) emphasize a vorticity and a heat imbalance problem which is well illustrated by these data sets.

If we consider only the large scale convergence (such as illustrated here), it is easy to note that an accumulation of vorticity would result below 400 mb and a depletion above 400 mb. In order to illustrate this, consider the vorticity equation:

$$\frac{\partial \zeta}{\partial t} = - \nabla \cdot (\zeta_a \vec{V}) - \frac{\partial}{\partial p} (\zeta_a \omega) - \zeta_a \nabla \cdot \vec{V} - \vec{k} \cdot \nabla \omega \times \frac{\partial \vec{V}}{\partial p}$$

Integrating this equation between 1000 and 400 mb, $-\nabla \cdot (\zeta_a \vec{V})$ would give a net convergence of flux of vorticity, since inflow correlates with cyclonic vorticity. $-\frac{\partial}{\partial p} \zeta_a \omega$ would be small since ω vanishes near the ground and ζ_a is very small at 400 mb. The term $-\zeta_a \nabla \cdot \vec{V}$ would give a net increase of vorticity because convergence correlates with cyclonic vorticity below 400 mb. $-\vec{k} \cdot \nabla \omega \times \frac{\partial \vec{V}}{\partial p}$ would be a small term for the large scale, since the vertical shear of wind is quite small below 400 mb. As a consequence, a vorticity budget below 400 mb yields:

$$\frac{1}{g} \int_{400}^{1000} \frac{\partial \zeta}{\partial t} dp > 0 \quad (3.3)$$

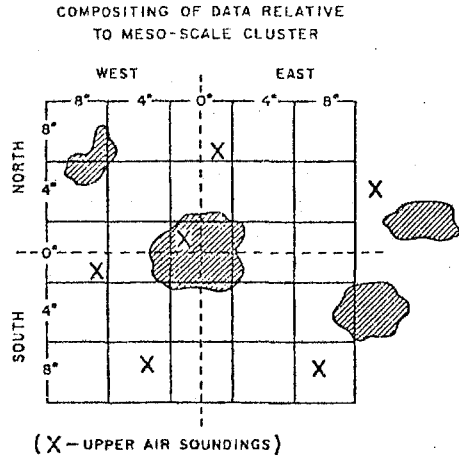
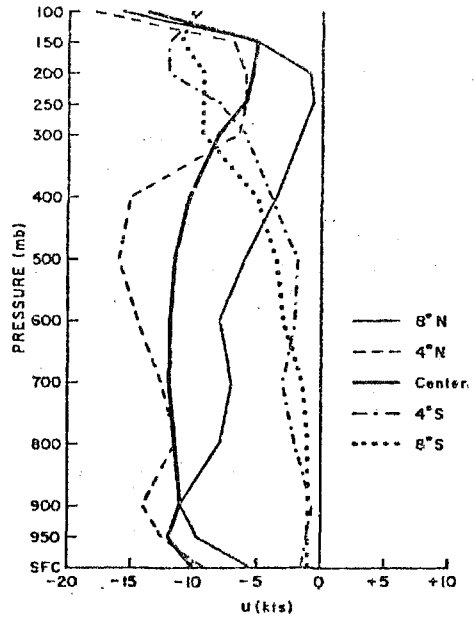
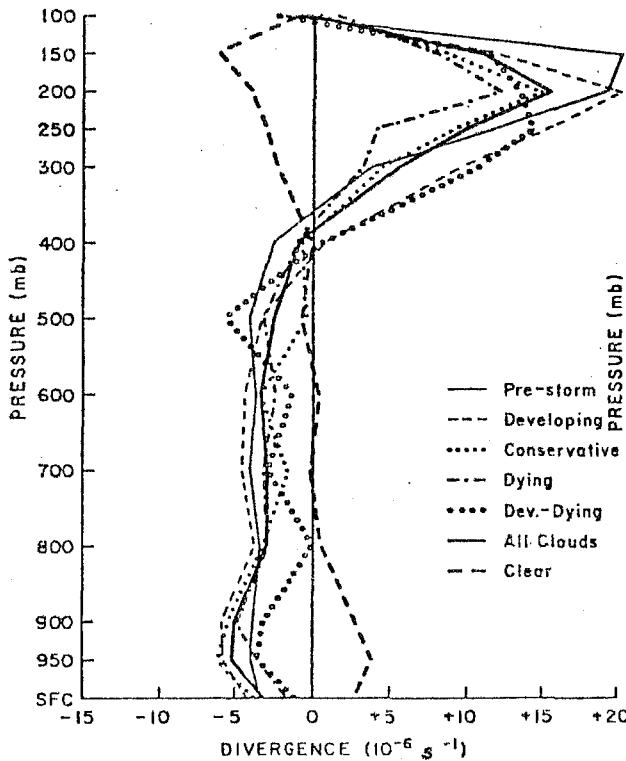


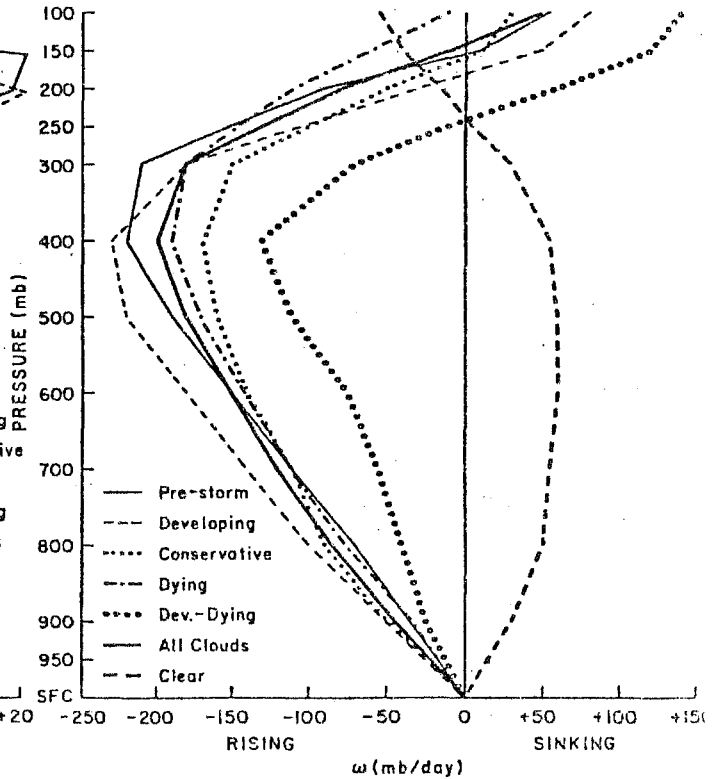
Illustration of compositing scheme and rectangular grid centre on cloud cluster



Vertical profiles of the zonal wind north of centre, at centre, and south of centre for conservative clusters



Vertical profiles of 4°-square area-average divergence at cluster centre



Profiles of 4°-square area average vertical velocity at cluster centre

Figure 3.4

The converse is the case above 400 mb. In this discussion, no mention is made of cumulus scale motions which would have to provide a balance for these slow moving conservative cloud clusters. The role of the cumulus scale would be to remove the excess vorticity from the lower levels and deposit it at the upper levels where a deficit is being created by the large scale motions. The precise manner by which this is accomplished is an unsolved problem.

The heat balance paradox is a similar story. Consider the following heat budget equation:

$$\frac{\partial}{\partial t} E_m = - \nabla \cdot (E_m \vec{V}_H) - \frac{\partial}{\partial p} (\omega E_m) + H_s + LE_B + H_R \quad (3.4)$$

= Lateral convergence + Vertical convergence + Boundary fluxes + Radiation

where E_m is the moist static energy,
 H_s is the sensible heat flux from the ocean,
 E_B is the evaporative flux of moisture from the ocean, and
 H_R is the net radiative warming.

The moist static energy E_m contains three parts:

$$E_m = gz + C_p T + Lq \quad (3.5)$$

= Potential energy + Enthalpy + Latent heat

The vertical profile of moist static energy has a minimum value generally near the 700 mb surface in the tropics. This is related to the large-scale conditional instability of the tropics. If a large scale three-dimensional mass of air is defined by a relation:

$$M = \frac{1}{g} \int_{p=700}^{1000} \iint dx dy dp \quad (3.6)$$

where the limits on x and y are of the order of several hundred km and the mass encloses the centre of the disturbance, then upon integration of the heat balance equation over the mass of the domain, we would note that boundary fluxes would supply energy to the box, lateral convergence $-\nabla \cdot \vec{V} E_m$ would bring in larger values of heat compared to what goes out at the top (i.e. $-\frac{\partial}{\partial p} (\omega E_m)$, the vertical flux term), and as a consequence a net accumulation of heat results in the lower box and the converse occurs above the 700 mb level. A near steady-state tropical disturbance cannot be maintained by the large scale mass inflows and outflows under these circumstances. Here again, one views the cumulus scale motions playing the role of removing the excess heat from the lower troposphere and depositing in the upper troposphere where there is a deficit. The precise manner by which this is accomplished in nature is a current major problem under the heading of "Parameterization of cumulus convection". This problem is receiving much attention in tropical meteorology today. We shall discuss this separately.

3.6 The Reed and Recker composite wave

This is another major study of the composite structure of some 18 disturbances in the west central Pacific over the Marshall Island network. Their reference for compositing was obtained by constructing a mean trough line (meridional wind $V = 0$) for the layer from the surface to 500 mb. For each day, a line was so identified and all the weather stations located relative to it. The structure yielded a composite which was divided into some 8 categories, i.e. from the ridge line to the trough line and on to the next ridge line. The raw data was first smoothed via a wide band pass filter that removed high frequency information below 2-day intervals and also removed low frequency information beyond 20 days. This procedure produced a data set that is currently much used by many research meteorologists.

Figure 3.5 illustrates the structure of Reed and Recker's composite wave. The salient features are quite similar to those noted by Williams and Gray. The composite wave was travelling at a speed of roughly 9 m s^{-1} or about 7° longitude day^{-1} . Its wave length was roughly 2000 km. The thermal amplitude of the wave is very small (0.5°C). This is probably an underestimate due to the compositing process. Likewise it seems that the relative vorticity is somewhat underestimated. An examination of the v -component and the relative vorticity suggests that the wave below 500 mb is cyclonic and above 300 mb has an anticyclonic circulation. There is a deep layer of convergence that extends to nearly 400 mb and in the upper troposphere there is divergence. As stated earlier, rainfall rates of the order of 1-2 cm day^{-1} were noted in this disturbance. Contrasted with other tropical disturbances, this is a very weak disturbance. One of the major accomplishments of this study was the determination that the vertical mass flux is in the cloudy part of the wave. An attempt was made to determine the vertical distribution of the heating function in the wave. We shall describe this elsewhere.

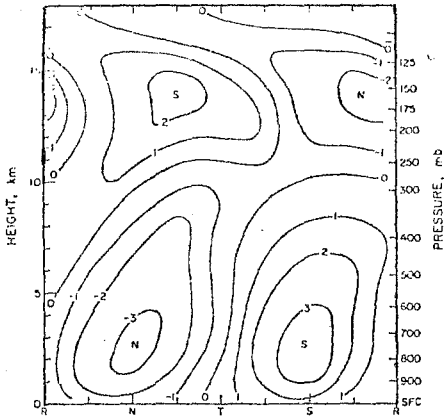
3.7 A composite West African wave

In a recent study (Reed *et al.*, 1977), the observations from the GARP Atlantic Tropical Experiment (GATE) were used to derive the composite structure of the West African wave disturbance. Figures 3.6a and b show the west/east vertical structure of the African wave during the northern summer months. The structure diagram contains the following parameters:

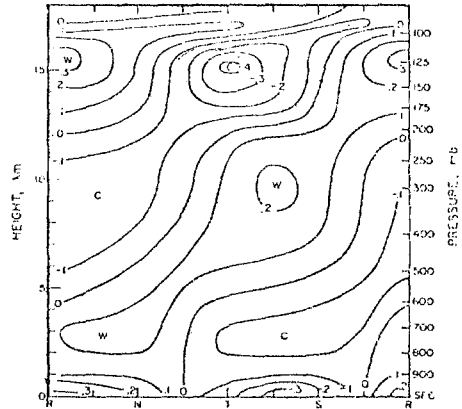
- (i) Meridional wind departure from a latitudinal average (m s^{-1})
- (ii) Zonal wind departure from a latitudinal average (m s^{-1})
- (iii) Vorticity (10^{-5} s^{-1})
- (iv) Divergence (10^{-6} s^{-1})
- (v) Vertical motion (mb h^{-1})
- (vi) Temperature deviation from latitudinal average ($^\circ\text{C}$)
- (vii) Relative humidity (per cent).

Here the latitudinal average refers to a distance equivalent to that of the wavelength of this composite disturbance.

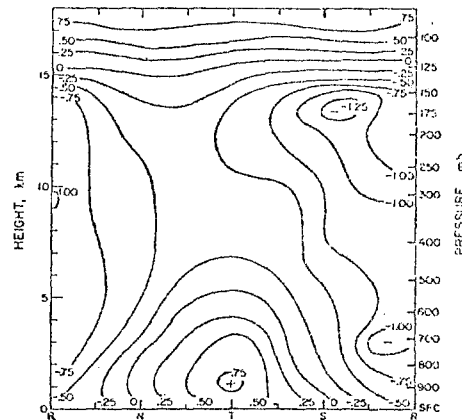
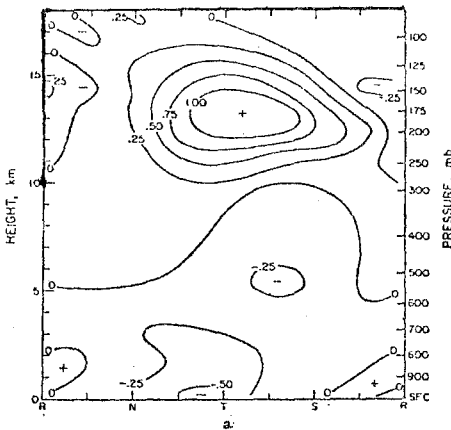
The abscissa in these diagrams denotes the categories of the wave (e.g. categories 2, 4, 6 and 8 are northerly (N), trough (T), southerly (S) and ridge (R) respectively).



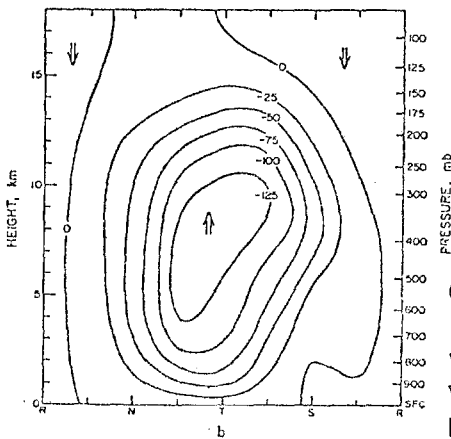
Composite diagram of meridional wind speed ($m s^{-1}$) for KEP. The letters R, N, T and S refer to the ridge, north wind, trough and south wind regions, respectively, of the wave as defined by its structure in the lower troposphere



Composite diagram of temperature deviations ($^{\circ}C$) at various levels from their respective mean values at KEP



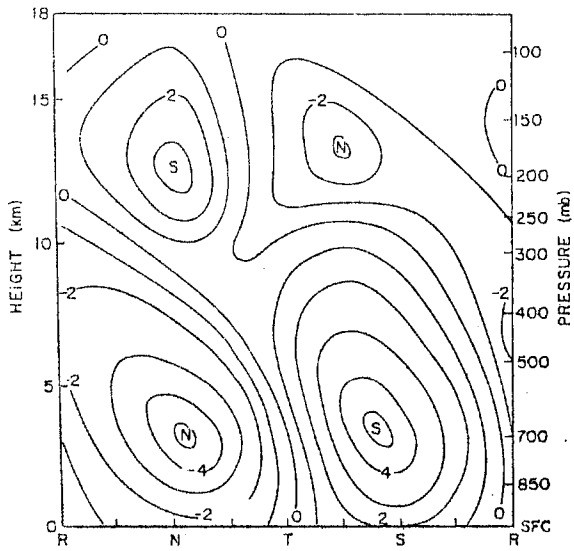
Composite diagram of vertical component of relative vorticity ($10^{-4} s^{-1}$) for KEP



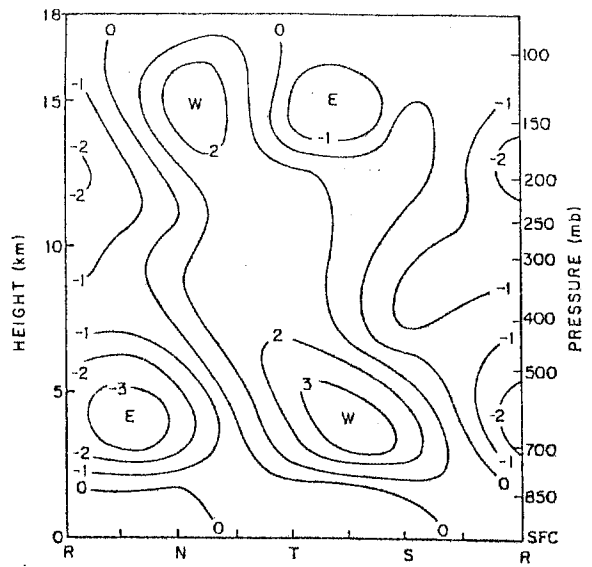
(KEP denotes: Kwajalein, Enewetok and Ponape.)

Composite of horizontal velocity divergence ($10^{-4} s^{-1}$) for KEP, (a); and corresponding vertical p velocity ($10^{-6} mb s^{-1}$), (b) (Analysed values give approximate displacement in millibars per day)

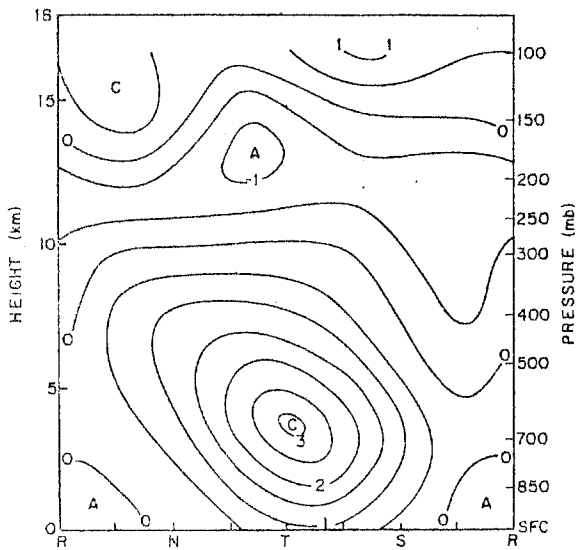
Figure 3.5



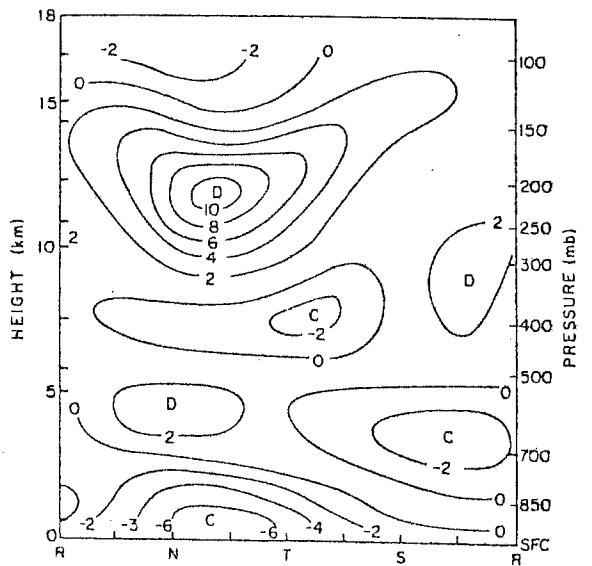
(i) Meridional wind ($m s^{-1}$)



(ii) Zonal wind ($m s^{-1}$)

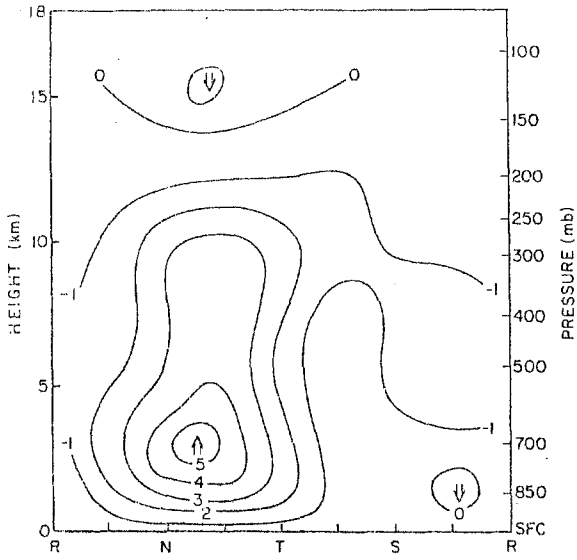


(iii) Relative vorticity ($10^{-5} s^{-1}$)

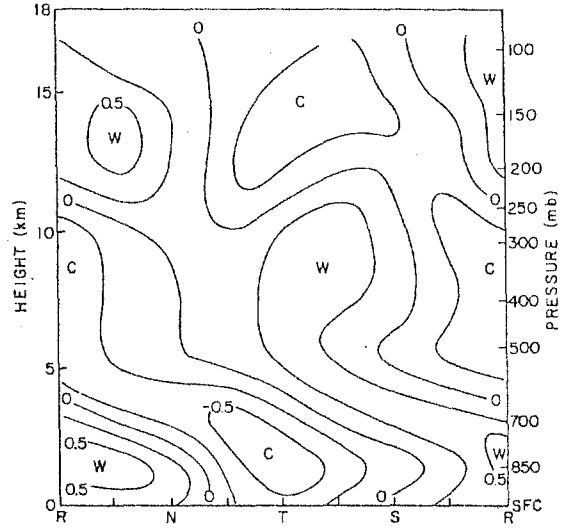


(iv) Divergence ($10^{-6} s^{-1}$)

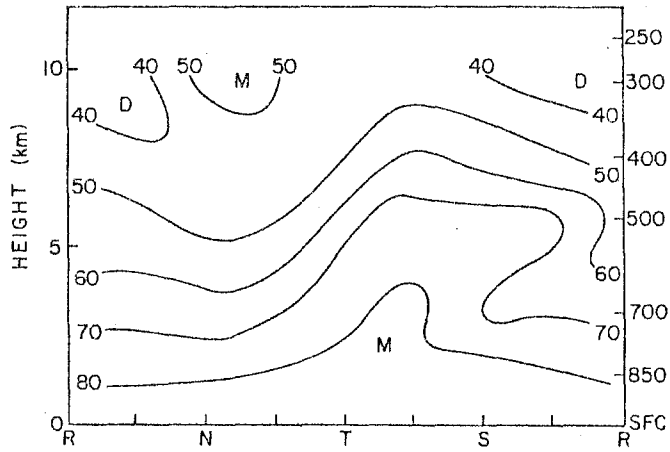
Figure 3.6a



(v) Vertical motion (mb h^{-1})



(vi) Temperature anomaly ($^{\circ}\text{C}$)



(vii) Relative humidity (per cent)

Figure 3.6b

The meridional wind of the composite African wave has its largest amplitude near the 650 mb level, and the intensity is around 5 m s^{-1} . The zonal wind structure shows westerlies and easterlies which correlate respectively with the southerlies and northerlies. This implies an Equatorward transport of westerly momentum ($\overline{u'v'} < 0$). The relative vorticity also has a maximum cyclonic value near the 650 mb level. An interesting aspect of the study made by Reed *et al.*, is the presence of an anti-cyclonic relative vorticity maximum at 200 mb. This shows that the composite disturbance is very deep in the vertical and must extend through the entire depth of the troposphere. The vertical structure of the convergence/divergence field in the illustration shows large convergence just ahead of the surface position of the trough. The largest horizontal mass divergence is naturally found near the 200 mb level over the same region. At the intermediate levels the vertical distribution of horizontal mass divergence is not too well defined. The associated vertical motion distribution illustrated in panel (v) shows a maximum vertical velocity at 700 mb and the intensity is around 5 mb h^{-1} (or $1 \text{ to } 2 \text{ cm s}^{-1}$). The largest upward motion occurs just ahead of the trough line of the West African disturbance. These results are in accordance with the findings of Pedgley and Krishnamurti (1976). However, this has been questioned by West African meteorologists who find satellite cloud cover on many occasions, and hence perhaps rising motion to the east of the trough line. This is a point that deserves further careful study. The thermal field exhibits a cold core below 700 mb for the West African composite wave disturbance, and a relatively warm core in the general area of 300 to 400 mb. At still higher levels, cold anomalies are again noted. The last structure diagram is that of the relative humidity. The dry air at low levels tends to be associated with northerlies and the moist air is located behind the trough in the southerlies. However, at higher levels, relatively moister air is found over the dry air of the lower troposphere, the converse being the case above the low level moist air. The reasons for this are not clear at present.

The composite African wave has a wavelength of roughly 2500 km and has a westward phase speed of roughly 5° to 7° longitude per day. Roughly one disturbance passes westward once every 3 to 4 days. This result is in accordance with the annual summaries of West African disturbances that pass Dakar (Frank, 1975). According to Frank, roughly 50 disturbances pass Dakar in a 7-month period (May through November) every year. This gives a frequency of one disturbance passage every 3 to 4 days.

There are several important reasons why the African wave disturbance has a significant place in tropical meteorology. One of these is the importance of the African wave in West African rainfall. Another reason is that some of these become hurricanes upon passage into the Atlantic ocean. These will be further discussed in the section on Atlantic disturbances.

This chapter giving a broad survey of synoptic disturbances has highlighted some salient structures. In the individual chapters relating to different regions we shall go into further detail on many other tropical systems.

Chapter 4

RADIATIVE PROCESSES IN THE TROPICS

4.1 Introduction

Radiative processes play a very important role in tropical weather systems. For an understanding of systems such as trade inversions, monsoons, heat lows, Hadley cells, African disturbances, tropical upper cold lows, etc., it is becoming clear that the role of radiation must be understood. Generally speaking, some measure of the total differential heating on the scale of disturbances or on domains of interest should be determined. The various components include heating at the Earth's surface and in the atmosphere. Short- and long-wave radiative processes are important in maintaining the quasi-steady thermal state of the tropical atmosphere. The temperature from one day to the next hardly changes, although the long-wave cooling may be of the order of a few degrees Celsius per day. The large scale tropical lapse rate is a consequence of both radiative and convective processes; the zonally asymmetric motion field also contributes significantly via advective processes towards the maintenance of the observed large-scale lapse rates. Without the radiative processes, the tropical weather systems cannot be maintained for time scales of the order of a week. In fact, for some phenomena such as sea breezes and low level jets, the radiative processes on much shorter time scales are important.

Summer-time tropical desert areas tend to be very hot, with ground temperatures rising to near 60°C (140°F). Night-time values of ground temperature over deserts are known to fall to near 10°C (50°F). The Hadley and east/west cells have a descending branch in the tropics and subtropics where the observed air temperatures cannot be maintained without substantial radiative cooling. The ever prevalent "tropical large scale conditional instability" is also maintained by substantial radiative cooling above the low-cloud layers. This latter phenomenon is also closely linked to the maintenance of the trade wind inversion. Diurnal change is not only observed over land areas near the Earth's surface, but also in the upper troposphere and over the oceanic tropics.

Many of these phenomena are discussed in some detail elsewhere in these notes. In this chapter we shall present an outline of the important processes and indicate how they may be measured and/or estimated.

4.2 Numerical calculations of radiative processes

This is one of the most important areas of Tropical Meteorology and its relevance to studies in many areas will be pointed out in later chapters.

In dealing with tropical weather systems, the following calculations are important.

- (i) Short-wave rate of warming of the atmosphere as a function of position and time (x, y, z, t).
- (ii) Long-wave net rate of warming/cooling of the atmosphere as a function of (x, y, z, t).
- (iii) Heat balance of the Earth's surface, as a function of (x, y, t).

In such calculations, prevailing conditions such as the vertical distribution of temperature and moisture, the surface temperature of the underlying surface, the cloud cover, cloud heights and depth and vertical extent of dust if available must be taken into account. Furthermore, soil properties such as the albedo of the Earth's surface, ground wetness and surface roughness are also important. Specific examples to illustrate the many possible tropical applications are not presented here; these will be considered in subsequent chapters where they are more relevant.

4.3 Short-wave radiation

The accepted value of the solar constant, S_0 , is $1360 \text{ W m}^{-2} = 1.997 \pm 0.04 \text{ cal cm}^{-2} \text{ min}^{-1}$. The zenith angle ζ is defined as the angle between the zenith direction and the sun. It is given by the relation:

$$\cos \zeta = \sin \phi \sin \delta + \cos \phi \cos \delta \cos h_r \quad (4.3.1)$$

where ϕ is the latitude, δ is the declination of the sun and h_r is the hour angle of the sun (measured from local solar noon, e.g. six hours = 90°). The declination of the sun is its angular distance north (+) or south (-) of the celestial equator. The optical depth of the atmosphere is a function of the mixing ratios of the atmospheric constituents, the pressure and the temperature distributions. It is usually expressed by the relation:

$$W(p) = \frac{1}{g} \int_0^p q (p/p_0)^{0.85} (T_0/T)^{0.5} dp \quad (4.3.2)$$

where the path length is estimated from the top of the atmosphere (i.e. $p = 0$) to a reference level p . In radiation flux calculations $W(p)$ is frequently regarded as a vertical coordinate increasing downwards. For tropospheric tropical problems water vapour is the principal constituent and may be incorporated using the specific humidity. The empirical coefficients are due to Kuhn (1963). The solar radiation incident at the top of the atmosphere is nowadays broken into a scattered and an absorbed part, Katayama (1972) and Joseph (1966). Short-wave radiation is depleted due to absorption by water vapour and Rayleigh scattering by aerosols. The treatment

of aerosols is poor in the present state of the art. Following Katayama we write:

$$\begin{aligned} \text{Scattered part} &= S^s = 0.651 S_0 \cos \zeta \\ \text{Absorbed part} &= S^a = 0.349 S_0 \cos \zeta \end{aligned} \quad (4.3.3)$$

It should be noted that we are primarily interested in illustrating a computational procedure for estimating the role of short-wave radiative warming of the atmosphere (or the Earth's surface). However, in discussing practical phenomenological problems in tropical meteorology, this kind of approach is also most useful. The above partition of the total radiation into two parts comes from the theory of Rayleigh scattering.

In the following analysis we shall first omit the attenuation of short-wave radiation by clouds. From empirical studies, Joseph (1966) has defined an Absorptivity function $A [W]$. This function tells us how much of the incoming solar radiation is depleted by the absorbing constituent, i.e. water vapour. Here W is the path length through which the radiation has to pass. He defines $A [W]$ by the relation:

$$A [W] = 0.271 (W \text{ Sec } \zeta)^{0.303} \quad (4.3.4)$$

The direct solar radiation reaching a reference level i may hence be written as:

$$S^a \left(1 - A \left[W_i \text{ Sec } \zeta \right] \right) \quad (4.3.5)$$

Note that only the "absorbed part" is attenuated by this process. In order to estimate the net downward flux of short-wave radiation at a reference level of the atmosphere we should take into account the amount of diffuse radiation that comes up from the Earth's surface. For this we should take into account the albedo of the Earth's surface, and also consider the absorptivity of the layer between the Earth's surface and the reference level i . $S^a \{1 - A [W_0]\} \alpha_s$ is the amount of diffuse short-wave radiation reflected by the Earth's surface. Note that the diffuse radiation is not a function of the zenith angle. Here α_s denotes the albedo of the Earth's surface.

The diffuse radiation experiences, in general, a longer path length compared to direct solar radiation. Joseph (1966) proposes that the absorptivity for diffuse radiation be written as $A [1.66 (W)]$ instead of $A [W]$. The factor 1.66 was shown to account for the increased path length. Hence, we can now write an expression for the diffuse radiation that reaches a level i from the Earth's surface, i.e.:

$$S^a \left\{ 1 - A \left[W_0 \text{ Sec } \zeta \right] \right\} \alpha_s \left\{ 1 - A \left[1.66 (W_0 - W_i) \right] \right\} \quad (4.3.6)$$

The total downward flux of shortwave radiation is then given by the relation:

$$S_i = S^a (1 - A [W_i \text{ Sec } \zeta]) - S^a \left\{ 1 - A [W_o \text{ Sec } \zeta] \right\} \alpha_s \times \left\{ 1 - A [1.66 (W_o - W_i)] \right\} \quad (4.3.7)$$

Next we shall outline what one can do to include clouds.

We shall consider only one layer of clouds.

S^a is the amount of absorbed short-wave radiation at the top of the atmosphere.

$$S^a (1 - A [W_i \text{ Sec } \zeta])$$

is the amount of short-wave radiation reaching a reference level i just above the cloud level. The diffuse radiation emanating upwards at the cloud level is given by $S^a (1 - A [W_{cT} \text{ Sec } \zeta]) \alpha_c$ where W_{cT} is the path length at the cloud top level and α_c is the albedo for the cloud. Part of this diffuse radiation would be absorbed prior to its arrival at the reference level i . The upward diffuse radiation reaching the level i is expressed by:

$$S^a (1 - A [W_{cT} \text{ Sec } \zeta]) \alpha_c (1 - A [1.66 (W_{cT} - W_i)])$$

The net absorbed downward flux of short-wave radiation passing through a reference level i when there is a cloud layer present below, is given by:

$$S_i^a = S^a (1 - A [W_i \text{ Sec } \zeta]) - S^a (1 - A [W_{cT} \text{ Sec } \zeta]) \alpha_c \times (1 - A [1.66 (W_{cT} - W_i)]) \quad (4.3.8)$$

The next logical step is to examine the amount of short-wave radiation passing through a cloud layer. For this purpose the absorptivity of the cloud must be defined. Since there is both liquid water and water vapour within clouds, Katayama (1972) defines the absorptivity of the clouds by a function $A [W_{ci}^*]$ where W_{ci}^* is the augmented path length which takes into account the equivalent amount of water vapour within the cloud. If S^a is the absorbed part of the short-wave radiation reaching the top of the atmosphere, we write $S^a (1 - A [W_{cT} \text{ Sec } \zeta])$ as the amount reaching the cloud top. The amount reaching below the cloud is written as:

$$S^a (1 - A [W_{cT} \text{ Sec } \zeta]) (1 - \alpha_c) (1 - A [W_{ci}^*])$$

To determine the downward flux of net short-wave below a single cloud in the atmosphere, the upward flux of the diffuse short-wave radiation rising from the Earth's surface must be considered. This latter calculation should be carried out as for the cloud-free case. The total downward flux of absorbed short-wave radiation at a reference below a single cloud atmosphere is thus given by:

$$S_i^a = S^a (1 - A \left[W_{cT} \text{Sec } \zeta \right]) (1 - \alpha_c) \left\{ 1 - A \left[W_c^* + 1.66 (W_i - W_{cb}) \right] - \right. \\ \left. (1 - A \left[W_c^* + 1.66 (W_o - W_{cb}) \right]) x_s (1 - A \left[1.66 (W_o - W_i) \right]) \right\} \quad (4.3.9)$$

where W_i is the path length at the reference level,

W_o is the path length at the ground,

W_{cb} is the path length at the cloud base, and

W_c^* is the equivalent path length of cloud.

If there is more than one cloud layer, a simple logical extension of the above analysis must be carried out (see Katayama, 1972).

Thus far we have not addressed the scattered part of the short-wave radiation. The student is recommended to read scattering theory. In general it can be said that the rate of warming of the atmosphere by the scattered part of the short-wave radiation is very small. This scattered part cannot, however, be neglected in the heat balance of the Earth's surface. The theory of scattering is too involved. Hence, we shall present two empirical formulae frequently used to define the scattered part of the short-wave radiation:

$$\alpha_o = 0.085 - 0.245 \log (p_s/p_o \text{Cos } \zeta) \quad \text{Chang (1977), for cloudless atmosphere,}$$

where α_o is the albedo of the atmosphere, p_s is the surface pressure and p_o is 1000 mb. The scattered part of the solar radiation reaching the Earth's surface is given by:

$$S_i^s = S^s (1 - \alpha_o) (1 - \alpha_o \cdot \alpha_s) \quad (4.3.10)$$

where S^s is the scattered part at the top of the atmosphere and α_s is the albedo of the Earth's surface. It can be shown that over periods of the order of several days this is not a negligible effect. We shall come back to this in our discussion of the heat balance of the Earth's surface.

4.4 Long-wave radiation

Here, again, the approach is one that emphasizes the computational aspects. We shall not review here the well-known Elsasser chart although the student unfamiliar with it should refer to a standard text on radiation. Whereas solar radiation is centred around the 0.474 micron wavelength band, we are referring here to emission centred around the 11.5 micron band. All of the long-wave radiation originates at the Earth's surface or from the atmosphere (and clouds). The atmosphere absorbs long-wave radiation much more strongly than solar radiation. The fundamental laws such as Wien's displacement law and Kirchoff's law are central to our discussions here. The concept of black-body radiation is implicit in much of our present analysis of long-wave radiation. Among ozone, water vapour and carbon dioxide, the absorption by water vapour is most important for tropospheric tropical meteorological problems. The water vapour absorption is strong around 6 and 20 microns (in the vibrational and the rotational bands respectively). The atmosphere both absorbs and re-emits long-wave radiation. We shall now consider the so-called Schwarzschild's equation:

$$dF_{\lambda} = K_{\lambda} \left[\Phi(\lambda, T) - E_{\lambda} \right] du \quad (4.4.1)$$

where K_{λ} is the absorption coefficient, dF_{λ} is the change in flux in a layer of optical thickness du , $\Phi(\lambda, T)$ is the black-body emission as given by Planck's equation and E_{λ} is the flux density at wave length λ . By Kirchoff's law, the emissivity of the layer is equal to the absorptivity ($K_{\lambda} du$). This equation expresses the difference between absorption and emission in a layer. In principle, this equation can be used for a model atmosphere. However, it is not well-suited for line absorbers since K_{λ} varies considerably. We shall therefore describe some simple calculation procedures for the evaluation of long-wave radiative flux divergence, the aim being to evaluate the rate of long-wave heating (or cooling) at the Earth's surface and in the atmosphere. Calculations for both clear-sky and cloudy situations are desirable.

First, we shall consider the cloud free case and describe the so-called emissivity method for estimating long-wave radiative effects. We shall examine the upward flux of long-wave radiation at a reference level i . This can be divided into two parts, part up to the level i from the Earth's surface (whose temperature is T_g), which can be written as:

$$F_g^{\uparrow} = \sigma T_g^4 (1 - \epsilon [W_B - W_i]) \quad (4.4.2)$$

and the part emitted by the layer between the reference level and the ground:

$$F_A^{\uparrow} = \int_{W_i}^{W_B} \sigma T^4 \frac{\partial}{\partial W} \epsilon [W - W_i] dW \quad (4.4.3)$$

where σ is the Stefan-Boltzman constant
 W_B is the path length at the ground,
 W_i is the path length at the reference level,
 ϵ is the emissivity.

It is possible to make use of tables of emissivity as a function of path length to obtain reliable estimates of the long-wave fluxes (Kuhn, 1963). Rodgers (1967) has shown that emissivity tabulations yield results almost as good as those obtained by exact integration of the transfer equation. The error estimates are of the order of $0.1^\circ \text{ day}^{-1}$ in the atmosphere, which is tolerable for most purposes. The total upward flux of longwave radiation at a reference level in the cloud free case is given by the sum of the two terms:

$$F_i^\uparrow = \sigma T_g^4 (1 - \epsilon [W_B - W_i]) + \int_{W_i}^{W_B} \sigma T^4 \frac{\partial \epsilon}{\partial W} [W - W_i] dW \quad (4.4.4)$$

Here $\frac{\partial \epsilon}{\partial W}$ is a measure of the change of emissivity with respect to the path length. The downward flux in the cloud free case is given by just one term, i.e.:

$$F_i^\downarrow = - \int_0^{W_i} \sigma T^4 \frac{\partial \epsilon}{\partial W} [W_i - W] dW + D \quad (4.4.5)$$

If we have one cloud layer above the reference level, then the cloud will affect the downward flux at the reference level. Here D stands for the incoming longwave radiation at the top of the model. In this case we write:

$$F_i^\downarrow = \sigma T_{cb}^4 (1 - \epsilon [W_i - W_{cb}]) - \int_{W_{cb}}^{W_i} \sigma T^4 \frac{\partial \epsilon}{\partial W} [W_i - W] dW \quad (4.4.6)$$

where T_{cb} is the temperature at the cloud base and W_{cb} is the path length at that level.

If there is one cloud layer below the reference level, then the formula for the upward flux of longwave radiative flux is:

$$F_i^\uparrow = \sigma T_{cT}^4 (1 - \epsilon [W_{cT} - W_i]) - \int_{W_i}^{W_{cT}} \sigma T^4 \frac{\partial \epsilon}{\partial W} [W - W_i] dW \quad (4.4.7)$$

Multiple cloud layers require a logical extension of the above principle. The question as to what one should do within a cloud remains an unsolved problem at this stage. In principle one could set the net heating (or cooling) equal to zero if the reference level falls within a cloud layer. The net longwave radiative flux at any level may be written as:

$$F = F_i^\downarrow - F_i^\uparrow \quad (4.4.8)$$

and the warming (or cooling) would be determined by the divergence (or convergence) of flux, i.e.:

$$C_p \left(\frac{\partial T}{\partial t} \right)_{\text{longwave}} = g \frac{\partial F}{\partial p} \quad (4.4.9)$$

The emissivity technique is fairly straightforward and can be used easily for evaluating the vertical profile of the long-wave radiative cooling rates. The specification of the vertical distribution of cloudiness is, however, a difficult problem.

4.4.1 The specification of cloudiness

The estimation of both short and longwave fluxes requires a specification of cloudiness. If one is interested in a local vertical distribution of the cooling rate, then observations of cloudiness should be used as far as is practically possible. Aircraft and satellite observations are, of course, very useful. There are inherent problems if more than one layer of cloud cover is present. Climatology of a local region may be extremely useful at times. Alternate ways of specifying cloud cover depend on empirical formulae relating vertical distribution of relative humidity and cloudiness. Such formulae have been presented by Smagorinsky (1960), Danard (1969), and Chang (1977). It should, however, be stated that none of these are very satisfactory for the whole of the tropics. According to Chang (1977), the following relations between cloud-cover and relative humidity may be used:

$$\begin{array}{l} \text{Low cloud} \\ \text{amounts} \end{array} \quad C_L = 3.3 \times RH_{900} - 1.98 \quad (4.4.10)$$

$$\begin{array}{l} \text{Middle cloud} \\ \text{amounts} \end{array} \quad C_M = 2.0 \times RH_{700} - 0.70 \quad (4.4.11)$$

$$\begin{array}{l} \text{High cloud} \\ \text{amounts} \end{array} \quad C_H = 1.8 \times RH_{500} - 0.50 \quad (4.4.12)$$

where RH_{900} , RH_{700} and RH_{500} respectively denote the relative humidities at the 900, 700 and 500 mb surfaces. These formulae are defective if the cloud amounts come out negative or exceed unity, in which case Chang sets the cloud amounts to zero or unity respectively. Some simple improvement on this is possible.

Finally, we shall show (Figure 4.1) a comparison of several calculated and observed profiles from a recent study of Ellingson (1972) for the tropics. In general, the agreement is within 1°C . Here "100 interval" utilizes many points in the vertical (i.e. ≈ 10 mb resolution), based on Ellingson's calculation. The radiosonde ascents made during BOMEX were available for this study. The radiometer-sonde is described later in this chapter. The Elsasser-Culbertson (1960) curve shown here is based on another well-known technique for the estimation of long-wave cooling rates.

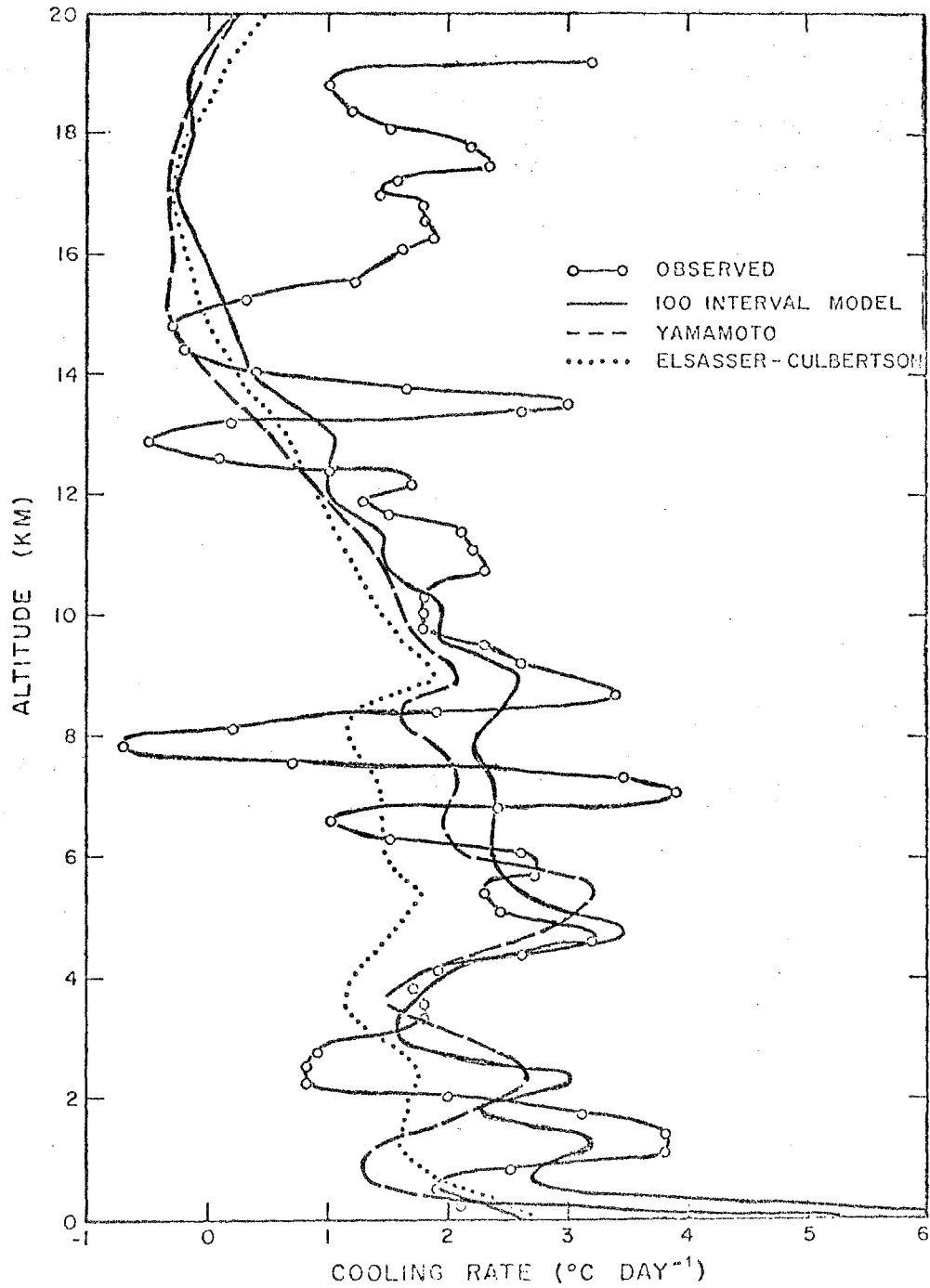


Figure 4.1 - An intercomparison of different model-point cooling-rate computations with the filtered cooling rates from the radiometersonde ascent from Discoverer on June 3, 1969

4.5 Heat balance of the Earth's surface

For most tropical meteorological problems the ocean is assumed to have an infinite heat capacity. Since the ocean's diurnal temperature changes are not as large as those for land areas, one does not address the problems of the heat balance of the ocean surface when small time-scales of atmospheric changes are considered. When one is concerned with monthly or seasonal changes, the oceanic problem becomes very important. The land-surface heat balance problem is very important from the point of view of both meteorology of motion systems and agriculture. As an example, the land surface of desert areas exhibits diurnal changes of the order of 30° to 40°C. The elements of the heat balance at the Earth's surface are the following:

- (i) Net incoming short-wave radiation at the Earth's surface:

$$F_s^\downarrow = (1 - \alpha_s) (S_o^s + S_o^a) \quad (4.5.1)$$

where α_s is the albedo of the Earth's surface and S_o^s and S_o^a are respectively the scattered and absorbed part of the solar radiation reaching the Earth's surface.

- (ii) Net downward flux of long-wave radiation at the Earth's surface:

$$F_L^\downarrow = F_o^\downarrow - \sigma T_g^4 \quad (4.5.2)$$

where F_o^\downarrow is the downward flux from the atmosphere and the clouds and T_g is the temperature of the ground surface.

- (iii) Upward (or downward) sensible heat flux over land areas, H_s .

- (iv) Upward (or downward) flux of latent heat over land areas, H_L .

The heat balance condition may be expressed by:

$$C \frac{\partial T_g}{\partial t} = F_s^\downarrow + F_L^\downarrow - H_s - H_L \quad (4.5.3)$$

where C is the heat capacity of the soil. We shall describe methods of estimating H_s and H_L in the next chapter on the boundary layer. They depend on a number of parameters such as ground wetness and surface roughness. If the heat capacity of the ground is assumed to be zero, then we can write:

$$F_s^\downarrow + F_L^\downarrow - H_s - H_L = 0 \quad (4.5.4)$$

This equation is used to solve for the diurnally varying surface temperature. Surface temperature appears generally in the formulations of F_s^\downarrow , F_L^\downarrow , H_s and H_L . This is a transcendental equation for the surface temperature, and numerical methods such as the Newton-Raphson method may be very useful in its determination. The diurnal change is incorporated by the inclusion of a varying zenith angle of the sun. In balanced state, diurnal variation over warm land areas is accompanied by substantial diurnal changes in the fluxes of F_s^\downarrow , F_L^\downarrow , H_s and H_L . The formulae should be tested against ground-based measurements of surface temperature. The energy-balance relation is also frequently used to estimate the maximum temperatures over land areas. The heat balance of the Earth's surface is central to our understanding of heat lows, monsoons, droughts and breaks in monsoons and deserts and we shall make further reference to this in other chapters. Here we shall present one example of this balance over West Africa based on recent observations and the above-mentioned calculations for the GARP Atlantic Tropical Experiment (GATE).

Figures 4.2 a, b, c show some observations over the Sahara desert based on the unpublished studies of Professor P. De Felice of the University of Paris. Professor Felice measured the surface temperature of the soil during the course of a day. Figure 4.2a shows the diurnal change of the soil temperature which varies between 45°C and 7°C during April. The atmospheric temperature at 5 cm and land temperature at the surface to 20 cm below the ground are shown in Figure 4.2b. This diagram may also be used to compare the diurnal change at the surface (7°C to 45°C) with that of the air at 5 cm height (between 8°C and 28°C) and at other depths (where the diurnal change decreases).

Professor Felice's measurements of conductive and convective heat flux over the Sahara are shown in Figure 4.2c. A marked diurnal change is evident; as much as 400 W m^{-2} goes up from the desert to the atmosphere during the noon hour with a reversal of the direction of heat flux at night. The values at night are around 40 W m^{-2} and the mean heat flux during the day is around 120 W m^{-2} . This heat is generally transferred by dry convection higher into the atmosphere. The surface-based radiation network is an important observing system over Africa (the surface-based instruments are discussed later in this chapter). We shall now show numerical calculations of the heat balance of the Earth's surface over the Sahara which yield similar results.

Figures 4.3a, b illustrate the diurnal cycle of the heat balance of the Earth's surface calculated from GATE observations at two selected sites over West Africa. The calculations are based entirely on the methods shown in these notes. Of interest in these calculations are the values taken for the surface albedo which are based on estimates by Posey and Clapp (1964); Figure 4.4 illustrates a map of surface albedo based on their study. As stated earlier, the albedo of West African deserts is around 0.3 (or 30%). At night-time there is a near balance between the incoming and out-going long-wave radiation, the other fluxes being small. During the daytime, the large fluxes of reflected short-wave radiation, the outgoing long-wave radiation and the sensible heat flux all add to the net warming of the air near the Earth's surface. This frequently results in the formation of superadiabatic lapse rates in the lowest 100 metres. Dry convection results in the removal of this excess heat. The importance of the surface albedo will be considered in the chapter on African disturbances. A detailed study of the heat balance of the Sahara desert is desirable. We have only presented the gross features of the surface diurnal change.

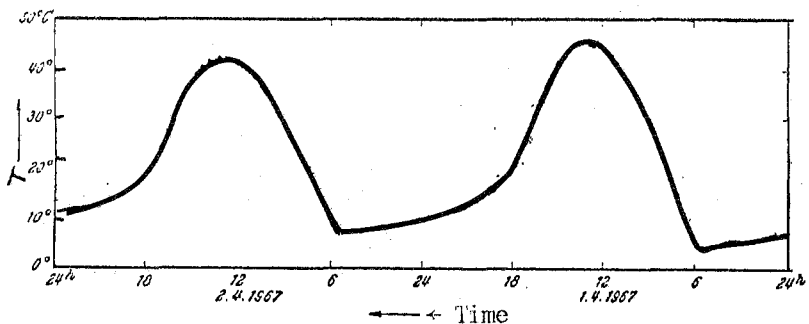


Figure 4.2a - Ground temperature of a sand dune (near Beni Abbes, Algeria) April 1-2, 1967

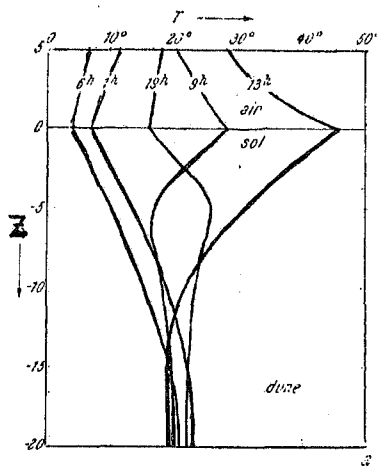


Figure 4.2b - Vertical profile of soil and air temperature near the surface during April 1, 1967 for a sand dune

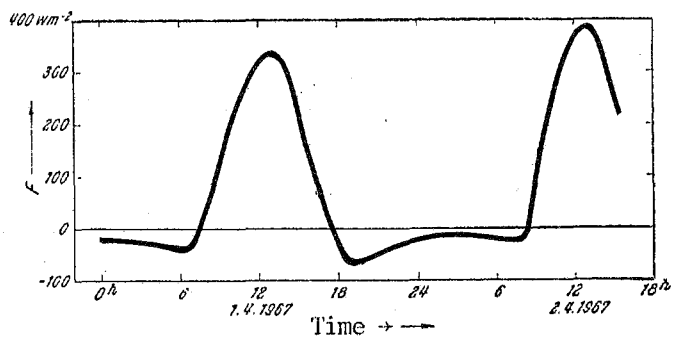
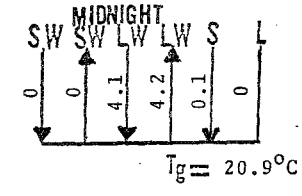
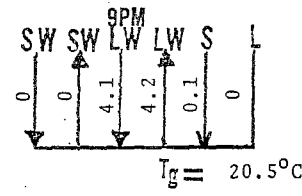
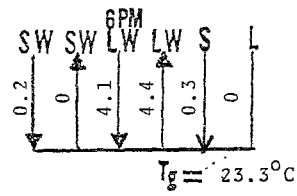
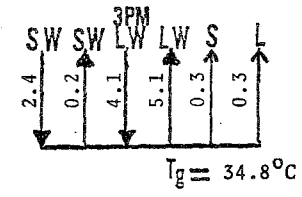
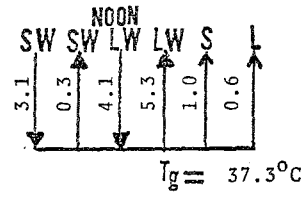
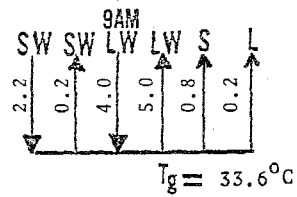
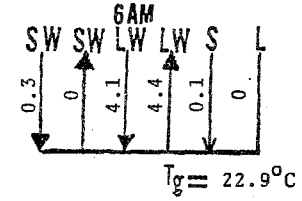
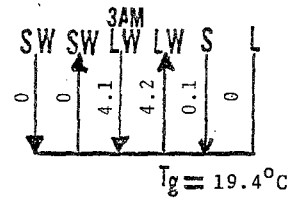
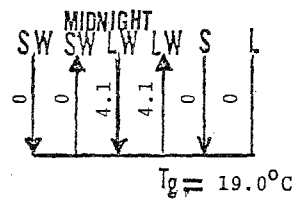
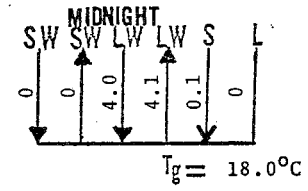
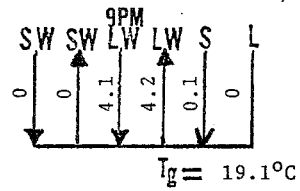
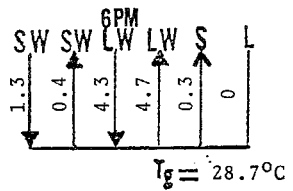
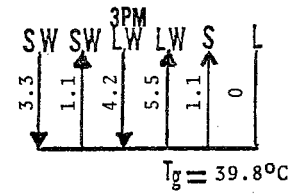
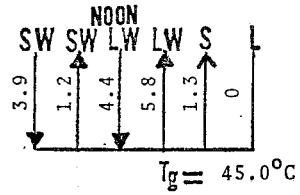
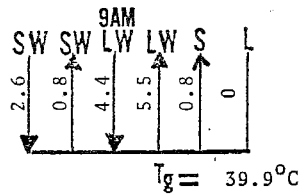
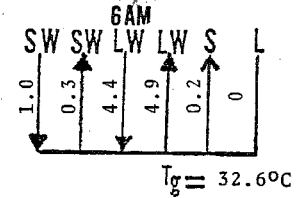
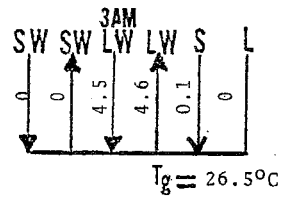
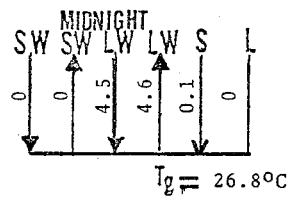


Figure 4.2c - Heat exchange at the ground/air interface by conduction and convection



date July 11
to July 12
albedo = 0.1
latitude = 6.6N
longitude = 3.4W

Figure 4.3a - Diurnal change of the heat balance at the Earth's surface over Africa. (SW = short wave, LW = long wave, S = sensible heat flux, L = latent heat flux, T_g = ground temperature)
Units (10^5 ergs $\text{cm}^{-2} \text{ s}^{-1} \equiv 10^2 \text{ W m}^{-2}$)



date July 11-12
 albedo = 0.3
 latitude = 13.5N
 longitude = 2.2W

Figure 4.3b - Diurnal change of the heat balance at the Earth's surface over Africa. (SW = short wave, LW = long wave, S = sensible heat flux, L = latent heat flux, T_g = ground temperature)
 Units ($10^5 \text{ ergs cm}^{-2} \text{ s}^{-1} \equiv 10^2 \text{ W m}^{-2}$)

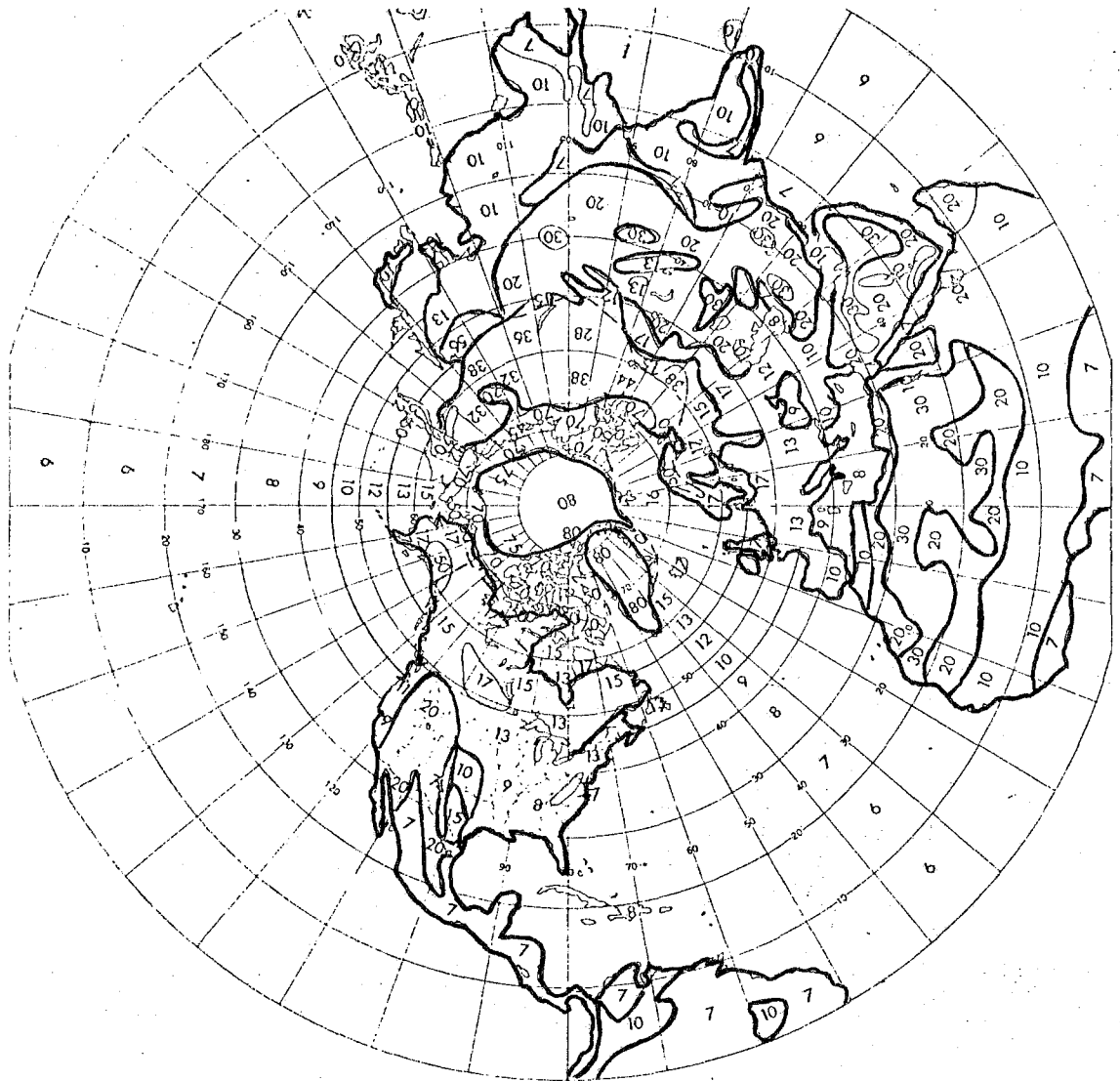


Figure 4.4 - "Surface albedo" during July based on Posey and Clapp (%)

4.6 Radiative heat balance at the top of the atmosphere

Measurements of the emitted long-wave radiation and the reflected solar radiation for the entire Earth/atmosphere system can be obtained by remote sensing from satellites. Sun-synchronous satellites pass over the same point of the Earth at the same local time each day. These measurements enable us to map the Earth's radiation budget and this type of mapping is very useful for climatic studies. Prominent studies in this area have been carried on by Professors Von der Haar, E. R. Raschke, V. Suomi and Dr. Jay Winston. Since Nimbus II was launched in 1966, reliable measures of these parameters have been mapped from the satellites. A knowledge of the solar constant ($1.95 \text{ cal cm}^{-2} \text{ min}^{-1}$) enables one to compare the incoming with the outgoing short-wave radiation. This in turn provides a mapping of the albedo of the planet. It is important to recognize that the atmospheric structure at any instant of time is a consequence of many non-linear feedback processes. The cloud cover is a consequence of dynamical processes and moisture distribution. The cloud cover has an important effect on the Earth's radiation budget. Here we shall illustrate some examples of the Earth's radiation budget during the northern summer season from a study of Raschke and Bandeen (1970).

Figure 4.4a illustrates the albedo for the first fifteen days of July 1966. The large values of albedo tend to occur over cloudy areas and over the deserts, while the clear oceanic areas tend to have small values. The two trade wind belts over the Atlantic and Pacific oceans show values as low as 10 %; low values are also found in the region of the monsoonal low level flows off the east African coast over the Indian ocean. The cloudy region of south-east Asia shows high values around 40 % to 50 % and the Sahara and Arabian desert regions also show high values, around 40 %. It should be noted that the patterns such as those shown here would change with the weather systems. In general, high-level cloudy overcasts have an albedo 40 % to 50 %. Deserts have similar high values. Clear oceanic areas have an albedo of around 7 %. Fractional cloud cover increases the values over the oceans.

Figure 4.4b illustrates the field of outgoing radiation for the same period. This radiation leaves the Earth and reflects a net cooling of the Earth/atmosphere system as a whole by this effect. There are two major subtropical belts, one around 30°N and the other around 20°S where large values are found. These are relatively cloud-free zones with low moisture and large surface temperatures. The deserts over the southwestern United States/Mexico, the Sahara, Arabia, and Pakistan all indicate large values around $0.40 \text{ cal cm}^{-2} \text{ min}^{-1}$. The region of the south central Pacific is usually characterized by subsidence and relatively warm oceans where large values are again found. The cloudy regions of the monsoons are characterized by values around 0.30 or less and the ITCZ has also values in the vicinity of 0.30.

Using satellite data one can also map the total absorbed solar radiation. This would be consistent with the albedo chart and the incoming solar radiation at normal incidence. Figure 4.4c is an illustration of this field for the same period as the above charts. The largest absorption of short-wave radiation during this fifteen day period during July 1966 occurs in the subtropics of the northern hemisphere. These values are around $0.50 \text{ cal cm}^{-2} \text{ min}^{-1}$. The largest absorption occurs over the summer hemisphere and this field is dominated by a pronounced zonal wave number 1. The northern summer tropical flow patterns and temperature fields are also dominated by a zonal wave number 1. These types of association are not usually easy to interpret.

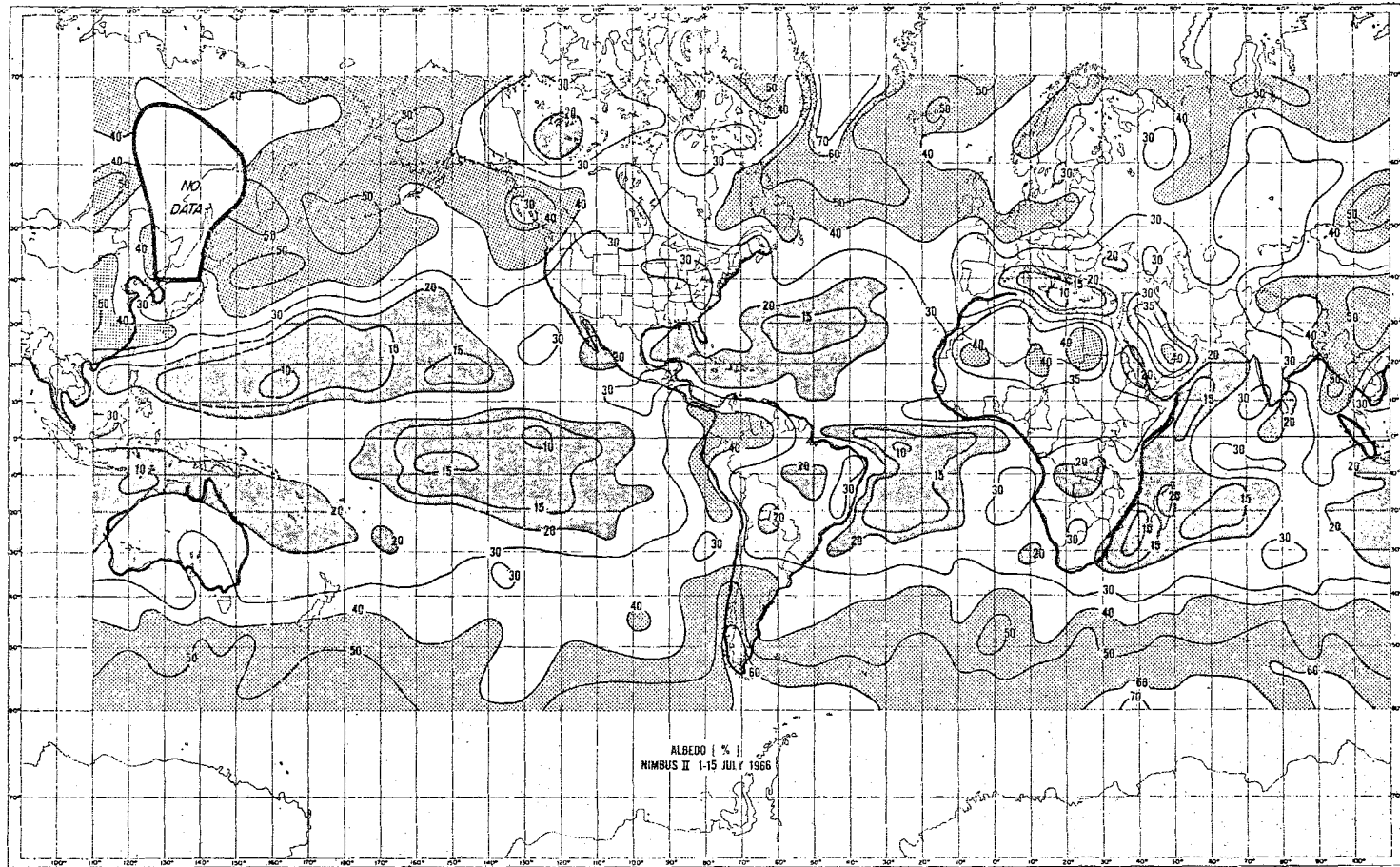


Figure 4.4a - E. Raschke and W. R. Bandeen

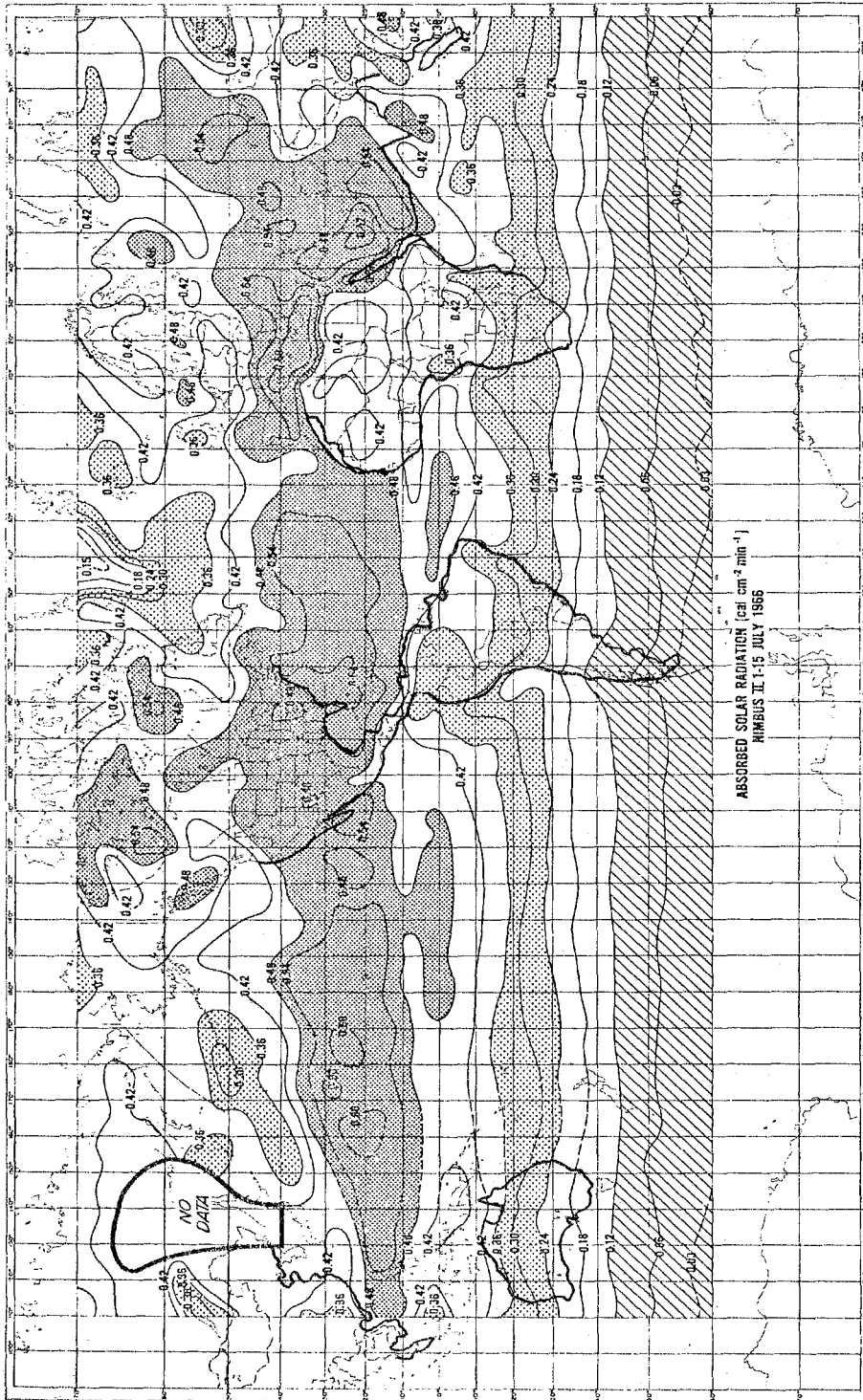


Figure 4.4c - E. Raschke and W. R. Bandeen

Our final figure in this sequence relating to the Earth's radiation budget (Figure 4.4d) illustrates the net radiation flux at the top of the atmosphere. The period here is the first two weeks of July 1966. North of roughly 10°S there is more radiation coming in compared to that going out at the top of the atmosphere. Over the subtropical oceans the net flux incoming is greater than $0.20 \text{ cal cm}^{-2} \text{ min}^{-1}$. The deserts of North Africa and Arabia are a major sink in the Earth's net radiation budget. This is a very striking result during the northern summer.

Although the deserts are so hot, this region radiates more energy to space than it receives. This is a consequence of the high albedo and the large nocturnal cooling.

If there were no land/ocean contrasts, then perhaps such large zonal asymmetries in these time-averaged fields would not be present. The southern hemisphere appears less asymmetric compared to the northern hemisphere. Regional mapping of fields, such as those shown here, have been published by a number of scientists. The usefulness of these products will become more and more evident as one collects many decades of such data.

In addition to the budget at the top of the atmosphere, the knowledge of the budget within the atmosphere and at the Earth's surface is extremely important for the understanding of tropical processes.

4.7 Radiation measurements with instrumented aircraft

In specially designed field experiments research aircraft play a major role in measuring the total infra-red and solar energy fluxes. Aircraft are capable of sampling cloud-free areas, dust layers, various types of recurrent cloud configurations noted in satellite photos and disturbed and undisturbed synoptic situations. In some of the sophisticated field experiments such as GATE, multiple-level flights were designed to study a number of relevant radiation problems. The kinds of instruments used in research aircraft are the following:

- (i) The Eppley Pyronometer for the measurement of upward and downward fluxes of short-wave radiation. It can also provide measurements as a function of the wavelength;
- (ii) The Eppley Pyrogeometer is frequently used to measure the upward and downward fluxes of long-wave radiation. In some aircraft, multichannel scanning radiometers are used to measure both the short- and long-wave radiation.

The reader interested in knowing more details of the instrumentation of aircraft is referred to GATE Report No. 4 (1973).

The sea-surface temperature or Earth's surface temperature (over land areas) can be obtained by a downward-pointed Eppley Pyrogeometer operating in the so-called window channel i.e. 9.5 to $11.5 \mu\text{m}$ band. It is, of course, essential that there are no intervening clouds, haze or smog conditions. The aircraft measurements should be calibrated against reliable surface-based observations to provide ground verification.

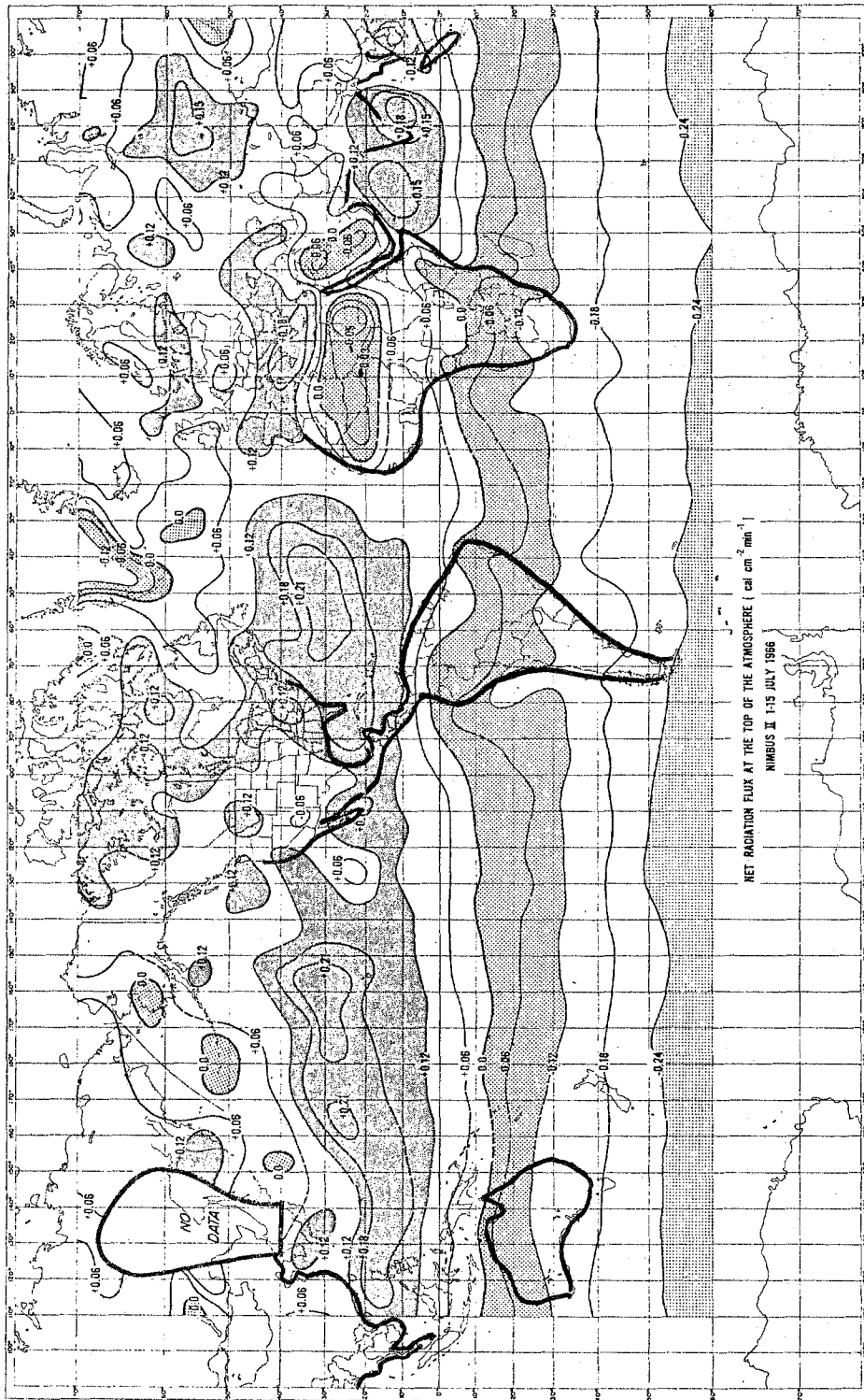


Figure 4.4d - E. Raschke and W. R. Bandeen

At present there is almost no other reliable means for obtaining detailed and accurate measurements of sea-surface temperatures for near coastal zones of upwelling where observations with a resolution of a few kilometres are usually desired. Future satellite-based measurements hold a similar promise in terms of accuracy and resolution. It is generally felt that sea-surface measurements should have an accuracy of at least 0.5°C.

Soviet research aircraft are known to carry spectrometers that provide an angular distribution of spectral radiation intensity in several wavelength bands such as: 2 to 5.5 μm (microns) at 1.5°, 6 to 14 μm at 1.5° and 0.4 to 2.5 μm at 30°.

Since aircraft are very expensive to use, it would simply not be possible to carry out field experiments whenever and wherever desirable. In the future, we must rely more and more on satellite-based observations and on detailed (or useful) numerical models which provide a four-dimensional view of the radiative processes. The main use of aircraft will thus lie in closing the gap in present uncertainties in numerical modelling and for providing some measure of ground verification for satellite-based observations.

We shall consider the typical magnitudes of the cooling and heating in the chapter on disturbances. The thermal amplitude of tropical waves is of the order of one degree in most oceanic pre-hurricane type disturbances. Here, the order of magnitude of radiative cooling is comparable to that of other processes on the time-scale of one to two days. This is one of many reasons why radiation processes need to be studied carefully in the tropics.

The research aircraft is a powerful platform in this regard since it is possible to obtain high accuracy in measurements of temperature, wind, and turbulent fluxes, etc. We discuss these elsewhere below.

4.8 Radiation measurements from balloon-borne radiometers

The Suomi-Kuhn radiometer (1958) is a very well-known instrument for measuring the total upward, downward and net long-wave radiative fluxes and cooling rates. It contains two identical radiometers mounted back to back. A blackened circular aluminium plate is connected to a circular polystyrene support and constitutes the temperature sensing surface. The upward and downward fluxes of long-wave radiation are measured by noting the energy balance of each sensing surface. According to Kuhn and Johnson (1966), the downward flux is given by the relation:

$$F_{\downarrow} = \epsilon \sigma \theta_{\epsilon}^4 + K_i \Delta \theta_i + K_{\epsilon} \Delta \theta_{\epsilon} + \lambda \Delta \theta_{\epsilon} / \Delta t$$

where σ is the Stephan-Boltzman constant

θ_{ϵ} is the temperature of the top plate

$\Delta \theta_i$ is the temperature difference between the surfaces of the two plates

K_i is a function of the thermal conductivity of the radiometer insulating material and the reflectivity of the polyethylene shields

ϵ is the emissivity of the sensor surface

$\Delta \theta_{\epsilon}, K_{\epsilon}$ are corresponding constants for a region which contains an air-cell between the sensor and the polyethylene

λ is a lag coefficient of the sensor system, and
 Δ_t is a time interval of measurement.

The student should clearly understand the physical interpretation of each of the terms of the above equation. This is a balance relation which determines the downward flux. There is an analogous equivalent formula for the upward flux.

Figure 4.5 shows the Suomi-Kuhn radiometer, based on a recent illustration from Ellingson (1972). It should be noted that this is a balloon-borne version of an instrument flown at night-time. The radiometer is generally launched with the radiosonde. One face of the radiometer faces down while the other faces up. The thermistors on the top and bottom plates transmit signals usually at 1/2 minute intervals; the entire radiometric instrument package is located roughly 30 metres below the balloon.

Standard errors in the estimate of net cooling rate for this kind of radiometer have been made by many scientists. It is generally felt that a cooling rate of roughly $2.5^{\circ}\text{C day}^{-1}$ may be in error by 10 % in these measurements (Kuhn and Johnson, 1966).

The student of tropical meteorology should also familiarize himself with the many other kinds of radiometers and their capabilities. The flat-plate radiometer is another frequently used instrument. Earlier we discussed numerical procedures for estimating the long-wave radiative cooling rates. It is desirable that such procedures be carefully tested and calibrated against observational methods. One should keep in perspective the kinds of error inherent in observations and in numerical methods.

4.9 Surface-based radiation instruments

The following are some of the standard radiation measuring instruments frequently used at surface radiation observing sites.

(i) The Pyrheliometer: This provides a measure of direct solar radiation at normal incidence. A number of such instruments are currently in use in tropical countries:

- (a) Angstrom compensation pyrheliometer,
- (b) Silver disc pyrheliometer,
- (c) Yanishevsky thermoelectric pyrheliometer,
- (d) Moll-Gorczyński pyrheliometer,
- (e) Eppley (normal incidence) pyrheliometer,
- (f) Linke-Fensner pyrheliometer,
- (g) Michelson pyrheliometer, and
- (h) Pacrad pyrheliometer.

The capabilities of these various instruments should be explored.

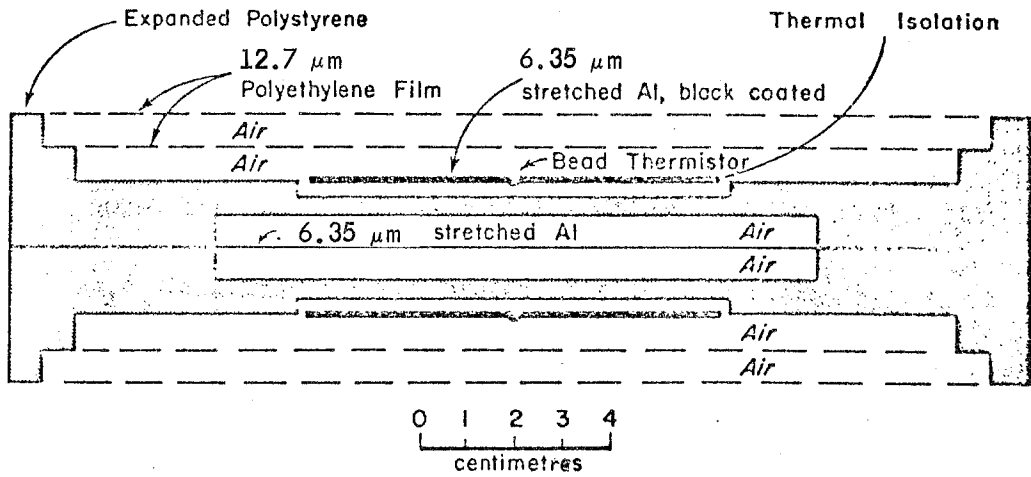


Figure 4.5 - Schematic vertical cross-section of the Suomi-Kuhn economical radiometer (From Kuhn and Sterns, 1971)

- (ii) The Pyranometer: This is a well-known instrument for the measurement of solar radiation received from the whole hemisphere. It is suitable for the measurement of the global or sky radiation. Some of the better-known instruments are the Moll-Gorczyński, Eppley models 15, 2, 849, Yanishevsky thermoelectric, Voloshine and Bimetallic actinographs of the Rabitzsch type pyranometer. Other frequently used instruments include:
- (iii) The Pyrgeometer: This instrument measures net atmospheric radiation on a horizontal "upward facing black surface" at the ambient air temperature.
- (iv) The Pyrradiometer: This instrument measures both solar and terrestrial radiation, i.e. the total radiation.
- (v) The net pyrradiometer: This instrument measures the net flux of downward and upward total (solar, terrestrial surface and atmospheric) radiation through a horizontal surface. The heat balance for a layer 2 to 5 metres below the Earth's surface is worth examining for the tropical land areas. The flux of short-wave radiation, S_o , should be measured, wherever possible, using pyrhelimeters. The flux of long-wave radiation, L_o , can be calculated from careful soil temperature measurements. The assumption here is that the Earth's surface radiates as a black body. One makes use of empirical formulae such as that given by Penman to estimate L_o from the soil temperature T_o . If T_o is the surface temperature of the soil (K), e is the surface vapour pressure in mb. Then, according to Penman, L_o can be expressed by:

$$L_o = \sigma T_o^4 (a - b \sqrt{e}) (c + d.S) \quad (4.9.1)$$

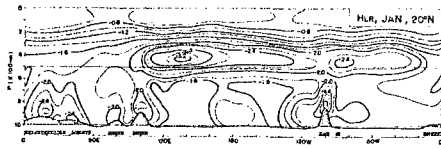
where σ is the Stephan-Boltzman constant, a , b , c and d have respectively the values 0.56, 0.092, 0.10 and 0.90, and S is the soil heat flux. The final units of L_o are Langley's day⁻¹ and for equatorial land areas $L_o \approx 150$ units.

The direct measurement of net radiation is generally very helpful in determining these empirical constants.

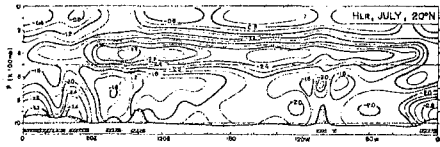
A number of these instruments are used in tropical countries.

4.10 Radiation climatology of the tropics

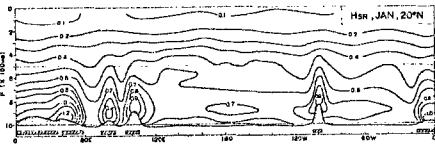
This chapter has emphasized the computational aspects of radiation since the value of the quantitative approach is now well-recognized. A student who has a few of these tools available can go a long way in setting up projects which provide a better understanding of weather systems. Next we shall present a brief outline of the radiation climatology of the tropical troposphere since this chapter on radiation would not be complete without a presentation of radiation climatology over the global



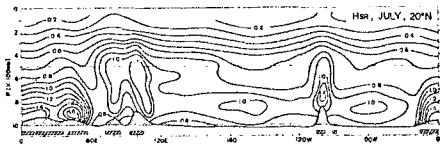
(a) Zonal cross-sections of heating rate by longwave radiation (H_{LR}) along $20^{\circ}N$, in January



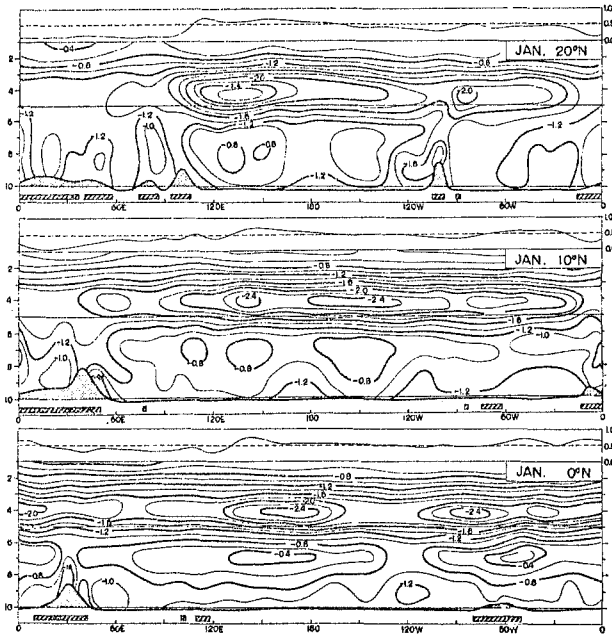
(b) Zonal cross-sections of heating rate by longwave radiation (H_{LR}) along $20^{\circ}N$, in July



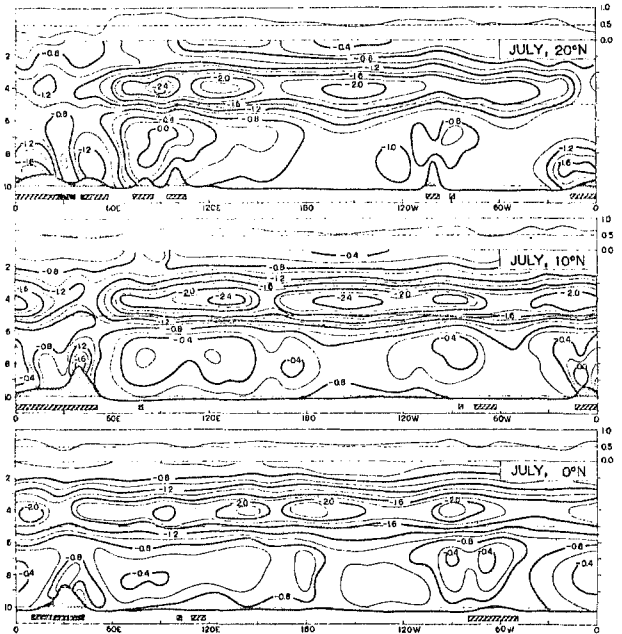
(c) Zonal cross-sections of heating rate by absorption of solar radiation (H_{SR}) along $20^{\circ}N$, in January



(d) Zonal cross-sections of heating rate by absorption of solar radiation (H_{SR}) along $20^{\circ}N$, in July



(e) Zonal cross-sections of heating rate by net radiative process ($H_{LR} + H_{SR}$) along $0^{\circ}N$, $10^{\circ}N$, $20^{\circ}N$, in January



(f) Zonal cross-sections of heating rate by net radiative process ($H_{LR} + H_{SR}$) along $0^{\circ}N$, $10^{\circ}N$, $20^{\circ}N$, in July

Figure 4.6 - based on Katayama (1967a)

tropics. For this purpose, we present some results based on a study by Katayama (1967). We illustrate vertical cross-sections, at the Equator, 10°N and 20°N (where available), of the heating due to absorption of solar radiation and the heating due to long-wave radiation (units $^{\circ}\text{C day}^{-1}$). Also presented are the sums, i.e. the net radiative warming over the tropics at 0° , 10° and 20°N . (See Figures 4.6a, b, c, d, e and f). The vertical scale is in hundreds of mb. It should be noted that the magnitude of the long-wave cooling is larger than that of the short-wave warming. The troposphere cools in the net. In fact, the cooling rate is large where the temperature is warm. As a consequence, the troposphere loses available potential energy. According to Katayama the largest cooling occurs near the 400 mb level, the intensity being around $2.5^{\circ}\text{C day}^{-1}$. The short-wave warming is largest in the low troposphere near the 900 mb level. The fields of Katayama need to be revised in the light of more recent observations, since they under-estimate the zonal asymmetry.

Chapter 5

THE TROPICAL BOUNDARY LAYER

In this chapter we shall present a brief outline of the tropical boundary layer. Its structure is very important for studies of tropical convection and tropical disturbances, especially hurricanes, the ITCZ, waves and low-level jets, all of which require a detailed knowledge of the lowest one kilometre of the atmosphere. In this region the air/sea interaction, the surface fluxes of heat, momentum and moisture, take place. These are somehow advected up to the cloud base which is located about one kilometre above the ocean surface. The clouds themselves have their own circulations that also constantly modify the structure of the lowest kilometre with their downdrafts.

The land area, referred to in the previous section, also contains a complex boundary layer where the surface fluxes of heat and moisture and the heat balance and ground hydrology are important. Understanding of these requires a knowledge of the boundary layer.

In this chapter we shall begin with the current status of observational knowledge. Some of the material presented here, although elementary, requires some knowledge of tropical convection and hence some reference to Chapter 6 may be necessary. We shall also present some empirical and dynamical aspects of the tropical boundary layer in this chapter. The rapid advances of observational, theoretical, modelling and numerical approaches in the field make it difficult to present a complete picture here and only an overview is given.

5.1 Empirical concepts

(a) The mixing-length concept

A perturbation quantity u' at height z is the difference between the value of the mean quantity \bar{u} at z and its value at some distance away at a level $z + \ell$, i.e.:

$$u' = \bar{u}(z + \ell) - \bar{u}(z) \quad (5.1)$$

A Taylor expansion gives $u' \approx \ell \frac{\partial \bar{u}}{\partial z}$

The quantity ℓ is representative of the local intensity of turbulence. Similar expressions can be written for θ' , ω' , and the moisture variable q' . If the flow is fully turbulent in three dimensions, then

$$|u'| \approx |v'| \approx |w'| \quad (5.2)$$

and hence

$$w' \approx \ell \left| \frac{\partial \bar{u}}{\partial z} \right| \quad (5.3)$$

The upward flux of momentum can be written as:

$$F_u = \rho \overline{w'u'} = - \rho \ell^2 \left(\frac{\partial u}{\partial z} \right) \left| \frac{\partial u}{\partial z} \right| \quad (5.4)$$

(The minus sign is introduced to ensure that the flux is positive down the flux gradient.)

The above formula gives a parameterization of the turbulent flux of momentum as a function of the variation of \bar{u} . However, it should be noted that \bar{u} varies very rapidly near the ground. Hence, it is still necessary to have some means of defining the profile of \bar{u} .

(b) The wind profile and surface drag

Near the ground one assumes that the mixing length is not related to the scale length of the large scale flow. It is assumed to be proportional to the distance from the ground, i.e.:

$$\ell \approx kz \quad (5.5)$$

The coefficient k is the Von Karman constant. The concept of friction velocity u_* is defined by the relation:

$$u_* = \left(\frac{1}{\rho} \right)^{1/2} (-F_{u0})^{1/2} \quad (5.6)$$

where ρ is the density of air and F_{u0} is the surface stress.

$$\text{Since } F_{u0} = - \rho \ell^2 \left(\frac{\partial \bar{u}}{\partial z} \right) \left| \frac{\partial \bar{u}}{\partial z} \right| \quad (5.7)$$

$$\text{we may write: } F_{u0}/\rho = \left[\ell \frac{\partial \bar{u}}{\partial z} \right]^2 \quad (5.8)$$

$$\text{or } u_*^2 = \left[kz \frac{\partial \bar{u}}{\partial z} \right]^2 \quad (5.9)$$

From this is obtained the logarithmic law:

$$\bar{u}(z) = \frac{u_*}{k} \ln(z/z_0) \quad (5.10)$$

where z_0 , the roughness length, is a characteristic of the underlying surface.

This formula relates the surface stress to the mean wind profile $\bar{u}(z)$ in the lowest layers, since:

$$\bar{u}(z) = \sqrt{-F_{u0}/\rho} \ 1/k \ln(z/z_0) \quad (5.11)$$

If values for the Von Karman constant k and the surface roughness z_0 are assumed then $\bar{u}(z)$ can be calculated from the above equation. It is important to recognize that empirical values are generally used for z_0 over tropical oceans, flat land areas and mountains; some typically assumed values are given in Table 5.1.

TABLE 5.1

Typical values of z_0		
Ocean	Flat land	Mountains
0.4	1.0	10.0
(based on Murakami <u>et al.</u> , 1970)		

The profile method has been used many times to estimate the magnitudes of turbulent momentum fluxes $\overline{u'w'}$. The procedure consists of making detailed measurements of the profile of $\bar{u}(z)$ from ship-tethered balloons, masts or towers. Knowing $\bar{u}(z)$, an estimate of $\overline{u'w'}$ is usually made from the relation:

$$\overline{u'w'} = - \ell^2 \left(\frac{\partial u}{\partial z} \right) \left| \frac{\partial u}{\partial z} \right| \quad (5.12)$$

Profile methods can also be used to estimate turbulent fluxes of heat and moisture.

(c) Bulk aerodynamic methods

These are the most widely-used methods for estimating transfers of heat, moisture and momentum from the ocean to the atmosphere. The flow over the oceans is always of the aerodynamically rough type, in which the ultimate transfer of momentum to the sea surface is through lateral pressure forces acting on the roughness elements of the surface. In the case of heat and water vapour, the transfer at the surface proceeds by molecular action. Upon integration, the flux equations for water vapour and heat lead respectively to:

$$E = \frac{\rho \kappa u_* (q_s - q_a)}{\ln \left(\frac{\kappa u_* a}{D} \right)} \quad \text{(surface evaporation rate)} \quad (5.13)$$

$$H = \frac{\rho \kappa u_* c_p (T_s - T_a)}{\ln \left(\frac{\kappa u_* a}{h} \right)} \quad \text{(surface sensible heat flux)} \quad (5.14)$$

Here the symbols denote the following:

D	Kinematic (molecular) viscosity
h	Thermometric conductivity
c _p	Specific heat of air at constant pressure
u*	Friction velocity
q _s , T _s	Specific humidity and temperature at the sea surface
q _a , T _a	Specific humidity and temperature at anemometer level (around 16 metres above mean sea level)
ρ	Density of air
κ	Von Karman's constant (0.4)
a	The anemometer height.

The above formulae are very frequently used for neutral conditions. Swinbank (1966) simplified these formulae for neutral as well as unstable cases and found that for the air-sea interaction problem we can approximate the fluxes by:

$E = 1.90 \times 10^{-8} U_a (q_s - q_a)$ and $H = 4.55 \times 10^{-9} U_a (T_s - T_a)$ where the units are: U_a ($m s^{-1}$), q_s, q_a ($g g^{-1}$), E ($g cm^{-2} s^{-1}$), H ($cal cm^{-2} s^{-1}$).

The momentum transfer is generally expressed as the shearing stress $\tau = \rho C_D U_a^2$. For neutral conditions, the logarithmic profile implies:

$$C_D = \kappa^2 (U_2 - U_1)^2 / U_a^2 \left[\ln \frac{z_2}{z_1} \right]^2$$

This requires wind observations at two levels, Z_1 and Z_2 . Deacon (1962) derived an empirical formula for C_D as a function of wind speed, viz.:

$$C_D = (1.00 + 0.07 U_a) 10^{-3}, \text{ where } U_a \text{ is measured in } m s^{-1}.$$

This formula has found wide application in numerical modelling. GATE observations suggest that this somewhat overestimates the magnitude of C_D . For most practical purposes the suggested value of C_D for wind speeds less than $15 m s^{-1}$ is 1.4×10^{-3} .

5.2 Observational aspects of the boundary layer

Observational studies of the turning of wind with height show that veering essentially dominates the flows north of the ITCZ in the northern hemisphere and backing is generally found south of the ITCZ. This was confirmed by data from the Line Island Experiment (2° to $6^\circ N$ and 157° to $162^\circ W$) by Robitaille and Zipser (1970) and also by Estoque (1971) from the Christmas Island data.

The tropical boundary layer characteristics in clear areas, undisturbed areas with shallow convection and disturbed areas are generally found to be quite different from each other.

In the clear or undisturbed trade wind regions the tropical boundary layer is known to have the following well-defined layers:

- (i) A surface layer in the lowest 20 metres where one finds a slight upward decrease of potential temperature and a decrease of moisture.
 - (ii) A mixed layer from a height of 20 metres above the surface to approximately 100 metres below the cloud base in which the potential temperature is nearly constant with height and the moisture content decreases only slightly with height.
 - (iii) A transitional layer located just above the well-mixed layer below cloud base. Here we note a stable layer with an increase of potential temperature and a decrease of moisture with height. This is usually a very thin layer with a thickness of the order of 100 metres or less.
 - (iv) A cloud layer usually several hundred metres deep where the moisture is still decreasing with height, the observed lapse rate in this region being close to the moist adiabatic lapse rate.
- and (v) An inversion layer on top of the cloud layer in which the potential temperature increases rapidly and the moisture decreases rapidly with height. Its base can be regarded as a reference level that defines the thickness of the boundary layer.

5.3 Recent observational findings

During the summer of 1977 some early observational findings in the planetary boundary layer of the Eastern Atlantic (the GATE Experiment) were reported by a number of workers in the field (J. Businger, W. Seguin, E. Augstein, M. Garstang, P. Lemone and others). A short summary of their important findings will be presented here. During the GATE Experiment the boundary layer of the tropical trade wind and ITCZ region was explored using ships, buoys, tethered balloons and research aircraft. The methods used for determining fluxes in the lowest kilometre included the bulk aerodynamic method, the profile method, the budget method and the dissipation method. (The drawings in this section were presented by the above authors).

Figure 5.1 illustrates the Meteor Profile Buoy. Instruments are mounted to measure profiles as well as eddy correlations at several heights in the lowest 8 metres. These types of buoy are extremely useful for determining the vertical structure of the boundary layer near the surface. There are different types of errors that arise in these types of measurements due to the orientation of the mast, rainfall on the anemometers and the effects of ocean waves.

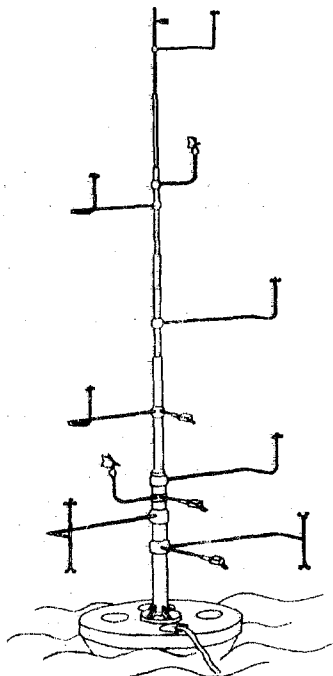


Figure 5.1 - Schematic drawing of the Meteor Profile Buoy

Garstang and his co-workers define 5 categories to illustrate the behaviour of the boundary layer. These are based on time-series of radar-echo percentage coverage. They can be defined as (1) stationary radar echoes with no precipitation, (2) growing radar echoes with precipitation, (3) decaying radar echoes, (4) disturbance wakes with no precipitation, and (5) stationary radar echoes with moderate convection.

The first stage signifies an undisturbed situation, the second stage the arrival of a disturbance, the third stage the period just after the passage of a disturbance, the fourth stage the wake some time after the disturbance passage and the final stage signifies a state close to the undisturbed situation. Figure 5.2 illustrates the mean vertical structure in the lowest 100 mb layer of the dry and moist static energy. (These parameters are defined in Chapter 6.) The moist static energy shows a substantial decrease from the undisturbed to the disturbed stage in the lowest km. The restoring of the mixed layer occurs with a gradual increase of static energy sequentially by classes. The dry static energy also shows a decrease as the disturbed state arrives over a station. Garstang also reported that the winds gradually increase in the lowest km from the undisturbed state (1) to the disturbed state (3).

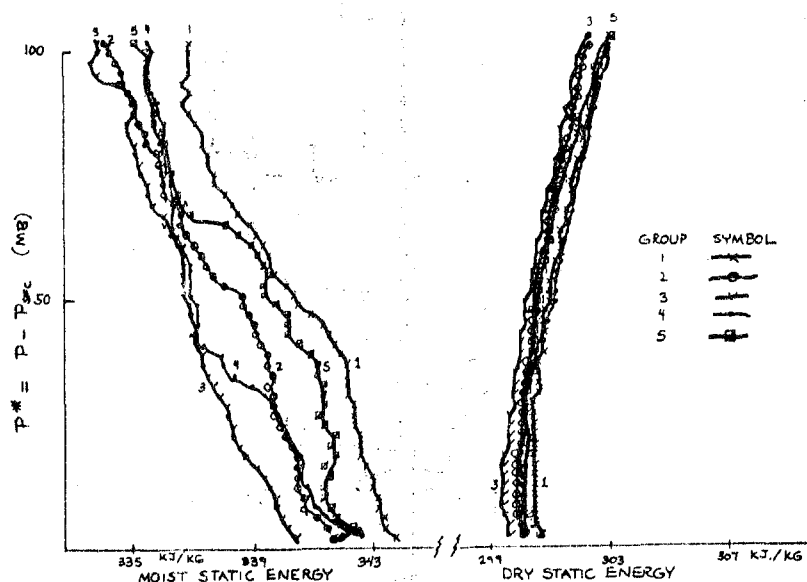


Figure 5.2 - Mean vertical structure by class (Fitzgerald) of moist and dry static energy

Figures 5.3 and 5.4 show typical sea-surface fluxes (during GATE) of the buoyancy, sensible heat and latent heat in undisturbed and disturbed conditions. We note here that the buoyancy flux increases from roughly 25 W m^{-2} to about 65 W m^{-2} from the undisturbed to the disturbed state. The corresponding increase for sensible heat flux is from 10 W m^{-2} to about 40 W m^{-2} while for the latent heat flux it is from roughly 80 W m^{-2} to 200 W m^{-2} . This is consistent with the gradual increase of the surface wind speed alluded to earlier. The height of the mixed layer is another important parameter. All the parameters are illustrated from GATE observations in Figures 5.5, 5.6 and 5.7. We note that the height of the mixed layer descends from roughly 550 metres (during the undisturbed state) to around 300 metres (in the moderately disturbed state). The lowering of the height of the mixed layer during disturbance passage is attributed to descending motion on large as well as small scales.

A long history of the height of the mixed layer for a 17-day period during GATE (from observations taken by 3 ships) is illustrated in Figure 5.7. It shows interesting fluctuations in both diurnal and 2- to 3-day time scales. The mean height is around 400 metres.

A summary of the structure of the planetary boundary layer is presented in Table 5.2, taken from the notes of the GATE Workshop (1977). Here the following parameters are contrasted for the disturbed and undisturbed categories:

- (i) Lifting condensation level,
- (ii) Cloud base height,
- (iii) Height of the base of the transition layer, and
- (iv) Depth of the transition layer.

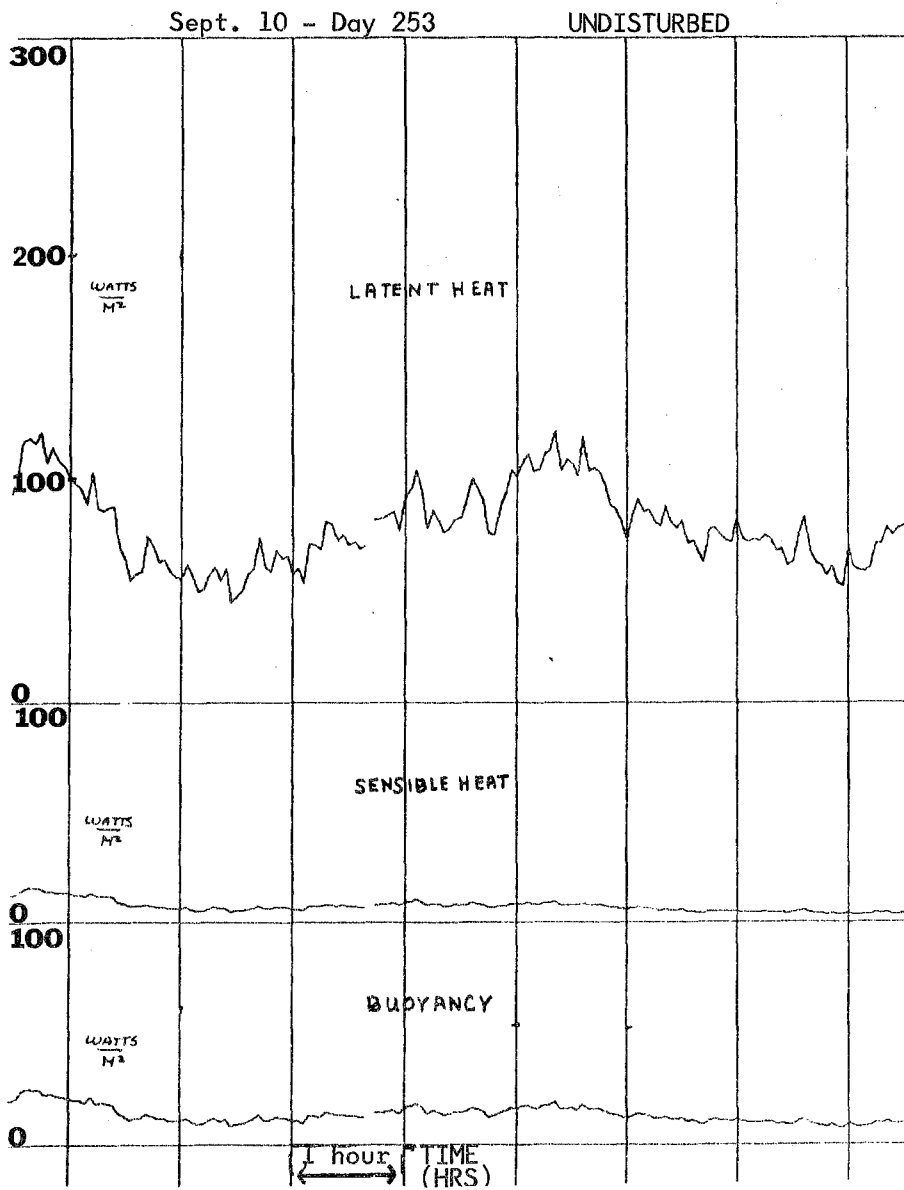


Figure 5.3 - Sea-surface fluxes during undisturbed conditions

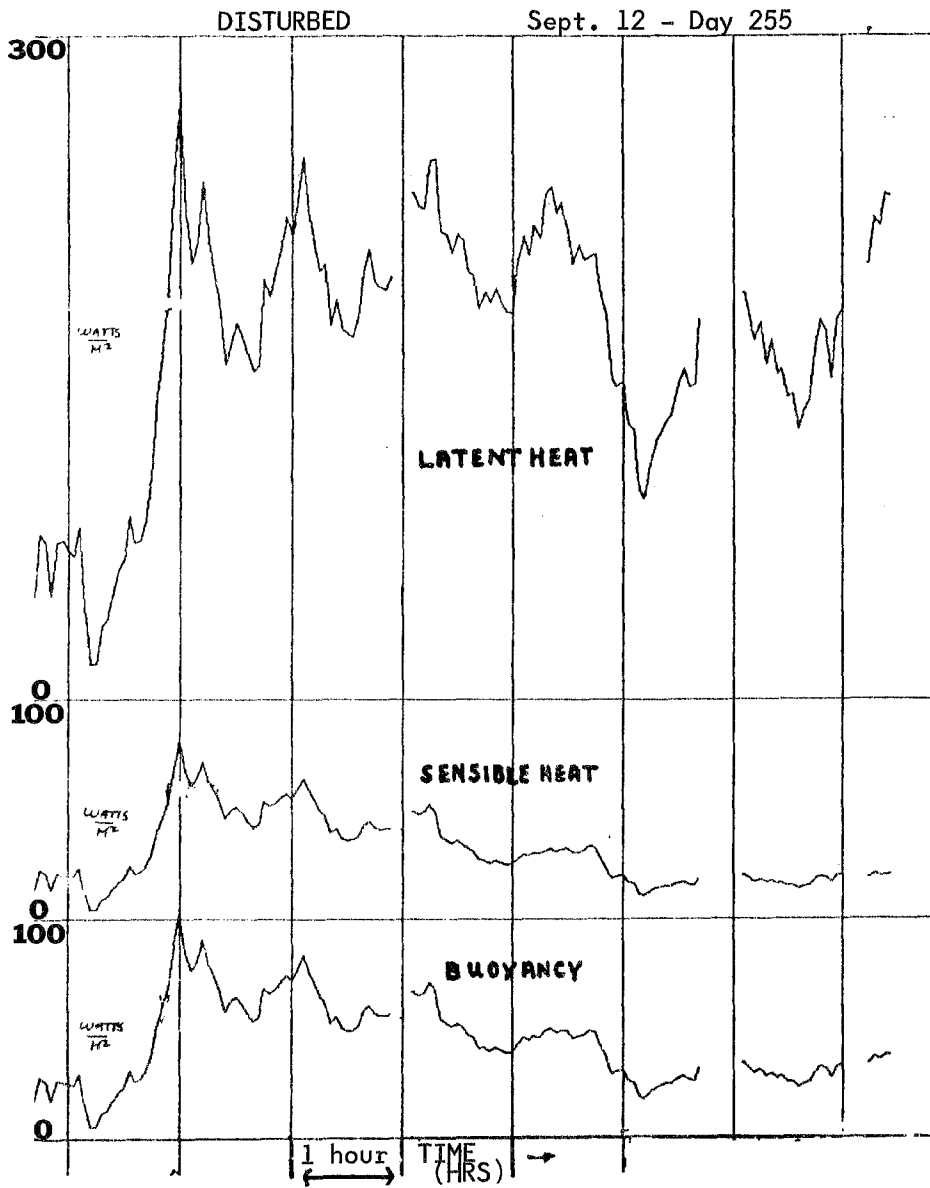


Figure 5.4 - Sea-surface fluxes in disturbed conditions

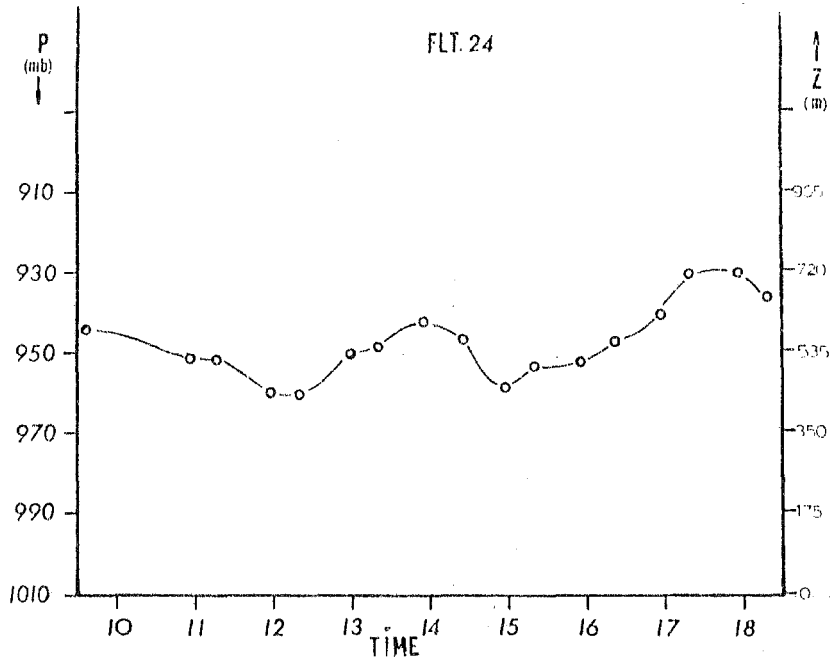


Figure 5.5 - Dallas BLIS, height of the undisturbed mixed layer

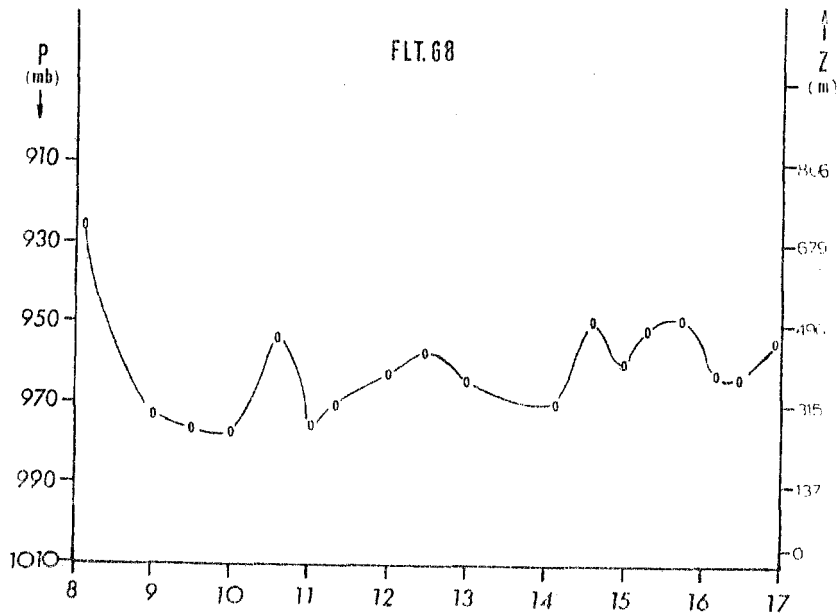


Figure 5.6 - Dallas BLIS, height of the moderately disturbed mixed layer

TABLE 5.2

Mean Transitional Layer and
Convective Cloud Base Properties

(Two classes)

Property	Undisturbed	Disturbed
Transitional layer depth	23 mb ± 15 mb 200 m ± 130 m	23 mb ± 14.7 mb 200 ± 130 m
Height of base of transitional layer	953 mb ± 11.4 mb 500 m ± 100 m	972 mb ± 14.9 mb 330 m ± 130 m
Height of cloud base	930 mb ± 14.6 mb 700 m ± 130 m	948 mb ± 19.0 mb 540 m ± 170 m
Height of lifting condensation level	937 mb ± 8.7 mb 640 m ± 75 m	952 mb ± 16.3 mb 510 m ± 140 m

TABLE 5.3

Values of I_1 , I_2 , and I_3 for GATE Phase III and Marshall Islands

n	GATE 85	Marshall Islands 390
I_1	180 ± 40 W m ⁻²	190 ± 10 W m ⁻²
I_2	280 ± 80 W m ⁻²	340 ± 20 W m ⁻²
I_3	460 ± 80 W m ⁻²	530 ± 20 W m ⁻²

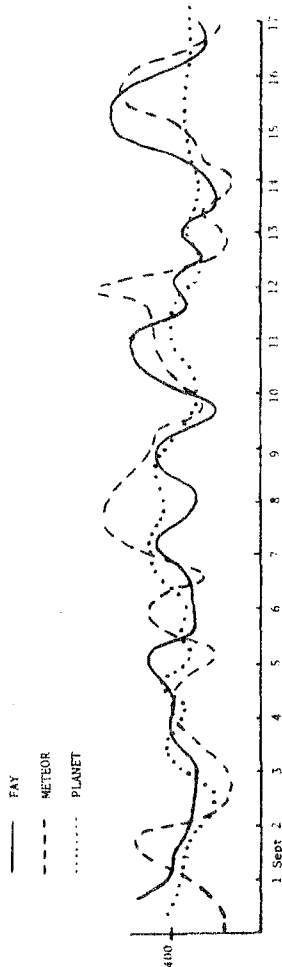


Figure 5.7 - Height of the mixed layer

A summary of the surface fluxes based on budget studies is provided in Table 5.3, again taken from the GATE Workshop (1977) results. The details of budget methods are presented in the next chapter. Here the symbols are:

- I_1 = total latent + sensible heat flux from the ocean;
- I_2 = surface precipitation minus evaporation in energy units; and
- I_3 = total net heating of the atmosphere due to condensation reaching the ground and sensible heat flux at the ocean.

Here a comparison of the results of the eastern Atlantic region (GATE) and the western Pacific region (Marshall Islands) are illustrated. It shows that convective activity (measured in terms of total condensation heating) was larger in the western Pacific ocean. This region is also further referred to in the next chapter.

The above results are taken entirely from the results of the GATE Workshop (1977). The final analysis of all of the GATE boundary layer sub-programme data will be of considerable interest. What is evident from much of this is that a more rational framework based on dynamical and thermodynamical principles is lacking. Hopefully, with further work such a basis will emerge to coordinate the many observational findings.

5.4 A simple model of the tropical boundary layer

The Ekman turning of wind with height may be inferred as follows. If the pressure field is prescribed and if it is assumed that the pressure gradients do not vary with height up to the gradient or geostrophic wind level, then the so-called Ekman problem can be solved. It is posed by the following equations:

$$-fv = -\frac{1}{\rho} \frac{\partial p}{\partial x} + \kappa \frac{\partial^2 u}{\partial z^2} \quad (5.15)$$

and

$$fu = -\frac{1}{\rho} \frac{\partial p}{\partial y} + \kappa \frac{\partial^2 v}{\partial z^2} \quad (5.16)$$

where κ is an eddy diffusion coefficient, together with the boundary conditions, $u \rightarrow u_g$ as $z \rightarrow \infty$ and $u, v = 0$ at $z = 0$,

This system was first solved by Akerblom for the atmosphere. The solution is of the form:

$$u = u_g (1 - e^{-\gamma z} \cos \gamma z) \quad (5.17)$$

and

$$v = u_g e^{-\gamma z} \sin \gamma z \quad (5.18)$$

where $\gamma = (f/2\kappa)^{1/2}$, and the geostrophic wind components are $(u_g, 0)$. The Ekman turning of wind with height is clockwise (veering) in the Northern Hemisphere and counterclockwise (backing) over the Southern Hemisphere. This analysis assumes that the geostrophic wind (and, consequently, the pressure gradient force) does not vary with height. To include such height variations (thermal wind effects) is a considerably more complicated matter but these can nevertheless be very important in all latitudes. If we assume that the variation of geostrophic wind with height is a constant in the boundary layer, we can prescribe the thermal wind corrections to the Ekman

formulae given above.

The corresponding formulae for u and v become:

$$u = (u_{go} - g/fT \frac{\partial T}{\partial y} z)(1 - e^{-\gamma z} \cos \gamma z) \quad (5.19)$$

and

$$v = (u_{go} - g/fT \frac{\partial T}{\partial y} z) e^{-\gamma z} \sin \gamma z \quad (5.20)$$

It has been found in practice that the thermal wind corrections provide an improvement when there are large cold surges and horizontal temperature contrasts. Applications of the above formulae have been described by Mendenhall (1967). Figure 5.8 from his study shows the close agreement between the observed and the calculated wind veer at Swan Island.

5.5 Scale analysis of the large-scale tropical boundary layer

The horizontal equations of motion can be scaled in an interesting manner to define in a gross way some realizable boundary layer structures. Here we shall follow the procedure outlined by Mahrt and Young (1972).

The zonal equation of motion may be written in the form:

$$\frac{\partial u}{\partial t} + u \frac{\partial u}{\partial x} + v \frac{\partial u}{\partial y} - fv = -g \frac{\partial z}{\partial x} + F_x \quad (5.21)$$

or

$$T + A + C = P + F \quad (5.22)$$

We shall use the following scaling to non-dimensionalize the above equation:

$$\begin{aligned} u &= Uu' \\ \frac{\partial}{\partial x} &= (U/\beta)^{1/2} \frac{\partial}{\partial x'} \\ f &= \beta y \quad (\text{usual beta plane approximation}) \\ \partial/\partial t &= \omega \partial/\partial t' \end{aligned}$$

where ω is a characteristic frequency. In the boundary layer P and F are expected to be dominant terms and we wish to compare T , A and C with these for different ranges of values of ω . The scaling of the above equations gives:

$$\omega U \left(\frac{\partial u'}{\partial t'} \right) + \frac{U^2}{(U/\beta)^{1/2}} \left[u' \frac{\partial u'}{\partial x'} + v' \frac{\partial u'}{\partial y'} \right] - f U v' = P + F \quad (5.23)$$

or

$$\omega \left(\frac{\partial u'}{\partial t'} \right) + (U\beta)^{1/2} \left[u' \frac{\partial u'}{\partial x'} + v' \frac{\partial u'}{\partial y'} \right] - \beta y v' = \frac{P}{U} + \frac{F}{U} \quad (5.24)$$

The vertical advection term is assumed to be small.

There are three time scales here, viz.:

$$\omega^{-1}, \quad (U\beta)^{-1/2} \quad \text{and} \quad (\beta y)^{-1}$$

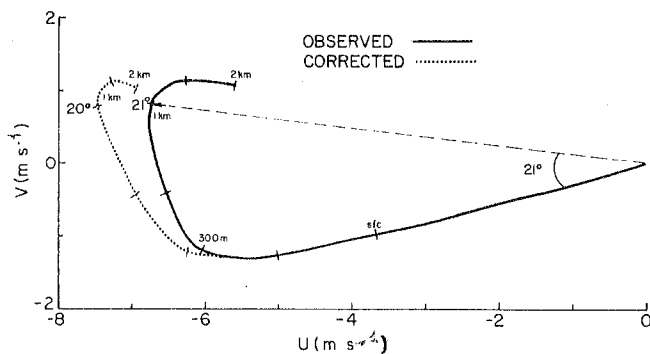


Figure 5.8 - Observed and geostrophically corrected hodographs at Swan Island derived from 2070 observations. Elevation marks are shown at the surface, 150, 300, 500, 1000, 1500, and 2000 m. Veering angle between the surface and 1000 m is noted on each hodograph. Observed veering is 21° and corrected veering, 20°

Consider the following three cases:

i) If $\omega < \beta y$ and $(U\beta)^{1/2} < \beta y$, then C, P, F , are the dominant terms, i.e., we expect an Ekman balance.

ii) Next let us consider the case:

$$f = \beta y < (U\beta)^{1/2}$$

$$\omega < (U\beta)^{1/2}$$

In this case the advective term A balances $P + F$ and we have what is called an advective or drift boundary layer.

iii) Finally, we may consider the case:

$$\omega > \beta y$$

$$\omega > (U\beta)^{1/2}$$

In this case the time dependent (i.e., $\partial/\partial t$ term) becomes dominant and there is a balance $T = P + F$. This is called a Stokes régime.

Young has illustrated these three régimes in an interesting diagram.

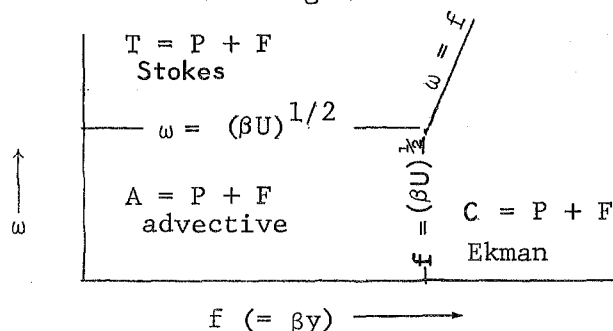


Figure 5.9 Régimes in the boundary layer

In the large-scale tropical boundary layer one is often interested in knowing which of the above three cases is the appropriate one in a given region. There also exist, of course, broad transition regions where one would expect to see the overlapping influence of two of the above regions at the same time. In middle latitudes the Ekman balance is a characteristic feature in the boundary layer (i.e., the lowest kilometre). In the Northern Hemisphere a veering (a clockwise turning) of wind with height is generally found, and in the Southern Hemisphere one should find a backing (or counterclockwise turning) with height.

5.6 Cross-equatorial flows and planetary boundary layer dynamics

An interesting series of numerical experiments on the dynamical structure of the boundary layer was carried out by Mahrt and Young (1972). Here the solutions of the following system of boundary layer equations were integrated for a prescribed pressure field:

Equations of motion:

$$\frac{\partial u}{\partial t} = -v \frac{\partial u}{\partial y} - w \frac{\partial u}{\partial z} + fv - 1/\rho_0 \frac{\partial p}{\partial x} + \kappa \frac{\partial^2 u}{\partial z^2} \quad (5.25)$$

$$\frac{\partial v}{\partial t} = -v \frac{\partial v}{\partial y} - w \frac{\partial v}{\partial z} + fu - 1/\rho_0 \frac{\partial p}{\partial y} + \kappa \frac{\partial^2 v}{\partial z^2} \quad (5.26)$$

Mass continuity equation:

$$\frac{\partial v}{\partial y} + \frac{\partial w}{\partial z} = 0 \quad (5.27)$$

The equations describe flows in a meridional vertical plane. The eddy diffusion coefficient is prescribed and the pressure field is given as a linear field of the form $p = ax + by + c$; the above system of three equations thus contains three unknowns, namely u , v and w . One integrates the above system from an initial Ekman solution. This is not possible near the Equator where a linear interpolation of the Ekman solution on either side of the Equator is necessary to define the initial wind field. The meridional plane usually extends from the middle latitudes of the two hemispheres and at the northern and southern boundaries one uses time invariant Ekman solutions to define the boundary conditions. We have already shown how one can express the Ekman profile as a function of the given pressure field. A good horizontal and vertical resolution is important for this numerical problem. Mahrt used a vertical resolution of 200 metres and a horizontal resolution of 50 km in his integration of the above system of equations.

Here we shall illustrate a particular application of Mahrt's framework that was recently carried out by Krishnamurti and Wong (1979) as part of the study of the boundary layer of the east African low-level jet of the northern summer. In this study the meridional distribution of the pressure gradient force was prescribed along 60°E . The model extends from 15° to 25°N . The major results of the boundary layer simulations are shown in Figs. 5.10 and 5.11. Figure 5.10 illustrates the horizontal winds in the meridional plane at 60°E , showing the cross-equatorial flows and a low level jet (the Somali jet) near 12°N . The simulated winds are reasonable when compared with observations (see Chapter 14). Knowing the long-term steady-state motion field one can compute the various terms in the equations of motion. The balance of forces in the boundary layer is found to settle to a set of values quite different from that of the initial Ekman layer (Coriolis + pressure gradient + friction ≈ 0). This is shown in Figure 5.11. Here, the simulations show a surface layer near the ground everywhere and the essential balance of forces is between the pressure gradient and friction forces (i.e. $P + F \approx 0$). Above the surface layer there is a friction layer where the essential balance of forces is of Ekman type (Coriolis + pressure gradient + friction ≈ 0) in the subtropics. However, nearer the Equator, an advective type boundary layer is found where the balance of forces is between horizontal advection, pressure gradient and friction terms at the Equator and among the horizontal advection, Coriolis, pressure gradient and frictional terms just away from the Equator. This is called an advective boundary layer. Aside from the important equatorial regions, there are two other features of interest in the boundary layer of this region: the Somali jet and an ITCZ over the northern Arabian sea. The calculations show that the Somali jet is located at the poleward edge of the region where the horizontal advective term becomes less important. The ITCZ is noted to form in the general region between the advective and Ekman boundary layers, a result first noted by Mahrt. The aforementioned study and the balance of force

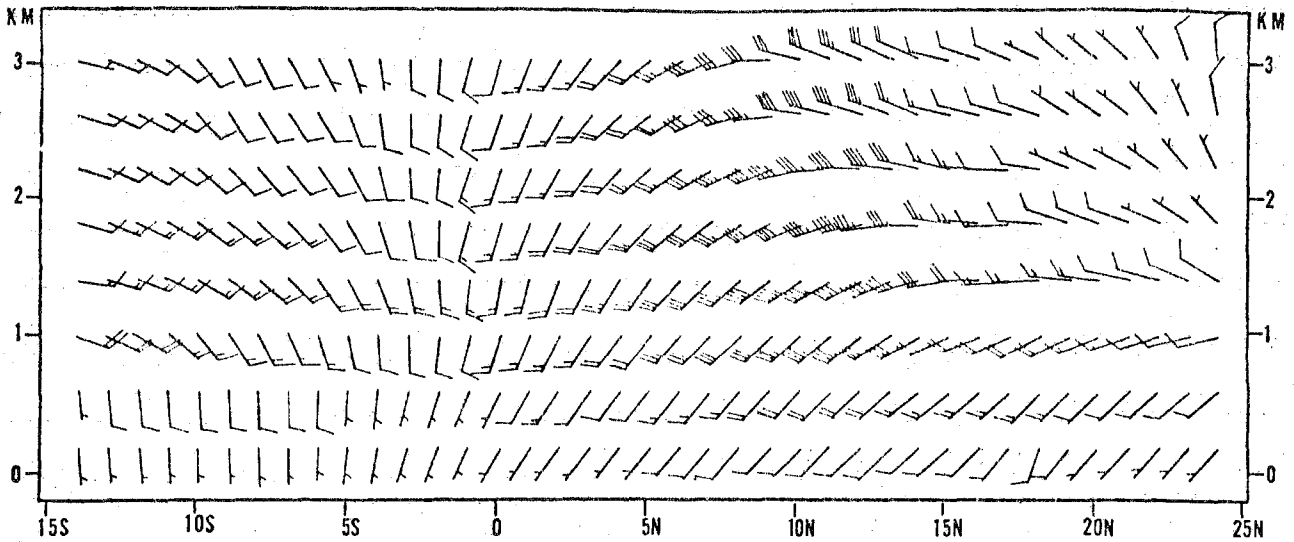


Figure 5.10 - Horizontal wind barbs in a meridional vertical plane for an experiment with a height-dependent diffusion coefficient K . The wind barbs are in the standard meteorological plotting convention, units: knots

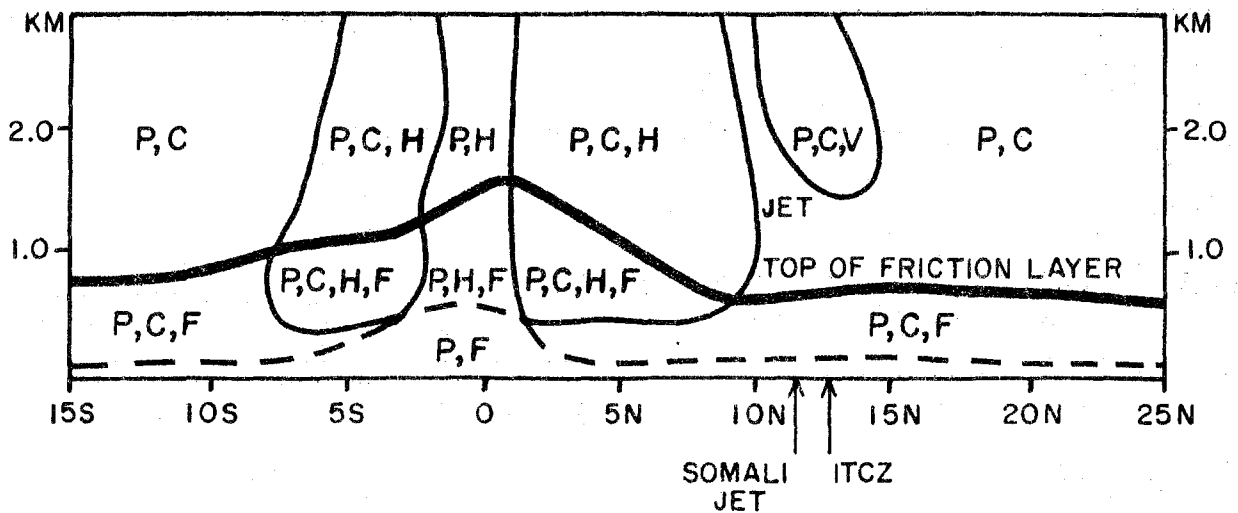


Figure 5.11 - A schematic illustration of various régimes and the significant "forces" in the boundary layer, from the solution at day 50. The letters P, C, H, V and F, respectively, stand for the pressure gradient, Coriolis, horizontal advection, vertical advection and the frictional terms. In the different régimes only those relative forces are identified whose magnitudes exceed 0.3. The dashed line indicates the top of the surface layer

diagram (Fig. 5.11) are very pertinent to the tropical boundary layer. This framework is not suited for investigating time variations of the boundary layer. By prescribing a pressure force, this framework also limits investigations of thermodynamic inputs such as air-sea interaction, diurnal variations, etc. Work in these important areas of the boundary layer structure would require a different approach.

Chapter 6

TROPICAL CUMULUS CONVECTION

6.1 Introduction

Convection is a central topic in tropical meteorology. Most of the tropical rainfall occurs from convective clouds. The oceanic undisturbed trade wind belt is covered with shallow cumulus clouds that reach up to the inversion level. These are non-precipitating cumuli. In tropical disturbances such as waves, vorticies and the ITCZ one finds an abundance of shallow as well as tall cumulus clouds. An understanding of the cloud population is important. In this chapter we shall emphasize some of the newer aspects of the important role of cumulus clouds for the maintenance of large-scale tropical disturbances. Tropical squall systems are another major convective-type disturbance which will be addressed in the section on African disturbances.

The geostationary satellite has become a powerful platform for providing very high resolution cloud imagery. We shall refer to these products quite frequently in these notes. Figures 6.1a and b are two recent photographs from geostationary satellites showing the cloud cover over the tropical belt. They are on two different resolutions. Among the many cloud features, the ITCZ and cloud clusters are easy to identify on these photographs.

In the budget studies of tropical disturbances the role of convection is being recognized as being very important. Innocuous westward motion of tropical disturbances occurs under very sensitive balances of mass, momentum, moisture, vorticity and heat. The role of convection is important in the dynamics of these motions. This chapter will emphasize some of these newer concepts in this area.

6.2 Parcel and slice methods

The student of tropical meteorology is expected to be familiar with the parcel and the slice methods of estimating stability. These are important and very fundamental concepts.

Given a sounding of temperature and dew point on a thermodynamic diagram, the parcel method consists in lifting a parcel of air from some pressure level along a dry adiabat until saturation is reached. Next it is lifted along a moist adiabat to the top of the sounding level. At those levels where the temperature of the lifted parcel is warmer than the environmental sounding, we state that there is parcel instability.



Figure 6.1a

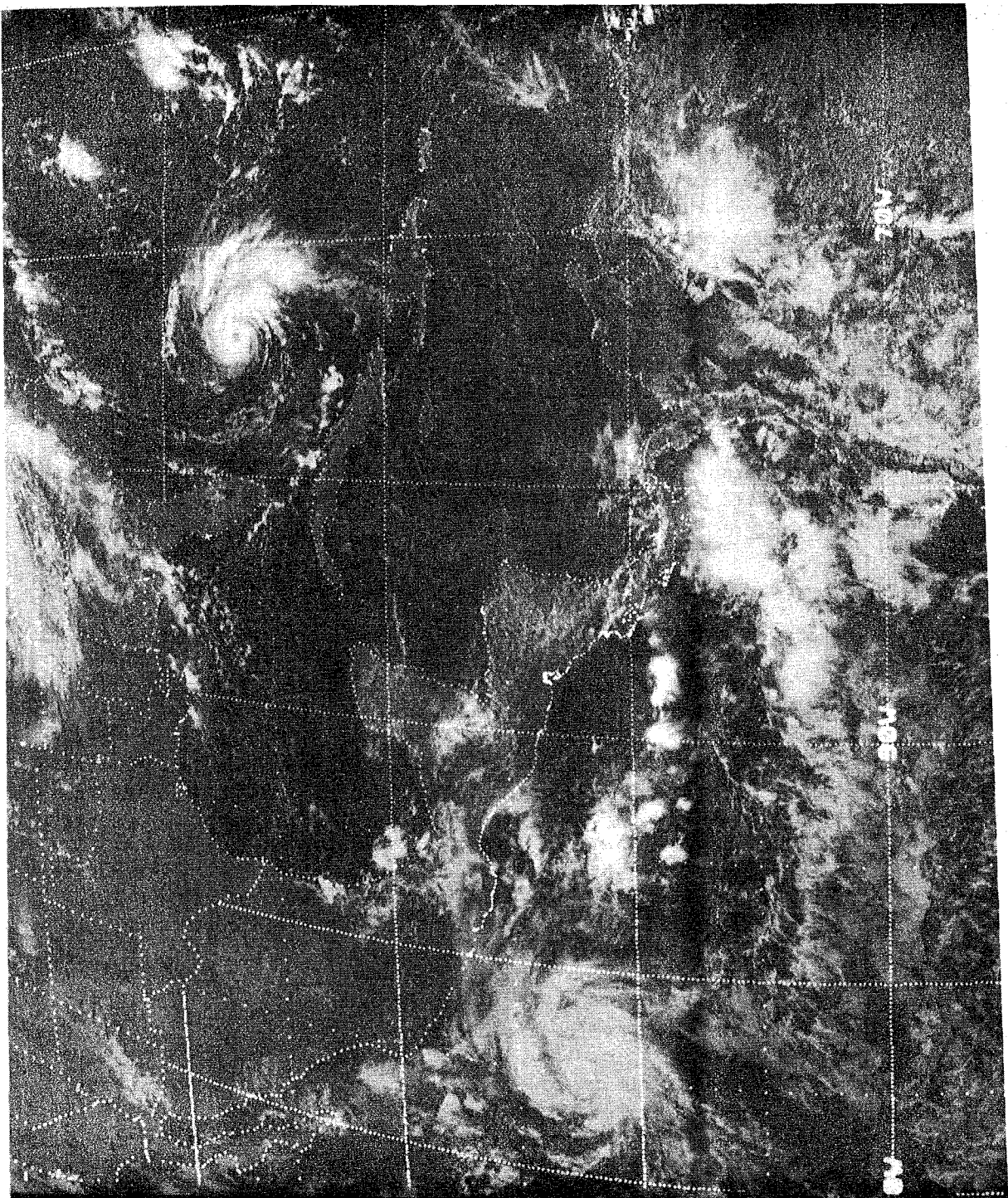


Figure 6.1b

If γ_d is the dry adiabatic lapse rate, γ is the prevailing lapse rate and γ_m is the moist adiabatic lapse rate, then the following definitions are important:

$\gamma > \gamma_d > \gamma_m$	absolute instability
$\gamma_d > \gamma > \gamma_m$	conditional instability
$\gamma_d > \gamma_m > \gamma$	absolute stability.

The tropical atmosphere on the large scale is nearly everywhere conditionally unstable below the 700 mb level. Many times the soundings in the lower troposphere may show the deceptive appearance of being stable; however, if an entire layer of the sounding were lifted to saturation via dry and moist adiabatic ascent, the lifted layer may exhibit absolute instability. Once a layer is lifted to such a level, it would become buoyant and vertical accelerations would be likely to occur. A quick check on a thermodynamic diagram can be very useful in this regard. The lifting of the layer, alluded to here, is usually accomplished by the passage of a disturbance, via its low level convergence and rising motions. The pre-existing weak disturbances are very important candidates for triggering convection over large areas which in turn can enhance the growth of the disturbance. The buoyancy acceleration of the parcel method is usually expressed by the relation:

$$\frac{dw}{dt} = g \frac{(T' - T)}{T} \quad (6.1)$$

where T' and T are the parcel and the ambient air virtual temperatures respectively.

The slice method is receiving more and more attention in tropical meteorology because it takes into account the thermodynamic change of the environment due to compensating descending motions around the regions of descent. This was first introduced by Bjerknes (1938). An excellent survey of this classical method is given in Petterssen (1956, Volume II, page 142) hence it will not be repeated here. In this section we will make use of more recent applications of these same principles.

We shall next review a simple cloud model which makes use of the buoyancy principle for the growth of a shallow cumulus cloud. We shall follow this up with some newer ideas on the problem of parameterization of cumulus which are very relevant to the studies of large-scale tropical circulations.

6.3 A simple cloud model (Murray and Anderson, 1965)

One of the simplest cloud models allows the formation of liquid water (cloud) if supersaturation occurs, and the liquid water (cloud) to evaporate if its environment is not saturated. In this simple model no rain fallout is permitted. The total moisture (liquid water and water vapour) over the domain in the phase change process is conserved. The basic equations for such a model are the so-called Boussinesq equations. Here we shall present an outline of the two-dimensional cloud model and show some preliminary results of interest. We shall not present more complex models. However, the interested student should look at published papers in this area.

Vorticity equation:

$$\frac{\partial}{\partial t} \nabla^2 \psi = - J(\psi, \nabla^2 \psi) + \frac{g}{T_M} \frac{\partial T'}{\partial x} + \nu_M \nabla^4 \psi \quad (6.2)$$

Local change
of
vorticity = Vorticity Advection + Buoyancy Term + Friction

Here ψ is a stream function in the vertical plane (x, z) where T_M is a mean temperature for the entire domain and is a constant. T' is a departure of the local temperature T from a horizontal (x) average. ν_M is a coefficient of eddy flux of momentum.

The stream function is related to the u and w velocity components via the relations:

$$\begin{aligned} \frac{\partial \psi}{\partial z} &= u \\ - \frac{\partial \psi}{\partial x} &= w \end{aligned} \quad (6.3)$$

and the continuity equation

$$\frac{\partial u}{\partial x} + \frac{\partial w}{\partial z} = 0 \quad \text{is satisfied by this stream function.}$$

If there is a buoyancy field

$$\frac{\partial T'}{\partial x} > 0$$

then it would contribute to vorticity generation, $\frac{\partial}{\partial t} \nabla^2 \psi > 0$

This increase of vorticity will, in general, lead to a cellular stream function geometry on the x - z plane with an enhancement of the velocities u and w in different parts of the buoyant cell. If there is an initial state of no motion, buoyancy can initiate a motion. If T' is large and positive locally, then on either side of it there would be regions of $\frac{\partial T'}{\partial x} > 0$ and $\frac{\partial T'}{\partial x} < 0$ respectively. The rising motion that

results at the centre will have two sinking lobes on either side. Any numerical model that is designed to study the time evolution of a phenomenon should have the following ingredients:

- (i) Independent variables;
- (ii) Dependent variables;
- (iii) Closed system of equations;
- (iv) Finite differencing schemes for above;
- (v) Boundary conditions; and
- (vi) Initial conditions.

For our problem, x, z, t are the independent variables. The dependent variables will be u, w, ψ, T', q_l, q_v , where q_l, q_v are, respectively, the specific liquid water content and humidity. We need six equations for the six unknowns to close this system.

The thermal energy equation is taken as:

$$\frac{dT}{dt} = -w \frac{g}{c_p} + \left(\frac{dT}{dt}\right)_{ph} + v_T \nabla^2 T \quad (6.4)$$

where

$$T = T_M + T_0(z) + T'$$

T_0 is the initial stratification of temperature of the undisturbed state and is known. Equation (6.4) describes the change of T_0 . $\left(\frac{dT}{dt}\right)_{ph}$ is the diabatic change of temperature due to (phase change) condensation heating or evaporative cooling. The equations for liquid water and water vapour respectively, are:

$$\frac{dq_l}{dt} = \left(\frac{dq_l}{dt}\right)_{ph} + v_q \nabla^2 q_l \quad (6.5)$$

$$\frac{dq_v}{dt} = \left(\frac{dq_v}{dt}\right)_{ph} + v_q \nabla^2 q_v \quad (6.6)$$

Equations (6.2) through (6.6) constitute the closed system provided we adequately define the phase change terms. They are estimated as follows:

One estimates a new value of q_v from the equation

$$\frac{\partial q_v}{\partial t} = - \left(u \frac{\partial q_v}{\partial x} + w \frac{\partial q_v}{\partial z} \right) + v_q \nabla^2 q_v \quad (6.7)$$

If $q_v > q_{vs}$, where q_{vs} is the saturation value, then

$$\left[\frac{dq_v}{dt}\right]_{ph} = - \frac{(q_v - q_{vs})}{\Delta t} \quad (6.8)$$

Once saturation is reached, the local change in equation (6.7) is set to zero. Furthermore, one sets

$$\left(\frac{dq_l}{dt}\right)_{ph} = - \left(\frac{dq_v}{dt}\right)_{ph}$$

Thus saturation results in removal of water vapour and the formation of an equivalent amount of liquid water. Liquid water in an unsaturated environment evaporates until the environment is saturated. This is given by the case:

$$\left[\frac{dq_l}{dt}\right]_{ph} = - \frac{(q_{vs} - q_v)}{\Delta t} \quad (6.9)$$

(6.9) is used in equation (6.5) to estimate $\frac{dq_l}{dt}$. Again an equivalent increase in water vapour is defined by the relation:

$$\left(\frac{dq_v}{dt}\right)_{ph} = - \left(\frac{dq_l}{dt}\right)_{ph} \quad (6.10)$$

The condensation heating or evaporative cooling for the thermal equation is next defined by the statement:

$$C_p \left(\frac{dT}{dt} \right)_{ph} = L \left(\frac{dq_v}{dt} \right)_{ph} = L \left(\frac{dq_l}{dt} \right)_{ph} \quad (6.11)$$

The diffusion terms are needed for the suppression of two grid length waves which would otherwise grow to an unrealistic size. We shall not discuss these here.

The system is now closed. The solution procedure involves the following steps:

- (i) An initial buoyancy and an initial state of no motion are specified to start the computation. The initial buoyancy can be in the T' field or it can be introduced via the moisture and thus in the initial horizontal gradient of virtual temperature.
- (ii) The vorticity equation (6.2) yields a new value of the stream function; this in turn gives the values of u and w from equation (6.3).
- (iii) The two moisture equations provide new values of q_l and q_v .
- (iv) The thermal equations (6.4) provide a prediction of the temperature T and thus the temperature deviation T' field.

Initial and boundary conditions and domain definition

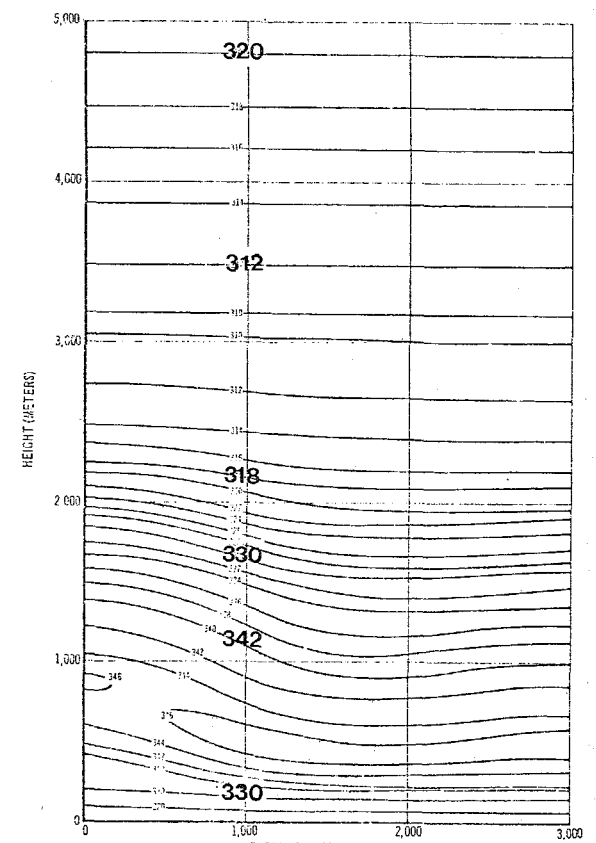
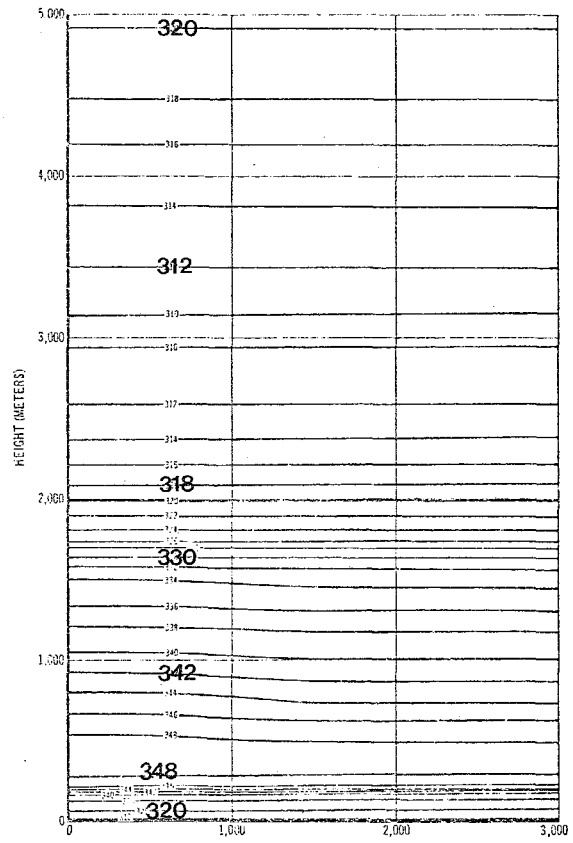
At $x = 0$, $\partial/\partial x$ of all quantities are set to zero, and the stream function is a constant at $z = 0$, $z = z_T$ and $x = x_R$. (The bottom, top and right boundaries of the domain.) The perturbation temperature T' vanishes at these same boundaries. Liquid water content $q_l = 0$ initially and, at the three boundaries, for all times. Initially, there is no horizontal gradient of water vapour q_v , and the value of q_v remains constant at all times although it has a vertical stratification. The initial thermal stratification shows a conditional instability for the $T(z)$ field in the lower troposphere. A perturbation in the T' field is used to initiate convection.

The domain is an 8 000 m square within which there are grid points at every 250 metres in the x and z directions. In the actual simulations of the cloud Murray and Anderson set $v_M = 500 \text{ m}^2 \text{ s}^{-1}$ and $v_G = v_T = 0$. The time step for calculations was 15 seconds which satisfies the linear stability criterion. One of the purposes of this study was to study the growth of a shallow cumulus cloud in a conditionally undisturbed atmosphere, and has considerable relevance to tropical cumulus cloud growth.

Results of numerical calculations

The temperature and moisture distributions can be used to construct the field of equivalent potential temperature for the initial as well as the predicted fields. Figures 6.2a and 6.2b show a time sequence of the evolution of the field of $\theta_e(x, z)$ at times $t = 0, 5, 15$ and 20 minutes. By 15 minutes the evolution of the cloud produces an interesting distortion of the θ_e field. Near the axis of the cloud, i.e., $x = 0$, the θ_e minimum, which was present initially at 3 km, is absent. A single shallow convective cloud is not able to stabilize the domain as much as many clouds might do over a period of time. Here we evaluated

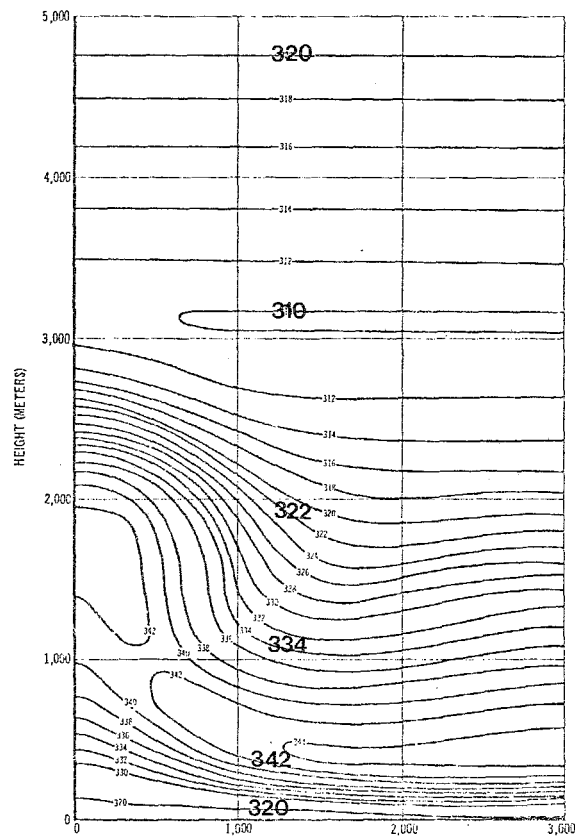
$$\int_0^{x_R} \theta_e dx / \int_0^{x_R} dx \quad (x_R \text{ is domain radius})$$



Radial distance (metres)

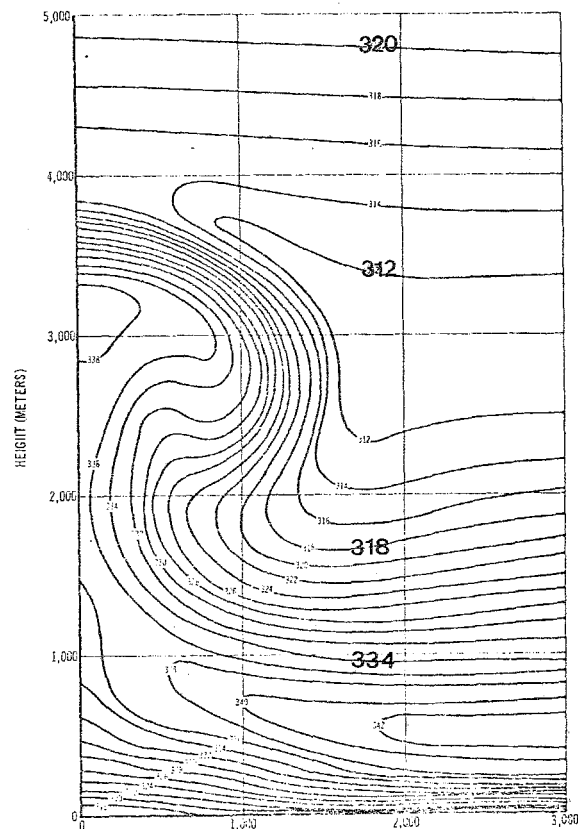
Figure 6.2a - Equivalent potential temperature, initial time

Equivalent potential temperature, 5 min



Radial distance (metres)

Figure 6.2b - Equivalent potential temperature, 10 min



Equivalent potential temperature, 15 min

at time zero and at 20 minutes. The integration provides a domain-averaged sounding of θ_e . We notice that the small cloud is able to reduce the intensity of the θ_e minimum somewhat and lift it upwards. This feature has also been noted in the atmosphere by Warsh *et al.*, (1971). Their results are shown in Fig. 6.3. It is important to note that conditional instability is usually very large prior to vigorous convection and after convection the θ_e profile shows less marked conditional instability. We next show two more interesting features of this cloud model. They are: time sections of vertical velocity W and temperature departure T' . (See Figs. 6.4a,b.) The vertical velocity clearly shows that the cloud grows for 20 minutes and thereafter the downward motions are associated with a decay of the cloud. The temperature anomaly shows a warming near the top of the cloud during the growing stage and a cooling above the cloud due to overshooting of the vertical velocity above. This is primarily due to adiabatic cooling that occurs in this region. Aircraft observations of clouds have confirmed the existence of such a cold region above the clouds although the model over-emphasizes its intensity. On the whole, this simple model is very satisfactory as a starting point for more sophisticated and better models. Although we shall not describe better and more detailed cloud models, the interested student should look at a number of other studies in this area. Some of these are:

- (i) Modelling deep convective clouds in an ambient atmosphere at rest (Murray, 1968);
- (ii) Modelling clouds in a vertically shearing environment (Asai, 1970);
- (iii) Modelling three-dimensional large thunderstorms (Ogura, 1975);
- (iv) Modelling squall lines, their formation and motion (Moncrieff and Miller, 1976).

In these studies the processes of entrainment of outside air into cloud, detrainment of cloud matter, rainfall mechanisms, cooling by evaporation, evaporative downdrafts, cloud regeneration, formation of solid phase, i.e., hail, etc. are included in a simple way.

If an observed cloud were to exhibit features identical to what is described in the simplest model presented above, it would take close to one million observations to describe all the details of the various dependent variables. Observations are expensive and it is, in fact, not necessary to observe all the details. For many problems in tropical meteorology, the large scale effect of an ensemble of clouds is more important than detailed knowledge of a single cloud.

6.4 Budget studies

Several interesting budgets of mass, momentum, kinetic energy, moisture and heat over tropical latitudes were carried out by Riehl and Malkus (1958, 1961). They were important studies in that they brought out clearly the need for the inclusion of the cumulus scale towards the understanding of the budgets of the larger scale. If we consider a tropical disturbance with small azimuthal asymmetries with respect to its instantaneous centre of reference, we may write the mass continuity equation as:

$$\frac{1}{r} \frac{\partial (v_r r)}{\partial r} + \frac{\partial \omega}{\partial p} = 0 \quad (6.12)$$

where v_r is an outward directed radial velocity.

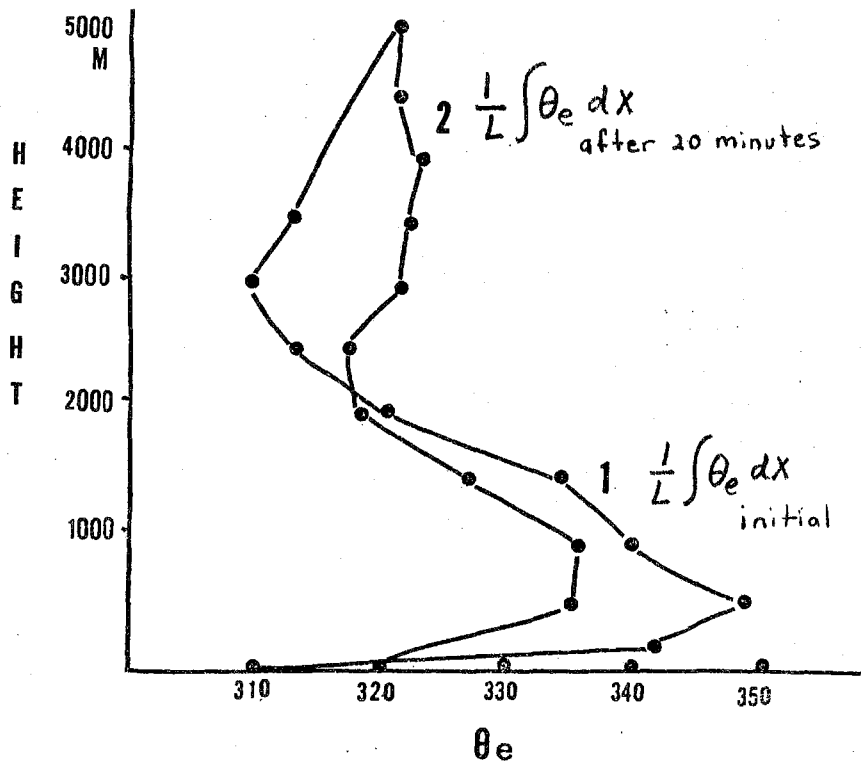
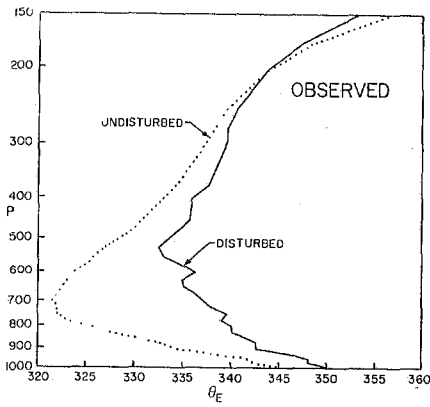


Figure 6.3

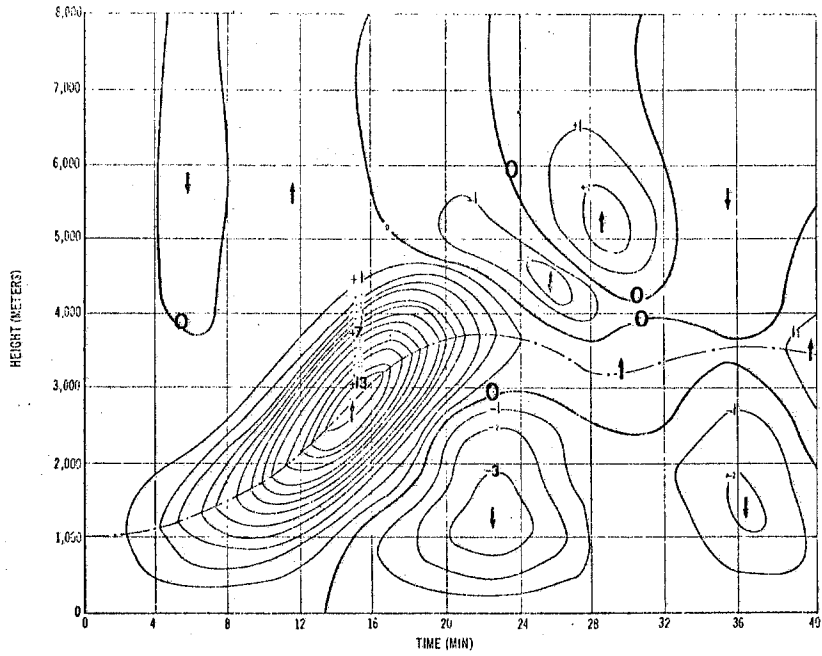


Figure 6.4a - Time section of vertical component of velocity on the central axis

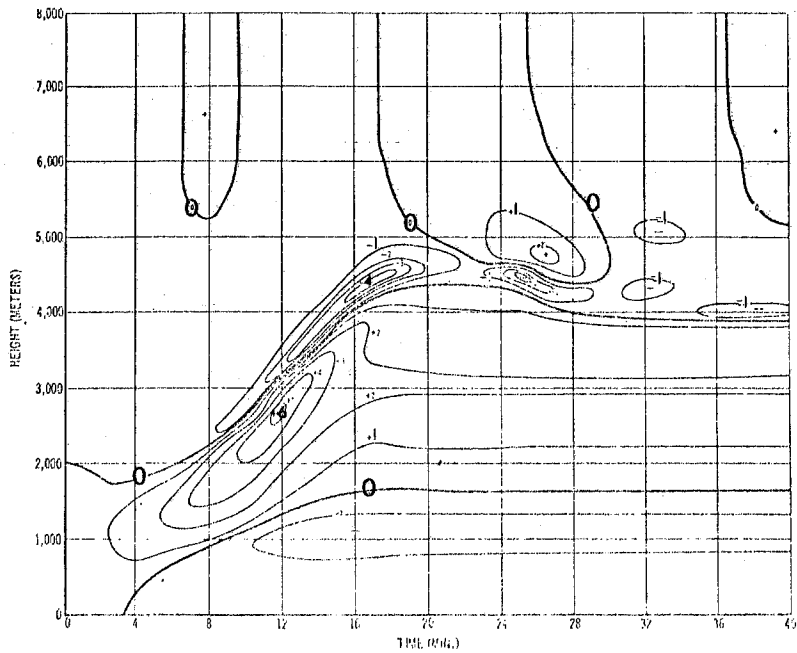


Figure 6.4b - Time section of temperature departure on the central axis

We take a cylindrical domain divided into two halves, as follows:

- (i) a lower tropospheric box below 500 mb and confined between $r = 0$ and $r = r_0$, an outer radius (a few hundred km), and
- (ii) an upper box between 500 and 0 mb.

An integration of equation (6.12) gives a mass budget relation, i.e.:

$$\frac{2\pi}{g} \iint \left(\frac{1}{r} \frac{\partial(v_r r)}{\partial r} + \frac{\partial\omega}{\partial p} \right) r \, dr \, dp = 0 \quad (6.13)$$

The lateral outward mass flux at $r = r_0$ for the lower troposphere is given by:

$$M_1 = \frac{2\pi}{g} \int_0^{r_0} \int_{500}^{1000} \frac{1}{r} \frac{\partial(v_r r)}{\partial r} r \, dr \, dp \quad (6.14)$$

and for the upper troposphere and stratosphere, by:

$$M_2 = \frac{2\pi}{g} \int_0^{r_0} \int_0^{500} \frac{1}{r} \frac{\partial(v_r r)}{\partial r} r \, dr \, dp \quad (6.15)$$

The downward mass flux at 500 mb is given by:

$$M_3 = -\frac{\pi}{g} \int_0^{r_0} \int_{500}^{1000} \frac{\partial\omega}{\partial p} r \, dr \, dp \quad (6.16)$$

Mass budget (based on mass balance) requires that $-M_1 = +M_2 = -M_3$, i.e., low level inflow \equiv high level outflow \equiv middle level upward flow. Meteorological observations, in general, do not satisfy this mass balance relation. Some adjustment is usually carried out to assure a mass balance and is a primary requirement for all mass budgets.

If Q is a property such as:

- (i) moisture content (specific humidity) per unit mass of air, q
- (ii) kinetic energy per unit mass of air, K
- (ii) heat content (moist static energy $gz + c_p T + Lq$) per unit mass of air, or
- (iv) momentum per unit mass of air u ; then Q satisfies an equation of the form

$$\frac{dQ}{dt} = P \quad (6.17)$$

where P defines the net sources and sinks that modify Q .

In the absence of sources and sinks

$$\frac{dQ}{dt} = 0 \quad (6.18)$$

By integration of the above equation over a mass of the two boxes we obtain outflow of Q from lower box ($Q_1 M_1$) and the outflow of Q from upper box ($Q_2 M_2$). The downward flow of Q from 500 mb is $Q_3 M_3$. If there were to be a steady state in the absence of heat sources and sinks and under the influence of the large scale inflows, upward flows and outflows ($-M_1, -M_3, M_2$), then we require that

$$-M_1 Q_1 = -M_3 Q_3 = M_2 Q_2 \quad (6.19)$$

Here subscript 1 denotes lower box, subscript 2 denotes the upper box and subscript 3 denotes the middle level. Low level of $Q \equiv$ middle level upward flow of $Q \equiv$ high level outflow of Q . It can be seen quite easily that such a balance of heat and vorticity is just not possible from considerations of one scale of inflow, outflow and upward flow.

6.4.1 Moist static energy ($Q = E$)

Let us consider the heat balance problem. The tropical atmosphere is conditionally unstable, i.e., $gz + c_p T + Lq = E$ has a minimum around 700 mb, i.e.:

$$\begin{aligned} E_1 &> E_3 \\ E_2 &> E_3 \end{aligned} \quad (6.20)$$

Furthermore $-M_1 = -M_3 = M_2$

for the lower box $-M_1 Q_1 + M_3 Q_3 > 0$

and for the upper box $-M_3 Q_3 - M_2 Q_2 > 0$ with low level inflow.

This results in an accumulation of heat in the lower box and a depletion (or removal) of heat from the upper box. If sensible heat flux from the lower box is introduced as a heat source 'P' then the imbalance is compounded further. The message that emerges clearly is that cumulus scale motions are required to remove the excess heat from the lower levels and deposit it at higher levels. This is a result of the conditional instability of tropical air masses.

6.4.2 Vorticity

If we are given a cyclonic tropical disturbance at lower levels and an anticyclonic circulation at higher levels, as is quite often the case over the Western Pacific Ocean, the divergence term and the advection terms of the vorticity equation both contribute to a net generation and excess of vorticity at low levels, the converse being the case at higher levels. Inclusion of surface friction (P) again compounds the imbalance and the disturbance cannot be maintained in a steady state by the broadscale low level inflow, middle level upwards flow and high level outflows (i.e., $-M_1$, $-M_3$ and M_2). The need to incorporate the cumulus scale becomes apparent here again.

Next we shall present a review of some of the major budget studies of the recent years that tell us how to determine the role of cumulus clouds influencing these budgets.

6.4.3 Western Pacific Marshall area budget studies

Notable contributions have come from Williams (1970), Reed and Recker (1971), Yanai et al., (1973), Ogura and Cho (1973) and others. Here we shall briefly review the approach of Yanai et al., (1973) and the extension by Ogura and Cho (1973) and others that have used a similar approach.

6.4.4 Basic budget equations

The equations for dry static energy and moisture form the basic equations. (The student should try to derive the following equations, see Appendix, and understand the underlying assumptions.)

Dry static energy:

$$\frac{\partial s}{\partial t} + \nabla \cdot s\mathbb{V} + \frac{\partial}{\partial p} s\omega = Q_R + L(c - e) \quad (6.21)$$

Here $s = gz + c_p T$ is the dry static energy, Q_R is the rate of radiative warming, c is condensation, and e is evaporation. The equation states that dry static energy s is conserved in the absence of radiation, condensation and evaporation processes. We next average the above equation over a horizontal area large enough to contain an ensemble of cumulus clouds, but smaller than the tropical synoptic-scale waves.

Next we write:

$$\frac{\partial}{\partial p} \overline{s\omega} = \frac{\partial}{\partial p} \overline{s} \overline{\omega} + \frac{\partial}{\partial p} \overline{s'\omega'} \quad (6.22)$$

and write the static energy equation in the form:

$$Q_1 = \frac{\partial \overline{s}}{\partial t} + \nabla \cdot \overline{s\mathbb{V}} + \frac{\partial}{\partial p} \overline{s} \overline{\omega} = Q_R + L(c-e) - \frac{\partial}{\partial p} \overline{s'\omega'} \quad (6.23)$$

Q_1 is called an apparent heat source, the following being the reason for this name: if only large scale observations are available, then one can in principle measure such quantities as \mathbb{V} , \overline{s} , $\overline{s\mathbb{V}}$ and $\overline{\omega}$, and if

$$\frac{\partial}{\partial t} \overline{s} + \nabla \cdot \overline{s\mathbb{V}} + \frac{\partial}{\partial p} \overline{s} \overline{\omega} \neq 0,$$

then its value is a measure of the apparent heating that the large scale experiences. This formalism was introduced by Yanai *et al.* (1973). A similar equation for the moisture variable q can be written in the same units:

$$Q_2 = -L \left[\frac{\partial \overline{q}}{\partial t} + \nabla \cdot \overline{q\mathbb{V}} + \frac{\partial}{\partial p} \overline{q} \overline{\omega} \right] = +L(c-e) + L \frac{\partial}{\partial p} \overline{q'\omega'} \quad (6.24)$$

Q_2 is called the apparent moisture sink. The reason for this being that the value of

$$\frac{\partial \overline{q}}{\partial t} + \nabla \cdot \overline{q\mathbb{V}} + \frac{\partial}{\partial p} \overline{q} \overline{\omega},$$

based on large scale data, tends to be negative. Although evaporation adds to the moisture, condensation and vertical divergence of eddy flux of moisture subtract from it. Q_2 , however, is defined so it is generally positive in regions of convective cloud clusters.

The above two equations are usually combined to yield:

$$Q_1 - Q_2 - Q_R = - \frac{\partial}{\partial p} \overline{(s' + Lq') \omega'} = - \frac{\partial}{\partial p} \overline{h'\omega'} \quad (6.25)$$

where $h = gz + c_p T + Lq$ is the moist static energy.

Yanai defines an average mass flux across a unit area by:

$$\overline{M} = - \overline{\omega} \quad (6.26)$$

which is divided into two parts:

$$\overline{M} = M_c + \tilde{M} \quad (6.27)$$

where M_c is the upward mass flux in cumulus clouds and \tilde{M} is the mass flux in the environment.

In a unit area, let σ denote the area occupied by cumulus clouds; $(1 - \sigma)$ is the area free from clouds.

If ω_c and $\tilde{\omega}$ are, respectively, the vertical velocity of the clouds and their environment we can write;

$$\begin{aligned} M_c &= -\sigma \omega_c \\ \tilde{M} &= -(1 - \sigma) \tilde{\omega} \end{aligned} \quad (6.28)$$

Furthermore, we can express other properties in the same way, i.e.:

$$\begin{aligned} \bar{s} &= \sigma s_c + (1 - \sigma) \tilde{s} \\ \bar{q} &= \sigma q_c + (1 - \sigma) \tilde{q} \end{aligned} \quad (6.29)$$

Next we shall derive a very useful relation, $-\overline{A'\omega'} = M_c(A_c - \tilde{A})$ where A is any property. We can write;

$$\bar{A} = \sigma A_c + (1 - \sigma) \tilde{A} \quad (6.30)$$

and

$$\begin{aligned} \bar{\omega} &= \sigma \omega_c + (1 - \sigma) \tilde{\omega} \\ \overline{A\omega} &= \sigma A_c \omega_c + (1 - \sigma) \tilde{A} \tilde{\omega} \end{aligned} \quad (6.31)$$

To the order σ we can write:

$$\bar{A} \bar{\omega} = \tilde{A} \tilde{\omega} - 2\sigma \tilde{A} \tilde{\omega} + \sigma(A_c \tilde{\omega} + \omega_c \tilde{A}) \quad (6.32)$$

and

$$\begin{aligned} \overline{A'\omega'} &= \overline{A\omega} - \bar{A} \bar{\omega} \text{ can be approximated} \\ &= +\sigma \omega_c (A_c - \tilde{A}) \\ &= -M_c (A_c - \tilde{A}) \end{aligned} \quad (6.33)$$

Here we assumed that $\sigma \ll 1, |\omega|_c > |\tilde{\omega}|, A_c - \tilde{A} < \tilde{A}$. Thus the eddy fluxes of s, q and h can be written in the form:

$$\begin{aligned} \overline{s'\omega'} &= -M_c (s_c - \tilde{s}) \\ \overline{q'\omega'} &= -M_c (q_c - \tilde{q}) \\ \overline{h'\omega'} &= -M_c (h_c - \tilde{h}) \end{aligned} \quad (6.34)$$

It should be noted here that we seek a closed system that describes the properties of a cloud ensemble and thus enables one to describe the eddy fluxes. Up to this point we have followed the presentation of Yanai *et al.*, (1973). We shall next outline a procedure given by Ogura and Cho (1973) for the determination of M_c , then proceed to show how the system is closed to perform a budget study.

Ogura and Cho proposed an elegant method for the determination of the vertical mass flux distribution function M_c that is now being used widely in diagnostic studies. Ogura, Cho, and others following Arakawa (1971) define a fractional entrainment rate ' λ ' to identify a cloud type within an ensemble.

$$\lambda = \frac{1}{m} \frac{\partial m}{\partial z} \quad (6.35)$$

where m is the total vertical mass flux within a plume (for one cloud type);

λ is assumed to be a constant for each cloud type. Using pressure as a vertical coordinate, we can write:

$$\frac{1}{m} \frac{\partial m}{\partial p} = - \frac{\lambda H}{p} \quad (6.36)$$

where $H = RT(p)/g$ is a scale height of the atmosphere.

If $m_B(\lambda)$ is the vertical mass flux at the base of a cloud type then one relates $m_B(\lambda)$ to $m(\lambda, p)$ via the relation:

$$m(\lambda, p) = m_B(\lambda) \eta(\lambda, p) \quad (6.37)$$

where η is a measure of the fraction of the cloud base mass flux that passes through a level p , and can be defined from equation (6.36).

$$\frac{\partial}{\partial p} \ln m = - \frac{\lambda H}{p} \quad (6.38)$$

$$\int_{p_B}^p \frac{\partial \ln m}{\partial p} = - \int_{p_B}^p \frac{\lambda H}{p} dp \quad (6.39)$$

$$m(\lambda, p) = m_B(\lambda) e^{-\int_{p_B}^p \frac{\lambda H}{p} dp} \quad (6.40)$$

or

$$\eta(\lambda, p) = e^{-\int_{p_B}^p \frac{\lambda H}{p} dp} \quad (6.41)$$

Next a continuity equation for a property Q is written as follows:

$$\frac{\partial}{\partial p} m Q_c = - \frac{\lambda H}{p} m \tilde{Q} + s \quad (6.42)$$

where Q_c is the property within the cloud, \tilde{Q} being that for the environment. The first term on the right hand side signifies entrainment of environmental property Q , and s is a source term. Using this notation, one can write down the cloud scale continuity equation for mass, static energy and moisture.

Mass continuity: $Q = 1, s = 0$

$$\frac{\partial m}{\partial p} + \frac{\lambda H}{p} m = 0 \quad (6.43)$$

Static energy: $Q = h, s = 0$

$$\frac{\partial}{\partial p} m h_c + \frac{\lambda H}{p} m \tilde{h} = 0 \quad (6.44)$$

Specific humidity: $Q = q_c, s = c$

where c is the total condensation rate within a cloud and it is a function of λ and p .

$$\frac{\partial}{\partial p} (m q_c) + \frac{\lambda H}{p} m \tilde{q} - c = 0 \quad (6.45)$$

or

$$m \frac{\partial q_c}{\partial p} + q_c \frac{\partial m}{\partial p} + \frac{\lambda H}{p} m \tilde{q} - c = 0 \quad (6.46)$$

from mass continuity, we can write the above equation:

$$m \frac{\partial q_c}{\partial p} + \frac{\lambda H}{p} m (\tilde{q} - q_c) - c = 0 \quad (6.47)$$

The treatment of liquid water:

The formation and detrainment of liquid water and associated warming and cooling are very important in the present parameterization theories of cumulus clouds in tropical circulation models. We shall here present a formulation for this important problem.

Since liquid water, q_{cl} , inside the cloud does not entrain from the environment, the continuity equation for liquid water is written by setting $Q = q_{cl}$, $s = c - D$, where c is the condensation rate, D is the rain fallout rate, and it was expressed by Ogura and Takahashi (1971) by the relation:

$$D = a c_0 q_{cl} \quad (6.48)$$

where a is an area of cross-section of the cloud, c_0^{-1} is the conversion time of cloud droplets to large raindrops. We also assume that raindrops once formed fall instantaneously out of the cloud. Taking all these processes into account, the liquid water continuity relation is expressed by:

$$\frac{\partial}{\partial p} m q_{cl} + c - a c_0 q_{cl} = 0 \quad (6.49)$$

The budget studies thus invoke processes like entrainment of environmental air into the cloud, detrainment of cloud water vapour and cloud liquid water from the cloud to the environment. Aside from the drying of air due to descent of the cloud environmental air, adiabatic warming in this region and cooling by evaporation are important mechanisms. The studies of westward motions and the maintenance of tropical disturbances bring out these concepts in the budget studies. A relation between q_c and h_c is shown in the Appendix.

The working equation for the solution of M_c involves some algebra and is presented next.

Earlier we had shown that:

$$\overline{s^* \omega^*} = - M_c (s_c - \tilde{s}) \quad (6.50)$$

when we consider an ensemble of clouds with each cloud type characterized by its own value of λ . We can write down the above equation in the form:

$$\overline{s^* \omega^*} = - \int_{\lambda} m(\lambda) (s_c - \tilde{s}) d\lambda \quad (6.51)$$

where $m(\lambda)$ is the upward mass flux for a cloud type, λ , and s_c , \tilde{s} now also refer to properties of a cloud type λ , and are thus functions of λ and p . Furthermore

$$M_c = \int_{\lambda} m(\lambda) d\lambda \quad (6.52)$$

Similarly

$$\overline{q^* \omega^*} = - \int_{\lambda} m(\lambda) (q_c - \tilde{q}) d\lambda \quad (6.53)$$

If we differentiate equation (6.51) by parts, we obtain:

$$\frac{\partial}{\partial p} \overline{s'w'} = - \frac{\partial}{\partial p} \int m(\lambda) s_c d\lambda + \frac{\partial \tilde{s}}{\partial p} \int m(\lambda) d\lambda + \tilde{s} \frac{\partial}{\partial p} \int m(\lambda) d\lambda \quad (6.54)$$

or

$$= \tilde{s} \frac{\partial M_c}{\partial p} + M_c \frac{\partial \tilde{s}}{\partial p} - \frac{\partial}{\partial p} \int m(\lambda) s_c d\lambda$$

The above equations can be simplified considerably by using the mass and dry static energy continuity equations:

$$\epsilon(p) - \delta(p) + \frac{\partial M_c}{\partial p} = 0 \quad (6.55)$$

and

$$\epsilon \tilde{s} - \delta \tilde{s} + \frac{\partial}{\partial p} \int m(\lambda) s_c d\lambda + Lc = 0 \quad (6.56)$$

where ϵ and δ are, respectively, the entrainment and detrainment coefficients. The total entrainment (ϵ) is defined by the relation:

$$\epsilon(p) = \int_0^{\lambda_D} \frac{\lambda H}{p} m(\lambda) d\lambda \quad (6.57)$$

where λ_D is the value of λ at the detrainment level which is explained a little later. The total detrainment at each level is given by:

$$\delta(p) = m(\lambda_D) \frac{d\lambda_D}{dp} = m_B(\lambda_D) \eta(\lambda_D, p) \frac{d\lambda_D}{dp} \quad (6.58)$$

Upon multiplication of the mass continuity equation by \tilde{s} and subtracting from the dry static energy continuity equation, we obtain:

$$\tilde{s} \frac{\partial M_c}{\partial p} - \frac{\partial}{\partial p} \int m(\lambda) s_c d\lambda = Lc \quad (6.59)$$

Here, we obtain:

$$\frac{\partial}{\partial p} \overline{s'w'} = M_c \frac{\partial \tilde{s}}{\partial p} + Lc \quad (6.60)$$

A similar treatment of the moisture equation yields:

$$\frac{\partial}{\partial p} \overline{q'w'} = M_c \frac{\partial \tilde{q}}{\partial p} - c - \delta(\tilde{q}^* - \tilde{q}) \quad (6.61)$$

Here the detrainment term requires an explanation.

Arakawa introduced the concept of a thin detrainment layer where the cloud loses its buoyancy. At this level = p_D the cloud properties are the same as the saturation properties of the environment, i.e.:

$$\begin{aligned} h_c(\lambda, p_D) &\equiv \tilde{h}^*(p_D) \\ q_c(\lambda, p_D) &\equiv \tilde{q}^*(p_D) \end{aligned} \quad (6.62)$$

and

$$s_c(\lambda, p_D) \equiv \tilde{s}^*(p_D)$$

Although entrainment, in principle, can be effective at all cloud levels, detrainment based on observational grounds is restricted to the level of vanishing buoyancy. Since one is dealing with an ensemble of clouds in which each individual cloud has a different top level, detrainment takes place at

different height levels. Furthermore, it should be noted that $\lambda_D(p)$ is an increasing function of height: hence shallower clouds have a greater rate of entrainment.

Next we shall write down the working equations for the budget study. Upon substitution of these expressions for the eddy fluxes of dry static energy and moisture, we obtain:

$$Q_1 - Q_R = -L \bar{e} - \frac{\partial \tilde{s}}{\partial p} \int_0^{\lambda_D} m_B(\lambda) \eta(\lambda, p) d\lambda \quad (6.63)$$

and

$$Q_2 = -L \delta(\tilde{q}^* - \tilde{q}) + L \frac{\partial \tilde{q}}{\partial p} \int_0^{\lambda_D} m_B(\lambda) \eta(\lambda, p) d\lambda - L \bar{e} \quad (6.64)$$

where $\bar{e}(p)$ is the total evaporation at any level. In budget studies large-scale observations are used to determine Q_1 and Q_2 . Q_R is either calculated or taken from past studies of radiative warming. Thus Q_1 , Q_2 and Q_R are to be regarded as known functions. If we subtract equation (6.64) from (6.63), we obtain the relation:

$$Q_1 - Q_2 - Q_R = L \delta(\tilde{q}^* - \tilde{q}) - \frac{\partial \tilde{h}}{\partial p} \int_0^{\lambda_D} m_B(\lambda) \eta(\lambda, p) d\lambda \quad (6.65)$$

A further assumption is made at this stage, namely $\bar{q} = \tilde{q}$, $\bar{q}^* = \tilde{q}^*$, i.e., the cloud environment and the large scale properties are identical. Thus, if the detrainment function $\delta(p)$ is determined from equation (6.58), we have one equation (6.64) for the one unknown $m_B(\lambda)$. This is an integral equation; the method of finding the vertical mass flux distribution function is called the spectral method. The solution of the above equation is obtained by assigning different values of λ_D (i.e., pressure). The above equation thus becomes a number of simultaneous equations, one for each value of pressure. The numerical technique generates a triangular matrix with more and more non-zero elements as one includes more and more vertical levels. The solution of the matrix equations yields the desired value of $m_B(\lambda)$ and using equations (6.37) and (6.52) one can then obtain $m(\lambda)$ and $M_C(p)$. The evaporation can next be determined from the relation:

$$\bar{e}(p) = \delta q_c(\lambda_D)$$

and the rainfall rate can be obtained from

$$R = - \int_{p_B}^{p_T} (\bar{c} - \bar{e}) \frac{dp}{g} = - \frac{1}{gL} \int_{p_B}^{p_T} Q_2 dp + \frac{M_C}{g} (\tilde{q}^* - \tilde{q}) \Big|_{p=p_B} \quad (6.66)$$

where p_T is the pressure at the tropopause.

What does all this accomplish?

The vertical eddy fluxes of heat and moisture are now easy to determine since the crucial parameter M_C is now known. Hence, one can answer the question: what role does the modelled cumulus scale motions play in the budgets of Q_1 and Q_2 , i.e., heat and moisture. From such budget studies we learn something about the detailed mechanisms in the scale interactions. These studies have many limitations:

- (i) Any large-scale imbalances in budgets are tacitly assumed to arise due to the contributions from the imbedded cumulus scale

which in turn are well defined functions of the large scale. This leaves no room for convection organized on the meso-scale and those having a weak coupling with the large scale;

- (ii) The more sophisticated budget studies seem to require a detailed prescription of cloud microphysical processes. These, according to Ogura and Cho (1973), are not being adequately handled;
- (iii) The knowledge gained from these studies has not had a serious impact on day-to-day weather prediction;
- (iv) The proposed budget study techniques are not unique and many versions of cloud models and specification of ensemble properties exist; it is very difficult to test the validity of these various, implied, subgrid scale processes.

Results of budget studies

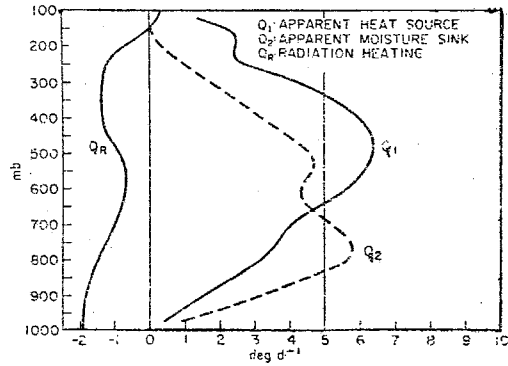
Figures 6.5 and 6.6 show recent results of budget studies over the western Pacific by Yanai et al., (1973) and by Cho and Ogura (1974). The latter authors used the well-known data set from Reed and Recker (1971).

Figure 6.5a is taken from Yanai et al., (1973). Here the data from the Marshall Island area were used to evaluate Q_1 and Q_2 , and Q_R was borrowed from other tropical studies.

One of the difficult problems in these budget studies is the estimate of Q_1 and Q_2 from large-scale data. The authors used a polygonal array of weather stations over the Marshall Island area during a few months of daily observations. The student should try an exercise in the evaluation of vertical motions using the Bellamy triangle method or a polygonal array method using line integral of mass flux around the domain. An adjustment of the vertical motions, to meet Dines' compensation, should be attempted as a laboratory exercise. The final values of divergence should satisfy the relation:

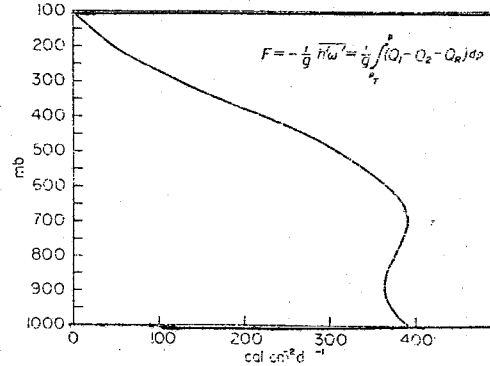
$$\int_0^{P_s} \nabla \cdot \mathbf{V}_H dp = 0$$

All the advection and transport terms should also be evaluated consistently with the adjusted motion field. This is not an easy matter. The vertical distributions of the apparent heat source Q_1 , the apparent moisture sink Q_2 , and of the radiational heating Q_R from Yanai et al., (1973) are shown in Fig. 6.5a. These are the three vertical distributions that are determined from the large-scale data. The question one must next ask is: How do the cumulus scale heating and the vertical eddy fluxes accomplish these large-scale (ensemble-averaged) distributions? In this diagram, it is worth noting that Q_1 is of the order of $70^\circ\text{C day}^{-1}$ at around 400 mb in these Marshall Island rain-producing disturbances. The apparent moisture sink Q_2 shows large drying due to descending motions around the cloud ($-M_c$) and has maxima around 800 and 550 mb. The diagnosed vertical distributions of the vertical eddy flux of moist static energy is shown in Figure 6.5b. This shows that above 700 mb there is a decrease of $-\overline{h'w'}$ implying a net divergence of flux of moist static energy by convection. This is an important deduction about the role of organized convection imbedded within large-scale disturbances in a conditionally unstable environment. Below 700 mb, the converse being the case, convection is trying to stabilize the large scale. The results of their calculations of \overline{M} , M_c and \tilde{M} are shown in Fig. 6.5c. Note that $M_c > \overline{M}$, where $M_c = \overline{M} - \tilde{M}$. The environmental descent is large at lower levels.



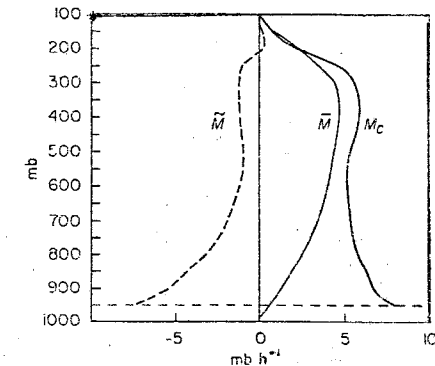
The mean apparent heat source Q_1 (solid) and moisture sink Q_2 (dashed). On the left is the radiational heating rate given by Doplick (1970)

Figure 6.5a



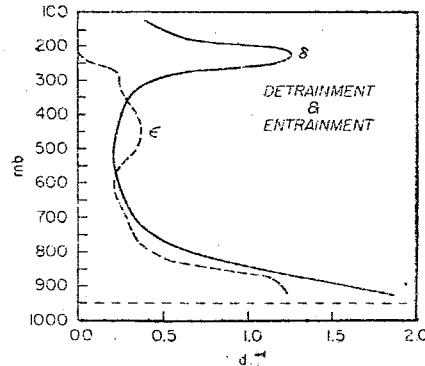
The derived vertical eddy heat flux

Figure 6.5b



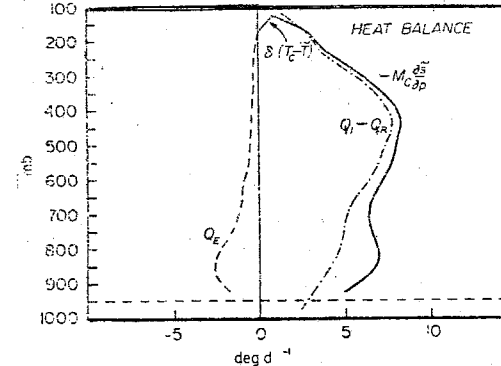
The average cloud mass flux M_c (solid), large-scale mass flux \bar{M} (thin solid), and residual mass flux \tilde{M} (dashed)

Figure 6.5c



The average detrainment δ (solid) and entrainment ϵ (dashed)

Figure 6.5d



The observed heat source $Q_1 - Q_R$ (dash-dotted) adiabatic heating by the compensating downward mass flux $-M_c (\partial \bar{s} / \partial p)$ (solid), evaporative cooling $-Q_E = -Le$ (dashed), and detrainment of heat $\delta (T_c - T)$ (thin solid)

Figure 6.5e

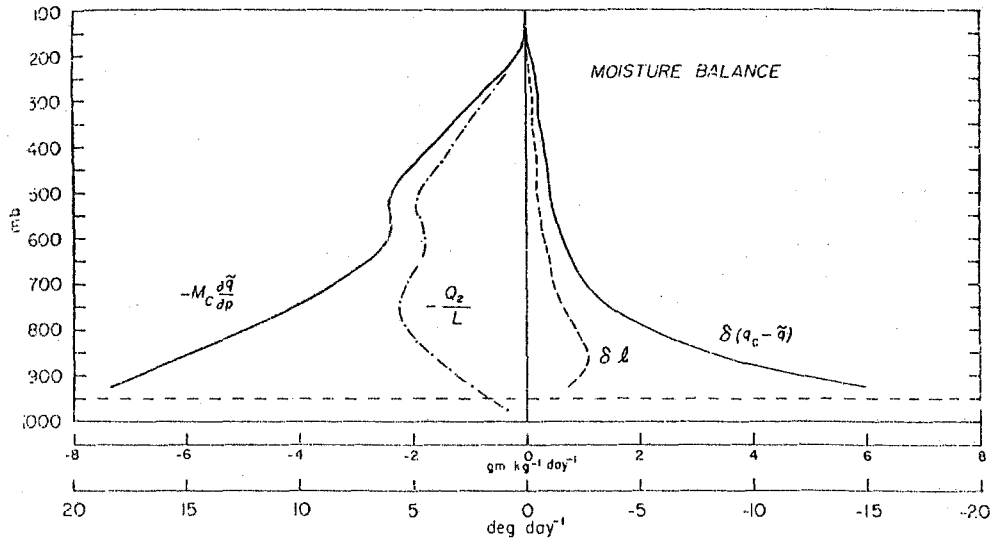


Figure 6.5f - The observed moisture source $-Q_2/L$ (dash-dotted), drying due to compensating sinking motion $-M_C(\partial\bar{q}/\partial p)$ (solid), detrainment of water vapour $\delta(\bar{q}_c - \bar{q})$ (thin solid), and detrainment of liquid water δL (dashed), in units of $\text{g kg}^{-1} \text{day}^{-1}$ and in equivalent heating units ($^{\circ}\text{C day}^{-1}$)

Although Yanai *et al.*, (1973) utilized a method different from that used by Ogura and Cho (1973), the two procedures yield not too dissimilar results. The M_c function is an important ingredient for budget studies and without this it is almost impossible to deduce what the cumulus scale motions are doing within the large scale. To the author's knowledge, there exist no shortcuts for the determination of this important function. It should be noted that M_c is an average for the entire ensemble of clouds and if one were to look at a single cloud type, then the values would be much larger. In the lower troposphere, the large scale upward mass flux \bar{M} is a small difference between upward cloud mass flux M_c and a large environmental descent \bar{M} . At the level of maximum heating Q_1 , \bar{M} is small and M_c is large, the implication being that the environmental descent is small where the heating is large, i.e., the middle troposphere. Yanai's (*et al.*) solutions of the entrainment and detrainment profiles are shown in Fig. 6.5d. Detrainment from the tops of very shallow and very tall clouds seems to be significant. The entrainment of environmental air is large for shallow clouds, which is consistent with the presence of a large population of smaller clouds that entrain dryer air and lose their buoyancy sooner. Another region of large entrainment is found below 400 mb where perhaps the tall clouds entrain large amounts of environmental air as they accelerate upwards.

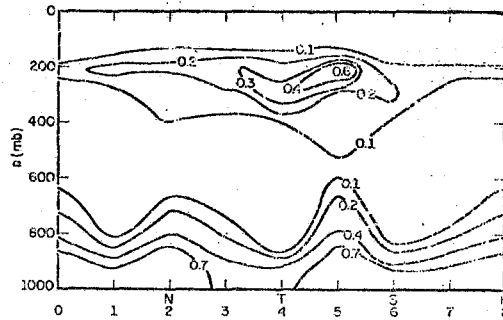
The heat and moisture balance of the cloud ensemble are shown from the study of Yanai *et al.*, (1973) in Figs. 6.5e and 6.5f. The major components of the heat balance are: (i) warming due to the descent of the cloud environment, i.e., $-M_c (\partial s / \partial p)$ and (ii) cooling due to evaporation of liquid water, i.e., $-Q_E = -L_e$. These bulk properties of the cloud clusters are indeed a major finding in the study of tropical convective disturbances.

The emphasis on warming due to descent in the cloud environment was made by Professor William Gray. The communication of cumulus-scale heating and the warming of the large scale thus appear to be somewhat indirect. The heat released provides warming (and buoyancy acceleration) to offset the adiabatic cooling in the ascending saturated cloud air. The buoyancy and upward motion in the cloud region (generating potential energy) require a net downward motion in the immediate environment of the ascending area. Here the potential energy (gz) of the descending air is converted to sensible heating ($C_p T$).

The picture of the moisture balance, Figure 6.5f, shows that the observed moisture source ($-Q_2/L$) is balanced by :

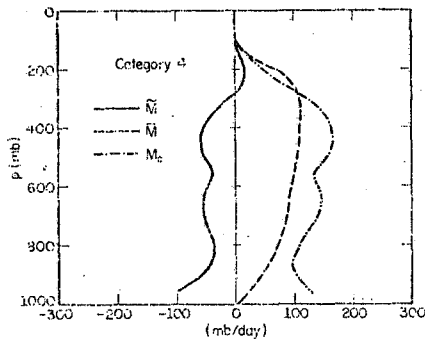
- (i) drying due to sinking motions;
- (ii) moistening due to the detrainment of liquid water; and
- (iii) moistening due to the detrainment of cloud water vapour.

These effects tend to be large below 700 mb and decrease rapidly above that level. The apparent moisture sink is a small difference between large source and sink terms and, as such, these internal aspects of the moisture budget are dependent on the sensitivity of the prescribed processes. There are a number of newer budget studies (Nitta, 1976, and others) that show somewhat different results. On the whole, these studies have provided new approaches to the studies of tropical weather systems. Another area of budget study where some progress is being made is in the understanding of the vertical flux of vorticity and momentum by the cumulus scale



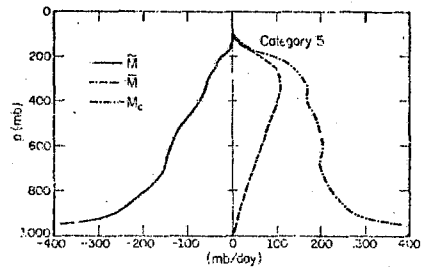
Composite of spectral distribution of the vertical mass flux at the cloud base as a function of the cloud top. Isoleths are in units of day^{-1} . Category 4 is centred on the trough axis, category 8 on the ridge

Figure 6.6a



Vertical distributions of the vertical mass flux due to all clouds (M_c), the mass flux in the environment (M) and the large-scale mass flux (M_e) for category 4

Figure 6.6b



As in Fig. 6.6b but for category 5

Figure 6.6c

motions, (Chu, 1977; and Godbole, 1977). We shall not review these here.

Figures 6.6a, b and c show three panels from the study of Cho and Ogura (1974). Figure 6.6a shows the vertical distribution of the vertical mass flux m_B . The abscissa is to be regarded as a line starting from the ridge, Category 1, (and also 8), of an ITCZ wave and it goes on to the Category 4 which is the trough line of the wave. The Reed and Becker wave is described elsewhere in this text. The bimodal vertical distribution of m_B signifies the predominance of shallow and deep convective clouds. The trough region is dominated by deep cloud while the ridge shows the dominance of shallow clouds in the relatively undisturbed environment. These results have also been confirmed and refined by Nitta et al., (1976). These studies provide the first diagnostic understanding of the dual cloud types in tropical disturbances.

Figure 6.6b shows the vertical distribution of Q_1 , Q_2 , and Q_R for the trough and the ridge regions. The solutions of M_c and M (the total mass flux of the environment) for the trough and ridge categories are illustrated in Figure 6.6c. The total vertical mass flux is small in the ridges and is downward while in the disturbed area of the trough the upward motions are larger and largely related to the distribution of M_c .

6.5 Parameterization theories

6.5.1 Introduction

We shall begin with a reference to the conditional instability of the tropics. On the large scale the tropical atmosphere is conditionally unstable almost everywhere and all the time. The following inequalities may be used to denote the instability:

$$- \frac{\partial}{\partial p} (gz + c_p T) > 0 \quad (6.67)$$

$$- \frac{\partial}{\partial p} (gz + c_p T + Lq_s) < 0 \quad (6.68)$$

where q_s is the saturation specific humidity at temperature T . The inequalities merely state that the atmospheric sounding lies between the dry and the moist adiabat, i.e., the sounding is conditionally unstable. If a saturated parcel were lifted from one level to another, then it would be warmer than the environment and become buoyant.

The definition of stable heating is extremely important in this context. If the atmosphere is absolutely stable, and if there exists ascent of saturated air, then the moist adiabatic local warming in any pressure surface may be expressed by the relation:

$$c_p \frac{T}{\theta} \frac{d\theta}{dt} = - L \frac{dq_s}{dt} \quad (6.69)$$

since the sounding is warmer than the dry and the moist adiabat in this case. The moist adiabatic warming, in fact, results in a net cooling of the area where the stable heating is invoked.

If the above stable heating is invoked in a conditionally unstable situation, it is clear that buoyant motions would occur everywhere. It has been shown from linear analysis of the growth rate of disturbances in such a conditionally unstable atmosphere that the maximum growth rate (in the frictionless atmosphere) occurs for scales that are infinitesimally small, that is of the order of 1 km. This kind of buoyant instability is recognized as the conditional instability of the first kind. This would suggest that the tropical atmosphere would be full of cumulus clouds everywhere. However, synoptic experience shows that there are, in fact, organized disturbances such as monsoon depressions, easterly waves, equatorial waves and hurricanes, etc., that move for several days preserving their scales. The fact that these large disturbances (larger than the cumulus scale) do not break down into the cumulus scale in a conditionally unstable atmosphere suggests that there is some kind of a cooperative interaction between the synoptic scales and the cumulus scales. This was first mentioned by Charney (1958), and by Charney and Eliassen (1964) and Ooyama (1969). The idea of the cooperative interactions gave birth to the notion of the conditional instability of the second kind (CISK). This new idea is a major concept in today's tropical meteorology. The first applications were made in the studies on the dynamics of hurricanes. The idea of cooperative interaction works for the development of a vortex as follows. The clouds supply the heating to drive the vortex. The vortex, by providing the moisture convergence, maintains and organizes the

cloud system. If there is a circular vortex in near gradient equilibrium over the ocean, its development into a hurricane by the CISK mechanism can be viewed as follows: frictional convergence provides the moisture supply in the boundary layer, mass and moisture will be transported upward in the cumulus clouds. The heat released in the upper levels of the clouds causes the warm core to be established and a lowering of the surface pressure. The increase of the pressure gradient at lower levels increases the vorticity of the near 'gradient wind' flows in the boundary layer. This results in an enhancement of the frictional convergence, which in turn increases the upward mass and moisture flux in the cloud and the entire development process keeps amplifying. However, the process does reach a limit. The limiting factor is the establishment of a moist adiabat beyond which no further warming and lowering of surface pressure is possible.

Practical proposals for shifting the scale of instability from the cumulus scale to larger synoptic scales in numerical models relate to the specifications of the convective heating function. This was shown, e.g., by Charney and Eliassen (1964), in their study of a hurricane depression. They considered a two-layer balanced model and showed that if the form of the convective heating was decoupled from the large-scale vertical velocity of the model, then gravitational instability is removed. They proposed a heating function which was proportional to the vertical velocity at the top of the boundary layer. This was defined using the so-called "Ekman Balance" in the boundary layer. In effect they use a heating function of the form:

$$H_c = - L \omega_B \frac{\partial q_s}{\partial p} \quad (6.70)$$

instead of

$$H_c = - L \omega \frac{\partial q}{\partial p}$$

where ω_B is the vertical velocity at the top of boundary layer. Charney and Eliassen show that disturbances with scales of the order of 100 km have large growth rates. A similar analysis was also carried out by Ooyama (1969) and by Syono and Yamasaki (1966). An important conclusion of these papers was that in order to describe near balanced flows in growing tropical disturbances, the heating function has to be decoupled from the large-scale vertical velocity. Several important propositions on the parameterization of cumulus convection soon emerged during the 1960's. One of the most widely used schemes was by Kuo (1965). We shall next review this scheme.

6.5.2 Kuo's parameterization procedure

This scheme invokes cumulus scale heating and a vertical flux of moisture if the following two conditions are met:

1) The sounding is conditionally unstable, which, for convenience, we define as in Krishnamurti et al. (1973) by the condition:

$$- \frac{\partial}{\partial p} (gz + c_p T) > 0 > - \frac{\partial}{\partial p} (gz + c_p T + Lq) \quad (6.71)$$

2) There exists a net large-scale convergence of flux of moisture in vertical columns, i.e.:

$$I = - \frac{1}{g} \int_{p_{Top}}^{p_{Bottom}} (\nabla \cdot q \nabla + \frac{\partial}{\partial p} q \omega) dp > 0 \quad (6.72)$$

In these regions where the above two conditions were met, Kuo used the following form of the moisture equation:

$$\frac{\partial q}{\partial t} = a \frac{(q_s - q)}{\Delta \tau} \quad (6.73)$$

where $\Delta \tau$ is a cloud time scale parameter and 'a' denotes the fractional area of the grid scale that would be covered by newly-formed convective clouds. The parameter 'a' is defined by the relation:

$$a = \frac{-\frac{1}{g} \int_{p_T}^{p_B} (\nabla \cdot qV + \frac{\partial}{\partial p} \omega q) dp}{\frac{1}{g} \int_{p_T}^{p_B} \left(\frac{c_p (T_s - T)}{L \Delta \tau} + \frac{q_s - q}{\Delta \tau} \right) dp} \quad (6.74)$$

In the following we shall use the symbol Q for the denominator of equation (6.74).

In this relation the denominator may be interpreted as the amount of moisture supply needed to cover the entire grid scale area by a model cloud (a local moist adiabat, T_s , q_s). The numerator, on the other hand, is a measure of the available moisture supply.

The total convective rainfall rate is given by the relation:

$$P_T = \frac{1}{g} \int_{p_T}^{p_B} \frac{a c_p (T_s - T)}{L \Delta \tau} dp \quad (6.75)$$

It should be noted that the definition of 'a' as given by equation (6.74) and the parameterization of the moisture in equation (6.73) are consistent with the principle of conservation of moisture. This can be shown by considering the moisture conservation law in the form:

$$\frac{\partial q}{\partial t} = -\nabla \cdot qV - \frac{\partial}{\partial p} (q\omega) + E - P \quad (6.76)$$

Upon integration of equation (6.76) from p_T to p_B with the assumption that evaporation E occurs only at the air-sea interface, i.e., below p_B , we obtain:

$$\frac{1}{g} \int_{p_T}^{p_B} \frac{\partial q}{\partial t} dp = I - P_T \quad (6.77)$$

where P_T is the total precipitation rate for the vertical column. Noting that

$$I = a Q = a \left[\frac{1}{g} \int_{p_T}^{p_B} c_p \frac{T_s - T}{\Delta \tau} dp + \frac{1}{g} \int_{p_T}^{p_B} \frac{q_s - q}{\Delta \tau} dp \right]$$

and substituting for P_T from equation (6.75) into equation (6.77) we obtain:

$$\frac{1}{g} \int_{p_T}^{p_B} \frac{\partial q}{\partial t} dp = \frac{1}{g} \int_{p_T}^{p_B} a \frac{q_s - q}{\Delta \tau} dp$$

Hence, the use of equation (6.74) is consistent with the moisture conservation law, i.e., equation (6.76).

We furthermore note that a part of the moisture convergence I is used for raising the level of moisture and a part of it goes into condensation heating. This partitioning may be expressed by the relation:

$$I = I_q + I_\theta \quad (6.78)$$

The convective heating function at any level is given by the expression:

$$H_c = \frac{a c_p (T_s - T)}{\Delta\tau} \quad (6.79)$$

The idea here is that clouds have temperature and humidity of a moist adiabat following a parcel that ascends from the sea level without entrainment. These clouds impart their properties to the macroscale by an instantaneous mixing in the horizontal with the cloud-free environment. This scheme has been used widely in the numerical simulation studies of the hurricane problem, e.g., Yamasaki, Rosenthal, Mathur, and many others. Versions of their scheme have also been used in real data forecasts by groups at Florida State University and at Bracknell in England. Some recent applications are discussed in Krishnamurti (1969; 1973a,b; and 1975, 1976). In these studies some limitations of Kuo's scheme were noted: in the tropics convective rain occurs frequently from meso-scale disturbances, implying that the convergence I in equation (6.77) should be measured on the scale of these meso-disturbances. Lack of observations on these smaller scales makes the field of I less intense than it should be. As a consequence, the convective heating and the associated rainfall is frequently greatly underestimated by Kuo's scheme. This problem does not appear to be serious for the hurricane problem where the scale on which I is resolved is much smaller. Another problem is a computational instability that arises in its application to large scale numerical weather prediction models. This relates to a disproportionate partitioning of I into I_q and I_θ initially. This can cause local instabilities. In the section on hurricanes we show some application of this procedure. It should be noted that the distribution of large-scale vertical wind shear and of the heating function are very important in the growth and decay of tropical disturbances. In Kuo's scheme the heating profile is restricted to the distribution of $(T_s - T)$. This limits the shape of the vertical distribution of heating. Detailed observational studies are needed to resolve the general validity of this shape.

We shall next make a few remarks on moist convective adjustment which is used in many numerical general circulation models. In this regard, reference may be made to the Princeton model (Hahn and Manabe, 1975), where its use has produced some very realistic fields of the tropical mean circulation patterns.

6.5.3 Moist convective adjustment

The idea here is to modify the sounding in a region where large-scale ascending motions occur in a conditionally unstable situation. This would be the so-called disturbed region of a tropical large-scale disturbance. The moist convective adjustment modifies the sounding in such a way that the total moist static energy remains invariant during adjustment.

Figure 6.7 shows a typical profile of moist static energy (E) before and (E_R) after the adjustment. Below a pressure level p_R the moist convective adjustment satisfies the relation:

$$\int_{P_R}^P E dp = E_R (p_R - p_0) \quad (6.80)$$

(Where p_0 is the surface pressure)

The values of temperature, moisture and geopotential along the adjusted sounding can be determined by integration of the following 6 equations for 6 unknowns:

$$gZ_s + c_p T_s + Lq = E_R \quad (6.81)$$

$$\frac{\partial}{\partial p} gZ_s = - \frac{RT_v}{p} \quad (6.82)$$

$$e_s = 6.11 e^{25.22 \left(1 - \frac{273}{T_s}\right) \left(\frac{273}{T_s}\right)^{5.31}} \quad (6.83)$$

$$q_s = 0.621 \frac{e_s}{(p - 0.379 e_s)} \quad (6.84)$$

$$T_v = T_s (1 + 0.61 q) \quad (6.85)$$

$$q = \mu q_s \quad (6.86)$$

where the subscript s refers to the saturation values, T_v stands for virtual temperature and μ defines a saturation criterion which may be arbitrarily chosen. Some studies use 0.8 as a value for this constant. The six unknowns are: Z_s , T_s , q_s , T_v , e_s , and q . The equations (6.83) and (6.84) express empirical relationships between the temperature, vapour pressure, and saturation specific humidity. The procedure for solution involves integrating downwards from the pressure level p_R using the following steps:

- (i) guess a temperature T_s at a pressure level $\Delta p + p_R$;
- (ii) compute e_s from (6.83);
- (iii) compute q_s from (6.84);
- (iv) compute q from (6.86);
- (v) compute T_v from (6.85);
- (vi) compute Z_s from (6.82);
- (vii) compute E_R from (6.81).

If E_R differs from what is shown in Fig. 6.7 make another guess till the procedure converges. Then proceed to pressure level $p_R + 2\Delta p$.

The adjusted sounding obtained by this procedure usually has temperature which varies from the original sounding by a few degrees (Celsius) and a moisture distribution differencing by a few $g\ kg^{-1}$. It has been shown by Krishnamurti and Moxim (1971) that in real data forecasts this can produce a drastic change from an initial state and produce shocks in the solution. Many tropical disturbances whose temperature amplitude is only about $1^\circ C$ can be ruined by such a convective adjustment. In general circulation models it is carried out every time step, hence the changes are smaller, however in these models the thermal and moisture structure of the disturbances in the vertical cannot be too realistic.

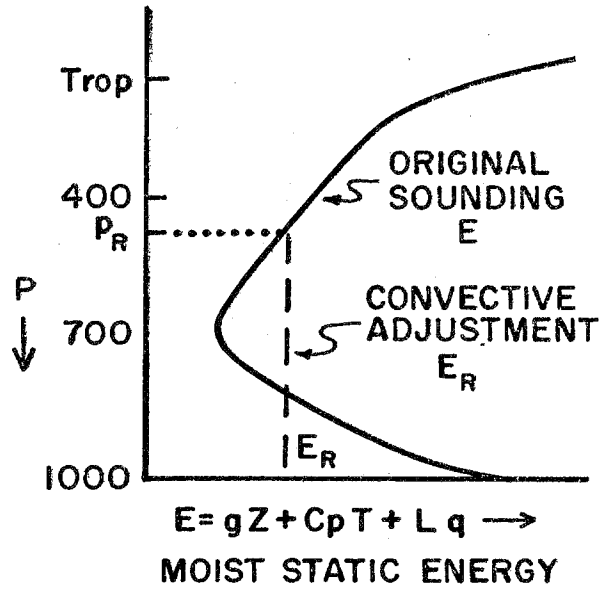


Figure 6.7

We shall next present a brief review of the current state of the art in the field of parameterization of cumulus convection.

6.5.4 Arakawa-Schubert theory

Arakawa's theory describes how an idealized cumulus ensemble and a large-scale field interact. The theory consists of three basic ingredients: feedback, static control, dynamic control (Fig. 6.8). The feedback loop explains how the cumulus transport terms and source terms modify the large-scale temperature and moisture fields. The control loops describe how the cloud ensemble properties are modulated by the large-scale fields. The basis of the theory is a quasi-equilibrium assumption (QEA) of the cloud work function $A(\lambda)$ which is discussed later. The large-scale field is divided into the subcloud mixed layer and the region above. Time changes of \bar{s} and \bar{q} are given by the heat and moisture budget equations. The depth of the mixed layer p_B (or Z_B) is also predicted.

The cumulus ensemble alters the large scale temperature and moisture fields through cumulus induced downdrafts and detrainment of cloud water. The downdrafts produce warming and drying and affect the depth of the mixed layer. Detrainment produces cooling and moistening. Three functions describing the cloud are introduced: entrainment (E), detrainment (D), vertical mass flux (M_c).

Entrainment due to the "ith" cloud (Fig. 6.9) is defined as:

$$E_i = \frac{\partial M_i}{\partial z} + \rho \frac{\partial \sigma_i}{\partial t} \quad (6.87)$$

where $(\partial M_i / \partial z)$ represents the mass (M_i) added per unit length and $(\partial \sigma_i / \partial t)$ represents the shrinking or expanding of the fractional area (σ_i) occupied by the cloud per unit time. Detrainment is defined as:

$$D_i = - \left(\frac{\partial M_i}{\partial z} + \rho \frac{\partial \sigma_i}{\partial t} \right) \quad (6.88)$$

$$E = \sum_i E_i, \quad D = \sum_i D_i, \quad M_c = \sum_i M_i \quad (6.89)$$

Σ_i denotes the summation over all clouds penetrating the level being considered. Budget equations in the entrainment and detrainment layer for the "ith" cloud are established for mass, static energy (s), water vapour (q) and liquid water (ρ). Entrainment is assumed to take place into the cloud at all levels whereas detrainment takes place in a thin layer at the cloud top (the level of vanishing buoyancy). As a result of the above budget two important relations are deduced:

$$\rho \frac{\partial \bar{s}}{\partial t} = D (\hat{s} - \bar{s} - L\hat{l}) + M_c \frac{\partial \bar{s}}{\partial z} - \rho \mathbb{V} \cdot \nabla \bar{s} - \rho \bar{w} \frac{\partial \bar{s}}{\partial z} + \bar{Q}_R \quad (6.90(a))$$

$$\rho \frac{\partial \bar{q}}{\partial t} = D (\hat{q}^* + \hat{l} - \bar{q}) + M_c \frac{\partial \bar{q}}{\partial z} - \rho \mathbb{V} \cdot \nabla \bar{q} - \rho \bar{w} \frac{\partial \bar{q}}{\partial z} \quad (6.90(b))$$

where $(\hat{\quad})$ refers to the level of vanishing buoyancy, and the environmental radiational heating is expressed as:

$$\bar{Q}_R = \tilde{Q}_R + \Sigma Q_{Ri} \quad (6.91)$$

Equations (6.90(a)) and (6.90(b)) relate the properties of the cloud ensemble to be evaluated so as to predict \bar{s} and \bar{q} . These properties are: (i) $D(z)$,

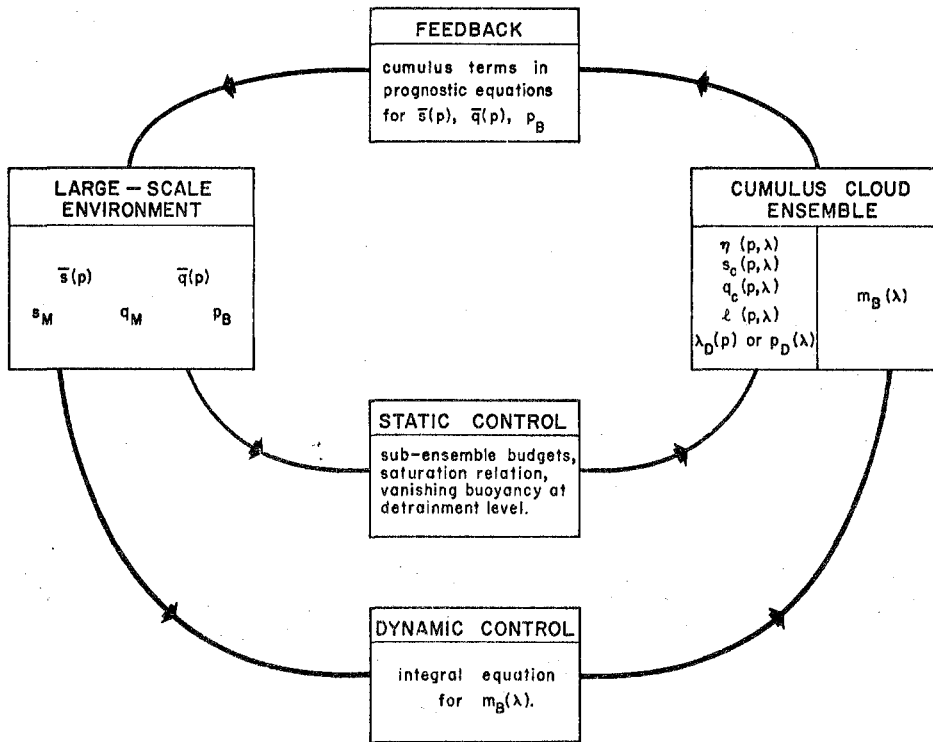


Figure 6.8 - Schematic representation of the mutual interaction of a cumulus cloud ensemble with the large-scale environment

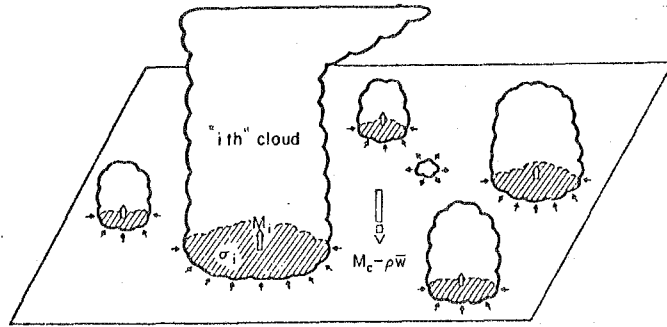


Figure 6.9 - A unit horizontal area at some level between cloud base and the highest cloud top. The taller clouds are shown penetrating this level and entraining environmental air. A cloud which has lost buoyancy is shown detraining cloud air into the environment

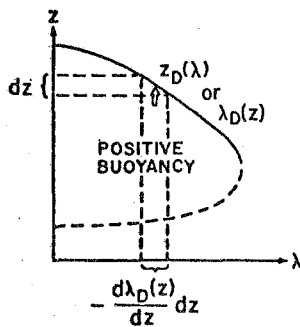


Figure 6.10 - The detrainment level z_D as a function of λ , or λ_D of the detraining clouds as a function of z

(ii) $M_c(z)$, and (iii) $\ell(z)$. Cumulus clouds also modify the large-scale temperature field via the radiational heating, ΣQ_{Ri} .

When the detrainment layer is very small, $D(z)\Delta z$ is equal to the total mass flux, at level z , of the clouds which lose buoyancy within that layer. To evaluate the vertical distributions of the above three properties, the cumulus ensemble is subdivided spectrally into subensembles according to cloud type characterized by the parameter λ called the fractional entrainment rate. The detrainment level z_D becomes a function of λ . This parameter is so chosen that $z_D(\lambda)$ decreases as λ increases (Fig. 6.10). The mass flux carried by the ensemble at level z is given by:

$$M_c(z) = \int_0^{\lambda_D(z)} m_B(\lambda) \eta(z, \lambda) d\lambda \quad (6.92)$$

where $\lambda_D(z)$ is the entrainment parameter for clouds detraining at level z and $\eta(z, \lambda)$ is a normalized mass flux as a function of height defined by the relation:

$$\eta(z, \lambda) = \begin{cases} \exp [\lambda(z - z_B)], & z_B \leq z \leq z_D(\lambda) \\ 0 & z \geq z_D(\lambda) \end{cases} \quad (6.93)$$

and $m_B(\lambda)$ is the mass flux at the base of clouds for a given entrainment parameter λ . For each subensemble, the budget equations for mass, moist static energy and total water content are computed. These determine the vertical mass flux $m_B(\lambda)$, the cloud moist static energy function $h_c(z, \lambda)$, the cloud specific humidity $q_c(z, \lambda)$, $\ell(z, \lambda)$, the level of vanishing buoyancy $z_D(\lambda)$ for each subensemble. A crude parameterization for the rainfall rate $r(z, \lambda)$ is made. $r(z, \lambda) = c_0 \ell(z, \lambda)$ where c_0 is a constant. The condition for vanishing buoyancy is given by:

$$h_c [z_D(\lambda), \lambda] = \hat{h}^* [z_D(\lambda)] \quad (6.94)$$

where \hat{h}^* is the saturation value of the moist static energy of the environment. Also,

$$\ell [z_D(\lambda), \lambda] = \hat{\ell}(z_D(\lambda)) \quad (6.95)$$

In order to evaluate $M_c(z)$ and $D(z)$ the mass flux $m_B(\lambda)$ needs to be known. The budgets for static energy and moisture of the mixed layer reveal that the mass flux in the mixed layer is determined by entrainment due to turbulent eddies. Without this entrainment, the top of the mixed layer is lowered by the subsidence. The cumulus clouds with their compensating induced subsidence determine the depth of the mixed layer. The budget equations enable the prognostic determination of z_B , s_M , q_M and hence h_M . It is assumed that the main role of the mixed layer (M) is to redistribute moisture and static energy to the cumulus clouds and hence we set:

$$\begin{aligned} s_c(z_B, \lambda) &= s_M \\ q_c(z_B, \lambda) &= q_M \\ h_c(z_B, \lambda) &= h_M \end{aligned} \quad (6.96)$$

Arakawa next defines a "cloud work function" $A(\lambda)$ for each sub-ensemble. This is a measure of kinetic energy generation by buoyancy per unit mass flux.

$$A(\lambda) = \int_{z_B}^{z_D(\lambda)} \eta(z, \lambda) \frac{g/c_p}{(1 + \gamma(z))\bar{T}(z)} \left(h_c(z, \lambda) - \bar{h}^*(z) \right) dz \quad (6.97)$$

where $\gamma = \frac{L}{c_p} \frac{\partial \bar{q}^*}{\partial \bar{T}}$ and $(\bar{\quad})$ are an area average. Without destabilization by the large-scale processes $A(\lambda)$ will decrease and environment will adjust towards a neutral state. The time scale for this adjustment is of the order of 10^3 - 10^4 s. To maintain the cumulus ensemble beyond that time scale, $A(\lambda)$ must increase due to large-scale processes. The time scale of large-scale processes is of the order 10^5 s, which is much larger than the adjustment time scale. As a result, the time rate of change of $A(\lambda)$ is almost zero. The subensemble is hence in a quasi-equilibrium with the large-scale forcing. This QEA is an assumption on "parameterizability" of cumulus convection.

By considering the balance between each sub-ensemble and the large scale forcing an integral equation to determine $m_B(\lambda)$ can be obtained. The constraints on the integral equation are:

$$\begin{aligned} m_B(\lambda) > 0, & \quad \int_0^{\lambda_{\max}} k(\lambda, \lambda') m_B(\lambda') d\lambda' + F(\lambda) = 0 \\ m_B(\lambda) = 0, & \quad \int_0^{\lambda_{\max}} k(\lambda, \lambda') m_B(\lambda') d\lambda' + F(\lambda) < 0. \end{aligned} \quad (6.98)$$

Here $F(\lambda)$ is the large scale forcing and $k(\lambda, \lambda')$ is the kernel representing the effect of different cloud types.

The theory can also be used for diagnostic studies by ignoring the dynamic control. At this stage, aspects of this theory have been verified by Betts (1974) and Yanai *et al.*, (1973). Practical application to problems of large-scale tropical weather prediction remains to be explored.

Chapter 7

SEA BREEZE AND DIURNAL CHANGES IN THE TROPICS

7.1 Introduction

The sea-breeze phenomenon is very striking over many parts of the tropics since it is known to produce cooling associated with afternoon showers that occur with regularity on most undisturbed days. Figure 7.1 from a classical diagram of Van Bemmelen (1922) illustrates the time evolution of the sea breeze in Batavia*. The Batavia sea-breeze time section shows that it is a shallow circulation confined essentially to the lowest 3 km. The intensity of the upper-land breeze is roughly a half that of the sea breeze. The land breeze during the early morning is much less intense by comparison. Extensive observational studies of sea breezes have been conducted by Hsu (1970), Flohn (1965) and many others. Hsu (1970) portrayed a schematic evolution of the land/sea-breeze phenomenon based on observations in the Texas Gulf Coast. Figure 7.2 illustrates this evolution, the diagram being self-explanatory. Here the horizontal and vertical extent of the wind system is enclosed within a heavy solid elliptical curve. This diagram of Hsu is adapted from Atkinson (1971).

Although the main intensity of the sea breeze is confined to the lower troposphere, the phenomenon of diurnal change is known to occur at all latitudes and even in the stratosphere. We recognize that the sea breeze is primarily driven by differential heating between land and sea. Simple numerical models have gone a long way towards exploring the role of such diurnally imposed heating cycles on the evolution of sea-breeze circulations. The problem is an important one, because, at times one can see a late evening line of coastal clouds for thousands of miles; occasional such examples of cloud lines have been observed on the Atlantic coast from Florida to Newfoundland during the summer months. Because of associated cumulonimbus convection, such a long line of convergence can have important implications in the atmospheric general circulation. We shall next address some of the well-known dynamical studies of the sea-breeze phenomenon.

7.2 Sea-breeze models

A large number of models have recently been described. Some of the well-known studies are by Estoque (1966 a, b, c) and by Pielke (1974).

Estoque considers the sea-breeze problem in an x - z plane where x is normal to the coastline and z is the vertical coordinate. The closed system of equations of the linear sea-breeze problem is:

* Now Jakarta.

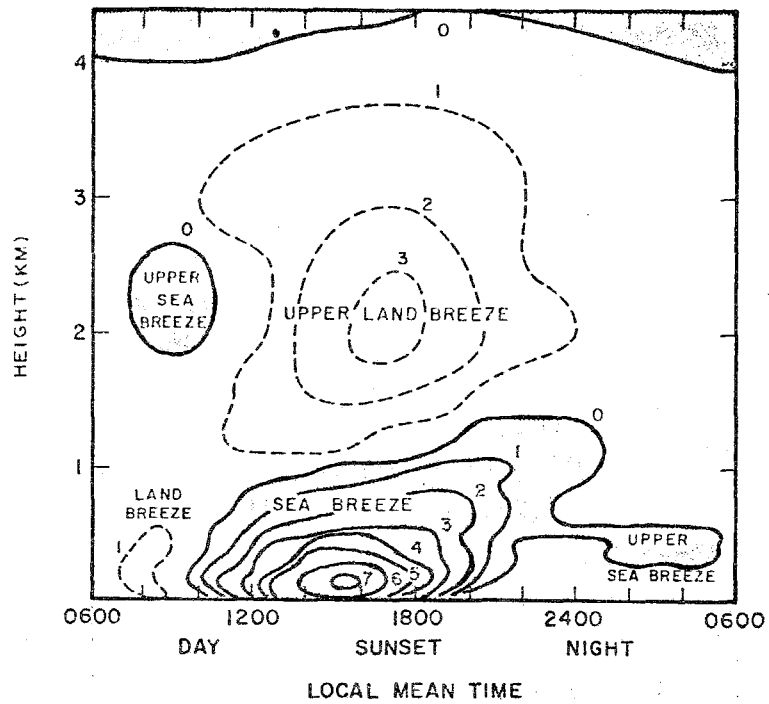


Figure 7.1 - Velocity isopleths (m s^{-1}) for the land/sea breeze in Batavia; shaded area indicates onshore flow and unshaded area offshore flow (after van Bemmelen)

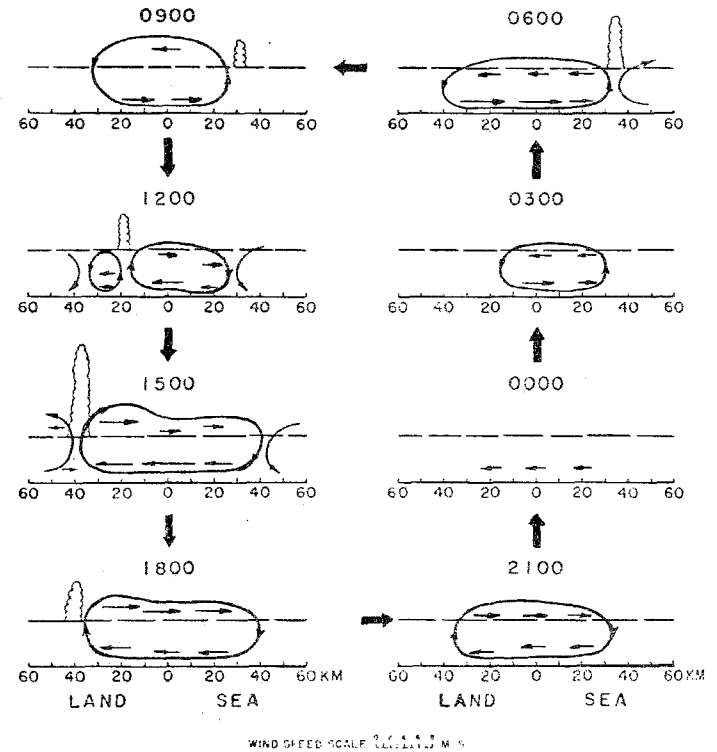


Figure 7.2 - Synthesized empirical model of the land/sea-breeze system along the Texas Gulf Coast. Arrow lengths proportional to wind speed. See text for discussion

Equation of motion:

$$\frac{\partial u}{\partial t} = fv - \sigma u - \frac{1}{\rho} \frac{\partial p}{\partial x} \quad (7.1)$$

$$\frac{\partial v}{\partial t} = -fu - \sigma v - \frac{1}{\rho} \frac{\partial p}{\partial y} \quad (7.2)$$

$$\frac{\partial w}{\partial t} = -\sigma w - \frac{1}{\rho} \frac{\partial p}{\partial z} - g \quad (7.3)$$

Mass continuity equation:

$$\frac{\partial u}{\partial x} + \frac{\partial w}{\partial z} = 0 \quad (7.4)$$

First law of thermodynamics:

$$\frac{\partial T}{\partial t} + \beta w = K \left(\frac{\partial^2 T}{\partial x^2} + \frac{\partial^2 T}{\partial z^2} \right) \quad (7.5)$$

The diurnal heating is introduced via a prescribed variation of surface temperature T by a relation of the form:

$$T = M e^{int} \sin \frac{2\pi x}{L} \quad (7.6)$$

Here u, v and w are the three velocity components, p is the density of air, f the Coriolis parameter and σ a coefficient of friction. K stands for a thermal diffusivity coefficient and β denotes the lapse rate of the undisturbed thermal stratification. The standard procedure of solving linear system of equation as those given above consists in assuming solutions of the form:

$$q = Q(z) e^{int} \frac{\cos}{\sin} mx \quad (7.7)$$

where q stands for one of the dependent variables u, v, w, T or p. The substitution of such forms of solutions with appropriately prescribed boundary conditions leads to a separation of variables in the x, z and t coordinates. The usual boundary conditions for this problem are:

$$z = 0 \rightarrow w = 0; \quad T = M e^{int} \sin mx; \quad m = \frac{2\pi}{L}$$

$$z = \alpha \rightarrow w = 0; \quad T = 0 \quad (7.8)$$

$$\text{Let } r = \frac{g}{\bar{T}} m^2 (\sigma + in) / \left\{ (\sigma + in)^2 + f^2 \right\}$$

The solutions are all periodic in x. Estoque's solutions for this problem are:

$$u = \frac{rM}{m(a^2 - b^2)} \left[ae^{az} + be^{-bz} \right] e^{int} \cos mx \quad (7.9)$$

$$v = \frac{frM}{m(\sigma + in)(a^2 - b^2)} \left[ae^{az} + be^{-bz} \right] e^{int} \cos mx \quad (7.10)$$

$$w = \frac{rM}{a^2 - b^2} [e^{az} - e^{-bz}] e^{int} \sin mx \quad (7.11)$$

$$T = Me^{-bz} + \frac{b^2 - s}{b^2 - a^2} [e^{az} - e^{-bz}] e^{int} \sin mx \quad (7.12)$$

M is an arbitrary amplitude function, and a and b are constants that are determined by the initial conditions. The symbols r and s respectively denote:

$$r = g \alpha m^2 (\sigma + in)^2 / \{f^2 + (\sigma + in)^2\} \quad (7.13)$$

$$s = \frac{in}{\kappa} + m^2 \quad (7.14)$$

α is a coefficient of thermal expansion

κ is the eddy diffusion coefficient.

Estoque used the following values of the constants to portray his solution of the linear sea-breeze problem.

$n = 7.273 \times 10^{-5} \text{ s}^{-1}$; $f = \text{Coriolis parameter at } 45^\circ\text{N}$; $\beta = 2.5 \times 10^{-5} \text{ deg cm}^{-1}$;
 $\sigma = 2.5 \times 10^{-4} \text{ s}^{-1}$; $g = 980 \text{ cm s}^{-2}$; $M = 2\pi/L$, where $L = 120 \text{ km}$ the lateral scale of the sea breeze; $\kappa = 2.25 \times 10^5 \text{ cm}^2 \text{ s}^{-1}$.

It should be emphasized again here that the sea breeze is driven by the imposed temperature perturbation in space and time along the lower boundary. How this temperature is realized is not addressed here. Estoque noted a number of interesting properties in this solution:

- (i) The maximum temperature at the surface occurs at noon, and later at higher levels. The vertical transport of heat is due to mixing and vertical advection.
- (ii) The motion field clearly shows a sea-breeze component. The lower branch of the sea breeze (ocean to land) is only 0.5 km deep, the return flow being much deeper. The maximum intensity of the sea breeze is reached about 1 hour after the maximum heating at the surface (i.e., 1 pm). Maximum vertical motion occurs at 0.4 km.
- (iii) A hodograph of the surface wind (u, v) showed that the sea breeze during the day and the land breeze at night were of equal intensity. This is unrealistic a consequence of the imposed periodic temperature cycle at the surface. The sea-breeze ellipse is usually pear-shaped (observationally).

- (iv) Estoque also noted that the solution depends strongly on the magnitude of the friction coefficient. The larger its value, the closer to the time of maximum heating do the stronger winds from the ocean tend to occur. The solutions from this linear theory appear quite realistic in many ways in spite of limitations such as artificially imposed cyclic conditions, lack of interaction with a basic large-scale prevailing synoptic situation and the surface heating.

In a further analysis, Estoque (1967) extended his studies to a non-linear two-dimensional model on a meridional vertical plane. The following 5 equations describe the closed system of this study:

$$\frac{\partial u}{\partial t} = -u \frac{\partial u}{\partial x} - w \frac{\partial u}{\partial z} + fv - \frac{RT}{p} \frac{\partial p}{\partial x} + \frac{\partial}{\partial z} \left(K \frac{\partial u}{\partial z} \right) \quad (7.15)$$

$$\frac{\partial v}{\partial t} = -u \frac{\partial v}{\partial x} - w \frac{\partial v}{\partial z} - fu - \frac{RT}{p} \frac{\partial p}{\partial y} + \frac{\partial}{\partial z} \left(K \frac{\partial v}{\partial z} \right) \quad (7.16)$$

$$\frac{\partial \theta}{\partial t} = -u \frac{\partial \theta}{\partial x} - w \frac{\partial \theta}{\partial z} + \frac{\partial}{\partial z} \left(K \frac{\partial \theta}{\partial z} \right) \quad (7.17)$$

$$\frac{\partial p}{\partial z} = \frac{p}{RT} g \quad (7.18)$$

$$\frac{1}{\rho} \frac{\partial \rho}{\partial t} = -\frac{\partial u}{\partial x} - \frac{\partial w}{\partial z} \quad (7.19)$$

The 5 unknowns of the problem are the velocity component, u , v , w ; pressure p ; and temperature T . K stands for the eddy diffusion coefficient, the other symbols are standard. A constant flux layer of thickness h near the Earth's surface has the property:

$$\frac{\partial}{\partial z} \left\{ \left(K \frac{\partial}{\partial z} \right) \begin{matrix} u \\ v \\ \theta \end{matrix} \right\} = 0 \quad (7.20)$$

By eliminating the density from equation (7.17) and (7.18) from (7.19), one obtains the relation:

$$p \frac{\partial^2 w}{\partial z^2} + \frac{\partial w}{\partial z} \frac{\partial p}{\partial z} = -p \frac{\partial}{\partial z} \left(\frac{\partial u}{\partial x} \right) + \frac{\partial}{\partial z} \left[\frac{p}{\theta} \frac{\partial}{\partial z} \left(K \frac{\partial \theta}{\partial z} \right) \right] - \frac{R}{c_p} \frac{\partial p}{\partial z} \left(\frac{\partial u}{\partial x} \right) - \frac{c_v}{c_p} \left(\frac{\partial u}{\partial z} \right) \frac{\partial p}{\partial x} \quad (7.21)$$

This is the equation for the vertical velocity w . Equation (7.20) replaces the mass continuity equation. For the variation of wind with height in the surface layer $0 \leq Z \leq h$, the logarithmic profile discussed in Chapter 5 was used. The method of initialization consists in defining a uniform potential temperature θ along horizontal surfaces. The pressure is deduced from the hydrostatic equation, initial winds are deduced from a geostrophic relation (although they could be zero everywhere at the start). The initial lapse rate is that of a standard atmosphere. The eddy diffusivity is determined in the boundary layer using mixing length ideas discussed in Chapter 5, above $z = h$, it is made to decrease linearly to zero at height H , the top of the computational domain. The numerical procedures include an upstream differencing scheme for the advection terms and a forward differencing scheme for the marching. The simulation cycle consists in first predicting u , v and θ and determining the pressure from the hydrostatic law and the vertical velocity from equation (7.20). Estoque ran two interesting experiments on the evolution of the sea breeze. In both cases the potential temperature variation at the lower boundary $z = 0$ was imposed as in the linear model, however, with more realistic values based on observations. The two experiments differentiate between a calm prevailing synoptic situation and one with a steady off-shore constant velocity. We show his results for the two experiments at 1700 local time in Figure 7.3. The calculations clearly show the major differences in the penetration of the sea breeze in the two experiments. The penetration of the sea breeze, in the calm case, extends to 30 km inland, while for the prevailing offshore wind case, it extends to 7 km inland. By 1700 hours the sea breeze was noted to have attained its maximum intensity (i.e. the vertical velocities were largest). In this diagram are also shown the isotherms as well as the isotachs. In these studies the computational domain extends to about 350 km in the lateral direction and does not have an imposed cyclic condition as did the linear problem. Aside from the proper handling of the penetration of the sea breeze inland, the solutions were also noted to be realistic in giving a reasonable vertical structure and depth of the entire circulation. The relative intensities of the sea and land breeze were more realistic. Furthermore, Estoque notes that observations usually show the formation of the cloud lines and associated diurnal rainfall and latent heat release; these are some of the factors not covered by this model since it is forced by the bottom boundary conditions. Estoque also felt that a time-dependent eddy viscosity coefficient was desirable for this problem.

Among the more recent advances in our understanding of sea-breeze dynamics, the studies by Pielke (1974) are noteworthy. Pielke integrated a three-dimensional hydrostatic system of primitive equations to study the sea breeze over south Florida. The forcing included surface heat and momentum fluxes as well as the influence of a prevailing synoptic situation. We shall not go into the details of the closed system of the primitive equations, although it should be emphasized that qualitative discussion of the results of a complex numerical model is no substitute for a detailed step-by-step understanding of the model, especially to those who wish to follow this approach towards understanding a phenomenon.

Pielke integrated the motion and thermal variables by a semi-implicit form of the upstream differencing scheme. The vertical velocity was determined from the vertical integration of the mass-continuity equation, and the pressure from an integration of the tendency equation. Pielke notes the following interesting results in his studies:

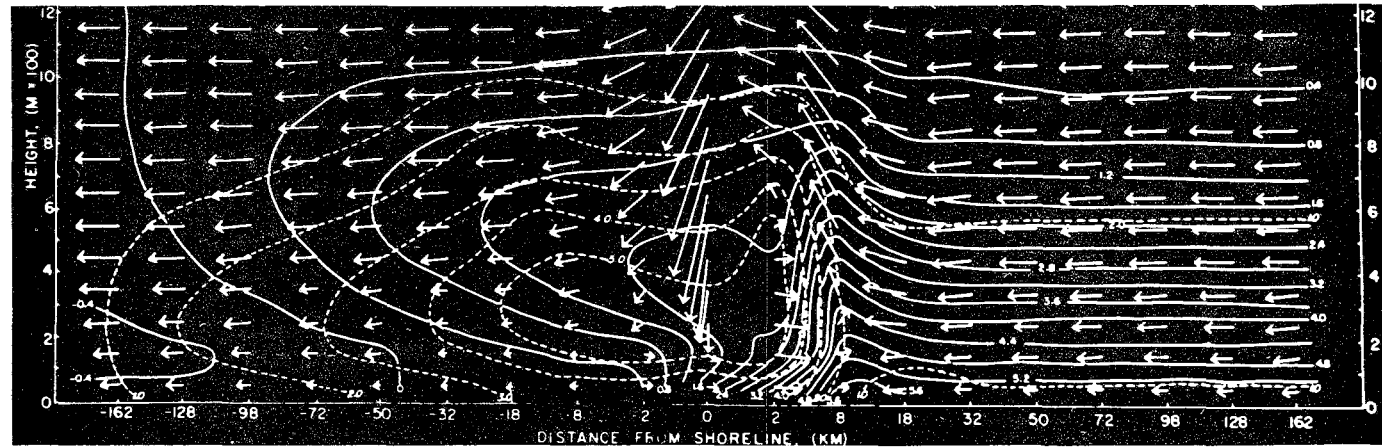
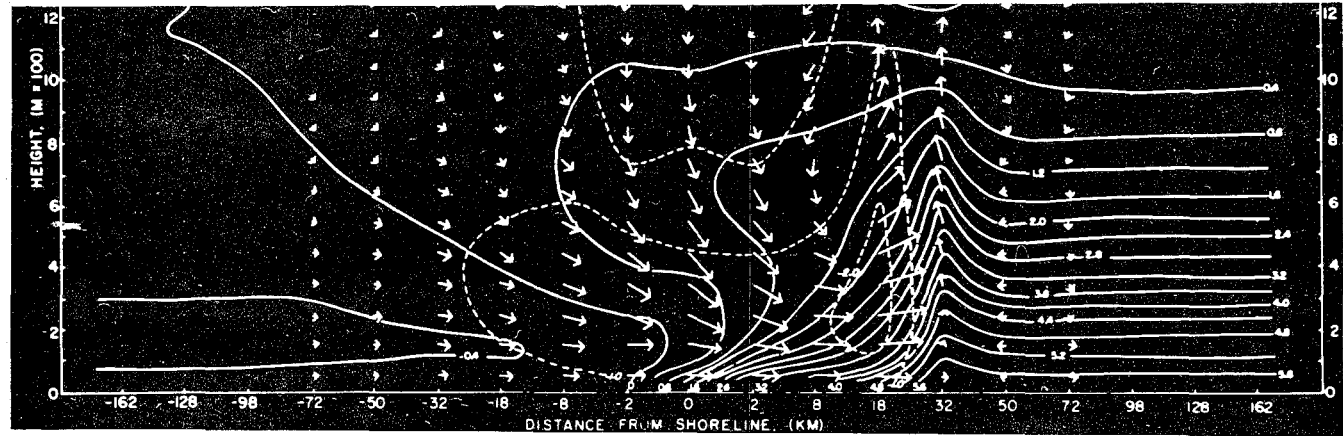


Figure 7.3 - Estoque's(1966) solution for the sea breeze at 1700 local time. Top panel shows no prevailing basic wind while bottom panel includes prevailing wind from the east. The wind arrows show a penetration of the sea breeze to 30 km inland top panel versus 7 km for the bottom panel. The solid lines indicate isotherms while the dashed lines show the speed field

- (i) The curvature of the coastline of south Florida has a significant influence on the location of the sea-breeze convergence zone.
- (ii) Under both southwesterly and southeasterly basic flows the convergence zone forms parallel and near the coast and moves inland during the day.
- (iii) Lake Okeechobee, located in central Florida, is a region of descent, this being a consequence of the cold water temperatures that are prescribed. It should be noted that, as in Estoque's formulation, at the surface of the earth, the potential temperature variation is described by an equation of the form:

$$\theta = A(x, y) \sin(2\pi t/T) \quad (7.22)$$

where A was chosen to be 10 K over land and 0 K over water. The period was taken as 13 hours, the duration of sunlight over Florida. The 10 K temperature differential between land and ocean is the critical factor in this problem; the absolute values of temperature do not explicitly enter the analysis.

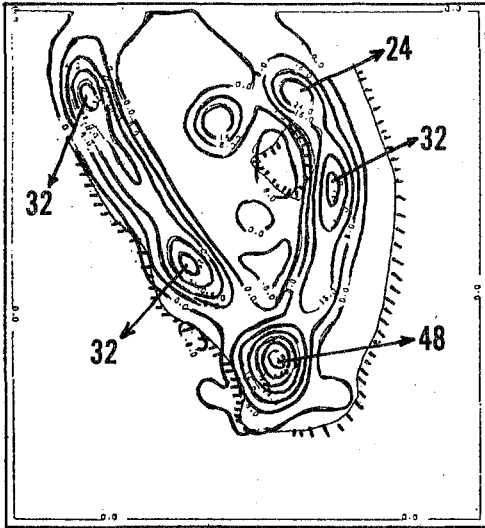
- (iv) The predicted evolution of the sea-breeze convergence zone is in close agreement with the organization of line convection over south Florida during undisturbed days.
- (v) Figure 7.4 shows the locations of cumulonimbus convection based on composite radar returns over Florida for a selected day and the numerically predicted field of vertical velocity around 3 and 4 pm, at the 1.22 km level. This comparison was a highlight of Pielke's simulation of the three-dimensional sea-breeze circulation. Studies along these lines can be formulated to investigate the coastal weather over many tropical land masses. Also studies of flows over small and large islands and peninsulas are other regions to which this approach can be applied. Models need to be further refined; however, in particular diurnal radiative heating, its feedback, convection (shallow, deep, dry and moist) require to be better formulated.

7.3 Some observational aspects of diurnal changes

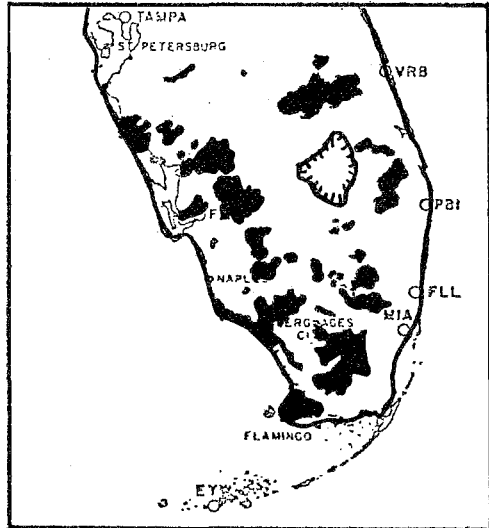
Lavoie (1963) presented a detailed investigation of the rainfall over oceanic atolls and showed the existence of a pronounced nocturnal rainfall maximum. The nocturnal or early morning maximum has been noted over different parts of the tropical oceans. Many hypotheses have been advanced for the nocturnal rainfall maximum such as: radiative effects due to differential heating over cloudy and cloud-free regions, radiative effects on the dry and moist static stability, radiative destabilization of the cloudy region at night, and tidal effects (diurnal as well as semidiurnal).

There exists an important semi-diurnal pressure wave in the tropics, also called the "S-2 wave". The semi-diurnal pressure wave is associated with a semi-diurnal oscillation of the surface divergence field. The amplitude of the diurnal

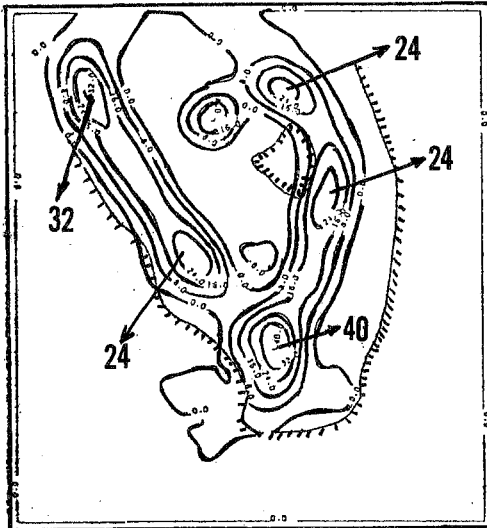
VERTICAL VELOCITY AT 1.22 km
GEOSTROPHIC WIND 2.5 m s^{-1} FROM 110°
HOUR 9.5 - CONTOUR INTERVAL 8 cm s^{-1}



COMPOSITE RADAR COVERAGE
1449 EST and 1544 EST 29 JUNE 1971



VERTICAL VELOCITY AT 1.22 km
GEOSTROPHIC WIND 2.5 m s^{-1} FROM 110°
HOUR 10.5 - CONTOUR INTERVAL 8 cm s^{-1}



COMPOSITE RADAR COVERAGE
1544 EST and 1644 EST 29 JUNE 1971

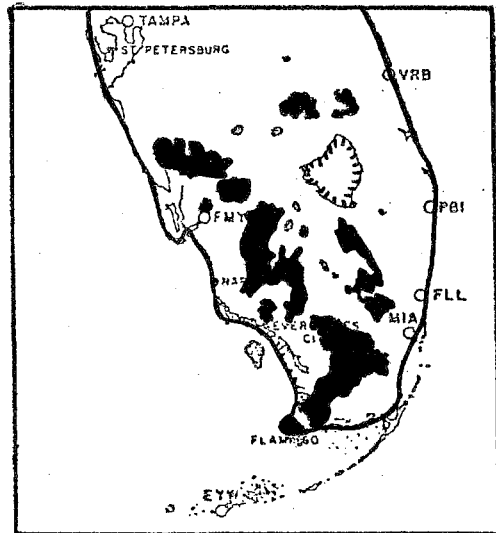
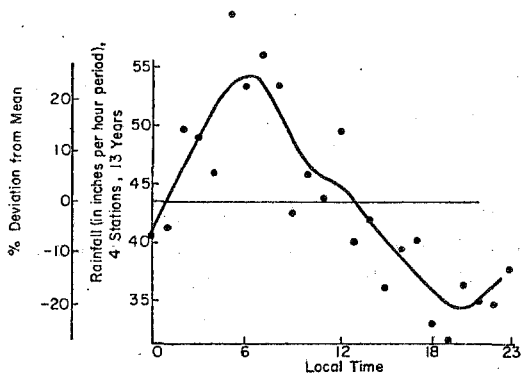


Figure 7.4 - Vertical motion prediction at 1.22 km and composite radar map for 29 June 1971 (Pielke, 1974)

pressure and the divergence oscillations were predicted by Lindzen (1967). However, most observations show that the amplitudes of diurnal oscillations are much larger than those given by simple tidal formulations. Nitta and Esbensen (1974) have presented such observational evidence.

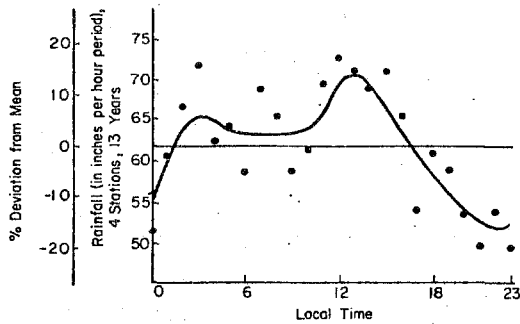
Gray and Jacobson (1977) have examined in some detail the diurnal variation of disturbance cloudiness over oceans. They found that oceanic intense rainfall from disturbances shows a maximum in the early morning hours. They found that this was true for most of the small islands, presumably due to the effect of the diurnal heating of the island, and a bimodal distribution of island rainfall was documented. Figures 7.5 and 7.6 from the study of Gray and Jacobson illustrate these features for small and large islands. The results here are based on observations over the western Pacific ocean. The small islands reflect oceanic conditions and show a maximum around 6 p.m. The large islands show the additional peak around 3 p.m. as well. Gray and Jacobson have analyzed this diurnal feature in some detail. They have, quite correctly, emphasized the importance of this problem for tropical meteorology. They found a marked difference in the vertical distributions of divergence between 00 and 12Z and an enhanced lower tropospheric convergence at 00Z (10 a.m.) compared with 12Z (10 p.m.). This was true for most of their categories shown in Figure 7.7 which illustrates these distributions. They offer the following explanation for the enhanced convergence in the early morning hours over the oceans: The disturbed region, with low-level convergence, has an excessive rainfall, this being a region with cloud cover. There exists a differential radiation field between the cloudy and surrounding clear regions. Figure 7.8 from the study of Gray and Jacobson shows what they consider are typical vertical profiles of net radiative warming (or cooling) rates within a tropical disturbance during the day and night. The intensity of differential heating between the cloudy and cloud-free regions is quite different for day-time and night-time conditions. Figure 7.9 also from the study of Gray and Jacobson describes in a schematic manner the influence of such a radiative effect on the enhancement of convergence during the early morning hours. Here the heating rates are implied to produce bulges in the thickness patterns between pressure surfaces leading to stronger horizontal pressure gradients, and the stronger cross-isobaric flows result in an enhancement of the low-level convergence and upper-level divergence distribution. Although this is a conceptual model it is worthy of detailed investigation.

The diurnal changes over Africa and over the GATE experimental region in the eastern Atlantic have been examined in considerable detail by McGarry and Reed (1978). They show that over northern Africa between 15° and 20°N thunderstorms are most prevalent in the late afternoon/early evening period. The convective cloud cover and the rainfall was, however, maximum just after midnight. They attributed this feature to the long-lived squall systems that form in the afternoon but take several hours to reach their maximum rain production. McGarry and Reed (1978) as well as Gray and Jacobson (1977) examined the rainfall over the eastern Atlantic and noted a distinct early afternoon maximum. This was also confirmed by Murakami (1978) from his analysis of satellite cloud cover distributions. The GATE region of the eastern Atlantic (defined in Chapter 20) is thus somewhat anomalous compared to the western Pacific ocean. No explanation was offered by McGarry and Reed for this anomalous behaviour.



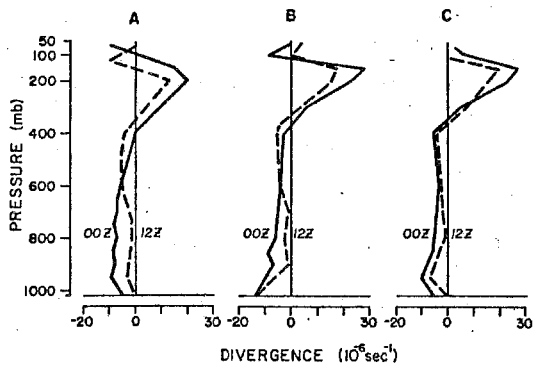
Precipitation curve for small islands in spring

Figure 7.5



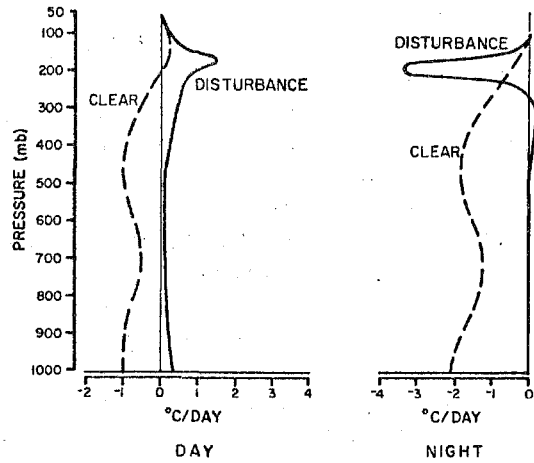
As in Fig. 7.5 but for large islands

Figure 7.6



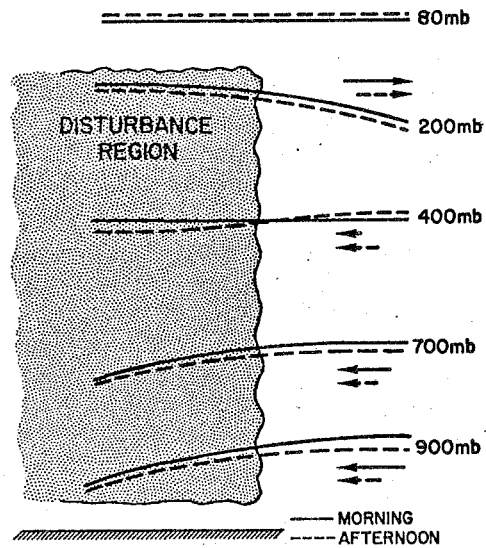
Average divergence profiles at 0000 and 1200 GMT for three groups of west Pacific cloud clusters: A, nonintensifying cloud clusters; B and C, cloud clusters which later develop into tropical cyclones. B is for clusters whose maximum sustained winds are less than $12-15 \text{ m s}^{-1}$, C for clusters whose maximum sustained winds are $\sim 20 \text{ m s}^{-1}$

Figure 7.7



Estimated typical day and night rates of net radiational warming within a tropical disturbance and in the surrounding clear or mostly clear regions

Figure 7.8



Idealized slope of a disturbance to surrounding clear region pressure surfaces during the day (dashed curve) and at night (solid curve) and the corresponding night versus day inward/outward radial wind patterns which are established

Figure 7.9

7.4 Diurnal variation in the monsoon belt

Ananthkrishnan (1977) has examined the diurnal changes of wind, pressure and temperature distribution over India. Figure 7.10 from his work illustrates the diurnal variation of winds (12Z minus 00Z winds) for four selected stations. The four stations are:

- (i) Madras, located on the south-east Indian coast, which experiences much of its rainfall in October and November;
- (ii) Bombay, located on the west Indian coast, which experiences most of its rainfall in June, July and August;
- (iii) Calcutta, located over coastal northeastern India, which also experiences most of its rainfall in June, July and August; and
- (iv) Delhi, located over north central India near a desert, experiencing most of its rainfall in July and August.

These diagrams are good illustrations of the vertical distributions of diurnal change phenomena.

Over Madras the 12Z (i.e. 5.30 p.m.) winds are easterlies, stronger than those at 00Z (5.30 a.m.) in the lowest kilometre. This is indicative of the sea breeze over Madras, where it is strongest during the summer months, at around 0.3 km above sea level. The depth of the sea breeze circulation is roughly 4 km.

Over Bombay the sea breeze is pronounced from September to May (i.e. the non-monsoon months). The depth of the sea breeze over Bombay can be as much as 5 to 6 km. This is noted between February and April. Over Madras as well as over Bombay, there exists a diurnal component between 9 and 12 km during the summer months. This is shown up in figure 7.10, i.e. diurnally stronger easterlies over Bombay and stronger westerlies over Madras. Although the amplitude of this phenomenon is only around 2 m s^{-1} , it is, however, significant, since the averages are based on roughly 10 years of observations. Thus an important question remaining unsolved here is "how is this diurnal feature maintained?". The axis of the tropical easterly jet of northern summer is located closer to Madras, and the above data implies that the jet is stronger at 00Z (i.e. 5.30 a.m.) than at 12 Z (i.e. 5.30 p.m.). This may be a reflection of radiative effects associated with diurnal variations of convection and cloud cover. Over Madras the rainfall maximum (see Table 7.1) occurs between 6 p.m. and midnight while at Bombay the period of most intense rainfall is between 6 a.m. and 9 a.m. This diurnal change over Bombay is more maritime (during June, July and August) while that of Madras seems more continental. Cloud cover and associated radiative cooling can affect the meridional thermal gradients and the winds may intensify or decrease accordingly at upper levels.

Over Delhi, located in north central India, there exists an interesting diurnal component during the summer monsoon months. Winds in the lowest 1 km are more from the east at 12Z (i.e. 5.30 p.m.) than at 00Z (i.e. 5.30 a.m.). Delhi is located on the eastern edge of the Rajputana desert. The diurnal change in winds at low levels is most likely in response to the diurnal heating of the desert and a flow towards it

TABLE 7.1
Diurnal variation of rainfall

Station	Elevation (m)	Season	Percentage of seasonal rainfall								Seasonal rainfall (mm)
			00-03 h IST	03-06	06-09	09-12	12-15	15-18	18-21	21-24	
1. Cherrapunji	1313	I	18.2	17.5	12.4	7.8	5.1	6.4	11.8	20.9	2360
		II	17.4	18.4	14.5	12.8	7.4	5.7	8.6	15.3	8481
		III	18.2	15.3	11.7	9.7	12.1	9.8	9.2	14.1	413
2. Mahabaleshwar	1382	I	7.7	6.4	2.5	1.2	12.1	40.0	18.0	12.1	104
		II	11.9	11.9	11.0	11.0	14.4	16.0	12.6	11.3	5521
		III	8.6	8.7	7.5	7.4	15.4	23.5	17.5	11.1	205
3. Bombay	11	I	58.4	16.8	9.3	3.4	0.0	2.1	3.1	6.9	29
		II	13.6	14.7	15.3	13.4	11.3	9.3	9.8	12.5	2116
		III	13.7	34.1	12.6	7.4	5.2	8.6	11.6	6.7	85
4. Madras	16	I	10.4	16.6	13.3	17.2	12.7	8.8	9.5	11.6	75
		II	19.0	12.8	3.3	2.4	3.9	14.2	22.1	22.3	421
		III	17.8	16.8	11.6	11.6	10.0	9.8	8.5	13.8	605
5. Sagar Island	3	I	11.0	6.6	10.6	8.6	5.4	11.3	24.4	22.1	127
		II	15.2	19.0	14.2	14.8	11.2	7.6	8.0	10.0	1208
		III	13.0	15.5	13.6	16.9	15.1	11.4	5.2	9.3	221
6. New Delhi	216	I	11.3	6.1	7.8	4.3	7.8	37.4	11.3	13.9	12
		II	8.5	15.2	14.7	15.1	16.1	16.9	7.4	6.1	539
		III	23.8	8.9	12.3	15.4	14.2	6.7	7.9	10.8	42
7. Jamshedpur	129	I	2.3	0.4	3.8	0.6	8.2	51.1	24.5	9.0	78
		II	8.9	9.2	7.9	9.6	17.8	23.3	14.1	9.2	1085
		III	12.4	14.1	9.4	7.6	16.0	18.4	11.6	10.4	89
8. Hyderabad	545	I	21.2	8.7	3.5	0.0	5.9	20.5	26.8	13.5	54
		II	14.5	10.6	5.0	4.9	9.7	18.4	18.1	18.7	605
		III	17.3	8.9	4.4	6.5	13.6	15.6	12.8	12.8	106

I: Apr + May; II: Jun + Jul + Aug + Sep; III: Oct + Nov + Dec

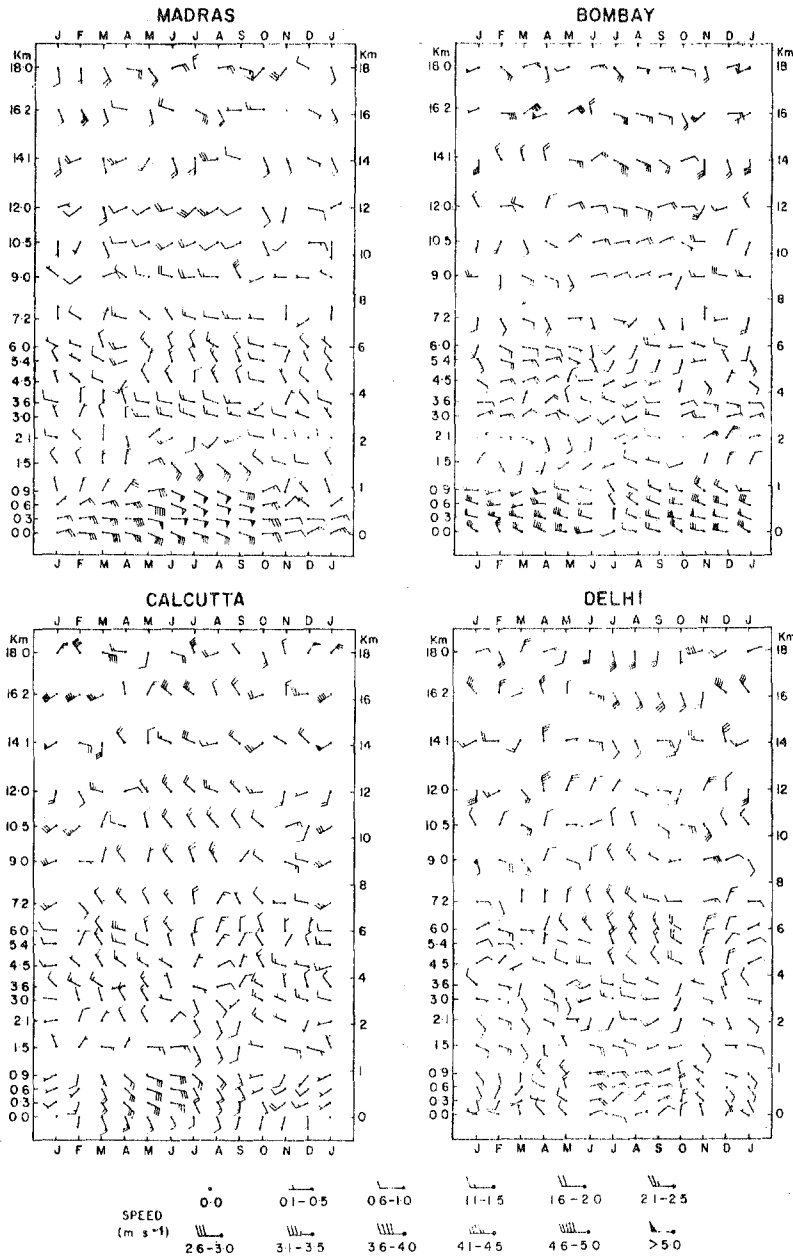


Figure 7.10 - Diurnal variation of upper winds (12 - 00)Z at Madras, Bombay, Calcutta and New Delhi

in the day-time. The reverse evidently occurs as a response to the cooling of the desert at night.

Calcutta, located in north-eastern India, experiences a strong diurnal component during April, May and June in the lowest km. This diurnal component is not well understood.

The diurnal component is important for several reasons. A proper understanding of the diurnal component of the motion field could provide a better understanding of the diurnal rainfall. Furthermore, there exists evidence that synoptic disturbances enhance and decay diurnally thus suggesting possible interactions of the synoptic and diurnal modes.

7.4.1 Diurnal variation in rainfall over India

Table 7.1 from Ananthakrishnan (1977) lists three-hourly rainfalls for a number of weather stations over India. Cherrapunji is one of the stations that experiences record rainfall amounts. Here the maximum rainfall occurs during the early morning between 03 and 06 h local time. The table is self-explanatory. Some of the stations show a single rainfall maximum around the early morning or late afternoon, while others display a bimodal character. During the summer monsoon, stations over north central India exhibit two maxima. A detailed explanation of the diurnal modes is presently lacking; the study of Gray and Jacobson (1977) provides important guidelines for further investigations of this problem.

A wind maximum around noon is shown up in the surface wind speed field. Figure 7.11, from Ananthakrishnan (1977), shows the hourly surface winds for four selected stations. The maximum wind for Port Blair, Madras and New Delhi is found during the northern summer months. A secondary maximum around 3 p.m. local time is also noted at New Delhi in the late winter months. The strong surface winds at noon over Port Blair and Madras are most probably related to the sea breeze. The strong winds at New Delhi are in response to the heating of the desert to the west and the diurnal strengthening of the heat low. Kodai-kanal is located at 1 200 m above sea level and is several hundred km from the Arabian Sea and Bay of Bengal coast. Here the surface wind speeds are out of phase with the coastal winds. A suggested explanation for this phase difference is based on momentum mixing in the vertical. Mixing is stronger in the summer months and tends to increase the surface winds while it reduces the winds at a higher elevation (such as at the level of Kodaikanal). The vertical distribution shows an increase of mean wind speed with height (with diurnal effects removed) above the surface at these locations. The amplitude of the diurnal change is found to be consistent with the mixing concept applied to the day-time hours. This implies a momentum mixing over a layer some 1 500 m deep. This is most probably brought about by the upward and downward fluxes of mass in and around the shallow convective clouds that are predominant during the summer months.

7.5 Final remarks

A vast body of literature exists on diurnal variations over continental areas of the tropics. Some of this is cited in Atkinson (1971). He notes that a

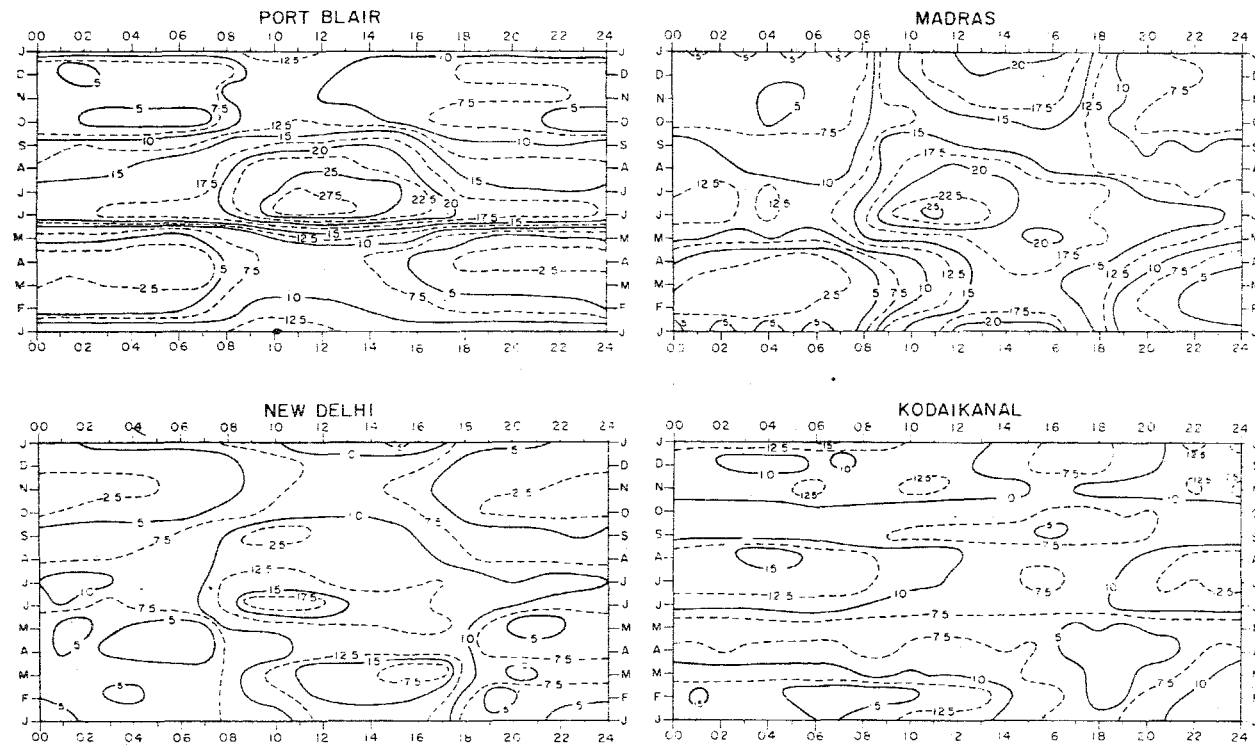


Figure 7.11.
Hourly variation of surface wind speeds (km h⁻¹) at Port Blair, Madras, New Delhi and Kodaikanal.

Figure 7.11- Hourly variation of surface wind speeds (km h⁻¹) at Port Blair, Madras, New Delhi and Kodaikanal

lack of order prevails in many areas; as an example: studies by Pedgley (1969) suggest that the diurnal change does not have the same phase in different sites of a region such as the Sudan. Diurnal change problems require further detailed observational and dynamical investigations.

Chapter 8

ATLANTIC DISTURBANCES

8.1 Introduction

The atmosphere over the tropical and the subtropical Atlantic oceanic regions is known for its subtropical high, tropical depressions, tropical storms, hurricanes, trade winds, easterly waves, "inverted V" cloud formations, cold upper lows, cloud clusters, squall lines, trade inversions, intertropical convergence zones, high level mid-oceanic troughs and low-and high-level easterly jets. Much of the weather activity is known to occur north of the Equator while the southern Atlantic is relatively free of disturbances and only the subtropical high, trades (with their fluctuations) and the trade inversion are well-known features. The apparent lack of disturbances south of the Equator has been recognized for some time. The intertropical convergence zone remains north of the Equator throughout the year and photographs from the geostationary satellite show a lack of cluster activity south of the Equator; the field of sea-surface temperature shows values much less than 26°C most of the time over the southern oceans. Furthermore, the southern hemisphere trade wind belt is observed to be quite close to the Equator. Tropical wave disturbances are known to form over West Africa and propagate westwards into the Atlantic. No counterpart of this is known to exist over the continent of Africa south of the Equator, although very heavy rainfall occurs in the near equatorial Zaire region during the northern winter months. The region south of the Equator is characterized during the southern summer season by low-level southeast trades and high-level westerlies (rather than easterlies). The vertical wind shear of the large-scale flow is large at 10°S and is comparable to that around 10°N during undisturbed periods. In this text we shall not say much about the region south of the Equator since not much is known at present. The region north of the Equator experiences fairly active weather between June and September, with greater activity in the latter months.

In this section we shall begin with a description of the so-called classical easterly wave.

8.2 Waves in the trade-wind belt

Case studies of tropical disturbances have been a very fruitful area of research in the Caribbean region. The easterly wave was extensively studied by Riehl (1945). In fact, the so-called classical easterly wave is based on his pioneering work in this area. Figure 8.1, based on his work, shows a time section at Grand Cayman Island during the passage of an easterly wave. This is one of the well-defined examples of wave passage. It shows the following features:

Wave trough - The wave trough tilts eastward with height (this is shown by the near-vertical dark line); the wave is moving westward and the upper part arrives later than the lower part. The wind shift shown by the directional change of wind barbs (knots) shows that the wave extends through the depth of the troposphere.

Thermal structure - The isotherms in this time section are shown as a departure of the observed temperature from a tropical standard atmosphere. We see here a cold core below the upper trough with higher temperatures to the east at low levels. The thermal amplitude of the wave at lower levels is somewhat large compared to other such examples. Between 500 and 250 mb a reversal in the thermal anomaly structures may be noted. The warm core above the low level cold core is attributed to the effects of cumulus convection. The thermal amplitude near 300 mb is about one half that at 900 mb.

The Moisture field - This is shown by the dashed lines (units $g\ kg^{-1}$). The region east of the wave trough is more moist than the region ahead (i.e. west) of it. The convective weather and large-scale upward rising motion tends to occur near the wave axis and to the east of it.

The horizontal structure of the Caribbean easterly wave has been analyzed by many scientists in the last twenty years. A detailed study was presented by Baumhefner (1968) based on a very careful analysis of the observations in this region. Figs. 8.2 through 8.5 are based on Baumhefner's analysis for August 13, 1961, 12Z. The wave has its largest amplitude near the 800 mb surface and the trough is located near $76^{\circ}W$ longitude. Figures 8.2, 8.3 and 8.4 illustrate the wind and temperature fields at 1 000, 800, 600, 400 and 200 mb. In this study the cold core is not discernible at the 1 000 mb surface; however, between 800 and 600 mb, the cold core is seen near the trough line and it tilts westward with height. The thermal field at 400 and 200 mb shows an upper cold low (located at $24^{\circ}N$ and $81^{\circ}W$). These tropical upper cold lows are transients within the quasi-stationary mid-oceanic long wave upper troughs.

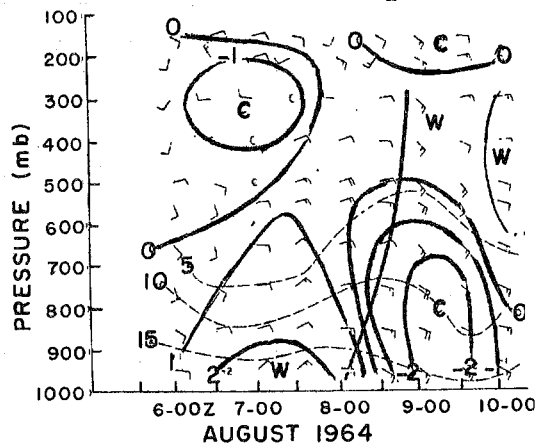


Figure 8.1.- A vertical time section showing winds (knots), temperature $^{\circ}C$ (solid lines) and specific humidity (dashed line) $g\ kg^{-1}$. The diagram is based on Riehl's study of easterly waves

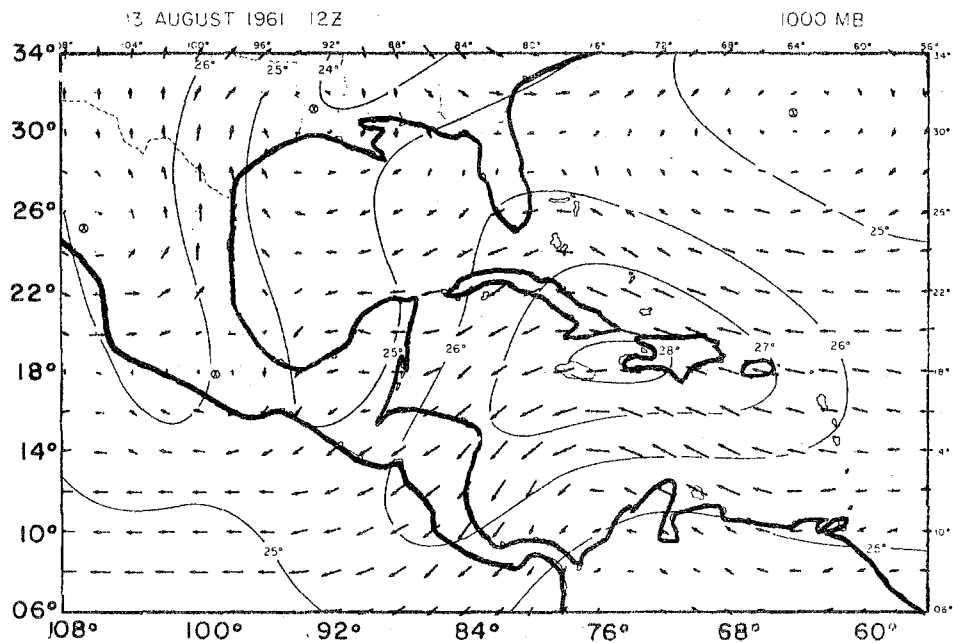
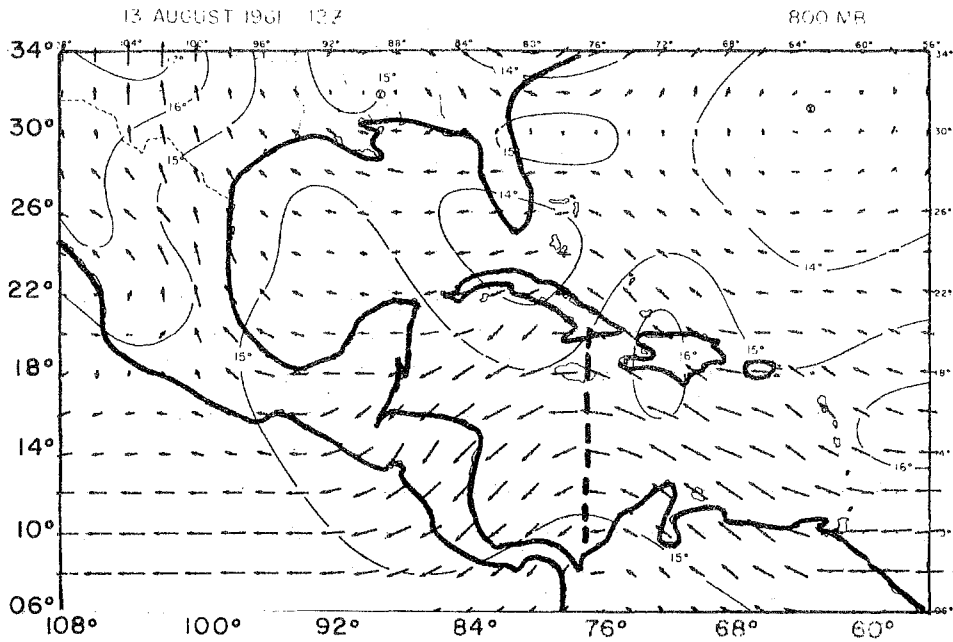


Figure 8.2. - Vector representation of the velocity field with the temperature. Vector length proportional to speed (0.4 centimetres equals 10 metres per second). Circled x's are closed centres of circulation. Temperature analysed every 1°C

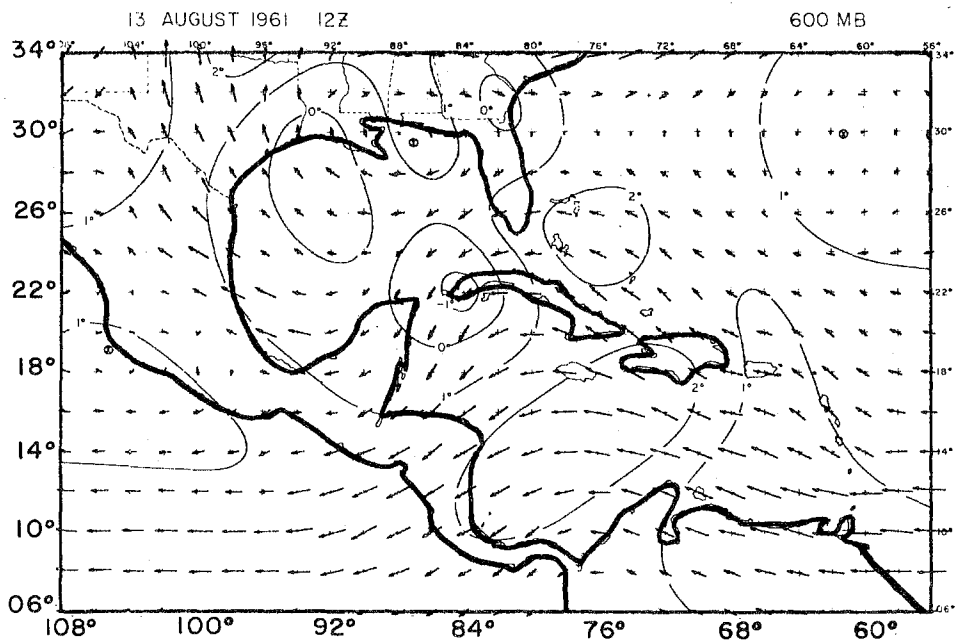
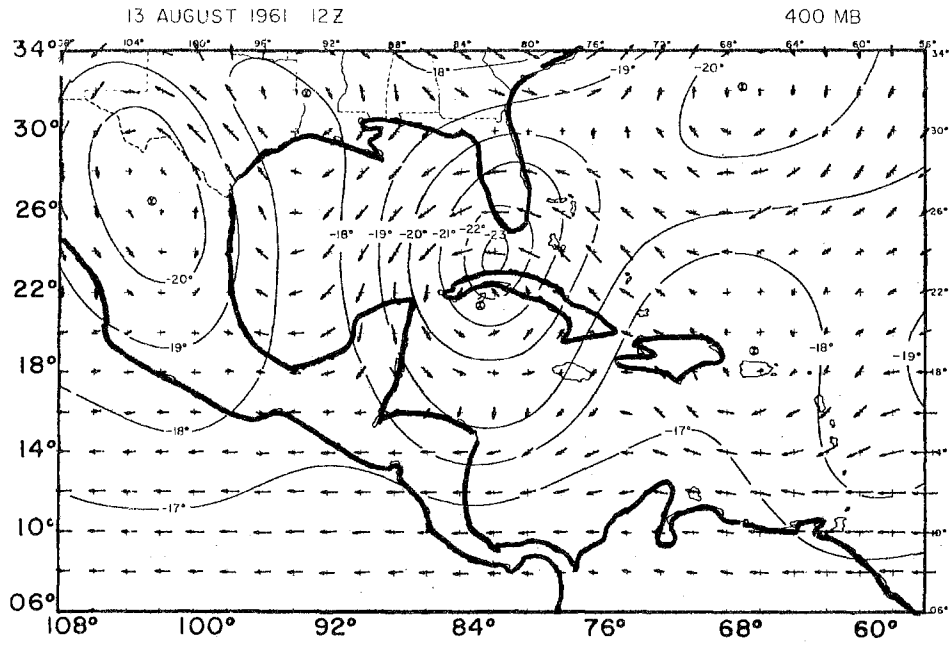


Figure 8.3 - Vector representation of the velocity field with the temperature. Vector length proportional to speed (0.4 centimetres equals 10 metres per second). Circled x's are closed centres of circulation. Temperature analysed every 1°C

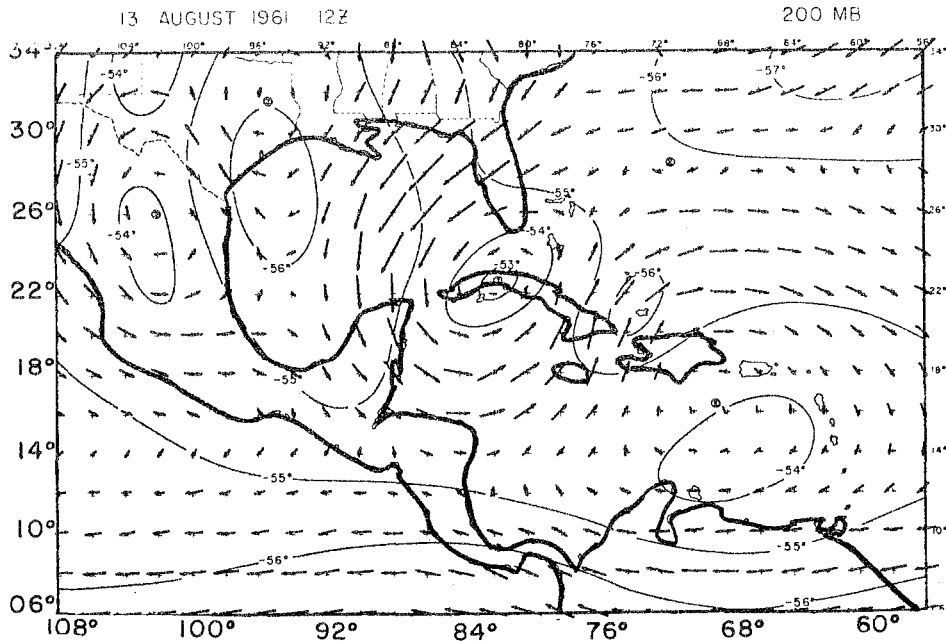


Figure 8.4a - Vector representation of the velocity field with the temperature. Vector length proportional to speed (0.4 centimetres equals 10 metres per second). Circled x's are closed centres of circulation. Temperature analysed every 1°C

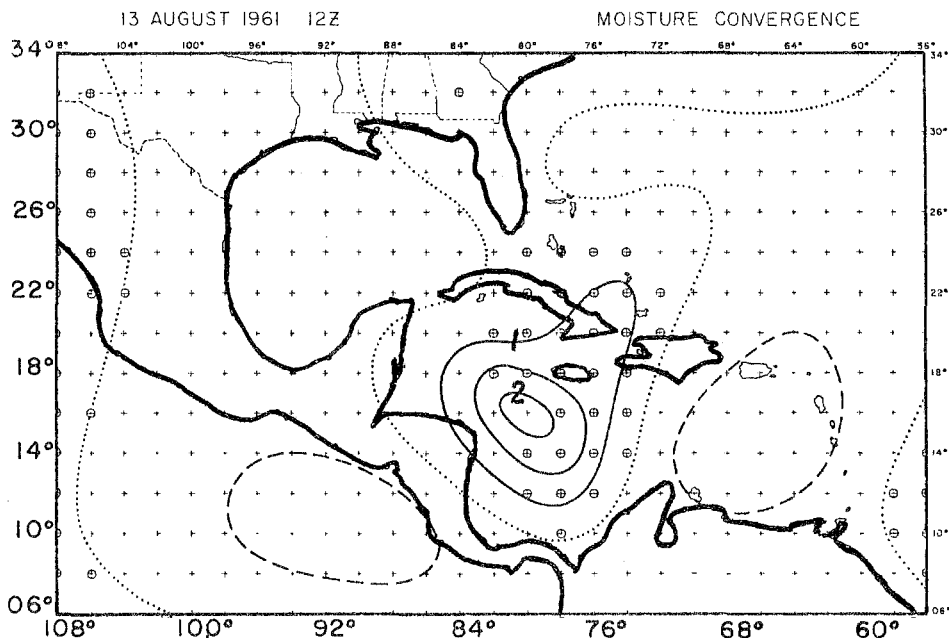


Figure 8.4b - Integrated moisture flux isolines are every $100 \times 10^{-6} \text{ mb s}^{-1}$. Solid lines are convergence, dotted lines are neutral, and dashed lines are divergence. Circled crosses are grid points of latent heat addition

The formation and maintenance of these easterly waves is difficult to understand. Frank (1976) has published an extremely valuable annual summary of Atlantic disturbances for the hurricane season. From operational daily surface and low-level weather charts and satellite photos, he has kept a seasonal diary of Atlantic disturbances that propagate westward from Africa. He notes that some 50 disturbances pass the coast of Senegal (Table 8.1 and Figure 8.6); that although several of these decay over the central Atlantic, roughly the same number are known to form there. A substantial number of these (around 20) are known to propagate westward across the central American highlands, and they move into the ITCZ disturbance belt of the eastern Pacific ocean. Although a qualitative count of these disturbances is now available, we still do not have sufficient information of their detailed structure. Unless and until we have more detailed information, it will be extremely difficult to predict which among these many disturbances will transform into hurricanes.

In the Appendix, we have provided a mathematical framework for the barotropic instability problem. The formation of easterly waves over West Africa has been studied by a number of scientists who have shown the importance of the barotropic mechanism. The disturbances that form over the Atlantic trade-wind belt have not been studied in sufficient detail. From an analysis of the detailed motion field at 850 mb utilizing cloud winds (Chapter 20), Tripoli and Krishnamurti (1975) concluded that over large portions of the eastern Atlantic, the wave disturbances receive energy barotropically. Thus their general feeling is that the barotropic mechanism may be most important during the initial formative stage of Atlantic waves. Over the western Atlantic, some of these waves are known to become hurricanes. In this region, statistically one finds that the disturbances lose energy to local zonal flows; thus the barotropic mechanism is perhaps not helpful in the maintenance of these waves and the role of convection is perhaps more important. In a study of a westward propagating easterly wave, Krishnamurti and Kanamitsu (1973) noted the following energy transformations (Figure 8.7) over the Caribbean. The principal mechanism is the transformation of eddy available potential energy into eddy kinetic energy which is found important for the maintenance of the easterly wave. The manner in which this mechanism operates is as follows.

Ascending motion occurs at the wave axis and to its rear. Over this region a warm core is present near the 500 mb surface. Subsidence occurs all around and ahead of the wave axis at the surface. The net result of this ascent of relatively warm moist air and descent of relatively colder and dry air is that a generation of eddy kinetic energy occurs from the eddy available potential energy.

Even the westward motion of a non-developing easterly wave is a fairly complex problem. Estimates of the various terms of the vorticity equation are generally used to determine which of these contribute to a positive tendency of vorticity west of the surface trough. This is what makes the disturbance move westwards.

Positive vorticity advection contributes most significantly to this local increase of vorticity ahead of the surface trough. This effect is somewhat counteracted by the divergence term of the vorticity equation.

TABLE 8.1

Results of 1975 compared with the previous seven years

	1968	1969	1970	1971	1972	1973	1974	7-year average	1975
Total systems (all types)	107	105	85	103	113	95	96	101	113
Dakar systems	57	58	54	56	57	56	52	56	61
Barbados systems	59	44	53	56	56	58	58	55	69
San Andres systems	40	43	45	58	49	54	52	49	64
Depressions	19	28	24	23	24	24	25	24	28
Named storms	7	13	7	12	4	7	7	8	8
Subtropical storms	?	?	?	?	4	1	4		2

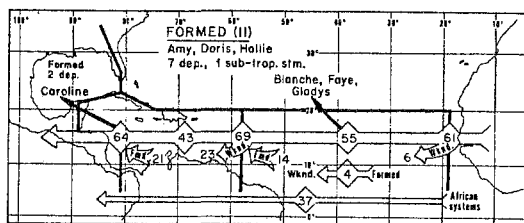


Figure 8.6 - Summary of tropical disturbances that passed three key stations (Dakar, Barbados, and San Andres) in 1975 and those maintaining their identity while crossing the Atlantic and Caribbean

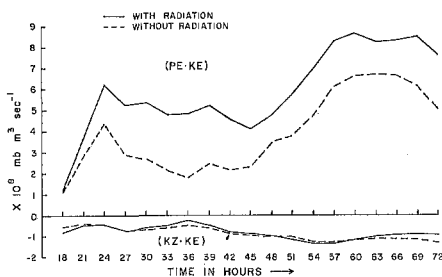


Figure 8.7 - Barotropic and baroclinic energy exchanges between 18 hours and 72 hours for two experiments, with and without long-wave radiative cooling effects. The energy exchanges are evaluated for a latitude belt 12° wide across the active part of the wave and between 100 and 1000 mb surfaces

In this example the easterly wave of the lower troposphere is close to the upper cold low. This is not always the case. This upper cold low extends down to 600 mb. Figure 8.4 (bottom panel) illustrates a computed field of moisture convergence based on Baumhefner's study. The heavy dark isopleths show a maximum of 2 units of moisture convergence. The field of total moisture convergence here is defined by the expression:

$$I = - \frac{1}{g} \int_{p_T}^{p_B} (\nabla \cdot \vec{V}_q + \frac{\partial}{\partial p} \omega q) dp$$

where q is the specific humidity, \vec{V}_q is horizontal velocity vector and ω is vertical velocity. It is generally recognized that large-scale net moisture convergence ($I > 0$) is encountered in regions where cloud clusters are found. As shown in Kuo's theory of parameterization (see Chapter 6), the cumulus scale vertical fluxes of moisture and heat are frequently parameterized as a function of the large scale field of moisture convergence, such as those shown here. In this instance, radar surveillance of convective cloud cover was available, and roughly 1 to 2 percent of the synoptic scale area was covered by hard core radar echoes. A schematic west/east cross-section (at 20°N) of the cloud representation is shown in Figure 8.5a along with the isopleths of moisture. This section is taken across the easterly wave shown above. The surface meteorological reports shown here were used in the cloud depiction by Baumhefner (1968). His study relates the cloud cover with the fields of large-scale vertical motion and moisture distribution. The latter are illustrated in Figure 8.5b. In general, the large-scale vertical velocity and cloud cover show very good correlation. In this example very dry air may be noted ahead, i.e. west of the wave axis. The estimation of vertical motion is difficult in the data-sparse tropics; Baumhefner's analysis was based on the solution of a non-linearly balanced omega-equation.

The structure can be summarized as follows:

Easterly waves have an approximate wave length ≈ 2000 km, over the Caribbean. They have been known to tilt eastward with height. The disturbance is known to have a cold core around 900 mb and a weak warm core around 500 mb. The active weather usually lags behind the trough line and very dry air with descending motion and associated low-level divergence is found ahead of the low-level trough line. This type of vertical structure by no means encompasses all cases. The vertical shear of the large-scale environmental flows varies considerably. One finds that the structure, the scale and the life cycle vary considerably from place to place. At times when the easterlies increase with height in the upper troposphere, the Atlantic waves have been known to resemble western Pacific easterly waves with an eastwards tilt and a reversal of the weather pattern with respect to the trough line.

On a satellite photograph, a Caribbean easterly wave resembles a cloud cluster with a dimension of roughly 500 km^2 . The cloud cluster is essentially a cirrus cover above active lines of cumulonimbus clouds. The fraction of the 500 km^2 area that is covered by deep convective clouds is usually only 1 to 2 per cent. There is usually also present a large area of shallow clouds which occupy roughly 30 per cent of this area.

In the final analysis on the maintenance of an easterly wave, one should consider the problem of detailed interaction of the cloud scale motion and the larger scale fields (Chapter 6). Thus a full description of an easterly wave may entail such processes as:

- (i) Dynamics of large scale motion system;
- (ii) Parameterization of deep convection;
- (iii) Treatment of shallow convection;
- (iv) Radiative effects; and
- (v) Air/sea interaction.

In general, one can incorporate such details only via use of diagnostic and prognostic numerical models.

8.3 Inverted V cloud formations

These are disturbances which were first recognized from satellite photographs by Neil Frank. They essentially comprise two cloud lines oriented to form an inverted V shape. Simpson and Simpson (1973) made the first definitive study of the cloud types in an inverted V using dropwindsonde aircraft. These are illustrated in Figure 8.8. The scale of the phenomenon appears to be around 1 000 km. The cloud-base is fairly high, i.e. 3 000 m or higher, and most clouds are of altocumulus and altostratus type. The sounding in the vicinity of the inverted V (Figure 8.9) shows a moist layer in the lower middle troposphere between 500 and 700 mb with drier air below and above. It is not quite clear whether or not it is a wave disturbance in the moist layer. Inverted V's have been noted to propagate all the way across the Atlantic ocean. Further work on their structure and dynamics is necessary to understand this phenomenon.

8.4 Squall lines over the Atlantic

Satellite photographs sometimes clearly indicate westward propagating squall lines over the Atlantic ocean. They have been known to propagate for periods of the order of several days from West Africa to Barbados. Strong trade winds are frequently noted on the east side of the squall line, compared to those on the west side. Large-scale convergence of mass is usually important in the low levels. The West African disturbance line is discussed in Chapter 14. Not much is known regarding the structure and dynamics of these squall systems. An analogy of Zipser's (1969) model of a Pacific squall system may provide a useful model for Atlantic squall systems. Zipser's model for the Pacific ocean is illustrated in Chapter 9. The results of the GATE Experiment are not fully available. However, we should expect to see, in the near future, some interesting three-dimensional structures for these Atlantic squall systems derived from observations.

8.5 Surges in the trades

The trade winds of the two hemispheres are known to fluctuate in their intensity. As stated in Chapter 2, the winter hemisphere trades are a little stronger than those of the summer hemisphere. During the last several years, geostationary

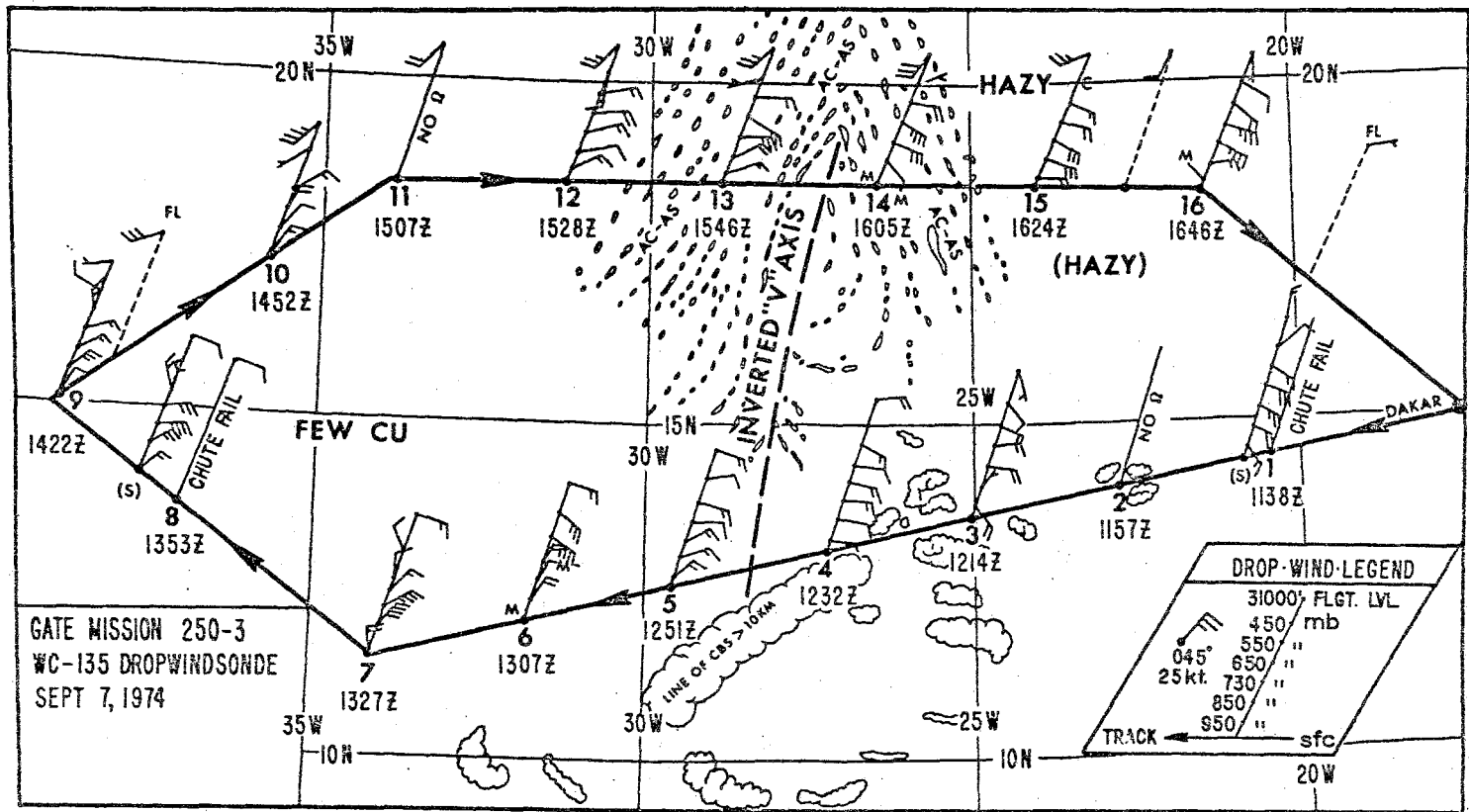


Figure 8.8 - A depiction of a dropwindsonde mission showing weather distributions observed (and extended in terms of satellite sector pictures) and the "wind ladders" for observed winds measured by the dropwindsonde instrument

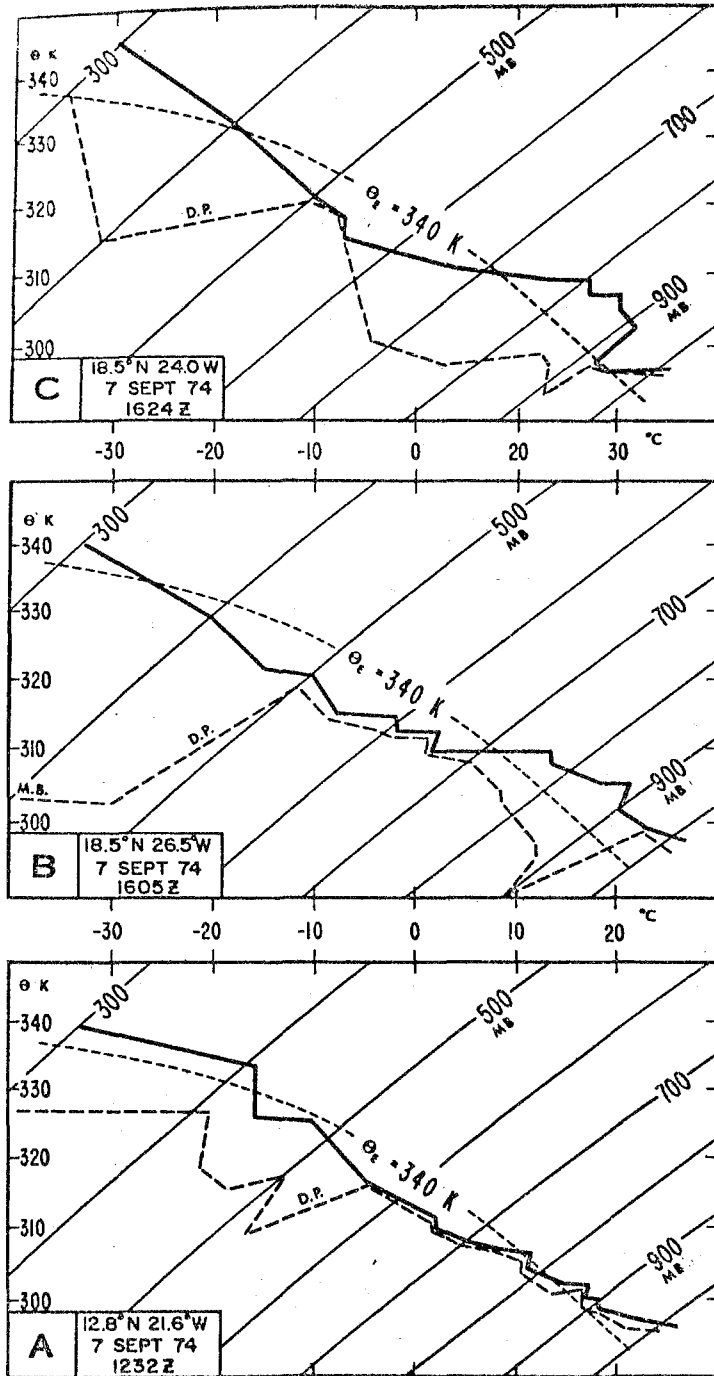


Figure 8.9 - Three soundings from a dropwindsonde mission on September 7, 1974: panel (a) in a disturbance near the ITCZ, panel (b) in an inverted V disturbance in the trade winds, and panel (c) in undisturbed trade winds near the Cape Verde Islands

satellites have been providing cloud motion vectors for the low and the high clouds. It is possible to map the trade-wind belt with a degree of detail that has never been possible before. In Chapter 20 we present examples of detailed low-cloud motion vectors and the 850 mb flows. These are based on recent work from Professor Fujita's group at the University of Chicago. The so-called undisturbed trades contain a very large number of cloud tracers. In fact, it is the undisturbed rather than the disturbed area where the low-level flows can be easily mapped using these cloud tracers. The high (800 m) resolution polar-orbiting satellite images indicate that cloud tracers are, in fact, present over most of the tropical oceans. When global coverage from several geostationary satellites is implemented, it should be possible to monitor global trade-wind systems very accurately.

The present data coverage over the Atlantic shows that there exists a near simultaneous surge in the intensity of the trade-wind systems of the two hemispheres (Krishnamurti *et al.*, 1975). They noted a dominant period of roughly two weeks in the oscillation of these systems. In fact, a famous explorer, Joshua Slocum (1910), traversing the trade-wind system in a sail boat noted, as far back as 1900, that the southern Atlantic trades exhibit a wind oscillation of a two-week duration. The full dynamical implication of this phenomenon is not clear. Figure 8.10 illustrates the wind speeds of the two trade-wind systems during 1974 over the Atlantic. Note how the two curves go up and down nearly simultaneously. The observations of the Atlantic trade-wind flows can be depicted in an animation movie showing vectors moving along the wind system. Such a film very clearly portrays the phenomenon of the simultaneous surges in the trades.

8.6 The ITCZ (Intertropical Convergence Zone) in the Atlantic

The near-equatorial rainfall belt may be identified as the ITCZ (The Intertropical Convergence Zone). At times this belt appears as an east/west elongated line located near 5°N latitude. At other times one notes westward propagating cloud clusters in this belt. There is a controversy as to whether or not there, in fact, exist two distinctly different disturbance regions: one around 12°N (the easterly waves) and the other around 7°N (the ITCZ waves). Satellite observations strongly suggest that the ITCZ waves (as revealed by cloud cluster passage) are, in fact, modulations of a quasi-stationary ITCZ by the westward passage of easterly waves farther north. Satellite photographs do not generally show two separate families of cloud clusters. A continuous cloud line near 7°N is frequently observed over the eastern Atlantic ocean.

8.6.1 Theories of the ITCZ

A number of theories of the ITCZ have been proposed in recent years. These theories have relevance to the ITCZ over the Atlantic, Pacific and Indian oceans. It would be appropriate to present a brief summary of these theories here.

Two interesting studies by Pike (1971, 1972) deal with the formation of ITCZ over high sea-surface temperatures. These studies are based on zonally symmetric numerical models. In these models primitive equations for the atmosphere are integrated and include the effects of air/sea interaction. Pike prescribed two belts of

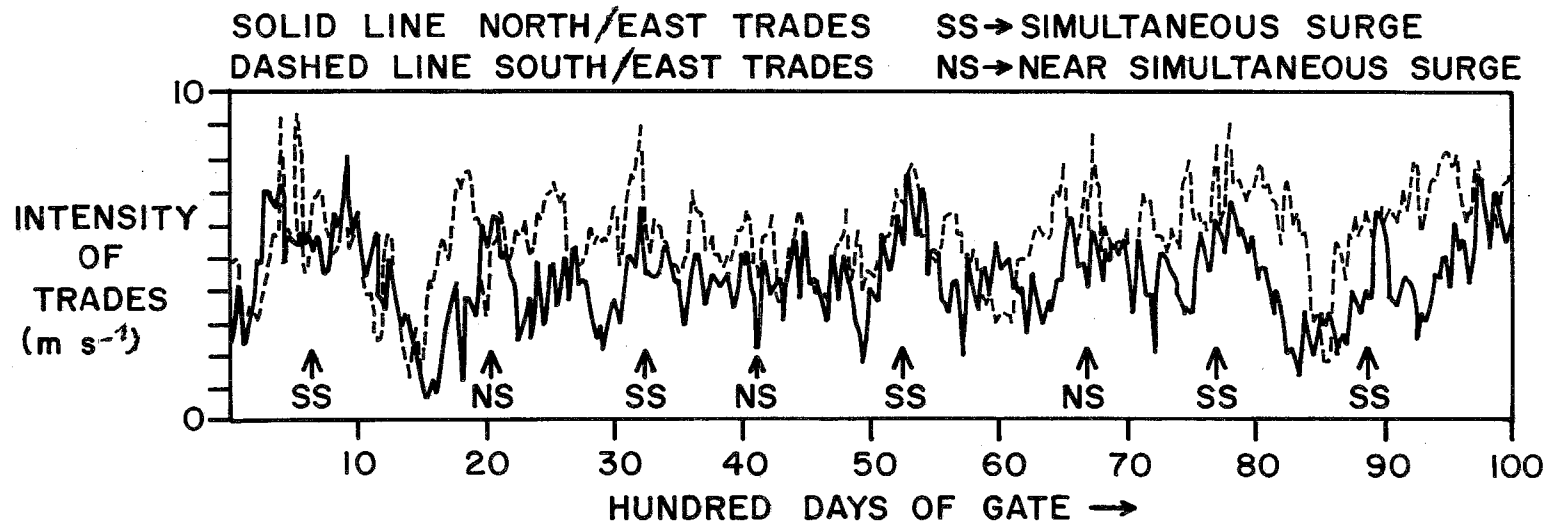


Figure 8.10 — Streamlines of 100 daytime averaged flows between 16 June 1974 and 23 September 1974 at 850 mb. The outline of the GATE A-scale is the large domain. Two inner domains over the Atlantic trade wind belts were also used for calculations (m s⁻¹)

high sea-surface temperature close to 10°N and at 10°S with a low-temperature belt near the Equator similar to what is generally observed. His integrations not only simulated a convergence zone with a rising centre but also showed a preference for a single ITCZ. This showed that although the sea-surface temperature forcing was symmetric about the Equator ($\pm 10^{\circ}\text{N}$), the solution nevertheless came out asymmetric (i.e. one ITCZ) as is generally observed in the atmosphere. Pike also carried out a seasonal cycle experiment with a combined atmosphere/ocean model including the radiative heat balance of the ocean. In this study, Pike showed a shift of the ITCZ from one hemisphere to the other with the march of the seasons. This model would be more relevant to parts of the Pacific and the Indian oceans. Pike also noted the preference for a single ITCZ in these studies, and he noted that the maximum sea-surface temperature lags behind the zenith sun by roughly 9 weeks, which is a reasonable lag time.

There is an essential difference between Pike's work and Charney's (1969) CISK ideas for the ITCZ. Here Charney views the ITCZ as a zone of cumulus convection which is controlled by the convergence of the moisture flux in the trades. This study of Charney is a line-symmetric analogue of the CISK model of a tropical cyclone. In his study, Charney presents a linear analysis for the growth rate of a line symmetric disturbance. He shows that the growth rate increases with the effect of the Earth's rotation (the Coriolis torque) due to (i) the frictional convergence (Ekman convergence) and (ii) the lapse rate of equivalent potential temperature. Charney shows that the combined effect of (i) and (ii) produces a maximum growth rate, i.e. an ITCZ, some 7° away from the Equator. Charney's theory prefers a double ITCZ: one on either side of the Equator. Furthermore, Charney's theory does not explicitly rely on the high sea-surface temperature.

Neither of the above theories account for the role of near equatorial wave disturbances in the formation of the ITCZ. It was a study by Holton *et al.* (1971) that examined this zonal asymmetry, i.e. the possible role of the westward propagating wave disturbances (see Reed and Recker, 1971, for a description of these). Satellite photographs frequently show cloud clusters along the ITCZ. Holton *et al.* show that there exists a critical latitude at which the angular frequency of a wave matches the Coriolis frequency. The theoretical analysis is based on the Ekman layer problem on a beta plane. They furthermore show that the Ekman convergence is concentrated near this latitude. This theory takes into account the obvious limitation of the CISK theory which depends on Ekman convergence and is invalid near and at the Equator. The theory of Holton *et al.* shows that the frequency spectrum of the westward propagating waves (being non-zero) matches the Coriolis frequency at a latitude close to 10°N where convergence, rising motion and the ITCZ would be expected. This theory thus takes into account the role of zonal asymmetry, i.e. the cloud clusters associated with the wave disturbances.

A fully three-dimensional model of the ITCZ has not been proposed to date. However, we should not underestimate the contributions by many global general circulation models in this area. The studies of Hahn and Manabe (1976) are one of many such important studies that provide valuable insights into the oceanic ITCZ. They find reasonable climatological positions of the ITCZ over the tropical oceans in the vicinity of the high sea-surface temperature belts and away from the Equator. Manabe and Smagorinsky (1967) have furthermore shown that the eddy kinetic energy along the ITCZ is primarily maintained by vertical overturning ($-\overline{W'T'} > 0$) with a conversion from eddy available potential energy — the latter being maintained by cumulus heating.

Estoque and Douglas (1978) have drawn a distinction between the ITCZ in the western as distinct from the eastern Atlantic. They showed that while the energetics of the ITCZ over the central and western Atlantic were similar to that noted by Manabe and Smagorinsky (1967), the eddy kinetic energy associated with the ITCZ over the eastern Atlantic seemed to be associated with other mechanisms such as lateral forcing from middle latitudes and by barotropic conversions.

8.7. Subtropical cyclones

Frequently observed phenomena over the Atlantic are the cyclones that form in subtropical latitudes. They possess gale force winds but lack the usual intense warm core that is found in tropical storms and hurricanes. They do not have the organized convection that is characteristic of the more intense disturbances. Many times during their life cycle, the subtropical cyclones show total lack of deep convection. Their formation is, at times, linked to a downward propagation of cyclonic vorticity from the upper cold lows. The size of these disturbances is between 500 and 1000 km, and is somewhat larger in scale than hurricanes. Similar disturbances have been noted in other oceans.

8.8. Other Atlantic disturbances

There are a variety of other phenomena that are of interest over the tropical Atlantic, e.g. upper cold lows, shear lines, areas of rapid cloud formation near the mid-Atlantic trough and dust outbreaks. We make reference to these in other sections.

Chapter 9

PACIFIC DISTURBANCES

The western Pacific typhoons are the most important among the many types of Pacific disturbances. On the average roughly 22 typhoons/year form over the western Pacific ocean. The western Pacific is far more active than the Atlantic or the Indian ocean. A large number of ITCZ waves propagate westwards around 10°N (see Chapter 3 for a review of the structure of ITCZ waves and Chapter 6 for a review of the budgets of heat and moisture; details of hurricanes (or typhoons) are addressed in Chapter 11). Gray (1968) has presented a clear account of the global climatology of tropical disturbances. He emphasizes the immediate poleward region of a doldrum ITCZ as a favourable region for the formation of tropical disturbances. The doldrum ITCZ is here identified as a region of weak winds, usually containing weak eddy motions at sea level and separated by the trade wind systems of the two hemispheres. The doldrum ITCZ is sometimes contrasted with a quasilinear ITCZ (or trade wind ITCZ) which contains a central asymptote of streamline convergence along which the speeds are of the order of 10 m s^{-1} . An easterly wave in the northern Atlantic ocean during the northern summer has been identified by Riehl (1945) and others as a wave disturbance that is distinctly different from ITCZ waves that are located farther to the south. In the Atlantic, the respective mean latitudes of westward propagation for easterly waves and ITCZ waves are stated to be roughly around 13°N and 7°N . Over the Pacific ocean, no such distinction is usually made.

9.1 Variations of sea-surface temperature (SST) over the Pacific Ocean and large-scale teleconnections

The most striking feature in the field of SST over the western Pacific ocean is the northward propagation of the axis of warm water temperatures. The monthly mean fields of SST (Figure 9.1) from the recent atlas of Alexander and Mobley (1974) produced at the Rand Corporation illustrate this phenomenon. The axis of warm temperatures migrates from 5°S during northern winter months to about 15°N during the northern summer months. The region of tropical wave activity as well as the ITCZ is also known to migrate northwards following these warm ocean temperatures. The north/south migration of the axis of warmest ocean temperatures is, by comparison, less in the eastern Pacific ocean. It stays north of the Equator all the year round, near 6°N during the northern winter and near 15°N during the northern summer. The location of the satellite brightness axis (defining the ITCZ) for the four seasons based on studies by Hubert *et al.*, (1969) is presented in Figure 9.2, the axis being indicated by a dashed line. The seasonal ITCZ migration is clearly portrayed. One

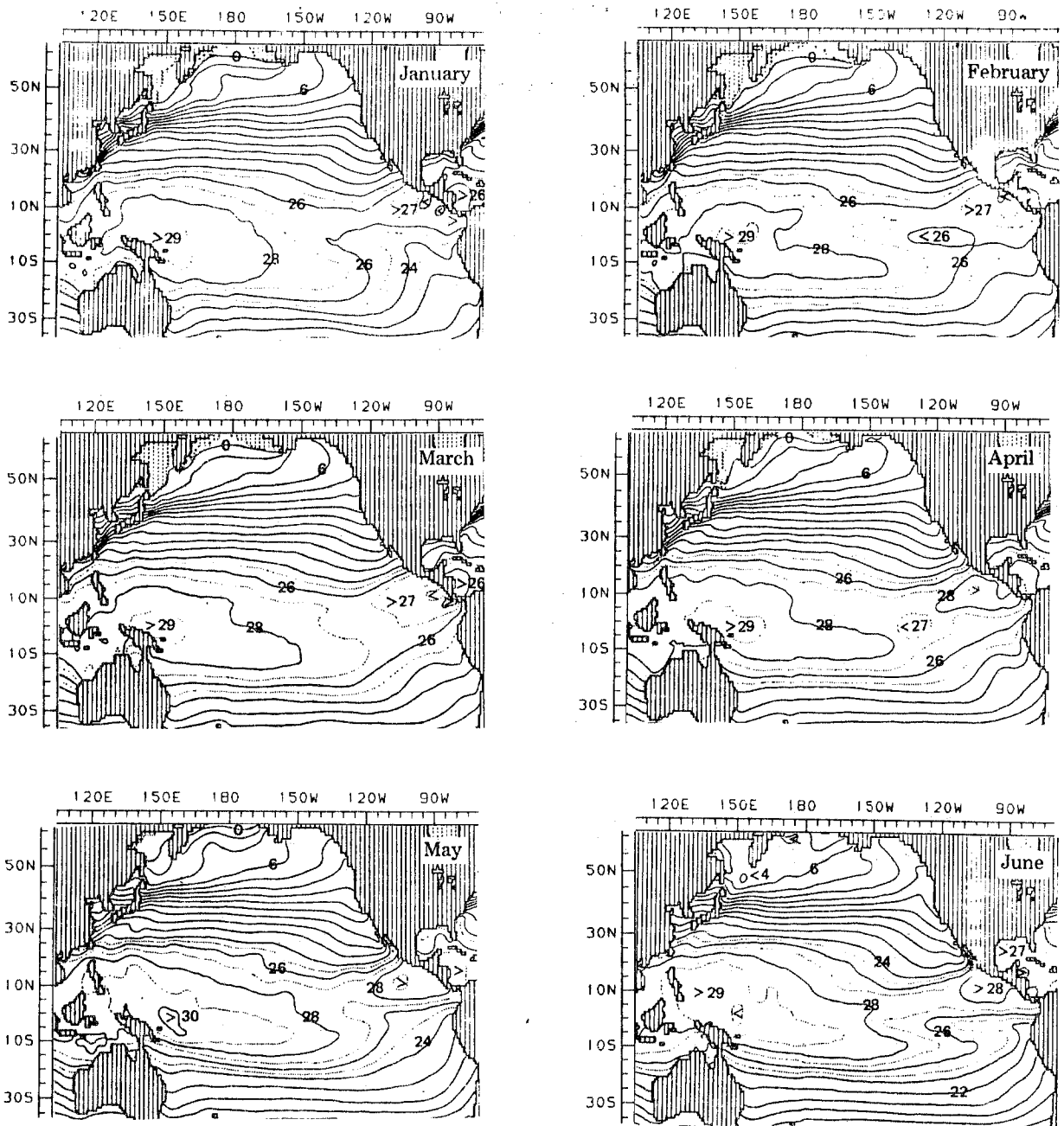


Figure 9.1a - Average ocean-surface temperatures ($^{\circ}\text{C}$) and ice-pack distributions (broken hash marks). Solid isolines denote 0° , 20° , 40° , 60° , etc. Dotted isolines in low latitudes denote 25° , 27° , and 29°C (Alexander and Mobley, 1974)

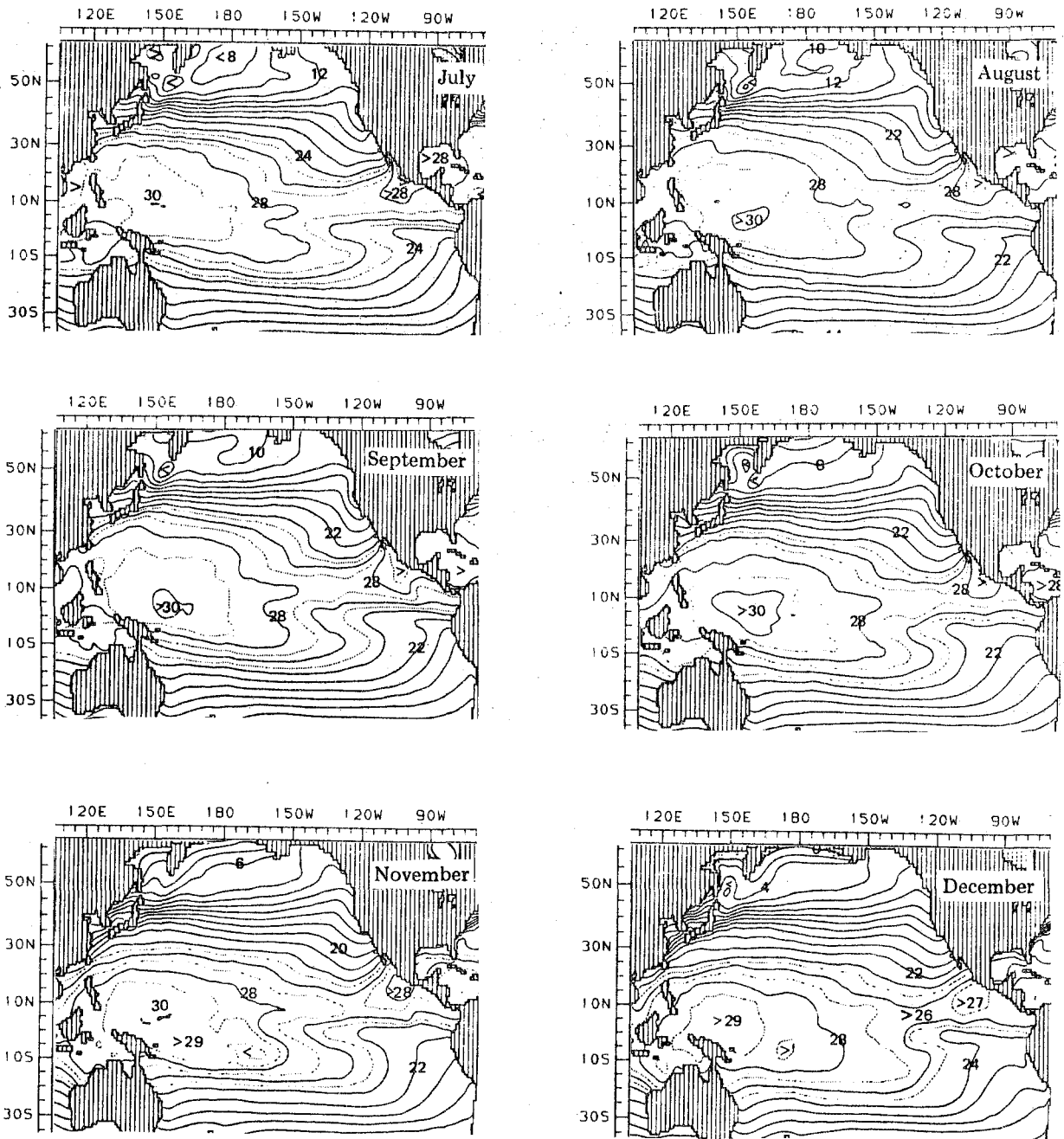


Figure 9.1b - Average ocean-surface temperatures ($^{\circ}\text{C}$) and ice-pack distributions (broken hash marks). Solid isolines denote 0° , 2° , 4° , 6°C , etc. Dotted isolines in low latitudes denote 25° , 27° , and 29°C (Alexander and Mobley, 1974)

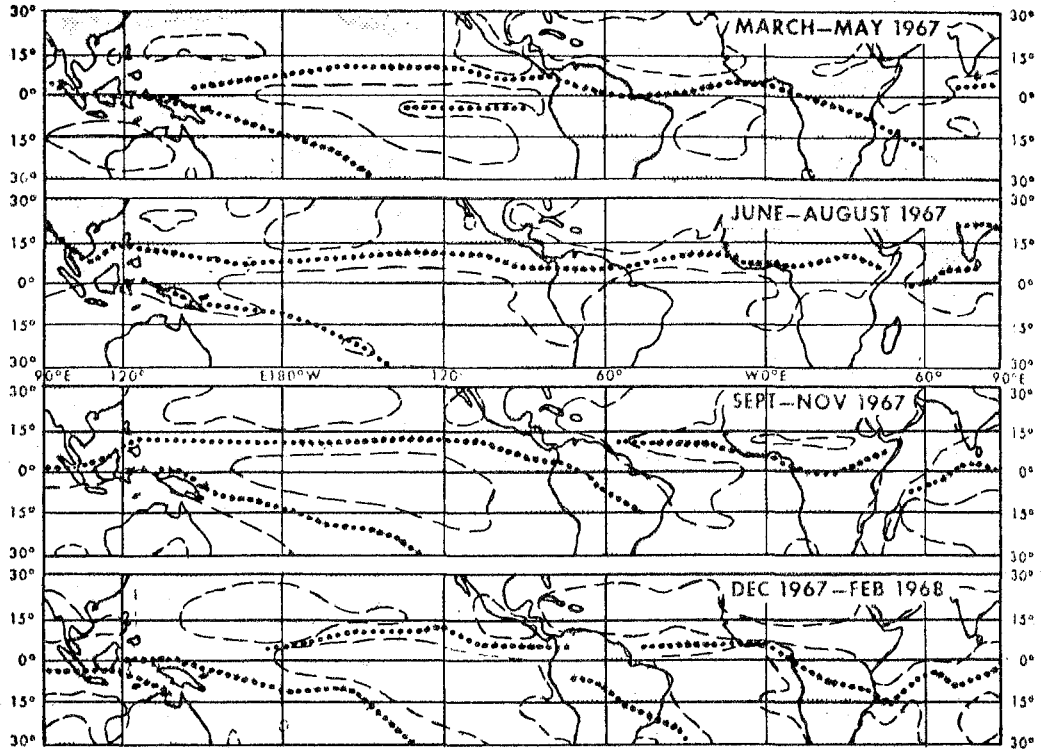


Figure 9.2 - Seasonal distribution of brightness from ESSA 3 and 5 digitized pictures over the tropics for the period March 1967-February 1968. The dashed lines enclose areas of minimum brightness, while stippling indicates regions of maximum brightness. The heavy dotted lines indicate the major zonally-oriented axes of maximum brightness (or cloudiness) (After Hubert et al., 1969)

of the enigmas of tropical meteorology is cloud line elongated from the north-west to the south-east in the western Pacific ocean of the southern hemisphere. This axis passes close to the Solomon and New Hebrides Islands where during the southern summer season rainfall amounts exceed 250 cm/season. This region of the Pacific ocean is characterized by warm sea-surface temperatures. In meteorological literature this rainfall belt of the southern hemisphere and the one north of the Equator near 10°N have been referred to as a double ITCZ, although Hubert *et al.*, (1969) have questioned this identification. This quasistationary rainfall belt north-east of Australia has not been properly investigated and deserves careful study. Among the transient features of the Pacific sea-surface temperatures, the occasional appearance of excessively warm water off the coast of Peru (called: El Niño) has attracted much interest in meteorology. In recent years these ocean temperatures were well above normal in 1957-58, 1965-66 and 1972-73. This warm water replaces colder waters in a region known for its upwelling. It has been suggested that this anomalous warming near the equatorial eastern Pacific between 80°W and 90°W has important implications for tropical atmospheric circulations, although this remains to be conclusively demonstrated. Sir Gilbert Walker (1923, 1924) introduced a concept called the "Southern oscillation" to describe a climatological relationship between the atmospheric variations over the Indian and Pacific oceans: Figure 9.3 from Berlage (1966) illustrates Walker's southern oscillation. It shows the distribution of the correlation coefficient between surface pressures over a large part of the globe with the pressure at Jakarta in Indonesia. The values over the southeastern Pacific region are opposite in phase to the pressure at Jakarta, i.e. when pressure is high in Jakarta, it is low over the eastern Pacific and vice-versa. This is, in fact, a planetary scale phenomenon, the largest amplitude being in zonal wave number 1. The phenomenon of the "East/west circulation" discussed in Chapter 2 seems to have some relation to the "Southern oscillation" and to these bursts of 'El Niño' warming.

9.2 Transient disturbances in the lower troposphere

The ITCZ waves were mentioned in Chapter 3. Budget studies such as those reviewed in Chapter 6 suggest strongly that such disturbances, once formed, are maintained by organized cumulus scale motions imbedded in them. Less is known about the initial formation of these wave disturbances, although several suggestions have been made. In a series of linear stability studies, Yamasaki (1969, 1971) has examined the question of the large-scale instability of the tropical conditionally unstable atmosphere. His analysis includes the effect of condensation heating by the so-called CISK mechanism. In fact, he shows that waves over a large part of the spectrum are unstable and thus one is led to believe that initial instability, at least theoretically, can be due to the CISK mechanism in a conditional unstable environment. This idea is sometimes not too appealing because some interpretations of CISK have insisted on the requirement for frictional convergence and strong large-scale cyclonic relative vorticity in the planetary boundary layer. Both Ooyama and Yamasaki have repeatedly insisted that this is a misinterpretation of CISK. The ITCZ waves form along the regions of east/west oriented cloud cover which on many occasions is already present and thus one cannot tacitly rule out this type of instability. Other notions of initial wave formation have emphasized the role of north/south shear of the basic easterly flow, i.e. barotropic instability. In two interesting papers, Yanai and itta (1968) and Nitta and Yanai (1969) have examined the basic easterly current of the western Pacific ocean in this context. Here it is necessary first to examine whether

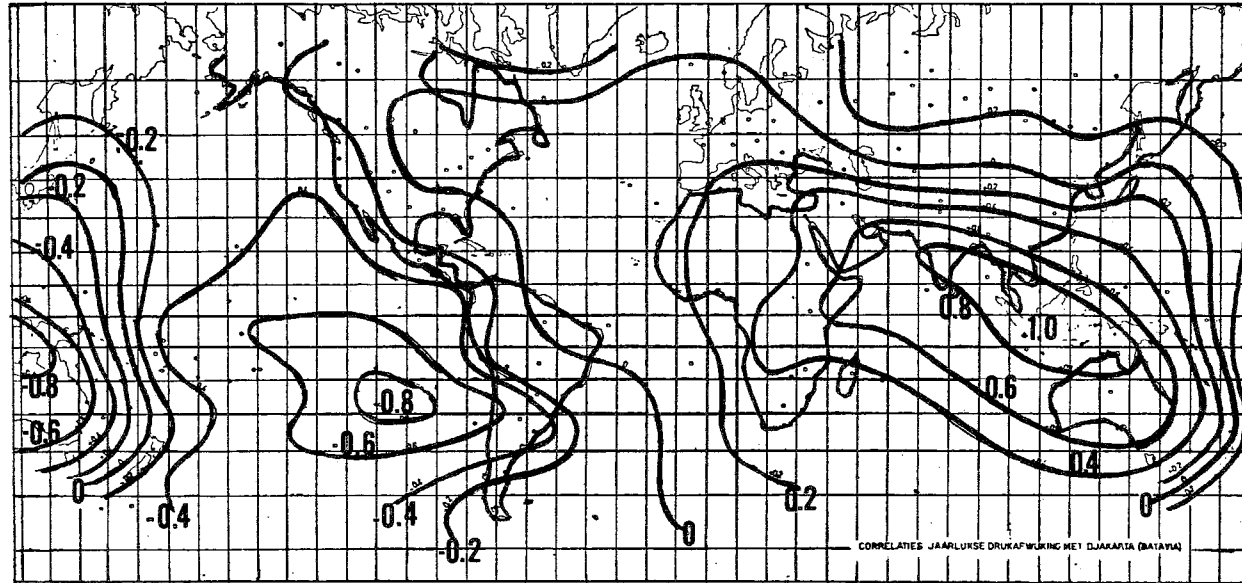


Figure 9.3 - Walker's southern oscillation as presented by Berlage (1966). The map shows worldwide distribution of correlations of annual pressure anomalies with simultaneous pressure anomalies in Jakarta, Indonesia

the necessary condition for the existence of barotropic instability is satisfied. (This is reviewed in the Appendix to these notes). It is that the meridional gradient of absolute vorticity vanishes at some latitude for the basic current under consideration. The stability problem, i.e. the determination of the growth rate as a function of scale, is examined by pursuing what is called the finite difference method for determining the barotropic stability. (This is also reviewed in the Appendix.) Figure 9.4a shows the meridional profile of the zonal surface wind in the western Pacific ocean based on the studies of Nitta and Yanai (1969). The strongest easterlies are about 8 m s^{-1} and located near 11°N . These are part of the trade wind easterly wind system of the western Pacific ocean. Figure 9.4b shows the corresponding meridional profile of absolute vorticity. This shows that around 10°N there is some evidence for the change in meridional slope ($\partial \zeta_a / \partial y$) of the absolute vorticity. Thus the necessary condition for the existence of barotropic instability seems to be satisfied by the easterlies in this region. It should be noted here that even this simple condition cannot be tested with most available data sets because the observations are generally too sparse, and computation of such slopes are not easy. Research aircraft data are most desirable for such studies. The diagram of linear stability (i.e. growth rate versus wave number) is illustrated in figure 9.4c, also taken from Nitta and Yanai (1969). It shows that for the profile shown in Figure 9.4a the most unstable wave has a scale of around 2 000 km. This is close to the wave length of observed near-equatorial ITCZ waves studied by Reed and Recker (1971). Thus one is led to believe that barotropic instability might be an important mechanism for the formation of these waves. Nitta and Yanai (1969) also examined the structure of this wave by computing the Eigen function for the most unstable mode. Their perturbation stream function is illustrated in figure 9.4d. It shows a perturbation stream function with a south-west to north-east tilt south of 10°N which thus transports westerly momentum northwards towards the axis of the strong zonal easterlies at 11°N , leading to a weakening of the easterlies (energetically) and a strengthening of the wave. These features of barotropically growing unstable waves are very common over many parts of the tropics. However, one should note that the southwest to northeast tilt will not always be present in tropical waves, the reason for this being that barotropic energy exchanges from zonal flows to waves and vice versa may alternate, with corresponding alterations in tilt. Synoptic analyses usually show waves with all types of tilt, any particular case having a sign depending on the stage of the life cycle of the disturbance. Thus, it is only at the initial barotropically unstable growing stage that one should expect to see a southwest to northeast tilt. These growing waves usually have their largest amplitude on the cyclonic shear side of the basic easterly jet.

Another mechanism that has been examined for the initial growth relates to the combined barotropic/baroclinic instability described in the Appendix and also applied to west African disturbances in Chapter 14 and to northern Australian disturbances in Chapter 10. This requires a stronger meridional temperature gradient (or vertical shear of horizontal wind) than is observed over the oceanic tropics. Thus it would seem that the initial growth of western Pacific ITCZ waves may not be due to the mechanism of combined barotropic/baroclinic instability.

9.3 Formation of near-equatorial anticyclonic eddies

According to LaSeur (1963) whenever the ITCZ or the near-equatorial low pressure trough line moves northwards from its climatological position by about 10°

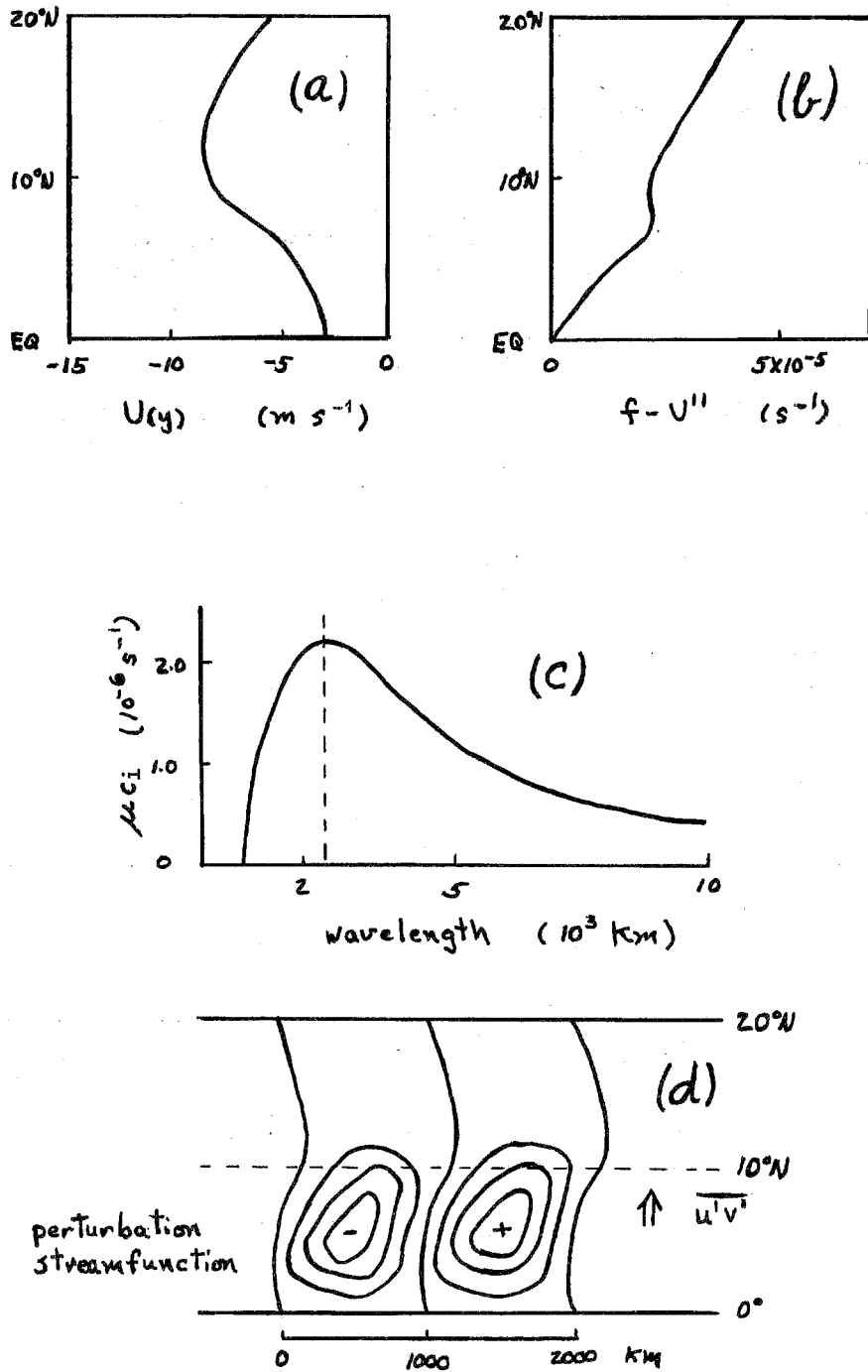


Figure 9.4 — (a) The meridional profile of surface zonal wind in the western Pacific during July; (b) The corresponding profile of absolute vorticity; (c) Plot of barotropic instability; growth rate (μ_{ci}) versus scale; and (d) The structure of the most unstable wave (Nitta and Yanai, 1969)

latitude, a tendency for the formation of near-equatorial surface anticyclones occurs. This has also been noted by many synoptic and operational meteorologists. Fujita et al., (1969) have studied the formation of these eddies using low cloud winds from geostationary satellite data over the eastern Pacific ocean. Figures 9.5a and b from the studies of Fujita et al., (1969) illustrate some stages in the formation and meridional motion of these near-equatorial anticyclonic eddies. They identify a sequence of stages in the evolution of these phenomena, identified in the diagrams as follows:

- (i) Pushing stage;
- (ii) Recurving stage;
- (iii) Cut-off stage;
- (iv) Mixing stage;
- (v) Burst stage; and
- (vi) Interacting stage.

A two-week cycle is schematically illustrated in Figure 9.5a and an actual sequence based on real data analysis is shown in Figure 9.5b. According to the authors (Fujita et al., 1969), the sequence starts with a northward push of southern hemisphere air. The initial flow contains large anticyclonic relative vorticity and divergence in low levels as the flows enter the northern hemisphere. The recurving stage is viewed as a consequence of gain in the anticyclonic relative vorticity.

The cutoff stage identifies the formation of a closed anticyclonic region. The anticyclone usually moves northwards with an associated band of convection moving to the south-west. The cloud band usually dissolves when it interacts with a cold front. A study of the dynamics of this synoptic model involving cross-equatorial flow must involve an examination of the boundary layer dynamics as well (see Chapter 5).

Fujita's analysis shown here, Figure 9.5b, is for selected days during September. During this two-week period between September 12th and 26th one can identify the sequence of evolution from the pushing stage (on the 12th near 100°W). Because of a lack of observations, the vertical structure of this phenomenon is not known. It should be noted that this sequence is based on very limited numbers of case studies. Much can be learned by careful analysis of a larger number of tropical maps using cloud winds as part of its data base.

9.4 The eastern Pacific Ocean

During the northern summer months the eastern Pacific is one of the most active regions of the tropics. A large number of tropical depressions, storms and hurricanes are known to form near 10°N. There are several factors that make this region unique from the point of view of tropical disturbance generation:

- (i) Sea-surface temperatures in the region are close to 29°C;
- (ii) A large number of western Atlantic easterly waves cross Central America and arrive over this region (see Chapter 8);
- (iii) The interaction of the Central American mountains with the prevailing easterly flows may be an important factor in the vorticity generation over this region;

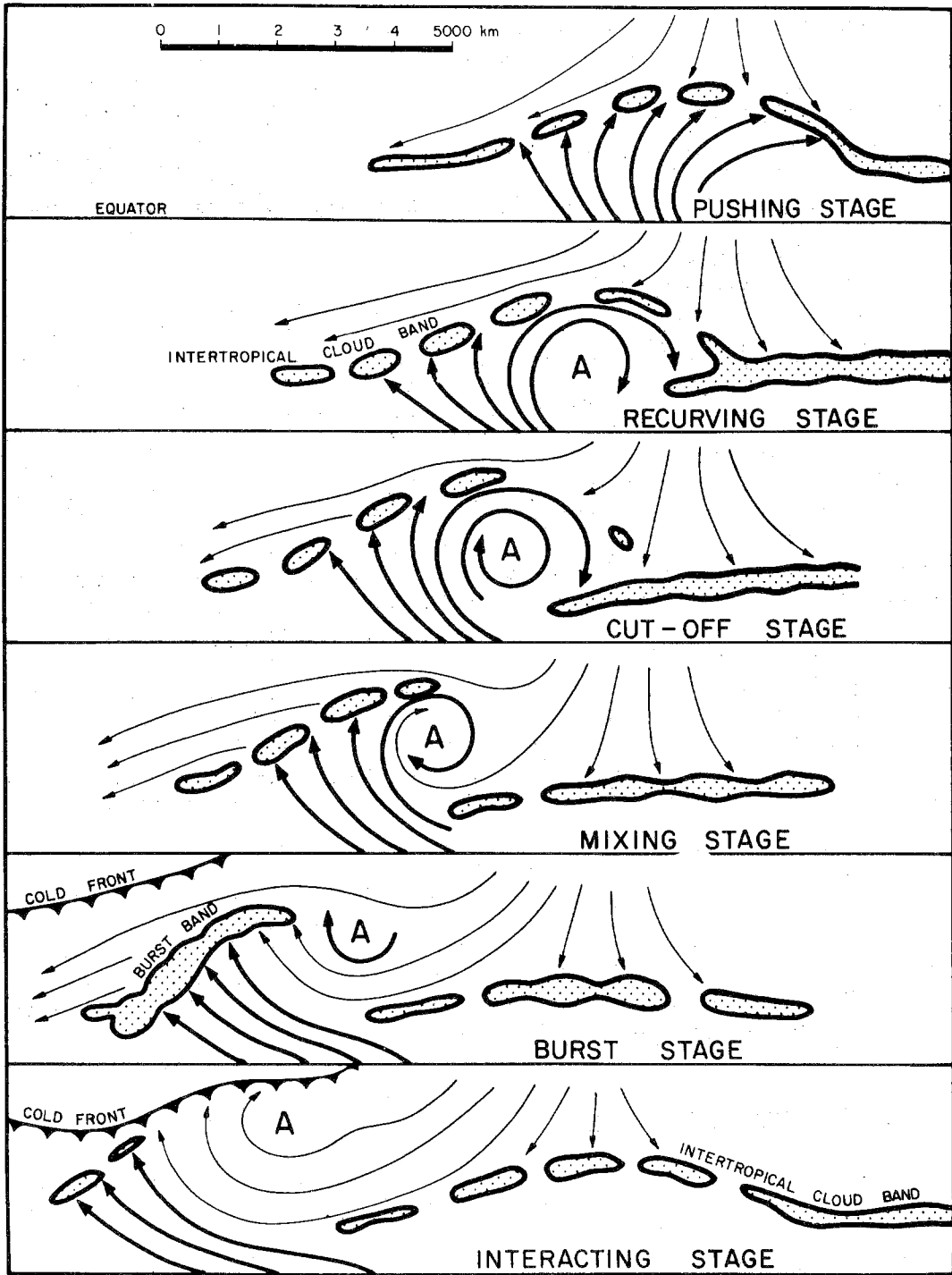


Figure 9.5a - A model illustrating six stages in the life cycle of a near-equatorial anticyclone

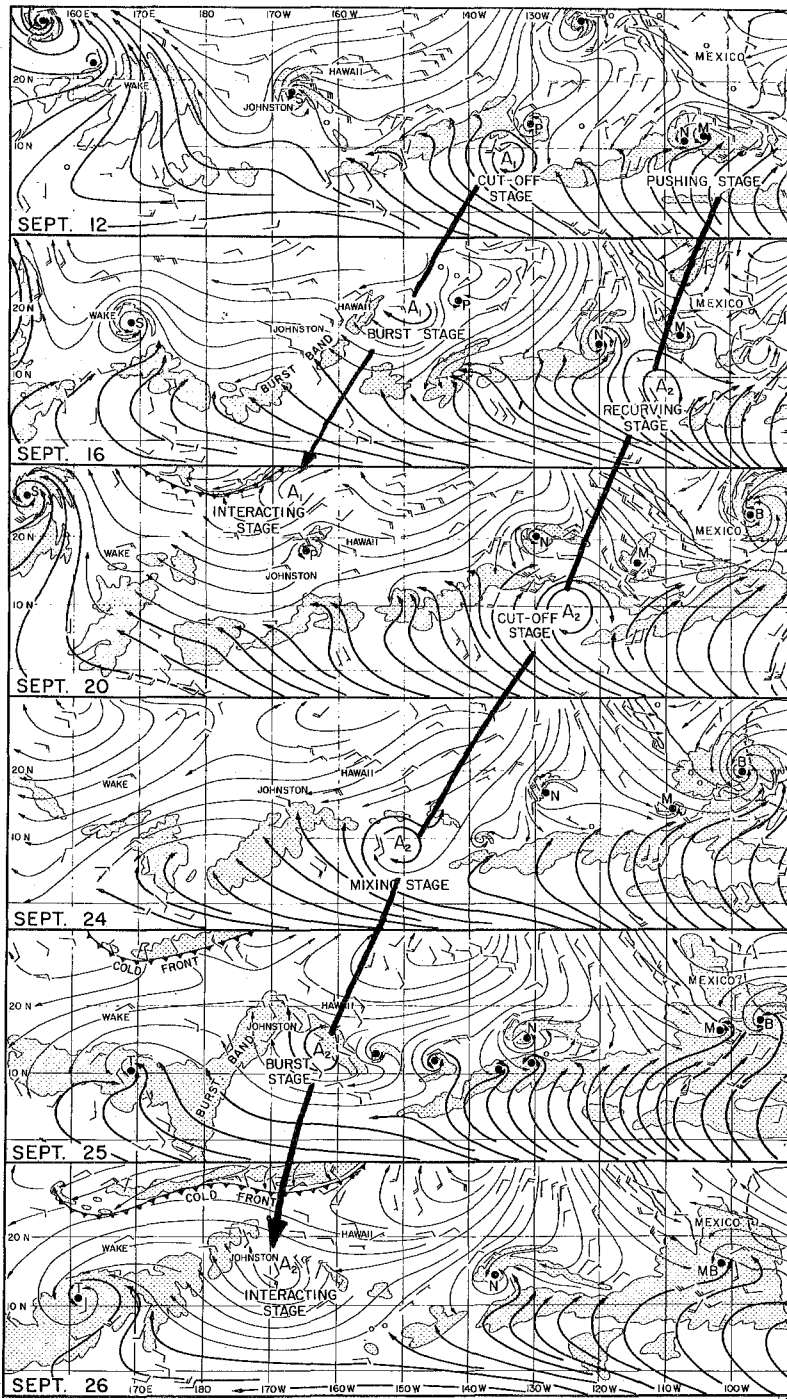


Figure 9.5b - Fujita's streamline analysis based on an analysis of real data

- (iv) This region is characterized by small vertical shear and large horizontal shear. Barotropic processes may be important here. Cloud winds from geostationary satellites are available for several years on a daily basis. A worthwhile research project would be to explore cyclogenesis in this region using these presently available observations. Figure 9.6 from Denney (1971) illustrates tracks of depressions, storms and hurricanes for a selected year. As may be noted, most of these hurricanes dissipate after a few days of westward (or northwestward) passage. Tables 9.1 and 9.2, based on Gunther (1977), illustrate the frequency of eastern Pacific tropical storms and hurricanes for the past decade. On average about 15 disturbances form per year in the eastern Pacific ocean, from among which about 50% are known to become hurricanes. The April issues of the Monthly Weather Review of recent years contain an annual storm summary for this region and this is an important source of reference.

Sadler (1972) has compiled a detailed wind climatology for the upper troposphere over the region of the eastern Pacific ocean. His analysis is based on an extensive use of commercial aircraft reports. This region has westerlies north of the Equator during the northern winter (Figure 9.7a) and northeasterlies during northern summer (Figure 9.7b). Over the southern hemisphere, the flows at 200 mb during the entire year are from the west. Sadler alludes to the establishment of an interesting buffer zone near the Equator during northern summer which separates the westerlies of the southern hemisphere from the northeasterlies to its north. The buffer zone cannot be identified as either a trough or a ridge line because of its proximity to the Equator. The dynamics of the buffer zone is another major unsolved problem in tropical meteorology because it comprises an important feature of the equatorial motion field.

The monthly mean sea-surface temperatures for the eastern Pacific ocean near 10°N may be noted in Figures 9.1 (a and b). This region is very warm around May (temperature close to 29°C); however, not many wave disturbances pass this region at this time. A slight cooling trend is usually noted during June and early July; thereafter sea-surface temperatures once again increase and values close to 30°C are frequently observed. This coincides with the high frequency of tropical storms that are noted to form in this region.

TABLE 9.1

Frequency of eastern Pacific tropical storms and hurricanes combined by month and year *

Year	May	June	July	August	September	October	November	Total
1966	0	1	0	4	6	2	0	13
1967	0	3	4	4	3	3	0	17
1968	0	1	4	8	3	3	0	19
1969	0	0	3	2	4	1	0	10
1970	1	3	6	4	1	2	1	18
1971	1	1	7	4	2	2	1	18
1972	1	0	1	6	2	1	1	12
1973	0	3	4	1	3	1	0	12
1974	1	3	3	6	2	2	0	17
1975	0	2	4	5	3	1	1	16
1976	0	2	4	4	3	1	0	14
Total	4	19	40	48	32	19	4	166
Aver.	0.4	1.7	3.6	4.4	2.9	1.7	0.4	15.1

TABLE 9.2

Number of eastern Pacific tropical storms reaching hurricane intensity by month and year *

1966	0	1	0	4	2	0	0	7
1967	0	1	0	2	1	2	0	6
1968	0	0	0	3	2	1	0	6
1969	0	0	1	1	1	1	0	4
1970	1	0	1	1	0	1	0	4
1971	1	1	5	2	2	1	0	12
1972	1	0	0	6	1	0	0	8
1973	0	1	3	0	2	1	0	7
1974	0	2	2	4	2	1	0	11
1975	0	1	2	3	1	1	0	8
1976	0	2	1	2	3	0	0	8
Total	3	9	15	28	17	9	0	81
Aver.	0.3	0.8	1.4	2.5	1.5	0.8	0	7.4

*Cyclones are ascribed to the month in which they began.

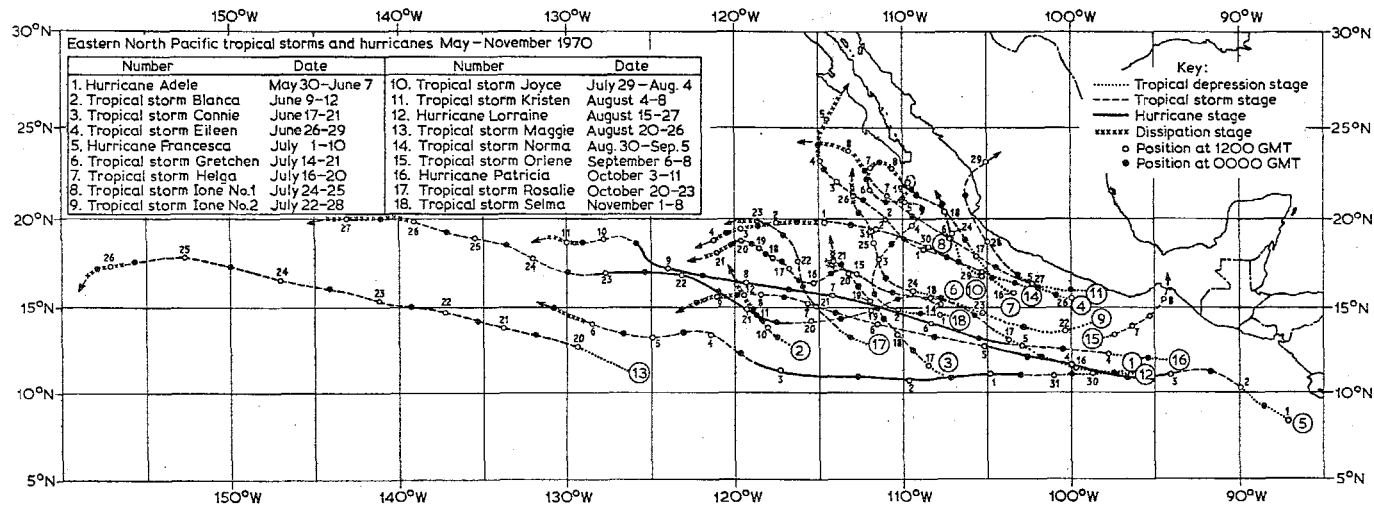


Figure 9.6 — Eastern north Pacific tropical storms and hurricanes from May to November 1970, largely from satellite evidence (After Denney, 1971)

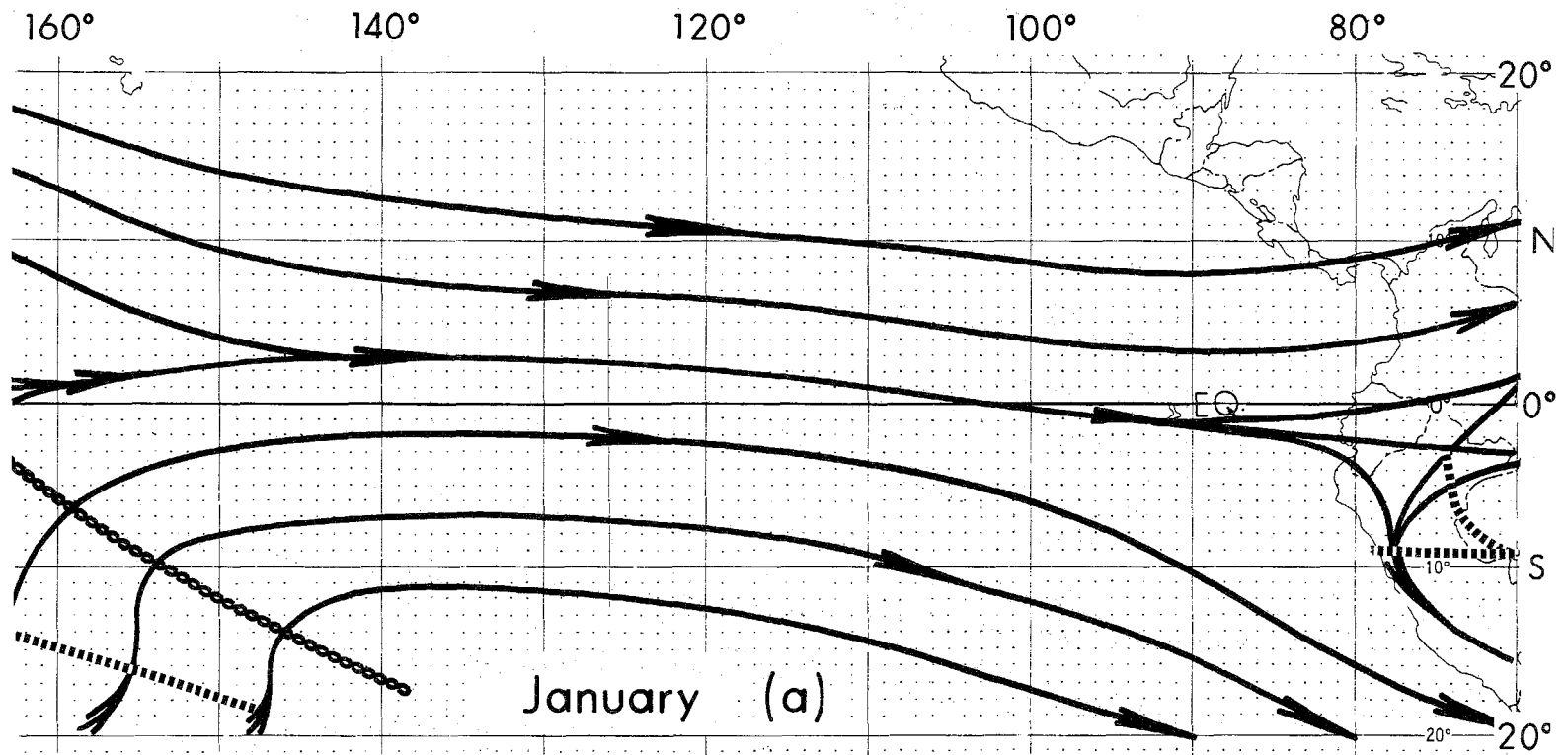


Figure 9.7a — Schematic of 200 mb ridge development in the Northern Hemisphere over the eastern Pacific and the concurrent establishment of a buffer system in an equatorial region (After Sadler, 1972)

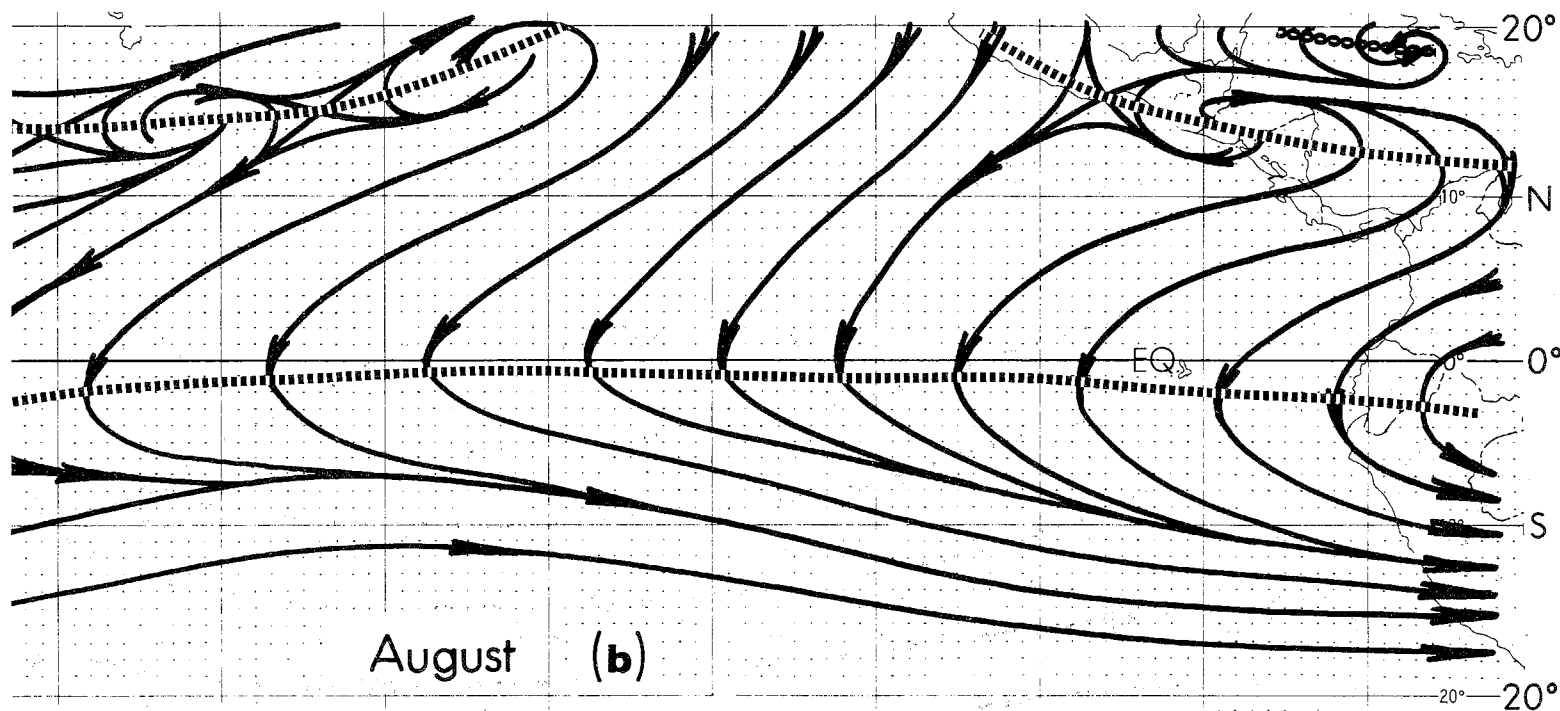


Figure 9.7b - Schematic of 200 mb ridge development in the Northern Hemisphere over the eastern Pacific and the concurrent establishment of a buffer system in an equatorial region (After Sadler, 1972)

Chapter 10

INDIAN OCEAN DISTURBANCES DURING THE NORTHERN WINTER SEASON

The atmosphere over the southern Indian ocean is very active during the northern winter season. A large number of wave disturbances form in the equatorial rain belt in the vicinity of Indonesia. These waves generally propagate westward along roughly 7°S latitude and a number of them become tropical storms prior to their recurvature southwestwards towards Malagasy (Madagascar) and the Mascarene Islands. Satellite observations are the major source of current data in the southern Indian ocean. Figure 10.1 illustrates a sample of daily photographs from polar orbiting satellites. This shows the westward passage and formation of tropical storms. The southern Indian ocean is unique in this respect compared to the southern Atlantic as well as the southern Pacific ocean since in these other regions there is a relative absence of storms. The field of sea-surface temperature over the southern Indian ocean (based on Alexander and Mobley, 1974) is shown in Figure 10.2. This region is characterized by high ocean temperatures. It thus seems that the formation and maintenance of these disturbances may be similar to their northern hemispheric counterparts. Figure 10.3 illustrates well documented tracks of tropical storms, based on the study of Crutcher and Quayle (1974), for the entire Indian ocean. The tracks north of the Equator represent storms over the Arabian sea and the Bay of Bengal for March, April, October and November while the tracks south of the Equator are for the northern winter months. The isopleths with numbers within this diagram show the most frequent direction from which the storm moved. The width of the heavy arrows represents the frequency of these storms, indicating that the southwestern Indian ocean is a very active region during this season. For comparison, we also show the west Pacific tracks which show a relatively higher frequency of tropical storm (typhoon) activity.

During the northern winter season, as stated earlier, the north easterly surface flows from the general region of the Siberian anticyclone move towards the low latitudes of the Indian ocean. These low-level flows encounter considerable air mass modification over the relative warm East and South China sea. Several observational studies suggest that the convection and heavy rainfall over the regions of southern Malaysia and Indonesia are related to the intensity fluctuation (surges, etc.) of the north-east monsoons. These surges in wind speed seem to occur over the south China sea. These low-level flows encounter a major obstacle, i.e. the mountains of Indonesia which are over 2 km in height between 5°S and 5°N latitude. Figure 10.4 based on Kuettner (1977) shows a possible interesting influence of the equatorial barrier on the north-easterlies at low levels. According to Kuettner, vortex pairs, one on either side of the Equator, form downstream from these mountains. Figure 10.4 left panel (from Kuettner, 1977) illustrates the tracks of a number of such vortex pairs, most of which formed during the northern winter season. These disturbances propagate westward in their respective hemispheres, and frequently become tropical storms in the central Indian Ocean. The right panel of Figure 10.4 (also from Kuettner, 1977) illustrates the westward displacement after the formation

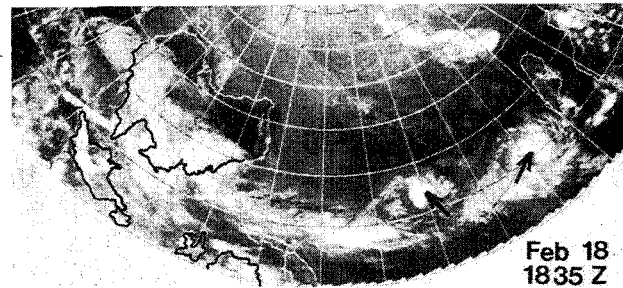
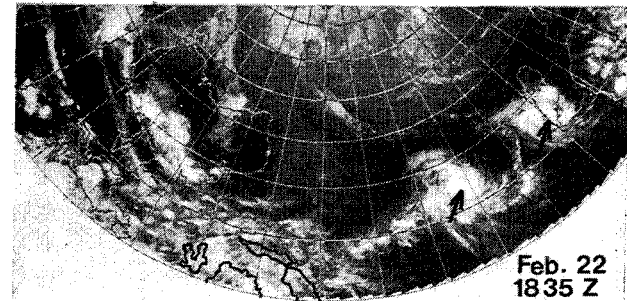
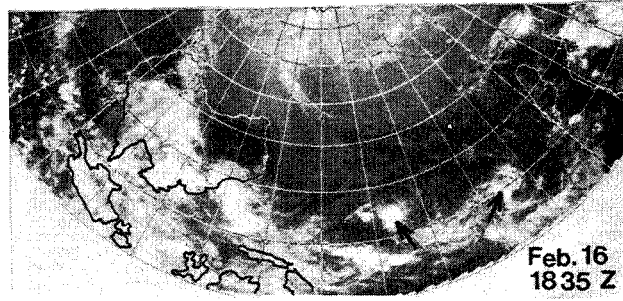
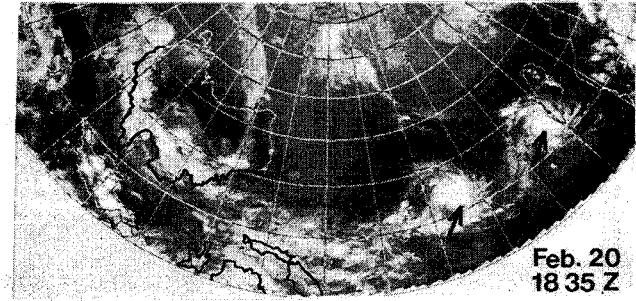
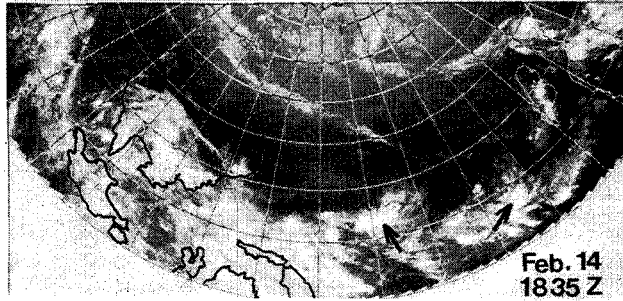


Figure 10.1 - Shows a sequence of satellite photographs between February 14 and February 22, 1977; illustrates the formation of two tropical storms over the southern Indian Ocean

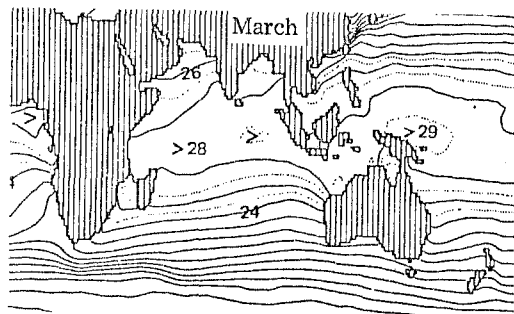
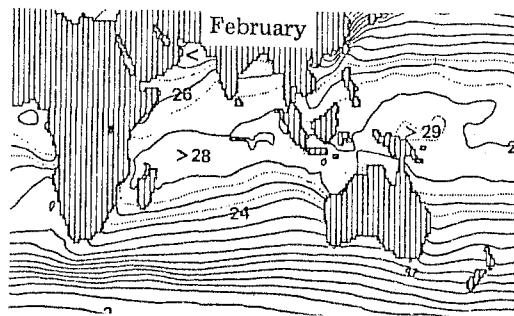
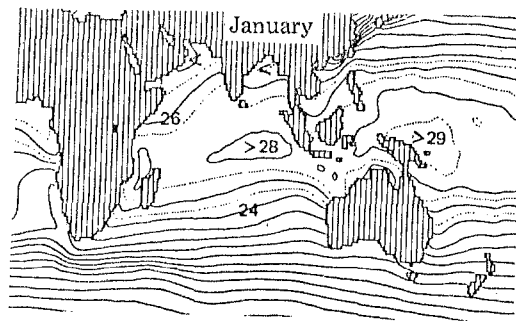


Figure 10.2 - Average ocean-surface temperatures ($^{\circ}\text{C}$); isolines denote 0° , 2° , 4° , 6°C , etc. Dotted isolines in low latitudes denote 25° , 27° , and 29°C

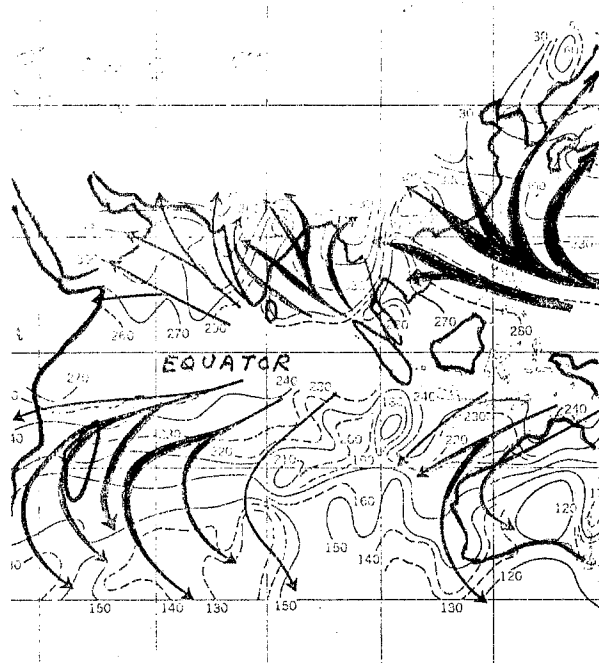


Figure 10.3 - Track of disturbances in the southern Indian Ocean during the northern winter season, as well as tracks of tropical storms and typhoons over the northern oceans in other seasons, based on Crutcher and Quayle (1974). The thin solid lines show isopleths of most frequent storm movement directions

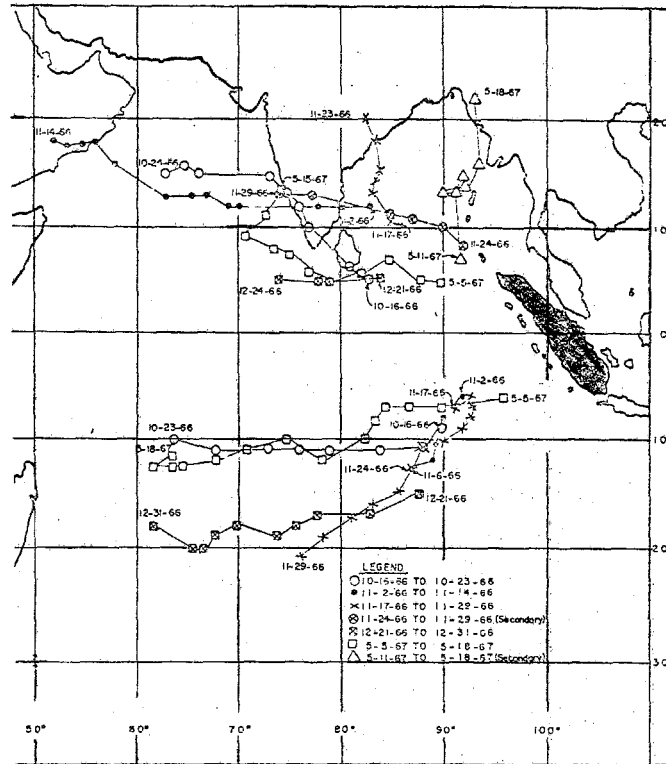


Figure 10.4 - (Left panel) Tracks of vortex pairs that formed in the Indian Ocean downstream from the Indonesian mountains (After Kuettner, 1977)

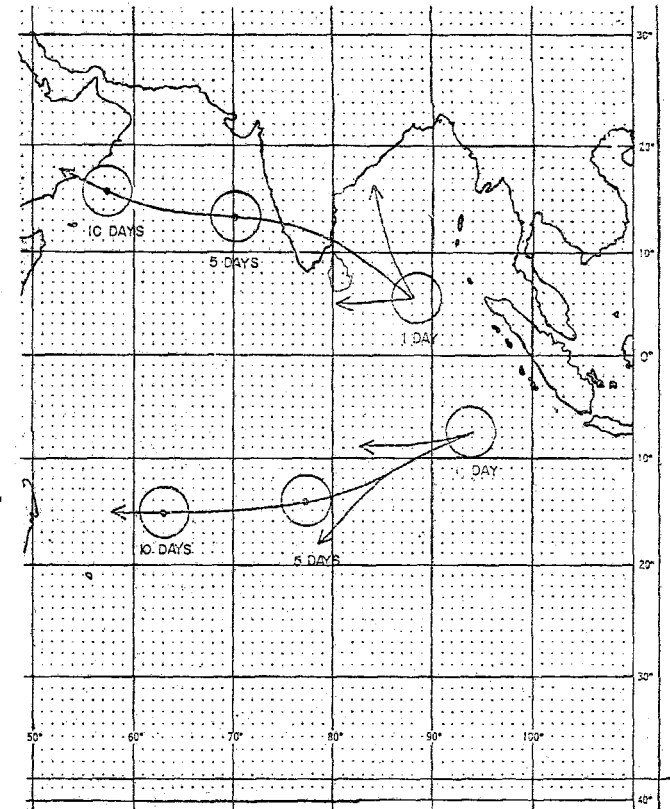


Figure 10.4 - (Right panel) Typical relative position of vortex pairs on days 5 and 10 after formation on day 1 (After Kuettner, 1977)

shown by day 1. The mechanism for the formation of these disturbances is not well understood. It would be desirable to study the influence of the Indonesian mountains on these low level flows by means of controlled numerical weather prediction experiments.

10.1 Climatology of flows over the southern Indian Ocean

Sadler and Harris (1970) provide an excellent climatology of the flow field in this region during the northern winter. In Figure 10.5 we present the map for February 1970, at the 600 metre level, 850, 700, 500, 300 and the 200 mb surfaces. Of major interest are the locations of major trough lines and near equatorial wind-shift lines. The pronounced Equator-ward tilt with height of the ridge line (located near 20°N at the 600 metre level) is one of the salient features in this climatology. On the other hand, the near-equatorial counterclockwise wind-shift line has a very small tilt up to 500 mb. The higher levels show a broad belt of easterlies between the Equator and 15°S where the tropical storms, discussed above, have a westward motion. It should be noted that year-to-year changes in the positions of these wind-shift lines are of major interest to the tropical climatologist.

This near-equatorial wind-shift zone, also called a buffer zone, is known to migrate more often to the summer hemisphere than to the winter hemisphere. Its anomalous meridional movement tends to bring in large-scale anticyclonic vorticity over the near-equatorial rainfall belt and causes temporary cessation or breaks in the rainfall. The precise mechanism of its meridional motions are not at present well understood.

10.2 The northern Australian low-level easterly jet

A remarkable similarity exists between the surface meteorological conditions over northwestern Australia and over western Africa. The Australian desert during the southern summer, see Figure 10.6, and the Sahara during the northern summer provide similar meridional thermal gradients on their Equatorward side in the lower troposphere. These regions of strong meridional thermal gradient are located near 15°S and 15°N , respectively. The lower tropospheric flows (Figure 10.7) are easterlies in this region during the respective summer seasons. A low-level easterly jet with maximum speed around 30 knots is frequently noted near 600 mb in both instances. Both horizontal and vertical shear of the wind is large below this level of maximum wind. The cyclonic shear side of the low-level jet (i.e. the Equatorward side) encounters lower tropospheric easterly wave activity in both regions. There are some major differences, as well, due to the different land/ocean configurations. The near-equatorial disturbances north of Australia traverse westward over a lower boundary consisting of both land as well as ocean. On the other hand, the large amplitude West African disturbances move over the continental areas near 10°N prior to their arrival at the Atlantic coast. It appears, from satellite imagery and infrared data, that the distribution and activity of convective disturbances are more vigorous over the near-equatorial region north of Australia than in the near-equatorial rainbelt over West Africa.

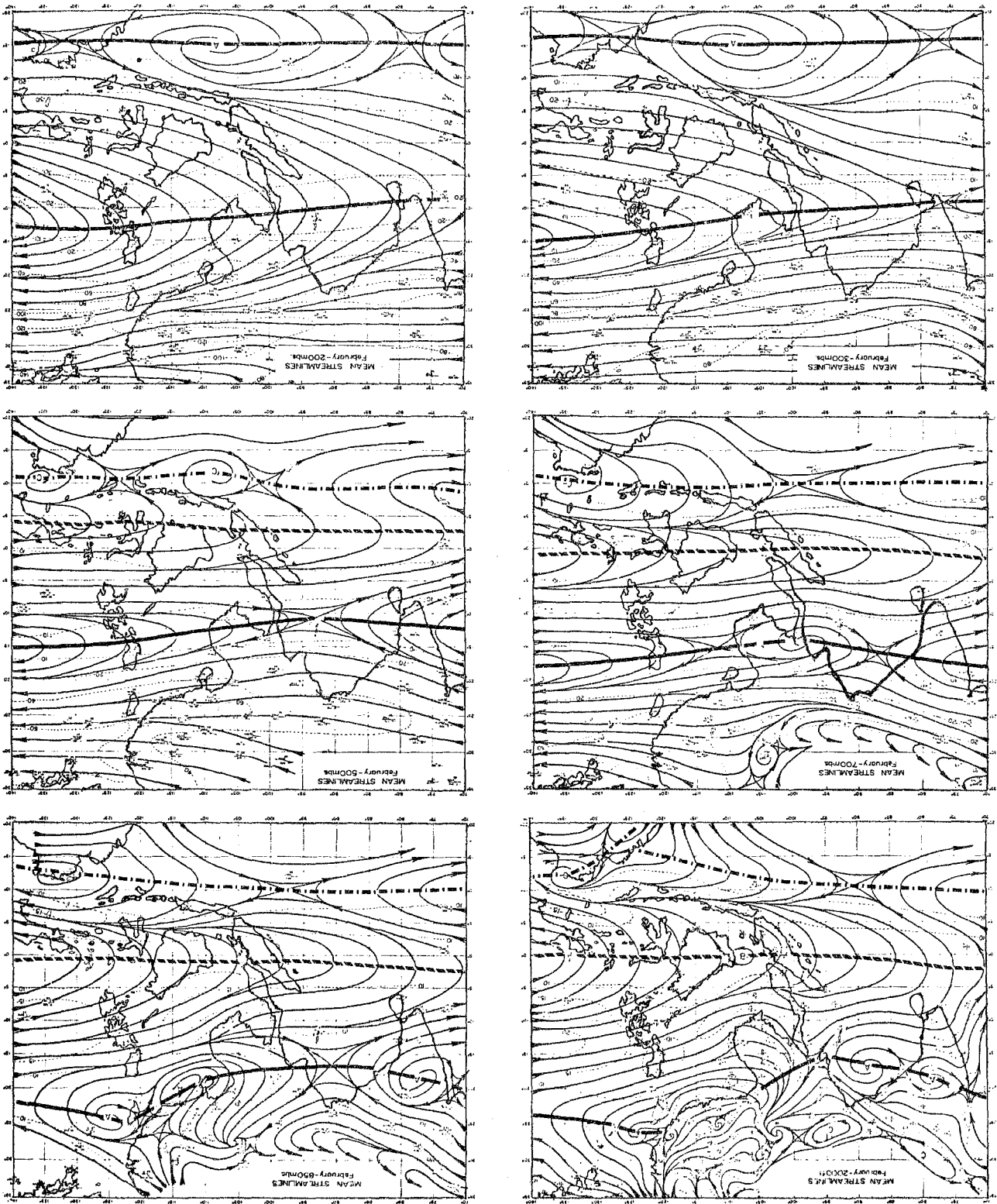


Figure 10.5 - Mean streamlines over the Indian Ocean for February (from Sadler and Harris, 1970) at surface, 850, 700, 500, 300, and 200 mb

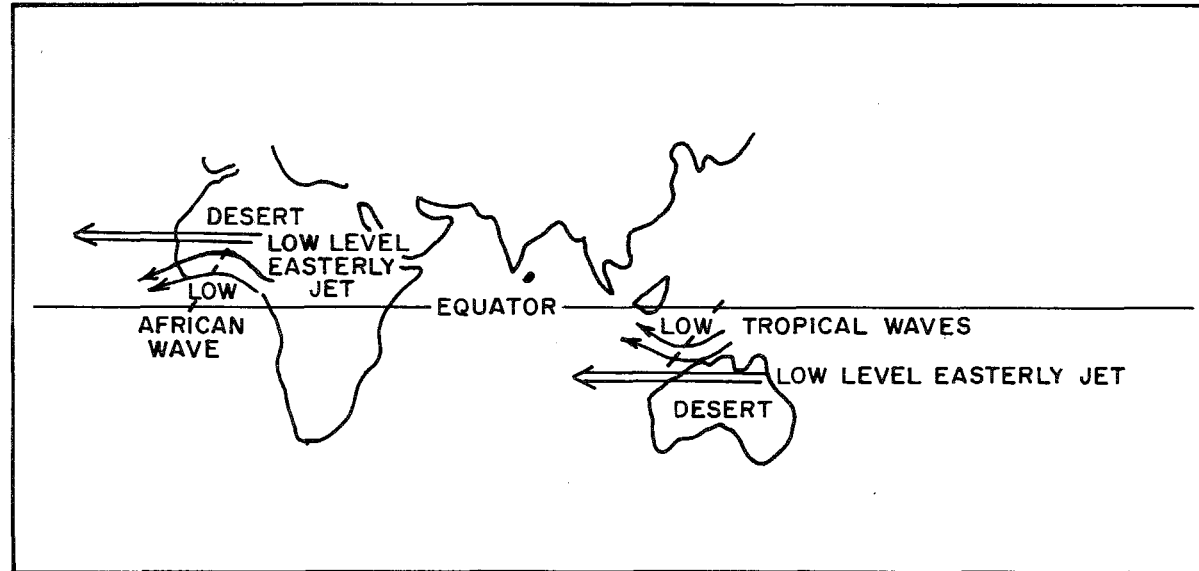


Figure 10.6 — A schematic diagram illustrating the similarity in the geometry of the low-level jets: over West Africa during northern summer and over northwestern Australia during northern winter. Wave disturbances form on the Equator-ward side, i.e. the cyclonic shear side of this low-level jet

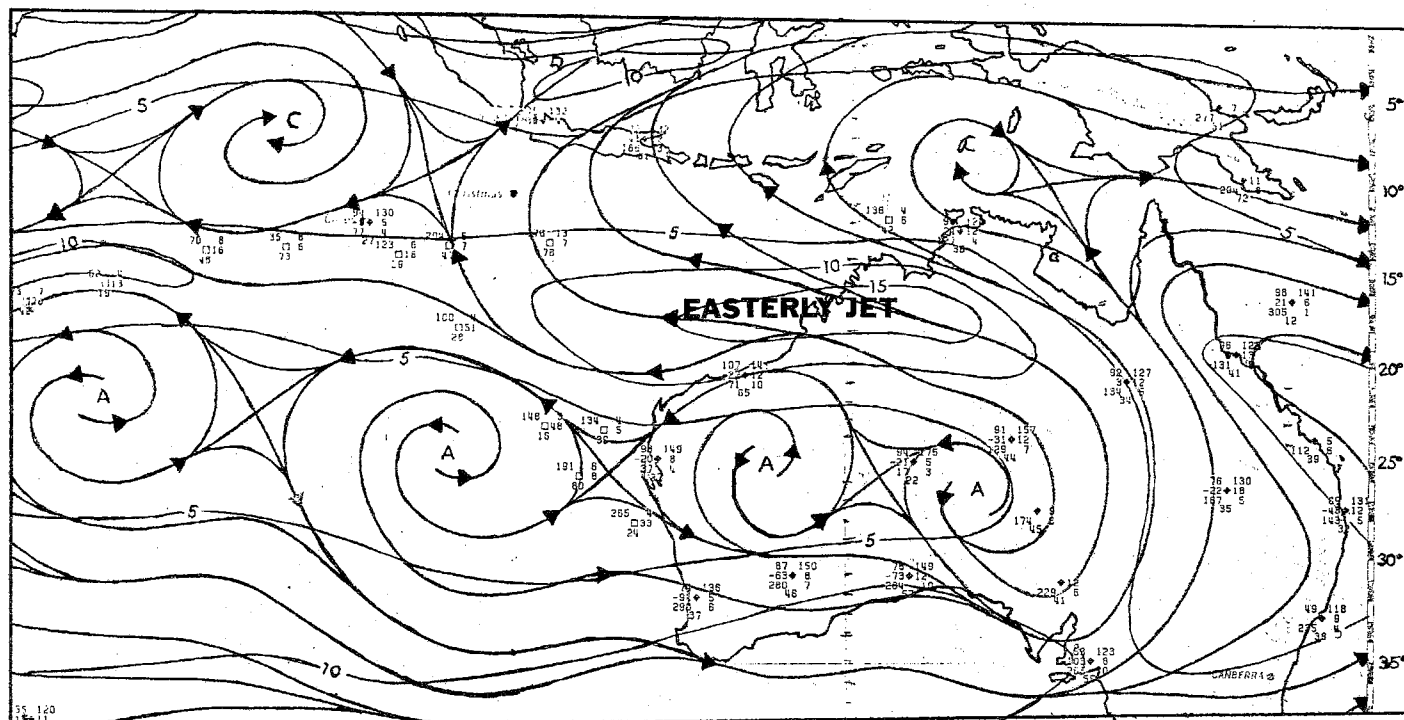


Figure 10.7 - 700 mb mean flows during February based on the analysis of Ramage and Raman (1974). The streamlines and isotachs (knots) are illustrated. The position of the low-level easterly jet is indicated here

TABLE 10.1

Estimates of individual terms in the horizontal gradient of mean potential vorticity in units of $10^{-11} \text{ m}^{-1} \text{ s}^{-1}$. Terms were evaluated at 700 mb from the monthly mean cross-section for August at 5°E based on Burpee (1972) over West Africa during northern summer

Latitude ϕ	$-\frac{\partial^2 \bar{u}}{\partial y^2}$	β	$-\frac{f_0^2}{N_s^2 \rho_s} \frac{\partial \rho_s}{\partial z} \frac{\partial \bar{u}}{\partial z}$	$-\frac{f_0^2}{N_s^2} \frac{\partial^2 \bar{u}}{\partial z^2}$	$\frac{\partial \zeta_p}{\partial y}$
5	4.8	2.2	-0.2	-2.0	4.8
7.5	6.4	2.2	-0.2	-2.0	6.4
10	-1.2	2.2	-0.3	-4.0	-3.3
12.5	-5.2	2.2	-0.4	-8.0	-11.4
15	-4.0	2.2	-0.3	-4.0	-6.1
17.5	0.0	2.2	-0.4	-2.0	-0.2
20	0.6	2.2	-0.2	-2.0	0.6
22.5	2.8	2.2	-0.1	0.0	4.9
25	0.0	2.2	0.0	0.0	2.2

TABLE 10.2

Same as above across the northwestern Australian low-level jet at 700 mb for southern summer (across 125°E longitude), based on unpublished work (Krishnamurti)

5°S	-0.3	2.2	4.6	2.5	9.0
7.5°S	-0.0	2.2	5.9	1.4	9.5
10	+0.3	2.2	-1.9	1.5	2.1
12.5	+3.5	2.2	-0.1	1.0	6.6
15	-0.2	2.2	-0.4	-1.8	-0.2
17.5	-5.8	2.2	0.3	-2.7	-6.0
20	-0.8	2.2	-0.2	-5.2	-4.0
22.5	+2.9	2.2	-0.1	-5.3	-0.3
25	+0.8	2.2	+0.2	-5.4	-2.2

There are also a number of dynamical parallels in these two easterly wind régimes.

10.3 Combined barotropic/baroclinic instability

A theory for the existence of combined barotropic and baroclinic instability is presented elsewhere (see Appendices). We have also discussed earlier that the West African wind and temperature observations satisfy the necessary condition for the existence of the so-called "combined instability" during northern summer. We shall show here that the low-level easterly jet over northwest Australia also satisfies the same conditions. If a data set satisfies the necessary condition for the existence of combined instability, then the meridional gradient of potential vorticity (ζ_p) must vanish somewhere within that region of interest. Tables 10.1 and 10.2 show the various terms in the expansion over West Africa from Burpee (1972) and over northwestern Australia based on the author's unpublished work. There are five columns showing respectively the horizontal shear, and the beta term, two terms showing the effects of vertical wind shear and the final column shows the sum of all the terms. The rows in the tables show different latitudes. The sum of the first two terms denotes the barotropic effects. A change of sign in the sum of the first two terms (as a function of latitude) reflects that the necessary condition for the existence of "barotropic" instability is satisfied by the data set. This is true for the two low-level jets considered here. The sum of all of the terms also shows a change of sign (as a function of latitude) thus satisfying the existence of the combined instability. The question naturally is asked: What is the implication, if the necessary condition is satisfied by a data set?

Here our interpretation is that wave disturbances propagating westward on the cyclonic shear side of the low-level jet could draw energy from the horizontal as well as the vertical shear of the basic current, i.e. the low-level jet. In order to go one step beyond this stage towards confirming whether such energy exchanges indeed occur in the maintenance of the wave disturbances, further diagnostic and prognostic studies are needed. Such studies have been carried out by Reed et al., (1977), Norquist et al., (1977), and by Krishnamurti et al., (1977) over West Africa. These studies essentially confirm the importance of baroclinic and barotropic energy exchanges for the maintenance of the wave disturbances.

Finally, it is important to recognize another point of similarity between these two wave disturbances. Most Atlantic hurricanes are known to form from the African waves; likewise a large number of tropical storms of the southern Indian Ocean form out of westward propagating wave disturbances that originate in the general region of north of Australia, Indonesia and southern Malaysia.

Chapter 11

HURRICANES

The amount of research that has gone on in this area is so large that it would be impossible to review the state of the art in one chapter. We shall first list some of the main areas of current studies.

- (i) Formation of hurricanes. Observational factors, instability, theories, numerical modelling;
- (ii) The mature hurricane structure, dynamics and numerical simulation;
- (iii) The track of hurricanes. Statistical and dynamical statistical methods, steering, numerical weather prediction;
- (iv) The land fall: decay of hurricanes, destruction, tornadoes associated with hurricanes at landfall, floods after storms move inland;
- (v) Storm surges;
- (vi) Modification of hurricanes;
- (vii) Cumulus convection and its parameterization in the numerical modelling of hurricanes;
- (viii) The hurricane rain bands;
- (ix) Dynamics and energetics of hurricanes.

11.1 Formation of hurricanes

Maps of tropical regions where hurricanes form may be found in studies such as those compiled by Gray (1968). Observations suggest that there exists a critical ocean temperature, i.e. 27°C , below which hurricanes do not usually form. Once formed, hurricanes are, however, known to move over middle latitude oceans where the ocean is colder. Some numerical models show that the maintenance of a mature hurricane depends crucially on the sea-surface temperature. The pattern on tropical weather maps during the initial stages of hurricane formation usually contain some clues. However, often the same pattern simply represents potential threat and no development occurs. Factors such as organized convection, large horizontal shearing currents in the lower troposphere, lack of vertical shear, high ocean temperatures, favorable high-level anticyclonic flows, etc., are usually quoted as being important. The number of such factors is so large that there are, in fact, no definitive empirical rules. Some studies, such as those by Dvorak (1973), indicate an expected sequence of satellite cloud cover during the formation of a hurricane (or typhoon). Such sequences can be somewhat misleading because they portray cloud patterns which are a consequence of the organization of the motion field and, in particular, the divergent part of the motion field. However, it provides some degree of satisfaction that one has looked at the evolution photographs. They do not provide too many clues about the formation process, which involves many dynamical and thermodynamical factors. Fig. 11.1 illustrates two sequences of photographs from Dvorak (1973) showing the satellite cloud cover (once per day) during the formation of hurricanes. The pictures clearly illustrate an organization of

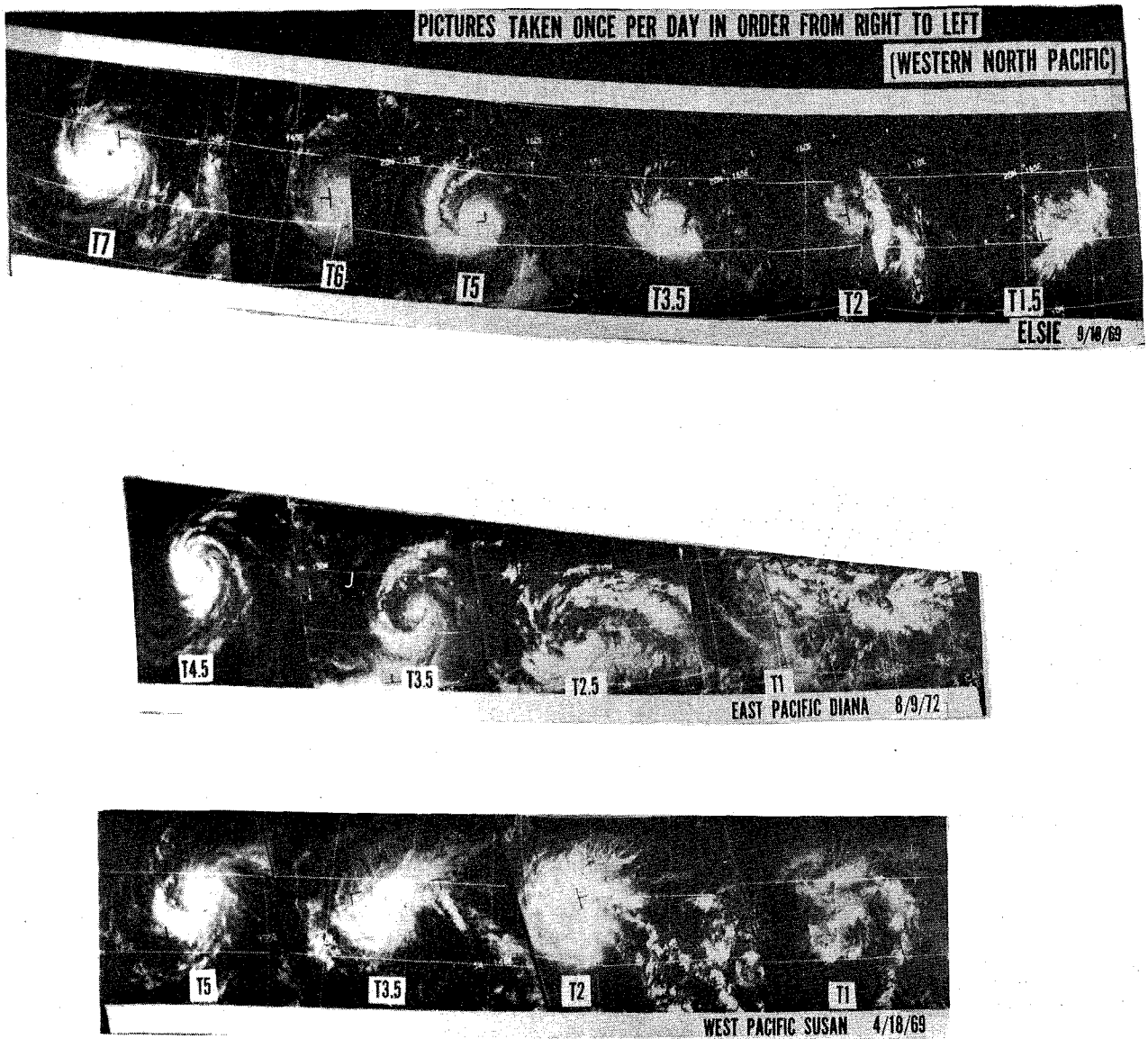


Figure 11.1 - Daily sequence of typhoon formation

convection. However, it does not explain why such an organized cloud structure evolved. It should be stated that experienced forecasters can, at times, find more than most people in such photographs to aid them in the

prediction of hurricane evolution. However, a formal documentation of their experience is usually not provided.

The map approach of identifying typical patterns which lead to hurricane development has similar limitations. Fig. 11.2 from a study of Fett (1966) gives schematic flow charts during the evolution of a typhoon. The idea is that if stage III follows II from an innocuous state I, then a forecast of stage IV is usually made. The limitation is that only in parts of the tropical oceans can one find a stage I type ITCZ and there are usually a myriad of cloud patterns that accompany flow patterns. This sequence evidently has met with some success over the central Pacific Ocean. Figure 11.3, according to Colon (1961), illustrates an example of a hurricane formation in an easterly current. The different panels illustrate the formation and northward motion of hurricane Helene. The broad scale flow is easterly both to the north and the south initially. The pattern is not quite the same as in Fig. 11.2 above. Late season storms frequently show this kind of evolution over the western Atlantic Ocean. Here again, the pattern alone can be very misleading at times. Operational weather maps from Weather Centers such as Miami and Guam provide many synoptic-scale examples of storm evolution. In this connection, reference should be made to the April issues of the Monthly Weather Review of the last several years. In these issues there are generally three review papers on the tropical disturbances and hurricanes of the preceding year over the Atlantic and eastern Pacific Oceans. Another important source of reference is the annual typhoon summary published by the Joint Typhoon Warning Center in Guam, the latter covering the western Pacific Ocean. In order to obtain a global coverage of the various storm episodes similar publications of several other countries, e.g. Australia, India, Mauritius are necessary. Although it appears that the ultimate understanding of hurricane formation will come only from a controlled numerical weather prediction approach, a knowledge of actual episodes is extremely important since they provide important background information.

11.2 Observed structure of a mature hurricane

In this section we shall present some of the structural details of hurricane Hilda (1964). Its structure was analysed by Hawkins and Rubsam (1968). Most of the analysis is based on research aircraft flights into the hurricane; four flights near 900 mb, 750 mb, 500 mb and 190 mb were carried out on October 1, 1964 when the storm was fully developed. Although there are four aircraft flight levels, the observations are still insufficient for full coverage. Observing a hurricane is an extremely expensive operation. Ideally one would like to see more than one plane flying at each of at least six pressure levels. Such an investment would provide a detailed and definitive structure of one hurricane. It may be desirable from the point of view of numerical modelling that some fairly detailed observational structures be determined and documented. As we shall see from the next section, numerical models produce what we think are very reasonable structures. We are, however, not in a position to determine their limitations.

Fig. 11.4 shows the observed vertical cross-sections of the following variables:

- (i) Temperature anomaly;
- (ii) D-value, which is a departure of the geopotential height from a standard atmosphere;

TYPHOON DEVELOPMENT WITHIN THE ZONE OF THE ITC

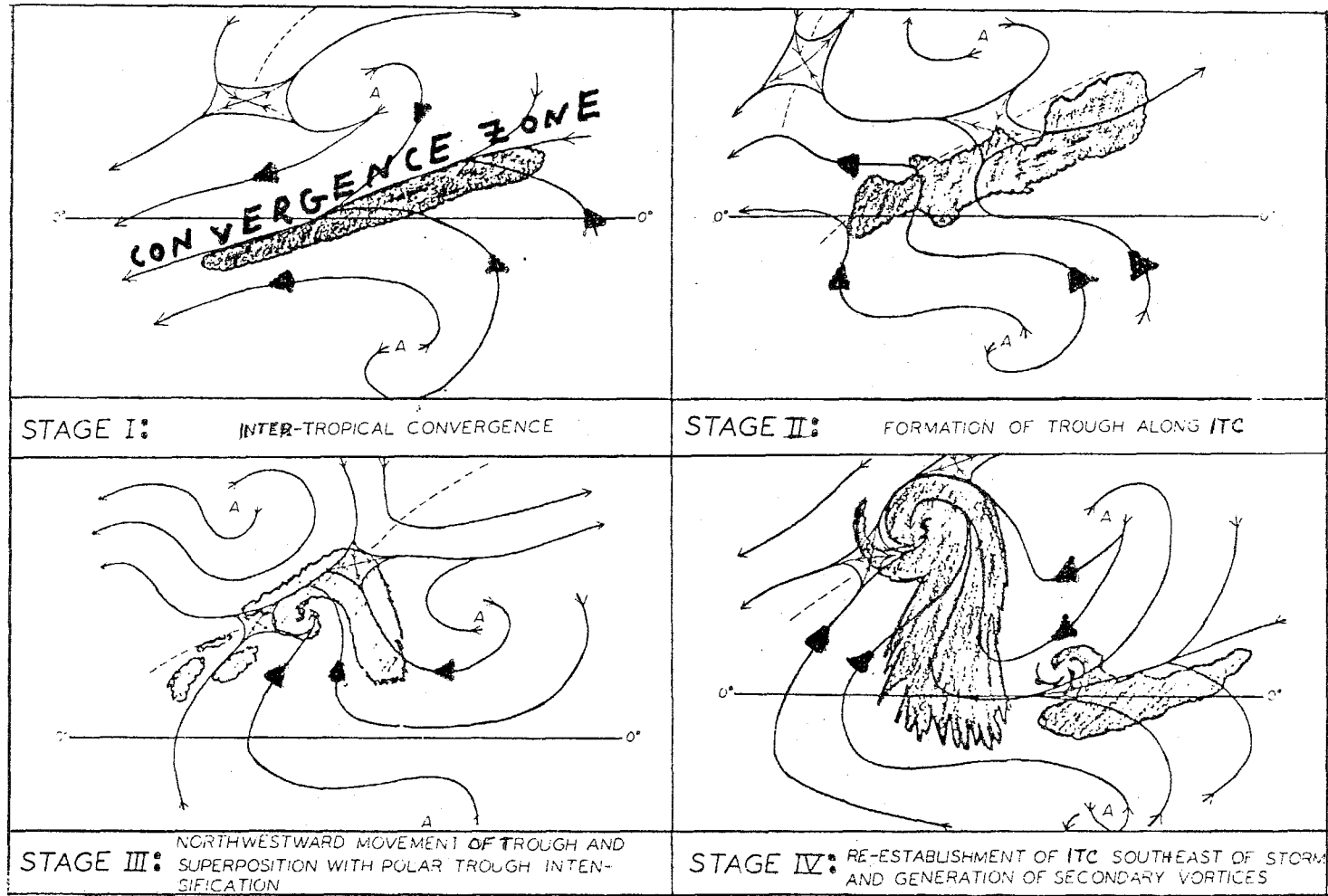
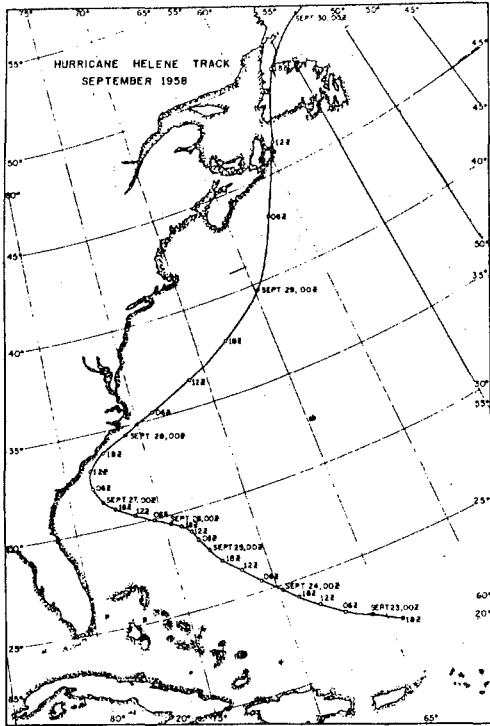
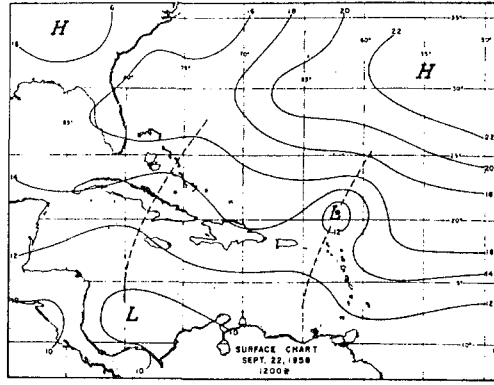


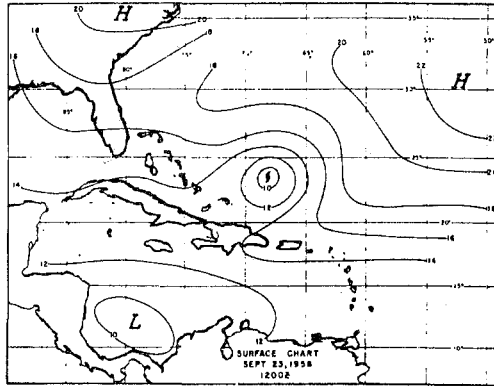
Figure 11.2



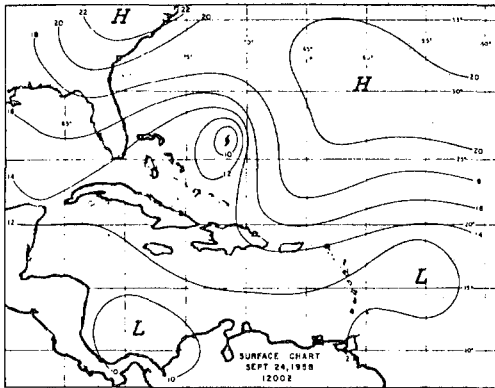
Track of hurricane Helene, September 29, 1958



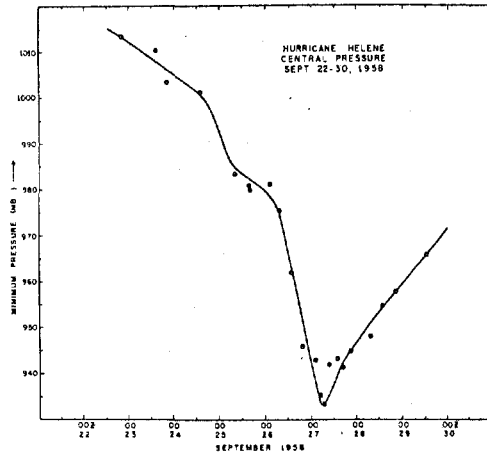
Surface chart, September 22, 1958



Surface chart, September 23, 1958

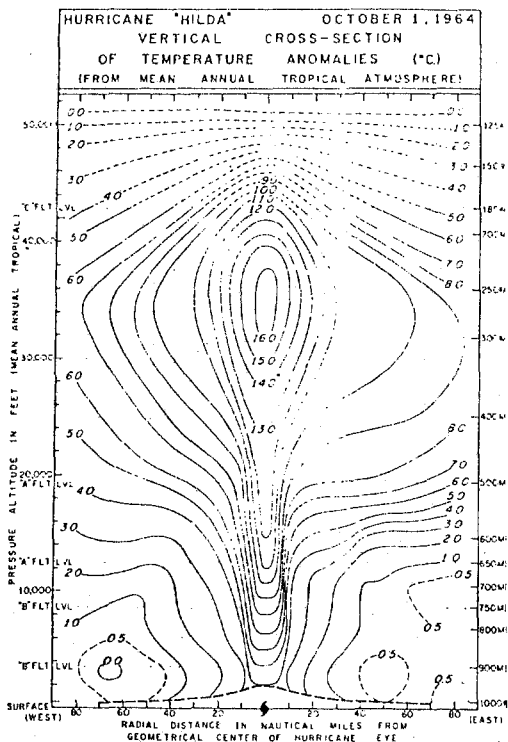


Surface chart, September 24, 1958

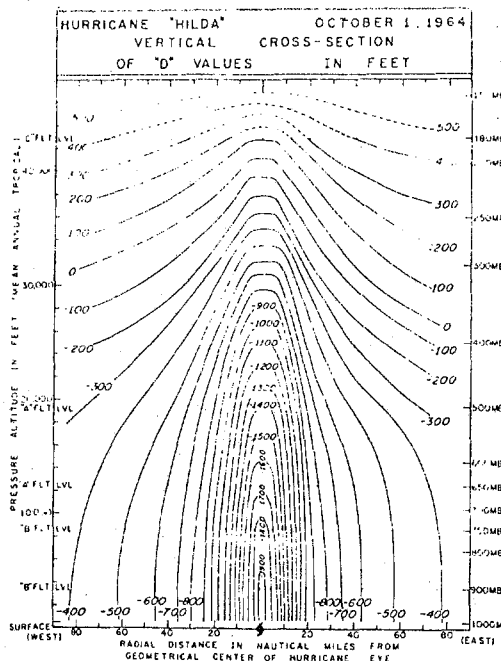


Time changes in the minimum central pressure in hurricane Helene

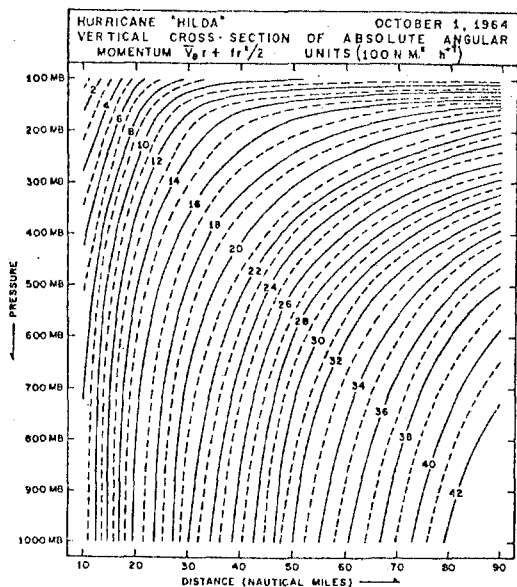
Figure 11.3



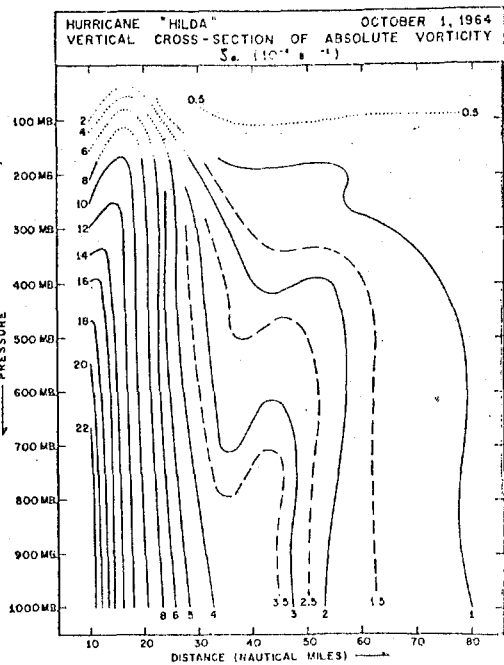
Vertical cross-section of temperature anomaly ($^{\circ}\text{C}$)



Vertical cross-section of D-values (from the mean tropical atmosphere)



Vertical cross-section of absolute angular momentum for tangential winds that have been averaged azimuthally about the moving storm



Vertical cross-section of absolute vorticity for the mean tangential relative winds

Figure 11.4

- (iii) Absolute angular momentum;
- (iv) Absolute vorticity.

Fig. 11.5 illustrates sections of:

- (v) Wind speed relative to moving centre;
- (vi) Radial velocity.

The temperature anomaly indicates a warm core with a maximum of 16°C near the 250 mb surface. The radial gradient of temperature is very large below 500 mb roughly 10 km from the storm's centre. It is clear from this detailed structure that a grid size of roughly 5 km may be required to resolve the observational details that are present here. The radial gradient of the thermal field is small over the ocean surface. The region above 200 mb is somewhat questionable in this section. There is a possibility that a very cold tropopause might be present above the hurricane, but this is not indicated by this section.

The D-values illustrate the region of large radial pressure gradient which is located 10 to 20 nautical miles from the storm's centre. Above 300 mb, this pressure gradient becomes considerably weaker. In this inner rain area, low pressure near the centre extends all the way up to 150 mb.

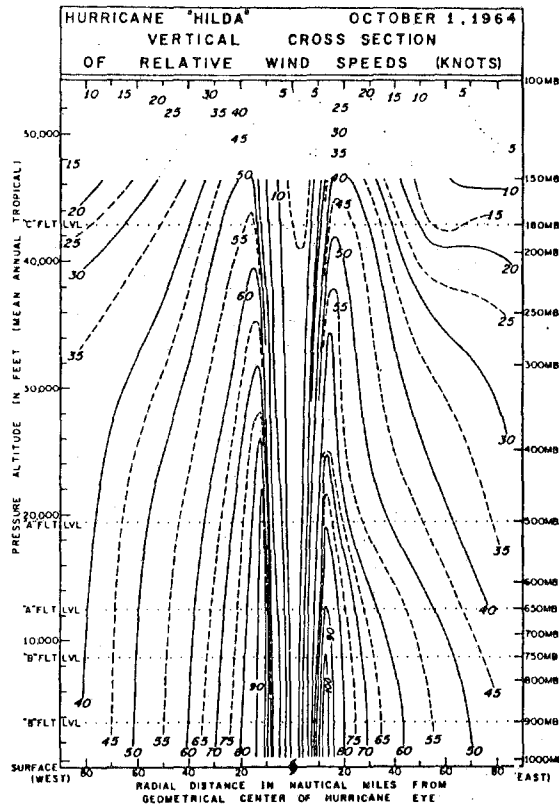
The radial mass inflow and outflows shown in the next figure (i.e. Fig. 11.5) indicate the largest inflows at the lowest level and outflows near the 200 mb surface. These inflow and outflow profiles at different radial distances have been adjusted for the condition of no net mass inflow. The horizontal wind speed relative to the moving centre is illustrated in the top panel of Figure 11.5.

The largest wind speed is of the order of 100 knots. Even after removal of the storm's motion, the left and the right sides are not symmetric about the storm's centre. Near the eye-wall, the vertical shear of the total wind is small. Speeds of the order of 45 to 55 knots are present even at 180 mb, the uppermost flight level where the storm was observed. It is of interest to note that the strong wind belt is confined to such a small area. At a radial distance of 80 nautical miles from the storm's centre, the speeds fall off to about 45 knots. This makes the forecasting of the land fall of strong winds a very difficult problem - since the accuracy requirements for the storm's track are extremely high.

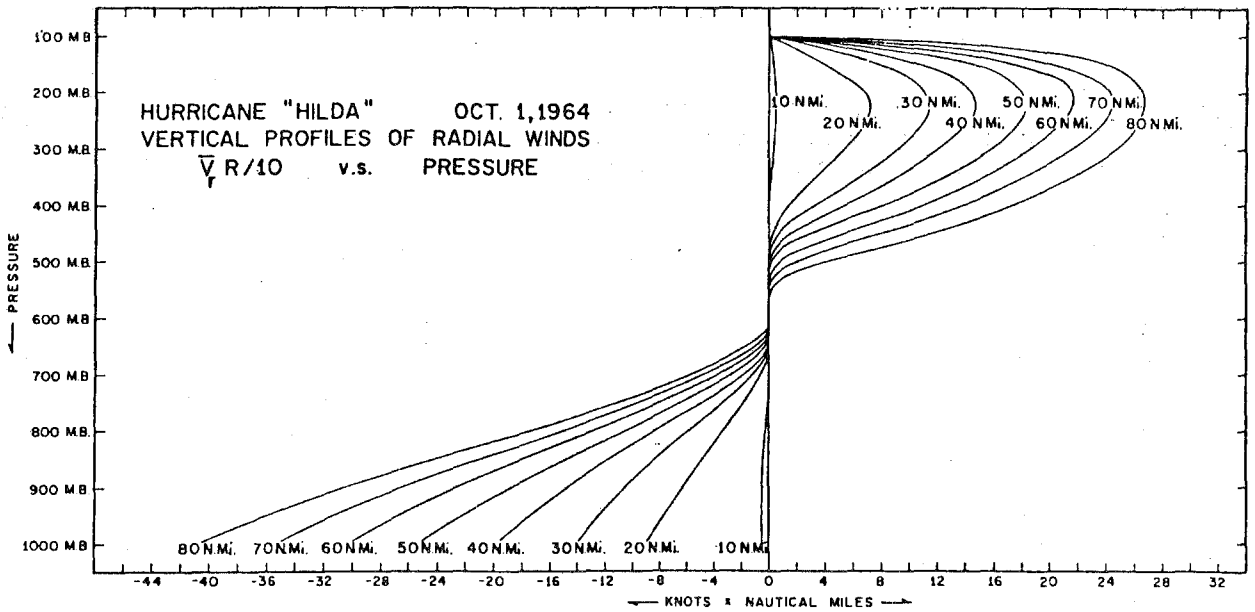
A vertical cross-section of the absolute angular momentum is given at the bottom of Fig. 11.4. The superposition of the mass inflow/outflow on this diagram reveals that at the lower level of the storm, parcels are moving towards smaller and smaller values of the angular momentum. Thus, there is an appreciable loss of angular momentum to the sea. At the higher levels, the outflows are more parallel to the isopleths of absolute angular momentum suggesting that the absolute angular momentum is nearly conserved.

The isopleths of absolute vorticity are illustrated at the bottom of Fig. 11.4. They show that the cyclonic vorticity of the storm has a maximum value of the order of $22 \times 10^{-4} \text{ s}^{-1}$. The vertical variation of the absolute vorticity is very small in the lower troposphere. The region of cyclonic vorticity (at about 25 nautical miles) extends all the way up to 100 mb.

The structure we have presented in the top panels of Figures 11.4 and



Vertical cross-section of wind speeds relative to the moving hurricane eye



Curves of radial velocity (in the form of $\bar{v}_r/10$) against pressure for various radii. Mass balance is satisfied at every radius

Figure 11.5

11.5 is of the storm's structure to the left and right of its centre with respect to its direction of motion. The other parts of these diagrams illustrate the symmetric structure of the storm.

11.3 The axially symmetric hurricane

The axially symmetric hurricane is a model hurricane that is stationary. These models have improved our understanding of the hurricane; but they have limitations.

In this section, we shall present a brief review of the state of the art in this area. The first successful numerical simulation of a hurricane came from the work of Ooyama (1969). The first study with a primitive equation model was carried out by Yamasaki (1968). Most subsequent contributions to the symmetrical model have been due to Rosenthal. His results appear in many papers published in the Monthly Weather Review. Sundquist (1972) has also contributed in this area.

11.3.1 The closed system of equations of the symmetric model

Cylindrical coordinates with pressure as a vertical coordinate are used in the following formulation. The independent variables are radial distance r , pressure p and time t . The dependent variables are the three velocity components u , v and ω , potential temperature, moisture variable q and the geopotential height of the pressure surface z .

The radial equation of motion is:

$$\frac{dv_r}{dt} - \left(f + \frac{v_\theta}{r} \right) v_\theta = - \frac{\partial \phi}{\partial r} + v \left(v^2 - \frac{1}{r^2} \right) v_r - g \frac{\partial \tau_r}{\partial p} \quad (11.1)$$

The tangential equation of motion is:

$$\frac{dv_\theta}{dt} + \left(f + \frac{v_\theta}{r} \right) v_r = v \left(v^2 - \frac{1}{r^2} \right) v_\theta - g \frac{\partial \tau_\theta}{\partial p} \quad (11.2)$$

The remaining equations are:

The hydrostatic law:

$$\frac{\partial \phi}{\partial p} = - \frac{R\pi}{p} \theta \quad (11.3)$$

The mass continuity equation:

$$\frac{1}{r} \frac{\partial}{\partial r} (rv_r) + \frac{\partial \omega}{\partial p} = 0 \quad (11.4)$$

The thermodynamic equation:

$$\frac{d\theta}{dt} = \frac{1}{c_p} Q + K v^2 \theta \quad (11.5)$$

The moisture equation:

$$\frac{dq}{dt} = E - P \quad (11.6)$$

where

$$\pi = T/\theta = (p/p_0)^{R/c_p}$$

and

$$\nabla^2 \equiv \frac{\partial^2}{\partial r^2} + \frac{1}{r} \frac{\partial}{\partial r}; \quad \frac{d}{dt} \equiv \frac{\partial}{\partial t} + v_r \frac{\partial}{\partial r} + \omega \frac{\partial}{\partial p}$$

The system of equations presented above requires definition of the friction, heating, precipitation and evaporative processes. If these are defined, then we have four prognostic equations for v_r , v_θ , θ and q and two diagnostic equations for ω and $\partial\phi/\partial p$. The system requires appropriate boundary conditions for these variables. The problem of a reference level specification for the geopotential ϕ is an important one.

Here we present the definition following Yamasaki (1968). In order to exclude external gravity waves from the system, ω was taken as zero at $p = p_0$ and at $p = p_T$, i.e., the bottom and top of the model atmosphere. The outward mass flux at a pressure level is proportional to $v_r r$. The net flux of mass radially in and out of a vertical column should be zero, i.e.:

$$\int_{p_T}^{p_0} v_r r dp = 0 \quad (11.7)$$

or, since $r = \text{constant}$,

$$\int_{p_T}^{p_0} v_r dp = 0 \quad (11.8)$$

Furthermore,

$$\frac{\partial}{\partial t} \int_{p_T}^{p_0} v_r dp = 0 \quad (11.9)$$

From equations (11.1) and (11.9) we obtain:

$$\int_{p_T}^{p_0} \left(A - \frac{\partial\phi}{\partial r} \right) dp = 0 \quad (11.10)$$

where

$$A = -v_r \frac{\partial v_r}{\partial r} - \omega \frac{\partial v_r}{\partial p} + \left(f + \frac{v_\theta}{r} \right) v_\theta + v (\nabla^2 - 1/r^2) v_r - g \frac{\partial \tau_r}{\partial p} \quad (11.11)$$

Using the hydrostatic law (11.3), we obtain:

$$\phi(p) = \phi(p_T) - \int_{p_T}^p \frac{R\pi\theta}{p} dp \quad (11.12)$$

and using (11.10), we obtain:

$$\begin{aligned} \phi(p_T) = \frac{1}{(p_0 - p_T)} \int_{p_T}^{p_0} dp \int_{p_T}^p \frac{R\pi\theta}{p} dp - \frac{1}{(p_0 - p_T)} \int_r^{r_0} \int_{p_T}^{p_0} A dp dr \\ + \frac{1}{(p_0 - p_T)} \left[\int_{p_T}^{p_0} \phi dp \right]_{r=r_0} \end{aligned} \quad (11.13)$$

This equation together with the hydrostatic law specifies ϕ at all levels.

The other boundary conditions are:

$$v_r = v_\theta = \frac{\partial \theta}{\partial r} = \frac{\partial q}{\partial r} = 0 \quad \text{at } r = 0 \quad \text{and} \quad r = r_0 \quad (11.14)$$

The stresses τ_r and τ_θ vanish at the top of the atmosphere. The stresses are defined above the surface by the relations,

$$\begin{vmatrix} \tau_r \\ \tau_\theta \end{vmatrix} = -\rho^2 g K \frac{\partial}{\partial p} \begin{vmatrix} v_r \\ v_\theta \end{vmatrix} \quad (11.15)$$

At the surface we define these by the usual relations:

$$\begin{vmatrix} \tau_{rs} \\ \tau_{\theta s} \end{vmatrix} = \rho_s C_D \left| v_s \right| \begin{vmatrix} v_{rs} \\ v_{\theta s} \end{vmatrix} \quad (11.16)$$

Furthermore,

$$\omega = 0 \quad \text{at} \quad p = p_0, p = p_T. \quad (11.17)$$

The vertical resolution of the numerical model is specified as:

$\Delta p = 25$ mb below 900 mb and $\Delta p = 100$ mb above. (Thirteen vertical levels in all).

The horizontal resolution is specified as:

$$\begin{aligned} \Delta r &= 20 \text{ km for } r < 100 \text{ km,} \\ \Delta r &= 50 \text{ km for } 100 \text{ km} < r < 450 \text{ km,} \\ \Delta r &= 100 \text{ km for } r > 500 \text{ km.} \end{aligned}$$

An upstream differencing scheme is used for horizontal advection. For the initial state, the following conditions are adopted:

Weak tangential velocity ($\approx 5 \text{ m s}^{-1}$), no initial radial or vertical motion. Initial geopotential derived from gradient balance of the weak circular vortex. The initial thermal stability is taken as slightly less than that of the so-called Jordan sounding.

11.3.2 The moisture distributions

In many of the symmetric hurricane models no explicit moisture variable is used. A steady source of moisture in the boundary layer is assumed and its effect in the thermal equation is introduced via the heating terms. An explicit water-vapour cycle was introduced by Rosenthal in a symmetric model. He discusses the so-called convective and non-convective precipitation for the hurricane problem. He showed that the non-convective component

was substantial for the hurricane intensification, a result also confirmed by Mathur in an asymmetric hurricane formation. Rosenthal essentially utilized an extension of Kuo's procedure for the parameterization of cumulus convection. The heating function

$$\dot{Q} = \frac{\lambda t}{\Delta t} \rightarrow 0 \left\{ \frac{c_p \Delta T}{\Delta t} \right\} \quad (11.18)$$

where ΔT is the net temperature change at a pressure level p due to n levels from which convection can originate and the convective precipitation rate for a column of unit area is

$$P = \frac{1}{g} \int \frac{\dot{Q}}{D} dp \quad (11.19)$$

(For a definition of ΔT refer to Kuo's procedure for parameterization of cumulus convection.) Large-scale condensation is invoked when there is saturation, ascending motion and a statically stable situation. Extreme care is exercised in assuring moisture conservation in the specification of the convective and non-convective heating and related precipitation. Since the saturation condition is a function of the models, super-saturated states can remain unaccounted for, and cause problems.

11.4 Results of numerical simulations of the symmetric hurricane

This review of hurricane simulation contains a mixture of contributions from different workers. We illustrate first some of the main results from Rosenthal's model with the explicit water vapour cycle. The simulations of Yamasaki (1968) and Rosenthal (1969) all seem to have much the same characteristics. Rosenthal uses a 10 km mesh size in his experiment. The results of his simulations, and especially the structure at the mature stage, are illustrated in Fig. 11.6. The following may be identified in these diagrams:

- (i) Evolution of the central pressure as a function of time;
- (ii) Evolution of maximum surface wind;
- (iii) Surface pressure as a function of radius at 144 hours;
- (iv) Convective plus nonconvective rainfall between 72 and 216 hours;
- (v) Tangential velocity at hour 144;
- (vi) Radial velocity at hour 144;
- (vii) Temperature anomaly at hour 144;
- (viii) Vertical velocity at hour 144.

At around hour 144, the central pressure reached a minimum value of around 975 mb and surface wind speeds approached 40 m s^{-1} . Let us redefine axial symmetry by the relation

$$\bar{Q}(r, z, t) = \frac{1}{2\pi} \oint Q(r, \theta, z, t) d\theta \quad (11.20)$$

where the integral is taken around any circle of the cylindrical coordinate system. In order to obtain a field of \bar{Q} (for any variable) based on observations, three-dimensional observations of the variable are required. It is safe to state that such detailed observations have not been made in any one storm. Data at a few levels from aircraft flights into hurricanes have provided much useful information on the inner structure of the storms. The gaps in data are quite large and no definitive detailed structure has been described. Some attempts at combining observations from many different storms have been very promising (Gray, 1974). Aside from the limitations of

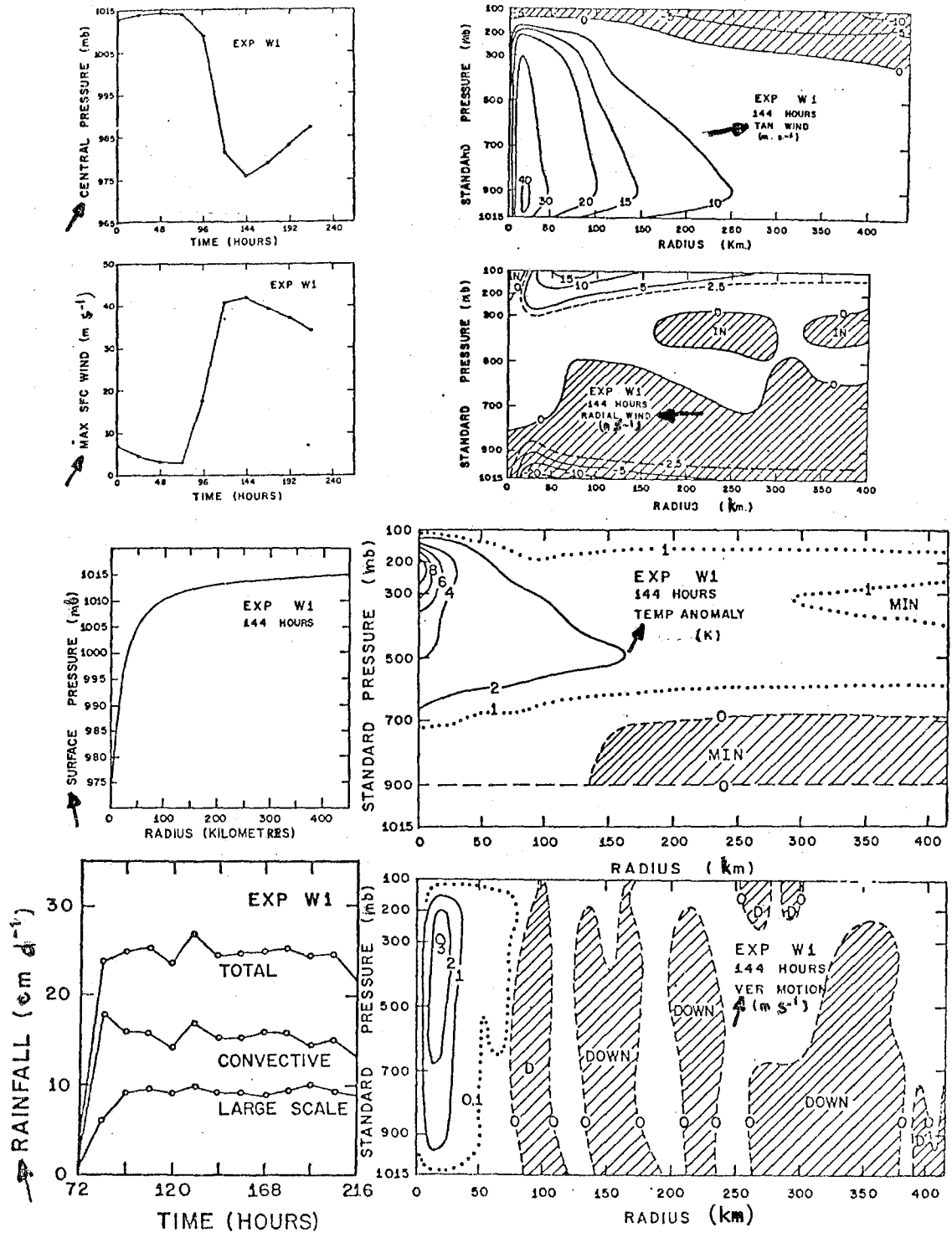


Figure 11.6

the lack of asymmetries and lack of motion of the storms, the calculations do seem to suggest a high degree of success in their simulation. The absence of a spin-up time of roughly 96 hours before any significant pressure drop occurs is a major defect of the present models. The long integration time, i.e., 144 hours, makes it difficult to assess the reality of the initial parameters of the model. In his experiment, Rosenthal felt that "the ultimate intensity of the storm is not greatly affected by the initial humidity conditions." This is evidently related to the long spin-up time. The simulation of the zonal, radial, and vertical velocities, and the temperature anomaly all seem quite realistic when compared with the presently available observed structures such as those we have presented in the previous section. The rainfall rates are reasonable and of interest here is the fact that a good proportion of the total rainfall is non-convective; out of a rate of about 25 cm per day about 7 to 10 cm per day are deposited from the non-convective process. This seems too high if we compare these rates with non-convective counterparts in middle latitude storms. This is primarily due to the intensity of the vertical motion ($\approx 3 \text{ m s}^{-1}$) in the upper, stable, saturated regions.

Several other remarkable findings have emerged from controlled numerical experiments with a symmetric hurricane. The following summary is based on Rosenthal's, Ooyama's and Yamasaki's contributions:

- (i) One of the problems examined was that of the role of inertial instability in the development of the hurricane. These studies all confirm that the appearance of a negative vorticity region is a consequence of the storm development and not the other way around;
- (ii) The vertical distribution of heating during the rapid intensification of the storm reaches the middle troposphere and even slightly lower. During this stage, the stratification of the upper levels becomes stable. The stratification near the centre becomes near neutral during the mature stage;
- (iii) The decaying stage of the storm was simulated in these studies. This occurs when the radial gradient of the temperature starts to decrease. This results in a decrease of the surface pressure gradient. The tangential velocity in the lower and middle layers starts to decrease. This decay of the storm is mostly a consequence of the model's tendency to produce near-neutral lapse rates over larger and larger areas near the centre of the storm. The weakening of the model storm is not due to a lowering of the sea-surface temperature or a simulated landfall. This type of weakening is not frequently observed;
- (iv) The model storm does weaken when the sea-surface temperature and/or the moisture supply from the ocean is cut off. The latter is a simulation of landfall;
- (v) Other major defects of the models relate to energy losses and momentum redistribution by the finite-difference procedures that act as pseudo-viscous effects.

11.5 Asymmetric aspects of hurricanes

We shall divide this section into two parts. First we discuss some salient observational aspects of the asymmetries.

11.5.1 Observational aspects

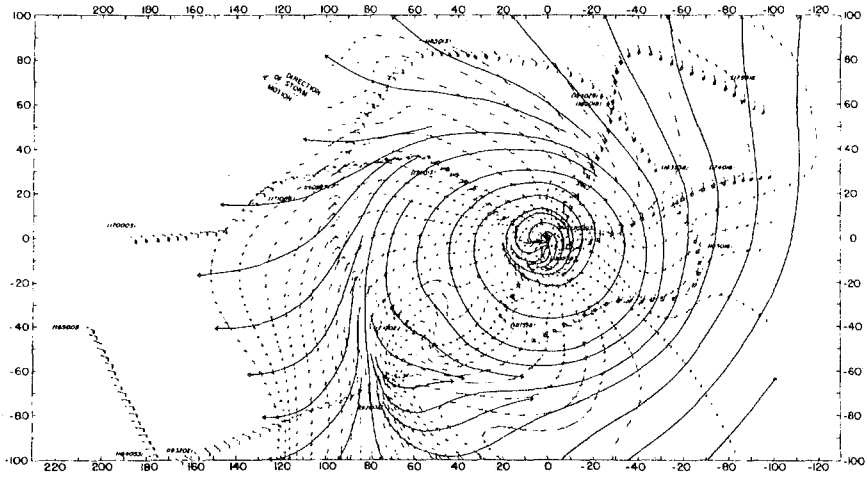
The major asymmetries are found in the motion field and in the distribution of cloud cover. The thermal and moisture fields have not been adequately observed. However, there is reason to believe that the moisture field above the boundary layer should be asymmetric with respect to the storm axis. Here again our interest is in the inner 100 km radius of the storm where most of the rainbelts are located. The upper tropospheric flows generally show an asymmetric flow distribution, which is illustrated in Fig. 11.7. The cyclonic outflows near the centre in the upper troposphere quickly change to anticyclonic outflow regions. Another salient asymmetry is in the isotach field of the lower troposphere. An example of the tangential velocity at 800 mb in a hurricane is illustrated in Fig. 11.7. This asymmetry of strong winds to the right of the direction of motion is not entirely due to the motion of the storm. A removal of the speed of motion of the storm still leaves some of the pronounced asymmetry in the tangential winds. The problem requires further observational exploration.

Finally, we show in Fig. 11.7 the asymmetries of the cloud cover from the radar composite for the same storm. The rainbands exhibit an asymmetry which is fairly typical of most hurricanes. The wind field in the boundary layer must be quite asymmetric with asymptotes of convergence beneath these rainbands. Lack of observations makes it difficult to construct any realistic detailed depiction of the streamline field over the ocean surface in the inner (100 km) rain area of the storm. The thermal and the pressure distributions are known to be the least asymmetric of the various observed fields.

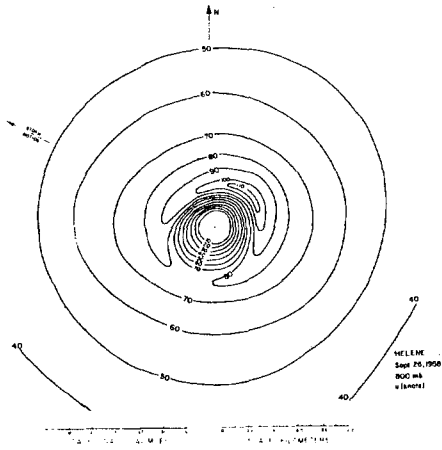
The rainbands illustrated in the diagram do not have quite the same structure in other storms. They frequently seem to contain a quasi-stationary part (with respect to the moving storm centre) and a transient part that moves outward from the storm centre. The latter has been related to the dynamic instability of the high level flows by Alaka (1961) and Black and Anthes (1972). Some storms have been observed to be far more symmetric than others.

11.5.2 Numerical modelling of the asymmetric hurricane

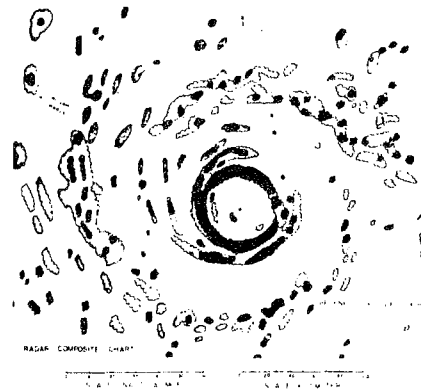
A four-dimensional numerical prediction or a simulation is a monumental computer problem. Only a few groups have ventured into a fine mesh numerical integration effort. Anthes (1972), Mathur (1971), Madala (1973) and Kurihara (1973) are some of the major contributors. Among these the formulations of Anthes, Madala and Kurihara are essentially extensions of the symmetric geometry. However, the work of Mathur is a real data hurricane prediction. All of these studies are very promising and there is no question that many other case studies are desirable. Anthes, Madala and Kurihara all started with a symmetric initial state and the asymmetries and rainbands developed after some 100 hours of integration. Their asymmetric flows appear to be similar to the observed counterparts illustrated above. We shall next review briefly the work of Mathur (1971) which is a four-day numerical forecast of hurricane Isabel of 1964. At the initial time, a depression located in the Caribbean Sea was moving northward and intensified into a hurricane. Fig. 11.8 shows the following four fields from the study of Mathur (1971);



200 mb STREAMLINES



800 mb ISOTACHS



RADAR COMPOSITE

Figure 11.7

- (i) Observed versus predicted track of storm;
- (ii) 1000 mb flows at time 0;
- (iii) 1000 mb flows after 96 hours; and
- (iv) 200 mb flows after 96 hours.

Mathur's predicted field possesses a remarkable degree of realism. The thermal field, central pressure and intensity of the motion field were quite close to the observed counterparts. There were three levels of aircraft missions in this storm that defined some mesoscale details of the initial state. In this study, Mathur used a 4-level model. A fine resolution near the storm's centre (≈ 37 km) was obtained through the use of a nested grid. His domain is illustrated in Fig. 11.8. The numerical model is a version of Florida State University's Tropical Prediction Model. The model uses a semi-Lagrangian advection scheme and an Euler backward time differencing scheme for a system of primitive equations. The basic equations consist of prognostic equations for the momentum, moisture and potential temperature, and diagnostic equations for the geopotential and the vertical velocity. The integration was from data for the 10th of October, 1964. The motion, thermal and moisture fields were analysed and the initial divergent motions were determined from quasi-geostrophic balanced models.

The specifications of physical effects were almost the same as those discussed in the moist symmetric models, i.e., surface friction is expressed in terms of the surface drag. Air/sea interaction is incorporated using bulk aerodynamic formulae. The stable heating formula is used as in the previous discussion and cumulus convection is incorporated following Kuo (1965). No radiation effects were included in this study.

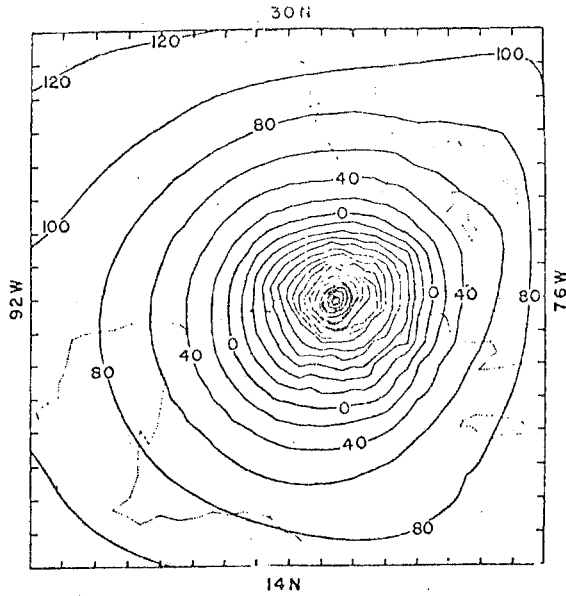
The numerical prediction over a limited area was carried out for a 96-hour period. The storm track illustrated in Fig. 11.8 shows that the track was predicted with a remarkable degree of success. The prediction was successful in many ways:

- (i) Stages of development, from depression to tropical storm to hurricane;
- (ii) Central pressure of storm;
- (iii) Temperature of the warm core;
- (iv) Maximum wind speed;
- (v) Position of storm;
- (vi) High level cyclonic outflows; and
- (vii) Banded fields of rising and sinking motion.

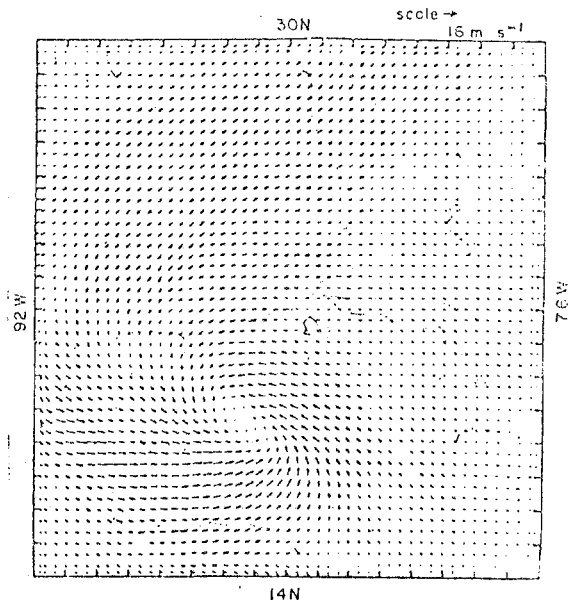
Figure 11.8 illustrates the 1000 mb height field and the horizontal motion field at 96 hours, showing a remarkable success of a real simulation. Unlike symmetric experiments, here there is no spin-up time; the evolution of the real data forecast is very realistic.

The undesirable aspects of the study relate to domain size and the smallest grid size. The domain should have been much larger to avoid contamination from boundary influences at 96 hours. The grid size of 37 km is too large to resolve the features suggested by observations. There is, of course, the need for much bigger computers and better models so one could carry out large numbers of such experiments. Only by such detailed experiments can one learn about the real mechanics of such complex weather systems.

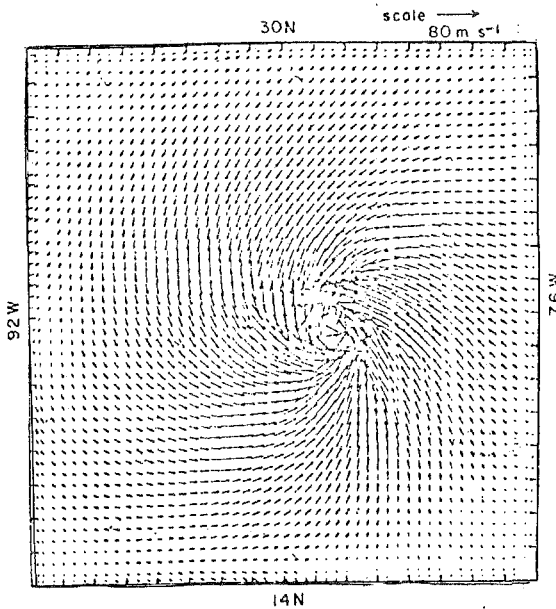
Many questions need to be asked in connection with the use of an asymmetric model. How much mesoscale input is required to produce high quality forecasts? What are the roles of the various initial asymmetries? What are the dynamics and energetics of the asymmetric hurricane? These questions remain to be explored.



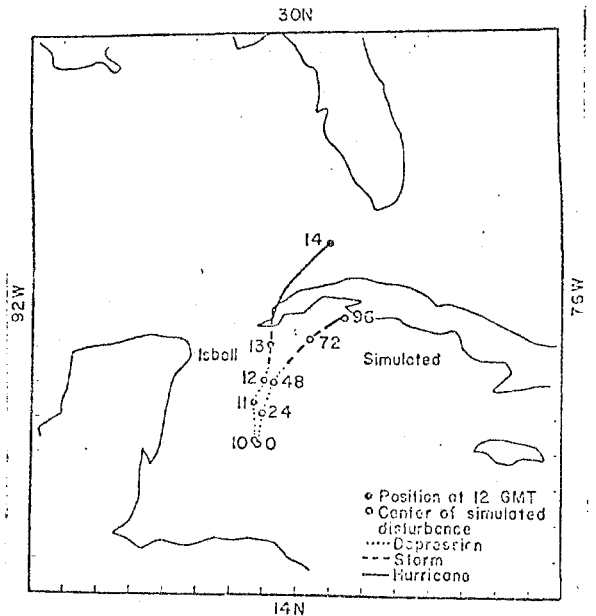
The tracks of hurricane Isabel and the simulated hurricane. Note that in both cases the intensification into a tropical storm takes place near 60 hours 00 GMT, 13 October, and the hurricane force winds appear after 72 hours (12 GMT, 13 October)



Initial wind field at 1 000 mb



The forecast field of the 1000 mb surface, t=96 hours. Isolines are labelled in metres



Wind at 1000 mb, t=96 hours

Figure 11.8

Chapter 12

THE TRADE-WIND INVERSION

Most of the undisturbed tropical oceans have a well-marked lower tropospheric inversion layer within which the temperature increases with height ($\partial T/\partial z > 0$) and the static stability ($\partial\theta/\partial z$) is large. The coastal regions of the west coasts of tropical and subtropical land masses generally have a very marked inversion layer some 1/4 km to 1 km above the ground. This is an important phenomenon simply because it is an integral part of the thermal structure of the tropical atmosphere over most regions outside of the ITCZ, the tropical waves, depressions and hurricanes. Since the structures and variability of the trade inversions are similar over most of the oceans, we shall first review the observational structure of the trade inversion based on some recent studies over the Pacific Ocean. We shall next address the question on the maintenance of the trade inversion based on recent budget studies.

12.1 Observational aspects

(a) Coastal marine inversion

Figure 12.1 shows the vertical thermal structure near the coast of southern California from the studies of Neiburger *et al.*, (1961). Here we note the following features:

- (i) The inversion base is 420 metres above the ground;
- (ii) The specific humidity decreases from 9 g kg⁻¹ at the base of the inversion to 3.9 g kg⁻¹ at the top of the inversion;
- (iii) The top of the inversion is at 1 870 metres; and
- (iv) The temperature increases from 12°C to 20°C across the inversion.

(b) Distribution of parameters along and away from the coast

The distribution of cloud cover as one moves westwards or Equatorwards from the west coast of continents plays an important role in the structure and intensity of the inversion. In general, the distribution of cloudiness changes from (i) fog and low stratus to (ii) stratocumulus (occasional polygonal-shaped cloud patterns) to (iii) undisturbed cumulus, and finally to (iv) the ITCZ, containing both deep and shallow convective clouds. In the southern oceans, especially the eastern Pacific and Atlantic, one only sees the first three categories frequently.

The following climatological maps are of considerable interest and are based on Neiburger *et al.*, (1961):

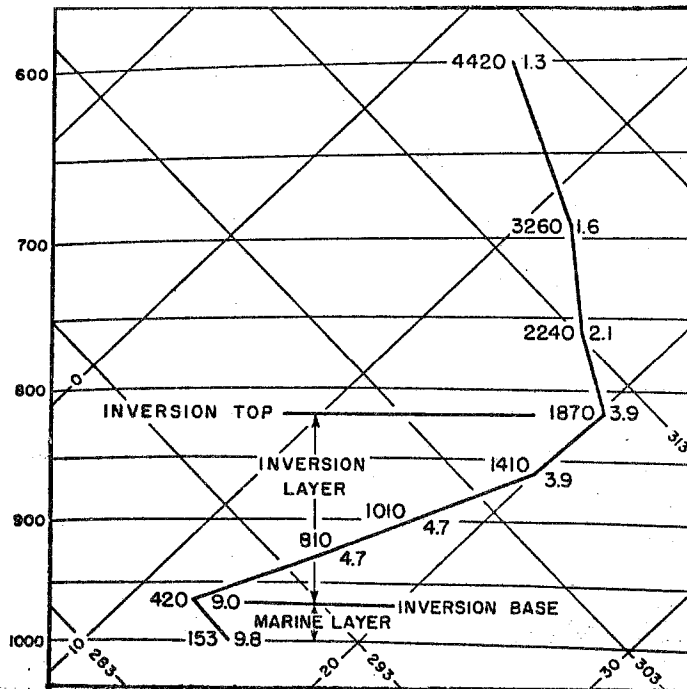


Figure 12.1a - Typical sounding of temperature showing the coastal marine inversion during the summer season (After Neiburger et al., 1961)

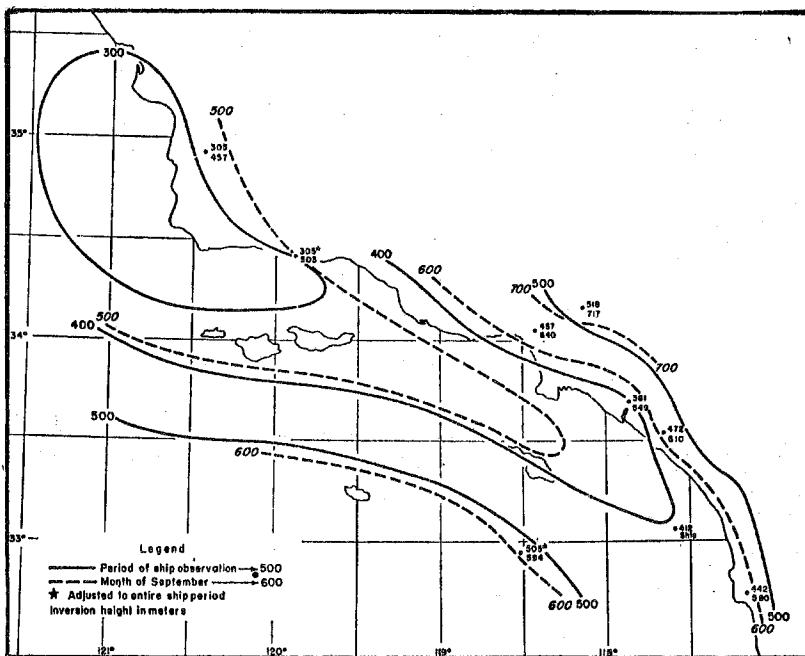


Figure 12.1b - The height of the base of marine coastal inversion in metres. Northern summer (After Neiburger et al., 1961)

- (i) Surface streamline and isotach fields during the summer season (Figure 12.2a);
- (ii) Divergence of the surface resultant wind field during the summer season (Figure 12.2b);
- (iii) The field of sea-surface temperature (Figure 12.2c); and
- (iv) The fields of vertical velocity and divergence above the inversion (Figure 12.2d).

We note in these diagrams that, over most of the regions of the eastern Pacific Ocean where the inversion is found, low-level flows are divergent at the surface level. The magnitude of the divergence is shown in Figure 12.2b. The divergence values are largest along the southern California/Baja California coast. In this region a tongue of low sea-surface temperature, Figure 12.2c, extends southwards. In general, the sea-surface temperature becomes higher both westwards and southwards from the coast. The fields of divergence and vertical velocity at 700 mb (i.e. above the inversion) are shown in Figure 12.2d. Over most of the eastern Pacific Ocean, divergence and downward motion prevail. Near the southern California coast, a field of convergence is seen in the analysis. Over most of these regions where the inversion is found, sinking motion and horizontal mass divergence prevail from 700 mb to sea level. It should be noted that this is based on a limited number of observations. Only some of the gross aspects of the circulations, mentioned here, are perhaps representative.

Next we shall examine the fields of the average heights of the top and base of the inversion. These are illustrated in Figures 12.3a and c. The inversion base rises from roughly 400 metres to 2 000 metres between the California coast and Hawaii, while the top of the inversion rises from roughly 1 000 metres to 2 400 metres. The average temperature at the top and base of the inversion are shown in the right-hand panel charts of Figure 12.3. Near the coast of California, the temperature at the top of the inversion is around 22°C while near Hawaii it is of the order of 14°C . The corresponding temperatures at the base of the inversion are nearly uniform around 10°C . The region of the east central Pacific Ocean along 135°W shows the lowest temperatures at the base of the inversion. This region is cold primarily because of the extensive stratocumulus cloud cover that inhibits warming by solar radiation. The top of the inversion in this same region also exhibits lower temperatures. The cooling is due primarily to the long-wave radiation fluxes from the cloud tops. The distribution of relative humidity at the top of the inversion is illustrated in Figure 12.4a. Here we note that the lowest values around 20% are found near the coastal region. The air is generally very dry everywhere and values near Hawaii are around 40%. The decrease of relative humidity between the base and top of the inversion is shown in Figure 12.4b. This clearly shows that the coastal region is more moist below the inversion than the region farther westwards. Finally, we present a composite west to east cross section, Figure 12.4c, of the temperature field for the summer season based on the studies of Neiburger *et al.*, (1961). It shows the rise of inversion from San Francisco to Honolulu. Similar structures have been found over the Atlantic Ocean. This diagram clearly identifies some of the thermal features we have described above.

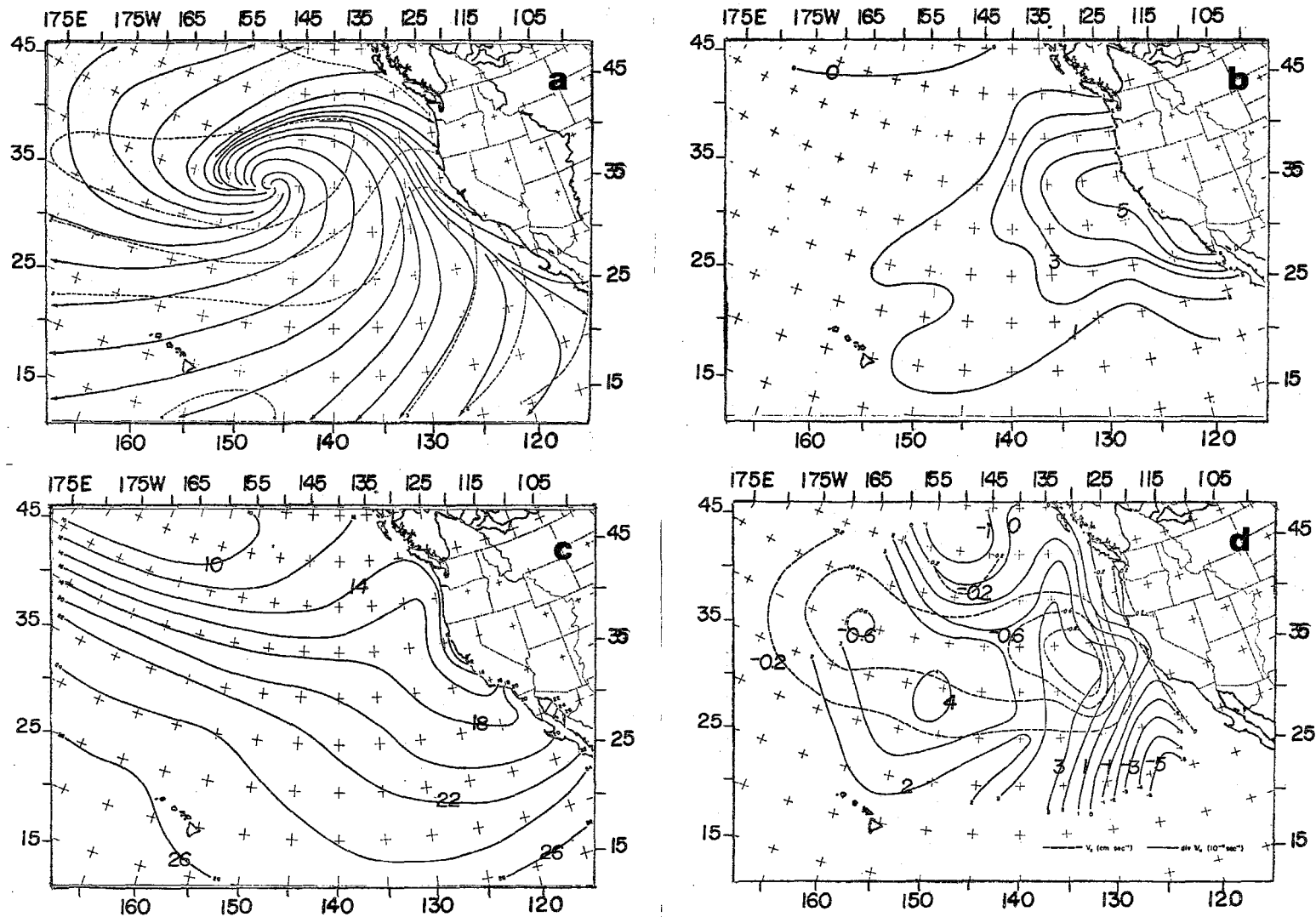


Figure 12.2 - (a) Surface streamlines and isotachs (interval 1 m s⁻¹) during northern summer; (b) divergence of surface wind x10⁻⁶ s⁻¹; (c) normal sea-surface temperature °C, July; (d) mean vertical velocity (dashed line cm s⁻¹) and divergence (solid line 10⁻⁶ s⁻¹) at 700 mb (Based on Neiburger et al., 1961)

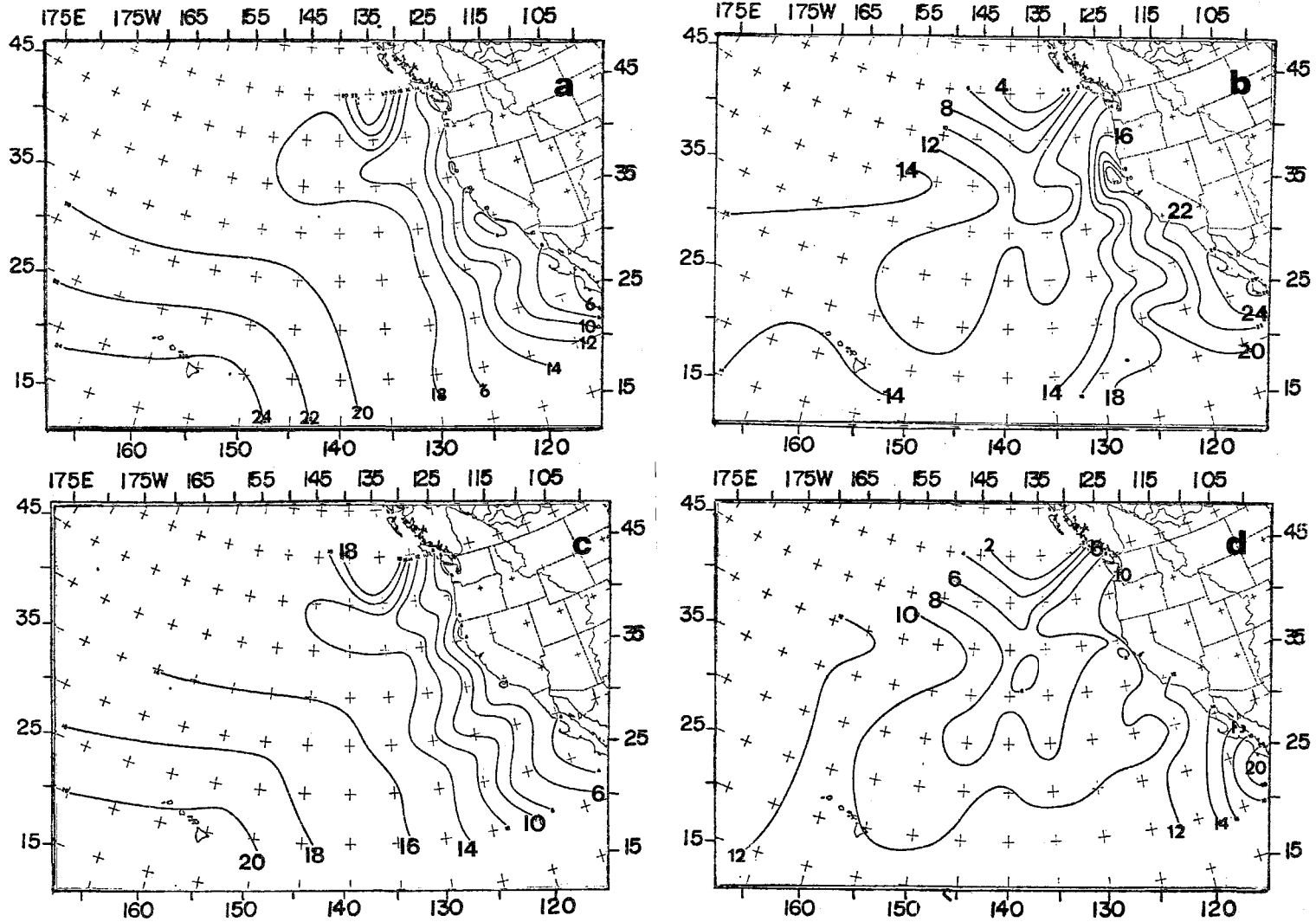


Figure 12.3 - Left panel : Average height (metres) of the top and bottom of the inversion during July; right panel : average temperature (°C) at the top and bottom of the inversion during July (After Neiburger et al., 1961)

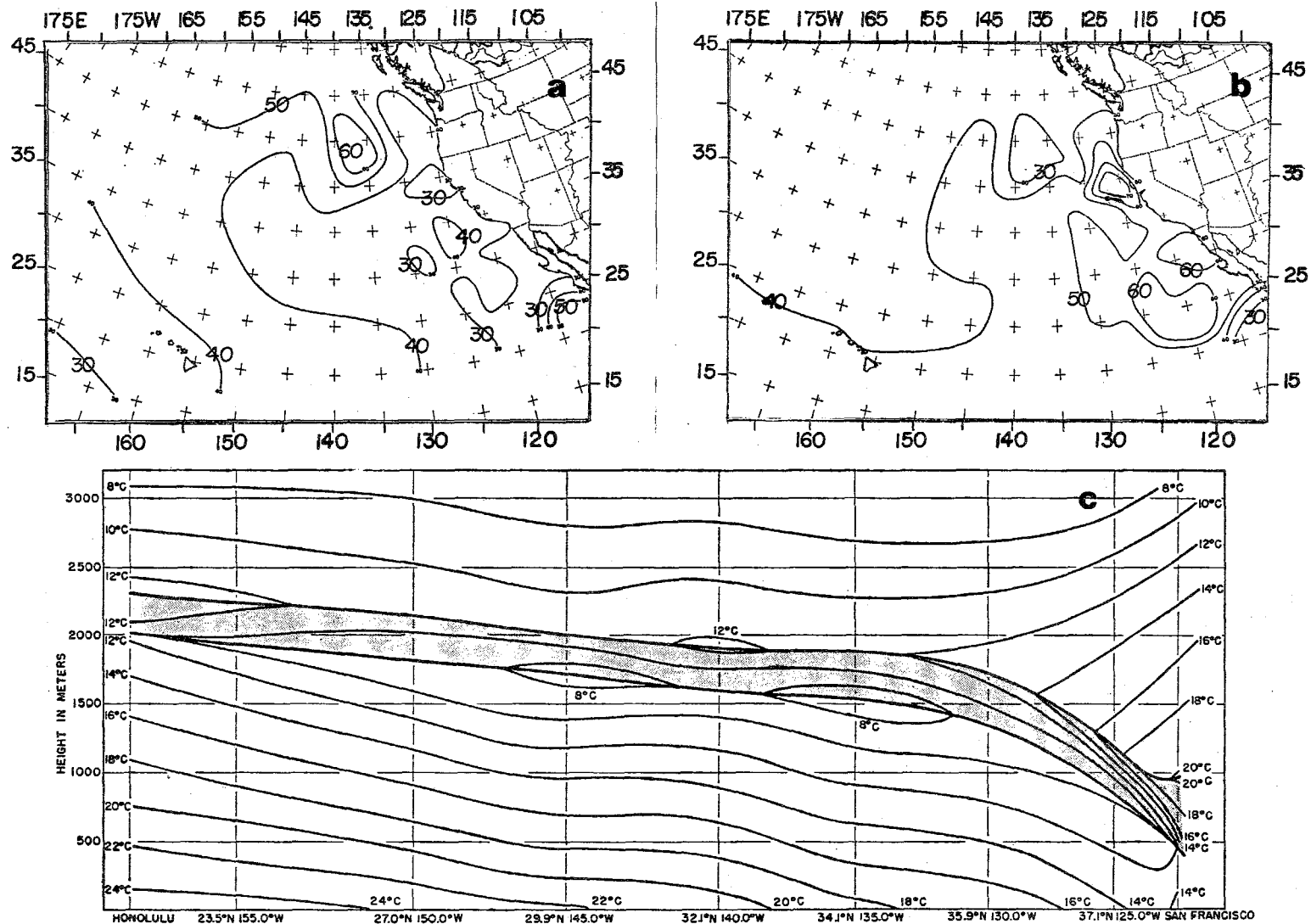


Figure 12.4 — (a) Distribution of relative humidity (per cent) at the top of the inversion during July; (b) decrease of relative humidity (per cent) from bottom to top of inversion; (c) west to east cross-section of temperature illustrating the inversion (Neiburger *et al.*, 1961)

(c) Field experiments

Two major field experiments, AMTEX conducted by Japan and ATEX conducted by West Germany, have added a lot to our present knowledge of the dynamics of the inversion. Many of the results of AMTEX have appeared in the recent issues of the Journal of the Meteorological Society of Japan, e.g. Nitta (1976). Here we shall present some of the observations over the Atlantic based on ATEX (Atlantic Tropical Experiment). This was a triangular array of ships (see Chapter 20) which made observations over the Atlantic trades during the winter of 1969. The period was well marked with a low-level inversion. Figures 12.5a and b respectively show the temperature and moisture soundings for the experiment. The soundings clearly demonstrate the presence of a persistent inversion in the ATEX ship array located around 37°W and 10°N. The moisture (specific humidity in g kg⁻¹) decreases rapidly and shows an interesting discontinuity above the inversion for the ships Discoverer and Planet.

The maintenance of this type of trade-wind inversion is addressed in the next section. There is some seasonal variability in the intensity of the trade inversion: during the winter season its intensity is strong over the trade-wind belt. However, in the coastal region the intensity is larger in the summer season than during winter. The coastal seasonal differences are largely due to lower sea-surface temperature, low stratus, and radiative cooling from the low cloud tops (Lilly, 1965) during the northern summer. The mid-ocean intensity of the trades is largely dictated by the intensity of the downward branch of the Hadley-type circulations which is strong in subtropical latitudes during the northern winter.

12.2 A theoretical framework for studying the trade-wind inversion

The trade-wind inversion is a large-scale phenomenon. Its formation, maintenance and dissolution seem to depend on both small- and large-scale processes. Many times we hear of the term "subsidence inversion". The reason for that simply is that subsidence is usually associated with lower tropospheric horizontal divergence and the latter can create static stability while convergence is known to destroy stability. It is very much easier to study this problem with reference to a framework which describes the change of large-scale dry static stability. This framework will be especially helpful for the interpretation of day-to-day changes in the structure of the stable layer.

We shall start with the first law of thermodynamics in the usual isobaric coordinates:

$$\frac{\partial \theta}{\partial t} = -V \cdot \nabla \theta - \omega \frac{\partial \theta}{\partial p} + \frac{1}{c_p} \left(\frac{p_0}{p} \right)^{R/c_p} \sum_i H_i \quad (12.1)$$

where H_i defines several forms of diabatic heating. We write the above in flux form and apply an averaging ($\bar{\quad}$) over a scale larger than the cumulus scale but smaller than that of the synoptic-scale systems. By this we mean that the averaging is over an

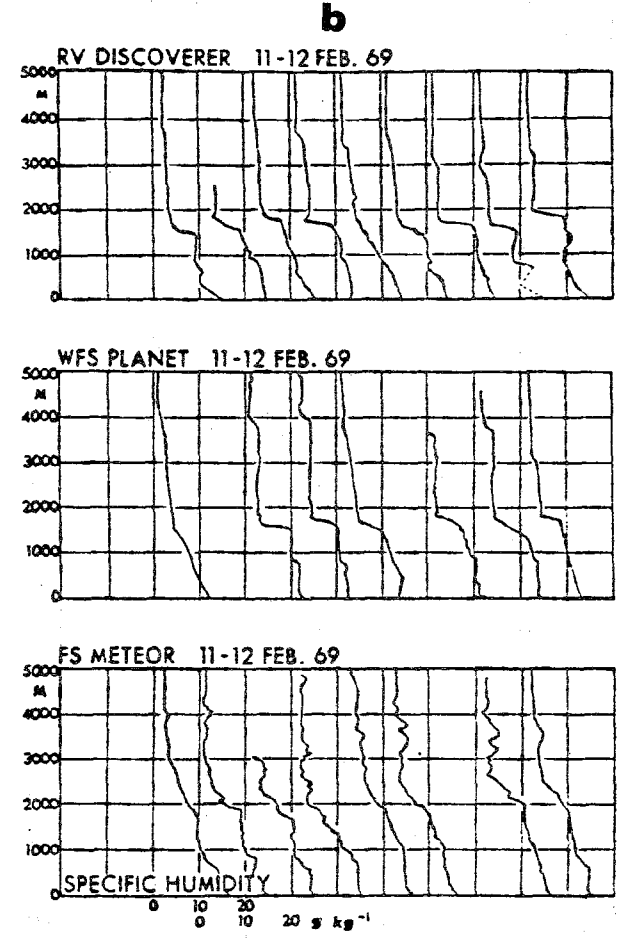
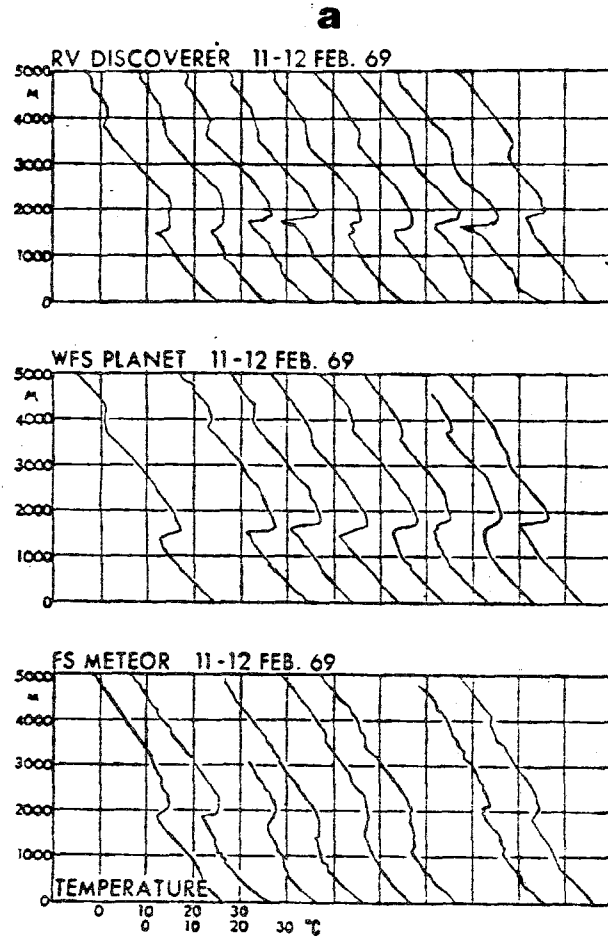


Figure 12.5— (a) Temperature profiles in lowest 5000 m of the ATEX ships in °C. (b) Specific humidity profiles in the lowest 5000 m of the ATEX ships in g kg⁻¹ (After Brummer et al., 1973)

ensemble whose time scale is of the order of a couple of hours and space scale about 100 km. Primes will denote sub-grid scale contributions from the cumulus scale.

$$\frac{\partial \bar{\theta}}{\partial t} = - \nabla \cdot \bar{\mathbf{V}} \bar{\theta} - \frac{\partial}{\partial p} \bar{\omega} \bar{\theta} - \nabla \cdot \bar{\mathbf{V}}' \theta' - \frac{\partial}{\partial p} \bar{\omega}' \theta' + \frac{1}{c_p} \left(\frac{p_0}{p} \right)^{R/c_p} \sum_i \bar{H}_i \quad (12.2)$$

Let $\bar{\Gamma}_d = - \frac{\partial \bar{\theta}}{\partial p}$. Upon differentiation of the above equations with respect to pressure we obtain:

$$\begin{aligned} \frac{\partial \bar{\Gamma}_d}{\partial t} = & - \nabla \cdot \bar{\mathbf{V}} \bar{\Gamma}_d - \frac{\partial}{\partial p} \bar{\omega} \bar{\Gamma}_d + \frac{\partial}{\partial p} \nabla \cdot \bar{\mathbf{V}}' \theta' + \frac{\partial^2}{\partial p^2} \bar{\omega}' \theta' \\ & - \frac{\partial}{\partial p} \left\{ \frac{1}{c_p} \left(\frac{p_0}{p} \right)^k \sum_i H_i \right\} - \bar{\Gamma}_d \frac{\partial \bar{\omega}}{\partial p} \end{aligned} \quad (12.3)$$

Here the left-hand side denotes the local time rate of change of large-scale dry static stability. Note that $\bar{\Gamma}_d$ is almost always positive. The exceptions are regions of superadiabatic lapse rate which are usually either short-term transients or those that form in the layer adjacent to the Earth's surface in the lowest 100 metres due to ground heating. We shall next present a brief discussion of the terms on the right-hand side of the above equation.

- (a) Horizontal advection: $(- \nabla \cdot \bar{\mathbf{V}} \bar{\Gamma}_d)$ is the horizontal advection of large-scale dry static stability by the large-scale horizontal motion field. If large observed changes call for formation or dissolution of the stable layer associated with the trade-wind inversion layer, then this term can only explain the observed changes if such features are already present in other regions and are being advected into the region in question. Horizontal advective processes are by no means negligible and can be very large and important locally. The reason for this is that the other processes are acting over very large areas of tropical oceans and their influence does get advected by strong lower tropospheric winds. Calculations show that for the maintenance of the trade-wind inversion, horizontal inhomogeneities of static stability and their advection cannot be ruled out for the description of day-to-day variations of the trade-wind inversion.
- (b) Vertical advection: $(- \bar{\omega} \frac{\partial \bar{\Gamma}_d}{\partial p})$. This term should not be confused with the so-called "subsidence inversion" effect — the latter is described in the next section. This vertical advection term is usually not very important for the formation, dissolution or maintenance of the inversion. The reason for this is that the magnitude of the large-scale vertical velocity $\bar{\omega}$ is usually very small and it would take several days (in contrast to the middle latitudes) for this effect to materialize.
- (c) Subsidence inversion effect: $(- \frac{\partial \bar{\omega}}{\partial p} \bar{\Gamma}_d)$. If this term alone were influencing the stability of a parcel, we might write:

$$\frac{d \bar{\Gamma}_d}{dt} = - \bar{\Gamma}_d \frac{\partial \bar{\omega}}{\partial p} \quad (12.4)$$

An analogous approximate vorticity equation may be written as:

$$\frac{d\bar{\zeta}_a}{dt} = + \bar{\zeta}_a \frac{\partial \bar{\omega}}{\partial p} \quad (12.5)$$

where $\frac{d}{dt} \equiv \frac{\partial}{\partial t} + \nabla_H \cdot \nabla$ denotes the substantial change following the parcel, moving only in the large-scale flows. The above two equations lead to the usual law of conservation of potential vorticity:

$$\frac{d}{dt} (\bar{\zeta}_a \bar{\Gamma}_d) = 0 \quad (12.6)$$

The guiding rules that emerge from the above equations are that, if parcels go through a region of horizontal divergence, they encounter (i) an increase of stability $\bar{\Gamma}_d$ and/or (ii) a decrease of absolute vorticity $\bar{\zeta}_a$. The converse is the case for the situation where parcels move through regions of horizontal convergence. The case of subsidence and lower-tropospheric divergence is the basic ingredient in the problem of formation and maintenance of trade-wind inversions. Since descending parcels encounter a field of horizontal divergence all the way to the ocean surface over the eastern tropical oceans, this effect alone will tend to produce the inversion at the ocean surface. However, the occurrence of the inversion base above the ocean surface is not explained by this term alone. Without a general large-scale descending motion it is not possible to produce the stable layer that is present over an area covering most of the tropical oceans. The maintenance of this stable layer at a level 1 km or so above the ocean is achieved primarily by other mechanisms. In order to explain the occurrence of the stable layer some distance above the ocean surface, one needs to look for destabilizing influences below the inversion layer that counteract the production of stability by large-scale horizontal divergence. We shall next illustrate some of these processes.

(d) Radiative cooling: This may be expressed mathematically as:

$$- \frac{\partial}{\partial p} \left\{ \frac{1}{c_p} \left(\frac{p_0}{p} \right)^{R/c_p} H_R \right\} .$$

Here H_R is the net radiative flux. Shallow convective cloud cover (stratocumulus) and a moist subcloud layer together usually give rise to large values of cooling near the base of the trade-wind inversion. The cooling near the ground in these situations is usually smaller by comparison. This strong cooling results in

- (i) $\frac{\partial H_R}{\partial p} > 0$ below the inversion, and
- (ii) $\frac{\partial H_R}{\partial p} < 0$ just above the inversion.

Such a vertical distribution of radiative cooling results in a stabilization above the inversion base and destabilization below. Although the exact figures for the vertical distribution of these long-wave cooling

rates seem to vary from case to case, there is reason to believe that this effect in the presence of stratocumulus cloud is extremely large and important. One should not lose sight of the fact that these processes are not inherently linear. For example, if one were studying the process of the formation of an inversion without there being one present in the initial state, the radiative effects may in fact evolve and grow as the inversion grows. The role of this important effect in the maintenance of the inversion can only be explored by detailed diagnostic studies.

(e) The sensible heat flux from the ocean:

The rate of cooling is:
$$- \frac{1}{c_p} \frac{\partial}{\partial p} \left\{ \left(\frac{p_0}{p} \right)^{R/c_p} H_s \right\}$$

where H_s is the upwards sensible heat flux. Since the heat is taken up from below, this term will in general have a destabilizing effect on the subcloud layer. The Bowen ratio over most of the tropics is small (≈ 0.1). Hence, this effect is not a dominant one on time-scales of a few days. The evaporative flux (latent heat) from the oceans is of course substantial over the tropics. However, the flux of latent heat from the ocean does not have a direct effect on the stability. It is only when this moisture condenses in the free atmosphere or re-evaporates thereafter that it has an influence on the dry static stability. Evaporation from the sea provides moisture to the subcloud layer. This moist layer is capped by a very dry layer above the inversion. Both radiative effects and the evaporation of cloud matter play a significant role in maintaining the trade inversion. For both of these effects, evaporation from the sea has an important indirect role.

(f) Evaporation of cloud matter: The region of the trade wind inversion over the oceans is usually covered with a myriad of shallow cloud elements. These small clouds are known to detrain liquid water which in turn evaporates and maintains a certain degree of cooling near the base of the inversion. These shallow clouds are usually non-precipitating elements. Because of the preponderance of shallow clouds, an understanding of the trade wind inversion cannot be complete without consideration of the conservation laws for water vapour and liquid water. In general, budget studies that invoke these effects find that this invariably requires much empiricism because of the need to parameterize cloud micro-physical processes.

12.3 The calculation of the heat and moisture budgets for the inversion

A number of important recent studies by Holland and Rasmussen (1973), Augstein et al., (1973), Nitta (1975), Betts (1973), and Ogura (1975, 1977) address this problem. Here we shall present a brief review of one such method based on a recent study of Oodally et al., (1977). We begin with the static stability equation in the form:

$$\frac{\partial^2}{\partial p^2} \overline{\omega' \theta'} = \frac{\partial \overline{\Gamma_d}}{\partial t} + \nabla \cdot \overline{\mathbf{V} \Gamma_d} + \frac{\partial}{\partial p} \overline{\omega \Gamma_d} + \overline{\Gamma_d} \frac{\partial \overline{\omega}}{\partial p} + \frac{\partial}{\partial p} \left\{ \frac{1}{c_p} \left(\frac{p_0}{p} \right)^{R/c_p} H_i \right\} \quad (12.7)$$

Here the large-scale variables are assumed to be known. Thus one can in principle evaluate the first four terms on the right-hand side of the above equation. $\sum_i H_i$ denotes the different types of heating that need to be parameterized. The moisture budget is considered in the same manner using an equation for the large-scale specific humidity (\bar{q}):

$$\frac{\partial}{\partial p} \overline{\omega'q'} = - \frac{\partial \bar{q}}{\partial t} - \nabla \cdot \overline{\nabla q} - \frac{\partial}{\partial p} \bar{\omega} \bar{q} + \bar{e} - \bar{c} \quad (12.8)$$

where \bar{e} and \bar{c} are respectively the evaporation and condensation per unit mass of air. Here \bar{e} and \bar{c} need to be defined.

- (a) Calculation of large-scale variables. Yanai et al. (1973), Reed and Recker (1971), and Reed et al. (1977) compute the large-scale terms using observations from an array of ships or weather stations. One of the harder problems is the estimation of $\bar{\omega}$, the field of large-scale vertical velocity. This is usually done using the so-called kinematic method. We have described a general method in the Appendix to these notes. It is most important that one adjust the divergence distribution in the vertical such that its vertical integral over the depth of the atmosphere vanishes. The calculations of divergence and curl of a vector integrated over the area of an array of ships or island stations are usually carried out using line integral methods, i.e. using relations of the type:

$$\overline{\nabla \cdot \nabla} = \frac{1}{A} \left[\oint u \, dy - \oint v \, dx \right] \quad (12.9)$$

$$\overline{\nabla \cdot \nabla Q} = \frac{1}{A} \left[\oint uQ \, dy - \oint vQ \, dx \right] \quad (12.10)$$

$$|\kappa \cdot \overline{\nabla \times \nabla Q}| = \frac{1}{A} \left[\oint uQ \, dx + \oint vQ \, dy \right] \quad (12.11)$$

$$\bar{\omega} = \int_{p_0}^P \overline{\nabla \cdot \nabla} \, dp \quad (12.12)$$

where Q is any scalar property,
 $|\kappa|$ is a unit vector in the vertical,
 u, v are velocity components, and
 A is the area of a domain bounded by ships or islands.

The line integral is taken cyclonically around the area A . The fields of mean dry static stability and of horizontal divergence and vertical velocity for the ATEX inversion region are shown in Figures 12.6a and 12.6e.

- (b) The detrainment of liquid water. The life-time of shallow cumulus clouds is very short, being of the order of 5 to 10 minutes on the average. Since a large population of shallow clouds is always present in the trade-wind belt, it is safe to state that some clouds are forming and others are

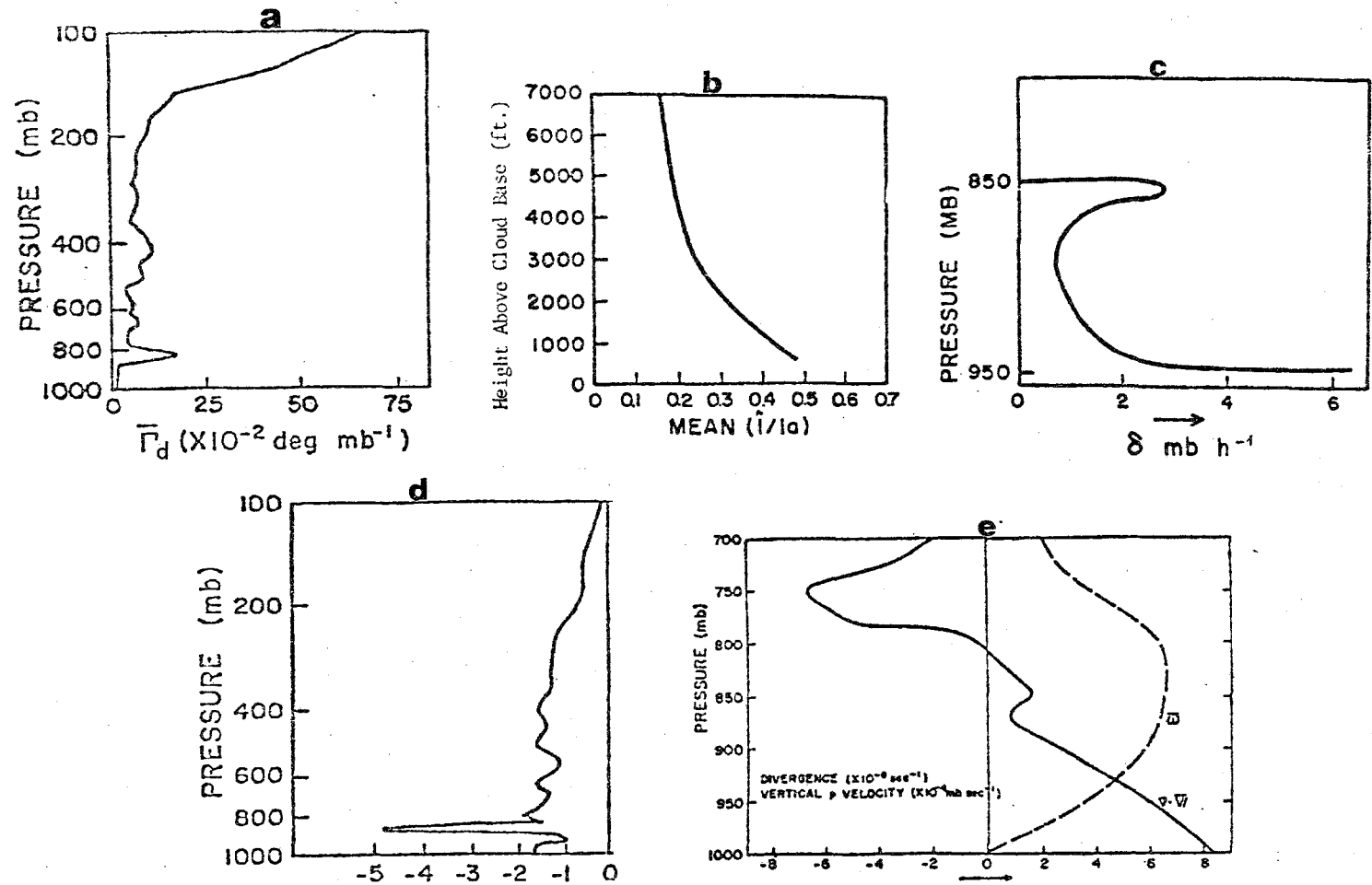


Figure 12.6 — (a) Large-scale dry static stability $\bar{\Gamma}_d$; (b) Warner's profile for estimating liquid water content of cloud; (c) detrainment profile adapted from Nitta (1975); (d) computed radiative cooling profile (Oodally *et al.*, 1977); (e) large scale divergence $\nabla_p \cdot \mathbf{V}$ and vertical p-velocity (Oodally *et al.*, 1977)

dying at any one time. If the water vapour condenses to form clouds and later the same liquid water detrains into the environment and evaporates at the same vertical level, then statistically we could state that there would be no net heating or cooling since the two processes would cancel each other. However, observational studies and budget estimates lead one to conclude that shallow clouds detrain liquid water near their top level, i.e. near the base of the inversion, while the rate of condensation is larger near the cloud base. The vertical difference of heating (condensation heating and re-evaporative cooling) is an important thermodynamical process, in many meteorological problems. The formula we present here is semi-empirical and by no means unique.

We are dealing with non-precipitating clouds. This means no rain falls out of the cloud and reaches the ground. Ships in the undisturbed trades do not usually note even a 'trace' of rainfall.

According to Rodgers (1967), we define a quantity l_a called the adiabatic liquid water content by the relation:

$$d l_a = - d \omega_s / (1 + \omega_s)$$

We examine the saturation mixing ratio W_s between the top and base of the cloud. Since at the cloud base we can take $l_a = 0$, we can write:

$$l_a \approx \frac{W_s \text{ (CLOUD BASE)} - W_s \text{ (CLOUD TOP)}}{1 + \{W_s \text{ (CLOUD BASE)} + W_s \text{ (CLOUD TOP)}\} / 2} \quad (12.13)$$

We next convert l_a into a measure of the liquid water content ' l ' by using results from field experiments. One such promising study was carried out by Warner (1955). Figure 12.6b shows Warner's graph (based on experimental data) where l/l_a is plotted against cloud depth. The depth of the cloud in question has to be known. If one assumes from observational knowledge of the phenomenon under study that the depth of the clouds are known, l_a is estimated from equation 12.13 and l is then determined from empirical graphs such as those of Warner.

The evaporation of liquid water is generally expressed by a relation of the type $\bar{e} = \delta l$, where δ is a detrainment parameter. Some of the more sophisticated budget studies, such as those discussed in Chapter 6, determine the vertical distribution of δ for an ensemble of clouds. Here we shall borrow one such profile from Nitta (1975) which is valid for an ensemble of shallow trade-wind clouds in an undisturbed environment. Figure 12.6c shows this profile. Now we have the necessary information to compute the evaporation rate by detrainment of liquid water. The corresponding cooling of the atmosphere at the cloud top level is given by:

$$H_e = - L \bar{e}$$

- (c) Condensation rate and associated heating. The condensation rate requires a knowledge of the upward mass flux in the clouds. Since the specific humidity decreases rapidly with height, the condensation rate is larger near the cloud base than near the cloud top. In Chapter 6 we discussed in detail the budget approach for this problem. Here again we shall use one such profile based on Nitta (1975) for the vertical distribution of condensation rate \bar{c} for an ensemble of shallow clouds in the undisturbed trade-wind environment. This is illustrated at the cloud base. The release of latent heat by condensation is next expressed by the relation:

$$H_c = + L\bar{c} \quad (12.14)$$

- (d) Calculation of the radiative heating/cooling rates. We shall not describe the methods for calculation of the radiative cooling (or heating) rates here. Suffice it to state that the methods described in Chapter 4 can be used to calculate the vertical profile of the rate of radiative warming provided that we are given:

- (i) vertical distributions of temperature and water vapour,
- (ii) the distribution of cloud layers, and
- (iii) the surface pressure.

Using a vertical resolution of 25 mb, the net upward and downward fluxes of radiation were calculated by Oodally *et al.*, (1977). Their profile of radiative cooling is consistent with a shallow cloud layer between 950 and 850 mb. Their profile is shown in Figure 12.6d. In many such studies one generally assumes a standard vertical distribution of radiative cooling. This can be, at times, inconsistent with the locations of the cloud layers. The largest cooling found by Oodally *et al.*, (1977) was at the top of the cloud and is of the order of 5°C d^{-1} . This has a very definite effect on the destabilizing below and stabilization above this level.

- (e) Air/sea interaction. The flux of sensible heat enters equation 12.7 while that of water vapour enters equation 12.8. In Chapter 5 we have reviewed the so-called bulk aerodynamic formulae for estimating the fluxes of sensible and latent heat from the ocean. These are most frequently used in tropical meteorology. We shall not repeat these formulae here. It suffices to state that given the surface wind speed, the temperature of the water as well as that of the air at the anemometer level and its dew point, one can estimate these fluxes at the lower boundary.

- (f) The calculation procedures for determining the static stability and the moisture budget. We now go back to equations 12.7 and 12.8. The unknowns of the problem were $\sum H_i$, \bar{e} and \bar{c} . The forms of heating that are generally consideredⁱ for the trade inversion problem are:

$$H_i = H_s + H_c + H_e + H_R \quad (12.15)$$

where H_s is the sensible heat flux from the ocean, H_c is the rate of

condensation heating, H_e the evaporative heating and H_R is the radiative heating per unit mass of air. We have shown how one can in principle make estimates of each of these forms of heating.

We have also shown in the previous section how \bar{e} and \bar{c} were estimated by Oodally *et al.*, (1977). Other studies such as those by Nitta (1976), Soong and Ogura (1976) and many others have provided useful formulations for these parameters.

Equations 12.7 and 12.8 are coupled through the condensation and evaporation processes. The question is: What are the vertical distributions of the eddy heat and moisture fluxes that are consistent with a complete specification of the remaining terms? The equations 12.7 and 12.8 are now written in the form:

$$\frac{\partial^2 \overline{\omega' \theta'}}{\partial p^2} = F(p) \quad (12.16)$$

$$\frac{\partial^2 \overline{\omega' q'}}{\partial p^2} = h(p) \quad (12.17)$$

These are treated as two independent ordinary differential equations for the unknowns $\overline{\omega' \theta'}$ and $\overline{\omega' q'}$. As boundary conditions one assumes $\overline{\omega' \theta'}$ and $\overline{\omega' q'}$ to vanish at the top of the atmosphere. At the ocean surface (or $p = p_s$ surface) one assumes that $\overline{\omega' \theta'}$ and $\overline{\omega' q'}$ are known and specified to be consistent with the air/sea transfers of sensible heat and water vapour respectively. This problem can be solved numerically by either standard relaxation or matrix inversion procedures. Knowing these fluxes one can then address the question of the maintenance of the trade-wind inversion.

12.4 On the maintenance of the trade-wind inversion

Here we use the above framework to examine the results for the budgets of dry static stability and moisture. We divide the atmosphere into four layers and examine the results in each layer separately.

- (a) Dry static stability. Figures 12.7a, b, c and d respectively illustrate the budgets for the subcloud layer, cloud layer, the inversion layer and above the inversion layer. In the subcloud layer, Figure 12.7a, we note that the destabilizing of static stability by turbulent flux of heat is balanced by the stabilization due to (i) differential condensation heating, (ii) convergence of flux of dry static energy by large scale downward vertical motion, (iii) subsidence effect, i.e. production of stability by horizontal divergence, and (iv) differential radiative cooling (i.e. more cooling near the ground and less near the cloud base).

In the cloud layer (Figure 12.7b) the destabilization primarily arises from (i) the radiative effects (more cooling around the cloud top) and (ii) the convergence of flux of heat by subgrid scale eddies. This is

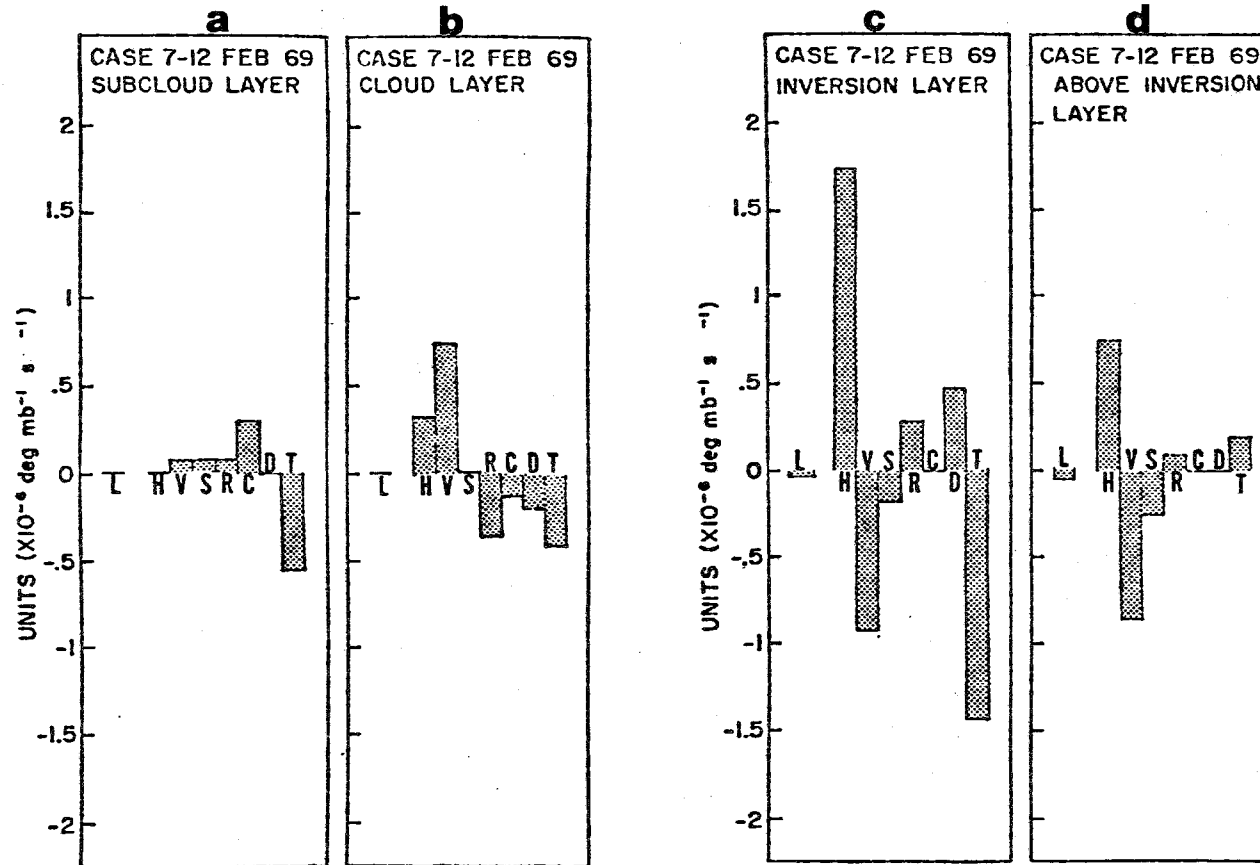


Figure 12.7 — Contributions of various terms of dry static stability equation to stabilizing and destabilizing in the (a) subcloud layer, (b) cloud layer, (c) inversion layer, (d) above the inversion layer (ATEX, 1969). L = local change, H = lateral convergence, V = vertical convergence, S = production by divergence, R = radiative effect, C = condensation, D = detrainment, T = vertical eddy flux

counteracted by a stabilization due to (i) large-scale horizontal advective processes and (ii) convergence of flux of static stability by large-scale vertical motion.

In the inversion layer (Figure 12.7c), we note that the destabilizing occurs due to (i) the turbulent flux of heat by subgrid scale eddies and (ii) the vertical divergence of flux of static stability by large-scale downward vertical velocity. This is counteracted by (i) large-scale horizontal convergence of flux of dry static stability (by the large-scale horizontal motion field), (ii) radiative effects, i.e. more cooling at the bottom of the inversion layer near the cloud top, and (iii) differential detrainment, i.e. more cooling near the cloud top which would be at the bottom of this layer.

In the layer above the inversion, the dominant balance is among the large-scale terms. Destabilizing occurs via (i) the large-scale convergence of flux of static energy from the descending motions and (ii) the destruction of large-scale dry static stability from the large-scale convergence field (since the largest downward motion occurs near the top of the inversion layer). This is counteracted by the stabilizing effects due to the convergence of flux of stability by the large-scale horizontal motion field; the results are illustrated in Figure 12.7d.

- (b) Moisture budget. In the subcloud layer, Figure 12.8a, convergence of flux of moisture $-\frac{\sigma}{\partial p} \overline{\omega q}$ results from large-scale descending motions at the top of this layer (note $\overline{\omega} = 0$ at the ground); this contributes to a moistening of the layer; the drying occurs due to the divergence of (large-scale) flux of moisture and the divergence of eddy flux (by subgrid scale eddies) in the vertical direction. This is an interesting result. However, it raises an important question: What is the role of the evaporation from the ocean in maintaining the moisture budget of the subcloud layer? The position of the ATEX triangle of ships has a considerable influence on the results obtained here. In this location, the evaporation from the ocean plus the supply of moisture by large-scale descending motion at the bottom of the cloud layer are both required to keep the subcloud layer moist. The former (evaporation from the sea) is not as large in this region as it is in other regions of the trades where the surface-wind speed is great (see Chapter 2). The results obtained here are consistent with the findings of Emmitt (1977).

In the cloud layer, Figure 12.8b, the downward flux of moisture by large-scale descending motion as well as the detrainment of the cloud liquid water contribute to moistening. This is counteracted by (i) divergence of flux of moisture by subgrid scale eddies, by (ii) condensation and by (iii) divergence of horizontal flux of moisture by the large-scale wind field. All of these aforementioned three processes contribute to drying of the cloud layer. In the inversion layer a sharp decrease (with height) of the moisture (specific humidity) occurs. Figure 12.8c: the large-scale downward mean motion causes drying of this region. This is offset primarily by moistening due to convergence of vertical eddy flux of

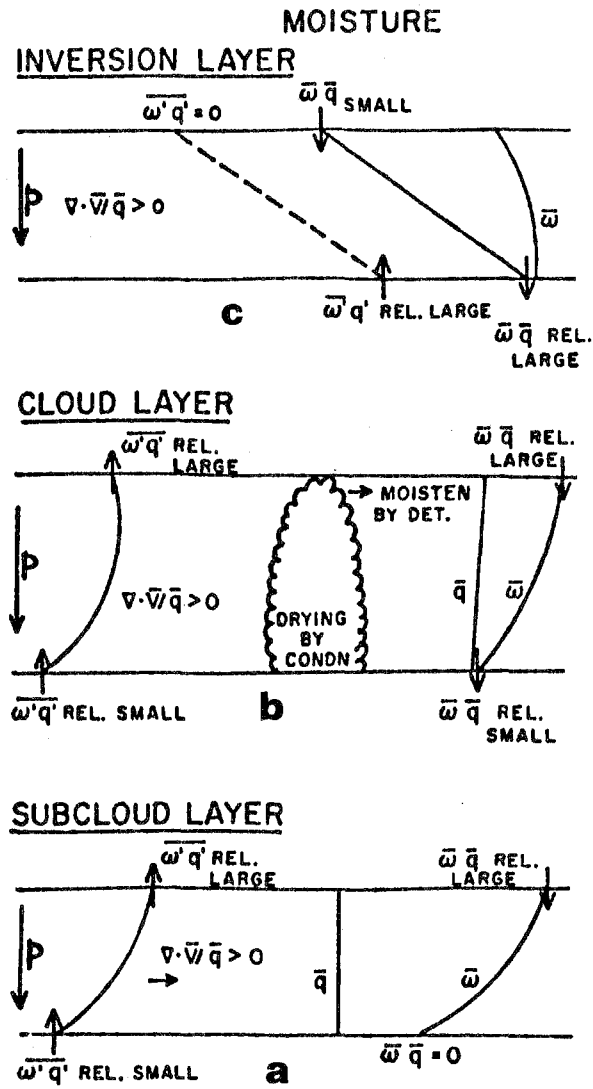


Figure 12.8 - Contributions of various terms of the moisture budget towards moistening or drying in the (a) subcloud layer, (b) cloud layer, and (c) the inversion layer

moisture (overshooting of cumulus clouds into the inversion layer). Thus the moisture balance of the inversion layer is roughly expressed by:

$$-\frac{\partial}{\partial p} (\bar{\omega} \bar{q}) - \frac{\partial}{\partial p} (\bar{\omega}' \bar{q}') = 0 \quad (12.18)$$

The region above the inversion is not particularly interesting from the point of view of moisture balance; here the essential balance is among the large-scale terms, i.e.:

$$\frac{\partial \bar{q}}{\partial t} = 0 \approx -\nabla \cdot \bar{q} \bar{V} - \frac{\partial}{\partial p} \bar{\omega} \bar{q} \quad (12.19)$$

It is important to note that the analysis presented in this chapter refers to a region during northern winter near 10°N and 40°W. This is not to be taken as representative for all of the regions in the trade-wind belt. The region of strong surface winds of the trade-wind belt has larger surface fluxes; the marine inversion is usually capped by low stratiform clouds and the role of radiation is also more important here. Thus the maintenance of the trade-wind inversion must not be expected to possess a simple explanation.

12.5 Summary

Inversion dynamics is a central part of tropical meteorology. Observational field programmes such as ATEX, AMTEX, BOMEX and GATE (see Chapter 20) provide some useful data sets for further detailed studies of this problem. There is need for further investigation in the following areas:

- (i) Structure and maintenance over different parts of the tropics (i.e. near the coast, away from the coast);
 - (ii) Detailed studies of the subcloud layer including its interaction with the cloud layer;
 - (iii) Recasting of the budget equations in a prognostic framework where the large-scale terms as well as their tendencies are treated as unknowns. Such a treatment of shallow convection and the inversion is essential for weather prediction studies; and
 - (iv) Diurnal changes.
-

Chapter 13

WEATHER SYSTEMS OVER ASIA

13.1 Introduction

The single most conspicuous weather system is the annual cycle of monsoons over Asia. This phenomenon has global as well as regional manifestations. A number of important publications exist on this topic:

- (i) Monsoon Meteorology, Ramage, 1971
- (ii) Monsoons of the World, India Meteorological Department, 1958
- (iii) Southwest Monsoons, Rao, 1976
- (iv) Meteorological results of the International Indian Ocean Expedition, WMO, Unesco, 1965
- (v) Proceedings of the Symposium on Tropical Meteorology, AMS, 1970
- (vi) Monsoon Meteorology, edited by Krishnamurti, 1977
- (vii) Monsoon Dynamics, edited by Lighthill and Pearce, Cambridge University Press, 1980.

This field has attracted a considerable interest in recent years. The variability of monsoon rainfall is the central problem because of its association with droughts and floods. Figure 13.1 following Khromov and Ramage identifies the Asian regions that experience a surface-wind direction reversal. During northern summer months the surface winds are south-westerly and during the northern winter months they tend to be more northerly or northeasterly. The primary driving force for the annual cycle of monsoons is the differential heating between land and ocean. The monsoon winds (as stated in Chapter 2) show a zonal asymmetry in many of their properties.

Much of our deeper understanding of the mechanisms of the monsoons has emerged from the interpretations of the results of general circulation model experiments. This approach to monsoonal evolution, dynamics, climatology and variability has been explored in a series of papers by a number of groups that have carried out long-term simulation experiments. A brief review of the major results obtained is presented in this chapter. Here we shall attempt to define the planetary scale monsoons, distinguish between the winter and summer monsoons of the northern hemisphere, discuss the air/sea interaction problem, describe the land/ocean contrast in heating which provides a framework for the broad-scale monsoons; finally, we shall briefly discuss some salient monsoon disturbances.

13.2 Planetary-scale monsoons

There exists a planetary-scale component of the monsoon which is best defined by the large amplitude quasi-stationary long waves of the tropical circulation. It is described by the first few zonal harmonics of the tropical stream function field in the latitude belt 10°N to 30°N . Observations during the northern summer show that

DOMAIN OF MONSOONS, REVERSAL OF SURFACE-WIND DIRECTIONS

-----> NORTHERN SUMMER MONSOONS
←----- NORTHERN WINTER MONSOONS

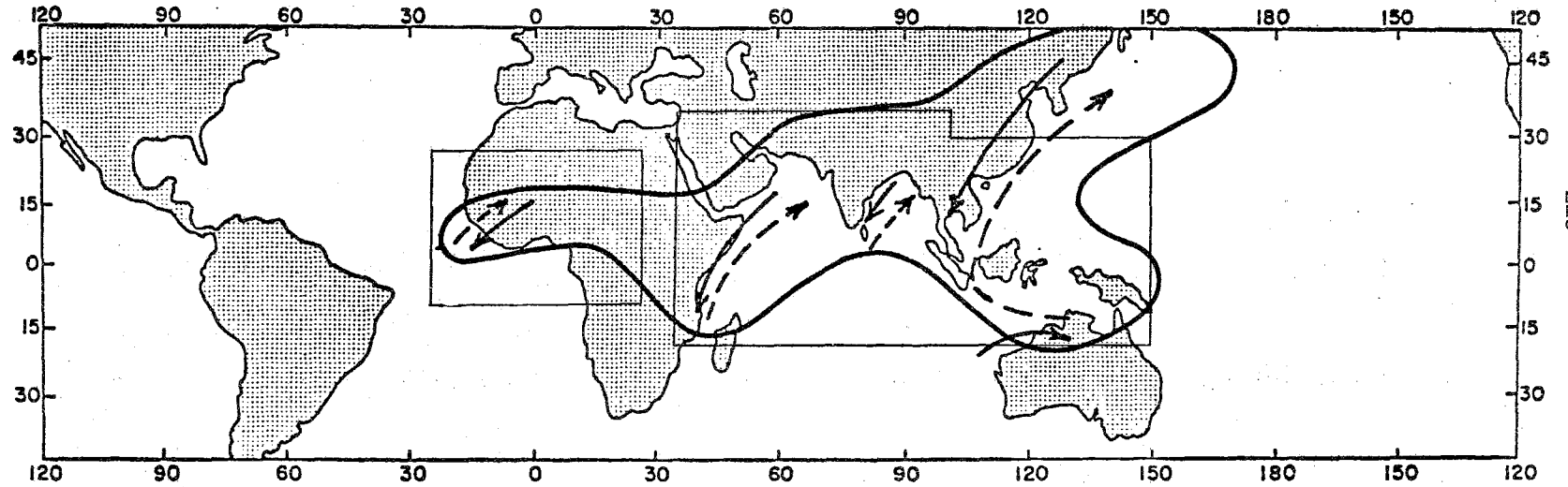


Figure 13.1

roughly 50% of the variance on these scales is carried by the quasistationary components. The pressure fields in the lower and upper troposphere appear to be nearly out of phase with respect to each other. The principal components that contribute to the planetary-scale monsoons are shown in Table 13.1. The climatological features shown here essentially describe the zonally asymmetric planetary-scale monsoons.

The amplitude of the above features of the planetary-scale monsoons is observed to increase around 20°N with the establishment of monsoon rainfall. Abbott (1977) has shown that this quasistationary system is driven by a zonal heating differential between land and ocean. An understanding of the planetary-scale monsoons requires a detailed knowledge of the heat sources and sinks.

The winter monsoons also possess both planetary- and regional-scale characteristics. The zonal asymmetry of the northern winter season's planetary-scale monsoon is largest in the upper troposphere over the subtropical latitudes, where the subtropical jet stream is found. In equatorial latitudes the most active region is located around the rainfall belts of the East China Sea, Malaysia and Indonesia. In Chapter 17 some of the prominent features of these zonally-asymmetric aspects are described.

13.3 Corresponding elements of winter and summer monsoon systems

The common elements in both the large-scale winter and summer monsoonal gyres include low-level flows from a large high-pressure area (1) to a monsoon trough (2). The flows accelerate occasionally between 1 and 2 and a low level wind maximum (3) (a jet or a surge) is frequently noted. Large areas of cloudiness and ascent (4) are a characteristic of the monsoon trough. The general rising air diverges out of an upper anticyclone (5) along an upper-level jet stream (6). These six major elements of the monsoon thus comprise a complex local Hadley-type vertical circulation. These are illustrated schematically in Figure 13.2. Here we shall tentatively equate the roles of:

- (1) The Siberian high of winter with that of the Mascarene high of northern summer;
- (2) The monsoon trough over northern India during summer with that of the trough over Indonesia during northern winter;
- (3) The cross-equatorial low-level jet over East Africa during northern summer with the lower tropospheric surges in the winter monsoons;
- (4) The northern summer monsoon rainfall and cloud cover over northern India with its counterpart near southern Malaysia and Indonesia during northern winter;
- (5) In the upper troposphere, the Tibetan high of northern summer with the western Pacific high of the northern winter;
- (6) The monsoonal tropical easterly jet stream of northern summer with the subtropical jet stream of winter.

These features describe broad-scale monsoon systems. A major difference between the two systems is in the geometry of the underlying surface: in the summer monsoons the general ascent and rainfall occur over warm land areas while the descent occurs over

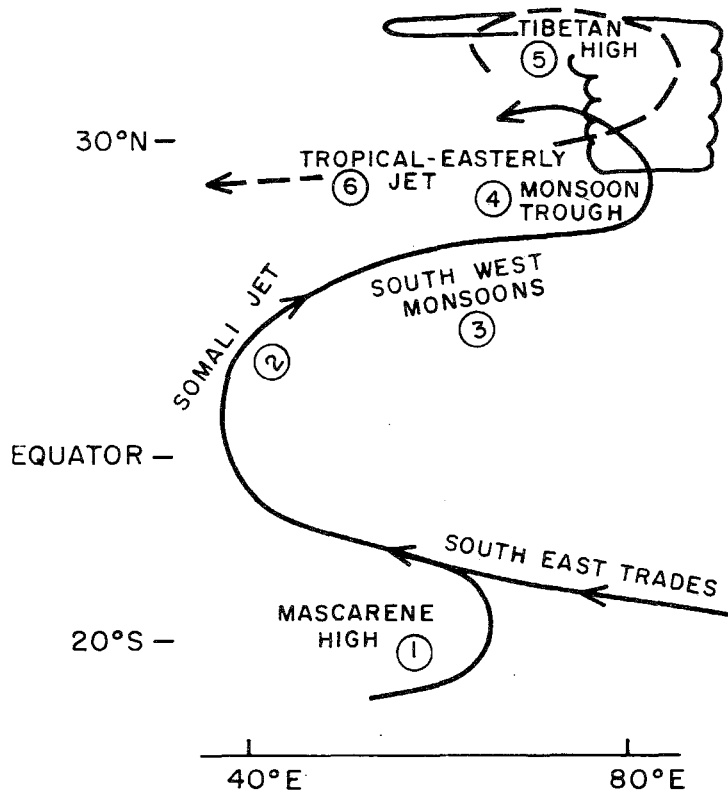
Table 13.1

Quasi-stationary planetary-scale monsoons between 10°N and 30°N

Parameter	Asia	Regional Features	
		Atlantic and Pacific Oceans	Central America
1. Pressure lower troposphere	Monsoon trough	Subtropical high	Mexican heat low
2. Pressure upper troposphere	Tibetan high	Mid-ocean trough	Mexican high
3. Tropospheric thermal field	warm	cold	warm
4. Tropospheric moisture field	moist	dry	moist
5. Large-scale vertical velocity	UP	DOWN	UP
6. Divergent circulation in the upper troposphere	outflow	inflow	outflow
7. Heating of the troposphere	net heating	net cooling	net heating to the south of the Mexican high
8. Cloudiness	cloud covered	relatively cloud free	cloudy southwest of the Mexican high
9. Mean winds at 200 mb	easterly	westerly	weak
10. Mean surface winds	south-westerly	northeasterly	northwesterly

SUMMER MONSOONS

LOWER TROPOSPHERE
UPPER TROPOSPHERE



WINTER MONSOONS

SOLID LINES
DASHED LINES

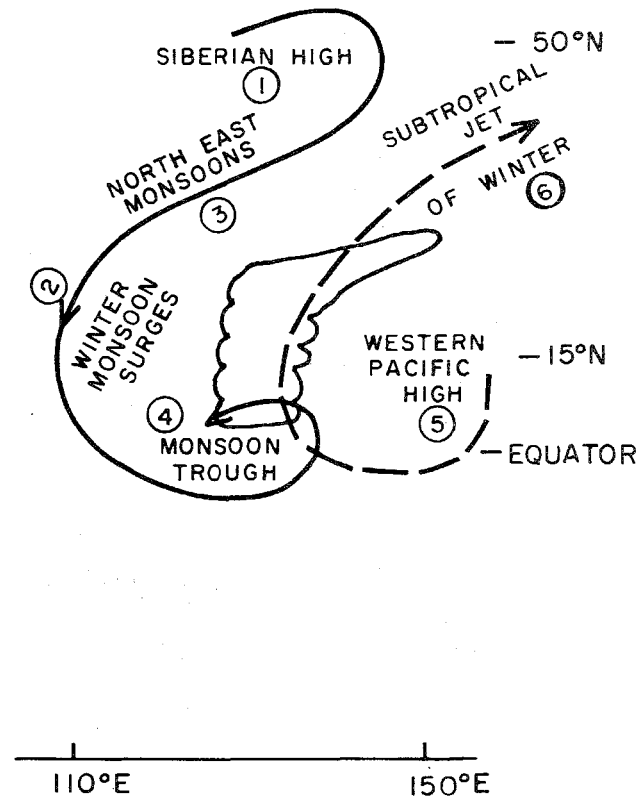


Figure 13.2 - A schematic distinction, summer and winter monsoons

the southern oceans. During the winter monsoons the general ascent and rainfall occur over a marine environment (the Maritime Continent according to Ramage, 1971) while the descent occurs over the land areas over eastern Asia and all the way to Siberia. It thus seems that a crucial element in the driving mechanism for the summer monsoons is the shortwave radiative warming over the land areas; while it is the longwave cooling over the land areas that seems to be more important for the winter monsoon.

The importance of the thermal differential that drives the monsoons was best illustrated in an interesting study by Murakami et al., (1970) which is described in the next section.

13.4 A simple theoretical framework for the monsoons

One of the simplest theoretical frameworks for the monsoon problem was presented by Murakami et al., (1970). Here the emphasis is on the differential heating between land and ocean. They integrated a set of zonally symmetric primitive equations using the Earth's surface as a coordinate surface. The Earth's surface was separated at 10°N between ocean to its south and land to the north. Smoothed mountains were included north of 25°N . The momentum, mass continuity, thermal and a moisture balance equation were integrated in a meridional vertical plane between the south and the north pole. The atmosphere started from a state of rest and was driven by differential heating between land and ocean. The components of heating that are important for the monsoon are:

- (i) The heat balance of the land area including the elevated Tibetan Plateau, viz.:
 - (a) sensible heat flux from the land surface,
 - (b) latent heat flux from the land surface,
 - (c) incoming minus outgoing (or reflected) shortwave radiation,
 - (d) incoming minus outgoing longwave radiation;
- (ii) Air/sea interaction, i.e., fluxes of latent and sensible heat from the ocean;
- (iii) Heating with the atmosphere which includes warming (or cooling) by the following processes:
 - (a) deep convection,
 - (b) shallow moist and dry convection,
 - (c) longwave radiation,
 - (d) shortwave radiation, and
 - (e) adiabatic processes.

Among the above processes the more important are: deep convection, all of the elements of heat balance of the Earth's surface, evaporative fluxes from the ocean, and the adiabatic warming and cooling within the atmosphere.

With the above framework Murakami et al., (1970) simulated a very realistic picture of the monsoons around 80°E longitude. Their simulations included the following features:

- (a) Realistic southeast trades south of the Equator with maximum speed near 900 mb;
- (b) Southwest monsoons over India with a maximum speed near 600 mb;
- (c) A tropical easterly jet in the upper troposphere near 150 km and around 10°N ;

- (d) Monsoon troughs (in the sea-level pressure field at 25°N);
- (e) A Tibetan high at 30°N and 200 mb;
- (f) A warm troposphere between the monsoon trough and the Tibetan high;
- (g) A rainfall maximum at around 20°N;
- (h) A Hadley cell with rising motion around 20°N and descent near 20°S with northeasterlies in the upper troposphere.

Much of what they simulated falls within the known range of observational variability of these well-known phenomena. The major drawback of this study is the absence of interactions of planetary-scale monsoon waves with the zonal flows and shorter scale waves (see Chapters 2 and 17).

A number of sensitivity studies were also conducted by Murakami *et al.*, (1970). The purpose of these sensitivity studies was to investigate what were some of the important (and also less important) parameters in the successful simulation of monsoons. They found that the Himalayan mountains were very important as well as the salient physical processes listed above. Surprisingly, they noted that the intensity of monsoons and of the differential heating was not changed much if the sea-surface temperatures were slightly altered. The ocean was found to be important for its supply of latent heat and the land for its heat balance and its warm temperatures. Finally, this framework is viewed as follows. The solar heating warms the land surface, the gradual increase of soil temperature results in dry adiabatic lapse rates and this is continuously removed in the model by dry convective adjustment over a substantial portion of the meridional belt. This results in the gradual formation and intensification of a heat low. Soon moist air from the ocean starts to converge into the general region of the heat low. Conditional instability over the land area grows and soon thereafter moist convection starts. Rainfall, warming of the troposphere, and the establishment of a Tibetan high, a monsoon trough and a Hadley cell follows. The upper level tropical easterly jet forms due to a transformation of kinetic energy of meridional motions into zonal motions. In many ways the Murakami *et al.* framework of broadscale monsoons is akin to a giant sea breeze whose scale is of the order of 6000 km and in which the effects of the Earth's rotation on the motions on the meridional plane become important.

13.5 The differential heating that drives the monsoons

Evidence based on rainfall observations, cloud distributions from satellites, surface-based radiation measurements, Earth's radiation budget measurements, and numerical modelling studies (Murakami *et al.*, 1970; Gilchrist, 1977) suggests that during summer monsoons a strong field of differential heating (VH) exists and is directed from the oceanic to the land areas of the monsoon belt. The components of large-scale heating include (i) the Earth's surface (the net short and longwave radiation, fluxes of sensible and latent heat and conductive heat fluxes into the soil), and (ii) within the atmosphere, heating by short and longwave radiative processes, dry convective processes, shallow and deep moist convection, sensible and latent heating fluxes from the Earth's surface, large-scale condensation and convergence by small scale eddy fluxes of heat. Gilchrist (1977) has mapped the field of vertically integrated total heating and has shown very clearly the field of differential heating within the atmosphere. Murakami's *et al.* (1970) study discussed in Section 13.4 also provides us with a simple framework relating the differential heating to the monsoon circulation. Table 13.2a illustrates the rate of total tropospheric heating based on Katayama (1964) over three regions of interest for the summer monsoon.

Table 13.2a Component heating rates for different regions of the monsoon
(Katayama, 1964)

Langley/day	Heat low over Saudi Arabia	Central Arabian Sea	Ganges Valley N.E. India
Total heating rate of the troposphere	-95	5	375
Q_R (radiation)	-130	-80	-25
Q_S (sensible heating)	20	-15	0
Q_C (condensation heating)	15	100	400

They are, respectively, the heat low to the northwest, the oceanic environment and the active monsoon disturbance region. The heat low region (the deserts) is primarily radiatively controlled, while the active monsoon region is convectively controlled; the oceanic environment falls somewhere in between. The meridional distribution of total heating along the west coast of India during the active monsoon period is shown in Table 13.2b. As one proceeds Equatorwards from the Himalayas, the field of differential heating from land to ocean is illustrated here. Near 20°N around Bombay, the total heating is largely convectively controlled. The radiative control gradually increases as one proceeds Equatorward over the oceanic areas.

Table 13.2b Meridional variation of heating rate along 73°E based on
Katayama (1964)

Langley/day	30°N	20°N	10°N	0°	10°S
Total heating	45	385	255	90	25
Q_R (radiation)	-75	-25	-25	-50	-75
Q_S (sensible heating)	20	10	-20	-10	0
Q_C (condensation)	100	400	300	150	100

The details of the differential heating for the winter monsoon including its spatial and vertical distribution within the atmosphere are not very well known.

13.6 Air/sea interaction

The bulk aerodynamic formulae are frequently used for estimating the transfers of sensible heat (F_S) and latent heat (F_L) from the ocean. A set of frequently used formulae is:

$$F_S = \rho c_p C_D |W_0| (T_w - T_o) \quad (13.1)$$

$$F_L = \rho C_D |W_0| (q_w - q_o) \quad (13.2)$$

where $|V_0|$ is the surface wind speed, T_w and q_w are the ocean temperature and the saturation specific humidity, respectively; while T_0 and q_0 , respectively, denote the air temperature and the specific humidity at the anemometer (or ship deck) level. If the wind speed is expressed in $m\ s^{-1}$ and the air/sea temperature and humidity differences for q_w and q_0 are respectively expressed in $^{\circ}C$ and $g\ kg^{-1}$ units, then F_S and F_L are in units of $cal\ cm^2\ d^{-1}$.

A number of atlases relating to the above parameters exist and they are very useful. Here we shall illustrate these fields for the months of the onset of the summer monsoon over south Asia (Figs. 13.3a and b). The most striking feature is a zonal belt of maximum air/sea energy transfer near $10^{\circ}S$ and another region over the Arabian Sea near $10^{\circ}N$. This axis of large air/sea transfer is located close to the region of the strongest surface winds which in turn are located near the axis of the major cross-equatorial low level jet of the Arabian Sea. The largest exchanges are of the order of 300 to 400 $cal\ cm^2\ d^{-1}$. Furthermore, it is important to note here that the Bowen ratio $B = F_S/F_L$ is of the order of 0.1 in the tropics, hence most of the energy transfers shown in these diagrams reflect latent heat fluxes. The distribution of sea-surface temperatures over this region is shown in Fig. 13.4.

The field of sea-surface temperature exhibits an interesting cooling trend over the Arabian Sea. During April and May values exceed $28^{\circ}C$ over most of the near-equatorial Indian Ocean and over the Arabian Sea and the Bay of Bengal. The cooling occurs along the east African coast and is well marked in June. At the height of the monsoon season (i.e., August), sea-surface temperatures over all of the Arabian Sea are cooler by about $2^{\circ}C$ than the values during June. This cooling is partly due to the intense coastal upwelling near the Somali and Arabian coast. Recent observations show that the coastal values of water temperatures approach around $15^{\circ}C$ on individual days (see Fig. 13.5). The general large-scale cooling of the Arabian Sea may be due to lateral spreading of cold upwelled water from coastal regions and possibly also to cloud and haze cover which increases between June and August, thus reducing the solar heating. The data for Fig. 13.5 were based on a special cruise of four U.S. naval vessels. The field of wind stress over the ocean can also be estimated by the use of standard drag formulae:

$$\begin{pmatrix} \tau_x \\ \tau_y \end{pmatrix} = C_D \rho_0 \left(u_0^2 + v_0^2 \right)^{1/2} \begin{pmatrix} u \\ v \end{pmatrix} \quad (13.3)$$

where C_D is the drag coefficient (1.4×10^{-3}); ρ_0 is the density of air at the surface; u and v are the zonal and meridional components of the wind and τ_x and τ_y are the stresses in the zonal and meridional directions. Hantel (1970) has produced a set of monthly mean maps of the curl of the surface-wind stress based on monthly mean wind stresses. The maps of Hantel (1970) are shown in Fig. 13.6. The curl of the wind stress is related to the intensity of the upwelling (from Ekman theory). His maps for July and August clearly show the positive values for the curl of the wind stress near the east African coast. Over most of the Arabian Sea, negative values (the shaded area) of the wind-stress curl prevail during the summer monsoon. Hantel notes that regions of positive relative vorticity (of the surface wind) are correlated with regions of positive curl of the wind stress. Hantel also noted a one month lag for the response time of the oceans to the wind stress.

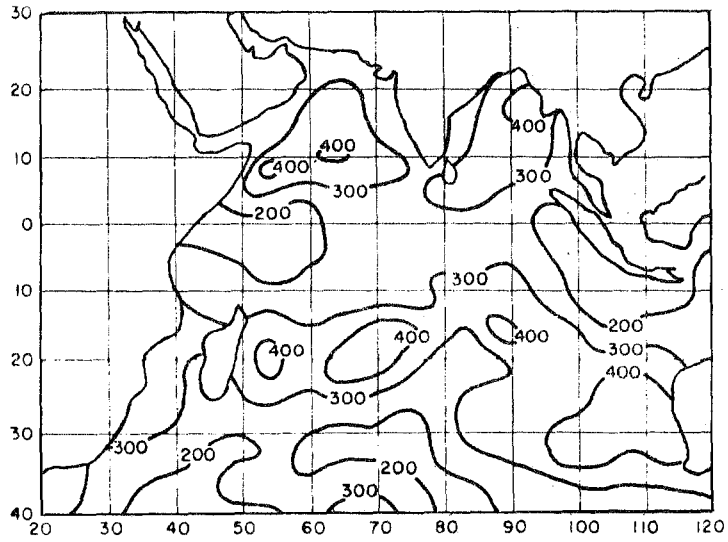


Figure 13.3a - Heat exchange at the sea surface in $\text{cal cm}^{-2} \text{d}^{-1}$ equivalent heat gain (latent plus sensible heat) May 1963

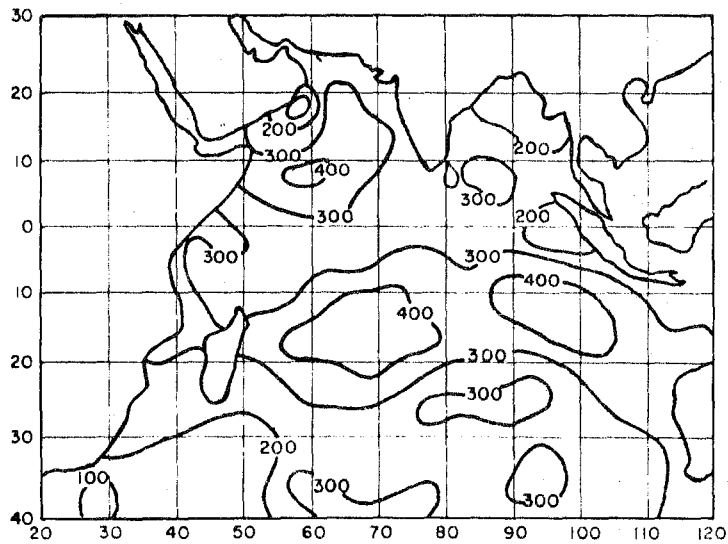


Figure 13.3b - Heat exchange at the sea surface in $\text{cal cm}^{-2} \text{d}^{-1}$ equivalent heat gain (latent plus sensible heat) June 1963

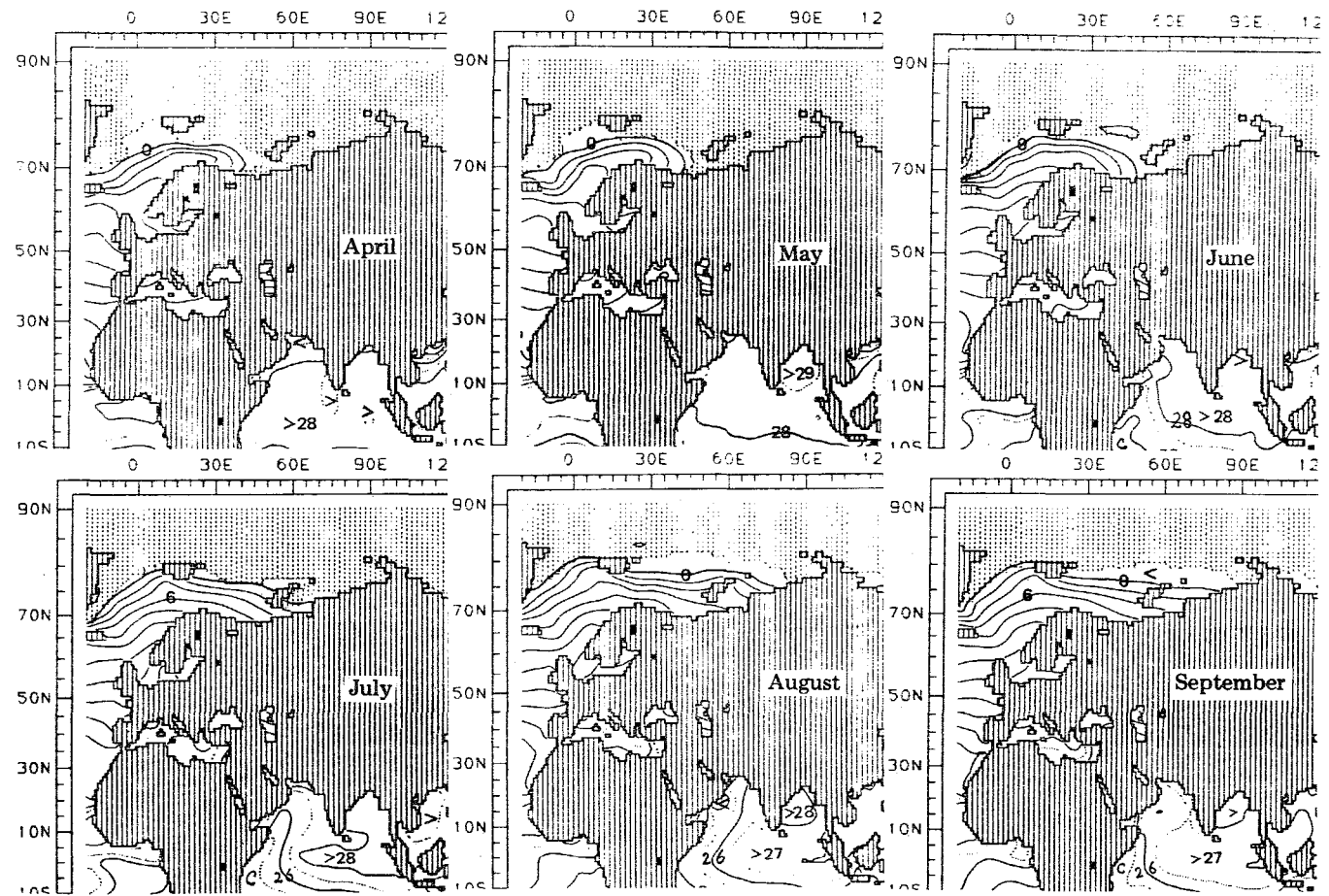


Figure 13.4 - Distribution of sea-surface temperature (Alexander and Mobley)

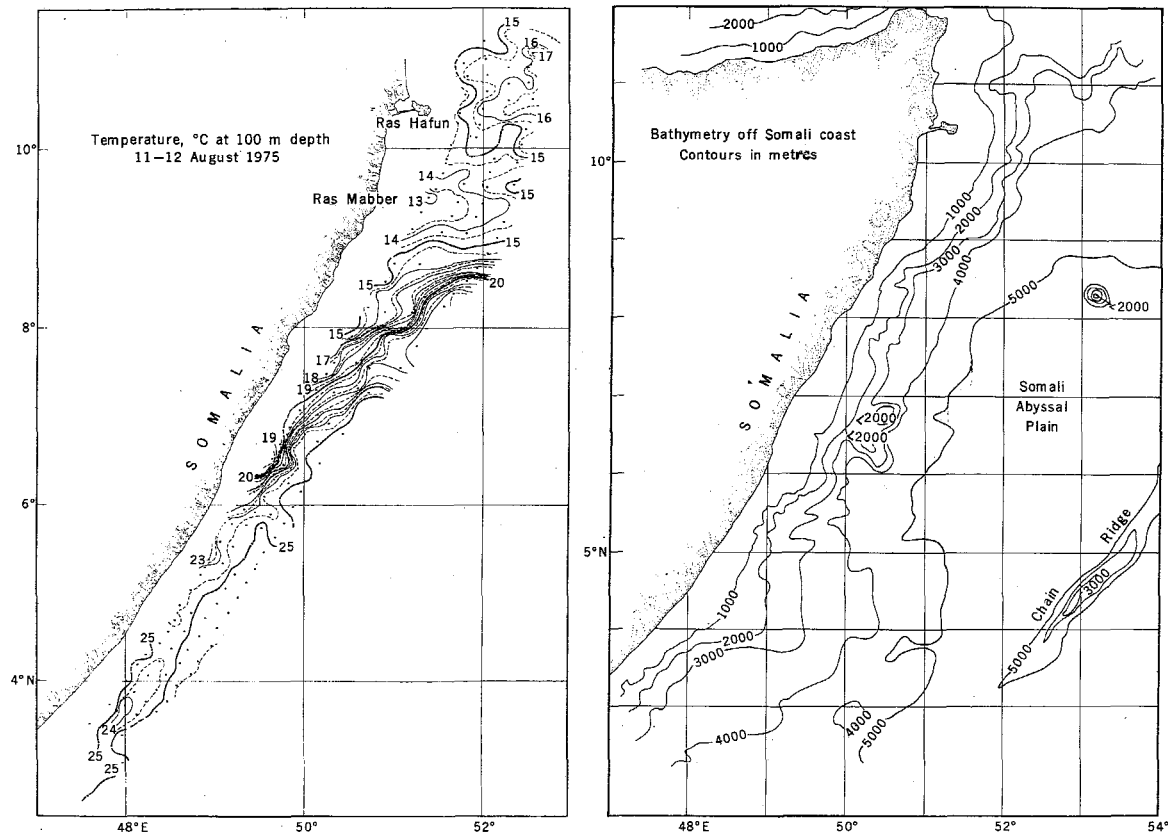


Figure 13.5a - (Left) Map of temperature contoured at a depth of 100 m in the Somali Current at approximately maximum strength during the southwest monsoon in 1975. Dots show XBT station positions from four U.S. Navy ships travelling abreast to the northeast along the coast from Greenwich mean time 1500, 11 August, to 2300, 12 August

Figure 13.5b - (Right) Bathymetric chart off the Somali coast based on a map by Laughton (Bruce 1973)

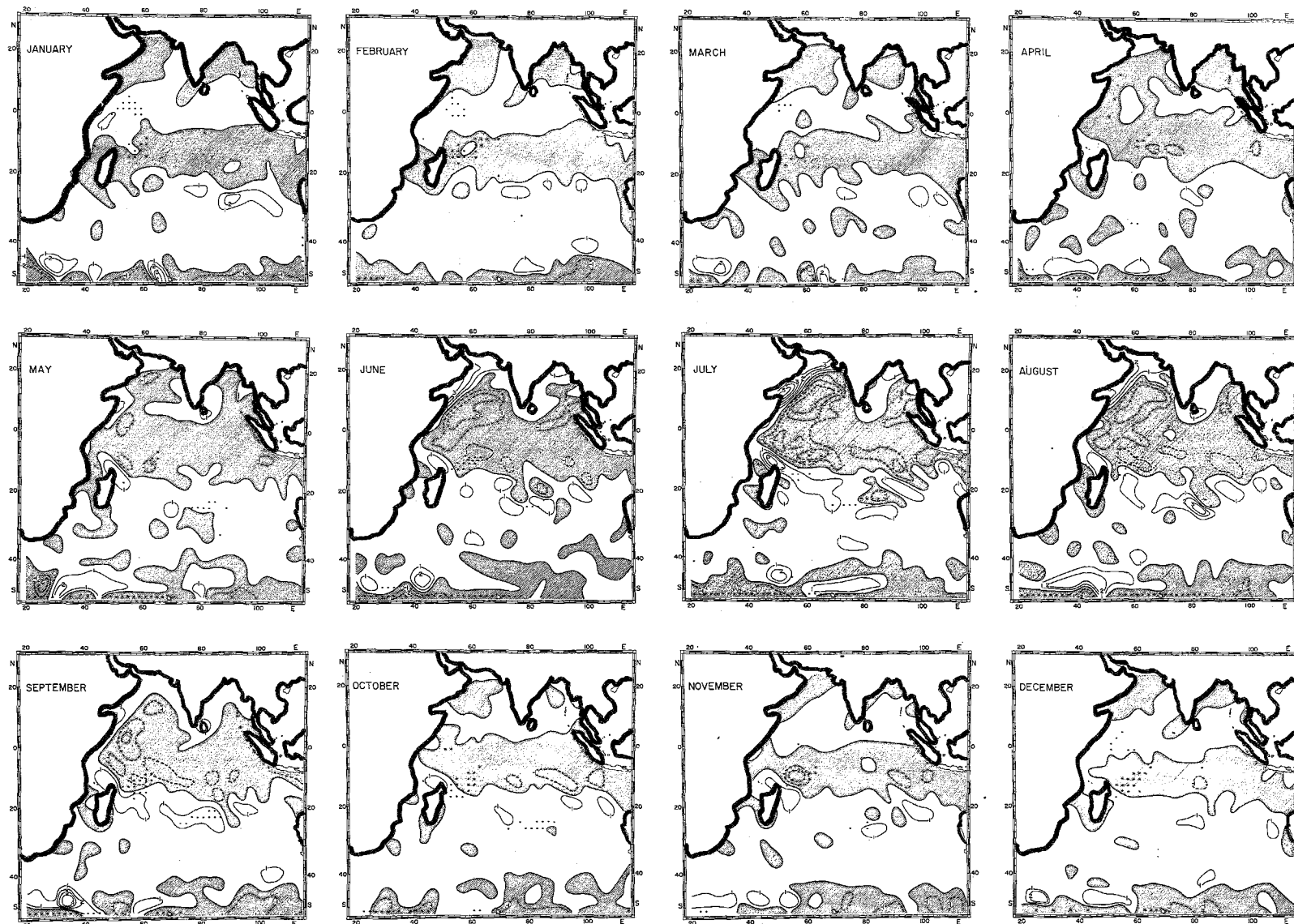


Figure 13.6 — Surface-wind stress curl over the Indian Ocean. Units, $10^{-7} \text{ kg m}^{-2} \text{ s}^{-1} = 10^{-8} \text{ dynes cm}^{-3}$. Negative areas are shaded. Dots indicate 2° squares without available wind data (Hantel, 1970)

13.7 The monsoonal inversion

The trade-wind inversion over the Arabian Sea during the summer monsoon months is low and intense along the near-equatorial east African coast, rises along the low-level monsoonal southwesterly, flows over the Arabian Sea and weakens near the Indian coast. This behaviour is opposite to that of the trade-wind belts. Bunker (1965) presented evidence of the above from drop-windsonde data taken during a field experiment. However, although his observations were interesting, the design of the field experiment did not permit an evaluation of the "inversion budget", which was possible for the ATEX Experiment discussed in Chapters 12 and 20. As shown in Chapter 12, a minimal observational system for budget studies requires a triangular network of upper-air stations. The "inversion budget" can be evaluated by a coupled system describing a balance of dry static stability and moisture. Several scientists have evaluated the balance of moisture over the Arabian Sea using line integral techniques over the entire region north of the Equator. Due to a lack of equatorial observations, these studies, e.g. those by Pisharoty (1965) and Saha and Bavadekar (1973) are not very conclusive. They attempted to relate the evaporation over the Arabian Sea to the cross-equatorial supply of moisture across the Equator in the rainfall budget. Although they both concluded that the evaporation over the Arabian Sea far exceeds the transport of moisture across the Equator, this important question deserves further observational studies. Perhaps in support of their work we might state that the near-equatorial dropsonde measurements during 1973 and Soviet ship soundings during 1973 and 1977 show that the atmosphere is indeed very dry and thus the transports of moisture along the cross-equatorial low-level jet may be very small. Table 13.3 shows the moisture budget over the Arabian Sea based on the studies of Saha and Bavadekar (1973). The lateral boundaries of their computational domain are shown in the columns showing the transports.

Table 13.3 Water vapour flux over Arabian Sea (10^{10} tons d^{-1})
(Saha and Bavadekar, 1973)

	Across				Net flux divergence	Estimated evaporation	Precipitation computed from water vapour budget	Estimated precipitation from rainfall charts
	42°E	26°N	75°E	Equator				
Sept. 1964	0.85	-1.09	-2.35	3.60	1.01	2.1	1.1	1.0
June 1964	0.11	-1.21	-3.38	4.99	0.51	3.5	3.0	2.5
July 1964	0.50	-1.53	-4.36	5.87	0.48	3.2	2.7	2.7
Aug. 1964	-0.67	-1.46	-3.89	5.75	-0.27	2.5	2.7	2.1
Sept. 1964	0.15	-1.27	-3.01	4.95	0.82	2.4	1.4	1.7

The field of large-scale vertical velocity generally shows descent over most of the Arabian Sea during the summer season (Depradine, 1978). Many individual case studies on vertical motion over the monsoon belt have shown that general descent prevails except in the vicinity of active disturbances. The inversion over the Arabian Sea thus appears to be similar

to the trade wind inversion; the general subsidence probably plays a major role in generating its large static stability. Some unanswered questions are:

(i) What are the relative roles of radiation, subcloud layer convection, and large-scale subsidence in the maintenance and variability of the monsoonal inversion?

(ii) What are the relative roles of processes that contribute to the moistening or drying of the subcloud layer, the cloud layer and the inversion layer over the Arabian Sea?

(iii) What factors determine the frequent inland penetration of the inversion during periods of inactive monsoons?

13.8 Onset, active and break monsoons

(a) The onset phenomenon:

The onset of monsoons is characterized by an abrupt increase in rainfall over a large area; this occurs during early June over many parts of India. The five-day mean rainfall averaged over calendar day intervals of 5 days is called Pentad rainfall. The Pentad rainfall for a weather station over India is illustrated in Figure 13.7. It shows the large increase of rainfall on the Pentad centered around the second of June. The area-averaged daily rainfall over large areas of central India is plotted every year by the Indian Weather Service. Figure 13.8 illustrates an example of this plot showing clearly the onset of monsoon rainfall around the 20th of June during 1972.

The dates of onset vary from year to year as well as from region to region. Normal dates of onset have been prepared by many weather services based on long-term rainfall records. It shows that a line (roughly from southwest to northeast) propagates northwestward. This line connects Sri Lanka and central Burma around the last week of May. It is located over northern India by the end of June. This line defines the isochrones of the normal onset of monsoons and is illustrated in Figure 13.9a. A reverse sequence between roughly the 15th of September and 1st of January describes the withdrawal of the monsoons (Fig. 13.9b).

The northwestward motion of the "onset isochrones" and the subsequent retreat of the "withdrawal isochrones" is an important part of the annual cycle of the monsoons. This sequence is not well understood at present. Differential heating between the land and the southern oceans and the moistening and increase of conditional instability over large areas are known to be associated with the onset phenomenon.

(b) Active and break monsoons:

Rainfall records such as those shown in Figure 13.10a are available for well over 80 years. They all show that monsoon rainfall exhibits considerable variability. There are active and inactive periods (called breaks) of rainfall. During drought years the breaks last for periods as long as one month. In years of near-normal rainfall the active and break spells alternate with an approximate period of one week each. Thus, a well-known quasi-biweekly oscillation in the monsoonal rainfall was noted by Krishnamurti and Bhalme (1976). Their analysis of the spectra of monsoon rainfall is illustrated in Figure 13.10b. It shows two pronounced peaks, one around 3 days related to passage of monsoon lows and the other around 15 days related to

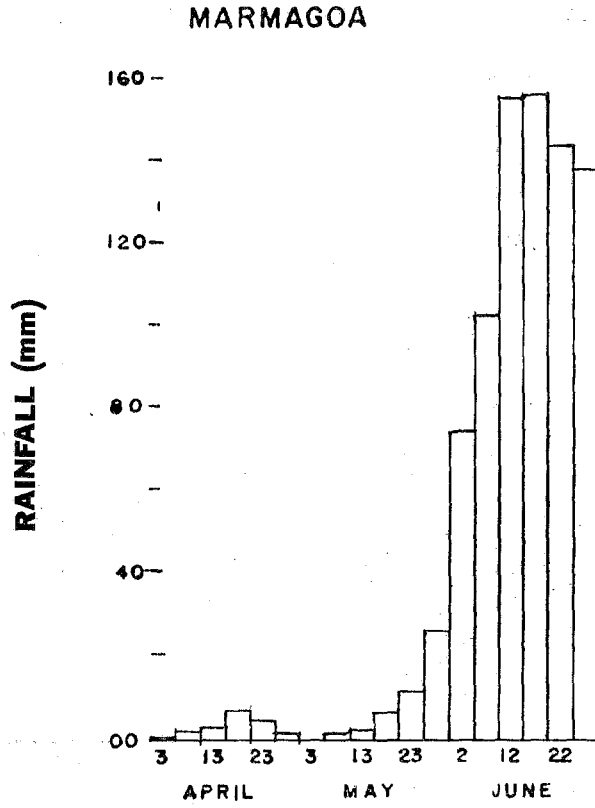


Figure 13.7 — Pentad rainfall over a weather station on the west coast of India

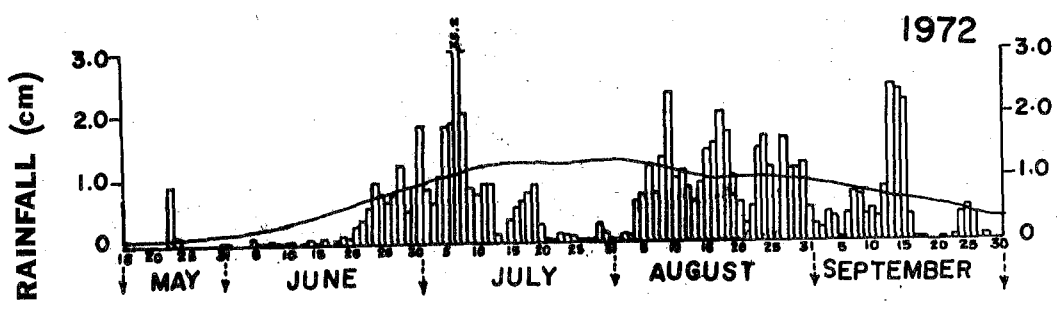
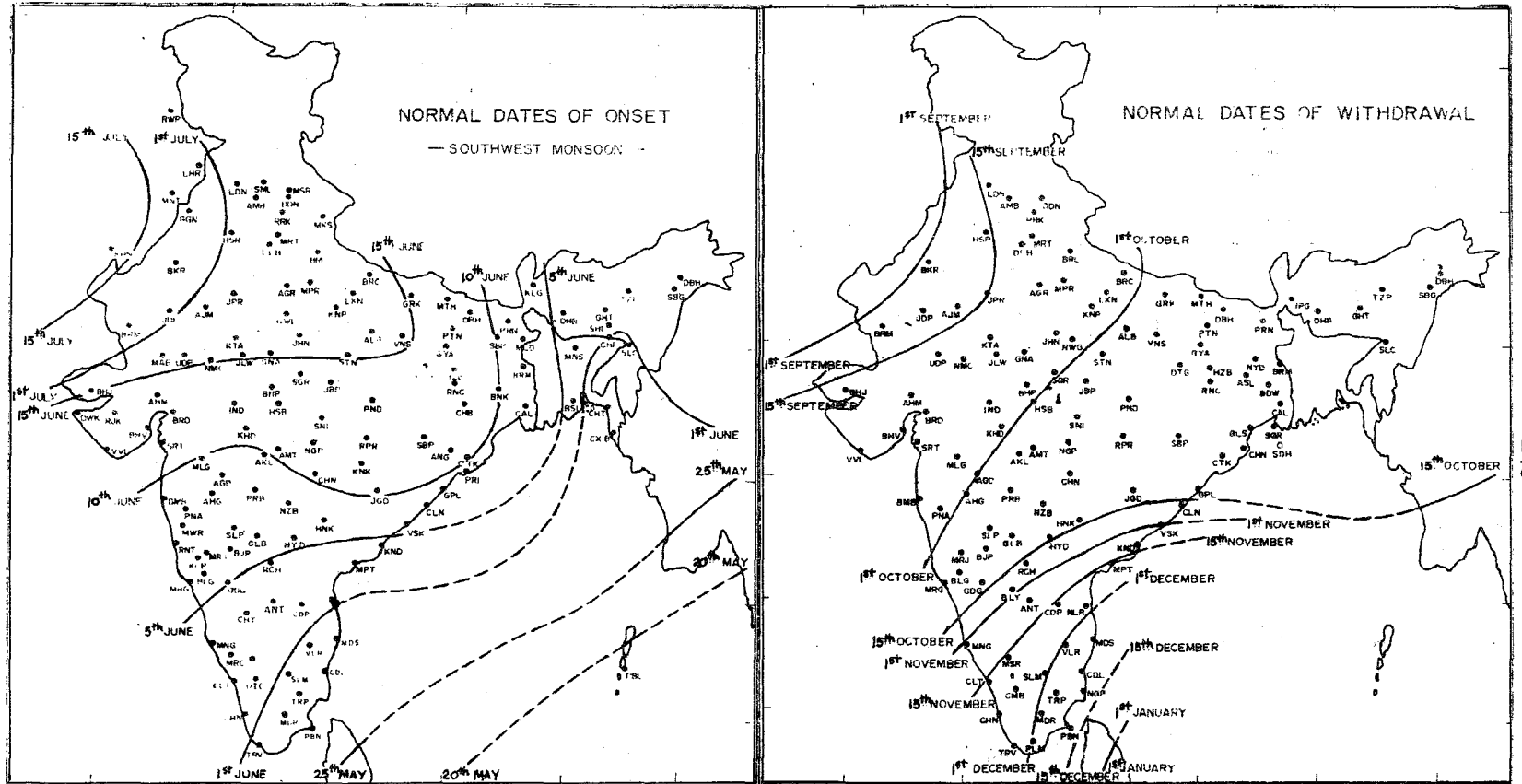


Figure 13.8 — Daily rainfall total during summer of 1972 over central India. The heavy dark line shows long term calendar day mean normal rainfall



(a) Isochrones of the normal onset dates of the monsoons (Rao, 1976)

(b) Isochrones of the normal withdrawal dates of the monsoons

Figure 13.9

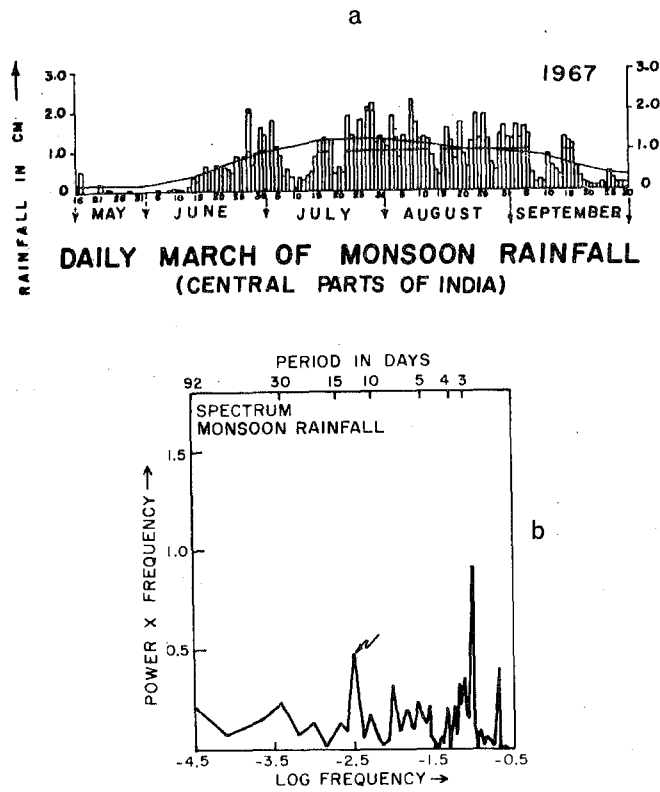


Figure 13.10 - (a) Daily values of monsoon rainfall averaged over central India and (b) the power spectrum for monsoon rainfall

active and break spells in monsoons. These active periods are generally associated with the passage of monsoon depressions that form over the Bay of Bengal and move northwestward. During break periods the active monsoon trough is known to move towards the Himalayas. The rainfall belt moves northward. During these periods most of central and northern India experiences a dry period. Another rainfall belt usually forms over southern India near 10°N during these breaks. The monsoon trough is replaced by a surface pressure ridge line around 20°N . Since the (zonally-oriented) pressure ridge line moves northward from equatorial latitudes toward 20°N , it is tempting to think that the cause of the breaks in the monsoon originates from near the Equator. Krishnamurti and Bhalme (1976) presented the following as a plausible hypothesis for this phenomenon. This is based on some preliminary results from a zonally symmetric monsoonal general circulation model (Murakami *et al.*, 1970). Here we note an oscillation between an active and an inactive (break) phase of the zonally symmetric monsoons. The heat balance of the Earth's surface around 25°N is crucial here. Net radiative effects warm the Earth's surface, the heat balance of which includes both sensible and evaporative fluxes. The fluxes gradually build dry and moist instabilities in the lower layers. Heat is transported up by the dry and moist convective adjustment processes. The heating is also augmented by large-scale condensation. As convection and condensation increase, cloudiness increases in the model. The gradual increase of cloudiness results in a gradual decrease in the incoming shortwave radiation reaching the Earth's surface. As a consequence, there occurs a gradual stabilizing of the lower layer and the dry and moist convective processes slowly decrease and the associated cloud cover also starts to decrease. The shortwave radiation now starts to become effective once again and the cycle starts all over again.

The hypothesis stated above requires further careful analysis. The symmetric models preclude any zonal interactions of the monsoons with other regions such as the Pacific. Observations, however, suggest that active monsoon spells are, in fact, related to activity in the western Pacific Ocean. One such interrelationship was recently explored by Krishnamurti *et al.*, (1976). Here the existence of an interesting phenomenon of downstream amplification for the monsoonal region was demonstrated from long-term surface pressure records. Figure 13.11a shows examples of downstream amplification that precedes an active monsoon period. Here the arrival of a typhoon (Fig. 13.11b) initiates a lowering of pressure near north Vietnam; this is followed by the formation of an anticyclone over central Indochina about a week later and the subsequent formation of a monsoon disturbance about another week later over the northern Bay of Bengal. Roughly 40 such examples were examined during the period 1939 to 1973. The slow rate of westward propagation of the amplification was attributed by Krishnamurti *et al.*, (1976) to a slow group velocity (slower than the phase velocity) in this region during northern summer. This is only one of several kinds of interactions of the disturbances over the Pacific Ocean with the activity of the monsoons.

The phenomenon of the breaks is fairly complex and not much is understood about it at present. Ramamurthy (1969) has published an exhaustive survey of the breaks in the monsoons covering an 80-year period, 1888-1967. During breaks, as the broad-scale surface pressure trough moves northward over the Indian subcontinent, westerly winds prevail and rainfall amounts over central India are small. Ramamurthy has used these characteristics in his definition of the breaks in the monsoon. He examined the months of July and August for 80 years of weather records. The breaks last for roughly 3-5 days in July and August. In the 80 years of records, there were no breaks during 12 of these years; one break per year during 25 of these years; two breaks per year during 22 of these years, three breaks per year during 9 of

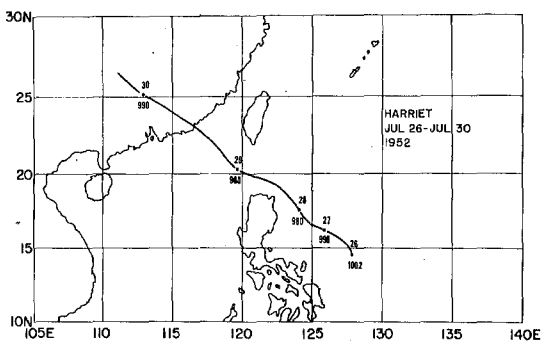
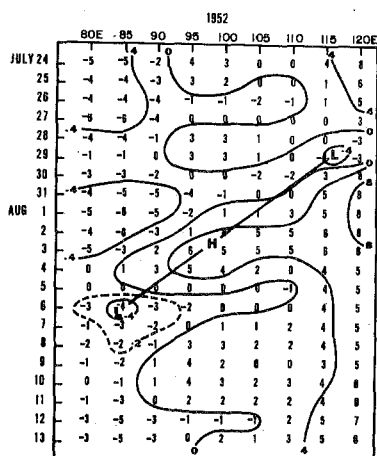
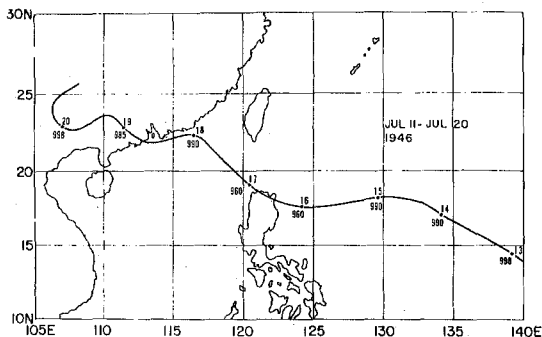
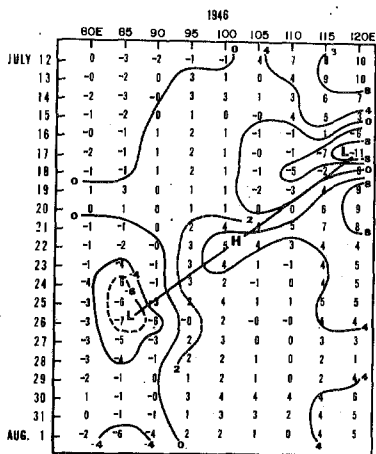
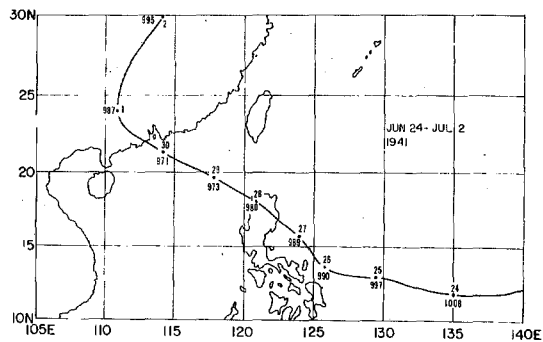
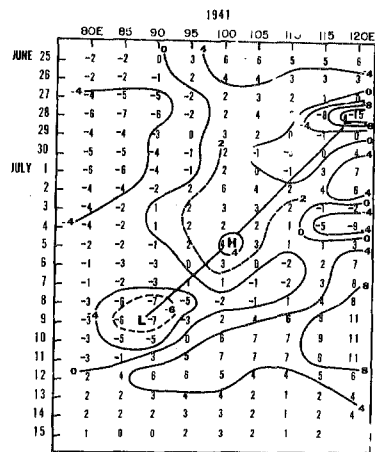


Figure 13.11 - (Left panel) Hovmöller diagrams of surface-pressure data at 20°N. The ordinate shows the date and the abscissa longitude. The surface pressures are departures from 1000 mb. (Right panel) Typhoon tracks for the downstream amplification illustrated in the left panel. Central pressures at 0000 GMT are shown, when available (Sources: Central Meteorological Observatory, Tokyo, 1951; Chin, 1958; U.S. Fleet Weather Central, 1960-1975)

these years, and 4 breaks per year during 2 of the 80 years. Thus, one or two major breaks in the monsoons is a frequent occurrence.

(c) An alternate definition of the onset of monsoons:

Prior to June 1st the lower troposphere is usually very warm and it cools very rapidly soon after the rainy season starts. The converse is true for the upper troposphere near the 300 mb surface.

The contribution to the time rate of change of total available potential energy from the monsoon belt shows a sudden decrease for the lower troposphere and a sudden increase in the upper troposphere after the start of the rainy season. This is related to the warming of the lower troposphere by shallow dry convection and sensible heat flux prior to the start of the monsoon rainfall and a warming of the upper troposphere subsequent to the start of the monsoon rains. The warming is primarily due to deep convection and associated large-scale subsidence warming.

If ΔP_E denotes the contribution to the total available potential energy from the monsoon belt, the onset of monsoons can be defined as the change in sign of the function, $\left(\frac{\partial}{\partial t} \frac{\Delta P_E}{\Delta p} \right)$ where $\frac{\Delta P_E}{\Delta p}$ is measured between 850 and 300 mb. This same function can be used to define planetary-scale monsoons by examining the growth and decay of the available potential energy of the long waves around $20^\circ N$ in the lower and upper troposphere. The advantage of this definition lies in the fact that it is based on changes of large-scale temperature field which is somewhat easier to measure, and it does not have to rely on rainfall patterns that usually differ from region to region.

13.9 Monsoon rainfall

Figure 13.12 shows the monthly mean rainfall (in mm) over the monsoon belt from a recent atlas prepared by Jaeger (1976). We show here the rainfall distribution for the summer monsoon, i.e., from May to October. This is one of the recently updated atlases containing a summary based on a large number of surface reports. The monthly total rainfall over India during May reflects premonsoon conditions while the totals for October are for a period just after the withdrawal of the monsoon over India. In this region, a large proportion of the rainfall occurs near the mountains such as the western Ghats, the west side of the Burmese mountains, the Arakans and the Khasi Hills along the Himalayas. Here the long-term monthly mean totals exceed 500 mm (20 inches) for July and August, the active monsoon months. The rainfall totals along parts of these mountain ranges are known to exceed 2540 mm a month. This sequence of diagrams clearly shows the importance of the monsoons.

The heavy winter monsoon rainfall is encountered over the land masses around the South China Sea. Figure 13.13 shows the monthly mean rainfall from Jaeger (1976) for the northern winter months, November to April. The large rainfall totals around the South China Sea are produced by synoptic and mesoscale disturbances. The structure of these disturbances is not too well known. The primary rainfall belt is located north of the Equator during November and December; however, it moves to the south of the Equator by February. Rainfall amounts during this month over Indonesia are comparable to those over eastern India during the summer months. It is expected that detailed analysis of the observations from the Monsoon Experiment during 1978-79 will provide a better understanding of the disturbances.

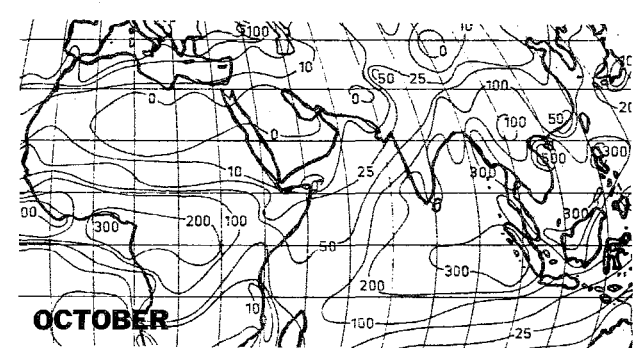
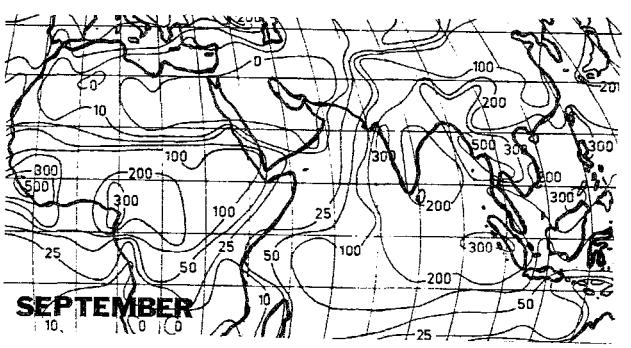
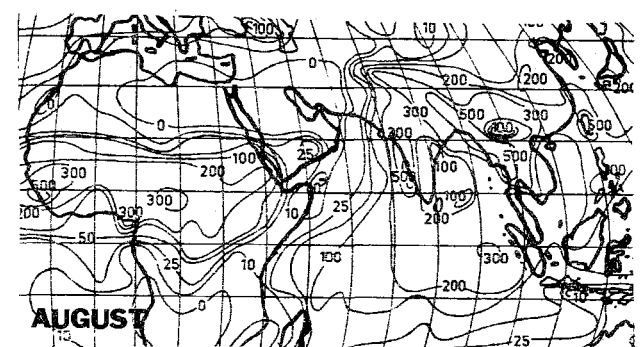
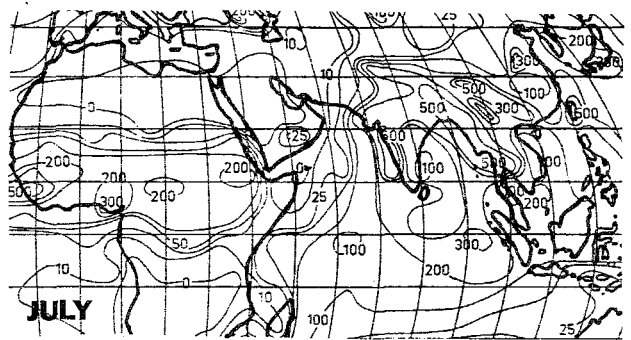
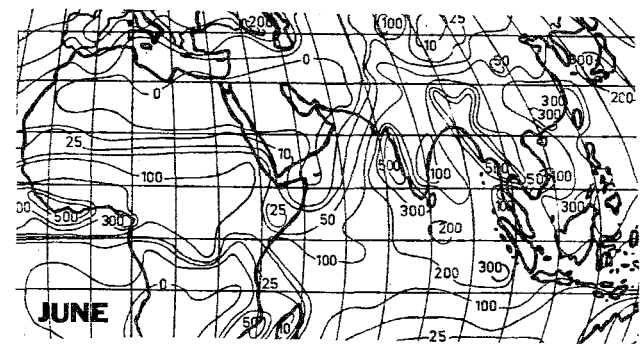
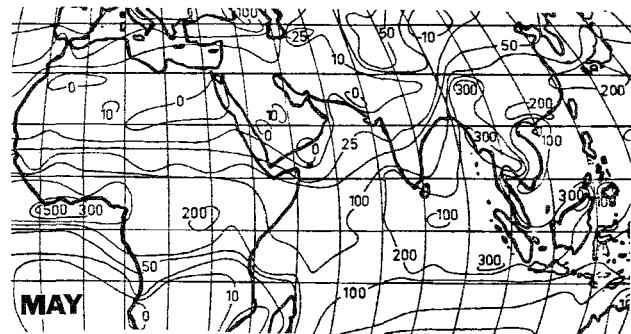
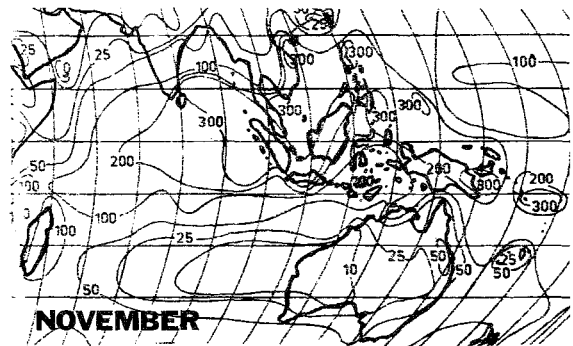
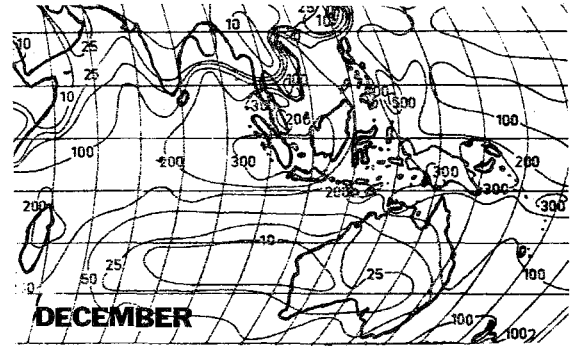


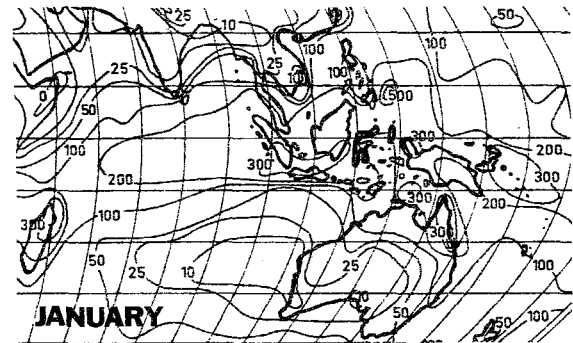
Figure 13.12 - Monthly mean rainfall (mm), Jaeger (1976), northern summer



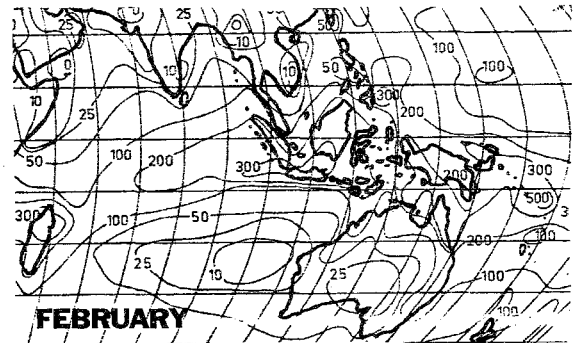
NOVEMBER



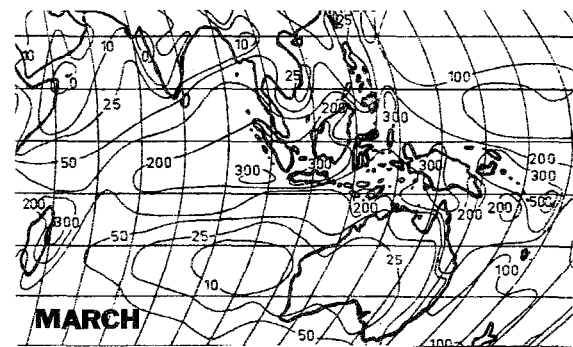
DECEMBER



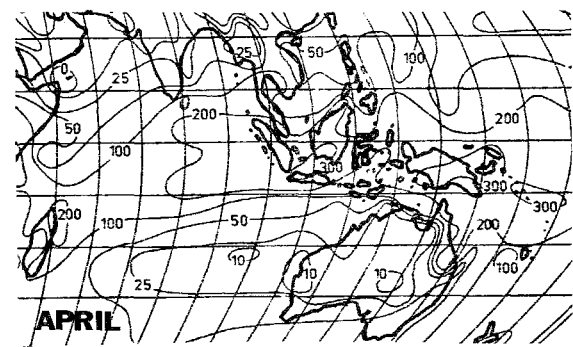
JANUARY



FEBRUARY



MARCH



APRIL

Figure 13.13 - Monthly mean rainfall (mm), Jaeger (1976), northern winter.

13.10 100 years of monsoon rainfall

Two recent studies (Raghavendra, 1973, and Banerjee and Raman, 1976) have examined 100 years records of monsoonal rainfall over India. Figures 13.14a and b illustrate the monsoonal rainfall for the months of June to September for 100 years over central peninsular India and over northwestern India. Also shown in these diagrams are the regional distributions (top right) and a spectral analysis (top left) of the rainfall. The rainfall amounts at the bottom also include a polynomial smoothing and a low pass smoothing of the rainfall amounts. Rainfall over India shows considerable interannual variability. Peninsular India (Figure 13.14a) shows a dominant peak around 2.7 years with minor peaks around 2.3 and 11 years. The 2.7 peak is statistically significant; it stands above the 95% confidence limit. The corresponding summer monsoon rainfall over northwest India also exhibits a significant peak in the 2.7 year period. It is a little difficult to understand what a 2.7 year period really is when data for June to September are averaged and used as a unit here. If one were to state that after a year of maximum rainfall the next one would be most likely to occur 2.7 years later, this would place that next maximum in a late winter season. This, of course, is an absurd interpretation. Our interpretation of the long-term record is that there probably exists a 2.7 year mode that excites monsoon rainfall whenever its phase occurs during the monsoonal months of June to September. Since the results are averages for a large area and therefore based on a large number of observations, the 2.7 year mode deserves very careful study. In their review of the long-term rainfall variability over east Africa (Chapter 14), a peak of around 3 to 4 years was noted by Rodhe and Virji (1976) over most regions. The long-term variability evidently has a complex geographical structure and no simple global patterns of rainfall variability can be identified. However, it should be noted that the east African annual rainfall is not associated with the same monsoonal period as in India. Pan (1978) and Joseph (1966) have noted oscillations in the planetary-scale circulations of the upper troposphere over the tropics with periods of around 2.6 years and 3 years, respectively. Although rainfall and circulations must have an association (since large rainfall amounts are accompanied by corresponding convergence patterns in the lower troposphere and divergence patterns in the upper troposphere) the phase relationship between rainfall and circulation has not been studied on these time scales.

13.11 Monsoon disturbances

During northern summer, the most common rain-producing disturbances are the monsoon lows and monsoon depressions. However, Pisharoty (1965) has illustrated situations of intense monsoon rainfall where synoptic-scale disturbances were not definable from the available observations on weather maps. It is thus possible that the broad-scale monsoonal current also contains mesoscale features that contribute to the monsoon rainfall. We shall not review this latter class of disturbance here since not much is at present known about its structure.

(a) Monsoon lows: Among others, Murakami (1977) has reviewed the literature on the structure and dynamics of monsoons using spectral analysis techniques. (The student studying these important papers should familiarize himself with some of the well-known techniques on statistical methods; a useful reference is the text by Jenkins and Watts, 1968) Because of the general lack of a dense network of observations, Murakami chose to carry out a spectral analysis based on upper-air observations for 1962 from a few observing sites over India. His results of the power spectra for the zonal

MONSOON (JUNE - SEPTEMBER) RAINFALL-NORTHWEST INDIA

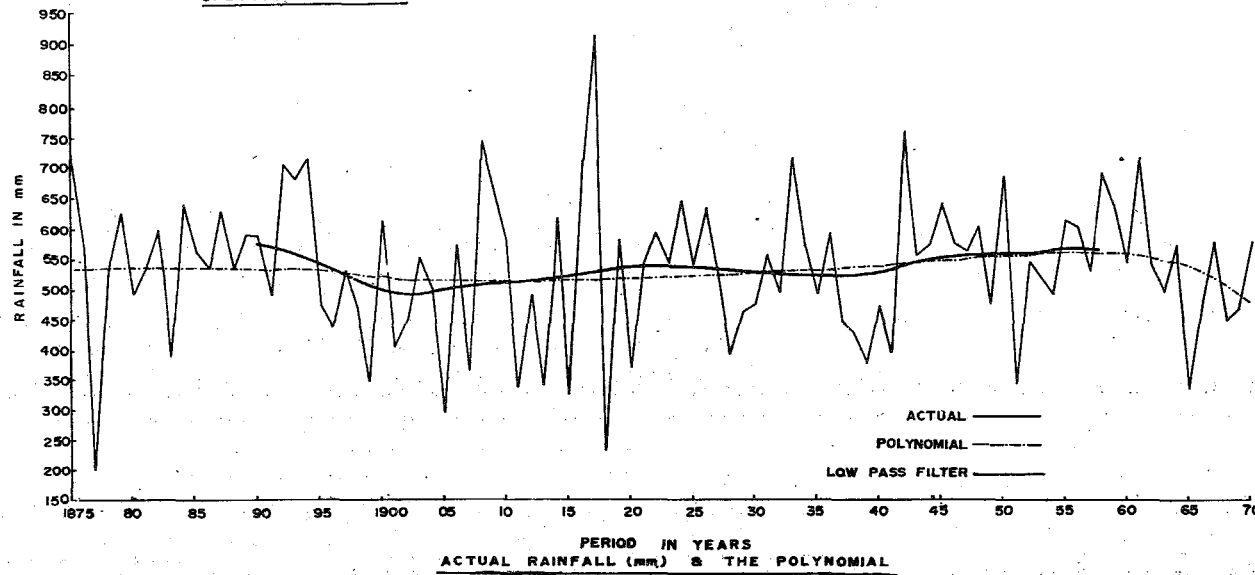
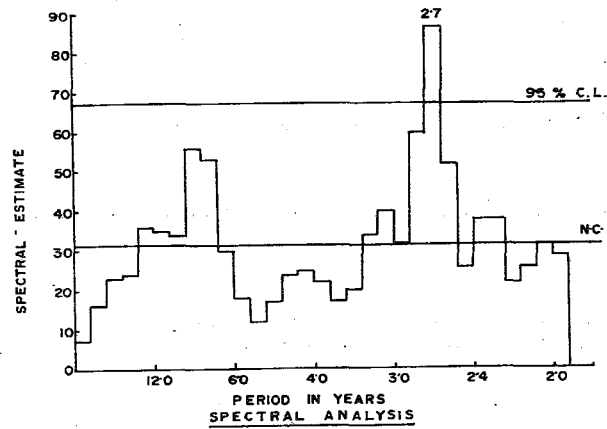


Figure 13.14a - Raghavendra (1973)

MONSOON (JUNE - SEPTEMBER) RAINFALL — PENINSULA

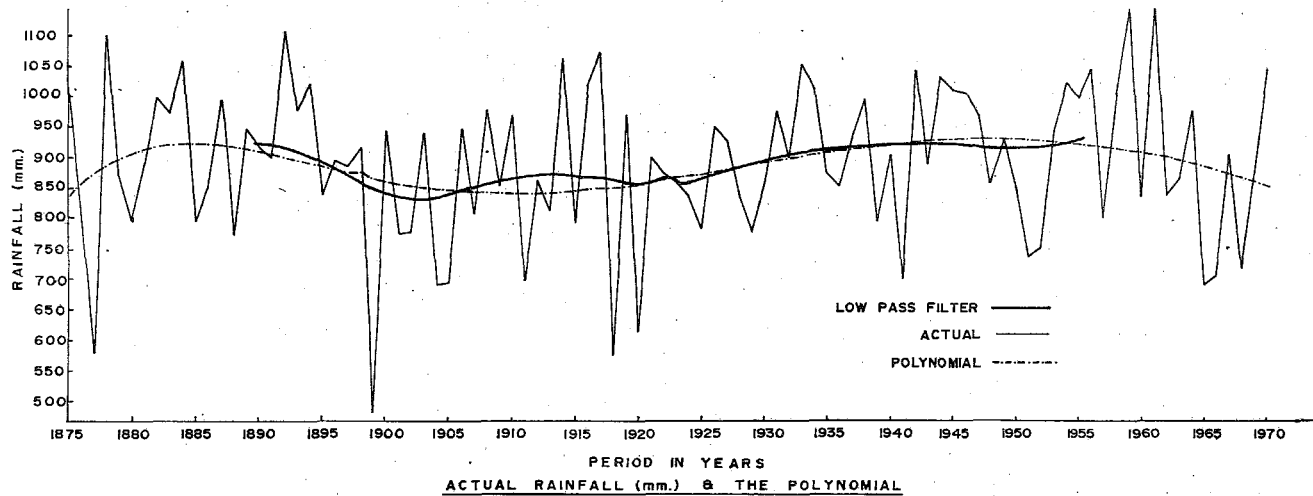
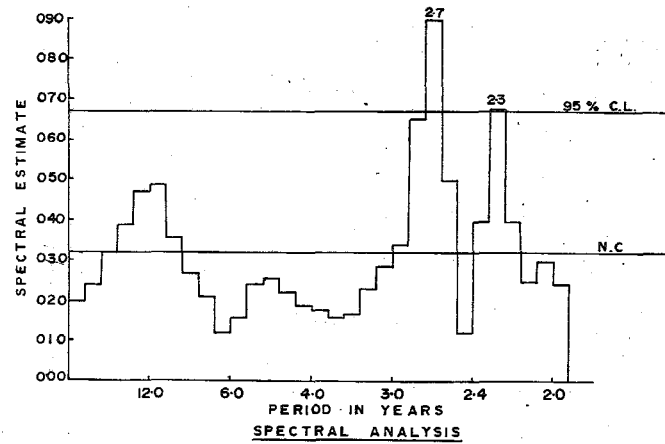


Figure 13.14b — Raghavendra (1973)

(u) and the meridional velocity (v) are shown in Figure 13.15 as a function of the vertical coordinate. The analysis clearly shows spectral peaks in the ranges 10 to 15 days and 4 to 5 days. The spectral peak around 15 days is quite clearly evident for the zonal velocity at all levels above 2 km (it shifts to longer time scales in the upper troposphere) while the 15-day mode is also evident for the meridional velocity around the 3 km level. The 4 to 5 day mode is well defined for both the zonal and the meridional velocity components. Murakami examined the geographical distribution of the variances of the meridional wind at 3 km in the 4 to 6 day range, and the variance of the zonal wind at 3 km in the 8.57 to 15 day range. These are illustrated in Figure 13.16. This study used only a limited number of upper-air stations over India, and the largest variances were found to be present over the northern part of the Bay of Bengal. It suggests that the Bay of Bengal is an important region for the growth of eddy motions on these scales around the 3 km level. The time-series technique can be used to estimate the horizontal scale and the speed of propagation of a wave disturbance by an extrapolation of the phase angle for adjacent weather stations. Murakami finds that the disturbances in the time frame of 4 to 6 days have a horizontal scale roughly 30° longitude (see Figure 13.17), and a westward phase speed of about 6° longitude d^{-1} . Based on available synoptic knowledge Murakami identifies these 4 to 6 day modes with the monsoon lows. An excellent survey of monsoon disturbances may be found in the recent text by Rao (1976). In order to study the vertical structure of these monsoon lows, Murakami carried out inter-level cross-spectral analysis using the 3 km level as a reference. He computed the vertical distributions of the variance, phase and coherence for the meridional wind, temperature and moisture distribution. The phases and variances for temperature and moisture are illustrated in Figure 13.18. The variance of temperature is large and increases in the lower troposphere while that of moisture is invariant with height. The phase distribution shows that the temperature anomaly tilts westward with height while the converse seems to be the case for the moisture in the lower troposphere. The derived vertical structure of the monsoon low for the meridional wind, temperature and moisture is shown in Figure 13.19. The trough line is identified as the vertical heavy line along which the meridional wind $v = 0$.

(b) Monsoon depressions:

The structure of the monsoon depression has recently been reviewed by Sikka (1977). The structures defined from aerological observations by Krishnamurti et al., (1975) and by Godbole (1975) contain descriptions of the mass, motion, thermal and moisture fields. Here we shall present some of the structures proposed by Godbole from a study using a compositing technique for many depressions.

The structure describes mature monsoon depressions. Figure 13.20 illustrates the composite motion field. The disturbance is most intense around 700 mb and the closed circulation can be seen from the surface to 400 mb but not at 200 mb. Here the compositing is based on many storms for the year 1973. Figure 13.21a illustrates the composite field of sea-level pressure showing that the depression pressure is around 990 mb. The depression is imbedded in the monsoon trough. Also shown in Figs. 13.21 a, b, c, d, e respectively, are vertical cross-sections of temperature along $23^\circ N$, relative humidity along $23^\circ N$, zonal wind along $83^\circ E$ and meridional wind along $23^\circ N$ and the vertical velocity along $23^\circ N$. The sections intersect the storm centre. We note here that the depression has a cold core below 700 mb; relative humidity shows fairly high values in the southerly flows. The zonal and meridional flows indicate clearly that the depression has very strong disturbance speeds exceeding 20 m s^{-1} . The vertical extent is best described

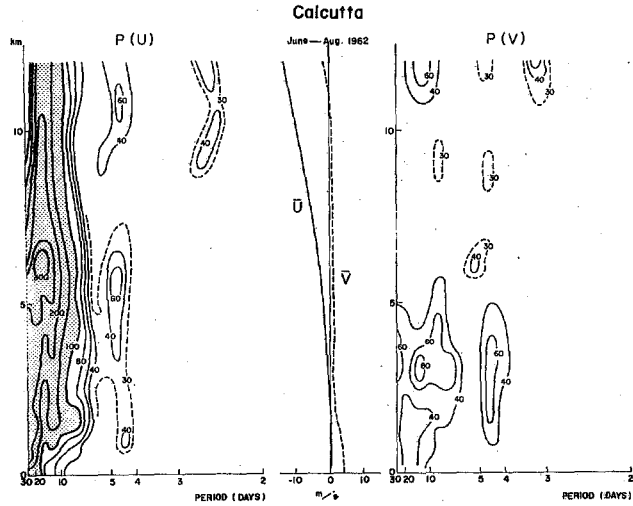


Figure 13.15 - Vertical distributions of the power spectra of the zonal (left) and the meridional (right) wind components and their mean values. Units of the power spectral densities are $(m\ s^{-1})^2\ d^{-1}$ and the values more than 100 are shaded. (After M. Murakami, 1977)

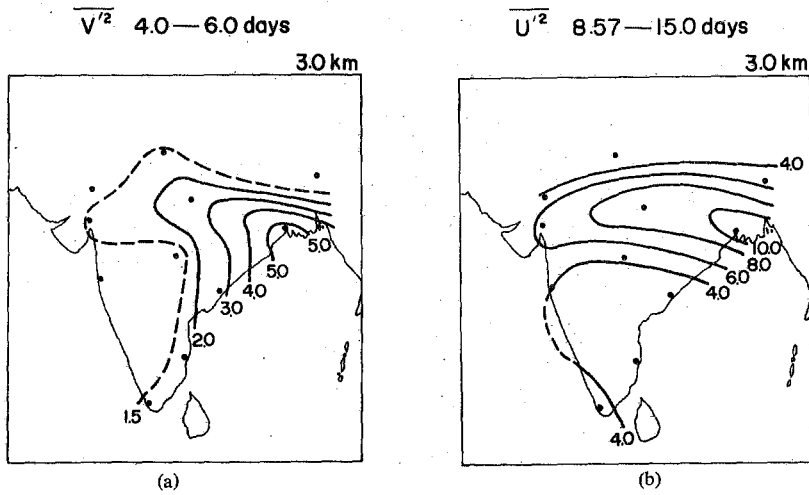


Figure 13.16 - Horizontal distribution of the variances at 3 km level produced by (a) the meridional wind in the period range 4.0 through 6.0 days and (b) the zonal wind in the period range 8.57 through 15.0 days. Units are $m^2\ s^{-2}$. (After Murakami, 1977)

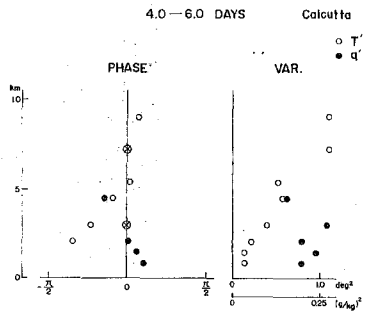
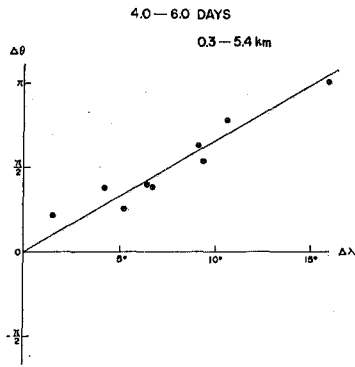


Figure 13.17 - Relation between the phase difference of the wind fluctuation ($\Delta\theta$) and the longitudinal difference ($\Delta\lambda$) of the stations in the period range 4.0 through 6.0 days

Figure 13.18 - Phase (left) and the variance (right) of the temperature (T') and the specific humidity (q')

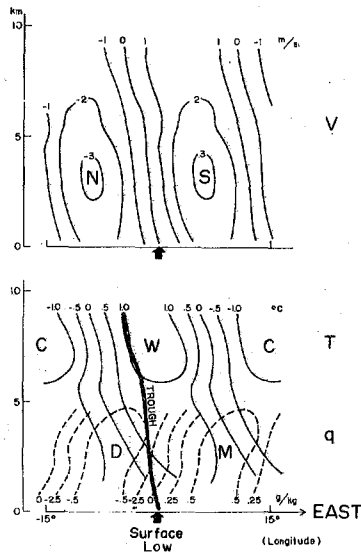


Figure 13.19 - Mean vertical structure of monsoon lows at Calcutta

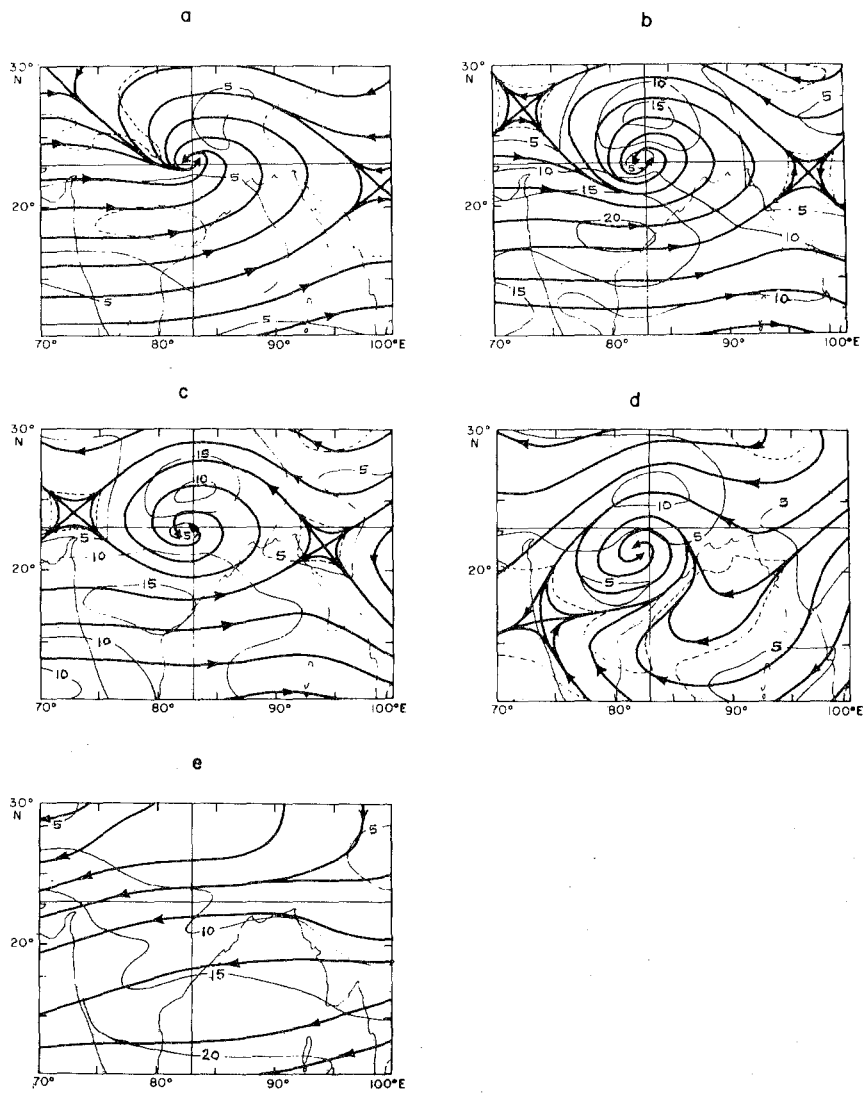
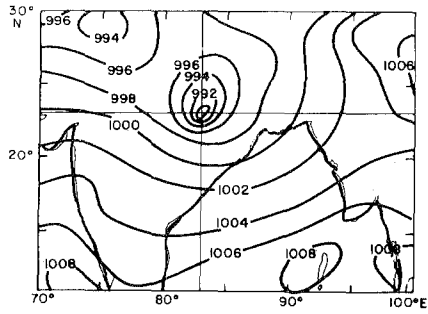
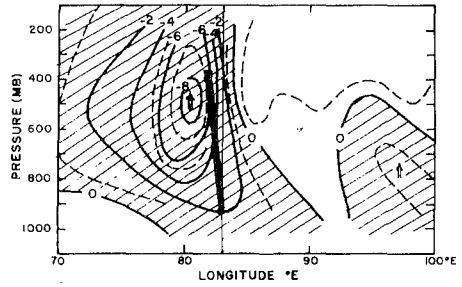


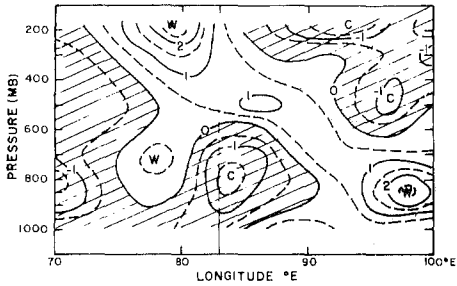
Figure 13.20 -- Streamline and isotach fields of the composite winds (m s⁻¹) at (a) the surface, (b) 800, (c) 600, (d) 400 and (e) 200 mb



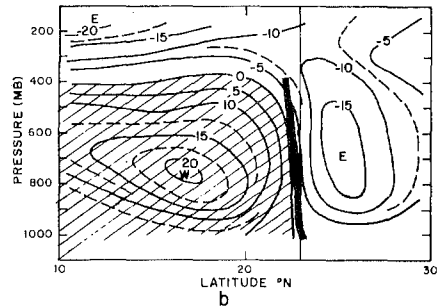
(a) Spatial distribution of the composite surface pressure (mb)



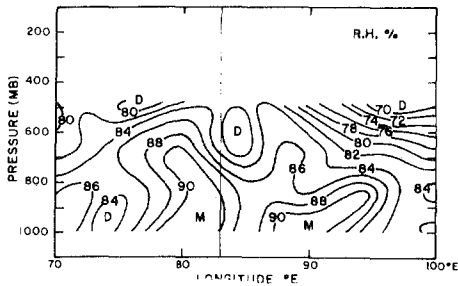
(d) The distribution of vertical velocity ($10^{-5} \text{ mb s}^{-1}$) at the vertical cross-section of the vertical velocity along 23°N



(b) The distribution of the temperature anomaly ($^{\circ}\text{C}$) at the vertical cross-section of the temperature anomaly along 23°N



(e) Vertical cross-section of (a) the zonal wind along 83°E and (b) the meridional wind along 23°N (m s^{-1}). The dark shaded line represents the axis of the depression in the wind field



(c) The distribution of the composite moisture field in terms of relative humidity (%) at the vertical cross-section of the relative humidity along 23°N .

Figure 13.21

in Figure 13.21d. The region of upward vertical velocity is described by the active region of cloud cover and rainfall, which occurs to the west of the depression. In this region typical rainfall amounts reach 10 to 20 cm d⁻¹. Not much is known about the formative stages of the depressions. Roughly two disturbances form every month during the summer monsoon months. Roughly 50% of the summer rainfall over India is accounted for by the passage of depressions.

Only a limited amount of theoretical work has been carried out to examine the instability mechanisms for the formation of monsoon depressions. Keshavamurthy (1972) and Shukla (1976) found that the barotropic and combined barotropic/baroclinic instability mechanisms may be important for the initial growth. The role of condensation heating (and CISK) was suggested as being important for the subsequent growth of the depression.

13.12 Mid-tropospheric cyclones of the southwest monsoons

These are mid-tropospheric vortices that frequently occur between 700 and 300 mb over the northwestern part of the Arabian Sea and occasionally over the northern part of the Bay of Bengal and over southern Indochina. The flows at the surface and at the 200 mb level do not show a closed circulation. This type of disturbance thus seems to be trapped in the middle troposphere. It is an important disturbance since its occurrence is associated with substantial amounts of rainfall. Rainfall rates of the order of 20 cm d⁻¹ are not uncommon.

A detailed review of the mid-tropospheric cyclones of the southwest monsoons was recently presented by Carr (1977). In this review Carr has addressed the questions of regional difference, and the formation and maintenance of these systems.

(a) Observational aspects

- (i) The vorticity maximum occurs between 700 and 500 mb;
- (ii) The scale of the disturbance is about 1000 km in the horizontal and about 6 km in the vertical;
- (iii) The largest vorticity in the disturbance is of the order of $16 \times 10^{-5} \text{ s}^{-1}$;
- (iv) The maximum upward motion occurs slightly to the southwest of the centre of the disturbance, the intensity of upward motion exceeding 10 cm s⁻¹ in these regions, where rainfall amounts of the order of 5 to 8 mm h⁻¹ have been noted. Horizontal convergence of the order of $6 \times 10^{-5} \text{ s}^{-1}$ have been noted at the base of these disturbances around the 600 mb surface;
- (v) The disturbances are essentially subtropical; the latitude where they are most frequently observed is around 20°N;
- (vi) Only one or two disturbances are known to form during each month of the monsoon season;
- (vii) The thermal structure of the disturbance shows a cold core below 500 mb and a warm core between 500 and 300 mb;
- (viii) Maximum horizontal winds are found near 600 mb where wind speeds of the order of 20 m s⁻¹ are frequently observed;

- (ix) The disturbance is known to be quasi-stationary; once formed over the northeastern part of the Arabian Sea it is known to remain nearly stationary for periods of as long as 3 to 7 days;
- (x) Below these disturbances at the surface, a weak trough is frequently noted near the western Ghats in the southwesterly flow;
- (xi) Above the disturbances, at 150 and 100 mb, one does not observe any semblance of a disturbance in the large-scale easterly flow fields, although this may not be true of the divergent part of the total motion field;
- (xii) The vertical structure of the moist static stability shows that the atmosphere below the mid-tropospheric cyclone possesses a high potential for deep convection since it exhibits a very high degree of conditional instability;
- (xiii) At 500 mb the region of the disturbance is fairly moist (relative humidity exceeds 50%). The large moisture contour is found to be advected horizontally from the Bay of Bengal in the upper-level easterlies and vertically from the Arabian Sea in cumulonimbus convection.

Next we shall illustrate some observational features of the mid-tropospheric cyclones. Figure 13.22a is a map of streamlines at 600 mb (dashed lines denote isotachs). This illustrates the mid-tropospheric cyclone from the study of Miller and Keshavamurthy (1968). Figures 13.22b, c and d illustrate vertical cross-sections in a zonal plane across a mid-tropospheric cyclone based on studies of Krishnamurti and Hawkins (1970). The parameters shown in these three diagrams are, respectively, the fields of absolute vorticity, temperature anomaly and vertical velocity.

(b) Dynamical aspects

One is interested in identifying the instability mechanism that might be responsible for the growth of the mid-tropospheric cyclones. A valid instability theory should be capable of describing the length scale, phase speed and structure of the growing wave in accordance with observations. Mak (1975) proposed a modified baroclinic instability theory which incorporates the vertical shear of the basic current in the zonal as well as in the meridional direction. This is called a modified Eady (1949) problem. Mak studied the linear growth in a quasi-geostrophic frame of reference and obtained very realistic results. However, his analysis has been questioned by Carr (1977a) on the grounds that the basic current used in Mak's analysis was too strong and thus not very realistic when compared with observations.

Another instability theory is that proposed by Charney and Eliassen (1964) and Ooyama (1963), which has been reviewed earlier, namely 'CISK', the conditional instability of the second kind. Since there is generally no surface disturbance below these mid-tropospheric cyclones, some authors felt that frictional convergence (which is proportional to the surface relative vorticity for a quasi-geostrophic Ekman theory; see Appendix for notes on this item) would be too weak and could not therefore account for the growth by the CISK process. However, no formal analysis with data sets for this region has yet been carried out.

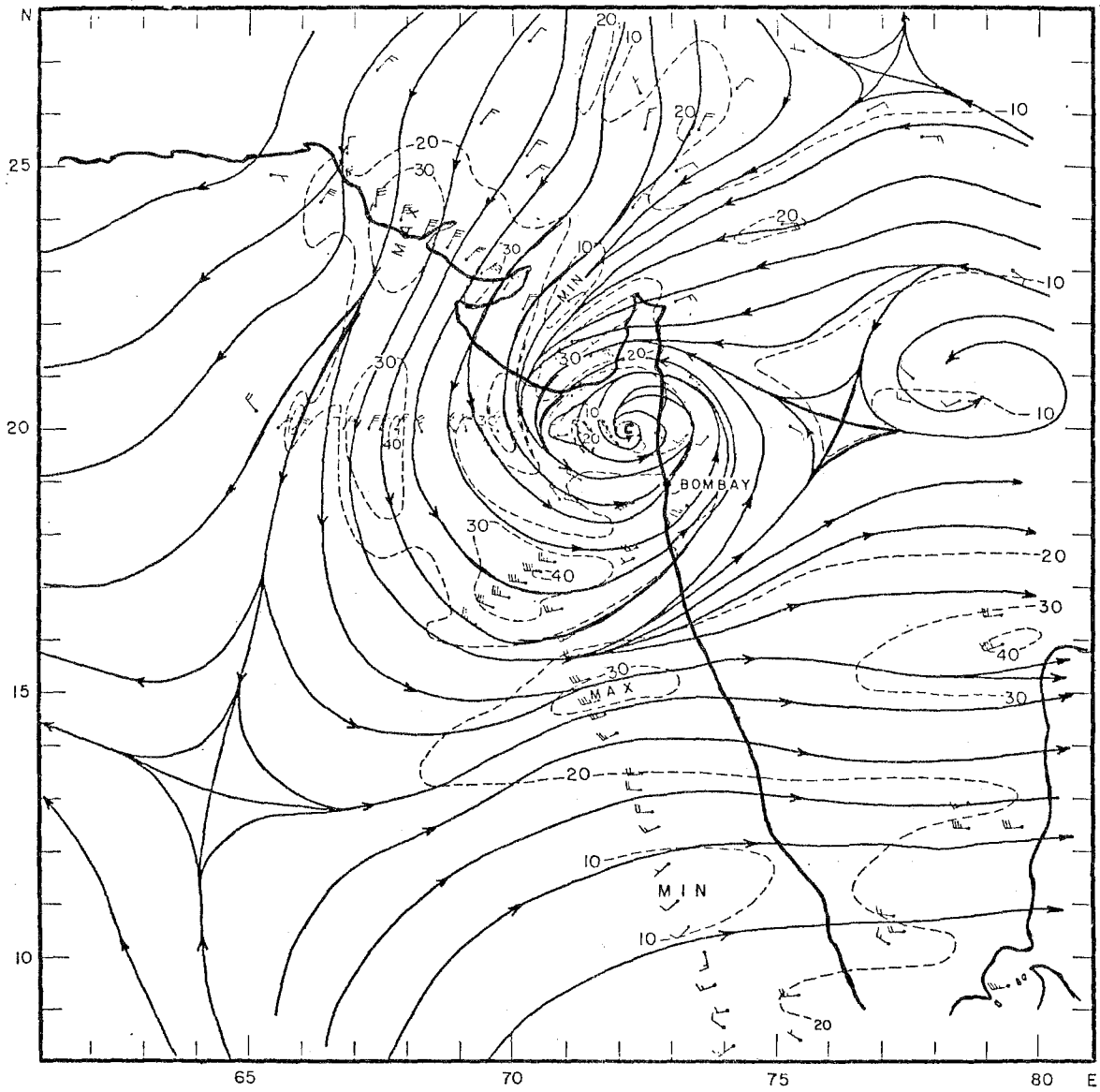
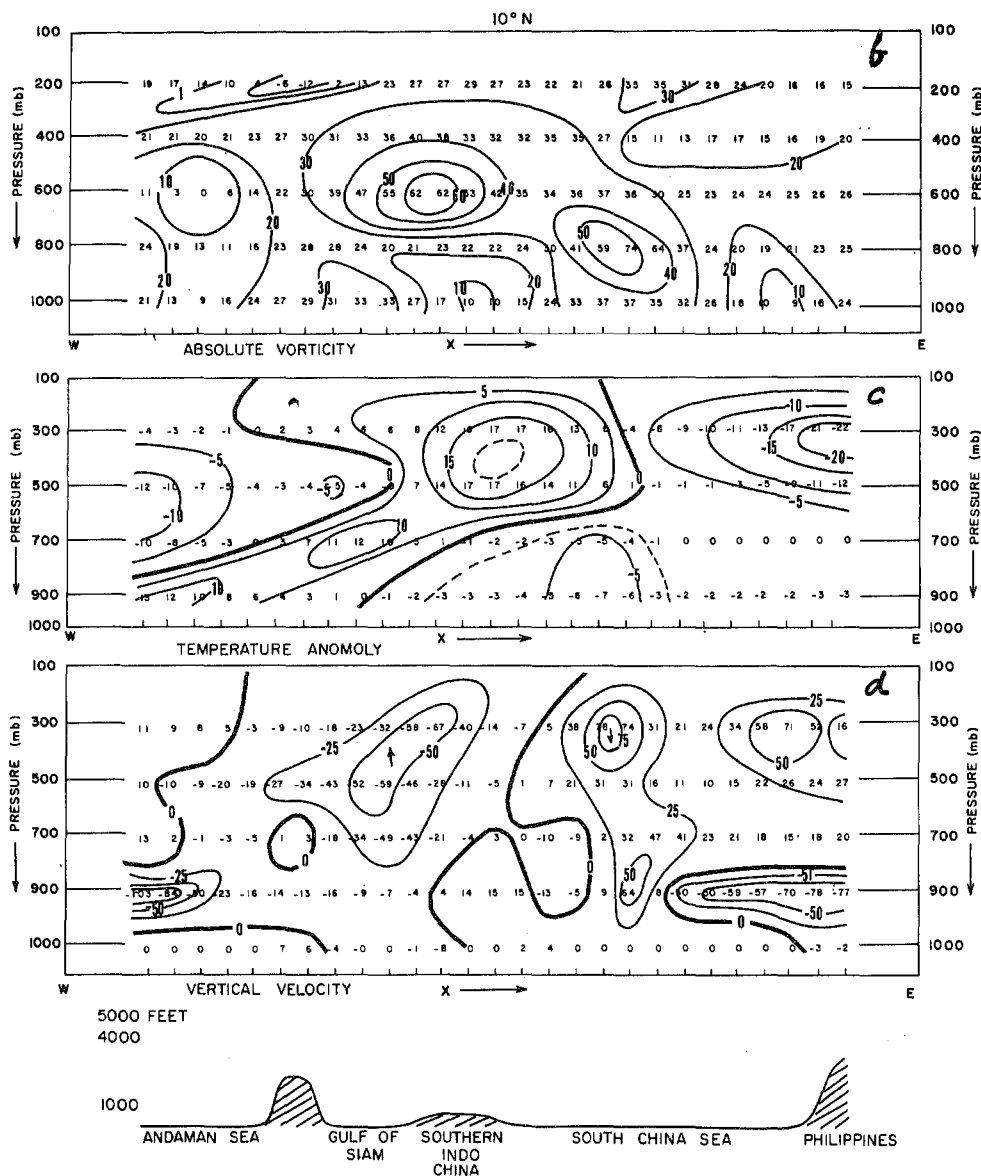


Figure 13.22a - Streamlines at 600 mb illustrating mid-tropospheric cyclone near Bombay (After Miller and Keshavamurthy, 1968)



Figures 13.22b,c,d - Vertical cross-section from west to east at 10°N for 0000 GMT 17 June 1966 through the mid-level cyclone over southern Indochina. Top: isopleths of absolute vorticity (10^{-5} s^{-1}); middle: isopleths of temperature anomaly ($10^{-1} \text{ }^{\circ}\text{C}$); bottom: isopleths of vertical velocity ($10^{-5} \text{ mb s}^{-1}$); A profile of the smoothed terrain is indicated at the bottom of the cross-sections

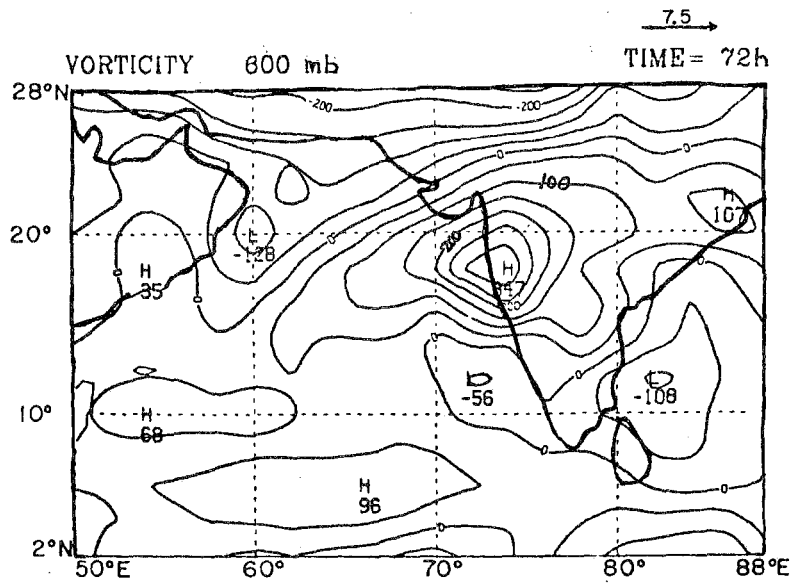


Figure 13.23 - Carr's simulation of the mid-tropospheric cyclone of the southwest monsoons. The field of absolute vorticity at 600 mb at hours 72 of simulation is shown here. (Units $\times 10^{-6} \text{ s}^{-1}$)

(c) Numerical modelling

Carr (1977b) has examined the problem of the maintenance of mid-tropospheric cyclones using controlled numerical experiments. He performed short-range forecasts with real initial data utilizing a multi-level primitive equation model (see Chapter 21). The disturbance was quasi-stationary and Carr was able to demonstrate quasi-stationarity as well as to simulate a very realistic structure of the disturbance. Carr constructed the convective heating profile based on the observed rainfall rate. This meant that his model did not itself determine the heating profile as a function of the evolving large-scale variables (such as wind, temperature, moisture and pressure). Figure 13.23 shows Carr's simulation of the mid-tropospheric absolute vorticity some 72 hours after initial time. This was based on one of his coarse resolution experiments. The maximum value of vorticity is of the order of $0.35 \times 10^{-5} \text{ s}^{-1}$ over western India. Carr's simulation of the structure of the dependent variables of the primitive equation model was extremely realistic and they are among the only available consistent dynamical structures of the mid-tropospheric cyclones. The structure is consistent in the sense that the rainfall rate one would infer from the dynamical structure is made to match the observed rainfall rates. Carr finally used the computed structure to examine the maintenance of the mid-tropospheric cyclones. His analysis shows that the major energy source for the maintenance of the system is the release of latent heat which generates both zonal as well as eddy available potential energy. The eddy kinetic energy of the mid-tropospheric cyclone is maintained by conversion of eddy available potential energy associated with rising of relatively warm air and a sinking of relatively colder air.

The formation of these disturbances is a major unsolved problem. Some of the monsoon depressions that form over the Bay of Bengal are known to propagate westward along roughly 20°N and weaken over the eastern Arabian Sea. A number of these disturbances are known to weaken at the surface while the middle tropospheric part of the circulation stays on as a mid-tropospheric cyclone for several days. This is only one of many ways the mid-tropospheric cyclones are known to form. Some form gradually and do not seem to bear much relationship to westward moving disturbances from the Bay of Bengal. More observations, better theory and better modelling efforts are needed to understand their formation and maintenance.

13.13 Final remarks

In this chapter the summer monsoon disturbances have been emphasized. Not much is known about the phenomena during the northern winter. Our knowledge of synoptic disturbances will improve with the analysis of the wind data from the recently launched geostationary satellites in this region. The references provided in section 13.1 contain a useful background for study of the climatology of this region.

Chapter 14

AFRICAN WEATHER SYSTEMS

14.1 Introduction

The continent of tropical Africa is very large and the lack of adequate observations makes it quite difficult to provide a description of its major weather systems.

There are essentially four sub-regions that one should consider in describing the weather systems over tropical Africa.

- (i) West Africa,
- (ii) The deserts,
- (iii) Somalia and east Africa, and
- (iv) Central Africa.

These four regions are, in fact, meteorologically quite different from each other. We shall begin with a quick review of the monthly mean rainfall over Africa.

14.2 Rainfall distribution

Figure 14.1 illustrates the monthly progression of African rainfall based on the work of Johnson (1975). The northward march of rainfall from winter to summer is somewhat dictated by the position of the sun. This belt of climatological rainfall moves more slowly than the sun. The surface albedo of West and North Africa increases rapidly northwards from 7% to 30%, from the near-equatorial rainy areas to the deserts. The surface albedo has a very strong influence on the meridional march of the rainfall belt during the summer season. Over the desert areas the strong diurnal heating tends to produce (during summer) a shallow heat low. A stable (or near neutral) lapse rate on the large scale is accomplished as a result of strong descent of upper tropospheric air, which we feel is an important aspect of the dynamics of the heat lows. This is accompanied by a tendency for strong drying of the air at lower levels which prevents a northward movement of the rainfall belt beyond roughly 15°N over Africa, since vertical development of clouds is inhibited in the very dry environment. The southward movement during the northern winter takes the rain belt south of 20°S (see January panel) over South Africa. Here the surface albedo is not very large and large-scale heat lows are not found. Although the above climatological picture is a broad overview, it should be recognized that the interannual variability is large and varies from region to region. Figures 14.2a and b show the variability in rainfall totals during July for 1967 and 1972. The latter year was well recognized as the start of the Sahelian drought. The Sahel region is located on the southern boundary of the Sahara Desert and the climatic

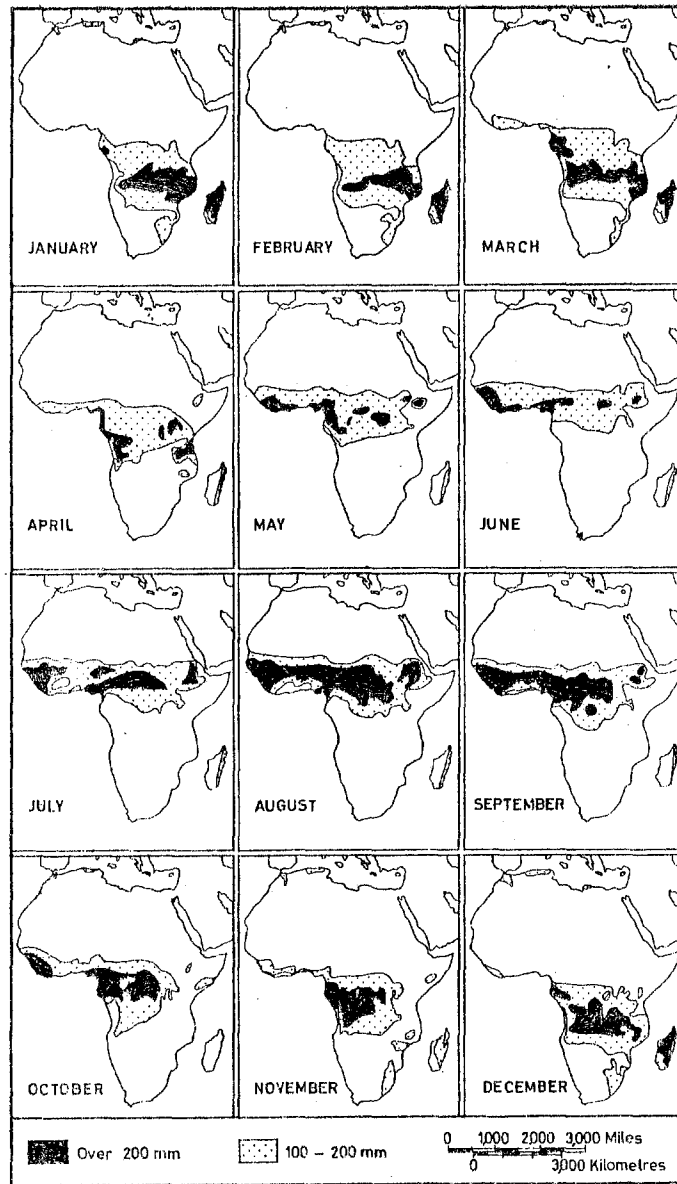


Figure 14.1 - Average monthly rainfall (showing only amounts greater than 100 and 200 mm/month) (After Johnson, 1975)

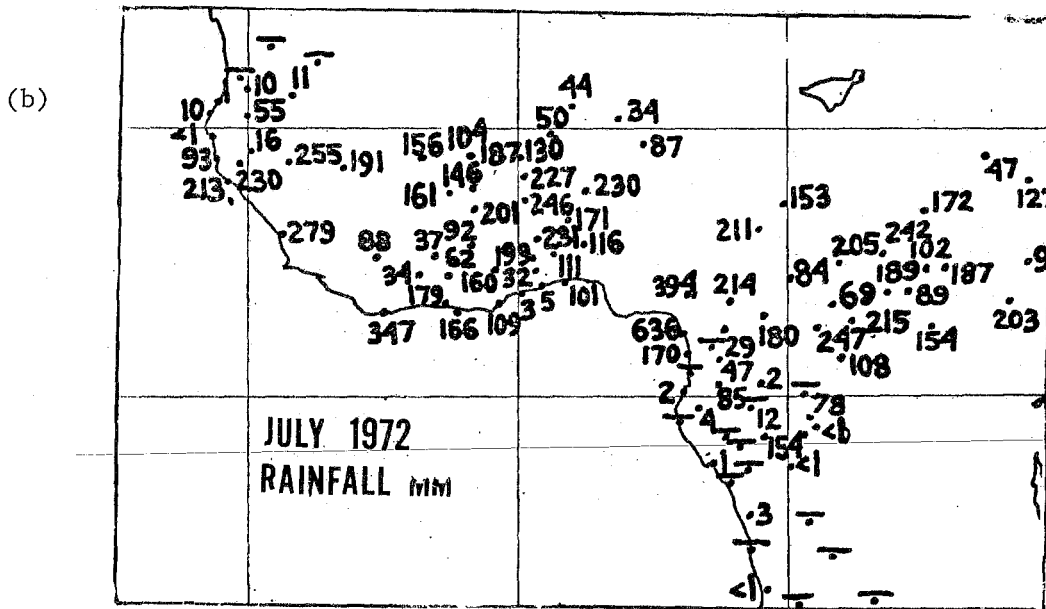
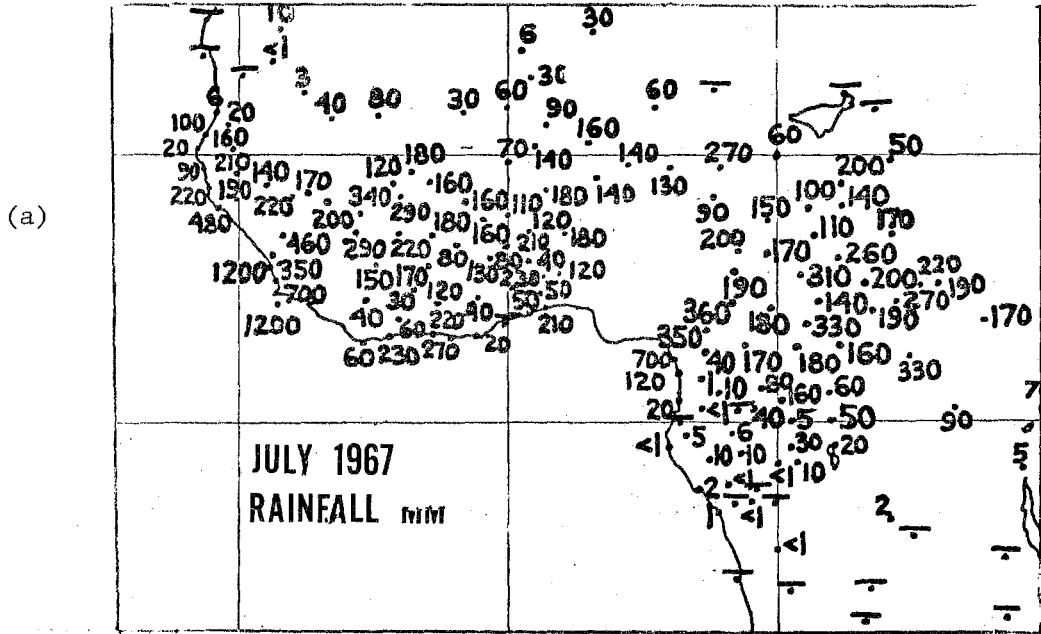


Figure 14.2 - Rainfall totals (mm/month) for July 1967 (a) a normal rainfall year, and (b) for July 1972 (a drought year)

change problem of this region has attracted considerable interest. Some scientists believe that the drought in this region is due to overgrazing of land which changes the surface albedo and results in dry conditions. The major drought of 1972, however, seemed to have occurred on a very large area extending from West Africa to Asia. The long term variability of rainfall at several selected African stations is shown in Figure 14.3. Spectral analysis of east African rainfall, Rodhe and Virji (1976) shows significant peaks in the ranges: 2-2.5 years, 3.5 years and 5-5.5 years over the coastal Tanzania regions, Kilimanjaro regions and Lake Victoria regions respectively. Although such spectral peaks have been noted in other parts of the tropics, their use in accurately predicting the possible occurrence of drought or rainy years has not proved possible.

A large amount of work over West Africa comes from studies conducted at Nigeria and by ASECNA (the Agency for Air Safety in Africa and Madagascar). Obasi (1977) has carried out a spectral analysis of rainfall using 80 years of data over Nigeria. This confirms the presence of 2 to 3 year modes in the rainfall variability.

As the rainfall belt migrates north and south during its annual cycle, the surface winds adjust to the pressure distribution on either side of the Equator. This problem has attracted considerable interest in African countries, especially as a result of the pioneering work of Johnson (1975). Figure 14.4a from Johnson (1975) illustrates the relationship between wind, pressure and rainfall belts during different configurations of the pressure distribution. Johnson and Mörth (1960) first showed these patterns and identified them by names such as duct, drift and bridge, etc. Figures 14.4b, c and d from Johnson and Mörth (1960) show idealized flow patterns for these duct, bridge and drift situations. Real data situations usually are combinations of several of these. Their dynamics is not well understood at present.

14.3 The time-averaged motion field over Africa during the winter and summer months

Here we refer to the analysis of Dean (1975) to show the fields of streamlines and isotachs for February and August, each based on one month's data. Figures 14.5a and b show the mean maps for 850, 700, 500, 300 and 200 mb. During February, we notice an anticyclonic circulation belt over North Africa at 850 mb. The axis of this anticyclonic belt is located at 20°N at 850 mb. A pronounced Equatorward tilt of this axis with height is a main feature of the winter charts. This axis is being found around 4°N at 200 mb. Consistent with this tilt, westerlies increase with height over North Africa and one notes westerly winds of the order of 40 to 50 knots at 200 mb. The easterlies near the West African coast at 850 mb are replaced by westerlies at 500 mb. The variation of wind with height near the Guinea coast is fairly complex; it is southerly at the surface level, backs with height becoming easterly by 800 mb and veers with height between 600 and 500 mb becoming westerly above that level. Over South Africa, the 850 mb temperatures are usually extremely high during the southern summer, and a heat low does exist over the mountainous land mass. The low is located around 18°W and 15°S at 850 mb in Figure 14.5a. The South African heat low is replaced by an anticyclone at upper levels which is well evident at and above 700 mb. The surface heat low is located over the Kalahari Desert. We discuss heat lows in some detail elsewhere in this chapter with reference to the North African desert heat lows. The student will find some parallels between North and South Africa in these phenomena.

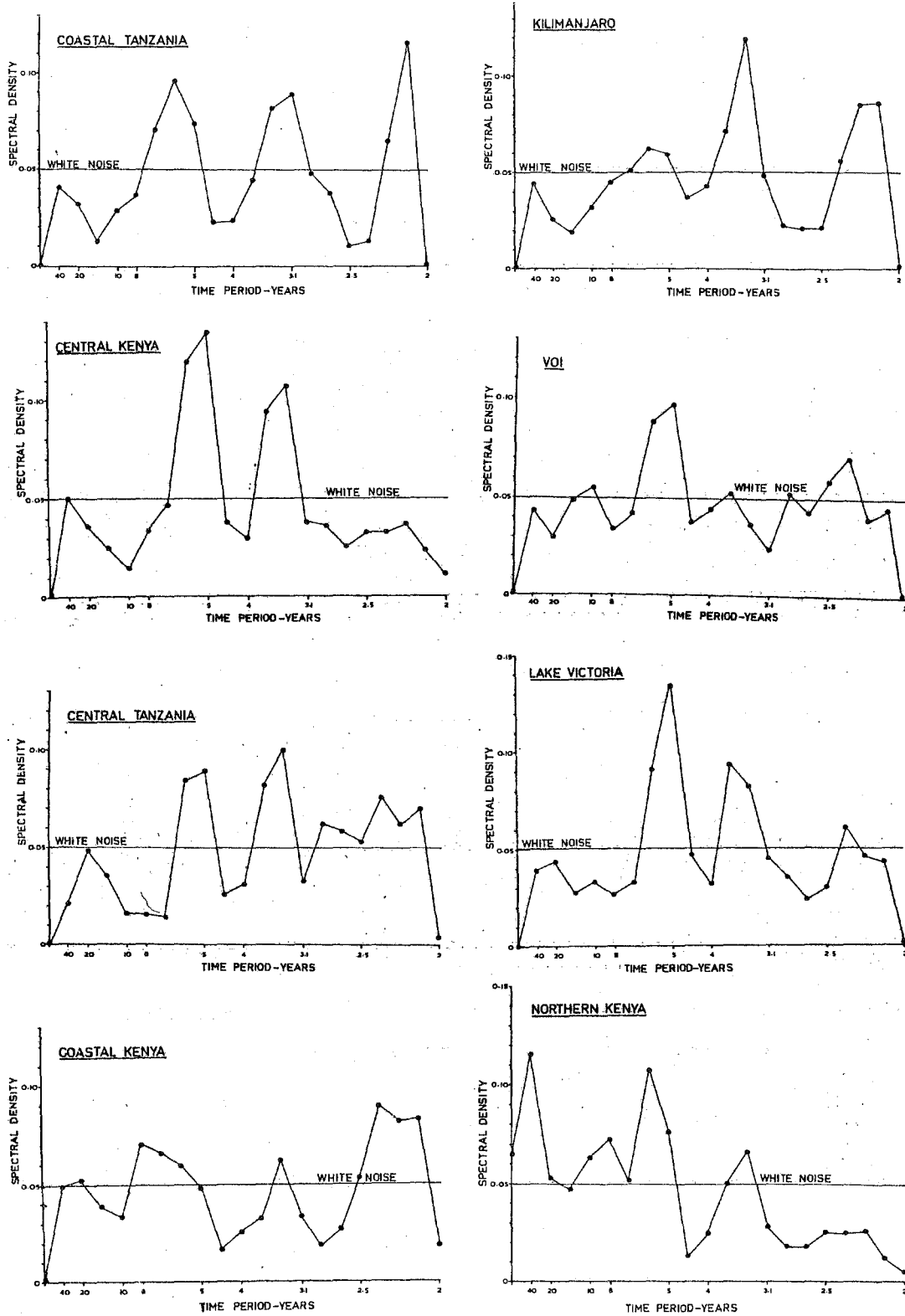


Figure 14.3 - Spectral analysis of rainfall over east Africa at selected stations (After Rodhe and Virji, 1976)

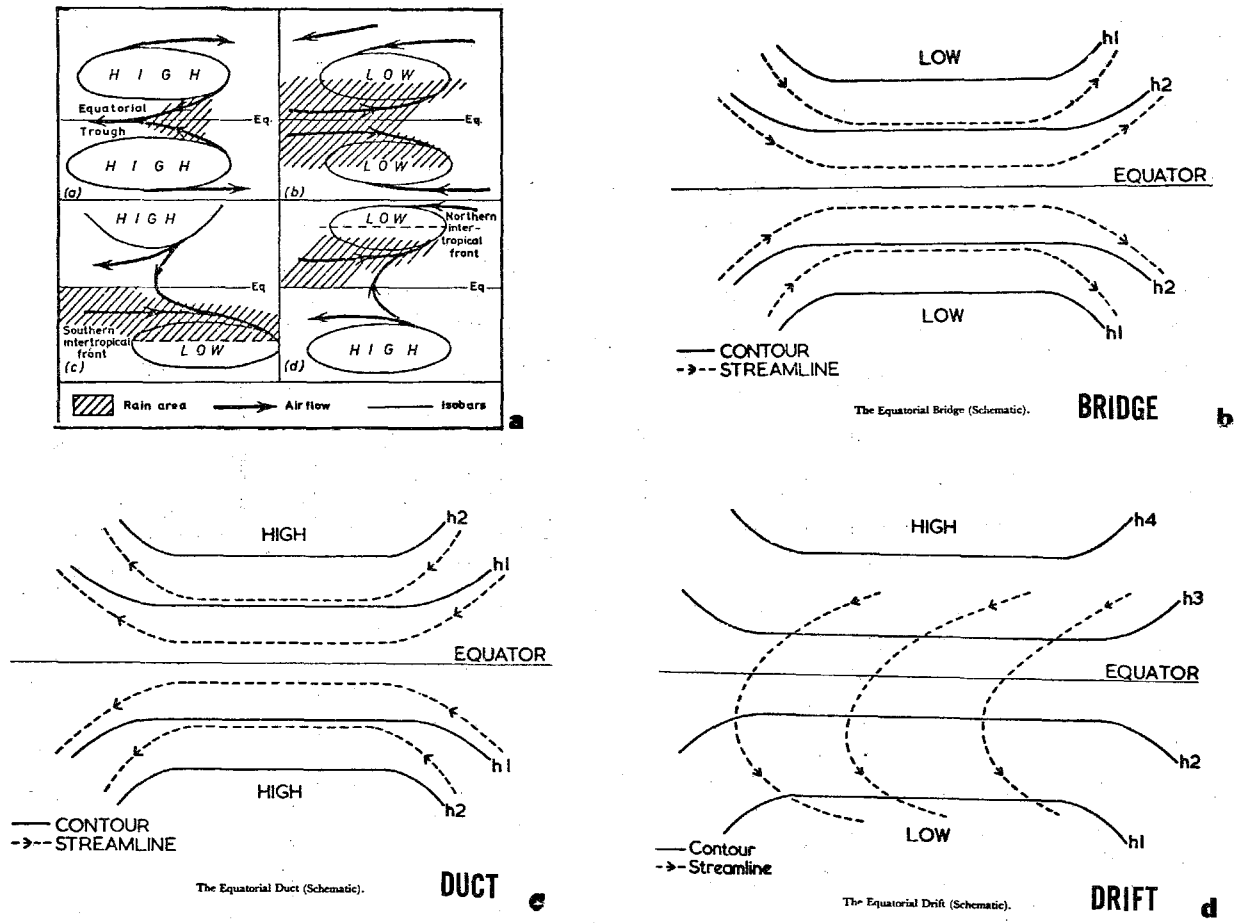


Figure 14.4 — Schematic pressure, wind and rainfall relationship over the equatorial belt of Africa during different times of the year (From Johnson, 1975)
 (b,c,d) Schematic pressure-wind relationships for idealized bridge, duct and drift geometries (based on Johnson and Mörth, 1960)

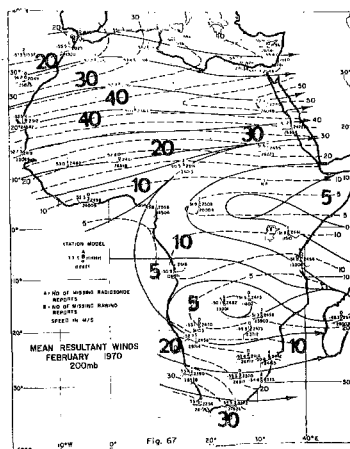
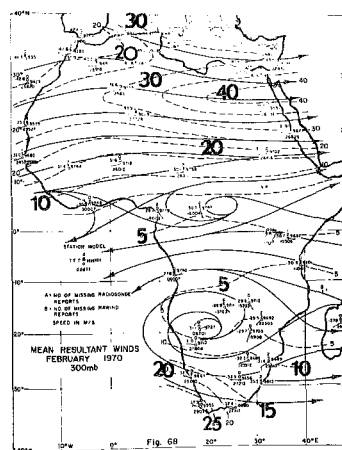
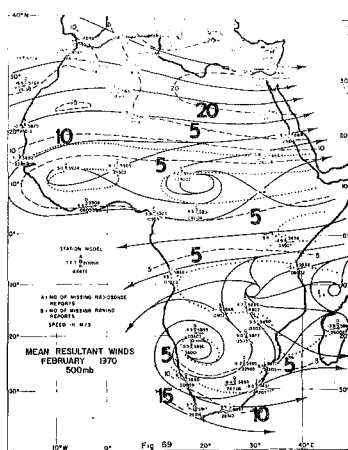
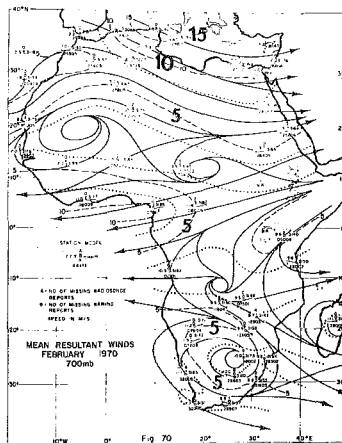
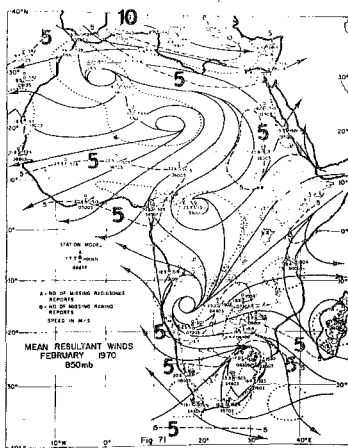


Figure 14.5a - Mean streamlines and isotachs ($m s^{-1}$) for February at 850, 700, 500, 300, 200 mb, based on Dean (1972)

The corresponding northern summer charts for August are shown in Figure 14.5b. They show at all levels the North African anticyclone above the Sahara heat low (at the surface not shown). The axis of this anticyclone tilts from 30°N at 850 mb to 25°N at 200 mb. The lower easterly jet at 700 mb near 15°N has a speed of around 15 m s^{-1} and the upper easterly jet indicated at 200 mb over the Guinea coast has a speed of around 20 m s^{-1} . The upper levels between 20°N and 10°S are usually characterized by a broad belt of easterlies.

14.4 The time-averaged temperature field over Africa during the winter and summer months

Figure 14.6 from Dean (1972) shows the winter season temperature field at 850, 700, 500, 300 and 200 mb. The belt of highest temperature over North Africa tilts equatorward from 12°N to 5°N as we go up from 850 mb to 200 mb. The meridional temperature gradient is quite large near the Mediterranean coast where the strongest winds associated with the subtropical jet are found at this time of the year. The warm Kalahari Desert area over South Africa at 850 mb is very striking in this diagram. In fact, the temperatures during January over this region are higher at 850 mb than those found over the Sahara Desert. The high temperature anomaly extends all the way up to 200 mb in the upper dynamic anticyclone over this region. The isothermal fields for northern summer from Dean (1972) are shown in Figure 14.6. Here the high temperatures around 30°C over the Sahara Desert and the baroclinic zone to its south are major features. This baroclinic zone becomes extremely weak at 15°N as one proceeds upwards to about 500 mb; however, one can trace an Equatorward tilt of the major thermal system and the associated thermal gradients. The major feature over South Africa during the southern winter is the gradual build-up of the thermal gradient which is strongest at 300 mb in association with the westerly subtropical jet stream of southern winter located near 25°S .

14.5 Surface-flow patterns over Africa (based on Dhonneur (1974))

Figure 14.7 shows the annual progression of the monthly mean streamlines over Africa as given by Dhonneur (1974). The heavy line separates different flow régimes. It is of interest to note that southerly flows cross the Equator northward into West Africa during all months of the year. Although this separation line stays north of the Equator over West Africa, its behaviour over east Africa is much influenced by the Asian monsoons. During the period of the winter monsoon, i.e. of northerly flows over east Africa between October and March, the wind separation line moves south of the Equator. The ITCZ over the Atlantic ocean as well as this wind separation line over West Africa stay north of the Equator all year long. Over the Indian Ocean the ITCZ moves from the southern hemisphere (around 15°S) to the northern hemisphere (around 20°N) between January and July. Thus east Africa encounters the largest meridional movement of this wind separation line. The double dashed line in these diagrams is another major wind separation which also exhibits humidity contrasts. The position of these lines migrates considerably with the season, staying for several months of the year (except May, June, July, August and September) close to the migrating rainfall belt shown in Figure 14.1.

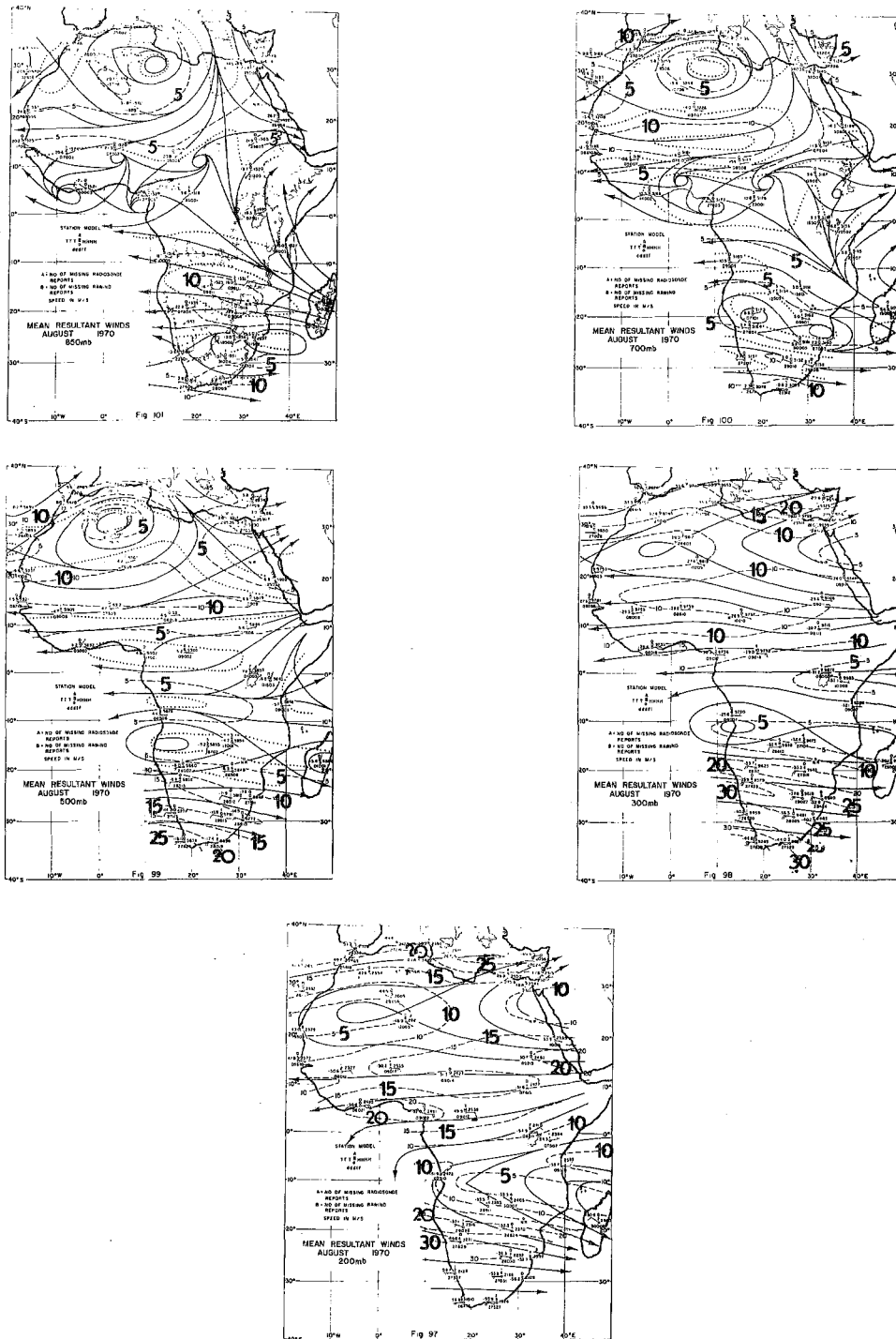


Figure 14.5b — Mean streamlines and isotachs ($m s^{-1}$) for August at 850, 700, 500, 300 and 200 mb, based on Dean (1972)

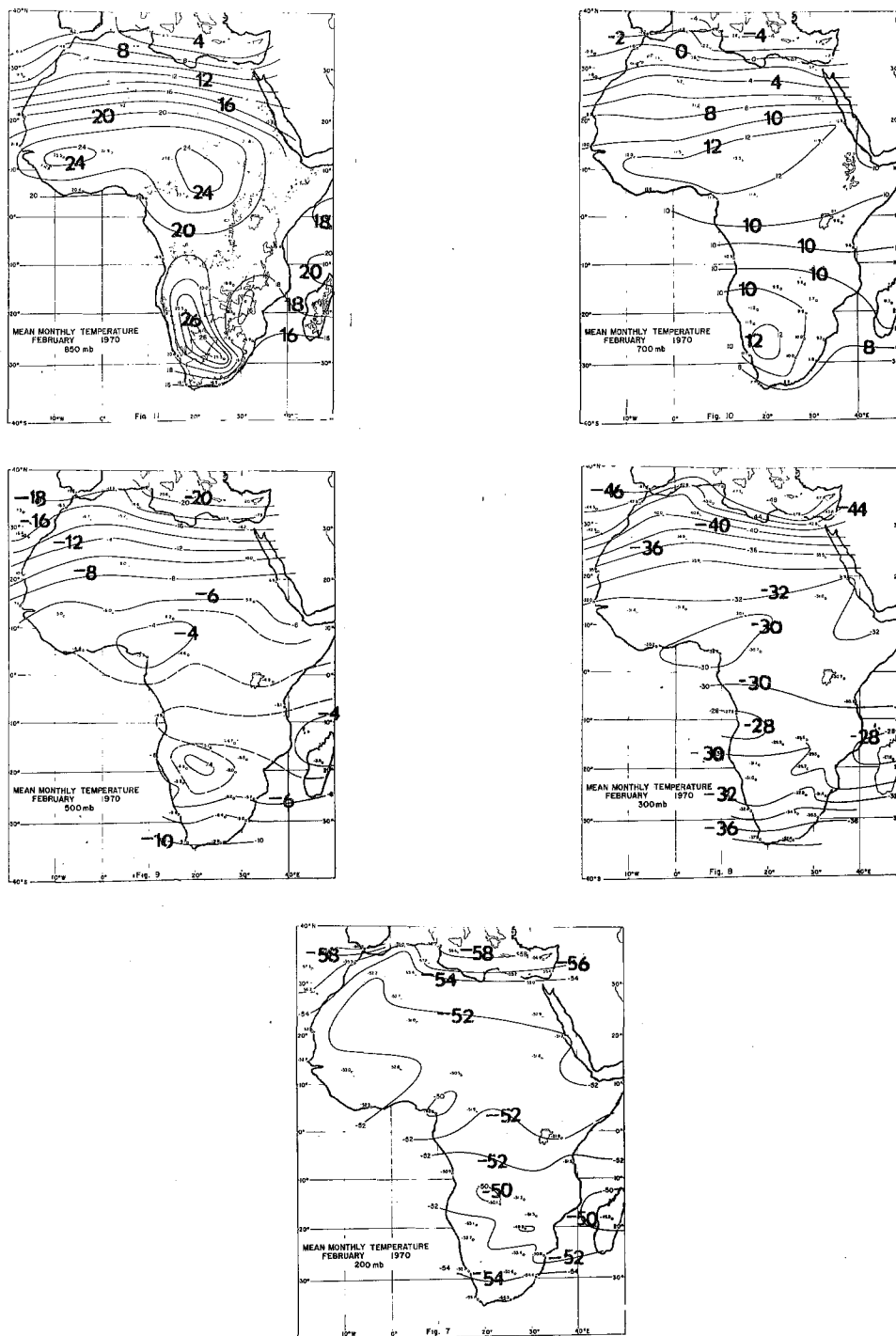


Figure 14.6a - Monthly mean temperature (°C) during February at 850, 700, 500, 300 and 200 mb (from Dean, 1972)

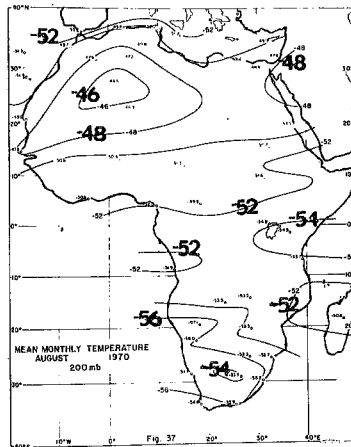
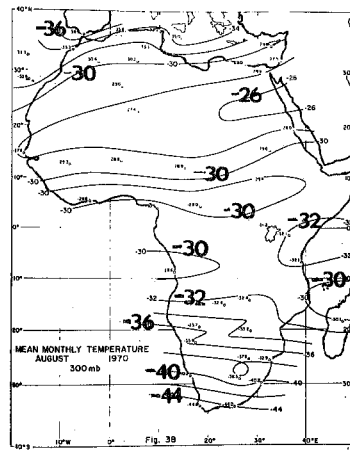
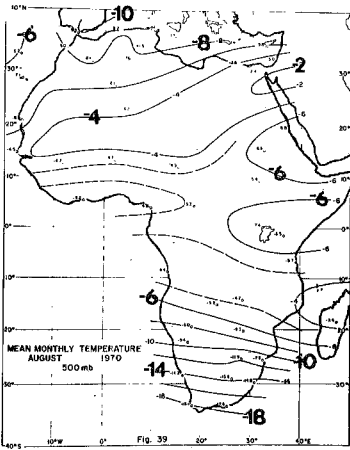
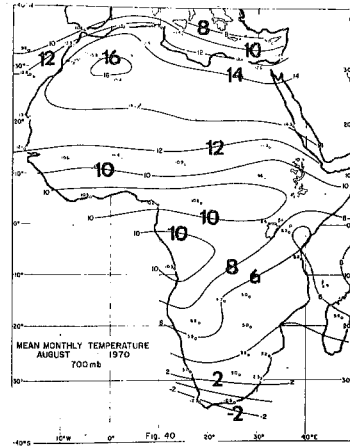
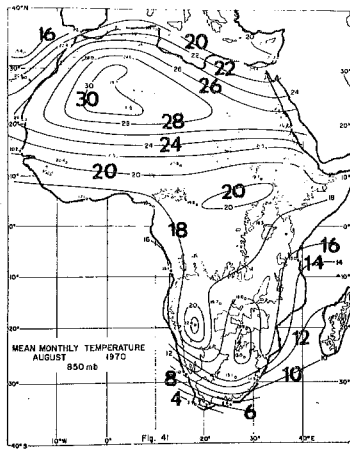


Figure 14.6b - Monthly mean temperature ($^{\circ}\text{C}$) during August at 850, 700, 300 and 200 mb (from Dean, 1972)

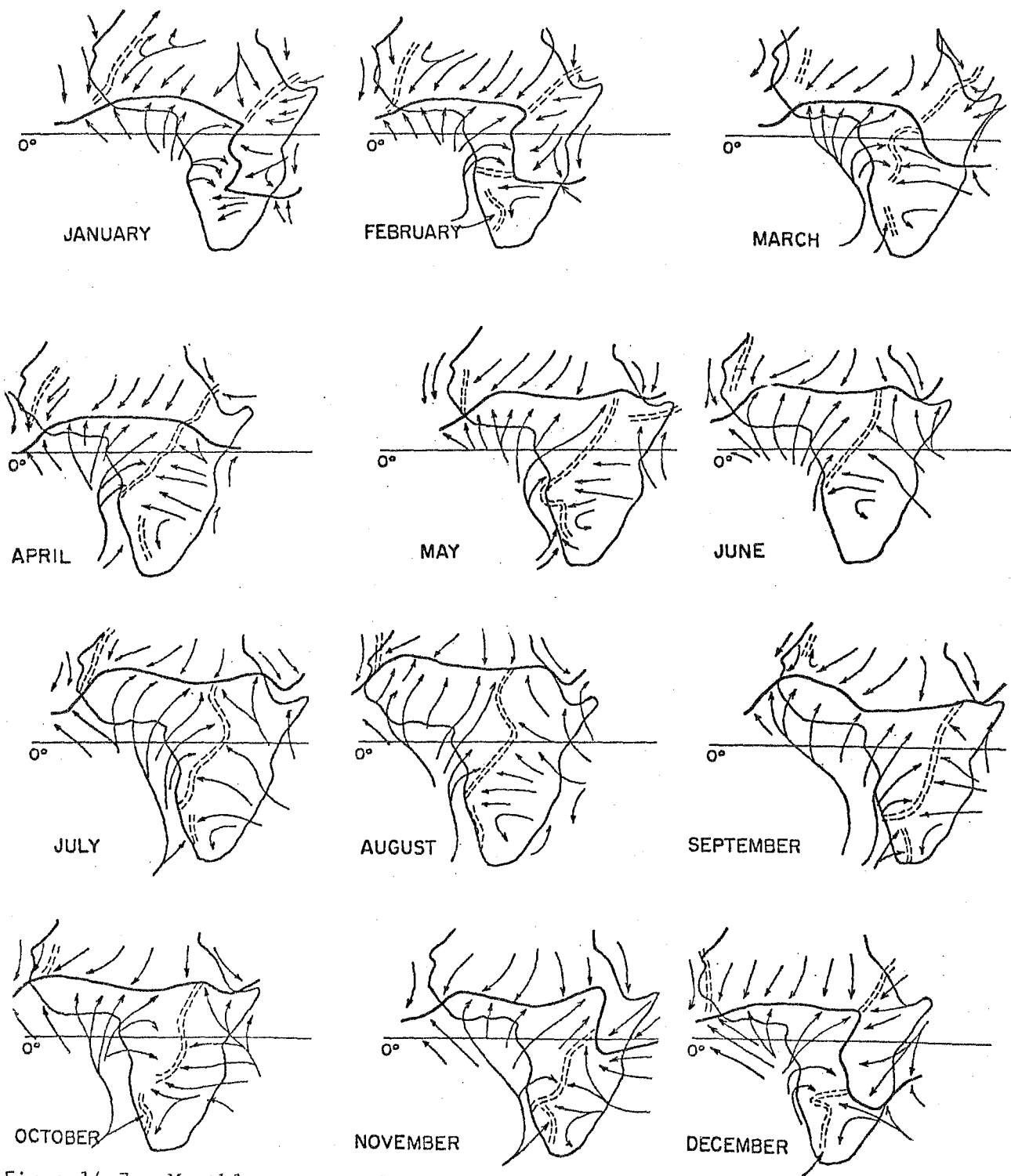


Figure 14.7 - Monthly mean surface streamlines over the surface based on Dhonneur (1974). Heavy and dashed lines indicate wind separation lines

14.5.1 Vertical slope of the pressure system

During northern summer the surface pressure trough over India and Africa occurs quite far north (compared to its position over the Atlantic and Pacific Oceans). This pressure trough has a very pronounced Equatorward slope with height, roughly 6 km/15° latitude. Figure 14.8 illustrates the trough line at surface, 850, 700 and 500 mb during July based on the study of Dhonneur (1974). Further refinements based on more recent data are necessary to construct such diagrams. However, the essential features are most probably correct.

14.6 Some climatological aspects of the Sahara Desert

In the section on radiative processes we discussed some aspects of the heat balance of the deserts. The surface climatology of the desert area is extremely important for the understanding of subtropical droughts. A few diagrams, Figure 14.9, illustrate the following (taken from Climate of Africa, Griffiths, 1972):

- (i) The extreme maximum surface air temperature is in °C. It shows that the air temperature gets as high as 55°C over the Sahara Desert. It should be noted that the soil temperature has been observed to be as high as 70°C in these same regions;
- (ii) The highest air temperatures move northwards between April and July. Near the West African coast the highest air temperatures are realized even later. The relative humidity shows a marked diurnal change. Near the West African coast the early morning values approach an uncomfortable 90% while during the afternoon hours drop down to near 65%. Over the Sahara the relative humidity fluctuates between 20 and 40% between 1300 hours and 0700 hours GMT;
- (iii) Figure 14.9 also shows a field of 'piche' evaporation for the month of June. These are the values of surface evaporation that would be realized from a pan if sufficient water were available. A parameter called "ground wetness" which takes into account the soil moisture would provide a better measure of true evaporation— which should be negligible over the deserts. A diagram of the surface network of meteorological observing sites over West Africa is also shown here. Although plenty of observations of different parameters are available, not many of these are used or properly archived.

14.7 Heat lows over the African deserts

The dynamics of the heat lows is intimately related to the understanding of the role of the deserts of Africa. In the chapter on radiation we showed the following interesting aspects of the radiative heat balance of this region. The desert region has a high albedo of the order of 30%; the heat balance of the Earth's atmosphere system, at the top of the atmosphere, as measured at satellite altitude,

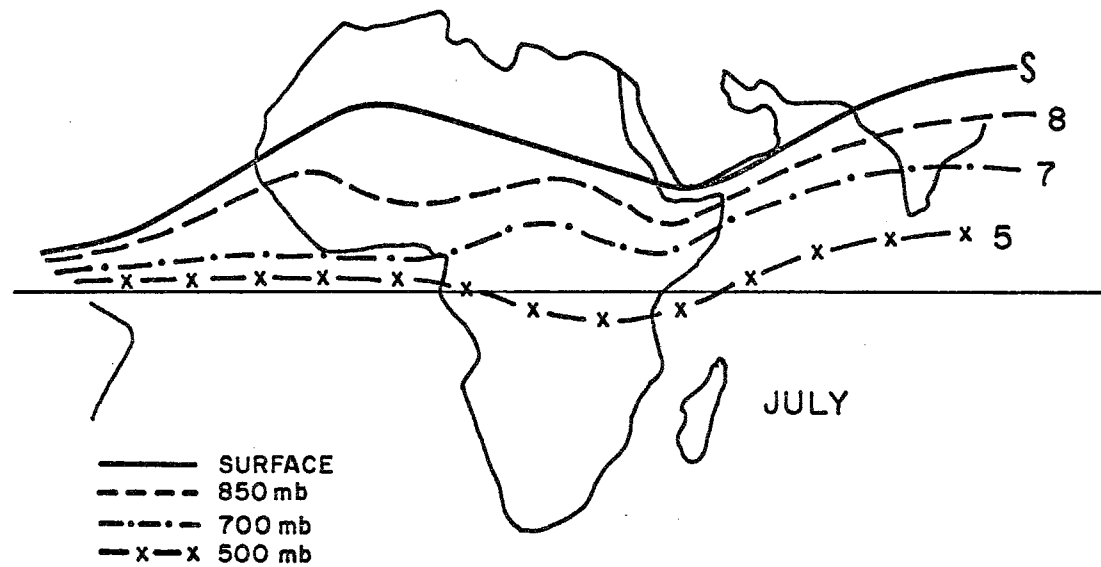
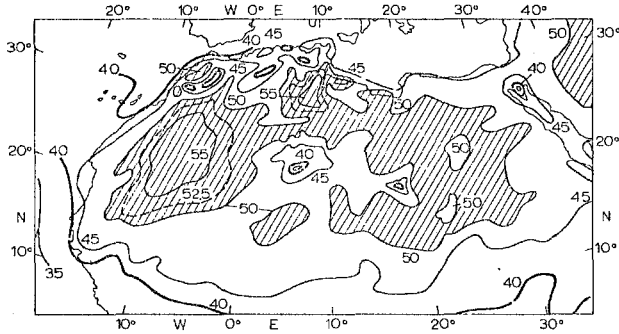
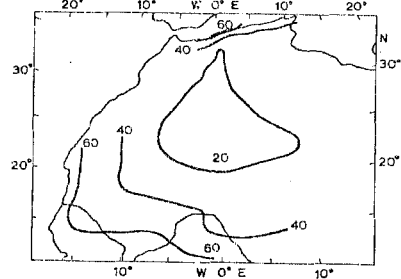


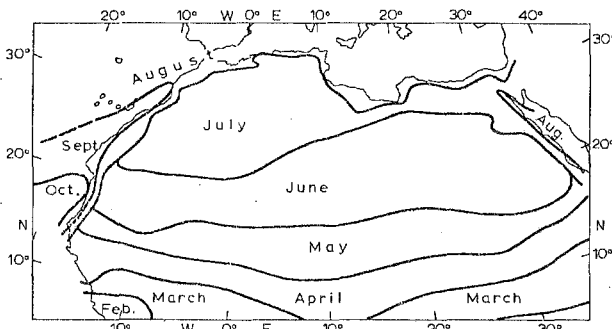
Figure 14.8 - Pressure trough line at surface, 850, 700 and 500 mb during July showing the pronounced Equatorward slope with height. (After Dhonneur, 1974.)



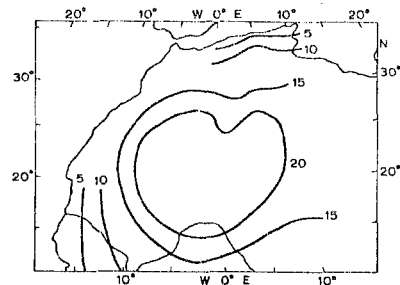
Extreme maximum temperature (°C), 1926-1950.



Mean relative humidity (%) at 13h00 G M T



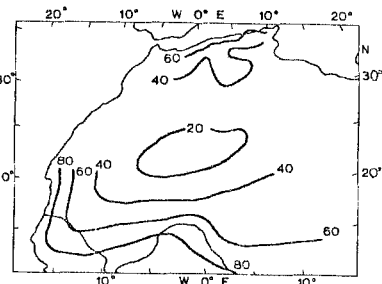
Month of highest monthly maximum temperature.



Mean "Piche" evaporation, June (mm/day).



Station locations in the northern desert.



Mean relative humidity (%) at 07h00 G M T

Figure 14.9 - Selected diagrams of surface climatology over West Africa during northern summer (After Griffiths, 1972)

shows that this region is an anomalous heat sink for these subtropical latitudes. Here, the net outgoing radiation exceeds the net incoming radiation. Tropospheric layers experience a net divergence of radiative flux. On the large scale there is a balance between the diabatic and adiabatic atmospheric temperature changes. As a consequence, one finds descent and drying of air on the large scale in the troposphere over this region. Near the surface, however, one notes a strong warming of air due to the large fluxes of long-wave radiation, reflected short-wave radiation and sensible heat flux from the Earth's surface during the day-time hours. Descending motion at the higher levels may be thought of as a dynamic response of the upper troposphere to this intense heating near the surface. The adiabatic warming of the descending air and dry convection near the ground provides a continuity of lapse rate (a stable lapse rate) in the vertical which is an essential adjustment that the atmosphere undergoes on the large scale. The heat low is a very shallow (in the vertical) feature of the atmosphere. There is large-scale ascending motion of the warm air in this lower atmosphere. The compensating descent evidently occurs between the heat low and the near-equatorial rainbelt around 5°N during the northern summer months. There is also a possibility that the descent occurs selectively in the preferred regions of West African disturbances that move westwards. The heat low thus shows a coupling with the westward propagating disturbances. The descending motion calls for an upper tropospheric convergence; on the other hand, the warm tropospheric columns call for an upper anticyclone. This is, in fact, observed over West Africa during northern summer; see Figure 14.5b. The upper anticyclone is a dynamic anticyclone which is characterized by descent and convergence and is most likely maintained by lateral input of anticyclonic relative vorticity in the upper troposphere. This lateral input can come from the Asian monsoon region where the poleward side of the tropical easterly jet contains large amounts of anticyclonic relative vorticity. This is steadily advected downstream, i.e. westwards over West Africa. Thus it appears that an understanding of the three-dimensional dynamics of the atmosphere over West Africa requires an understanding of the coupling of this region with the Asian monsoons to the east. If the coupling at the upper levels is weak, then it would be difficult to maintain an upper anticyclone over the deserts dynamically and the heat low would most likely have anomalous characteristics in such situations. Although heat lows exist in many parts of the world, similar upper level features are generally noted to exist over most of them. Figure 14.10 shows a schematic meridional cross-section of the vertical circulation over this region near the Greenwich meridian. The heat low produces an anomaly in an otherwise conventional pattern of ascent near 5°N and descent near 35°N ; the heat low induces additional local meridional cells over the desert around 20°N in the lower troposphere. The schematic diagram places the following phenomena in their (plausible) perspective:

- (i) Heat low;
- (ii) Major rain belt;
- (iii) Upper easterly jet; and
- (iv) Lower easterly jet.

The diagram shown here has a southerly flow that extends across the Equator all the way to the heat low at 20°N ; however, the major convergence and ascent are shown to occur near the major rain belt near 6°N . Speed convergence rather than directional convergence is more important at the surface level. The surface air undergoes strong mixing with the descending warm dry air as it moves northward towards the heat low.

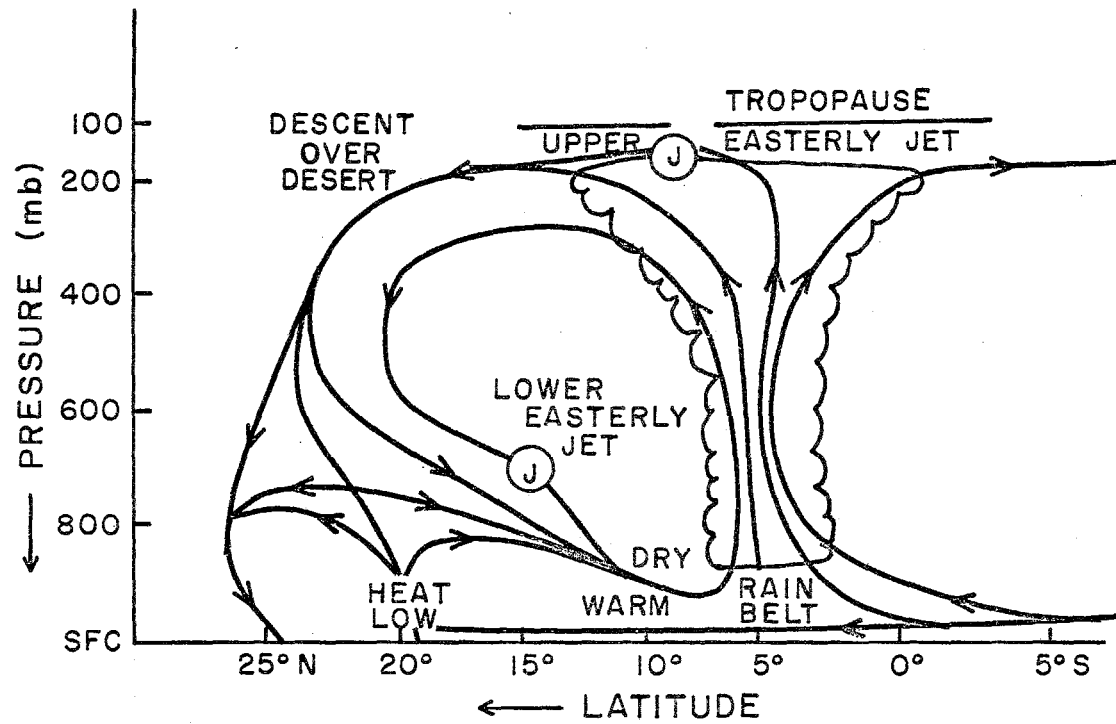


Figure 14.10.— Schematic vertical circulation in a meridional plane over West Africa

The schematic picture of the local Hadley cell is somewhat complex, primarily due to the distortion produced by the heat low over the desert.

The dynamics of the heat low deserves detailed investigations. The African monsoons, the Asian monsoons and the thermodynamics of the deserts are all interrelated and the ultimate understanding of the Sahara heat low during the summer months will only be possible when the interrelations of all of these phenomena are understood.

14.8 West African wave disturbances

In the broad survey of tropical zonal asymmetry in Chapter 3, we have already discussed the structure of African wave disturbances and hence we shall not repeat this here. Here we shall present a brief account of the dynamics of these disturbances. The West African wave disturbances are known to pass westwards over the region of strong meridional temperature gradient near 13°N (i.e., just south of the warm Saharan belt). This region is characterized by a strong horizontal as well as vertical wind shear (see Figure 14.5b). It was shown by Burpee (1972) that these shears are sufficiently large that they satisfy the necessary conditions for the existence of combined barotropic/baroclinic instability (see mathematical Appendix). A wave of the typical horizontal scale of a few thousand km is maintained by drawing energy both from the horizontal and the vertical shears of the environmental flows over this region. Burpee carried out calculations of the co-variances of the zonal and the meridional wind ($\overline{u'v'}$) and of temperature and meridional wind ($\overline{T'v'}$) at several West African weather stations. He noted that the time-average value ($\overline{u'v'}$) of the flux of westerly momentum was directed towards the low-level African easterly jet. This would tend to weaken the lower-level West African easterly jet and thus give rise to an energy exchange from the zonal kinetic energy K_Z to the eddy kinetic energy, K_E which may be expressed as:

$$\langle K_Z \cdot K_E \rangle = \bar{u} \frac{\partial}{\partial y} \overline{u'v'}$$

Here $\bar{u} < 0$ and $\frac{\partial}{\partial y} \overline{u'v'} < 0$. This relates to the barotropic energy exchange. Burpee furthermore noted that $\overline{v'T'} < 0$, i.e., sensible heat is transported equatorward, and $\frac{\partial \bar{T}}{\partial y} > 0$, i.e., mean temperature increases northwards. This down-the-gradient heat transfer is consistent with properties of baroclinic waves; thus the African wave is thought to be maintained from horizontal and vertical shear.

With the coming of the GATE data, much further progress has been made in observational compositing of West African disturbances. Aside from the distributions of the horizontal motion, temperature and moisture, it has been noted that ascent and clouds and rain tend to occur to the west of the trough line. This was noted by Pedgley and Krishnamurti (1976) and Reed et al., (1977). This region ahead of the wave trough is moist with relative humidities around 70 to 80% in the subcloud layer; however, the upper troposphere over this region tends to be very dry. We shall discuss this region, where severe weather is frequently encountered, in the next section.

14.9 West African disturbance lines

Squall lines are known to propagate westwards from the Sudan area towards the west coast of West Africa during the northern summer months (Hamilton and Archbold, 1945; Eldridge, 1957; and Obasi, 1974).

Roughly 7 disturbances are known to propagate westward during each month. From time-sections of surface and upper-air data, Obasi (1974) has constructed some interesting west to east cross-sections relevant to their passage across Lagos (Nigeria). Figure 14.11 from Obasi (1974) illustrates the variations, from west to east, of surface temperature, relative humidity, pressure and the 900 mb relative humidity. Prior to a squall line passage, surface temperature and the 900 mb humidity show larger than normal values, reflecting larger values of θ_e near the ground and conditional instability. A pressure rise somewhat analogous to a pressure jump is found just after the temperature drops. The latter is used here as a reference to define the local passage of the disturbance line.

14.9.1 Squall lines "An Integral Part of the African Wave"

A recent study by Reed et al., (1977) and by their associates, Payne and McGarry (1977), provides an entirely new picture of the West African squall line. The idea is roughly as follows.

Although a squall line may move faster than the westward propagating African wave disturbance, they note that the squall line is most active just to the west of the trough line. They, in fact, identify a beginning of a squall and an active squall at different distances west of the wave trough. Figure 14.12 from their study shows that the frequency of occurrence of cloud clusters as well as squall is largest in categories 2 to 4, which are located roughly 300 km to the west of the trough line. These results are obtained by compositing a large number of episodes with reference to a trough line identified by category 4.

This study does raise the question as to whether squall lines ever go past African waves without any significant interactions and the answer is that some of them probably do. An important question that needs to be addressed here is "Why is the region ahead of the trough line preferred for the development of squall lines?" The answer to that must lie in the configuration of moist static stability and the vertical distribution of the horizontal wind. The moist southwesterly monsoonal low-level flows are capped by dry east north-easterlies ahead of the trough line. The mid-tropospheric easterly jet at 600 mb and the moist southwesterly monsoonal current provide conditions quite similar to those encountered in the continental United States (see Petterssen, 1956). Thus there may be some measure of similarity between the tropical and the extratropical squall systems.

14.9.2 Other squall line models

From an analysis of GATE data, Mower (1977) (Fig. 14.13) suggests the following schematic outline of a squall line over the eastern Atlantic ocean. This may be thought of as the structure of a West African squall line after it crosses over to the oceanic region. Mower notes the following features:

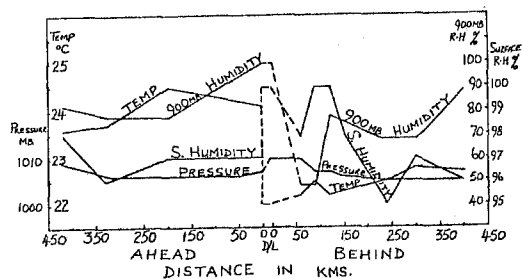


Figure 14.11 - West to east cross-section across a model disturbance line showing the surface temperature, relative humidity and pressure. Also shown is the 900 mb relative humidity (After Obasi, 1974)

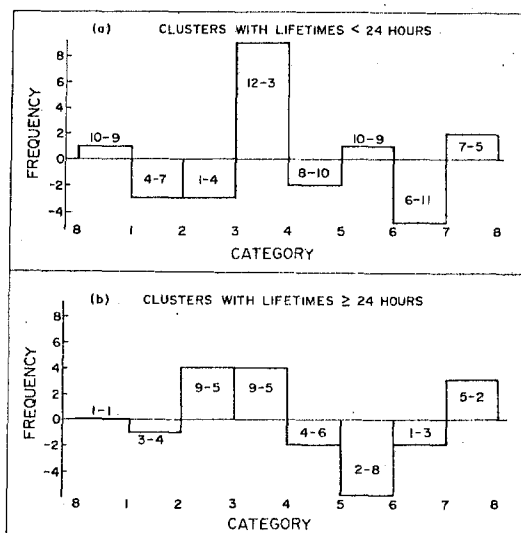


Figure 14.12 - Frequency distribution of the excess (positive ordinate values) or deficit (negative ordinate values) of cluster genesis over cluster decay by wave phase category for clusters (a) with lifetimes <24 h and (b) with lifetimes ≥24 h (After Payne and McGarry, 1977)

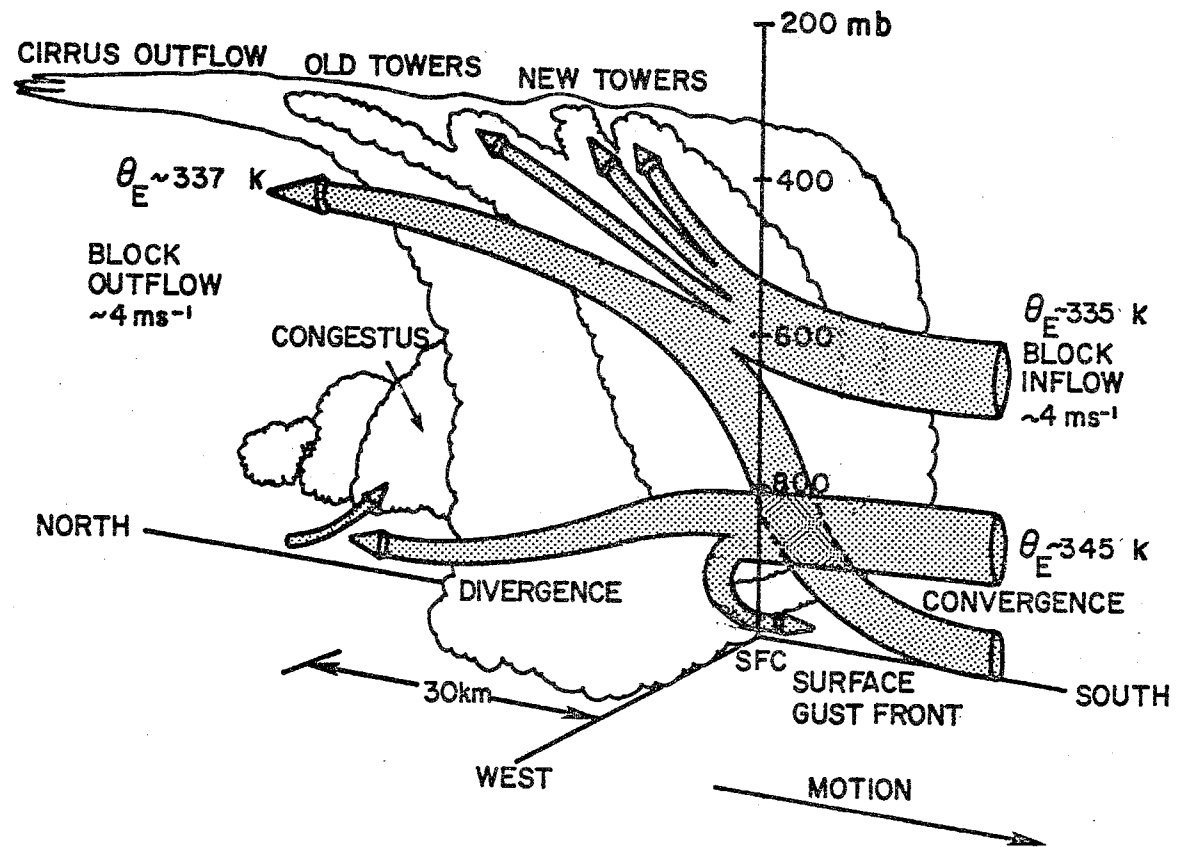


Figure 14.13 — Schematic of stream tubes and characteristics of this line of convection

- (a) Sharp convergence of high θ_e air at the "leading" edge of the lines (10^{-3} s^{-1});
- (b) Strong divergence of slightly smaller magnitude to the rear;
- (c) Large drop in θ_e indicating the presence of a downdraft at the surface with its origins in the 900-800 mb layer;
- (d) Cooling at the surface after the line passage of 1.5 K (small);
- (e) Small, but sharp, pressure drop with a large decrease in incoming solar radiation, together with a lowering of cloud base.

The wind profiles showed:

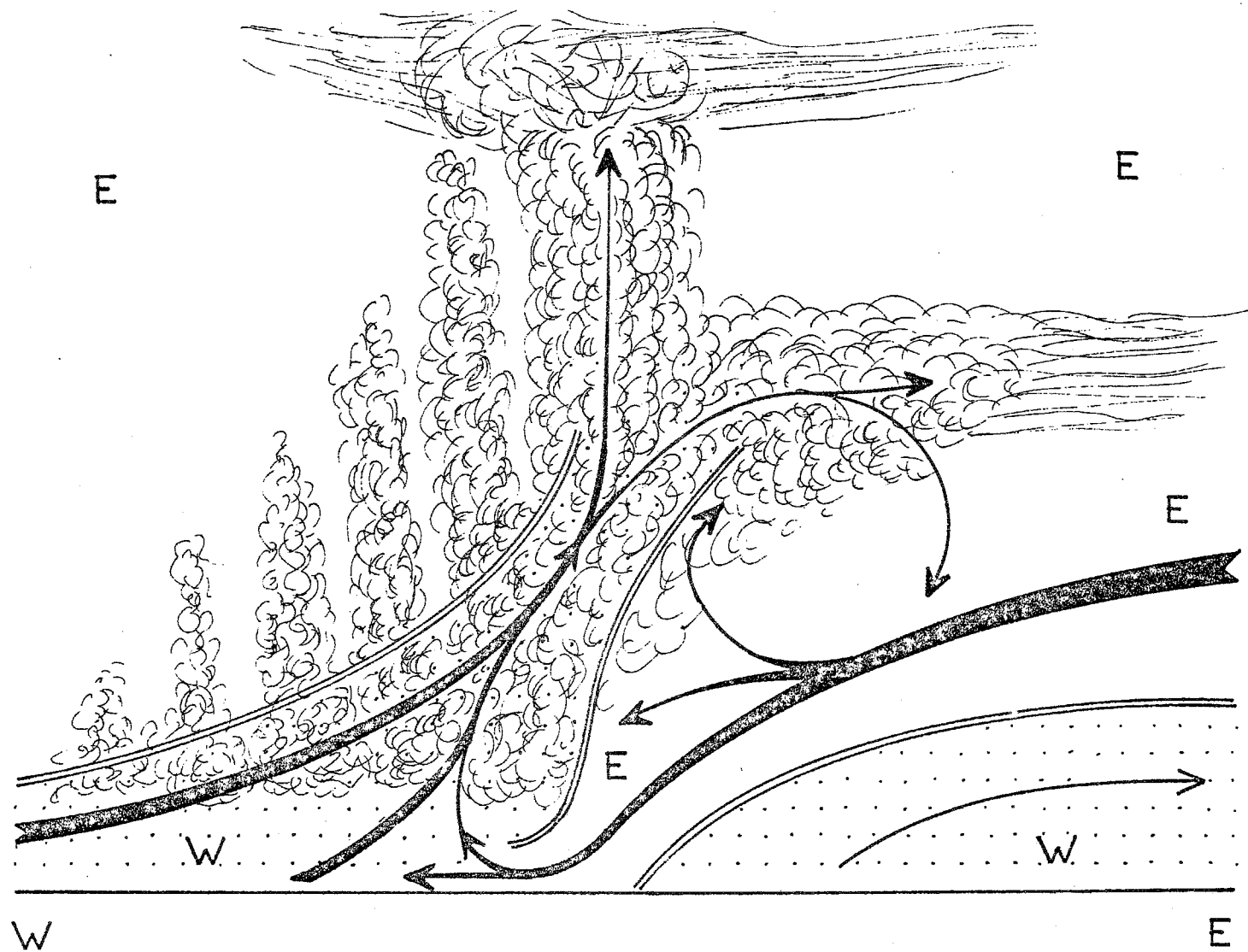
- (a) Surface westerlies ahead of the line;
- (b) Very little vertical shear in both wind components;
- (c) No observable steering level;
- (d) Lines are embedded in a larger-scale motion field which is convergent and cyclonic from the surface to 700 mb.

The thermodynamic profiles showed:

- (e) Drying in the lowest 50 mb resulting from the downdraft;
- (f) Drying at the surface and moistening above;
- (g) Cooling at the surface of 1.5 K with warming aloft; and
- (h) A large θ_e drop in the mixed layer.

The schematic diagram is drawn relative to the moving squall line. The driving mechanism for the squall line is thought to be an abundant supply of warm moist air in the subcloud layer with high enough value of θ_e ; the convergence and ascending motion are maintained by the downdraft reaching the ground; this seems to originate from a rather low level, i.e., 900-800 mb in this situation. This picture by Mower does not require a large-scale shearing environment (i.e., vertical shear of the horizontal wind) for the maintenance of the squall system. In this regard it is different from that of squall line in middle latitudes. Mower's picture of the squall system is somewhat similar to that presented by Moncrieff and Miller (1976), a three-dimensional numerical model which describes the passage of the squall line. In this study, the downdraft air is shown to originate from a rather low level just above the subcloud layer. The downdraft air is warmed adiabatically during the descent and is cooled by evaporation of the liquid water and rain. The final configuration of the surface air was noted to depend on the intensities of these opposing effects.

In another recent study, Leroux (1976) presents a different view of the squall system where the effect of the shearing environment is emphasized. Figure 14.14 from the study of Leroux (1976) shows a schematic outline of the West African squall line. The emphasis here is on the downward flux of easterly momentum from the middle tropospheric easterlies over West Africa. The hypothesis of Leroux needs to be tested more closely with observations. According to this hypothesis, the convergence at the surface occurs at the leading edge of the strong surface easterly surges. The southwesterly monsoon current is split into two parts by this easterly current. The precise reasons for the downward flux of easterly momentum is not explained by this study. The proposal of Laroux (1976) is not too different from that of Obasi (1974). Obasi noted strong easterlies with speeds ≈ 30 to 35 knots



COUPE VERTICALE SCHEMATIQUE D'UNE LIGNE DE GRAINS

Figure 14.14 — Schematic vertical cross-sections across African squall line from Leroux (1976)

in the lower troposphere (700 to 900 mb) and at roughly 100 km to the rear of the disturbance line. Ahead of this line he found weak westerlies in this region. This asymmetry of the zonal flow provides a sustained field of low-level mass convergence ($\partial u/\partial x < 0$) across the disturbance line. Squall line passages over the Atlantic Ocean are known to exhibit similar strong zonal flow asymmetries. The dynamics of the initiation of a strong surge in the easterlies is an unsolved problem in tropical meteorology. It is observed to occur over many parts of the global tropical belt. Over West Africa this sudden surge of easterlies may be due to downward motion and a downward flux of easterly momentum from higher levels. This descent may be the mass compensation for the active ascent over an ITCZ disturbance in the near-equatorial rain belt. Once such a surge of easterlies is established, local convergence lines and the squall system could perhaps maintain themselves via mechanisms such as those proposed by Moncrieff and Miller (1976).

Finally, the student should examine the structures illustrated here with that of the oceanic squall system proposed by Zipser (1969) for studies over the Line Islands over the Pacific Ocean. This is described elsewhere in the section on Pacific Ocean disturbances.

14.10 Central Africa

Although rainfall amounts exceed 2 540 mm a year in parts of the near-equatorial rainbelts, we know very little about the disturbances that produce these rainfall amounts. Since the major rainfall belt migrates from 20°S to 7°N during the year arriving at 20°S during the northern winter, the near-equatorial regions encounter two rainfall seasons associated with the northward as well as the southward passage of the rainfall belt. Some interesting mean cross-sections of the atmospheric structure over central Africa were recently presented by Dean (1975). The rest of this section describes cross-sections that were based on data obtained during the International Geophysical Year in 1957 and 1958. Figure 14.15 is a station locator chart that was used by Dean. Here we shall only look at his sections for some selected stations near and south of the Equator. Figures 14.16a, b, c show these sections for Bangui at 4°N, Coquilhatville at the Equator, Luluabourg at 5°S, Albertville at 5°S, Elisabethville at 11°S and Broken Hill at 14°S. The left panels in these three diagrams show the meridional (top) and the zonal (bottom) velocity in m s^{-1} during the year. Dean has also included the monthly mean rainfall totals in mm at the bottom. We note the following interesting features. As one proceeds south from the Equator, the rainfall totals decrease if the lower tropospheric flows are from the east. This is partly due to the fact that low-level easterly flows are of continental origin and are dry since the Indian Ocean moist trajectories do not cross the east African highlands. The westerly winds are of oceanic origin (Atlantic) and are moister.

At Bangui and at Coquilhatville the low-level westerlies are weak in all seasons except the summer. During these months when the westerlies are weak, the easterlies at 4 km are fairly strong. As one proceeds southwards the low-level westerlies are replaced by low-level easterlies and the winter hemisphere high-level westerlies appear in these sections. The strength of strong easterlies ($\approx 10 \text{ m s}^{-1}$) in the lowest km over Elisabethville and Broken Hill, i.e., south of 10°S are extremely interesting features. There does not seem to exist any simple relationship between monthly mean rainfall and the meridional wind.

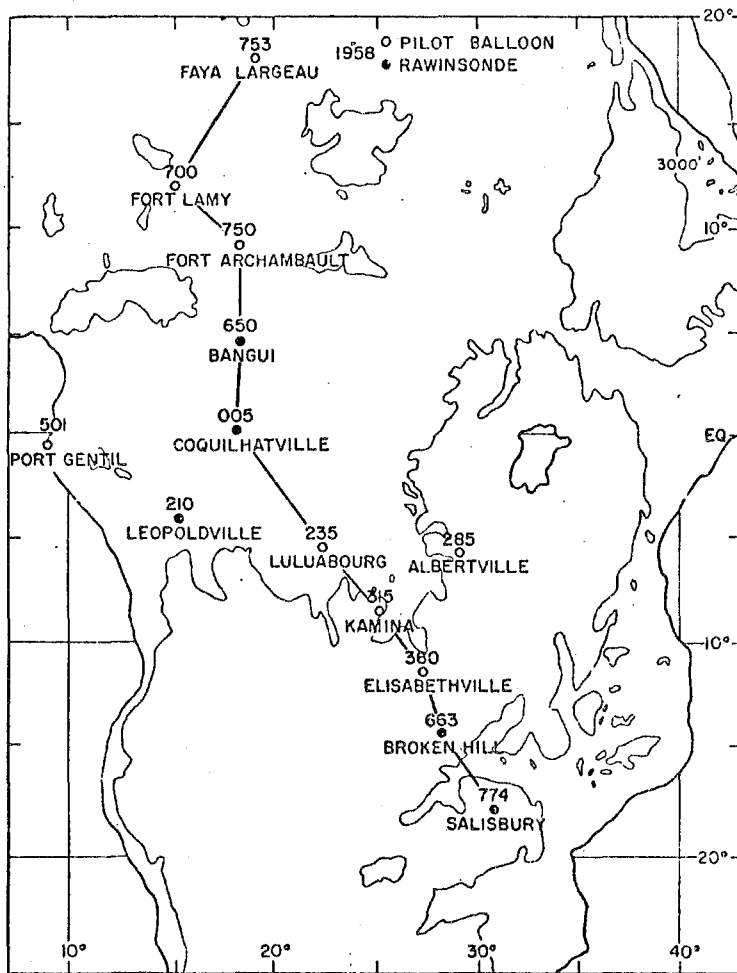
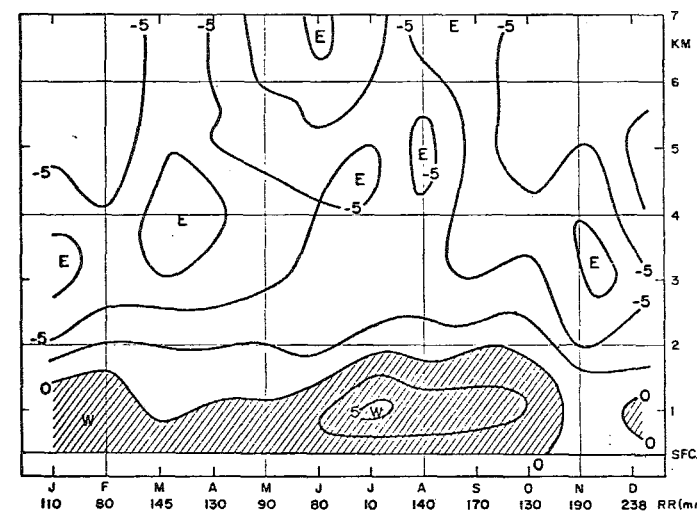
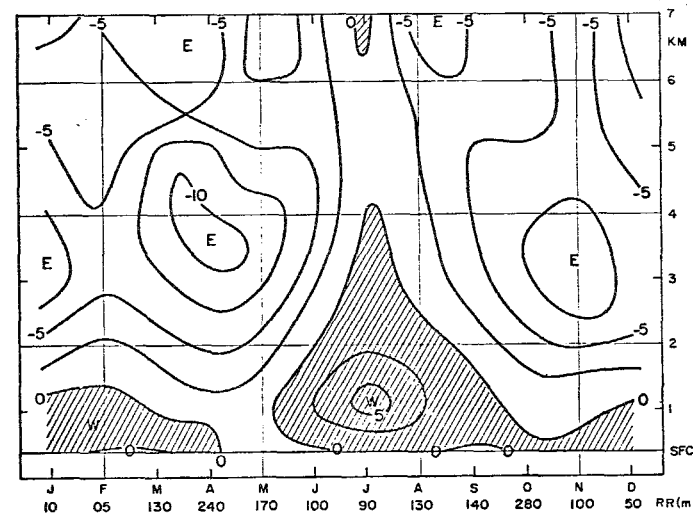
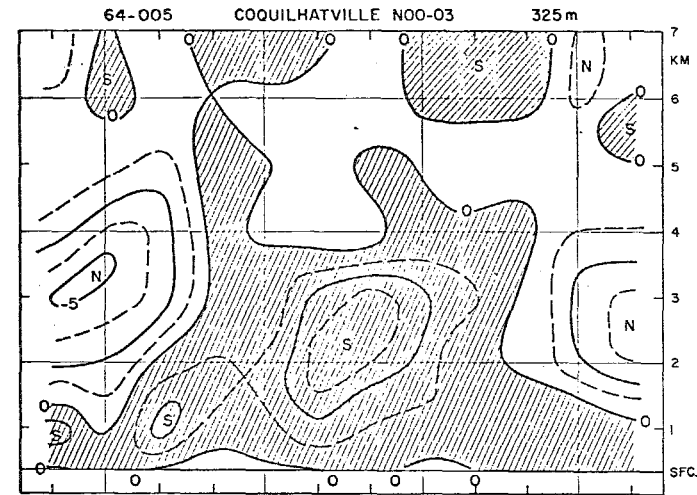
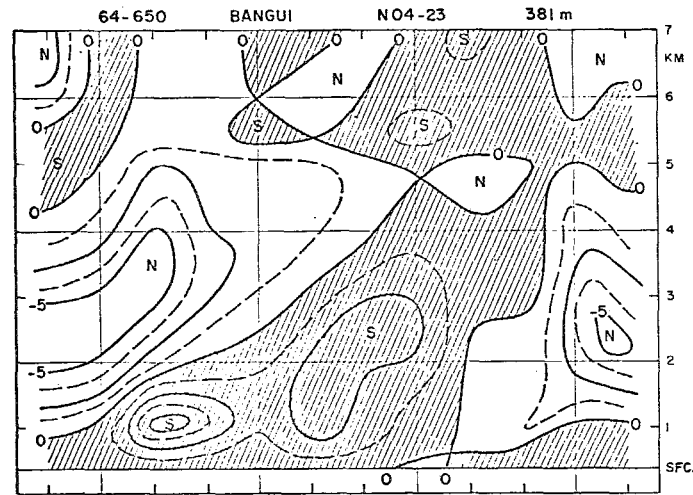


Figure 14.15— Station locator chart over Africa, from Dean (1975)



TIME SECTION OF 1958 MEAN MONTHLY RESULTANT WIND COMPONENTS IN ms^{-1} .

TIME SECTION OF 1958 MEAN MONTHLY RESULTANT WIND COMPONENTS IN ms^{-1} .

Figure 14.16a

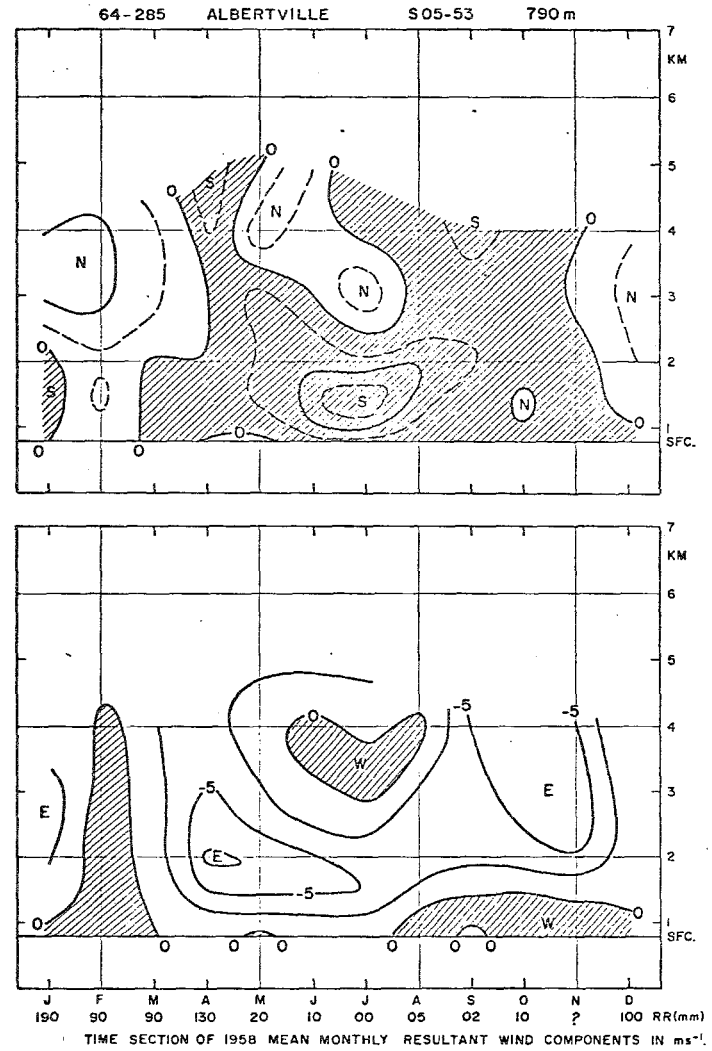
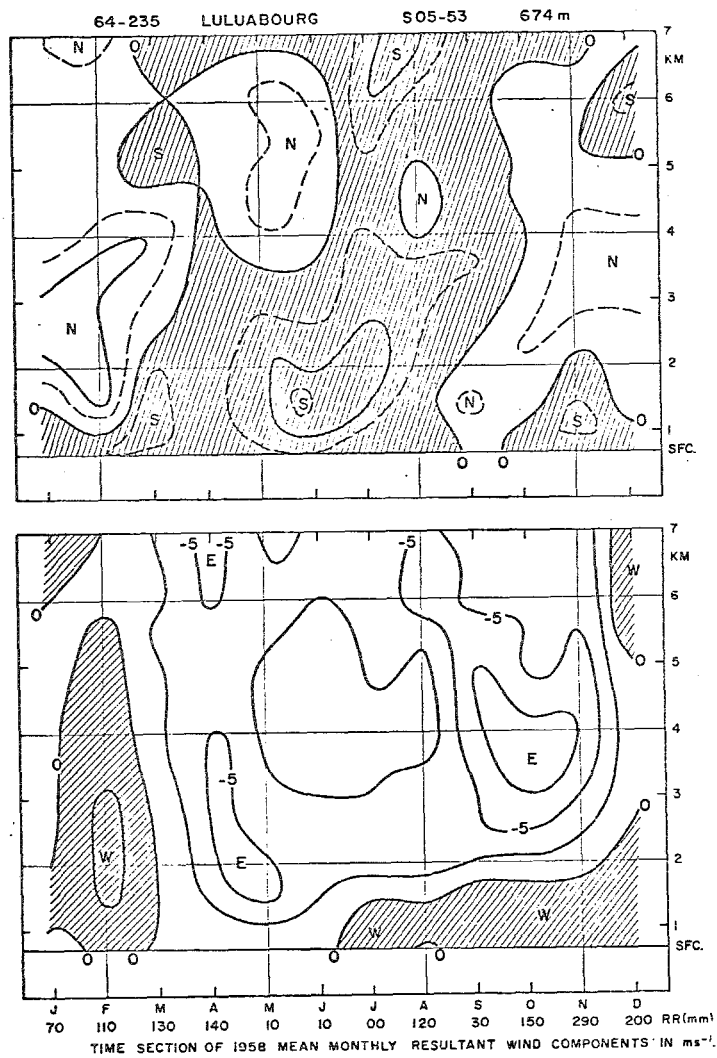


Figure 14.16b

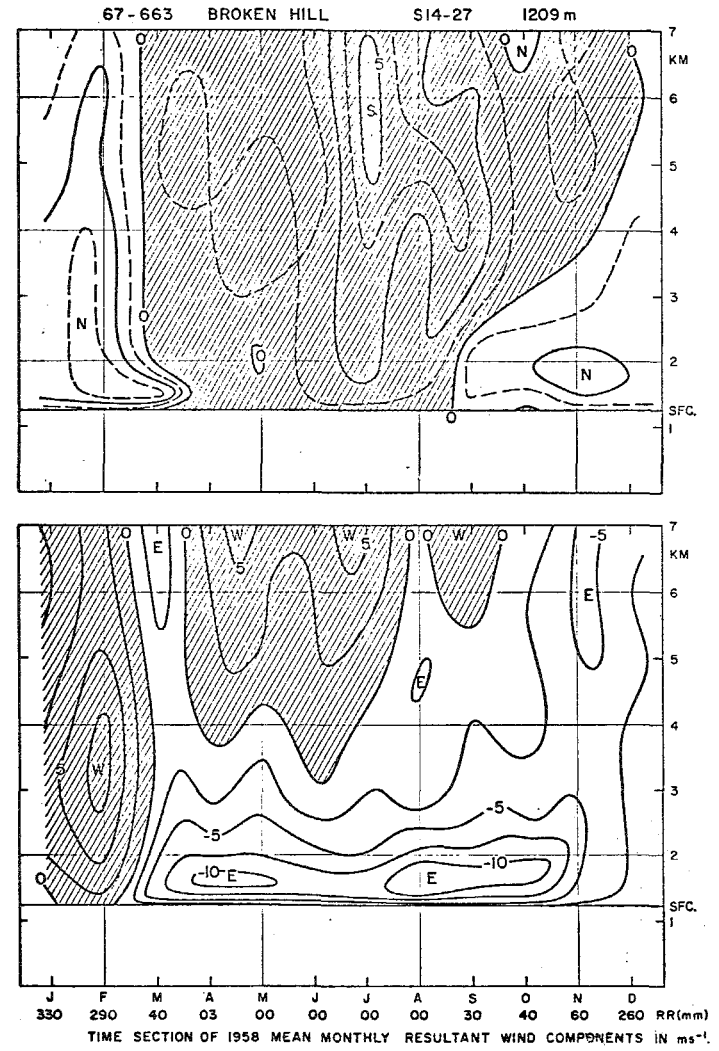
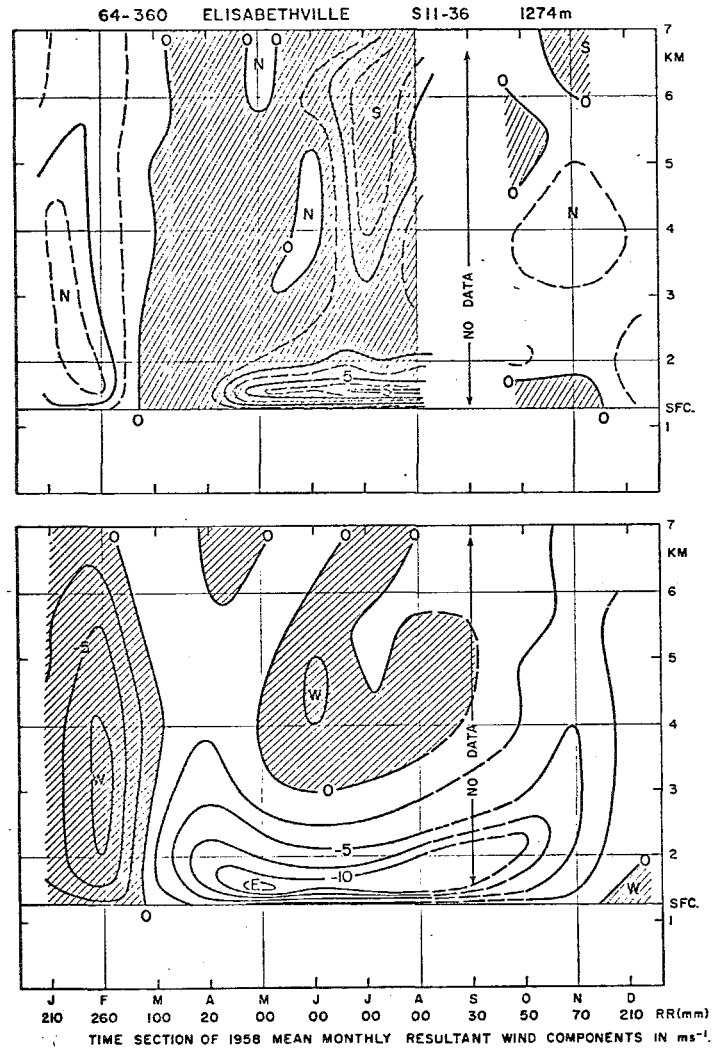


Figure 14.16c

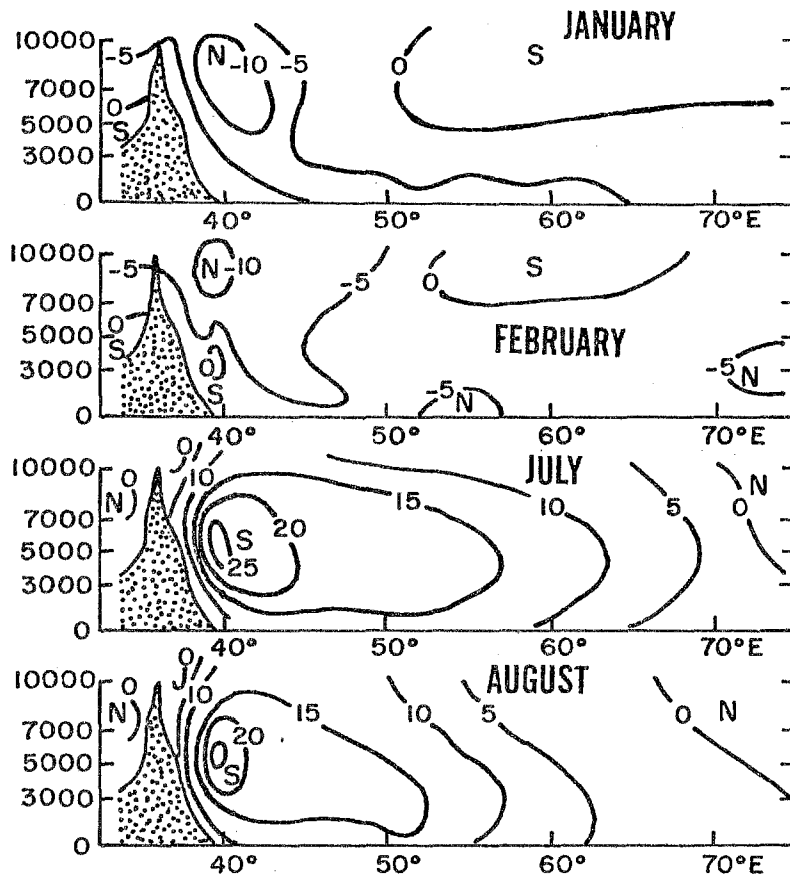


Figure 14.17 — Zonal vertical cross-section of the monthly mean meridional wind speed near the Equator (following Findlater, 1971). Areas of wind speed larger than 20 knots are shaded. The mountains illustrated here are the Kenya highlands

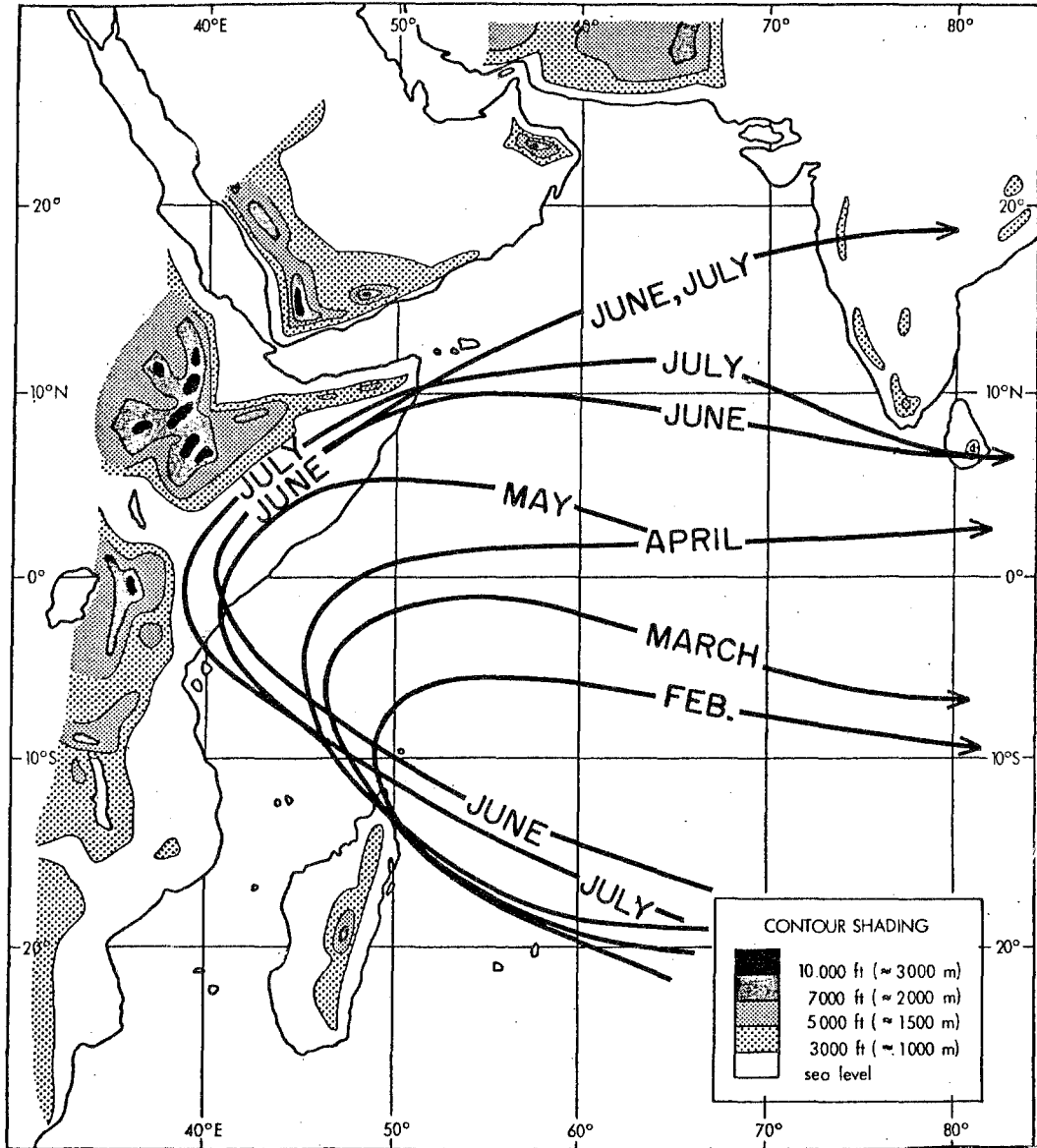


Figure 14.18 -- Month-by-month progress of the axis of the low-level cross-equatorial jet. Note the split in the axis of the jet in June and July. The east African mountains are also indicated in this diagram

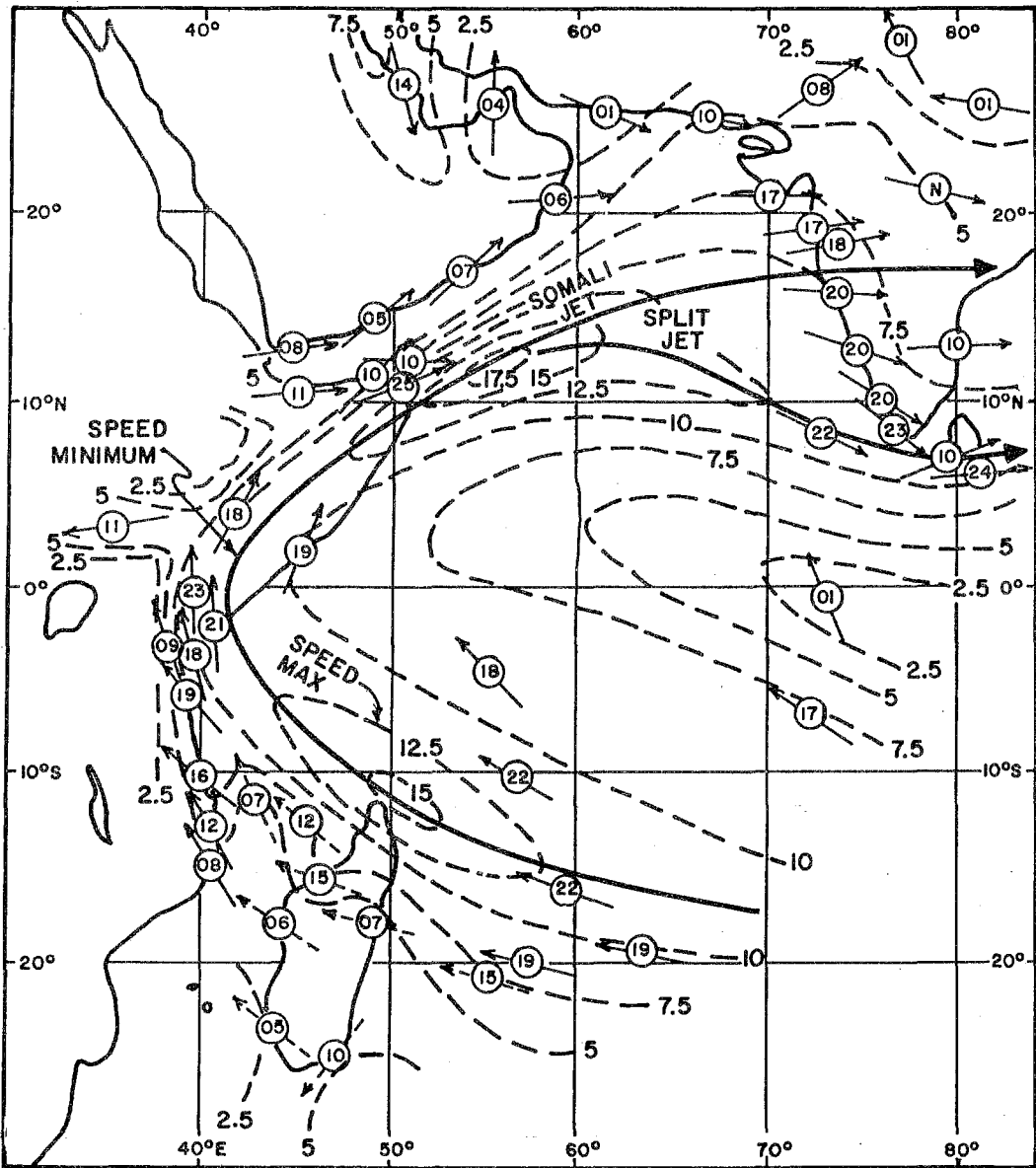


Figure 14.19 — 1 km flows for August over the Arabian Sea/Indian Ocean region based on Findlater (1971). Speed lines are in $m s^{-1}$. Station values within circles are in knots. The solid line indicates the axis of the low-level jet

14.11 Cross-equatorial flow near the east African coast

During the summer as well as the winter monsoon months strong cross-equatorial flows near the 1.5 km level develop along the east African coast of the Indian Ocean. The southerlies during the summer monsoons and the northerlies during the winter monsoons are a regular part of the annual cycle of flows in this region. Figures 14.17a, b show (Findlater, 1969) vertical cross-sections from west to east near the Equator, illustrating this wind reversal. The Kenya highlands lie to the west of the low-level cross-equatorial flows in these cross-sections. Findlater has shown that a substantial part of the monsoonal cross-equatorial flows occurs in this low-level jet. An interesting clockwise gyre of low-level flows is usually found over the southern Indian Ocean in February, and this gradually moves north-westward and becomes a quasi-stationary summer monsoon flow by June (see Fig. 14.18, which is based on Findlater's data). The low-level jet remains quasi-stationary during June, July and August and thereafter the gyre slowly retreats southeastwards with the arrival of the northeast monsoons. Figure 14.19, from Findlater's work, shows a well-known monthly mean isotach field illustrating the major cross-equatorial low-level jet. Findlater's (1971) report contains the mean maps for the entire year and shows the annual cycle of the cross-equatorial flows. The August mean map illustrated here contains the following interesting features:

- (i) A low-level jet extending from the southern Indian Ocean meridionally along east Africa towards Somalia and then eastwards over the Indian Ocean;
- (ii) Strong winds are noted (at the 1 km level) just downstream of the Malagasy Republic and downstream from the coast of the Somali Republic over the Arabian Sea;
- (iii) A split in the axis of the jet is noted over the Arabian Sea. The split may be a reflection of barotropic instability of the strong jet near Somalia. The Ethiopian mountains are noted to be an important factor in determining the strength of the Somali jet.

The weather over Somalia is dry and lacking in clouds during the summer monsoon months; however, the sky is usually covered by a haze layer that extends to a height of a few kilometres. The speed of the cross-equatorial jet exhibits interesting fluctuations on time scales less than 6 days and around 18 days. Findlater has noted some interesting lag relationships between the occurrence of velocity maxima along the east African coast and the subsequent rainfall over western India. This study is a preliminary one and deserves further careful analysis.

Chapter 15

SOUTH AMERICAN NEAR-EQUATORIAL RAINBELTS AND DRY ZONES

15.1 Rainfall and lower tropospheric flow fields

Figures 15.1a, b, c and d portray the rainfall for February, May, August and November based on a recent atlas of Dean (1971). The near-equatorial rainfall maxima in May are found over Brazil and Colombia. The disturbances that account for nearly 30 cm of rainfall in one month are not well described in the literature. A major field experiment to determine the structure of these disturbances is evidently needed. By August the rainfall maximum moves to 10°N along the Venezuelan coast south of Barbados. By November the rainfall belt moves southwards towards eastern Peru near 10°S , east of the Andes. Much of this rainfall is orographic. February is the period of most widespread rainfall over the Amazon valley and western Brazil. Figures 15.2a, b, c and d portray the mean 850 mb flow field during these four months based on Dean's atlas. Figure 15.3 shows a recent map of the upper-air stations over Brazil.

15.2 The low-level easterly wind maximum during February

During February an easterly wind maximum is found over the Equator, near the 2 km level. This is very clearly illustrated in the vertical cross-section of the zonal wind shown in Figure 15.4. The Amazon rainfall belt is located south of the easterly wind maxima on its cyclonic shear side. The cyclonic shear side of this jet (often as strong as 30 knots) contains the path of many westward moving rain-producing cyclonic wave disturbances. This region is somewhat similar to the West Africa rainfall belt of northern summer. A calculation of the meridional distribution of absolute vorticity across this easterly jet shows a weak change of sign in the gradient of absolute vorticity. This suggests the possibility of barotropic instability in these Amazon disturbances. This is a region that deserves much further study.

15.3 Northeast Brazil

This is a unique region of the tropics south of the Equator. An interesting dry belt (located near 10°S and 40°W) has perplexed meteorologists for some time. Rainfall increases westward from the region. The rainy season from January through April in this near-equatorial belt shows considerable variability over South America. Figure 15.5 shows the normal monthly precipitation based on a 30-year period from the study of Ramos (1974). The annual total of 474 mm (18 inches) at Petrolina reflects very dry conditions for these latitudes. The region is under the influence of the western Atlantic oceanic flow régimes which exhibit, in the mean, a low level diffluence during the rainy season; see Figure 15.6, Ramos (1974). The rainfall characteristics show a maximum during the early morning hours and minimum in the

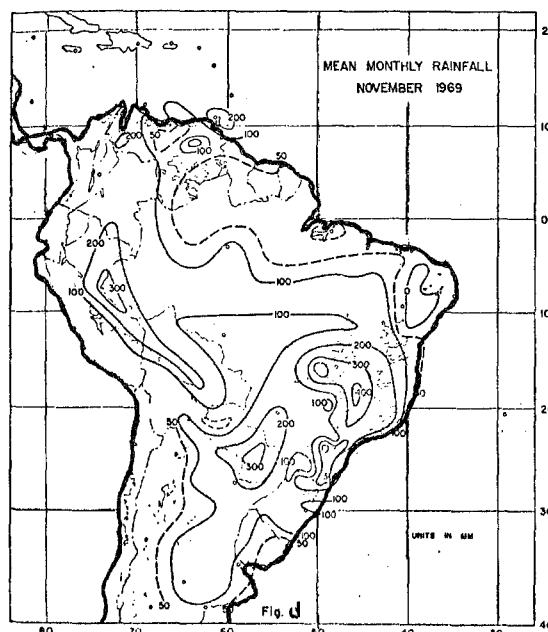
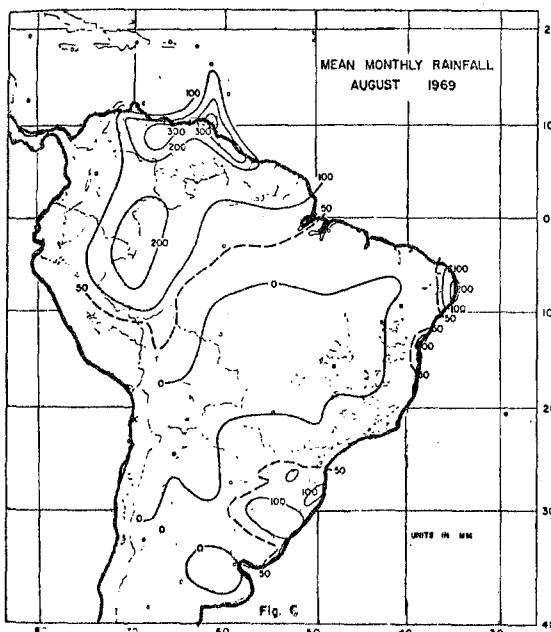
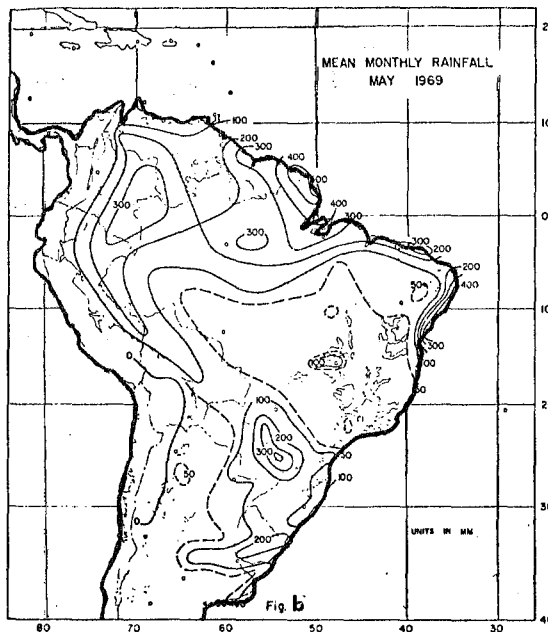
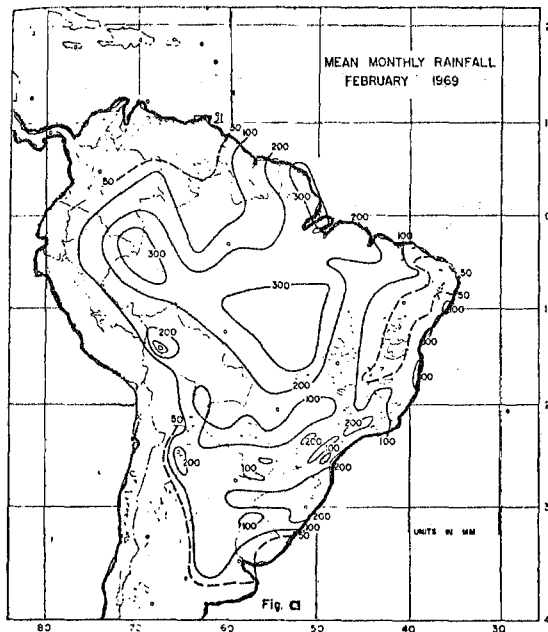


Figure 15.1 (a,b,c,d)

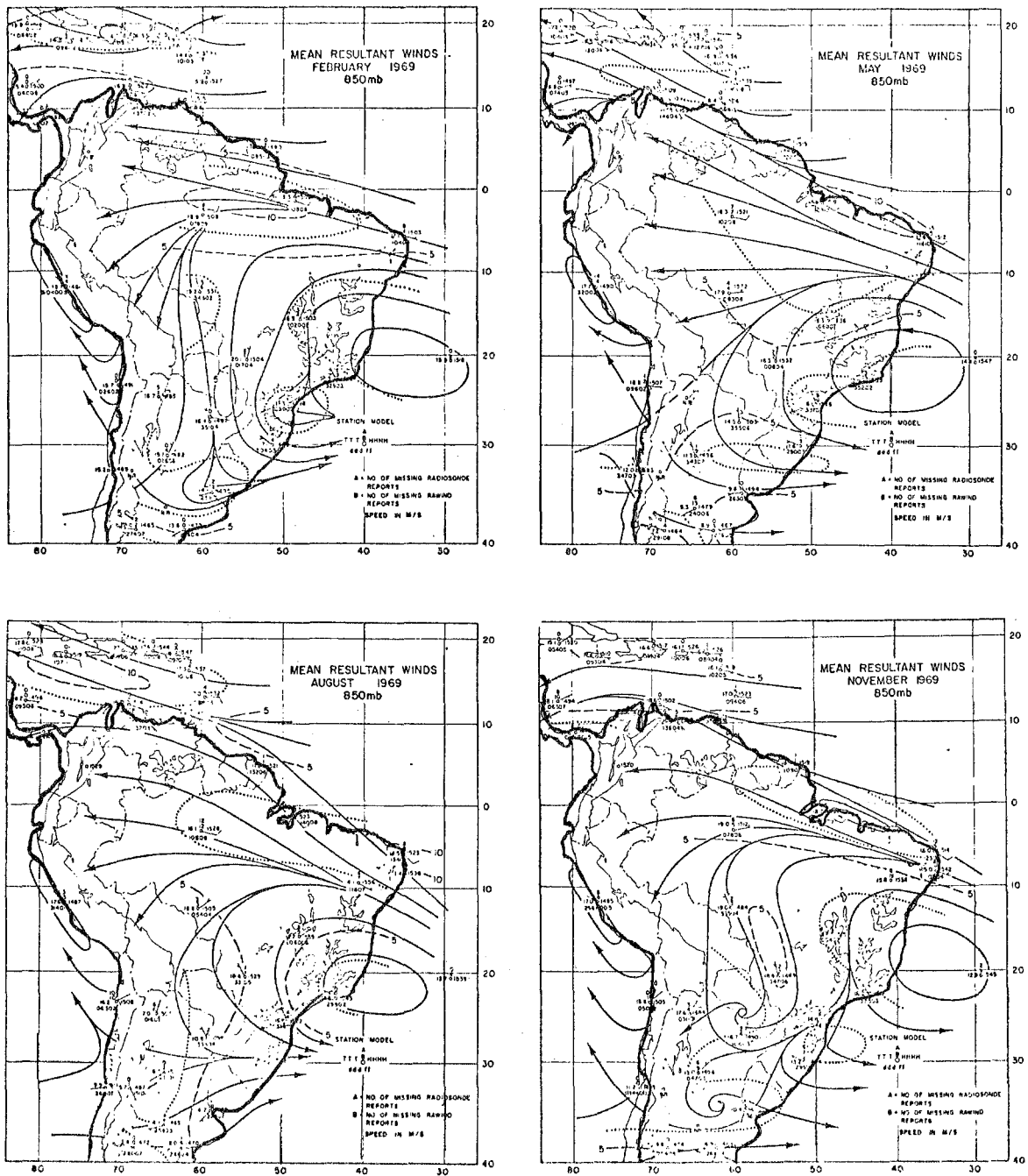


Figure 15.2 (a,b,c,d)

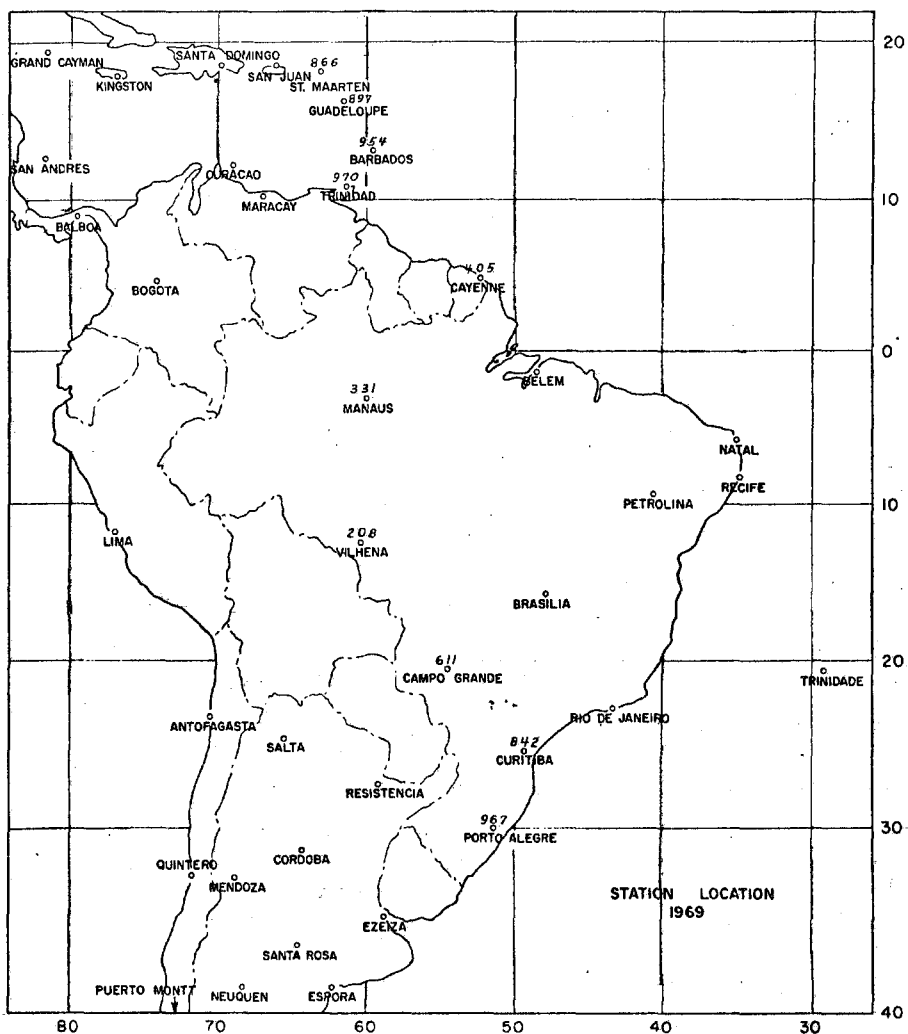
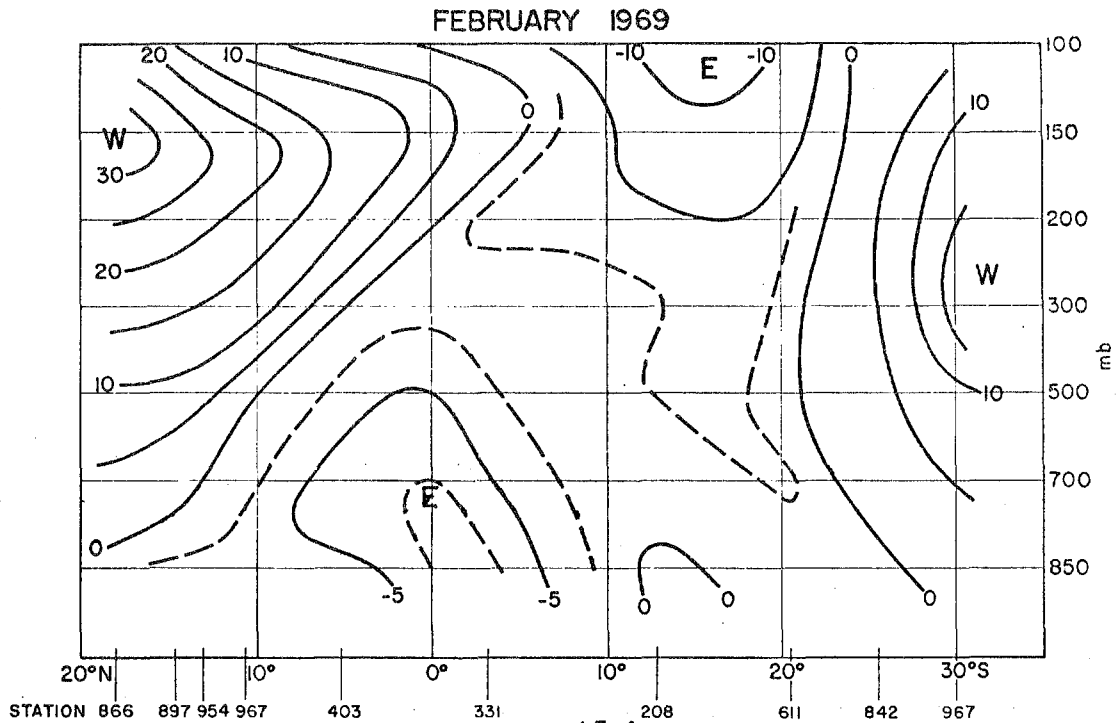
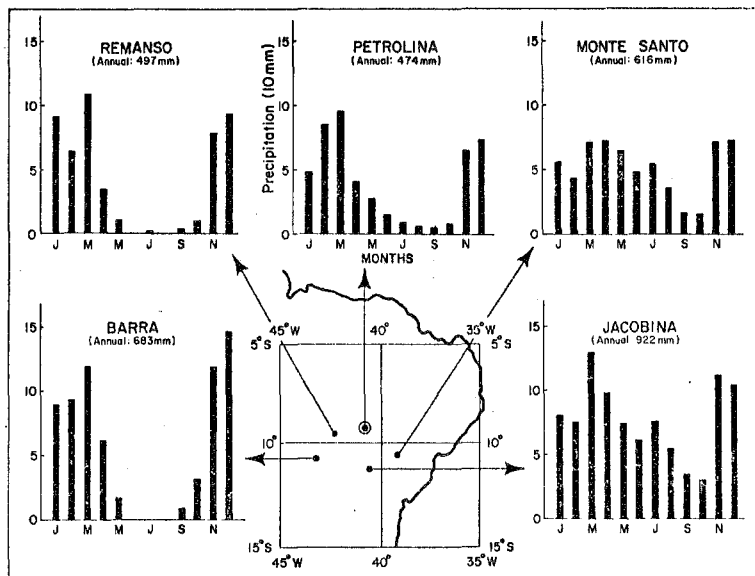


Figure 15.3

Location of rawinsonde stations in South America during 1969



Cross-section of the mean zonal wind component in $m s^{-1}$ near $60^{\circ}W$, February 1969



Normal annual precipitation for the period 1931-1960 given in millimetres for five cities in the northeast Brazil dry region

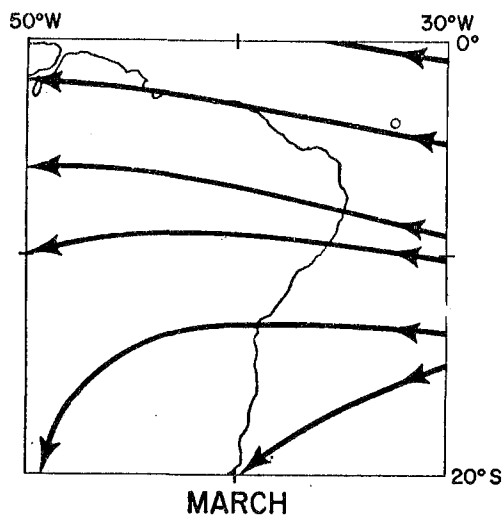


Figure 15.6

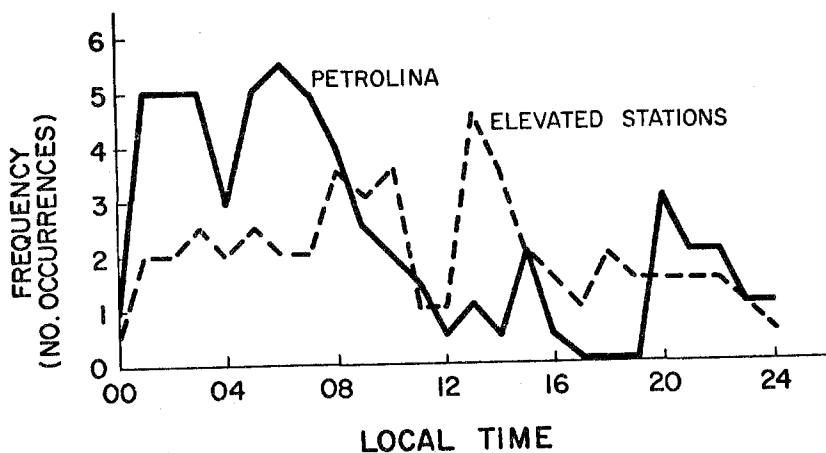


Figure 15.7

Diurnal rainfall frequency for the seven rain periods. Averaged data from Petrolina region (solid curve) and averaged data from three elevated terrain stations to the west of Petrolina (dashed curve).

afternoon hours; Figure 15.7, Ramos (1974). This is a feature of rainfall over the oceanic tropics. As one proceeds westwards the afternoon maximum in the rainfall is clearly dominant. Ramos has emphasized the importance of orographic heating to explain the diurnal variation of rainfall. It is, however, recognized that there exist westward propagating disturbances which account for the observed rainfall, most of which is observed to occur within a few days. The few storms that do reach this region are on the average as intense as the Caribbean easterly waves. The large-scale mean low-level diffluence pattern over the region is a semi-permanent feature; it is characterized by broad-scale descent and an intense inversion.

15.4 Synoptic maps during the rainy season

We present a sequence of 850 and 200 mb maps (based on Rocha de Aragão, 1975) over South America during the rainy season (see Figures 15.8a, b, c and d). The maps illustrate the formation of cyclonic disturbances. The sequence of maps is for January 20th through 23rd at 1200 GMT, 1970. The most interesting feature is an anticyclone situation (on the 20th) at around 20°S, 37.5°W. The northerly flows west of the anticyclone undergoes a marked turn towards northwesterlies in the next 48-hour period. Two major cyclonic disturbances form and they are evident on the 22nd with a separation or scale of around 1500 km. They seem to form in the cyclonic shear zone of the westerlies in this instance around the 22nd and move westwards with a speed of roughly 5° longitude/day. The 200 mb flows in this sequence show a rapid eastward motion of an upper trough with a subsequent formation of an upper closed low on the east coast. Not much is known about these types of rain-producing disturbances over western Brazil. As stated earlier, it is desirable that a major field project be organized to study the dynamical and thermodynamical structure of the rainy season disturbances over the Brazilian rainbelts.

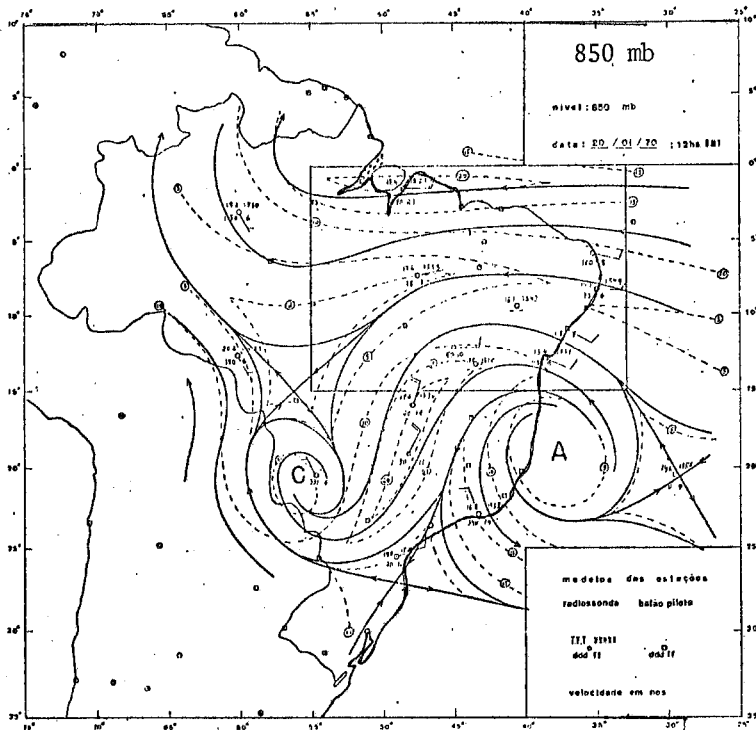
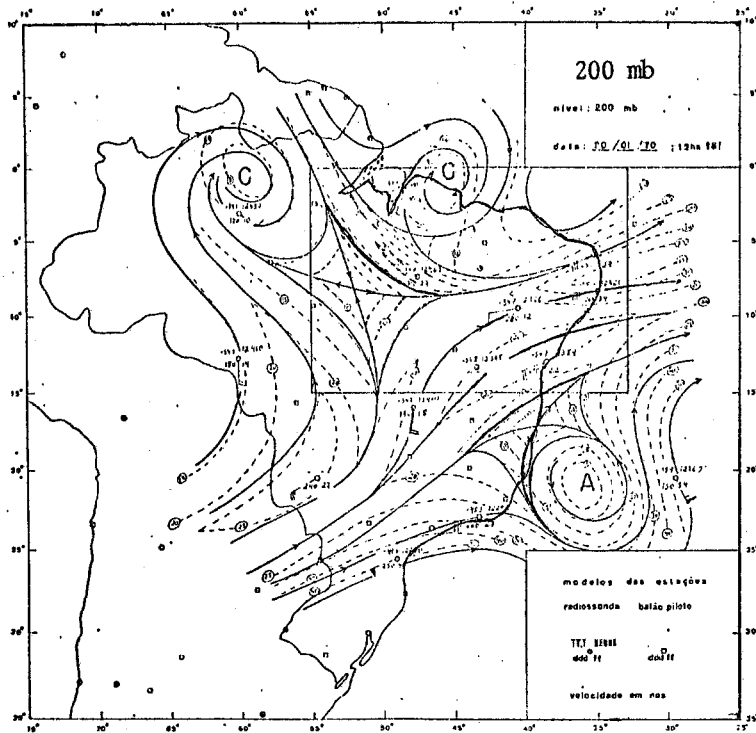


Figure 15.8a



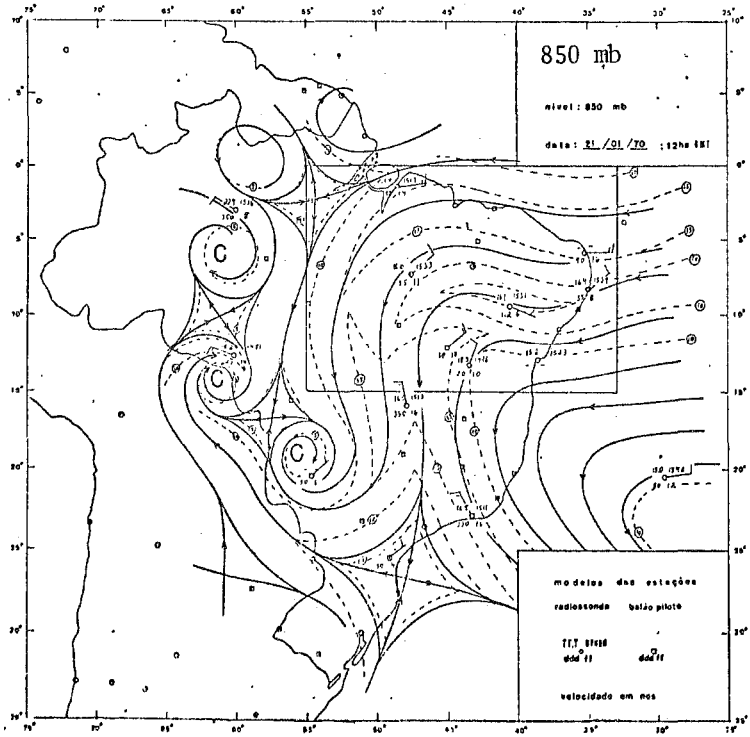
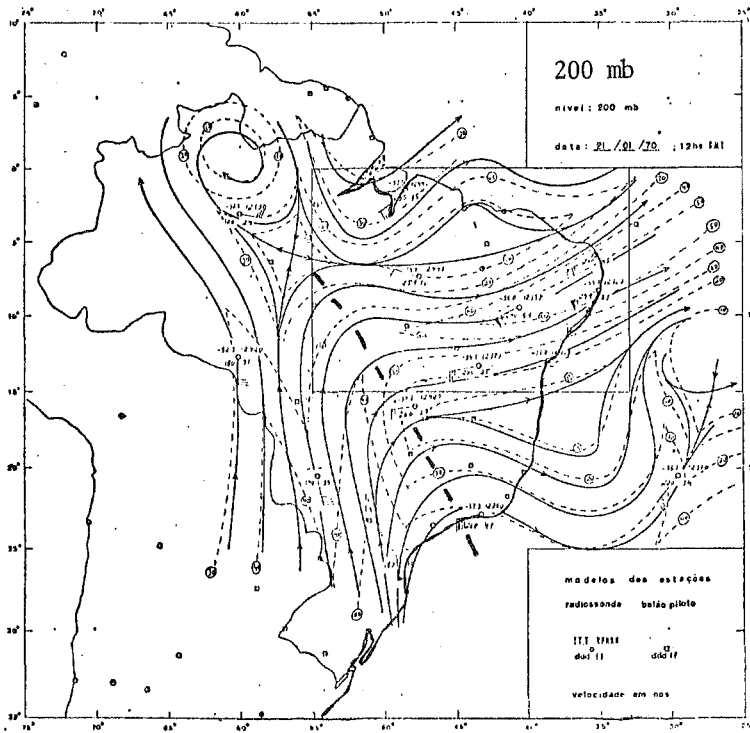


Figure 15.8b



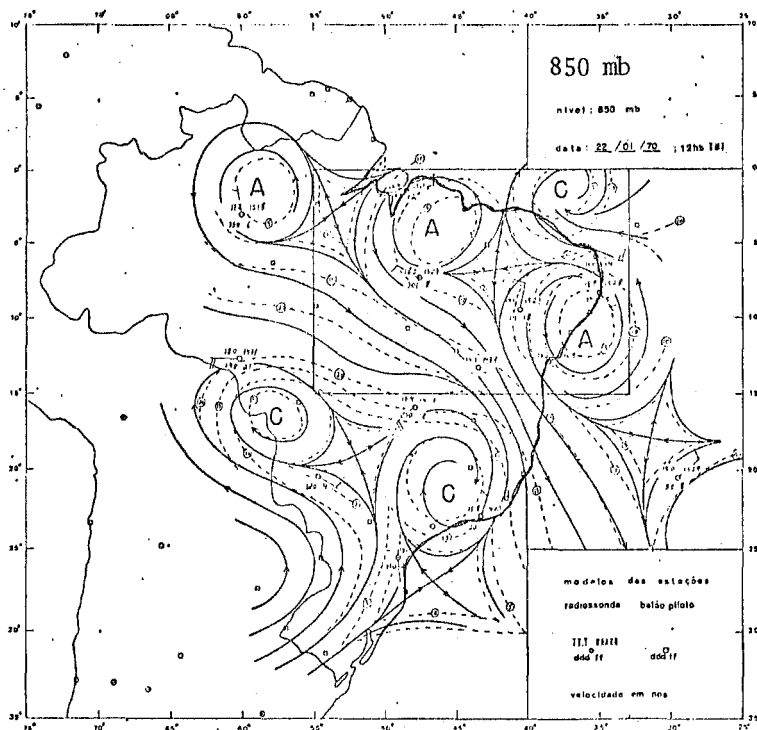
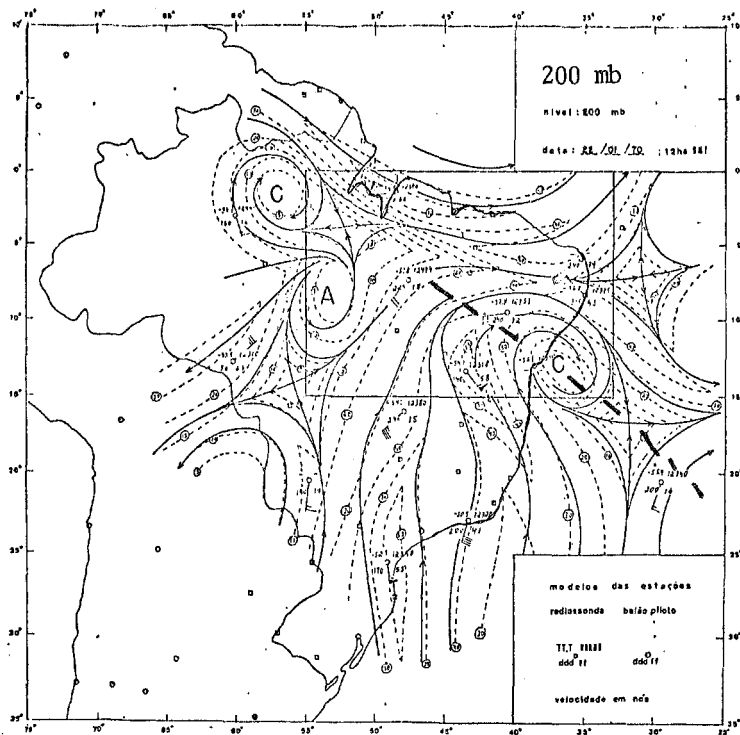


Figure 15.8c



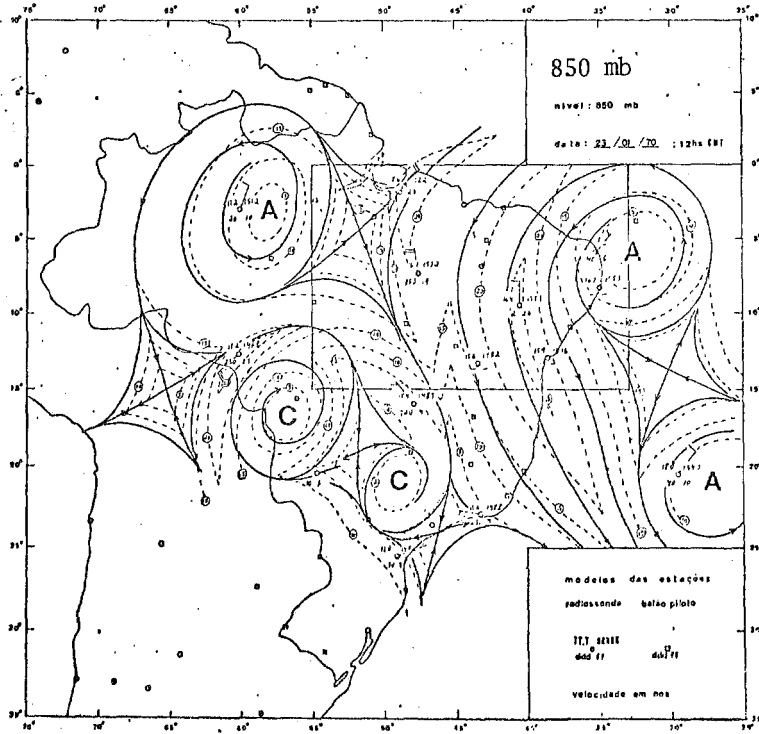
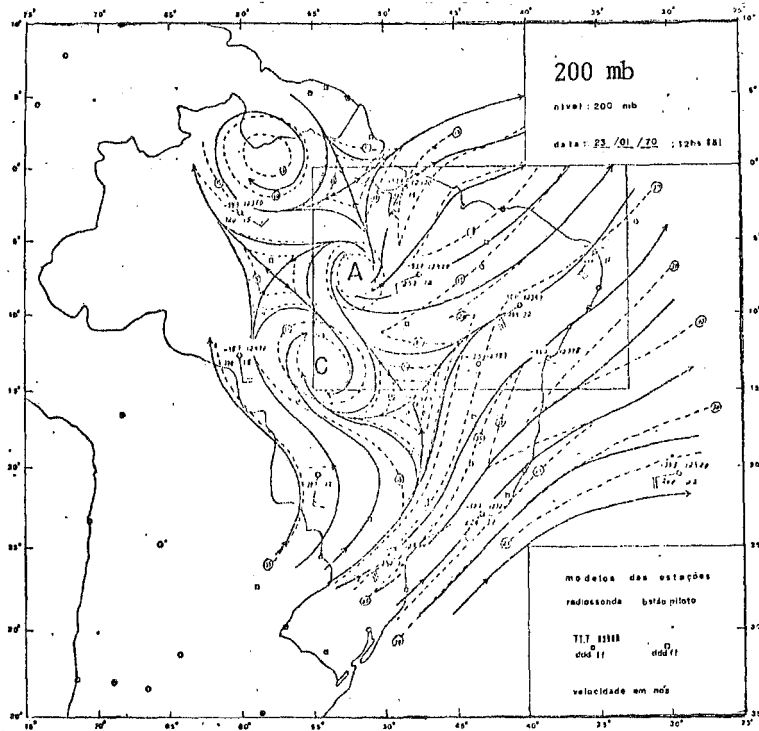


Figure 15.8d



Chapter 16

TROPICAL CLOUD COVER, RAINFALL AND SATELLITE METEOROLOGY

16.1 Introduction

Near the west coasts of continents (North and South America, Africa) one usually notes low stratus and fog during the summer season. As one proceeds westward and equatorwards along the trades the low stratus breaks down into stratocumulus and then into fair weather cumulus régimes. As one approaches the ITCZ the occurrence of tall cumulonimbus becomes predominant. In propagating disturbances such as easterly waves, equatorial waves and hurricanes, the cloud cover is mostly convective, containing a mixture of shallow and deep clouds.

Figures 16.1a, b, c and d illustrate monthly mean cloud cover over the global tropical belt from the tabulation of Sadler (1970) based on several years of satellite data. The illustrations are for January, April, July and October. The isopleths are in units of 1/8, 2/8,to 8/8, i.e. oktas of cloud cover. The types of clouds are here identified in terms of coastal stratus, ITCZ clouds (convective), monsoonal (convective) and frontal, for the sake of convenience in identification.

The axis of the ITCZ cloud cover (5 to 6 oktas) remains north of the Equator over the Atlantic and the eastern Pacific Oceans, while over the western Pacific and the Indian Oceans it is found south of the Equator during the northern winter. The band of convective cloudiness northeast of Australia is an interesting and year-long feature. This region of convective cloudiness extends from northwest to southeast merging with the active frontal regions of the southern hemisphere. The existence of this extremely intriguing phenomenon is as yet unexplained.

In order to study tropical cloud cover, its areal extent, its day-to-day variations and its interseasonal and annual variations the satellite is without doubt the best tool. Satellite cloud cover information is nowadays presented in digital form from the visible and the infrared radiation received at the satellite altitude. These data are archived at different resolutions, these depending on the types of satellite resolution and the scientists' requirements. An example of satellite brightness data for northern summer is shown in Figure 16.2. This is based on studies of Krishnamurti and Bhalme (1976). The satellite brightness data over the global tropics for a whole year were recently examined by Gruber (1974). His major interest was in the examination of what we call space-time spectra of this data set. The student should familiarize himself with relevant statistical techniques that may be useful for studies of meteorological space-time spectra. The original data for the satellite brightness are tabulated on a 5° latitude by 5° longitude mesh of grid points. The smallest resolvable spatial scale is of the order of 1 000 km in this data set. Taking the entire year of tropical data, Gruber found that there exist dominant westward propagating "brightness waves". Zonal wave number 5 had a period of around 12.5 days and zonal wave number 9 had a period of around 6 days. Tropical

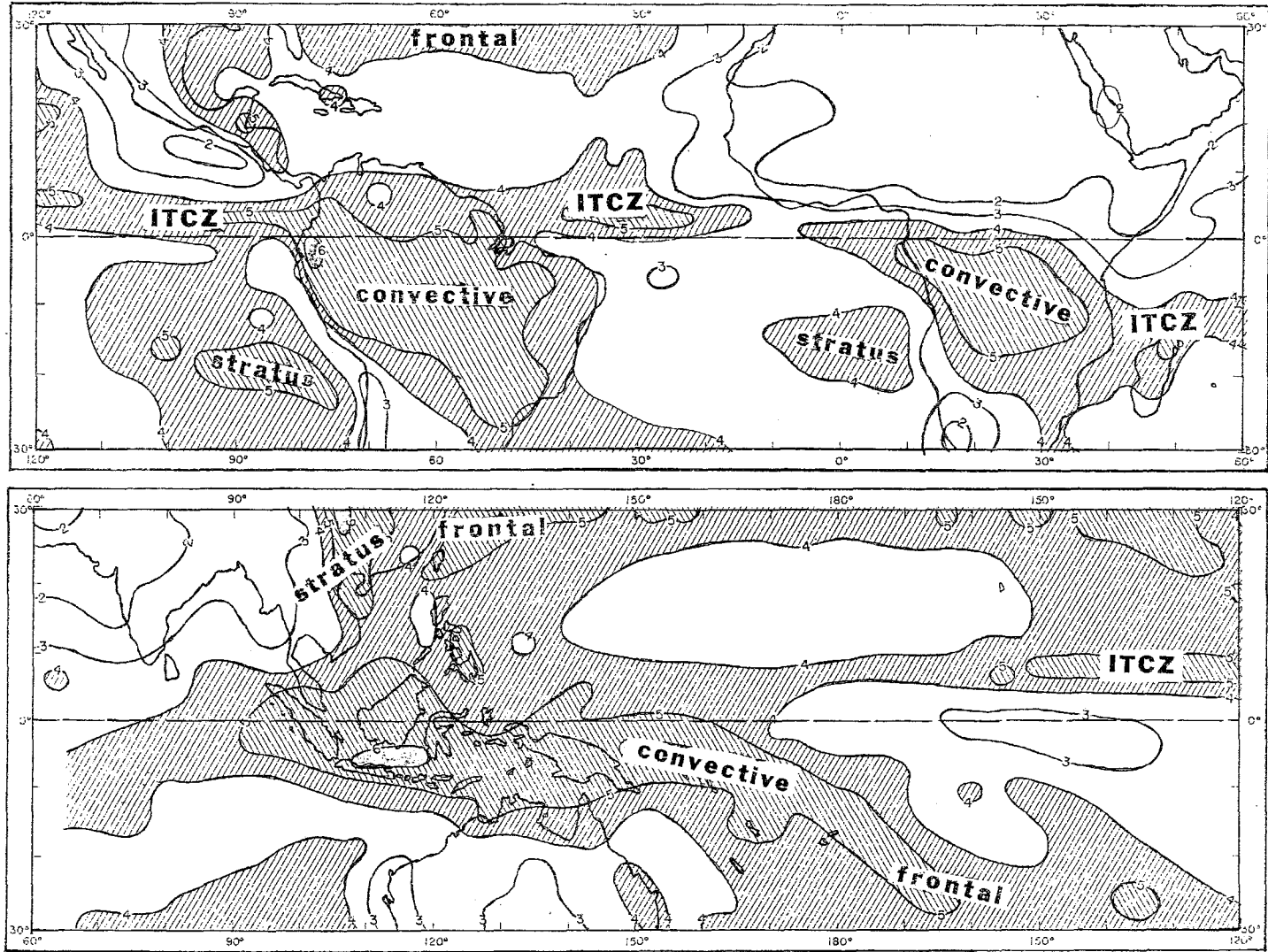


Figure 16.1a - Climatological cloud cover. JANUARY. Sadler (1970)

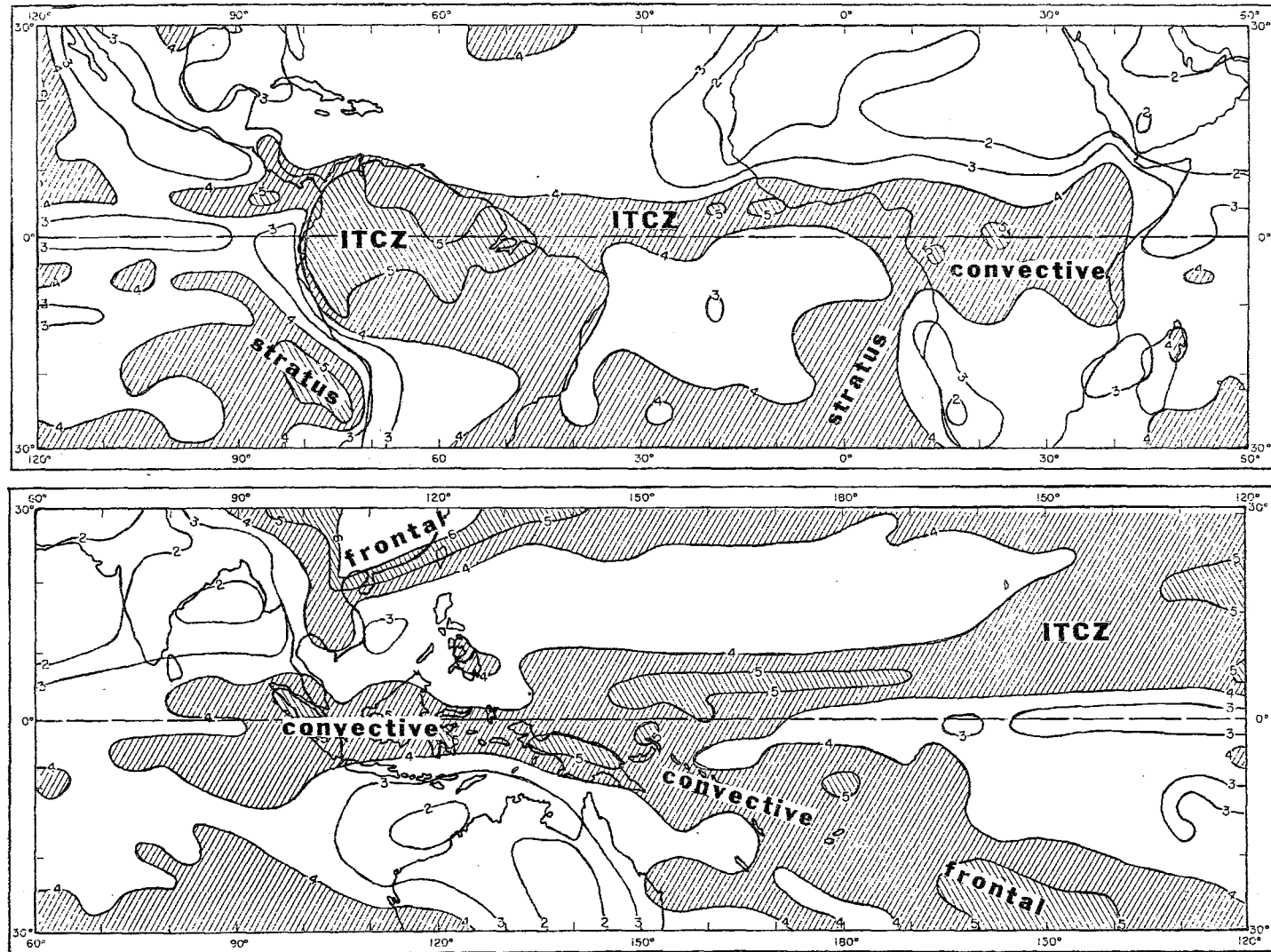


Figure 16.1b - Climatological cloud cover. APRIL. Sadler (1970)

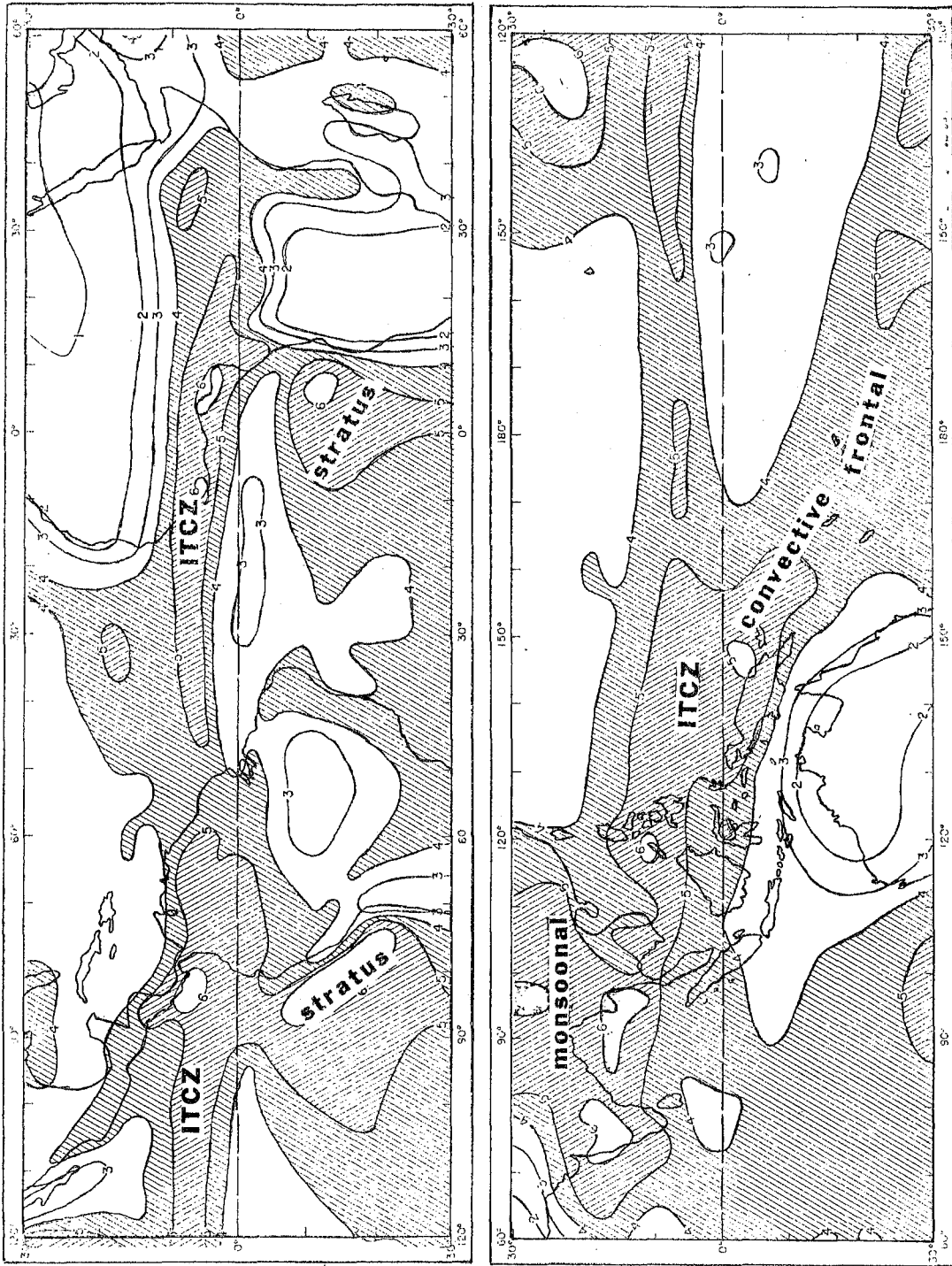


Figure 16.lc - Climatological cloud cover. JULY. Sadler (1970)

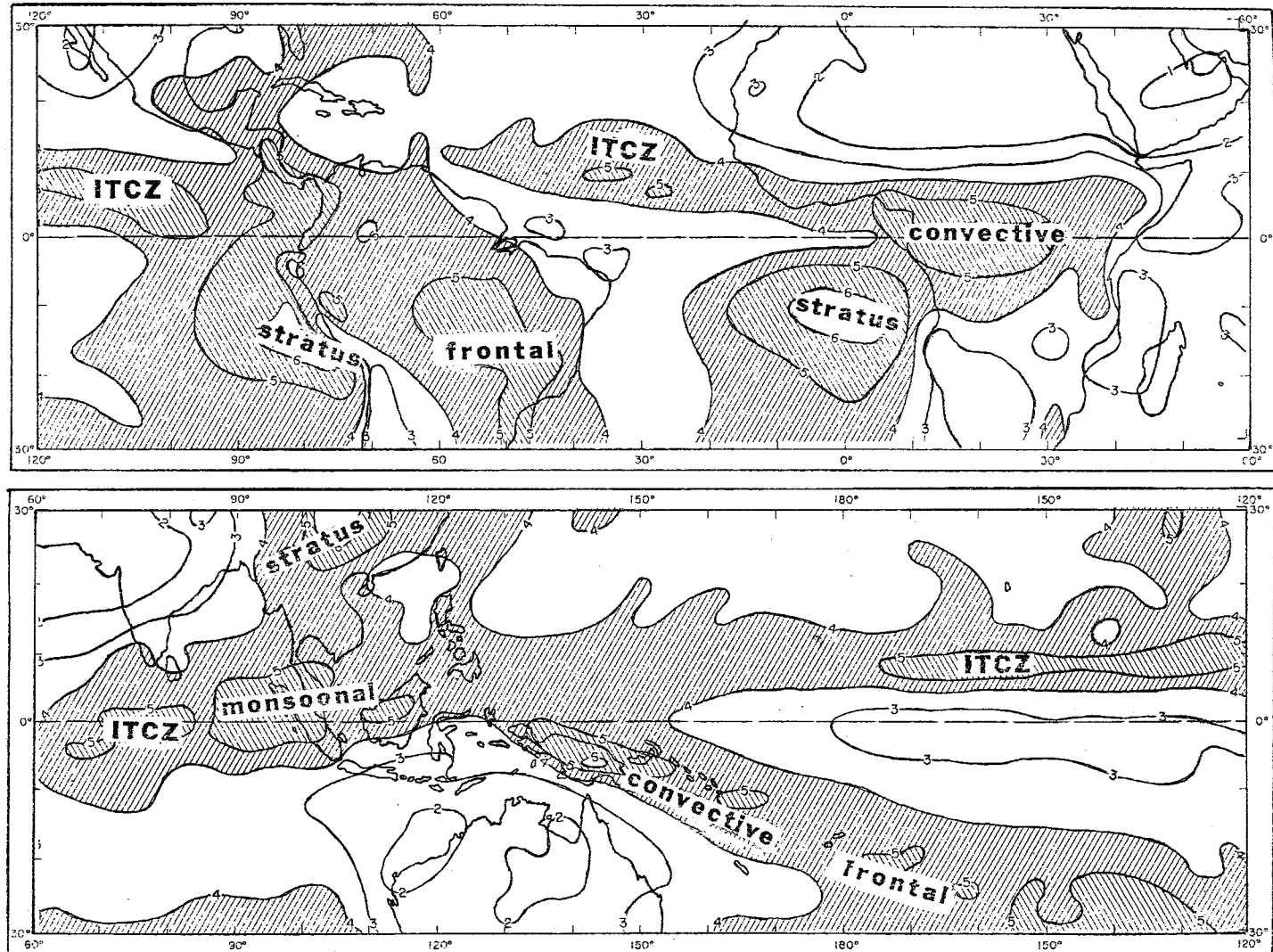


Figure 16.1d - Climatological cloud cover. OCTOBER. Sadler (1970)

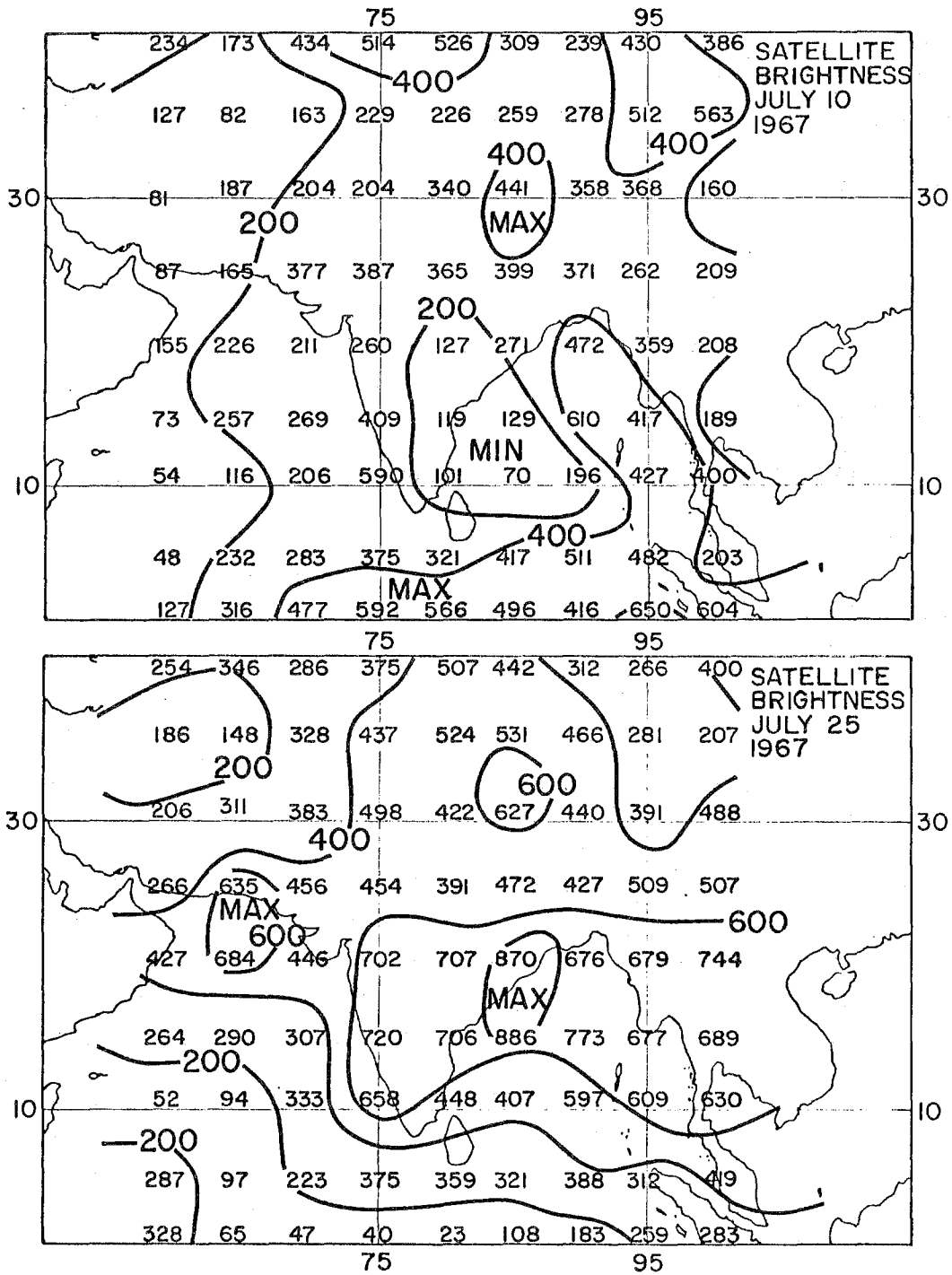


Figure 16.2 - Satellite brightness data over India on a "break" monsoon day during July 1967 (top)
- Satellite brightness data over India on an "active" monsoon day during July 1967 (bottom)

meteorological literature nowadays contains an abundance of such information on space-time spectra for many different parameters. The transient waves defined by the brightness data spectra are extremely interesting. Gruber feels that these are respectively related to Rossby waves and easterly waves. The near 15-day oscillation in the satellite brightness data was also noted by Krishnamurti and Bhalme (1976) over the Asian summer monsoonal belt. It is generally felt that the cause of this oscillation, which also shows up in many other meteorological parameters, is not understood at this time.

16.2 Tropical rainfall climatological aspects

Two excellent references on tropical rainfall are: (i) the tabulation of Wernstedt published in 1972 and (ii) the recent monthly rainfall maps published by Jaeger (1976). Wernstedt's compilation contains a vast climatological data collection for the tropics; as an example, data for well over 500 raingauge stations over the islands of Indonesia were processed. Most of these tabulations are averages for at least 20 to 30 years of data. Jaeger's maps are generally based on 30-year averages between 1931 and 1960. Here we shall present four of his maps for January, April, July and October. These maps, Figures 16.3a, b, c and d, the result of painstaking effort, are about the most reliable compilation to date that exists over the oceans. The four maps shown here contain the geographical distribution of rainfall. This original text of Jaeger is an important reference for the annual variability of rainfall on a month-by-month basis. Here we present selected charts from his text.

- (a) January rainfall, Figure 16.3a. The maximum rainfall over the eastern Pacific Ocean of over 200 mm is found between 5° and 10° N along the ITCZ. The rainfall totals over the central part of South America near 5° S over western Brazil exceed 300 mm. The ITCZ over the Atlantic remains north of the Equator in January and the rainfall maximum occurs near 5° N with values near 200 mm. The rainfall maximum over Africa has its larger value between 10° S and 20° S with magnitudes reaching as high as 300 mm. This maximum extends eastwards towards the northern part of the Malagasy Republic. The Indian Ocean just south of the Equator is an active disturbance area where roughly 200 mm of rainfall occur in January. The rainfall amounts gradually increase as one proceeds eastwards and over Indonesia the rainfall totals for January exceed 300 mm. The extremely dry belt over Australia and the pronounced rainfall minimum near 25° S is a very interesting feature during January. The local Hadley-type overturning has a rising branch centred near Indonesia, the sinking branches are located near 25° S and also near 25° N. The subtropical westerly jets near southern Japan and over Australia are both closely related to these Hadley-type overturnings. This entire region between 30° S to 30° N is an extremely interesting region for studies of the Winter Monsoon phenomenon. The rainfall over the western Pacific has a maximum of around 300 mm during January. This is related to the cloudiness maximum we earlier referred to in some detail. From these large rainfall amounts one can infer that this region east of Australia over the New Hebrides Islands is mostly convective. This is a quasistationary rainfall belt elongated from the Equator south/southwestwards into the southern Pacific Ocean. As stated earlier, the quasistationarity of this large-scale rainfall belt poses an unsolved problem.

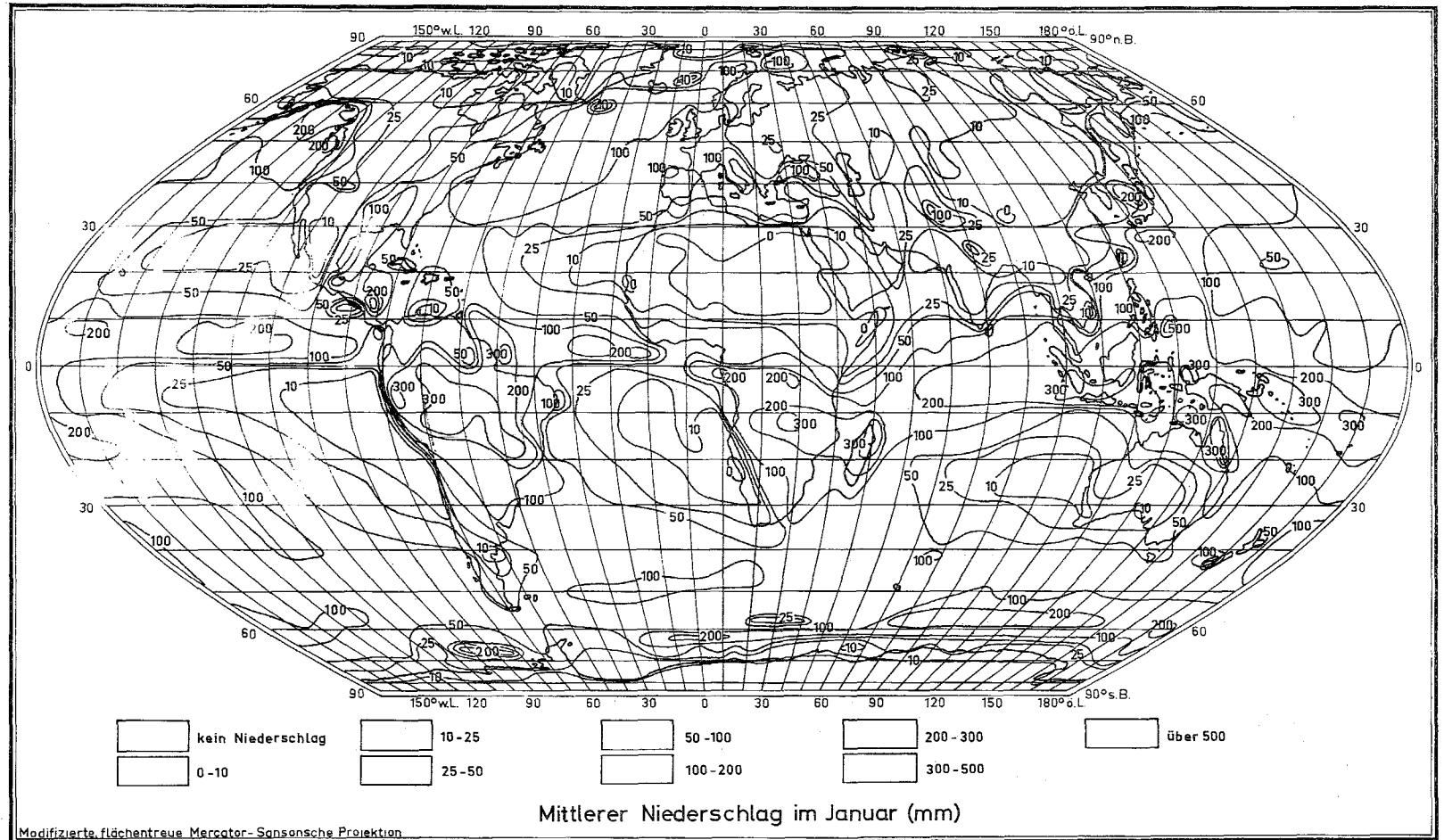


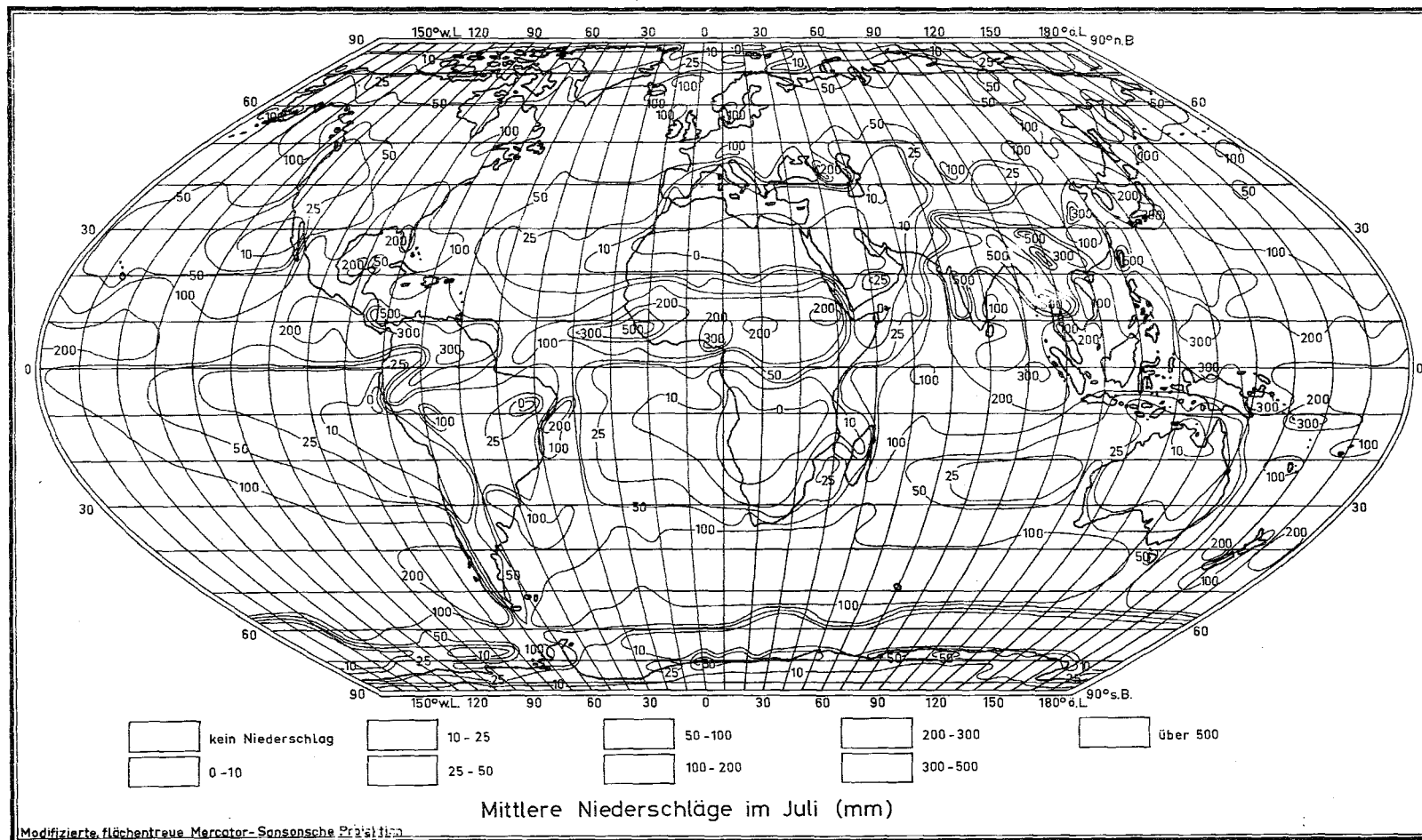
Figure 16.3a - Climatological rainfall. JANUARY. Jaeger (1976)

- (b) April rainfall totals, Figure 16.3b. The rainfall maps change considerably over the land areas and the Indian Ocean, but less so over the Atlantic and Pacific Oceans. Over the land masses of South America and Africa the belt of rainfall maximum (around 200 to 300 mm) moves Equatorward. This is the period of heavy rain over northern Brazil and equatorial and east African countries. A number of countries, such as Kenya, publish their own climatological rainfall maps. These are very detailed and contain far more information than it is possible to include in a global chart. The rainfall belt over Indonesia and the dry belt over Australia remain until April and are prominent features.
- (c) July rainfall totals, Figure 16.3c. This is the period of intense summer monsoon activity over Asia and West Africa. During this month the totals begin to exceed 500 mm over several regions, such as:
- (i) The west coast of India;
 - (ii) Bengal, Bangladesh and the Burma coast;
 - (iii) Central America;
 - (iv) The Philippines; and
 - (v) The West African Guinea coast.

Most of the active rainfall is north of the Equator during this month. The western and eastern Pacific both indicate rainfall amounts in excess of 200 mm along the ITCZ which is located between 5° and 10° N. A rainfall maximum at 10° S on the Brazilian coast is related to the surges in the southeast trades of the southern Atlantic Ocean. This belt is located just adjacent to the dry zone of northeast Brazil where one notes negligible rainfall totals during July. These are two interesting orographically controlled features. In order to study the summer local rainfall problem in further detail the student should examine the tabulations of Wernstedt or regional climatic publications.

- (d) October rainfall totals, Figure 16.3d. The regions of intense rainfall exceeding 300 mm are:
- (i) The West African coastal area;
 - (ii) Malaysia;
 - (iii) The Indian Ocean extending eastwards over Indonesia to the Philippines;
 - (iv) Northeast of Australia along the island chain;
 - (v) Central America; and
 - (vi) Along the north Vietnam coast.

The ITCZ rainfall totals over the southern Indian Ocean, western Pacific and eastern Atlantic are quite large. The activity along the eastern Pacific and western Indian and Atlantic Oceans has weakened by October.



Bericht Deutscher Wetterdienst Nr. 139 (1976)

Figure 16.3c - Climatological rainfall. JULY. Jaeger (1976)

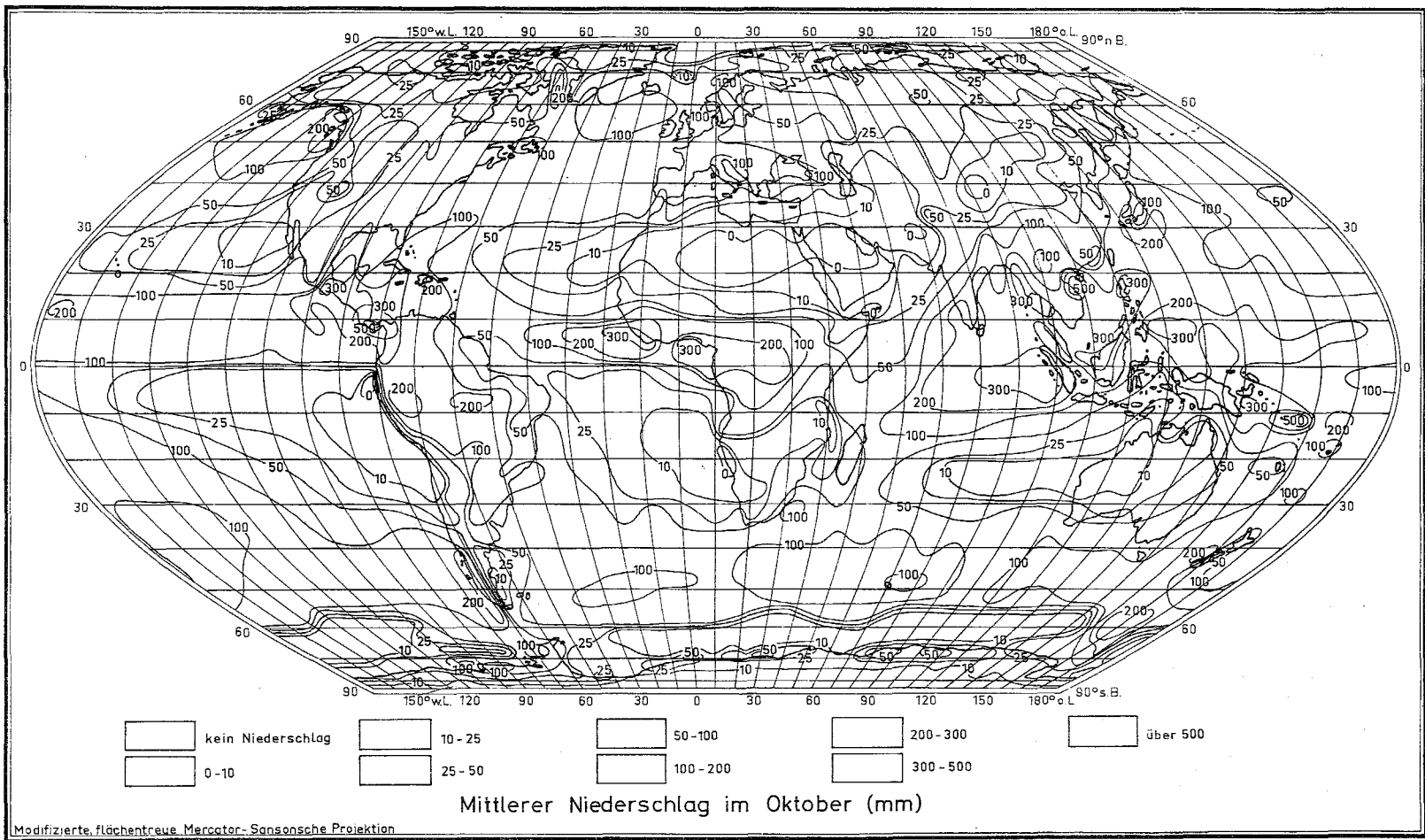


Figure 16.3d - Climatological rainfall. OCTOBER. Jaeger (1976)

16.3 Mapping of rainfall rates from satellite brightness data

When one intercompares observed rainfall rates with satellite brightness the one-to-one correspondence is not always apparent over all regions. The reason for this is that although satellite brightness of newly-forming clouds has some correspondence to rainfall rates, older and long-lasting clouds and their anvils do not exhibit the same kind of relationship. The latter account for a large fraction of the total cloud cover. A closer examination of data shows that the time change of satellite brightness measured from several frames, bears a better relationship to observed rainfall rates. Hence, it is desirable to collect satellite brightness information from several successive observations (roughly 30 minutes apart) from geostationary satellites. Griffiths *et al.*, (1978) have outlined a procedure for mapping rainfall rates from satellite data of cloud brightness measured from visible as well as infrared digital products. A three-way interrelationship among (i) rain-gauge measurements, (ii) radar reflectivity, and (iii) satellite brightness is obtained in these studies. The following is a summary of their method.

- (i) The negatives of the satellite brightness (obtained from satellite photographs) are magnified roughly 33 times using a densitometer. A densitometer can display on a monitor (in either black and white or in colour) all or part of the image of a film transparency. It can enhance a brightness contrast and also colour code a satellite photograph's relative brightness over its different regions. The colour scheme (called false-colour coding) can be used to provide a clear distinction between low and high clouds, oceans and land. A digital count in the range of 0 to roughly 250 units is used to describe a satellite photograph.
- (ii) The next step is to define a test area where a good network of raingauges exists. Here one should recognize the limitations of rainfall measurements from raingauges due to unrepresentativeness of the sites where they are placed. Buildings, hills and local effects can influence the rainfall measurements and may not be representative of the scales in which one is interested. Thus, the data from a network of raingauges are better suited for the calibration of the satellite-derived products.
- (iii) The radar is able to provide a better integrated picture of meso-scale rainfall if the radar reflectivity is calibrated with the rain-gauge data. Here one constructs a nomogram of the echo area (as sensed by raingauges) over a region of good surface observations and radar coverage. Such a nomogram requires to be fine-tuned for each region; furthermore, it should also take into consideration the representativeness of rain-gauge data. Figure 16.4 shows a map of rainfall (measured over 24 hours) based on rain-gauge data which was extended using a standard Z-R relationship using radar data: ($Z = 230 R^{1.25}$). This map was prepared for a period during the GATE Experiment.

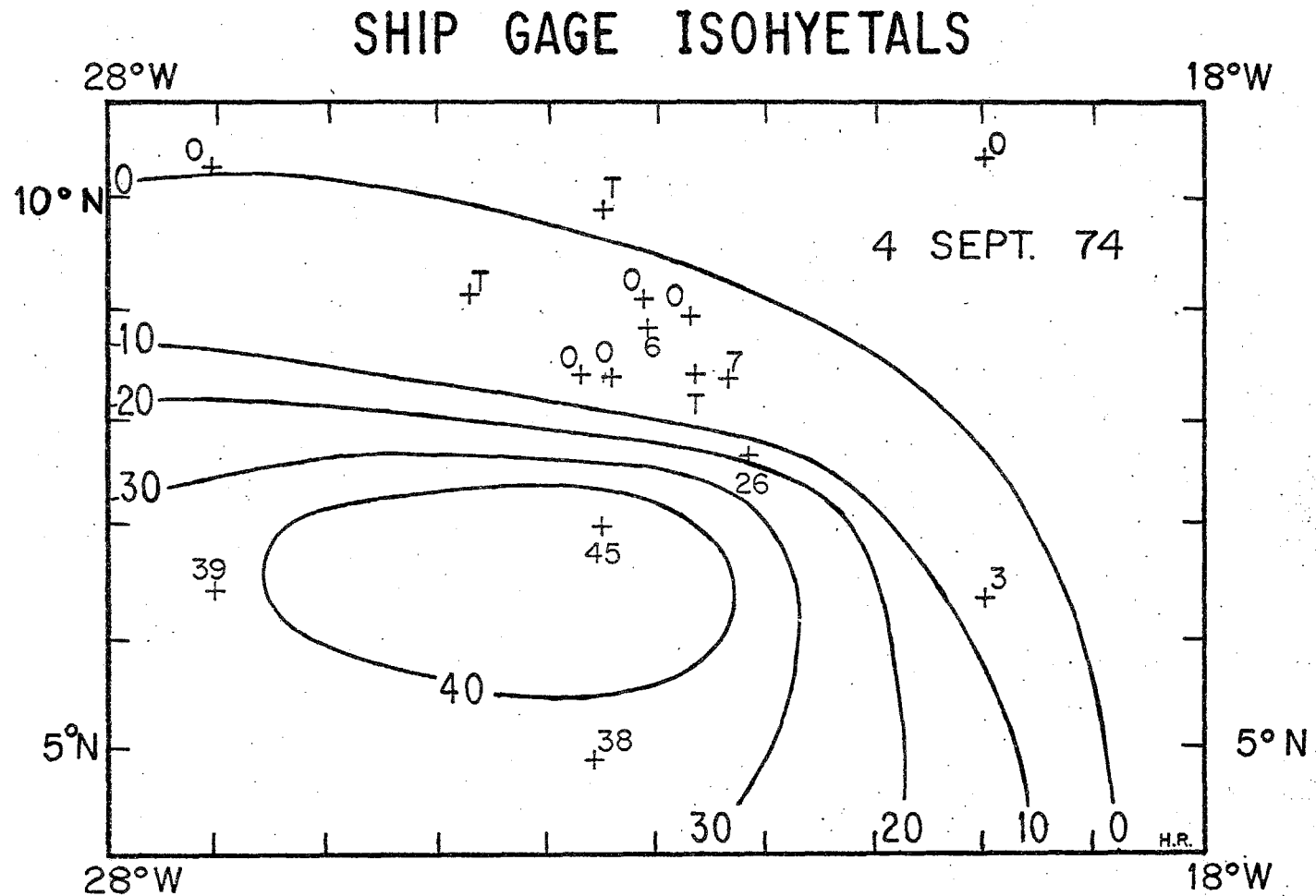


Figure 16.4 - Isohyetal analysis of the 18 ship gauge daily rainfalls (mm) over the A/B-scale for 4 September 1974. Ship positions and gauge readings have been plotted. "T" denotes trace. Analysis kindly provided by H. Riehl. Compare with the satellite-estimated rainfall of Figure 16.6.

(From Griffiths, Woodley et al.)

- (iv) Calibration of satellite-derived products. Figure 16.5 illustrates a relationship between the area of clouds A_c (measured from satellites) and the area of the cloud echoes A_e (measured from radar). Here both A_c and A_e are nondimensionalized with respect to a maximum cloud area; A_m defined as 80 digital counts on a brightness scale. The graph distinguishes between a period of increasing cloud area and one of a decreasing area. This distinction is important because non-precipitating anvils can occupy a large area in the later stage of a cloud's life cycle.

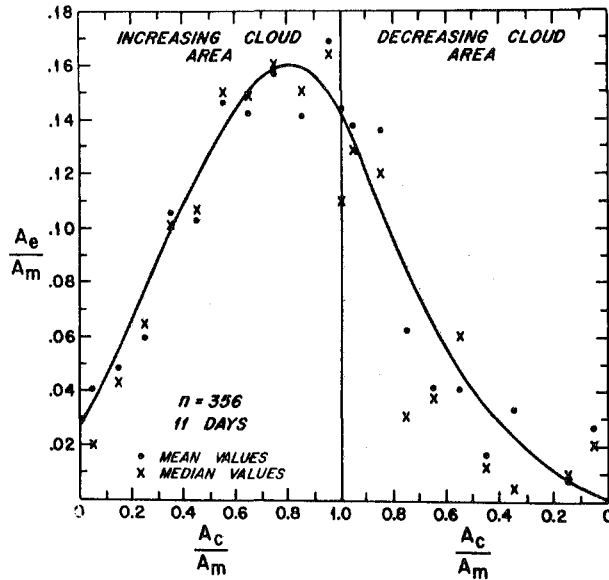


Figure 16.5 - The cloud area / echo area relationship. Both cloud (A_c) and echo (A_e) areas have been normalized to the (relative) maximum cloud area (A_m). Data have been averaged over intervals of $0.10 \times A_c/A_m$. The curve is an eyeball fit to the mean data. Median values are also plotted

(From Griffiths, Woodley et al.)

Finally, in Figure 16.6 we illustrate a rainfall chart during GATE obtained from the satellite products. The calculations shown here should be compared with Figure 16.4 which shows the field based on surface-based observations.

16.4 Rainfall maps from microwave radiometer data

The microwave radiometer is another powerful tool that is becoming increasingly important for the mapping of rainfall over tropical oceans. Rao *et al.* (1976) have prepared an atlas of this product based on satellite observations made by an Electrically Scanning Microwave Radiometer (called ESMR). The ESMR operates at 19.35 GHz (band with 250 MHz). The oceans provide a nearly uniform background for the estimation of rainfall rates. Here one uses ESMR brightness temperature to map the rainfall. The brightness temperature is a product of the emissivity of water near 19 GHz and the thermodynamic temperature. Figure 16.7 shows a nomogram prepared for ESMR by Rao *et al.*, (1977) for the rainfall atlas. They studied the rainfall over global oceans during 1973 and 1974 by this method. They note large interannual variations in the rainfall over the Pacific and Indian Oceans. Their studies also indicate an interesting region of large rainfall over the southwestern Atlantic Ocean during the southern winter season. It is most probably related to quasistationary frontal zones that are oriented southeast to northwest. Figure 16.8 from this study illustrates the inter-annual variability over the Pacific Ocean.

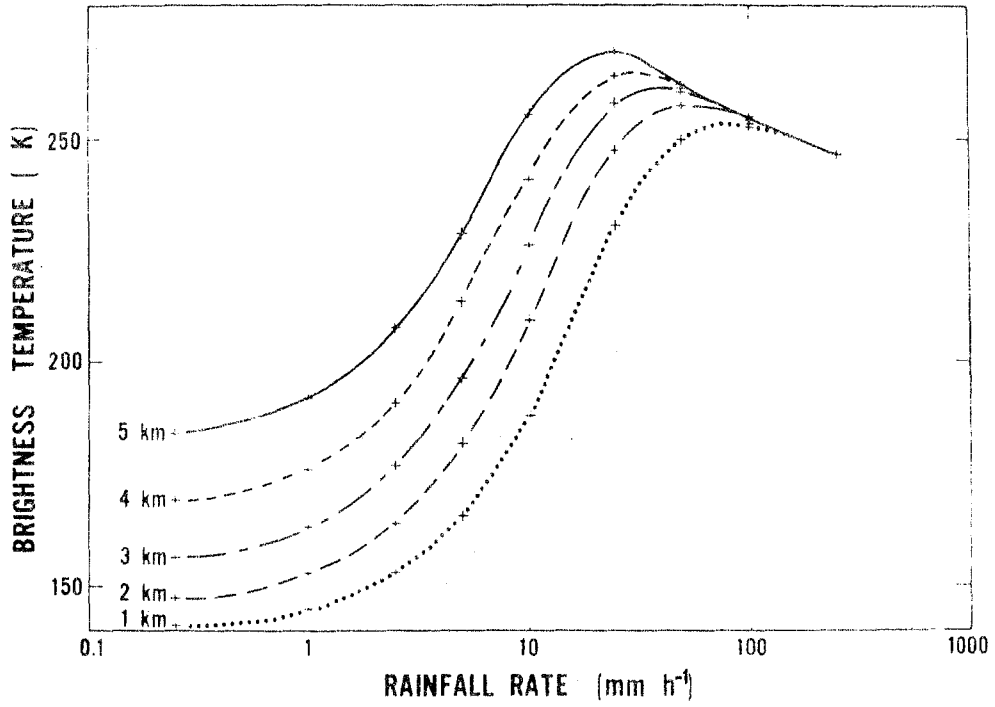


Figure 16.7 - Rainfall rate (mm h^{-1}) versus brightness temperature (K) at different freezing levels

(From Rao et al., 1976)

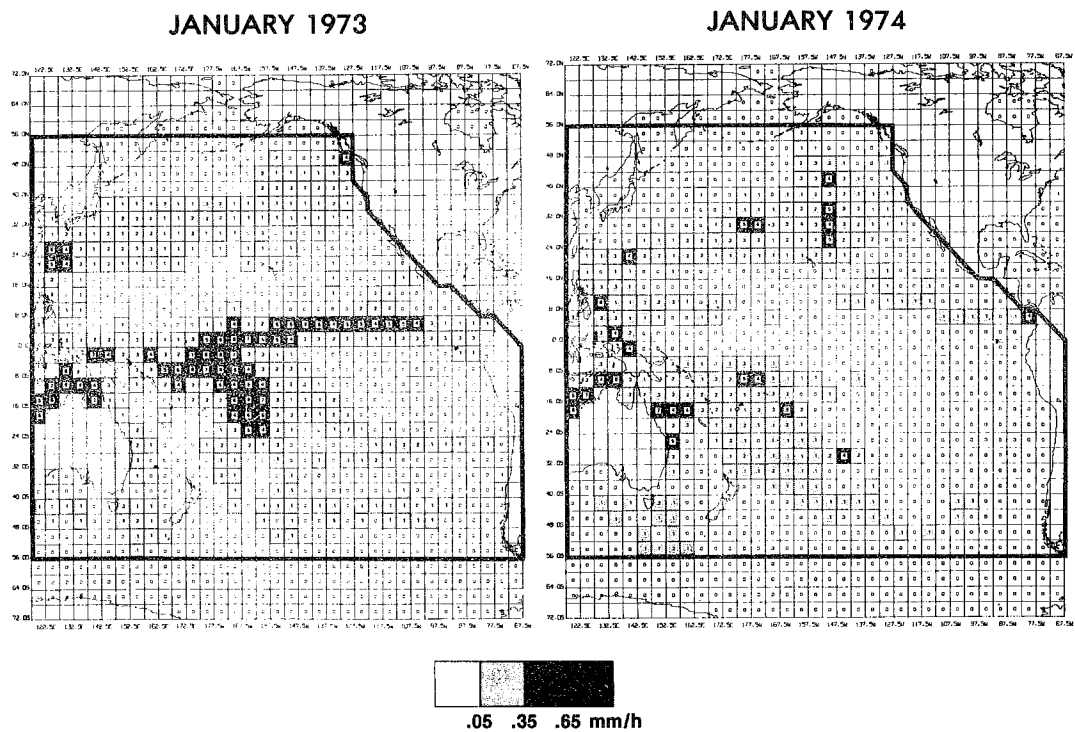


Figure 16.8 - ESMR-derived Pacific Ocean average rainfall rate for January 1973 (el Niño year) and January 1974 (non-el Niño year)

(From Rao et al., 1976)

Chapter 17

TROPICAL UPPER-TROPOSPHERIC PHENOMENA

The tropical upper troposphere contains a variety of disturbances such as jet streams, quasi-stationary troughs and ridges, transient waves, upper cold lows and dynamic and thermal anticyclones. There are two major jet streams: (i) the subtropical jet stream of winter (e.g. see Krishnamurti, 1961) and (ii) the tropical easterly jet stream of northern summer. The quasi-stationary troughs are the mid-oceanic troughs that were discussed in Chapter 2; the quasi-stationary ridges are found over continents during the summer seasons. Transient waves are usually observed on the cyclonic shear side of the tropical easterly jet. Upper cold lows are frequently found in the summer hemispheres near 20°N and 20°S latitude. These are very slowly westward-moving transient systems and occur within the quasi-stationary long-wave mid-oceanic troughs.

The formation and maintenance of these upper tropospheric disturbances are usually discussed in terms of calculations of their energetics. In this section, we shall present a brief review of the jet streams, upper cold lows, warm anticyclones and upper waves and their maintenance.

Many studies show that the scales, speeds of propagation, structure and life cycle of the lower and upper-tropospheric disturbances are different and that they are often decoupled. However, there also exist upper anticyclones which are an integral part of the lower-tropospheric cyclonic disturbances; also, one frequently observes upper-closed lows over the oceanic tropics that are coupled to lower-tropospheric cyclonic wave disturbances.

17.1 The subtropical jet stream of winter

The subtropical jet stream of winter was investigated by Defant and Taba (1957) and Krishnamurti (1961). These studies were based on aerological observations for the winter of 1955 and 1956. The data coverage of the present day is of an order of magnitude better than during that year. The jet is known to be located near the 200 mb surface. The precise mechanisms for the formation of the subtropical jet stream of winter are not well understood. From global observations and results of general circulation models one gets the impression that the following sequence may be important for our understanding of this phenomenon.

- (i) The heat balance of the Siberian area results in a net cooling of air at low levels.
- (ii) The mountains to the west, east and south of Siberia traps this cold air at low levels.

- (iii) The atmosphere tends to balance this intense rate of cooling by creating downward motion and adiabatic warming of air at low levels.
- (iv) The descending air spreads at the surface under the influence of surface friction and a polar anticyclone forms over this region which is called the Siberian high of the winter season.
- (v) A south-north directed sea-level pressure gradient extends all the way to the Equator.
- (vi) The flows from the north develop at the surface down this pressure gradient. Parts of these flows are called the north-east monsoons.
- (vii) This air converges and ascends along the ITCZ over the southern Indian Ocean near 5°S and over Indonesia and southern Malaysia.
- (viii) On a vertical cross-section near 120°E or 140°E , the ascending branch of a local Hadley type overturning occurs between roughly 5°S and the Equator. The Hadley type overturning is enhanced and maintained by the heat released in the convective region near 5°S , and by the descending motions near 30°N which are partly forced by the descent of the Siberian air at these latitudes. A strong westerly jet forms at the poleward edge (i.e. near 30°N) of this local Hadley cell located around 120°E to 140°E .
- (ix) From here on the influence of the mountains, primarily the Himalayas, seems crucial in determining the global geometry of the subtropical jet stream of winter.
- (x) The heat balance of the atmosphere over Tibet also has a crucial influence in locating the axis of the subtropical jet south of the Himalayas. A cold troposphere is found over the Tibetan Plateau during northern winter.
- (xi) One wave of the axis of the subtropical jet stream of winter extends from northern India towards Japan, the ridge being located slightly east of Japan near 30°N . The strong influence of Siberia (its heat balance), the Himalayas, and Tibet (its heat balance) anchors this wave in a quasi-stationary position.

- (xii) A quasi-stationary three-wave pattern forms over the globe around roughly 27°N ; ridges being located east of Japan, east of the southeast coast of the United States and over the Mediterranean Sea; and troughs being located over the Arabian Sea, central Pacific Ocean and central Atlantic Ocean.
- (xiii) The speed of the jet is found to be a maximum in the ridges and weaker in the troughs. The stronger winds in the ridges are related to strong ageostrophic south-easterly flows towards lower pressure in the ridges. Northwesterly flows are found upstream from the troughs. These flows are also somewhat ageostrophic and towards higher pressure, the net result being that troughs tend to exhibit a minimum in the speed.
- (xiv) The ageostrophic flows in the southwesterly branch of the the subtropical jet is, in fact, seen to originate from the ITCZ. This air moves northeastwards crossing towards lower pressure, giving rise to strong winds in the ridges of the subtropical jet stream of winter. There exists a one-to-one relationship between the three ridges of the subtropical jet stream and the following three well-known rainfall belts of the northern winter season:
 - (i) The Indonesia - southern Malaysia region;
 - (ii) Equatorial central Africa; and
 - (iii) The Amazon and the northwestern part of South America.

This activity in these land-area (ITCZ) rainfall belts may, in fact, be a consequence of the formation of the global subtropical jet stream of winter. There most likely exists a major influence of the Siberian, Tibetan and Himalayan region on the circulation over the rest of the global tropics. This can be established only by carefully controlled numerical experiments. Figure 17.1 provides a schematic outline of the major upper tropospheric phenomena that are relevant to the understanding of the subtropical jet stream of winter. The three major tropical rainfall belts provide a link between the northern and southern hemisphere phenomena.

- (xv) During the northern winter three middle-oceanic quasi-stationary troughs are found in the southern oceans, the divergent upper level outflows from the near-equatorial rainbelts converging into these upper troughs. For the maintenance of these mid-oceanic troughs, the vorticity generation by these east/west overturnings shown in Figure 17.1 are considered to be important.

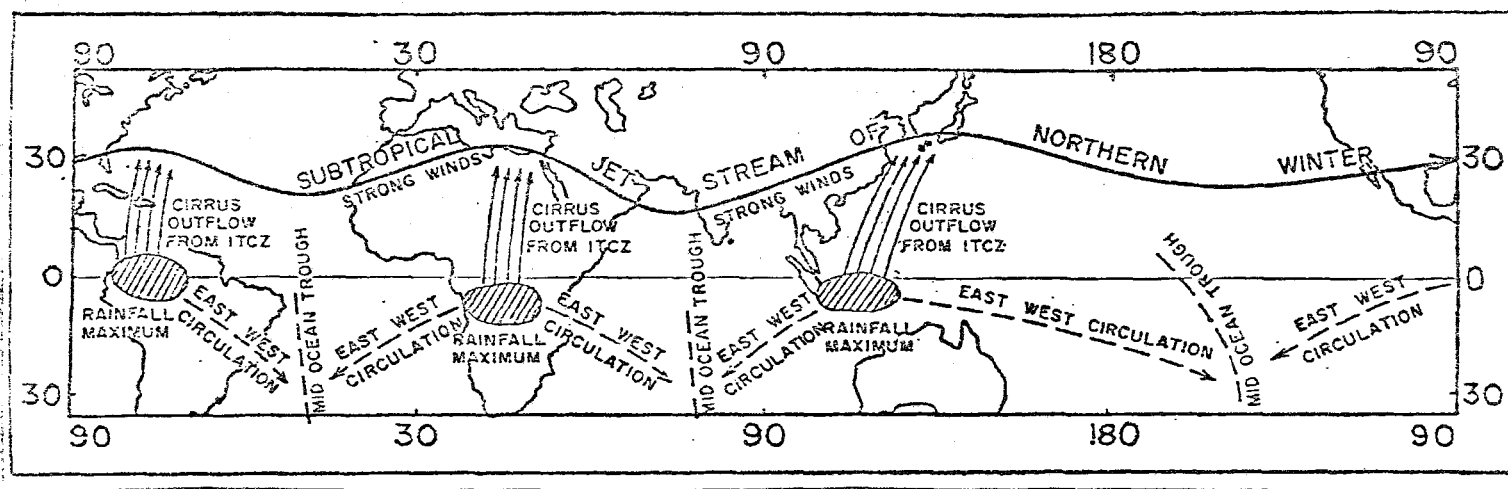


Figure 17.1— A schematic illustration of the subtropical jet stream and some associated features during northern winter

The fifteen points presented here do not give a very convincing explanation of the existence of the global subtropical jet. Maybe they should emphasize more clearly the global aspects. In the upper troposphere the mid-oceanic troughs have relatively lower temperatures than the rest of the tropics. The tropical upper-cold lows are an interesting phenomenon and are discussed in section 17.4.

The southern oceans are data void and the only useful source of data is commercial aircraft wind reports. Much of our present knowledge is based on this data source. Subtropical fronts are upper tropospheric frontal zones that are found below the subtropical jet stream of winter. These were first noted by Defant and Taba (1957). They do not usually extend down below 600 mb. They most likely form as a result of geostrophic adjustment of the mass field to the strong winds aloft, thus providing thermal wind consistency in these subtropical latitudes. We shall not go into a detailed description of the tropical easterly jet here since it is described elsewhere as a monsoon problem.

17.2 Barotropic instability of the tropical upper-level jets

(a) Subtropical westerly jet of winter

In Chapter 2 we discussed the climatology of this jet. The meridionally varying zonal flow of this jet at different longitudes was subjected to the following two tests (see the Appendix for theoretical discussions):

- (i) Whether or not the condition for the existence of barotropic instability was satisfied by the data along different meridians; and, if the above criterion was satisfied;
- (ii) The determination of the scales and growth rates of the most unstable barotropic waves.

As stated earlier, the interesting regions of the subtropical jet stream of winter are located near: the western Atlantic Ocean (near 30°N), south of the Mediterranean Sea, over India near 90°E, and the western Pacific Ocean (near 30°N and 140°E).

In all these four regions the data sets of the summer mean zonal flows satisfy the necessary condition for the existence of barotropic instability. This is determined by noting that the meridional gradient of absolute vorticity $\frac{\partial}{\partial y} \left(-\frac{\partial \bar{u}}{\partial y} + f \right)$ vanishes somewhere within 10° latitude on either side of the subtropical jet stream of winter.

Figure 17.2 shows the graphs of the growth rate versus the scales for barotropic instability in these four regions of the subtropical jet stream of winter. These graphs are based on calculations of the linear stability using the so-called finite-difference method, described in the Appendix to these notes. The region downstream from the southeastern United States shows a very weak growth rate for a scale of the 3 500 km waves. The interesting region of the subtropical jet stream

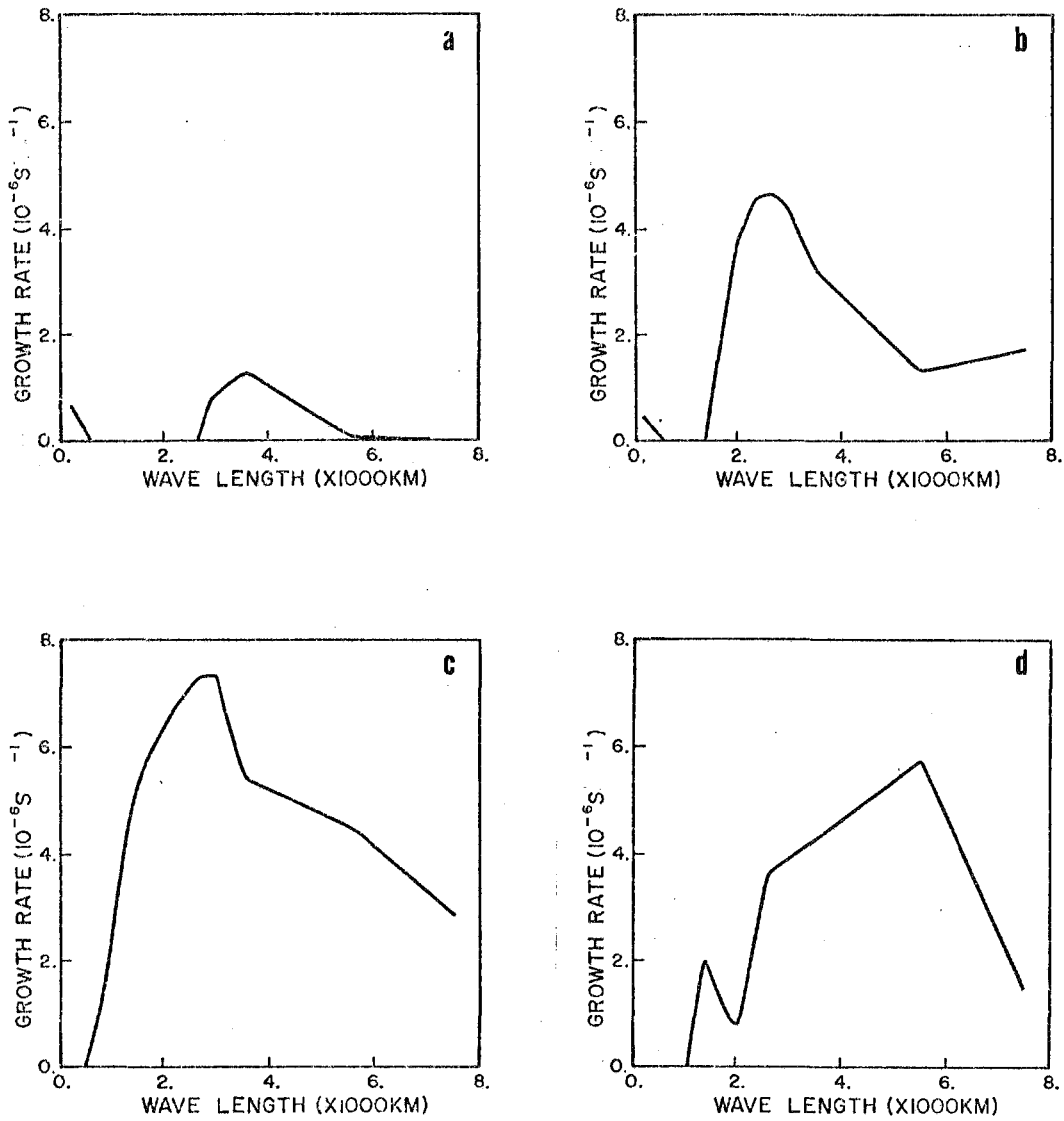


Figure 17.2 - The growth rate versus the scales of the disturbances on January mean map of: (a) west Atlantic Ocean (near 30°N), (b) southeast of the Mediterranean Sea (near 45°E), (c) Indian Ocean (near 90°E), and (d) western Pacific Ocean (near 30°N and 140°E)

of winter extends from North Africa to the strong wind region near Japan. Here the growth rates are very large, i.e. with a doubling time of 2-3 days (Figure 17.2) and the scale of the maximum growth rate gradually increases as one proceeds eastwards:

- (i) Mediterranean - 2 200 km ;
- (ii) India - 2 800 km ;
- (iii) Near Japan - 5 500 km .

This downstream increase in the scale of instability is not well understood. Wind observations along the subtropical jet stream of winter do exhibit small amplitude fluctuations on the time scale of a few days. These are evidently the transients driven by the barotropic instability. The dominant modes, however, are the quasi-stationary long waves of the subtropical jet which are primarily driven by the Hadley and east/west type overturnings. These studies suggest that the upper-level shorter waves draw energy from local zonal flows barotropically, while the longer waves are baroclinic and it is necessary to invoke the effects of vertical circulations to explain their maintenance.

(b) The tropical (monsoonal) easterly jet of the upper troposphere during northern summer

The climatology of this jet was reviewed in Chapter 2. Its dynamics is presented in Chapter 13. Here again we examine the (i) necessary condition for the existence of barotropic instability, and (ii) the scales and growth rates of maximum instability along the easterly jet.

All along the tropical easterly jet from its entrance region near 150°E to the exit region near the Greenwich meridian, the local meridional profile of the monthly mean zonal flows (across the jet) satisfies the necessary condition for the existence of barotropic instability. The results of calculations of the growth rates of barotropic instability as a function of scale are shown in Figure 17.3. The most remarkable result here is a decrease in the growth rate along the jet from the western Pacific to the west coast of West Africa. The scale of maximum growth rates (as in the case of winter) also increases downstream along the easterly jet stream; these are at:

- (i) Western Pacific Ocean - 2 000 km;
- (ii) Indian Ocean (70°E) - 3 000 km;
- (iii) West Africa - 7 000 km.

This downstream increase in the scale of barotropic instability is not well understood.

A number of films of tropical upper level flows based on real data during northern summer indeed show that the eastern hemisphere, from the date line to the Greenwich meridian, has very interesting wave motions on scales between 2 000 and 6 000 km. These may be driven by barotropic instability of local meridional flows.

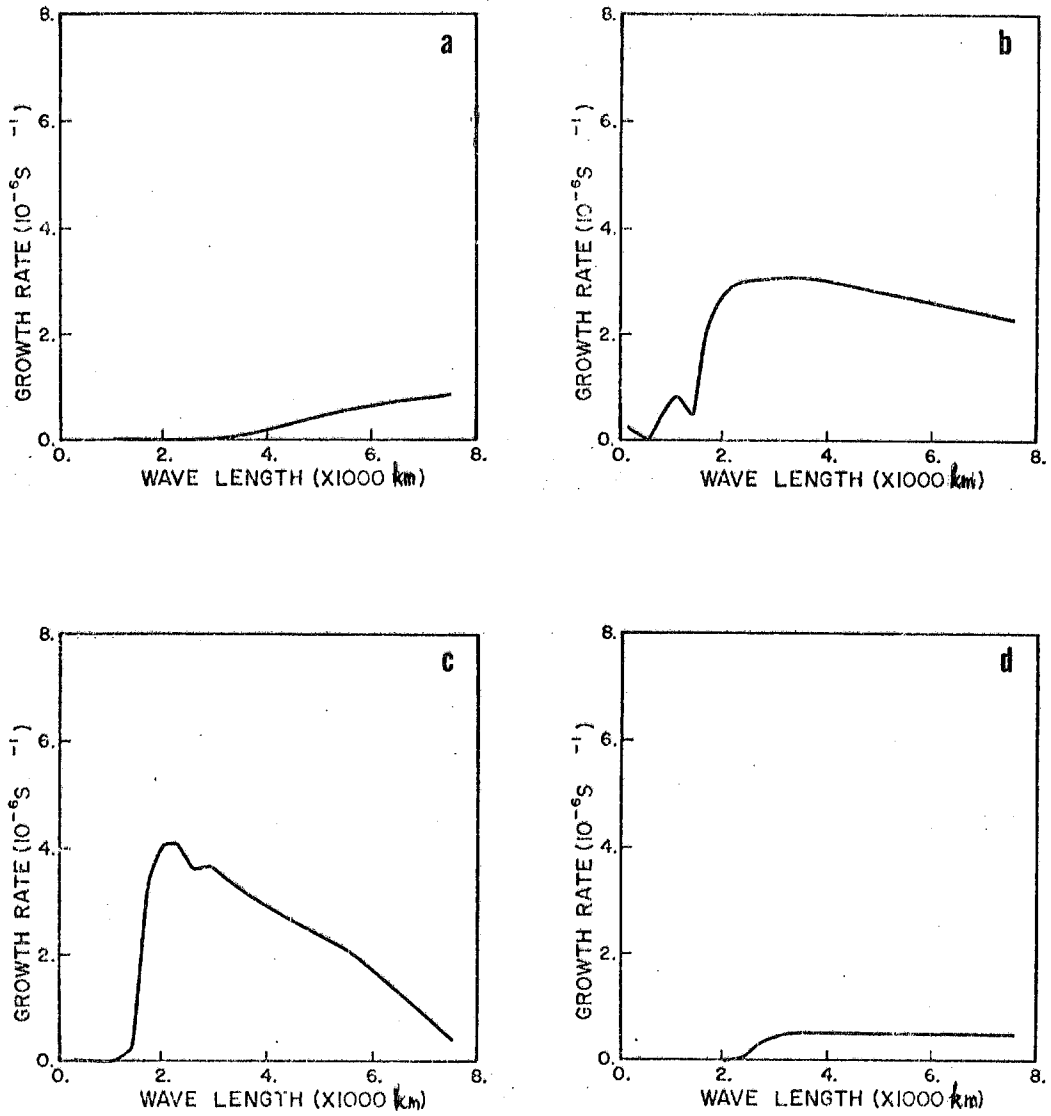


Figure 17.3 - The growth rate versus the scales of the disturbances on July mean map of: (a) West Africa, (b) Indian Ocean (near $70^{\circ}E$), (c) West Pacific Ocean and (d) mid-Pacific Ocean (near $170^{\circ}W$ and $10^{\circ}S$)

(c) The meridional as well as the zonal variation of the basic zonal current and barotropic instability

The analysis presented above does not take into account the zonal asymmetry of the tropical zonal currents which was emphasized in Chapter 3. This is an important addition that needs to be done to determine what kind of difference would arise if the zonal variation of the speed of the easterly jet were invoked in the stability analysis.

Tupaz et al., (1978) has presented an interesting analysis of a zonally varying easterly zonal jet. He shows that the major difference is that the maximum growth rate and instability occur not at the longitude of the strongest local instability but some distance downstream from it. Furthermore, the waves are shown to draw energy from the zonal jet in the region of instability, transfer it downstream where, if local conditions favour barotropic stability, this energy is transferred back to the zonal current. Tupaz's study is amenable to the analysis of a number of questions regarding the behaviour of tropical upper-tropospheric waves.

17.3 The northward seasonal march of the Tibetan high

During June, July and August the upper-tropospheric circulations over Asia are dominated by the Tibetan high. In a recent atlas by Chin and Lai (1974) the seasonal progression of this anticyclone at 200 mb is very clearly portrayed. The following diagrams (Figures 17.4 a and b) based on their study illustrated this. This upper anticyclone is recognized as a warm thermal high maintained by condensation heating. It is first seen over the South China Sea in April; it then gradually moves northwestwards until June when it is located over Tibet. The retreat starts in September and the anticyclone loses its identity by December.

During different years this event occurs at somewhat different rates and the onset and withdrawal of monsoons is evidently related to this phenomenon. One of the most important questions here is the speed of north-westward motion of this system during early summer. This is not very well understood. It is evidently related to a number of factors such as the heat balance of the land areas to the northwest and the gradual intensification of the differential heating between land and sea.

17.4 Tropical oceanic upper-level cold lows

A review of the climatology of the mid-oceanic tropical upper-level troughs is essential in this context. Figure 17.5 shows a mean map of the tropical upper-level mid-oceanic trough, following Frank (1970). The time-averaged map shows the mean trough. On daily maps one quite frequently finds in its vicinity transient upper-tropospheric cold lows. These lows generally move very slowly westwards and have a lifetime of 4 to 7 days. A large frequency of transient upper lows in the same general vicinity of the mean trough is observed. Tropical motions in the vicinity of these upper lows are often decoupled in the vertical. Below 600 mb, one frequently observes westward propagating wave disturbances and vortices. The phase speed of the latter is usually 5° to 7° longitude/day and thus much faster than that of the upper cold lows. Coupling and decoupling of these disturbances in the vertical

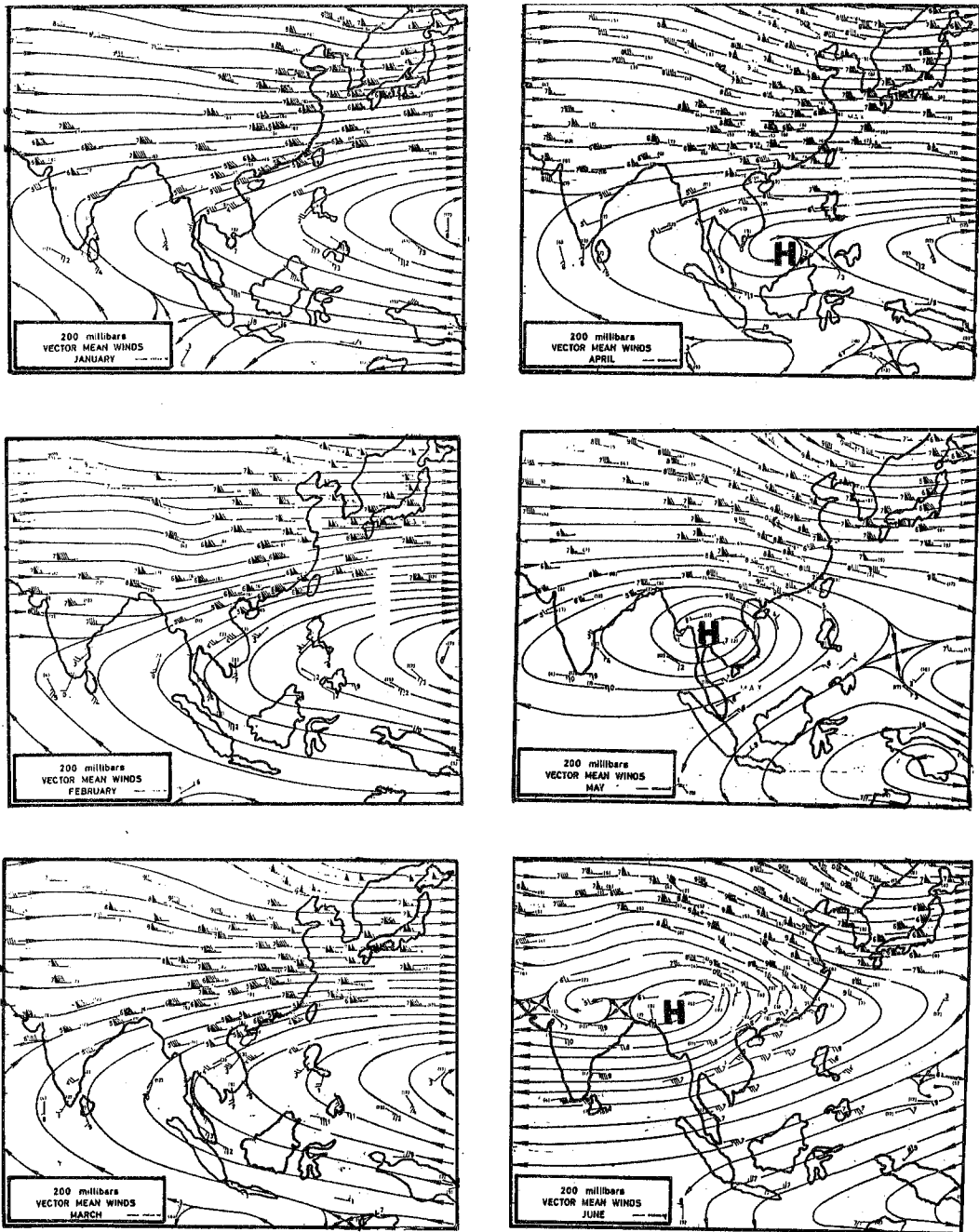


Figure 17.4a -- Monthly mean 200 mb wind field over Asia from January to June
(Based on Chin and Lai, 1974)

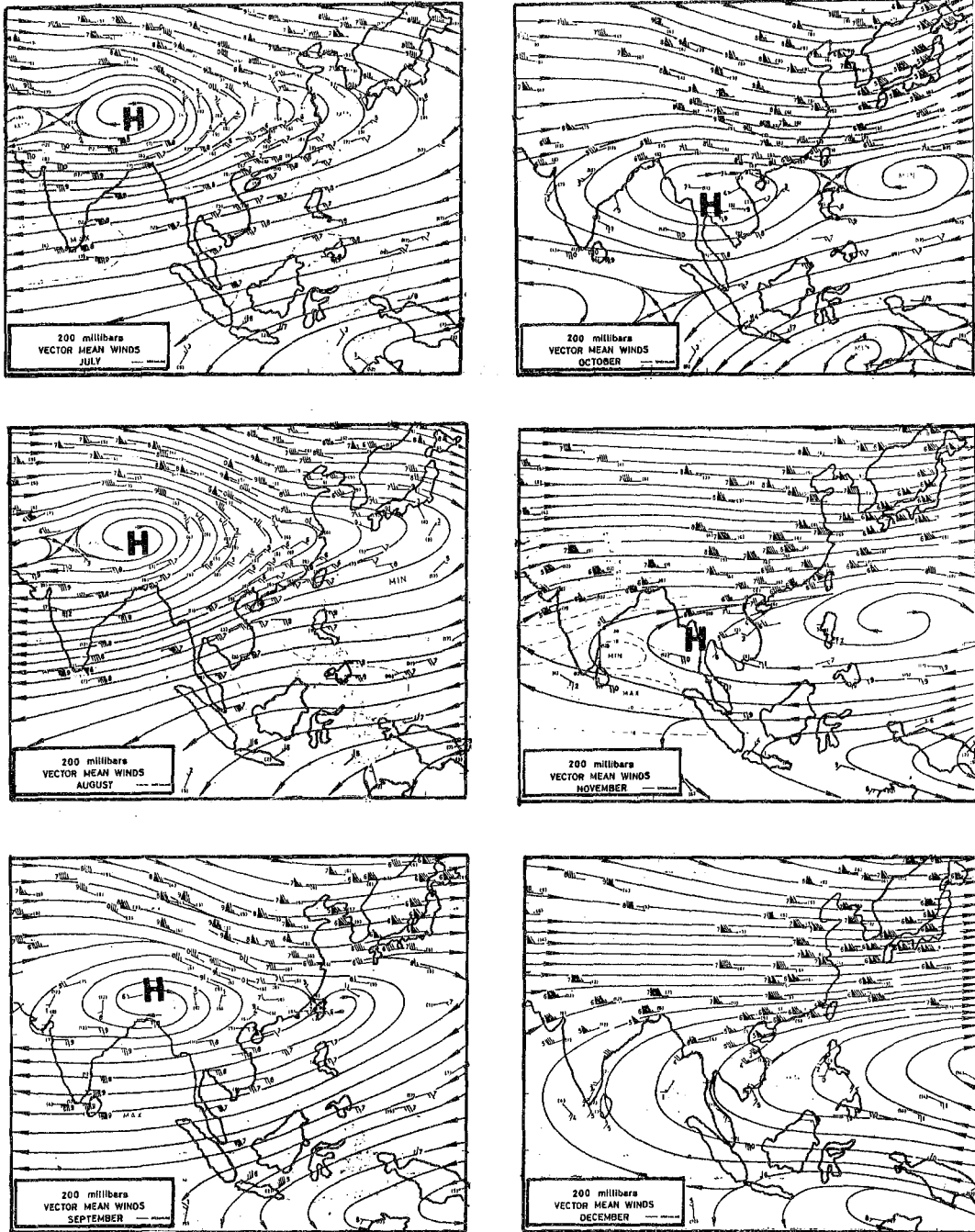


Figure 17.4b - As in Fig. 17.4a except from July to December

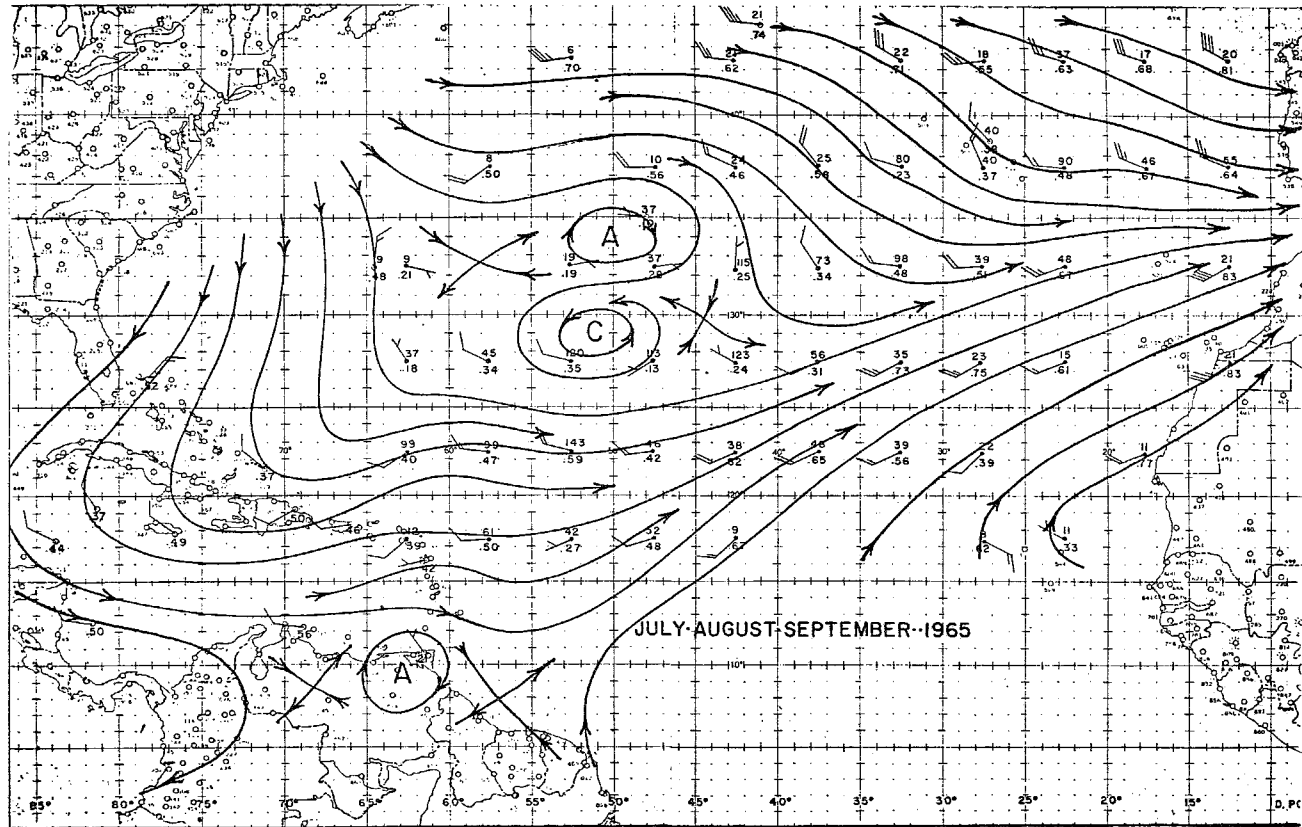


Figure 17.5 - Mean upper-tropospheric winds and streamlines for July to September 1965

are often noted. The "flare up" of the lower-tropospheric disturbances often occurs when these arrive just to the east of the upper centre. Southwesterly flows aloft usually go with ascending motions near the upper trough. This is a region where surface development of disturbances sometimes occurs. However, frequently, as the faster moving lower-tropospheric disturbances pass to the west of the upper trough, upper-level descending motions inhibit their further growth. Many lower-tropospheric disturbances weaken in this region. Frank (1970) identifies two types of upper-cold lows of the tropics. One type has a cloud-free region near the centre surrounded by a region of clouds. Figures 17.6 and 17.7 illustrate an example of such an upper low from Frank (1970). The other type of upper-cold lows contains clouds in the centre of the low with surrounding clear areas. Figure 17.8 is an illustration of such a disturbance from a study of Frank (1970). In order to appreciate the lateral and vertical scale of this phenomenon, we present a space and a time section in Figures 17.9 and 17.10. Figure 17.9 shows a detailed vertical cross-section following Erickson (1969). In this drawing, the temperature anomaly isopleths are shown (see figure caption). The thermal amplitude of the cold-core low is largest at 300 mb. It is about 4°C colder than the Jordan sounding. In fact, the cold core extends all the way up from 850 mb to roughly 250 mb. The big enigma here is the lower stratosphere. An intense warm anomaly above the cold core is found in the observations. The intensity of this lower-stratospheric warm core is much larger than that of the cold core. The cold-core low has the largest amplitude in its motion field at 200 mb where the winds (Figure 17.10) are strongest. This cross-section passes through a cold-core low of category one, i.e. it is relatively cloud-free at the centre and surrounded by cloudiness. Figure 17.11 (also from Erickson, 1969) shows a vertical time section illustrating the passage of this upper-cold low.

17.4.1 The maintenance of the cold low

A number of interesting questions arise that have not been adequately answered in the literature. How do these transient disturbances form? This question has not been addressed properly since there are no detailed observational studies in four dimensions that describe its formation. Unless such documentation is available, it will be difficult to properly pose the problem. The two categories of the cold lows raise a number of questions. The second category with clouds near the centre must have downward motions in the centre where it is coldest and thus eddy kinetic energy must be converted to eddy available potential energy by the indirect circulation. For the maintenance of this system, an energy source would be required. If we examine the following framework for this problem, we can make some speculations regarding the maintenance of this system (see Lateef, 1964):

$$\begin{aligned}
 \frac{\partial}{\partial t} \int K \, dm &= \int_{p_0}^P \oint_L v_n K \, dL \frac{dp}{g} + \int_{p_0}^P \frac{\partial}{\partial p} \int_A \omega K \, dA \frac{dp}{g} \\
 &+ \int_{p_0}^P v_n' \phi' \, dL \frac{dp}{g} + \int_{p_0}^P \frac{\partial}{\partial p} \int_A \omega' \phi' \, dA \frac{dp}{g} \\
 &+ R \int_{\ln p_0}^{\ln p} \oint_A \omega' T' \, dA \frac{d \ln p}{g} + \int_{p_0}^P \int_A \nabla \omega \cdot \frac{\partial \tau_0}{\partial p} \, dA \, dp
 \end{aligned} \tag{17.1}$$

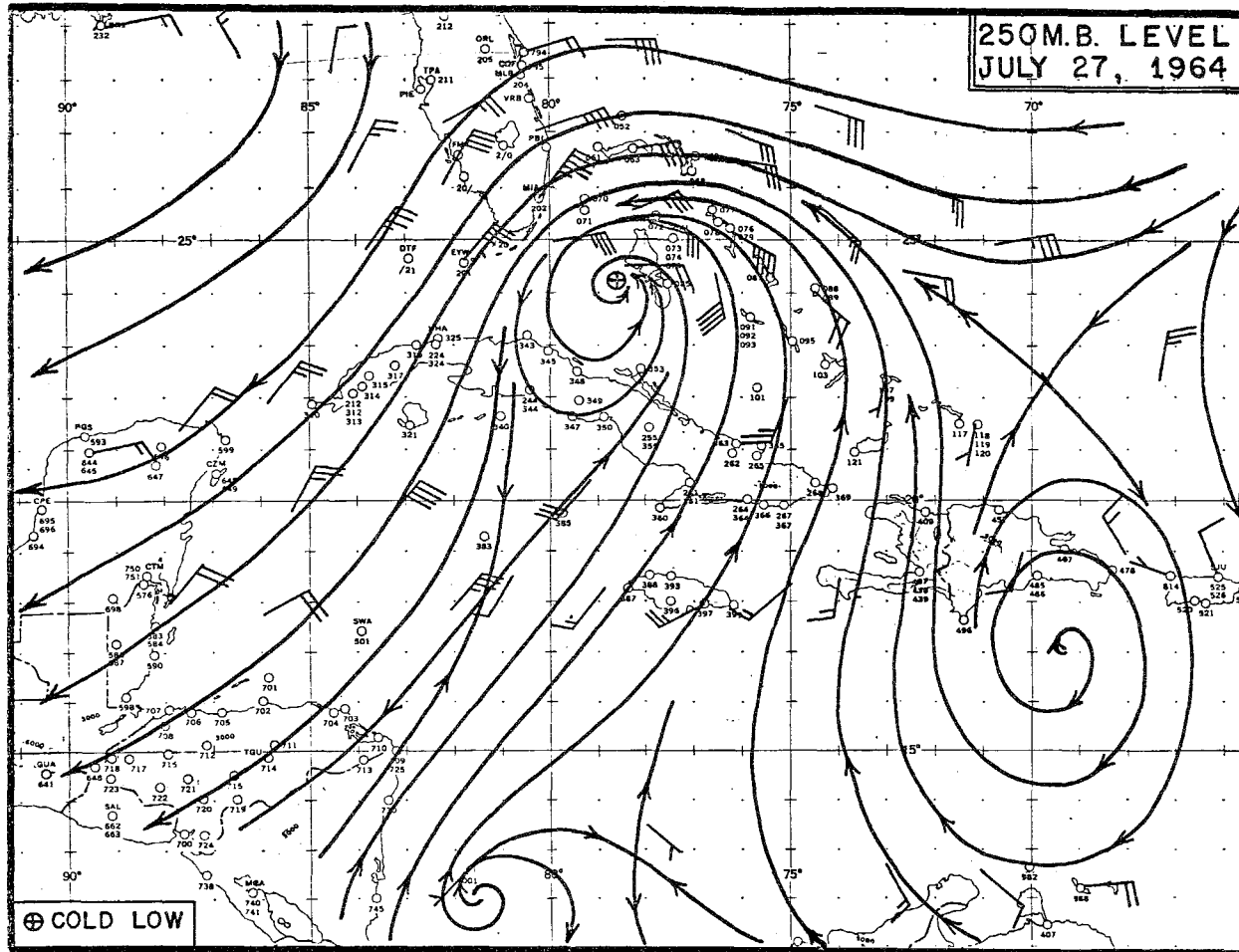


Figure 17.6 - 250 mb streamlines July 26-28, 1964

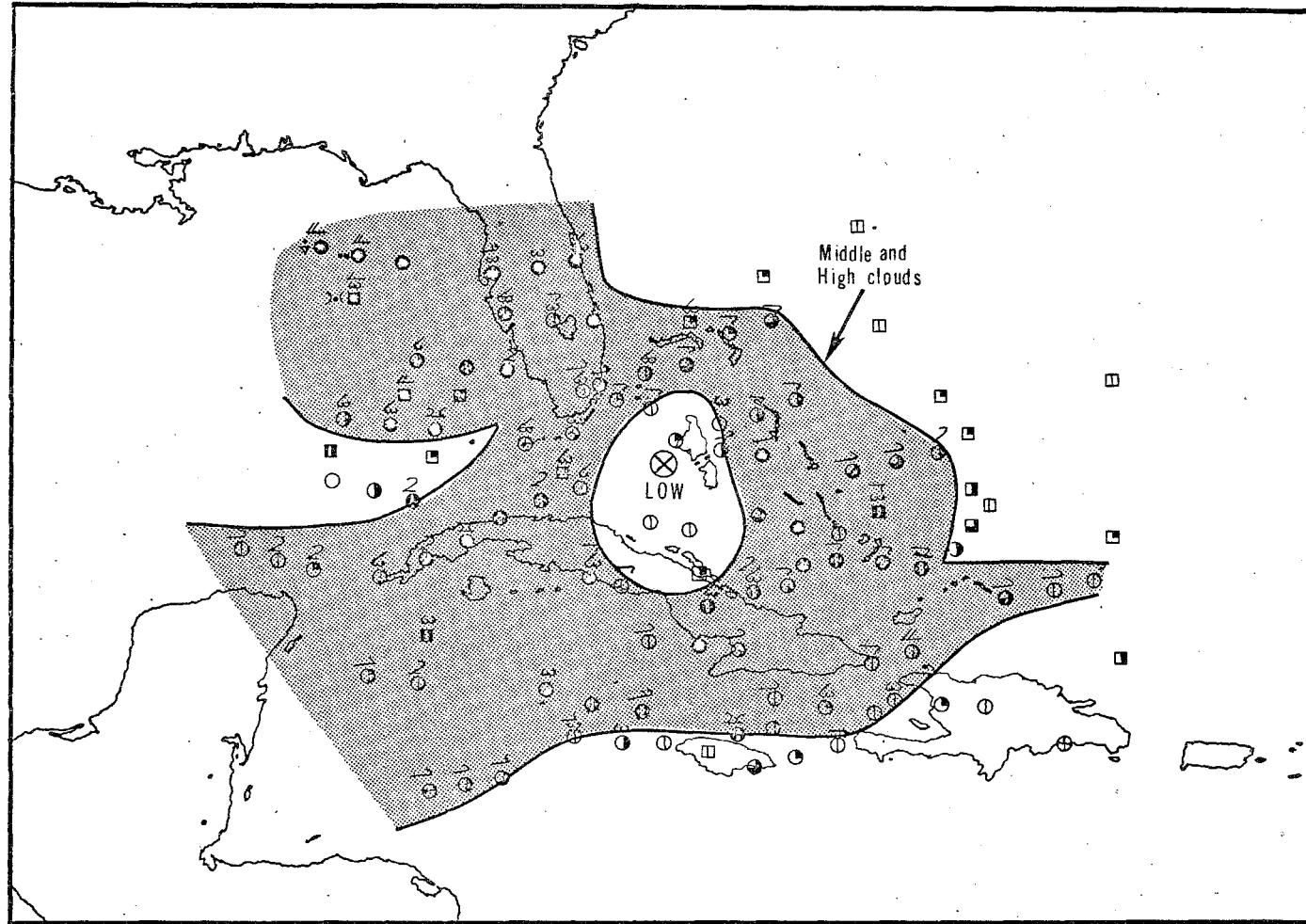


Figure 17.7 - 48-hour composite of cloud reports for the July low 1964. The scalloped line encloses reports of middle and/or high clouds

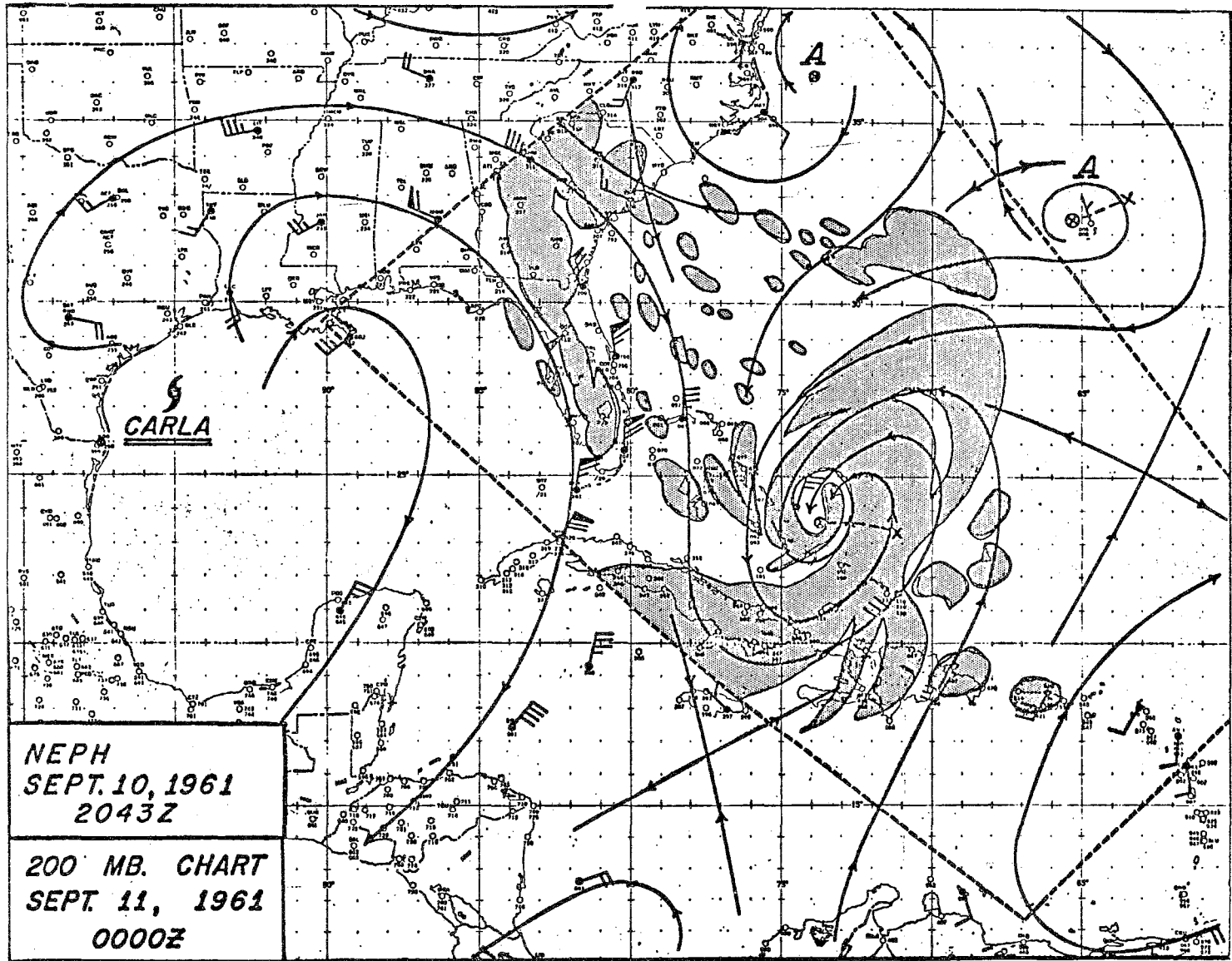


Figure 17.8 - 200 mb chart, September 11, 1961, 0000Z

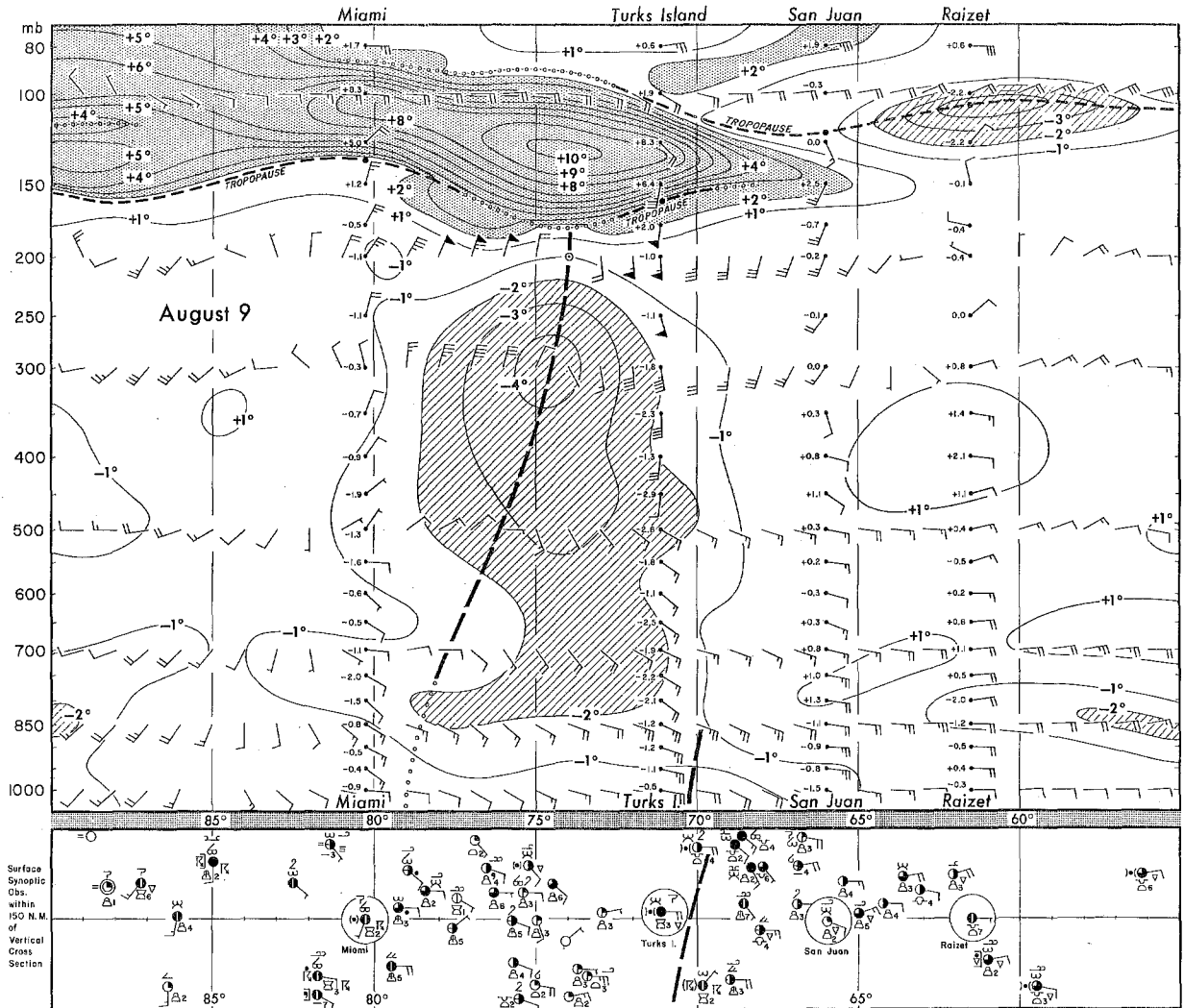


Figure 17.9 -- Vertical cross-section for 1200 GMT, August 9, 1966, along a line through Miami, Florida, and Raizet, Guadeloupe. Isolines are temperature deviations ($^{\circ}\text{C}$) from mean Caribbean atmosphere for August (Jordan, 1958) and are based on smoothed analyses at constant pressure levels. Areas of deviations exceeding 2°C are shaded. Unsmoothed data are plotted at four individual stations. Intermediate winds along standard isobaric levels are interpolated from streamline-isotach analyses. All winds, both surface and aloft, are plotted in the standard synoptic convention (one full barb = 10 kts, wind directly from left of page is from west, from bottom south, etc.). Heavy dashed lines near 75° and 70°W are axes of upper-level cyclonic curvature and low-level wave, respectively

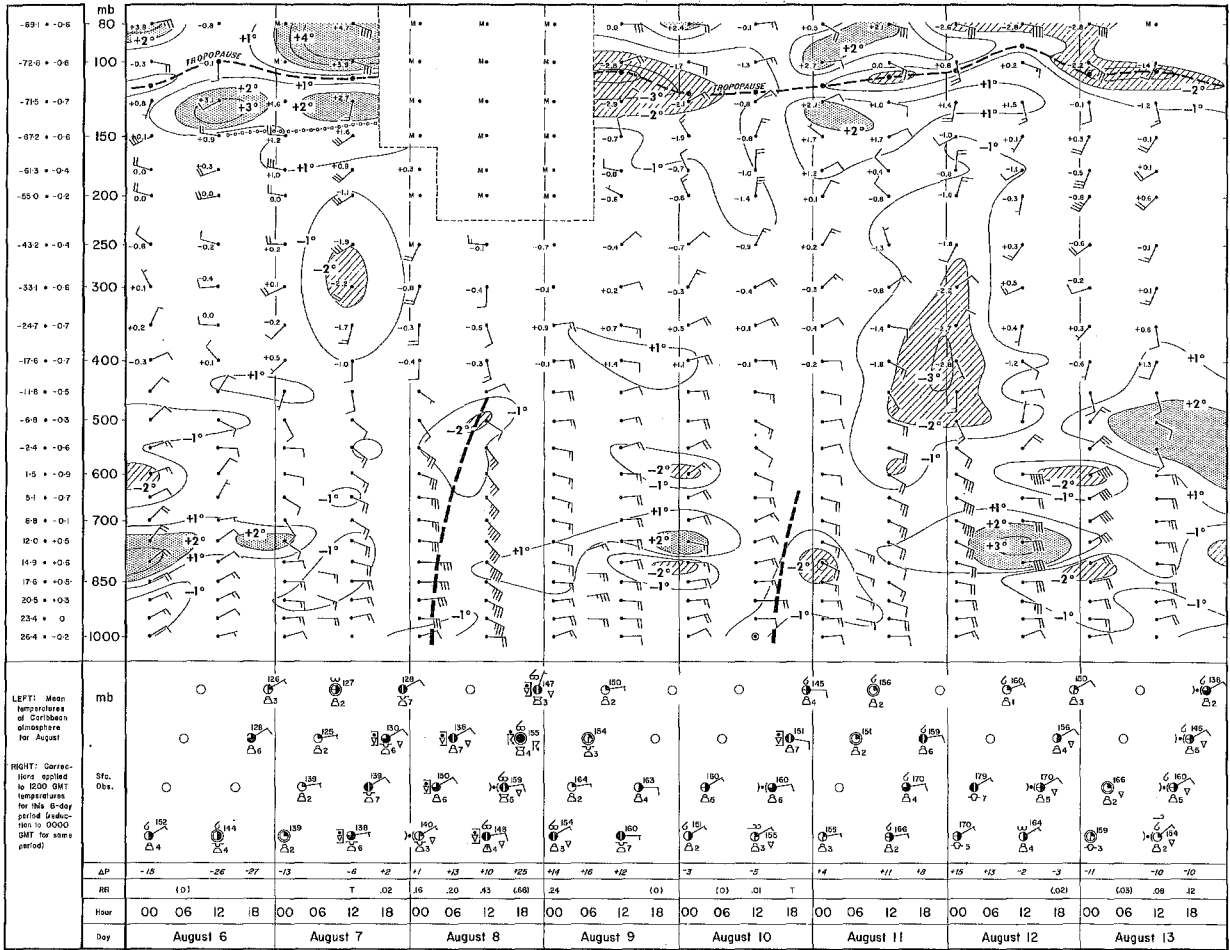


Figure 17.11 — Vertical time-section for Raizet, Guadeloupe (16°N, 61.5°W), August 6-13, 1966. Isolines are temperature deviations (°C) from mean Caribbean atmosphere for August (Jordan, 1958). Heavy dashed lines are axes of low-level waves. ΔP is 24-hour sea-level pressure tendency (to 0.1 mb) for period ending at indicated hour. RR is 6-hourly rainfall amount (to 0.01 inch, parenthetical values are estimated)

This equation is obtained by integrating the kinetic energy equation over a horizontal area A and, in the vertical, between pressure levels at the surface p_0 and the top reference level p . The various terms on the right-hand side have the usual interpretation, i.e.:

- I Lateral inward flux of kinetic energy into area A,
- II Vertical inward flux of kinetic energy into area A,
- III Lateral inward flux of eddy potential energy into area A,
- IV Vertical inward flux of eddy potential energy into area A,
- V Internal conversion of eddy available potential to eddy kinetic energy inside domain A,
- VI Frictional dissipation of kinetic energy inside domain A.

If we extend the integrations from the Earth's surface to the top of the atmosphere, then the terms II and IV are small. Table 17.1, from a study of Frank's, illustrates the magnitude of these various terms for the two categories, i.e. the dry and the wet lows. The domain was roughly a 1,000 km square. It contained the cloudy areas within it for both categories. The wet lows were decaying in time, as may be noted from the last column. The lateral pressure work term indicates that it has opposite signs for the dry and wet lows. For the former, kinetic energy is generated by the pressure work at the boundaries and thus the maintenance of this system, i.e. the dry low, depends on the boundary forcing. For the wet lows, the only source of kinetic energy is the internal conversion of eddy potential to eddy kinetic energy.

Table 17.1

Kinetic energy budgets for the three "dry" lows and the "wet" low of two days (Frank, 1970)

	Horizontal advection I	Vertical advection II	Horizontal work III	Vertical work IV	Conversion V	Residual (friction) VI	Tendency
<u>Dry Lows</u>							
July 27, 1964	-12.6	0.0	11.5	0.1	16.4	-15.4	0.0
Aug. 12, 1961	-10.9	0.0	22.7	0.1	3.0	-14.8	0.0
July 22, 1961	- 8.3	-0.1	28.2	0.0	7.2	-27.0	0.0
<u>Wet Lows</u>							
Sept. 14, 1965	- 9.5	0.0	-29.0	0.1	14.9	-18.9	-42.4
Sept. 15, 1965	-14.7	0.0	-28.9	-0.1	13.7	-11.6	-48.4

All of the other terms act to destroy kinetic energy of the wet low. Thus the magnitudes of these numbers in Table 17.1 suggest that the dry lows require a boundary forcing for their maintenance, while the wet lows depend on the internal generation mechanism.

Next consider the thermal balance. The first law of thermodynamics may be written in the form:

$$\frac{\partial \theta}{\partial t} = -\mathbf{V} \cdot \nabla \theta - \omega \frac{\partial \theta}{\partial p} + \frac{1}{c_p} \left(\frac{p_0}{p} \right)^{R/c_p} [H_s + H_c + HR] \quad (17.2)$$

where H_s stands for the convergence of the sensible heat flux from below,
 H_c stands for condensation heating, and
 HR stands for radiative warming.

For the near steady-state maintenance of the cold low, radiative cooling in the tropical upper troposphere plays an important forcing role. Frank (1970) and Pellissier (1972) both drew attention to the importance of radiative cooling in these systems. It is quite clear that, for the dry lows with descending motion ($-\omega \frac{\partial \theta}{\partial p} > 0$) and inflow ($-\mathbf{V} \cdot \nabla \theta > 0$), radiative cooling would be essential for the maintenance of a thermal balance.

The aforementioned observational studies do not provide very convincing estimates of the detailed structure of these upper-cold lows. The results presented in Table 17.1 do not seem very definitive. Since the distribution of radiative cooling seems so important, it appears that detailed observations of the vertical distribution of moisture are required. Such observations are not available except perhaps from some of the ships during the GATE Experiment. The presence of middle- and high-level clouds would help to produce large long-wave radiative cooling rates in the upper troposphere. Detailed infrared radiometric measurements and observations of cloud distributions should be made to obtain reliable cooling rates.

A successful numerical simulation would go a long way towards providing a better understanding of the phenomena. Other questions such as the coupling of the transient cold lows with the planetary scale mid-oceanic troughs need to be explored. The entire question of the high lower-stratospheric temperatures (Figure 17.10) remains unexplored at this stage. It is conceivable that this is due to net radiative warming (rather than descent). Furthermore, descending motion in the lower stratosphere may be a part of a thermally indirect lower-stratospheric east/west circulation. The latter remains to be mapped as well. The currently available lower-stratospheric data suggest strongly that in the lower stratosphere there exists a strong thermally indirect east to west circulation; cold air ascends over the Asian monsoon belt and warm air descends in the regions of these mid-oceanic troughs.

17.5 A review of tropical upper-tropospheric energetics during the northern summer

Because of the large number of wind reports from commercial aircraft and "cloud winds" from high cloud motions, it has been possible to analyze the upper-tropospheric motion field between 300 and 200 millibars in considerable detail on a daily basis. Analysis groups at a number of institutions such as Florida State University, University of Hawaii, the National Meteorological Center in the United States have exploited this data source very extensively. One of the most complete studies on tropical upper-tropospheric energetics was recently carried out by Depradine (1978). His work complements the earlier contribution of Kanamitsu et al., (1972) and Murakami (1977).

The region considered here extends between 25°S and 45°N around the globe. For this region, Depradine made estimates of energy variables and their transformations. The basic energy equations are usually written in the form:

$$\frac{\partial \bar{P}}{\partial t} = \langle \bar{K} \cdot \bar{P} \rangle - \langle \bar{P} \cdot P' \rangle + \bar{G} + B_{\bar{P}} \quad (17.3)$$

$$\frac{\partial P'}{\partial t} = \langle K' \cdot P' \rangle + \langle \bar{P} \cdot P' \rangle + G' + B_{P'} \quad (17.4)$$

$$\frac{\partial \bar{K}}{\partial t} = - \langle \bar{K} \cdot \bar{P} \rangle - \langle \bar{K} \cdot K' \rangle - \bar{D} + B_{\bar{K}} \quad (17.5)$$

$$\frac{\partial K'}{\partial t} = - \langle K' \cdot P' \rangle + \langle \bar{K} \cdot K' \rangle - D' + B_{K'} \quad (17.6)$$

where the symbol B denotes the boundary fluxes, and $\langle A \cdot B \rangle$ denotes an energy transfer from A to B. \bar{P} , P' , \bar{K} and K' , are, respectively, the zonal available potential energy, eddy available potential energy, zonal kinetic energy and eddy kinetic energy over a domain bounded between two latitude circles around the globe and in the vertical bounded between 100 mb and 300 mb. The definition of available potential energy over a limited domain is not a valid one; the rationale one adopts is that these energy transformations and generation terms represent contributions by the selected domain to the global energetics. A somewhat more detailed explanation of the energy equations is given in the Appendix. Here we will point out some important avenues of current tropical research into these problems.

It is possible to cast the above energy equations in a wave number domain. This enables one to ask what the principle energy exchanges and generation (or dissipation) terms are for different scales of motion. This kind of analysis from observations was first presented by Saltzman (1957) for atmospheric data fields. Saltzman's (1970) review of this work essentially outlines the energetics north of 30°N. Here one obtains equations of the type:

$$\frac{\partial P_o}{\partial t} = \langle K_o \cdot P_o \rangle + \langle \text{WAVE}_n \cdot \text{ZONAL}_o \rangle_P + G_o + B_{P_o} \quad (17.7)$$

$$\frac{\partial P_n}{\partial t} = -\langle P_n \cdot K_n \rangle - \langle \text{WAVE}_n \cdot \text{ZONAL}_o \rangle_P + \langle \text{WAVE}_{m,n,p} \cdot \text{WAVE} \rangle_P + G_n + B_{P_n} \quad (17.8)$$

$$\frac{\partial K_o}{\partial t} = -\langle K_o \cdot P_o \rangle + \langle \text{WAVE}_n \cdot \text{ZONAL}_o \rangle_K - D_o + B_{K_o} \quad (17.9)$$

$$\frac{\partial K_n}{\partial t} = +\langle P_n \cdot K_n \rangle - \langle \text{WAVE}_n \cdot \text{ZONAL}_o \rangle_K + \langle \text{WAVE}_{m,n,p} \cdot \text{WAVE} \rangle_K - D_n + B_{K_n} \quad (17.10)$$

We shall not go into a detailed derivation of the above in these tropical notes. Reference may be made to papers by Saltzman (1970) and Depradine (1978) for further details.

The following are important definitions:

K_n refers to the kinetic energy of a zonal wave number n ;

P_n refers to the available potential energy of zonal wave number n ;

K_o refers to the zonal kinetic energy; and

P_o refers to the zonally available potential energy.

$\langle \rangle$ represents a mass integral over the entire mass of the atmosphere being considered here.

$\langle A \cdot B \rangle$ denotes an energy exchange from A to B.

$\langle P_o \cdot K_o \rangle$ denotes the generation of zonal kinetic energy from Hadley type overturning.

$\langle P_n \cdot K_n \rangle$ denotes the generation of eddy kinetic energy due to the ascent of warm air and descent of relative colder air on the scale n .

$\langle \text{WAVE}_n \cdot \text{ZONAL}_o \rangle_P$ is the eddy available potential energy exchange from the wave, n , to the zonal flows.

$\langle \text{WAVE}_n \cdot \text{ZONAL}_o \rangle_K$ denotes the kinetic energy exchange from wave, n , to the zonal flows.

$\langle \text{WAVE}_{m,n,p} \cdot \text{WAVE} \rangle_K$ denotes the gain of eddy available potential energy by a scale n , due to its interaction with scales m and p where $p = m \pm n$.

- $\langle \text{WAVE} \cdot \text{WAVE} \rangle_{m,n,p}$ denotes the gain of eddy kinetic energy by a scale n , due to its interactions with scales m and p , where $p = m \pm n$.
- G_o G_n denote generation terms for the zonal and the eddy (of scale n) available potential energy, respectively.
- D_o D_n denotes dissipation terms for the zonal and the eddy (of scale n) kinetic energy, respectively.
- B_{p_o} B_{p_n} Boundary fluxes in the zonal and eddy available potential energy equations, respectively.
- B_{K_o} B_{K_n} denotes boundary fluxes in the zonal and eddy kinetic energy equations, respectively.

Depradine used global observations of the wind for the period of the GATE Experiment. He analyzed the daily motion field at 300, 250 and 200 mb for a 100-day period. From these winds he determined the geopotential field at these three levels using a dynamical initialization technique (this is discussed in Chapter 21). From the geopotential fields at 300, 250 and 200 mb, he deduced the temperature field at 225 and 275 mb using the hydrostatic relation. Using the above data set, Depradine estimated the various terms of the above stated spectral energy equations. We shall next present a brief review of his important results.

A grouping of scales can be made as follows:

- (i) Zonally averaged state wave number 0.
- (ii) Long waves: Zonal wave numbers 1 and 2.
- (iii) Short waves: Zonal wave numbers 3 through 15.

The reason for defining 1 and 2 as long waves is because a large proportion of the variance of the motion field (i.e., the tropical stream function) is accounted for by the quasi-stationary part of the flows which are closely related to the land/ocean configuration, i.e., troughs over the mid-Atlantic and Pacific Oceans and ridges over Asia, Africa and over the southwestern United States. Furthermore, observational studies show that much of the variance in zonal wave numbers 3 through 15 is accounted for by transients.

The results of the energetics are presented for the layer between 200 mb and 300 mb and between the Equator and 30°N around the globe zonally. Fig. 17.12 is a schematic outline of the observational energetics.

Kinetic energy: Calculations based on observations show that kinetic energy transfer occurs from long waves to the zonal flows. This is related to the observations that long waves have a very pronounced tilt from southwest to northeast and they transfer westerly momentum away from the latitude of the mean zonal easterly jet, thus strengthening the easterlies barotropically. One could state that, with respect to the long waves, the tropical zonal flows are barotropically stable during the northern summer season.

Results of the analysis of observations also show that an exchange of kinetic energy occurs from the zonal flows to the short waves (with a pronounced peak around zonal wave number 8). Thus, it seems that zonal flows

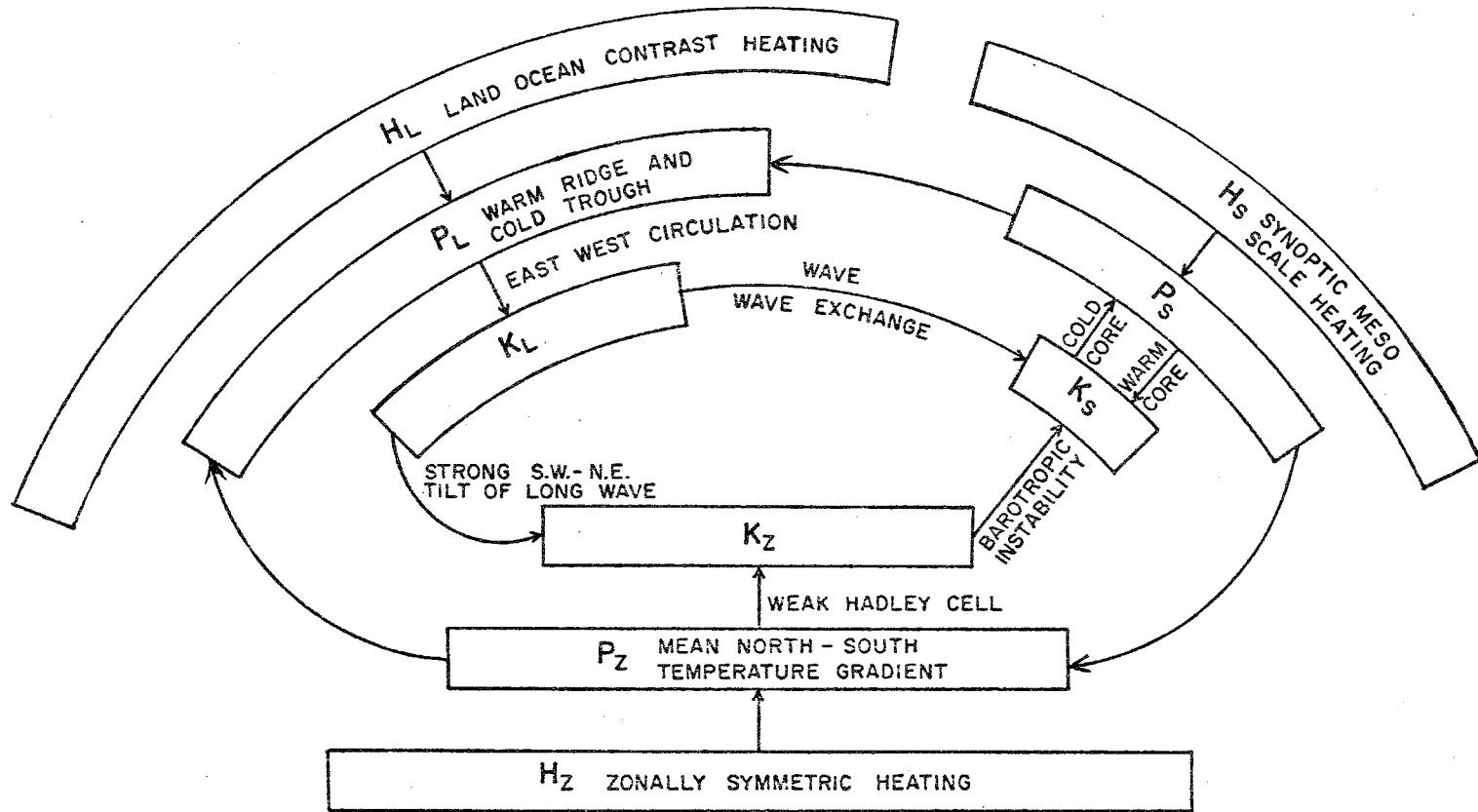


Figure 17.12 - A schematic diagram of tropical energetics based on Depradine (1978)

are unstable (barotropically) to smaller scales. Calculations of kinetic energy exchanges among waves show that the long waves are a source of kinetic energy for all other waves. The wave-wave energy exchanges occur in association with three-wave interactions (wave numbers m , n and p). The selection rules require that $p = m + n$ or $p = m - n$; and the mutual interaction of m , n , and p would either increase or decrease the kinetic energy of m . The largest such interaction occurs at low wave numbers. The potential energy exchanges over the tropics have been estimated by Kanamitsu (1975) and Depradine (1978). The most important results are that the short waves (i.e., zonal wave numbers 3 through 15) supply available potential energy to longer waves (via wave-wave interactions) and the zonal flow (via wave-zonal interactions). This is also indicated in Figure 17.12. Furthermore a weak transfer of available potential energy also occurs from the zonal to the long waves (via wave-zonal interactions). No simple synoptic interpretation exists for the wave-wave exchanges of kinetic or eddy available potential energy between different scales. It is desirable to determine map features in the motion and thermal fields that relate to such energy transfers.

In summary we can state that shorter waves are a source of available potential energy for the long waves and the zonal flow, while the longer waves are a source of kinetic energy for shorter waves as well as to the zonal flows. Kanamitsu (1975) also estimated the generation terms (i.e., generation of available potential energy by different heating terms) and noted that cumulus convective heating contributes quite significantly to the generation of zonal, long- and shorter-scale eddy available potential energy. Such a generation occurs if the covariance of the heating and temperature ($H_0 T_0$ or $H'T'$) is positive for the scale in question. The energetics of the tropical easterly jet is also indicated by Figure 17.12. According to this diagram, the tropical easterly jet (i.e., the K_z box) receives energy from the Hadley-type overturning as well as from the wave-zonal transfers from the long waves. The latter is found to be the more important of the two.

17.5.1 Normal versus anomalous years

The circulation patterns as well as the associated energetics vary somewhat from year to year. The major differences appear when one compares normal rainfall years with drought years. It has been shown by Kanamitsu and Krishnamurti (1978) that during a drought year, e.g. the year 1972 when tropical rainfall was quite deficient over India and West Africa, the long waves did not develop in the same way as they did during normal rainfall years (for example, 1967). In the drought year, the zonal flows were the source of kinetic energy for all other waves and the Hadley cell was energetically more active. Energetics fluctuations on time scales of several decades pose an important problem.

17.6 On the quasi-stationarity of the upper-tropospheric climatology

A perplexing question that has drawn considerable interest in recent years relates to the maintenance of the quasi-stationarity of the large amplitude upper-tropospheric map features such as the Tibetan high, mid-oceanic troughs, the Mexican high and the tropical easterly jet. As stated earlier, the stationary part of these circulations carries a large proportion of the variance of the total motion field. These large amplitude disturbances show up on most daily maps, but they do not move westwards as they should if the beta term in the vorticity equation were a dominant effect.

One of the observational findings at 200 mb during the northern summer is that the divergence and the vorticity fields are nearly out of phase (Krishnamurti, 1971a; Holton and Colton, 1972). Since the maximum values of the horizontal advection of vorticity would be located some distance away from the minimum value of relative vorticity, the advection term is not able to balance the production of vorticity by the divergence term. The latter occurs over regions of maximum and minimum vorticity (and not vorticity advection). Holton and Colton proposed a viscous drag coefficient with a value of $1.5 \times 10^{-5} \text{ s}^{-1}$ and introduced a viscous dissipation term in their vorticity equation. Such a mechanism is able to dissipate the vorticity that was advected, to the west of the disturbances, in a matter of some 19 hours. Quasi-stationarity was actually achieved in a time integration of the vorticity equation with the above specifications. Although such a large dissipation may be rationalized as a parameterization of the vertical transport of vorticity by the deep cumulus convection, this required finding "negative hot towers" in the regions of the upper troughs over oceans. The "negative hot towers" would have to transport cyclonic vorticity down via sub-grid scale eddy motions. This does not seem reasonable observationally.

This problem is very succinctly presented by Fein (1977). The problem was also addressed by Abbott (1977).

In another recent study, Kanamitsu (1977) described an alternate mechanism for the maintenance of quasi-stationarity. His analysis utilizes a Fourier transformed vorticity equation in wave number domain using zonal harmonics. The basic equation used in Kanamitsu's study is of the form:

$$\frac{\partial \zeta_n}{\partial t} = \langle \text{Adv} (m, n-m) \rangle + \langle \text{div} (m, n-m) \rangle - f \text{div} (n) - \langle \beta v(n) \rangle + \langle \text{TWISTING} (m, n-m) \rangle + F (n) \quad (17.11)$$

where the terms denote:

Left-hand side: local change of vorticity for zonal wave number n.

Right-hand side:

- (i) First term - horizontal as well as vertical advection of relative vorticity;
- (ii) Second term - contribution by the product of divergence and relative vorticity; this invokes wave-wave as well as wave-zonal interactions, e.g., the divergence of wave number n interacts with the vorticity of waves with wave numbers n and n-m to give a rate of increase of vorticity of wave number n;
- (iii) Third term is the contribution from the product of the Earth's vorticity and divergence;
- (iv) The fourth term is the contribution from the beta term of the vorticity equation;
- (v) The fifth term is the contribution by the twisting term and it also includes wave-zonal and wave-wave interactions;
- (vi) The sixth term denotes a frictional term. Here the symbol denotes a summation over all wave numbers m ($-\alpha$ to $+\alpha$).

For a derivation of the above equation reference may be made to Kanamitsu (1977). Kanamitsu first accomplished the desired quasi-stationarity by showing a reasonable numerical weather prediction over a global tropical belt

between 25° N and 45° N and from 100 mb to 1000 mb. The model included the salient physical features that are used in the most sophisticated primitive equation prediction models.

He diagnosed the quasi-stationarity from the above-stated spectral vorticity equation by examining the balance of vorticity for the long waves ($n = 1, 2$) which were noted to be nearly stationary.

Kanamitsu's major conclusions on the quasi-stationarity of the long waves were that: (i) the long waves "by themselves" do not have a vorticity balance; their quasi-stationarity requires that other scales be involved. By themselves they retrograde westward due to the phase-shifts between the production by divergence and the beta term; (ii) the non-linear advective term supplies cyclonic vorticity primarily via wave-wave interactions to the west of upper anticyclones and anticyclonic relative vorticity to the east. He notes that the smaller waves (through their contributions to wave-wave interactions) play an important role in supplying the needed vorticity to the longer waves and thus contribute to the quasi-stationarity of the long waves, and (iii) he attributes the major differences between his results and those of Holton and Colton (1972) and Abbott (1977) to the non-linear advection by the divergent part of the motion field.

Chapter 18

THE TROPICAL LOWER STRATOSPHERE

In this text we shall examine the structure of the atmosphere only below 30 kilometres.

18.1 The quasi-biennial oscillation (QBO)

The most spectacular phenomenon is the well-known quasi-biennial oscillation. An excellent review of this topic appears in a recent study by Hopewood (1972).

A major reversal of wind direction, westerly for roughly one year and easterly for another year was noted by Graystone (1959), Reed *et al.*, (1961) and many others. The period of this oscillation varies between 22 and 29 months. According to Reed and his co-workers, the amplitude and phase of the phenomenon vary little with longitude. The phenomenon disappears at the tropopause. Its largest amplitude is near the 25 km level. Above that level the easterlies are more frequent than the westerlies. However, the phase varies with height; the westerlies or easterlies first appear at about 30 km and propagate downward at a rate of about 1 km/month. The largest amplitude occurs at the Equator. The amplitude decreases as we go poleward, and it is very small at 30°N and S latitudes. Figure 18.1 from Wallace (1973) shows a time-section of the wind reversal as a function of height. This illustrates some of the findings mentioned above.

The amplitude, period and the rate of downward propagation seem to vary somewhat from one cycle to the next. The temperature field also exhibits some oscillation in this same time frame of nearly 2 years. Reed (1964) noted that temperature oscillations have an amplitude of around 2°C near 25 km but this decreases as one goes down to the 100 mb level (≈ 16 km). The amplitude is largest near the Equator, but decreases poleward, being almost negligible at 17°N. The amplitude, however, increases once again towards the subtropics. The highest temperature of the cycle in the 0° - 17°N belt is found to precede the maximum of the west wind at 20°N by some 5 months at the 20 mb level. The subtropical cycle appears to be out of phase with respect to the near-equatorial cycle.

One of the convenient ways to handle data in reference to this phenomenon is to use 12-monthly running means of the data sets. This also has some limitations. Although it achieves the desired result of suppressing the annual cycle, other cycles are also attenuated. To avoid this problem, one has to resort to harmonic analysis.

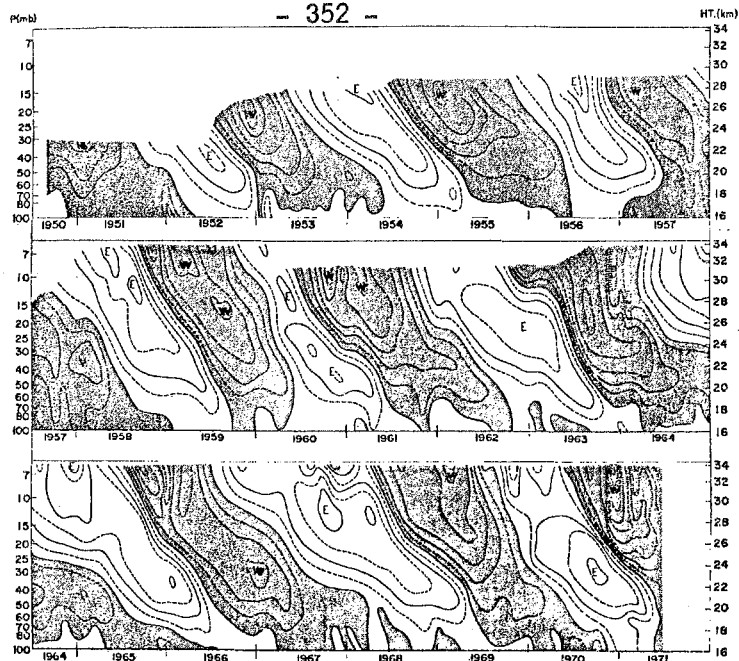


Figure 18.1 - Time-height section of zonal wind at the Canal Zone station through June 1970 and at Kwajalein from July 1970 to June 1971 with the 15-year average (1956-1970) of the monthly means subtracted to remove annual and semi-annual cycles. Both stations are located near 9°N

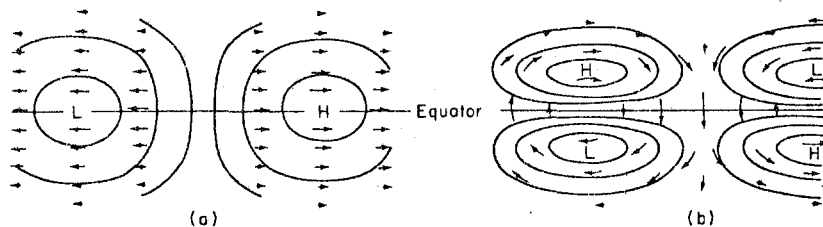


Figure 18.2 - Schematic illustration (adapted from Matsuno, 1966) of pressure and streamline patterns for (a) the Kelvin wave and (b) the mixed Rossby-gravity wave

The discovery of the oscillation of the zonal wind component in the tropical stratosphere led investigators to attempt to develop a theory which could explain the cause, dynamics and structure of the oscillation. A satisfactory theoretical model of the QBO should successfully explain the three most striking features of the oscillation: (1) the approximate biennial periodicity, (2) the downward propagation without loss of amplitude, and (3) the occurrence of zonally symmetric westerlies at the Equator.

A number of theories have been proposed to explain the main features of the QBO. Most of these have failed in some way to fully explain the phenomenon. We shall review some of these theories and discuss the theory which is now considered most reliable in explaining the major features of the QBO. No attempt will be made to give mathematical details of any of the theories.

Early attempts at a theoretical explanation of the QBO were generally based on thermal forcing by some variation in solar output. Shapiro and Ward (1962) associated the oscillation with variations of solar ultraviolet radiation caused by a small hitherto neglected sunspot maximum with a period of 25 months. Staley (1963) suggested that the zonal wind oscillation in the equatorial stratosphere was a forced geostrophic wave resulting from downward propagating heat supplied, presumably, by a solar source of ultraviolet radiation with a period of about 26 months. The heat was assumed to propagate downward by eddy diffusion, although radiative transfer was thought to be of significance. Reed (1964) rejected Staley's suggestion of a 26-month fluctuation of solar radiation and postulated as a possible agent the annual heating cycle. The QBO was regarded as a subharmonic response to this cycle. Both Reed and Staley presented theoretical models to support their suggestions. However, neither of the models was able to account for the downward propagation of the oscillation without loss of amplitude.

In the theories based on thermal forcing, the zonal wind field is coupled to the heating field through a system of zonally symmetric circulation cells driven by differential heating. These motions produce a local change in the zonal wind by advecting absolute angular momentum in the meridional plane. In a rotating frame of reference the local changes in angular momentum arise mainly as a result of Coriolis torques produced by the mean meridional circulation. However, this mechanism is not very effective near the Equator, where the Coriolis parameter is small. In addition, the mean meridional circulation is incapable of producing any sizeable westerly momentum near the Equator. As a result, there must be some other mechanism capable of providing a source of westerly momentum near the Equator.

The inability of the thermal forcing theories to fully describe the main features of the QBO led Tucker (1964) to look for a possible momentum source for the oscillation. Tucker examined the transient eddy statistics for evidence of long-term fluctuations in the meridional flux divergence of zonal momentum in the tropical stratosphere. At the 25 km level he found evidence of fluctuations that seemed to be related to the QBO. Wallace and Newell (1966) also indicated a biennial periodicity in horizontal eddy momentum fluxes in the middle latitudes above 30 mb. However, the evidence for these fluxes in the tropical latitudes was not very convincing, and the amplitude of such variations was too small to account for the QBO.

The above type of forcing does not explain how an oscillation in momentum fluxes could generate the downward propagation of the oscillation. Tucker (1964) suggested that the observed downward propagation was mainly a result of advection produced by a mean sinking motion throughout the tropical stratosphere. Such a wide region of subsidence would, by continuity, require a strong Equatorward meridional flow, and consequently unrealistically large mean easterlies a few degrees from the Equator. Hence, it might be possible that the downward propagation was due to a combination of thermal and dynamical forcing.

To test this hypothesis, Wallace and Holton (1968) developed a diagnostic numerical model of the QBO based on the equations of motion, the continuity equation, and the thermodynamic energy equation for a geostrophically balanced vortex. The model tested various time-dependent distributions of thermal and dynamical forcing in order to obtain some understanding of which physical mechanism might be responsible for the observed wind and temperature oscillations. Numerical results of the model indicated that it is possible to obtain a solution which resembles in some respects the QBO. However, it was impossible to produce the observed amplitude of the oscillation without assuming a larger variation in solar output than is observed. Neither thermal nor dynamical forcing could produce the observed downward propagation without loss of amplitude. Wallace and Holton concluded that the only way to account for the downward propagation is to resort to a momentum flux oscillation which propagates downward.

Observations and theory now provide evidence that long-period vertically propagating planetary wave disturbances are the momentum source, and can explain the quasi-biennial periodicity as well as providing a source of westerly momentum generation at the Equator. The interaction of these waves with the zonal wind provides the basis of the theory for the QBO as proposed by Lindzen and Holton (1968) and revised by Holton and Lindzen (1972).

Before discussing this theory, a brief description of the waves and other observed zonal wind oscillations in the equatorial stratosphere will be given.

Reed (1965, 1966) and others have noted, in addition to the QBO, an annual and semi-annual oscillation in the tropical stratosphere. The annual cycle is pronounced between 36 and 40 km, while the semi-annual cycle is prominent above 40 km and is strongest at equatorial latitudes.

Two types of wave disturbances are found in the equatorial stratosphere. These are the Kelvin waves and the mixed Rossby-gravity waves. The Kelvin wave is an eastward travelling wave which has a distribution of pressure and zonal velocity which is symmetric about the Equator, and has essentially no meridional velocity component. The mixed Rossby-gravity wave, on the other hand, has distributions of pressure and zonal velocity which are antisymmetric about the Equator, and has a distribution of meridional velocity which is symmetric. Both of these waves transport zonal momentum upward; the Kelvin wave transports westerly momentum and the mixed Rossby-gravity wave transports easterly momentum. As these waves propagate upward, they are attenuated primarily by infrared cooling and their momentum is absorbed by the mean zonal flow. The greatest absorption tends to occur near the transition between easterlies and westerlies. When this occurs, the mean momentum which is deposited in the mean zonal flow produces an acceleration which is westerly for the Kelvin wave and easterly for

the mixed Rossby-gravity wave. This acceleration then alters the original mean zonal wind distribution in such a manner as to cause a downward propagation of the shear zone. This in turn causes the wave to be absorbed at lower levels, so that the shear zone is lowered further. The process continues until the shear zone approaches the tropopause level.

Lindzen and Holton (1968) assumed that a spectrum of gravity waves, generated in the neighbourhood of the tropopause and propagating upward, are the momentum source of the QBO. The vertical flux of momentum due to the waves is deposited in the mean flow at critical levels where the waves are absorbed by the mean flow. An interaction is assumed to take place with the semi-annual zone wind oscillation above 40 km. The region above the critical level at which the interaction takes place is shielded from the action of the waves by a "velocity ledge" or zone of strong wind shear which is produced by the interaction. As a result, the interaction will then take place at a lower level and the shear zone will propagate downward. When the zone descends below the tropopause, there is no longer any shielding effect, and the waves are again able to propagate upward to interact with the semi-annual oscillation, which by this time has changed phase. The process is repeated, this time with a shear zone opposite in sign to the previous one propagating downward.

Lindzen and Holton (1968) noted the need for improvement and extension of some details of the theory, including a better understanding of gravity waves and their interaction with the mean flow without assuming separation of scales.

Observational and theoretical developments have provided a better understanding of planetary-scale wave disturbances in the tropical stratosphere. Evidence now indicates that the waves consist primarily of a single westerly Kelvin wave during the descending westerlies phase of the QBO and in a single easterly mixed Rossby-gravity wave during the descending easterly phase. This information led to a revision of the theory of Lindzen and Holton (1968) by Holton and Lindzen (1972). In this theory, the assumption of a critical-level absorption mechanism is replaced by a more realistic mechanism wherein damping of the short period Kelvin and mixed Rossby-gravity waves by infrared cooling produces the necessary momentum flux necessary to accelerate the mean flow. As a result, there is no longer the need for the full spectrum of gravity waves and the semi-annual oscillation, while important, is no longer essential to the overall theory.

In order to understand the theory, assume that a Kelvin wave is allowed to propagate upward from the tropopause through a mean wind profile which is easterly at all levels. The wave will be attenuated slightly until it reaches near 30 km where attenuation will become rapid, leading to a pronounced acceleration of the mean flow. Once this shear zone is established, it will propagate downward as a result of absorption taking place within it.

When the westerly régime reaches the tropopause, the mixed Rossby-gravity wave, which was previously absorbed by the lower stratospheric easterlies, becomes free to propagate upward until an upper level easterly shear zone is encountered. This will then cause an easterly régime to propagate downward to the tropopause, where the cycle begins anew.

The upper-level shear zones may be produced either as a result of continued absorption of the wave at upper levels, or be provided by the semi-annual oscillation above 40 km.

A numerical model, which included the above mechanisms based on the theories of Lindzen and Holton (1968) and Holton and Lindzen (1972), was able to simulate the main features of the QBO. The model was a simplification of that used by Wallace and Holton (1968) with height-dependent dynamical forcing.

There is strong observational and theoretical support for all the crucial requirements of Lindzen and Holton's mechanism; however, there are still more uncertainties to be cleared up. Despite these remaining uncertainties, the theory has been able to explain the major features of the quasi-biennial oscillation and produce some understanding of its origin.

18.2 Spectral analysis in the tropical lower stratosphere

The Kelvin wave and the mixed Rossby-gravity wave have been studied extensively from tropical time-series of long data records. Wallace (1973) has presented an excellent summary of these waves. We have referred to these two waves in the previous section. Table 18.1 from Wallace (1973) describes the essential characteristics of these two types of waves.

Table 18.1 Description of vertically propagating wave modes in the tropical stratosphere

	Yanai and Maruyama	Wallace and Kousky
Theoretical description	mixed Rossby-gravity wave	Kelvin wave
Frequency ω (ground based)	$2\pi/4-5$ days	$2\pi/15$ days
Horizontal wave length L	10 000 km	30 000 km
Zonal wave number k	4	1-2
Vertical wavelength D	4-8 km	6-10 km
Structure	Fig. 18.2b, 18.3a	Fig. 18.2a, 18.3b
Average phase speed relative to ground	-23 m s ⁻¹	+25 m s ⁻¹
Average phase speed relative to zonal wind	-30 m s ⁻¹ §	+50 m s ⁻¹ §§
Doppler-shifted frequency ω'	$2\pi/3$ days§	$2\pi/8$ days§§
Amplitudes		
Zonal wind u^*	2-3 m s ⁻¹	8 m s ⁻¹
Meridional wind v^*	2-3 m s ⁻¹	0
Temperature T^*	1°C	2°-3°C
Geopotential height z^*	30 metres	4 metres
Vertical velocity w^*	0.15 cm s ⁻¹	0.15 cm s ⁻¹

§ Near level of maximum westerly winds, where $U \approx 7$ m s⁻¹

§§ Near level of maximum easterly winds, where $U \approx -25$ m s⁻¹

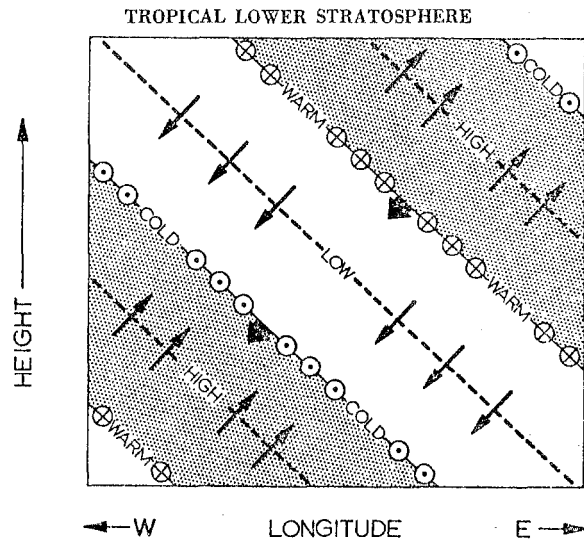


Figure 18.3a — Idealized longitude-height section through a mixed Rossby-gravity wave at a latitude north of the Equator showing maximum and minimum pressure, temperature, vertical motion (indicated by vertical component of small arrows), zonal wind (indicated by horizontal component of small arrows), and meridional wind (indicated by arrows pointing into the page for northward flow and out of the page for southward flow). Heavy arrows indicate the direction of phase propagation (Figure supplied by J. R. Holton)

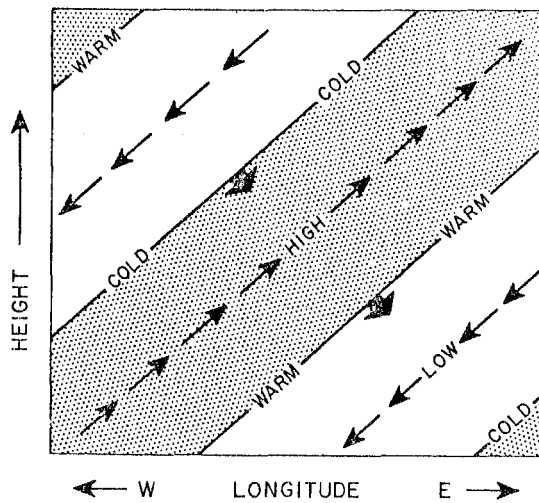


Figure 18.3b — Idealized cross-section along a latitude circle showing phases of the zonal wind, temperature, and pressure and vertical motion oscillations associated with Kelvin waves (adapted from Wallace and Kousky, 1968). Conventions are the same as those in Figure 18.3a

The horizontal structure of these waves is of considerable interest. The pressure and streamline charts of the Kelvin and Rossby waves are shown in Figure 18.2. These are based on the theoretical analysis of Matsuno (1966). The Kelvin wave shown on the left panel propagates eastward and has an even symmetry about the Equator for the zonal wind and the pressure. The mixed Rossby wave shown on the right panel propagates westward, the meridional wind exhibits an even symmetry while the zonal wind and pressure show odd symmetry about the Equator. Here we define even and odd symmetry by the usual rules:

even = 0 at the Equator odd = \pm at the Equator

Figure 18.2 is a schematic representation. In practice, real data and weather maps are more complicated. Many scales are usually present, although winds sometimes show such geometrical patterns. The pressure data are almost impossible to analyse because of the extremely weak gradients. These are both transient waves that, as indicated in Table 18.1, move either westward or eastward. The tropics are characterized by a dominant quasi-stationary stratospheric equatorial waves remains an unsolved problem to date. The stratospheric Kelvin and Rossby-gravity waves are forced from below and they require a tropospheric source of excitation. Figures 18.3a and b show idealized longitude-height cross-sections on a vertical plane of the structures of the Kelvin and the mixed Rossby-gravity waves, respectively, based on Wallace, Kousky and Holton. The arrows in these diagrams are interpreted to have a zonal and a vertical component. The diagrams indicate the vertical tilt of the disturbance, and the wind, temperature and pressure relationships. For the case of the mixed Rossby-gravity wave, the maximum temperature coincides with the maximum poleward wind component.

As stated earlier, the tropical stratospheric weather maps show a great degree of complexity. This is evident if one examines stratospheric time-height cross-section of wind data. The reason for this is that these motions are not only excited from below but there exists also a variety of local instabilities and energy exchanges among scales (stationary and transient). Except for the interests of the stratospheric supersonic jet aircraft, and the monitoring of stratospheric aerosols, there is not much interest in day-to-day forecasting of the stratospheric variables. The influence of the stratosphere on the tropical troposphere is considered very small.

18.3 The large quasi-stationary gyres

A large proportion of the total variance of the zonal velocity and temperature fields is accounted for by the long quasi-stationary components of the zonal harmonics. This has been noted at 150 and 100 mb in the tropics. The maintenance of these large amplitude quasi-stationary gyres is an unsolved problem.

Chapter 19

MISCELLANEOUS PHENOMENA AND PROBLEMS IN THE TROPICS

In this section we shall present a very brief overview of a few interesting problem areas that are not covered in the main text. These appear to be very interesting although not much is known about them at present.

19.1 Diurnal changes in near-equatorial continental regions away from the coast

Observations in many places (e.g. Zaire and Brazil) exhibit a dominant diurnal mode which is not simply explained as a sea-breeze phenomenon since the regions in question are quite far away from the coast. There are no well-defined westward (or eastward) passing wave disturbances over Zaire that account for the major rainfall during March and April around 0° to 5°S . The observed rainfall seems to have a large diurnal component associated with convergence of mass which also exhibits a pronounced diurnal change. The region is far away from the coastal region and hence the phenomenon is not easily explained. Figures 19.1a and b illustrate the diurnal change in the surface divergence field during February and March, the rainfall months. A dense network of surface stations provides wind observations on a three-hourly basis. The divergence here is based on these 3-hourly maps of the wind field over a domain between 14°S and 4°N and 12°E to 32°E . The graphs are of average values centred at 3°S and 21°E .

19.2 Diurnal changes over the open oceans

Observations over tropical oceans far away from continental influences usually indicate interesting diurnal fluctuations in rainfall, surface pressure, wind and even sea-surface temperatures. We have addressed the general problem of diurnal change in Chapter 7. This is, without doubt, an important problem of tropical meteorology. In 1969 a field experiment called BOMEX (see Chapter 20) was carried out to study tropical budgets during both disturbed and undisturbed periods. Nitta and Esbensen (1974) examined the diurnal variation over the western Atlantic trades utilizing the BOMEX data sets. Figures 19.2a, b, c, d and e illustrate the diurnal changes (obtained by averaging 7 days of hourly data) of the following parameters over open ocean (15°N , 56°W):

- (i) Horizontal divergence;
- (ii) Relative vorticity;
- (iii) Eastward wind;
- (iv) Northward wind;
- (v) Vertical velocity.

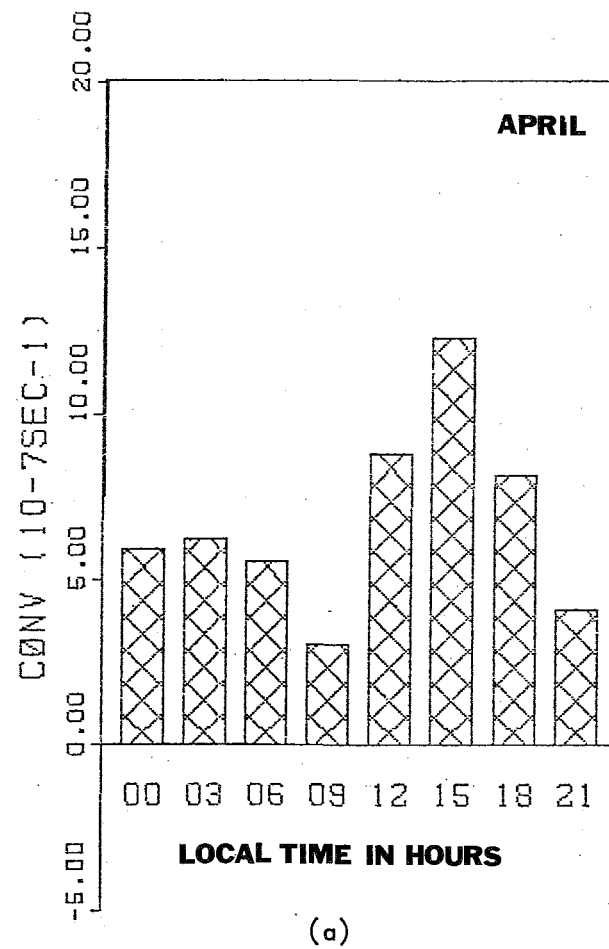
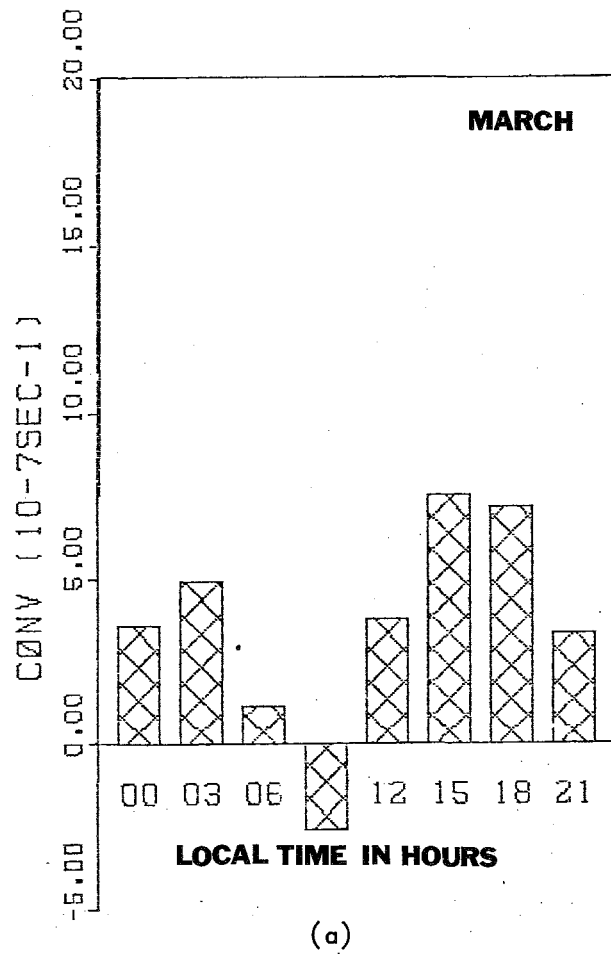


Figure 19.1 — (a and b) shows diurnal change in surface horizontal convergence at Zaire during the rainy months

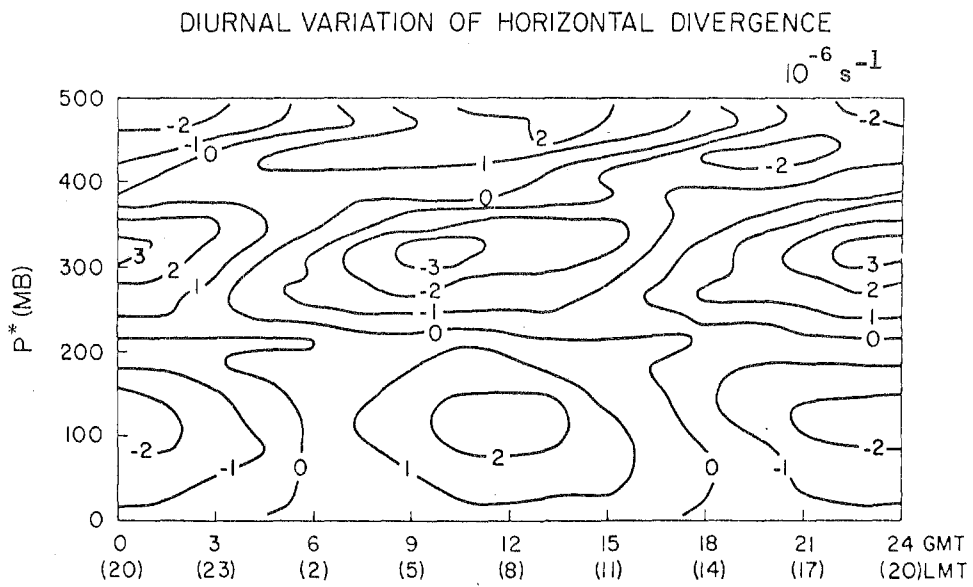


Figure 19.2a - (Nitta and Esbensen)

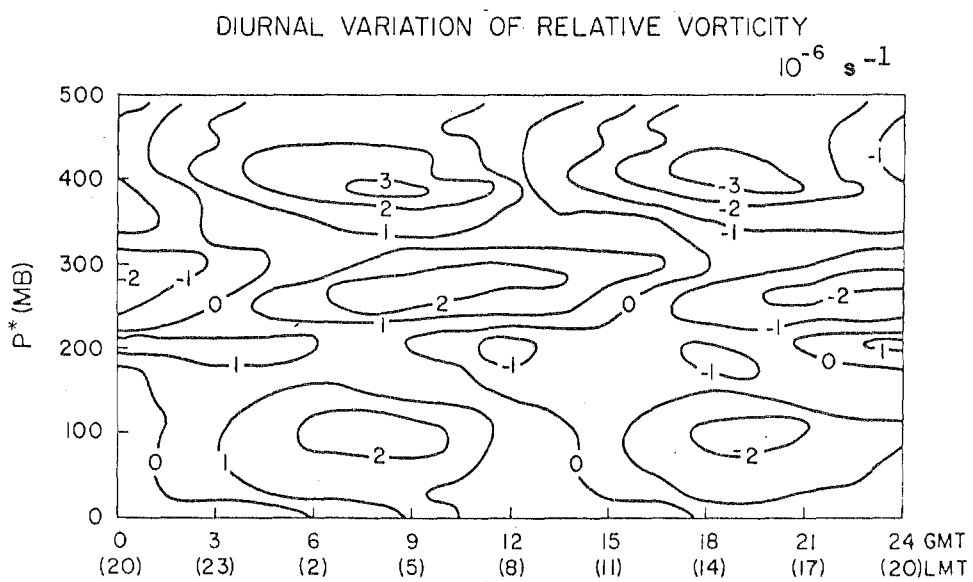


Figure 19.2b - (Nitta and Esbensen)

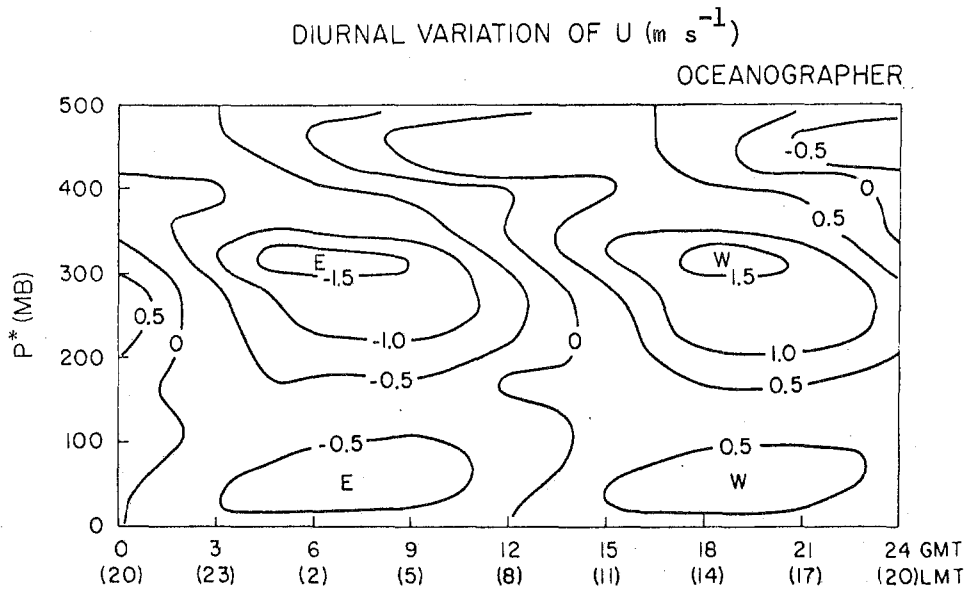


Figure 19.2c - (Nitta and Esbensen)

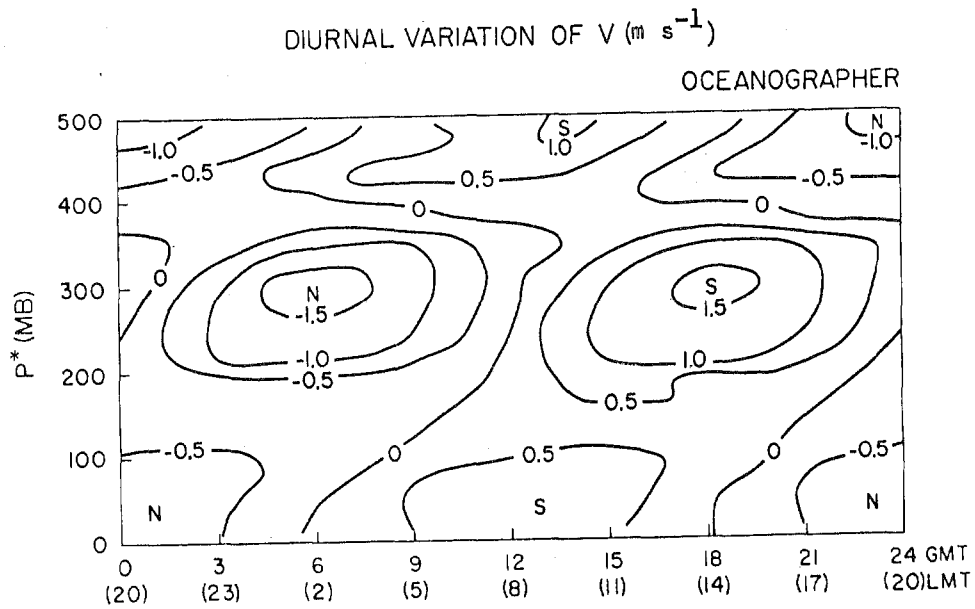


Figure 19.2d - (Nitta and Esbensen)

DIURNAL VARIATION OF ω^* (MB/HOUR)

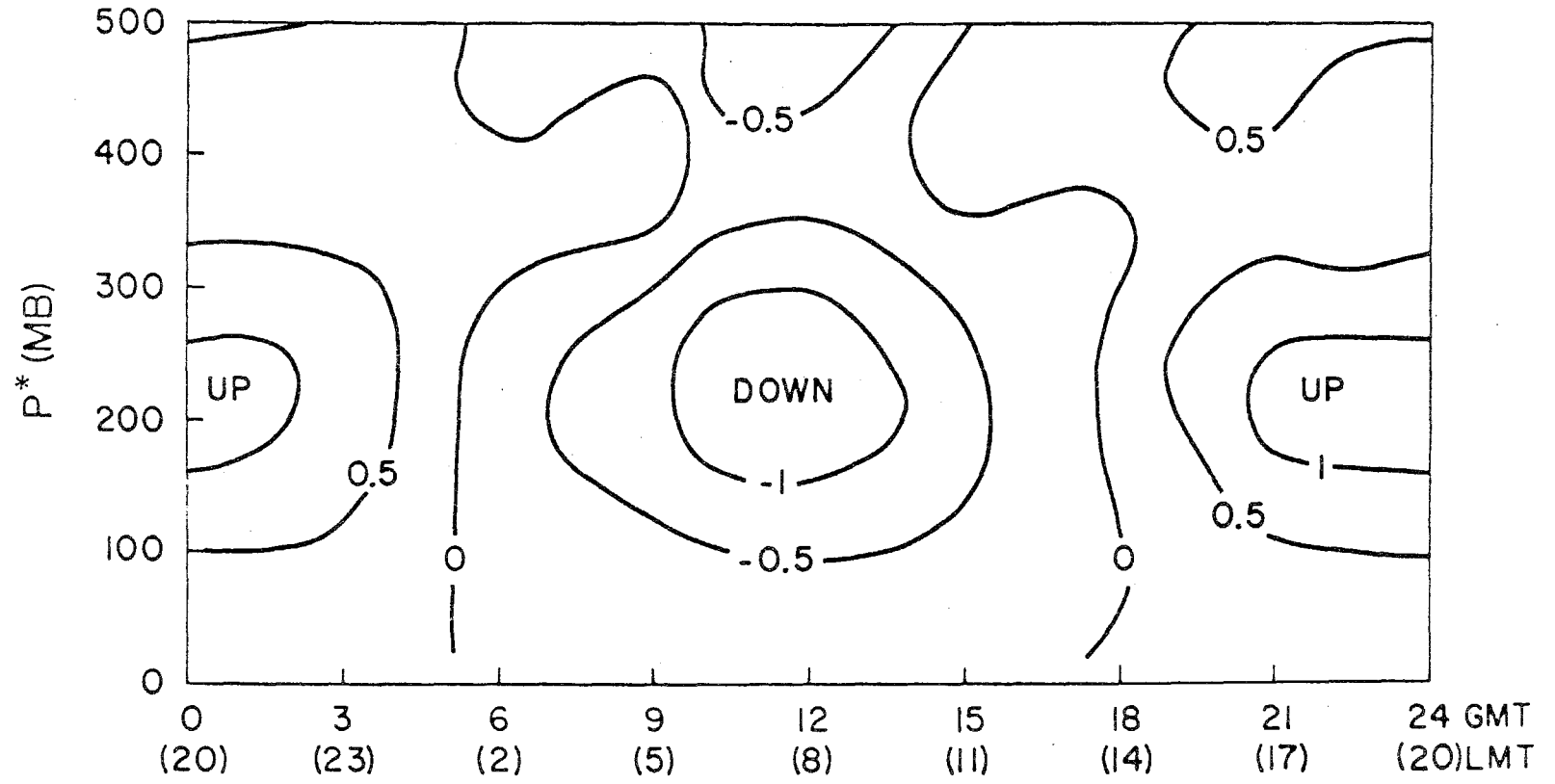


Figure 19.2e - (Nitta and Esbensen)

Here Nitta and Esbensen use p^* as the ordinate where $p^* = p_s - p$ where p_s and p respectively are the surface pressure and pressure at some upper level.

Table 19.1 summarizes the diurnal changes illustrated in the five diagrams.

Table 19.1
Diurnal change in the trade-wind belt over the oceans

	AMPLITUDE	LOCAL TIME OF MAXIMUM	LOCAL TIME OF MINIMUM
Divergence below 800 mbs	$2 \times 10^{-6} \text{ s}^{-1}$	8 a.m.	8 p.m. (Maximum convergence)
Relative vorticity	$2 \times 10^{-6} \text{ s}^{-1}$	4 a.m. (cyclonic)	4 p.m. (anticyclonic)
Zonal wind near the ground	0.5 m s^{-1}	4 a.m. (max easterly)	4 p.m. (max westerly)
Meridional wind below 900 mbs	0.5 m s^{-1}	Maximum southerly at 10 a.m.	Maximum northerly at 10 p.m.
Meridional wind at 700 mbs	1.5 m s^{-1}	Maximum northerly at 6 a.m.	Maximum southerly at 6 p.m.
Vertical velocity	1 mb h^{-1}	Maximum downward motion at 8 a.m.	Maximum upward motion around 8 p.m.

These calculations with the BOMEX data over the open oceans have not been adequately explained. It has been shown by Hudlow (1970) that radar echoes exhibit a maximum activity in the early morning some 6 hours after the occurrence of maximum upward motion. Over oceans the minimum echo activity occurs around noon some 4 hours after the occurrence of largest downward velocity. It is believed that these diurnal variations are related to a complex structure of the mixed layer.

19.3 Diurnal change of the monsoon trough

Figure 19.3 from Kreitzberg et al., (1969) illustrates the diurnal change in surface pressure over Indochina based on observations made at 0500 and 1700 LST. This is a region of the monsoon trough. The mean pressure for June over this region changes from a low value in the daytime to a high value during the night. The 24-hourly average pressure shows pressure in this region to be low. This is a phenomenon of diurnal change over an area on a scale of 1500 km^2 . Surface winds are noted to respond to this diurnal change. Kreitzberg et al., (1969) also examined the diurnal

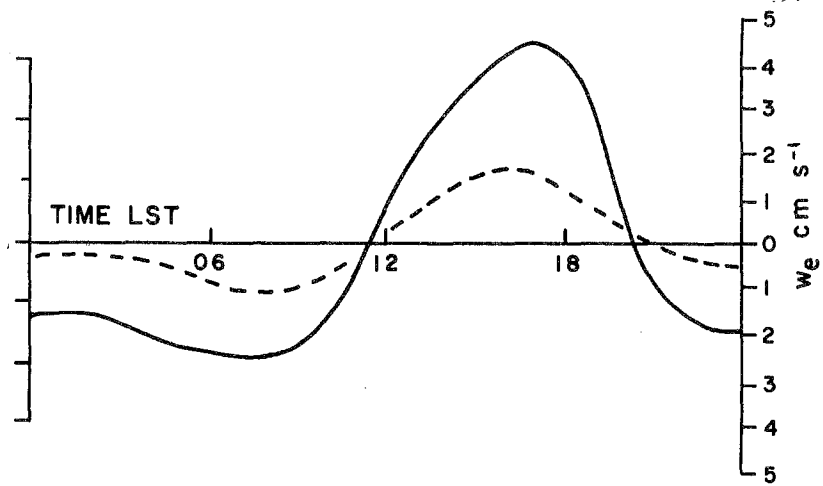


Figure 19.3 — Diurnal variation of equivalent vertical motions determined from moisture changes (solid) and temperature changes (dashed) at 5.5 km (Kreitzberg *et al.*, 1969)

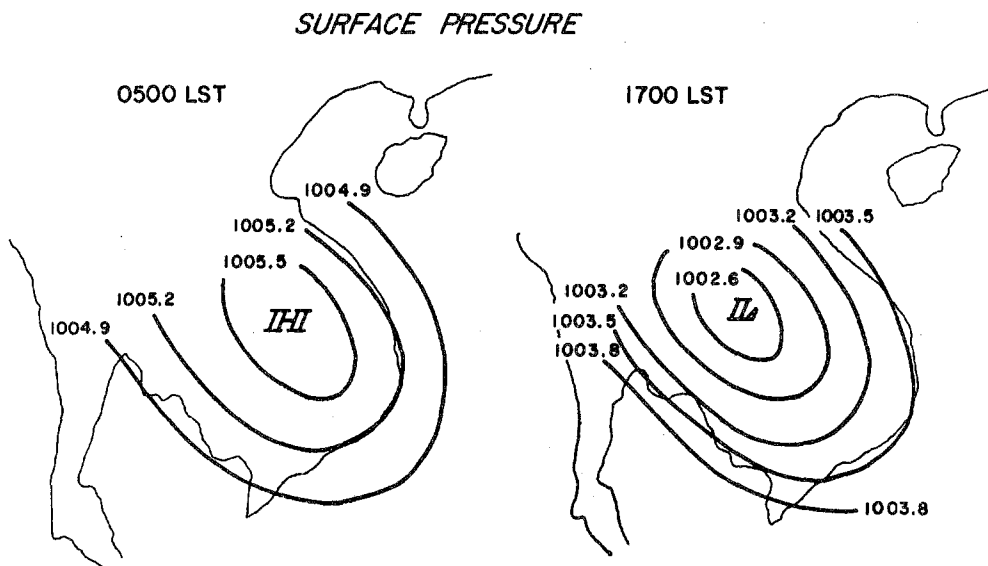


Figure 19.4 — Charts of mean sea-level pressure over Indochina in June at 0500 and 1700 LST (Kreitzberg *et al.*, 1969)

changes in the vertical velocity over this region and their graphs, based on thermal and humidity changes, are illustrated in Figure 19.4. This is an important diurnal change phenomenon on the continental scale whose implications and interaction with the passing disturbances are worthy of detailed examination.

19.4 Wave CISK

This is a new concept in tropical meteorology developed for studies of interaction of cumulus convection and wave disturbances by Yamasaki (1969), Hayashi (1970), Lindzen (1974), Chang (1978), Stevens et al., (1977) and Stevens and Lindzen (1978). Moisture convergence associated with the wave fields provides the water vapour which condenses in cumulus clouds; the heating of the atmosphere occurs in the space and time scales of the wave itself. It departs from the idea of CISK presented in Chapter 6 where frictional convergence in the boundary layer rather than an explicit wave scale was emphasized.

19.5 Sea-surface temperature anomalies over the tropics and tropical weather

A number of interesting studies, primarily using numerical general circulation models, have examined the influence of warm (or cold) sea-temperature anomalies on tropical weather; Shukla (1975) and Washington et al., (1977).

The basic strategy in these studies is to compare the results of two long-term integration experiments: (i) where climatological values of sea-surface temperatures are used (called a standard run), and (ii) an anomaly run where a previously observed sea-surface temperature anomaly is used over a portion of a tropical ocean. An example of a well-known sea-surface temperature anomaly is that which occurred during 1972 when the central and eastern Pacific sea-surface temperatures (in the near-equatorial latitudes) were noted to be some 2° to 3°C warmer than the climatological values. This was a year of rather unusual circulations over the tropics, recently discussed by Kanamitsu and Krishnamurti (1978). Washington et al., (1977) introduced (in three separate studies) sea-surface temperature anomalies over the western Arabian Sea, eastern Arabian Sea and over the central Indian Ocean. They examined the 30-day evolution of the monsoonal rainfall in a general circulation model which was designed to simulate the weather conditions (and their anomalies) during July. They found that no significant changes in monsoon rainfall occurred over India in these simulations. In this sense, their results are not in agreement with an experiment (on imposed cold sea-surface temperature anomaly over the western Indian Ocean) carried out by Shukla, who noted a significant reduction in rainfall totals over India. This suggests that further studies along these lines are necessary to examine the reasons for the differences among different models. Washington et al., (1977), however, note that when a warm anomaly (+ 3°C) is introduced in the central Indian Ocean, it leads to an increased rainfall and an enhanced upward vertical velocity over the region of the anomaly. However, this effect is known to decay rapidly with distance away from the imposed anomaly with a reversal in the sign of the vertical velocity. In this case they noted a reduction of rainfall over Malaysia and the western Pacific Ocean. This is an interesting and important tropical problem and deserves further careful studies.

Chapter 20

FIELD EXPERIMENTS OVER THE TROPICS AND FUTURE TROPICAL OBSERVING SYSTEMS

20.1 Introduction

A number of very important field experiments have been conducted in recent years to study the behaviour of the tropical atmosphere. Among these are the following:

(i) Line Island Experiment (south of Hawaii near the Equator) for study of ITCZ, 1970;

(ii) BOMEX. Polygonal array of ships east of Barbados to study the undisturbed and disturbed trades, 1969;

(iii) ATEX. To study wintertime trades in the North Atlantic Ocean, 1970;

(iv) AMTEX. To study air-mass transformations over the western Pacific Ocean south of Japan, 1972-1973;

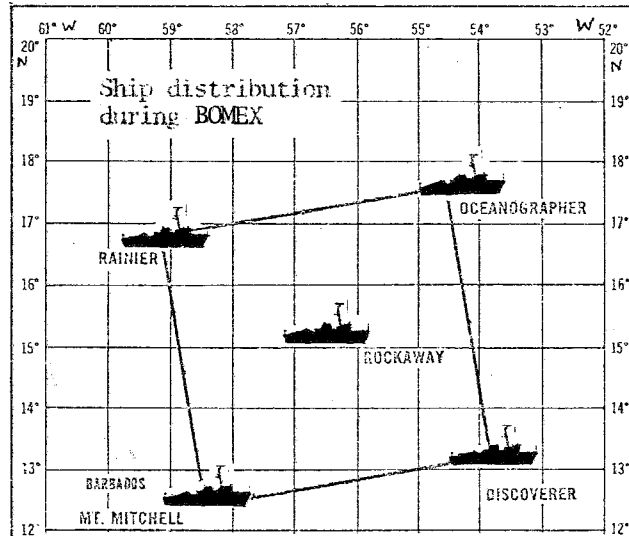
(v) GATE. The most detailed field experiment to date to study the interaction of cumulus with larger-scale tropical motions, 1974.

The following is a list of some important platforms used in field experiments:

(a) Research aircraft: They provide wind, temperature, moisture, pressure, turbulent flux, radiative flux, sea-surface temperature and cloud microphysical measurements.

(b) Research ships: These are usually placed at strategic positions to study important scientific problems. Triangular and polygonal arrays of ships with the capability of upper-air atmospheric measurements are most often used for tropical budget studies. A number of important findings have emerged on shallow and deep convection and studies of the trade-wind inversion using these ship configurations. Fig. 20.1 shows ship arrays for ATEX, BOMEX, AMTEX and GATE.

(c) Geostationary satellites: The products from geostationary satellites play an important part in operational weather prediction. Special efforts to collect data from these products have improved the overall data base in field experiments. Day and night cloud imagery (or cloud photographs) and cloud-motion vectors are used to determine the wind from daily film loops of visible and infrared images. The "cloud winds", as they are called, are an indispensable product for tropical meteorology. It has been shown by a number of workers in this field that three levels of cloud-motion vectors can be mapped depending, of course, on the availability of cloud tracers. The undisturbed trades are usually covered with low-cloud tracers because of the preponderance of shallow convection over oceans. Fig. 20.2 shows an example that illustrates this point (based on Prof. Fujita's work at the University of Chicago) of the low cloud-motion vectors over the Atlantic. Over a disturbed region, the high cloud-motion vectors are usually abundant. Fig. 20.3 shows an analysis of the motion field over the Atlantic at 850 and 200 mb that exploits this important data source. The determination



UPPER AIR OBSERVATIONAL NETWORK IN THE AMTEX

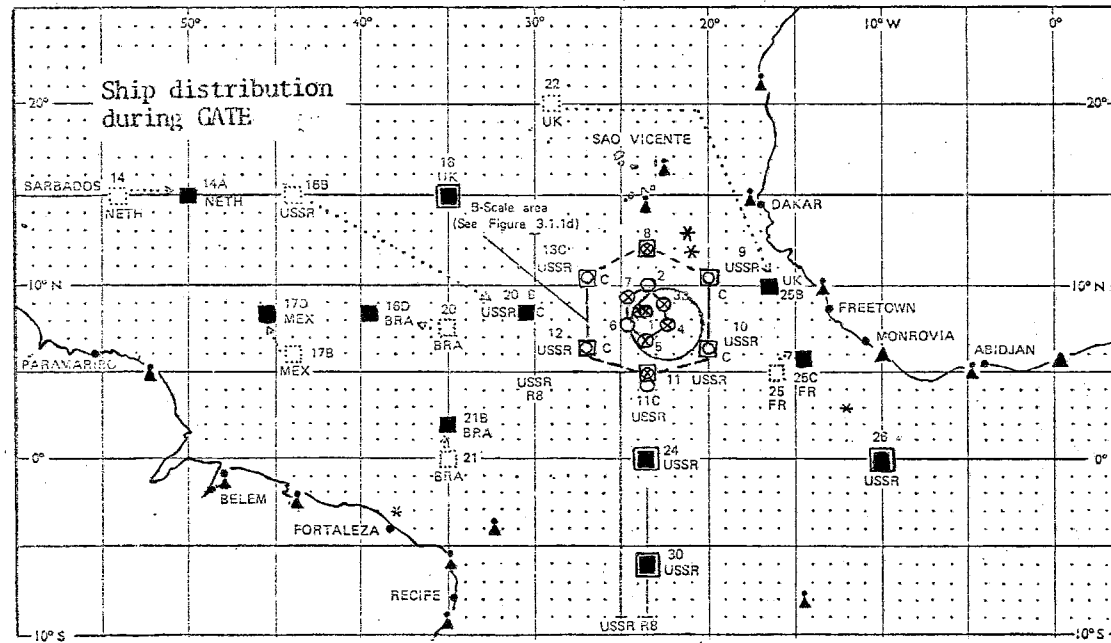
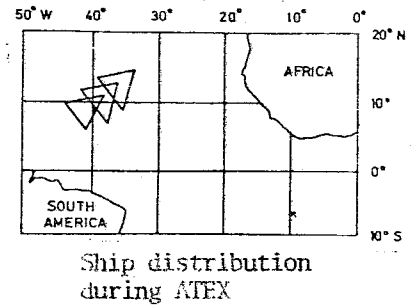
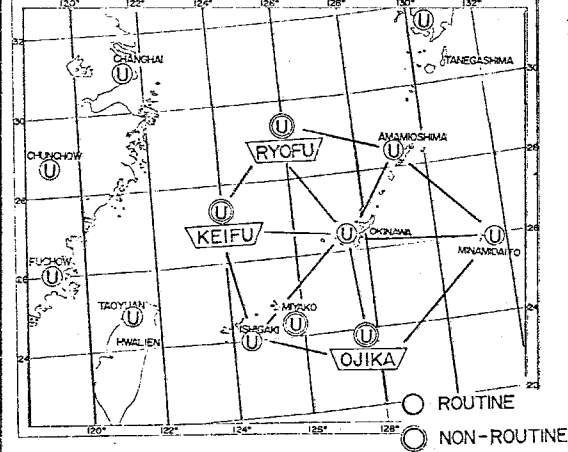


Figure 20.1

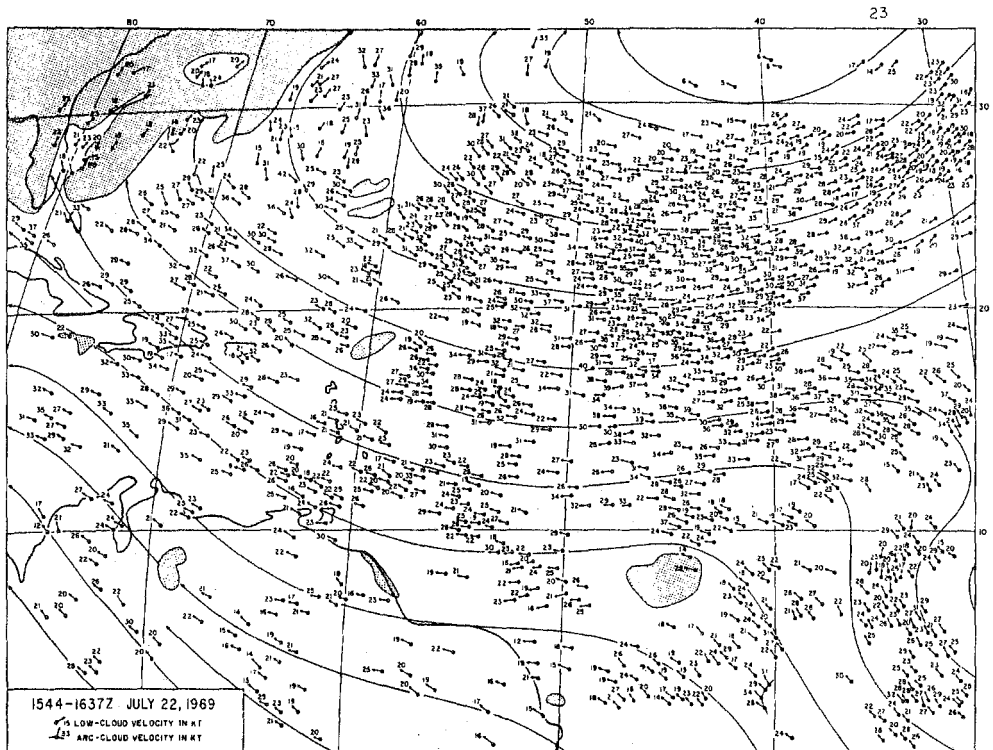


Figure 20.2 — Velocity vectors of low clouds over the Atlantic Ocean for July 22, 1969. A sequence of five pictures taken between 1544 and 1637 GMT is used for the computation. Cloud elements in an arc cloud are connected with a heavy line. High-cloud areas are shaded. Flow patterns are shown with streamlines drawn to fit cloud velocities

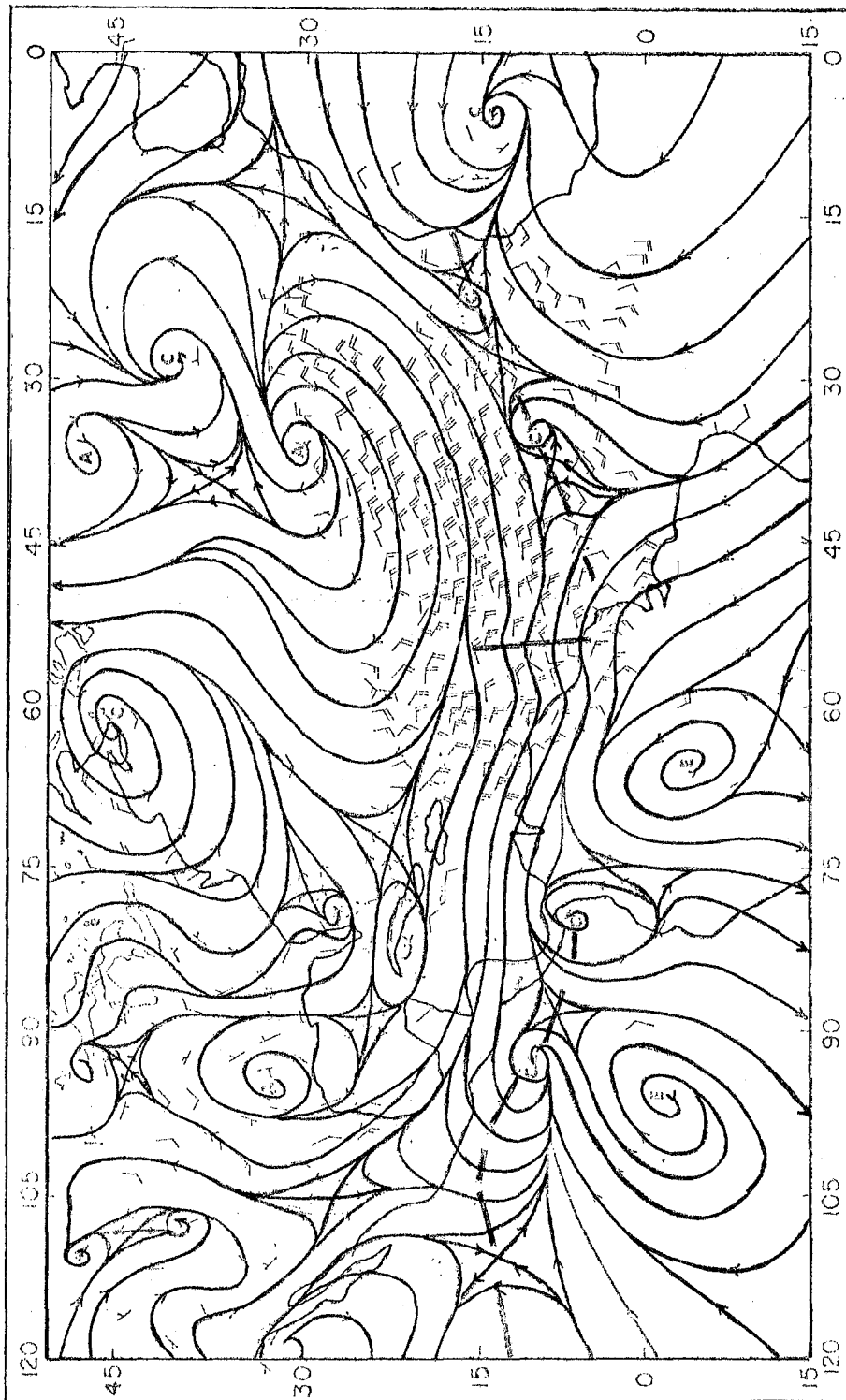


Figure 20.3a

Wind vectors at 850 mb over the Atlantic inferred from cloud displacement

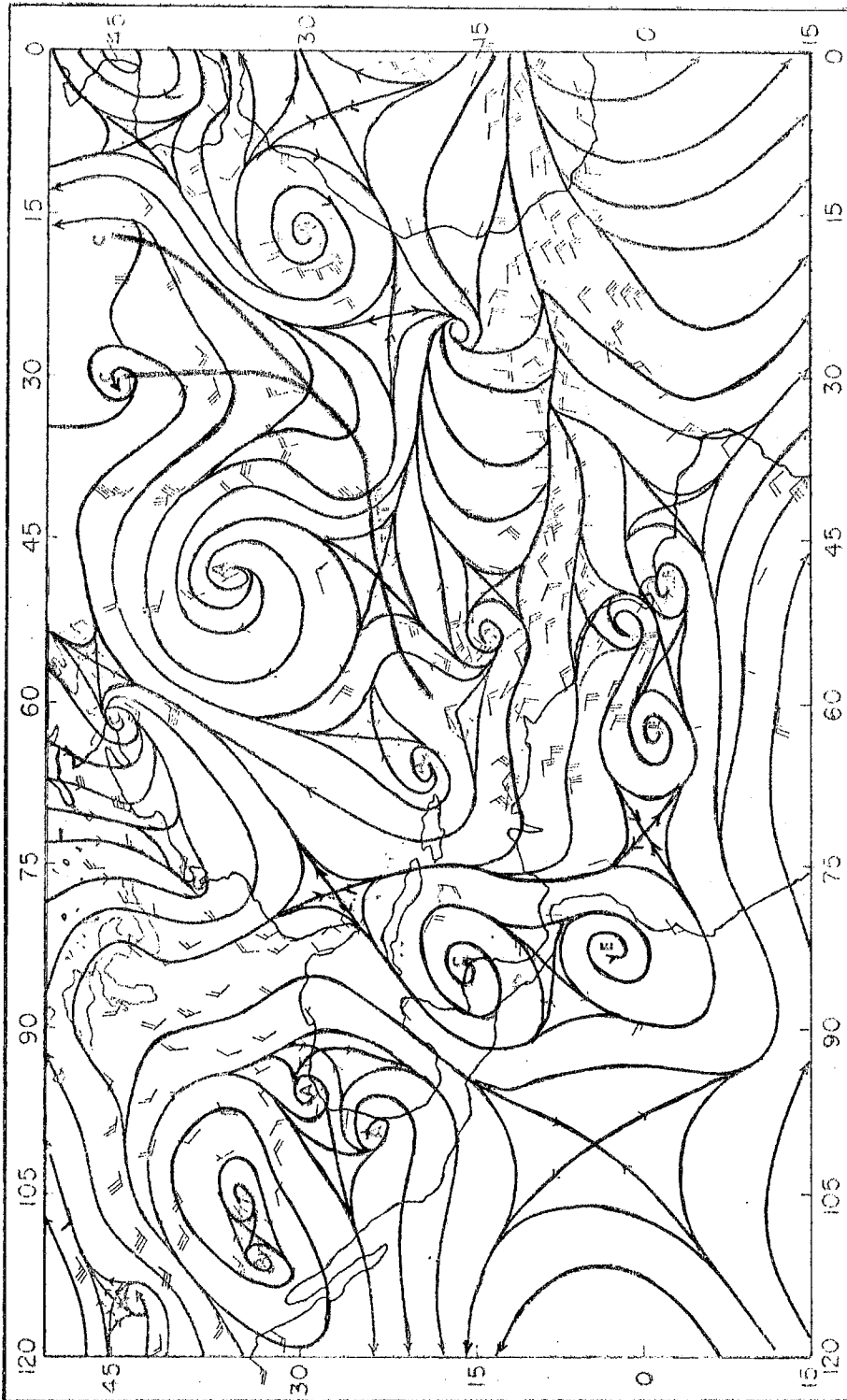


Figure 20.3b

Wind vectors at 200 mb over the Atlantic inferred from cloud displacement

of the vertical level of best fit for these cloud winds is a difficult problem. The present feeling based on a number of comparisons of the rawinsonde winds in the cloud-vector winds suggests that the low cloud-motion vectors should be assigned a level close to 900 mb over the tropics while the high cloud-motion vectors belong near the 200 mb surface.

The satellite photographs and film loops with an 800 m resolution provide a powerful research tool. The ground equipment to receive such satellite products is a worthwhile investment for developing tropical countries.

(d) Polar orbiting satellites: Aside from the Earth's radiation budget (see Chapter 3), a number of other products from the polar orbiting satellites are extremely valuable for tropical meteorology. The microwave radiometer on board satellites such as the NIMBUS series provides a measure of the total precipitable water. Maps of total precipitable water can be obtained from the digital products. The horizontal resolution of this product is at present somewhere around 50 km. A simple technique was proposed by Haydu and Krishnamurti (1978) to calibrate this satellite-derived product for ground truth. The procedure consists of obtaining a finite difference Laplacian of the satellite-derived precipitable water field on a horizontal mesh of five grid points. The radiosonde observation locations are projected to their nearest grid points. These values are kept fixed during a relaxation of the Laplacian field. As boundary conditions, one uses assigned normal gradients. The final solution matches the radiosonde values at their nearest grid points and it matches the Laplacian of the satellite-derived product elsewhere. Once the total precipitable water ('Q') is calibrated for ground truth, then, using a vertical structure function for specific humidity, one can map the field of specific humidity "q" at several levels in the atmosphere. An exponential variation of specific humidity with height is a reasonable structure function. This field satisfies the relation:

$$Q = \frac{1}{g} \int_0^{p_s} q \, dp$$

where p_s is the surface pressure. The maps of q at each level can also be calibrated for ground truth (i.e., radiosonde measurements) by an analysis technique such that the final values of q still satisfy the integral constraint stated above. This procedure is known to produce an analysis of the vertical distribution of the moisture field with sufficient detail to enable its horizontal gradients to be meaningful and compatible with satellite photographs. It should be stated here that this satellite-derived product of total precipitable water is only reliable over oceans since the microwave radiometer is an unreliable instrument over land areas.

Another useful product that one can map in the tropics is the satellite-derived sea-surface temperature distribution generally obtained from polar-orbiting satellites. In clear sky conditions, the black body radiation emitted by the ocean surface is usually calibrated to determine the field of sea-surface temperature. Low clouds, excessive water vapour and aerosols (dust) all tend to contaminate this field. Hence, a careful calibration of this product is essential. It is generally believed that under clear sky conditions the gradients of the satellite-derived field of sea-surface temperatures are more reliable than their absolute values. Generally, one computes a finite difference Laplacian of the satellite-derived sea-surface temperature on a fine mesh. This field is inverted. However, in this process one keeps the values fixed at those interior points which are closest to the station locations, the station values being assigned to these nearest grid points. Furthermore, it is desirable to use normal gradient boundary conditions and thus only the gradients, and not the absolute values, enter the analysis.

(e) Commercial ships: The merchant ship fleet provides an extremely valuable data base for research. Whenever field experiments are designed in and around oceans, special efforts are usually made to collect surface meteorological observations from a large number of merchant ships. During GATE, on the average, close to 1000 ship observations per day were collected over the tropical Atlantic Ocean. The surface observations include the usual parameters such as pressure, temperature, dew point, wind direction and speed, state of sky (cloud amount and type, visibility and sea-surface temperature, and sea state). Fig. 20.4 provides an illustration of the commercial ship distribution during the GATE.

(f) Commercial aircraft: This is an extremely valuable data source in the upper troposphere. A large number of wide-bodied jets carry several inertial navigation systems and, as a result, this stable platform enables one to measure high-level winds very reliably, especially between 300 and 200 mb. Although the temperature reports are not usually very reliable, the wind accuracy matches that from any other observational platform. Tropical oceans are usually data-void and the collection of commercial aircraft wind reports is very important. During the GATE, well over 1000 commercial aircraft wind reports were collected on a daily basis. Fig. 20.5 shows recent routes of commercial aircraft over the global tropics. This, of course, includes a number of smaller aircraft that depend on the global OMEGA navigation system for determining their position but the winds derived from these aircraft are slightly less accurate.

Several plans are under consideration by the global meteorological community to implement automatic collection of commercial aircraft wind reports for a selected number of wide-bodied jets. Data from these aircraft would be available for global weather prediction in near-real time. Wind data are transmitted from the aircraft to a satellite and then on to a data collection centre. Fig. 20.6 shows an example of global tropical wind analysis where commercial aircraft provide the bulk of the data.

(g) Boundary layer instrumentation: In the section on boundary layers, we made reference to some of the observations that are being made in order to obtain a better definition of the tropical boundary layer. The GATE contained within it a very sophisticated boundary layer subprogramme. This included both low-level research aircraft flights and ship-based tethered balloon measurements. The aircraft measurements included vertical eddy fluxes (with respect to flight leg averages) of moisture, sensible heat and momentum. A boom approximately 2.5 m long in front of the nose of the aircraft carries the small bead thermistor for temperature measurement and a fractometer cavity for water-vapour measurements. A gust probe measures the three components of air motion relative to the aircraft.

The ship observational program in GATE included tethered balloons and ascending and descending sondes. They are instrumented to provide the vertical distributions of moisture, temperature, and pressure and their fluctuations. The primary aim here is to examine the structure of the sub-cloud layer under a hierarchy of cloud convection régimes.

(h) Buoys: The deployment of moored and drifting buoys is a very useful way of getting oceanic observations. In addition to the usual surface meteorological and oceanographic measurements such as pressure, temperature, moisture and sea-surface temperature, they can be designed to provide real-time flux computations of sensible heat, momentum and water vapour. These are called "Spar Buoys." They provide fast-response measurements of the vertical wind component as well as temperature, wind and humidity on a similar time resolution.

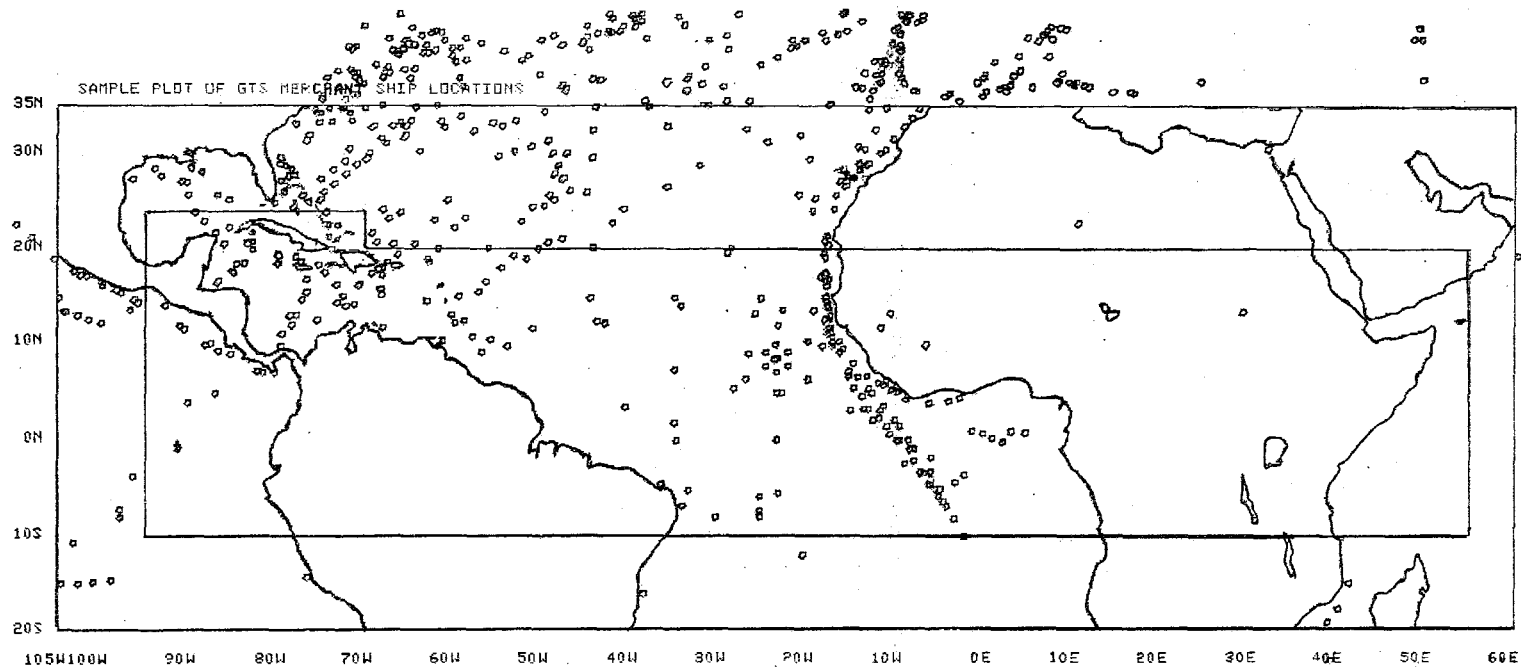


Figure 20.4 — A sample plot of location of merchant ships on one day during GATE (GTS tapes only)

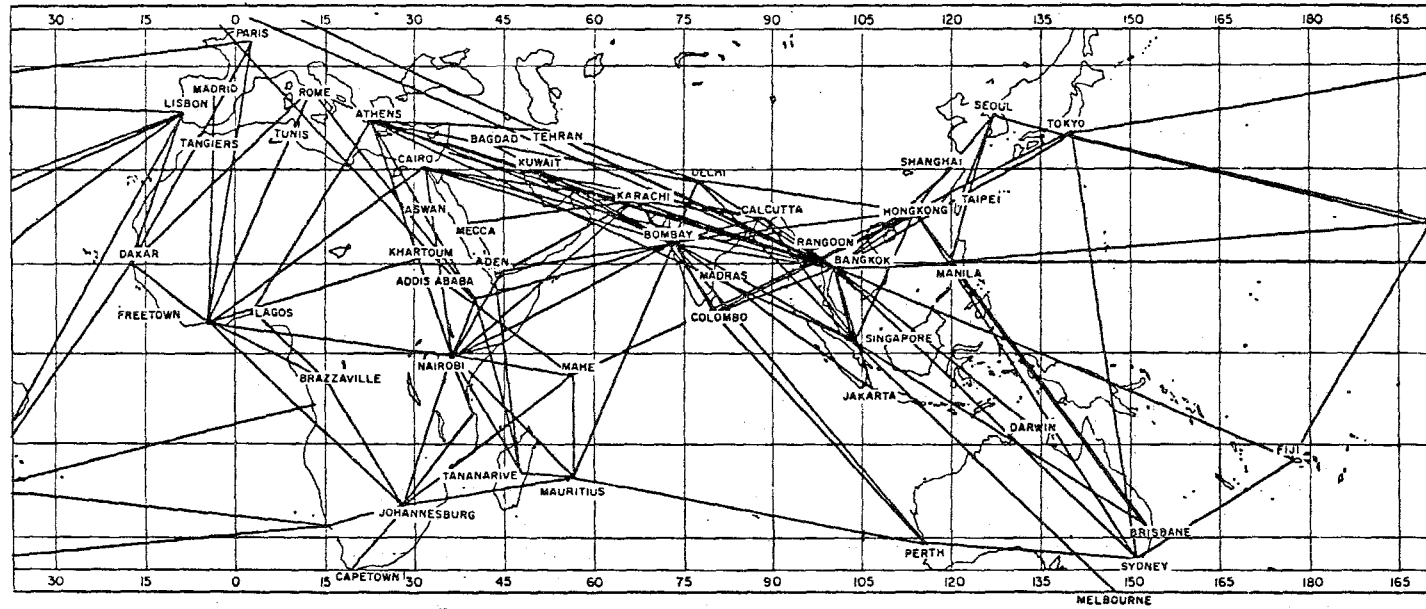


Figure 20.5 — Commercial aircraft routes between major airports

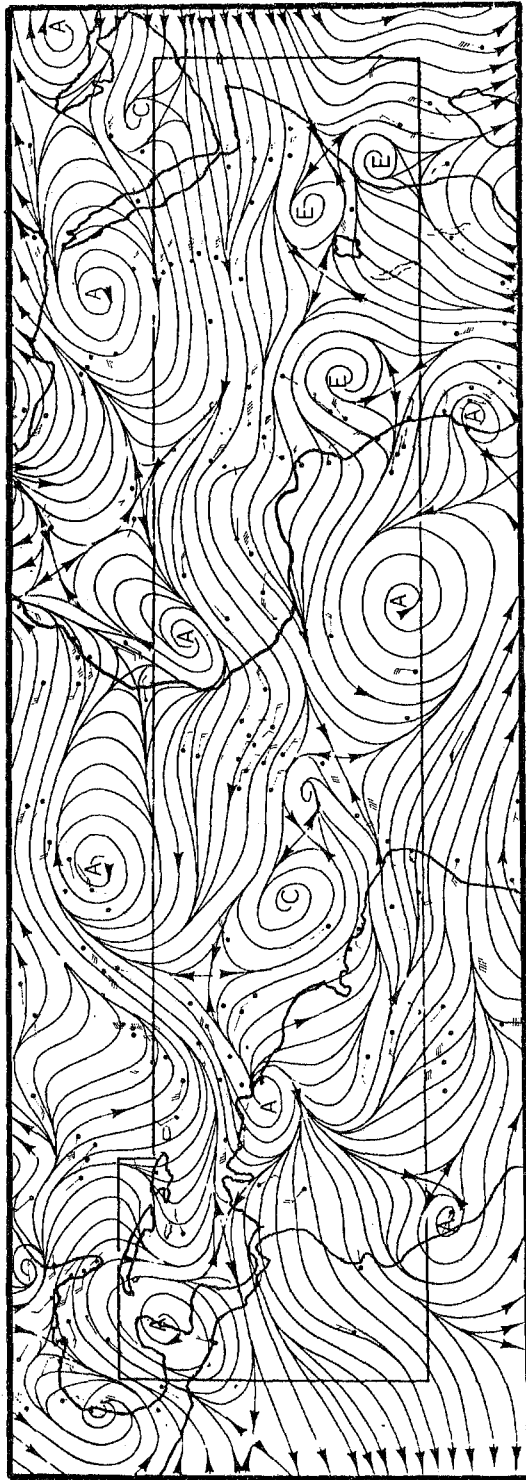


Figure 20.6
Example of global tropical wind analysis at 200 mb based on commercial aircraft reports

(i) Shipboard radar: 3 and 5 cm radars are generally carried on ships with a stabilized platform. The radar observations of echo intensity are extremely useful for the mapping of oceanic rainfall intensity. A very careful calibration is required. Calibration is usually carried out by performing drop-size spectra measurements by aircraft and ships in a well-coordinated field experiment such as GATE. The digital product can be used to construct vertical cross-sections as a function of time. They reveal a lot about the meso-scale cloud structures in evolving disturbances.

Chapter 21

NUMERICAL WEATHER PREDICTION OVER THE TROPICS

In this text on tropical meteorology, it is felt appropriate to present some of the fundamentals of the numerical prediction models suitable for this region. Since this is an area where much effort is expected from developing countries, it would be well worthwhile for the student interested in tropical meteorology to understand the ingredients of a tropical numerical prediction model.

21.1 Filtered barotropic model

As a starting point in the development of numerical weather prediction models for the tropics, the simplest barotropic model is very useful. This model will take as input the streamlines and isotachs of a limited area weather map and provide a forecast of the flow field at that level. For operational and research work, the various advances that have been made in this model should be exploited. Factors such as analysis of the initial map, domain size, grid size, handling of north/south and east/west boundaries, and the finite-difference techniques all deserve very careful examination. This type of model can be very useful by providing a quick look prediction for a typical tropical wave-type disturbance that may be identified on the initial map. To consider an example, let us assume that a model is being constructed for the West African region.

The African waves have their largest amplitude near the 700 mb level. Their scale is roughly 2000 km and their speed of westward propagation is 5° to 10° longitude/day. Barotropic energy conversions are largest near the 700 mb level because of the presence of the West African low-level jet at this level. The choice of 700 mb as an appropriate level for making barotropic forecasts is appealing on these grounds. However, the forecast will be of marginal value if the level of non-divergence is far away from this level. Experience shows that the barotropic model behaves far better at 700 mb than at the 850 and 200 mb levels over Africa. Because of the extreme simplicity of the model, the suggestion was advanced that it should be made a "model zero" for operational purposes and twice daily forecasts should be attempted. Only by making a large number of forecasts can one assess the value of the product. Furthermore, by watching the day-to-day behaviour of the forecasts on facsimile charts, experienced synoptic meteorologists quickly gain enough insight to assess its good and bad features. Such an experience adds to the possibility of issuing a revised subjective forecast where the experienced meteorologist adds his own evaluation of the product.

A systematic development and evaluation of a hierarchy of models is essential. Failures of simpler versions of models can be due to a number of factors such as: inadequate observations to define the initial and the verification maps, poor physics, poor numerical techniques, and unrepresentativeness of the scales being studied. We shall next go into the details of designing of a simple barotropic model.

21.2 The basic dynamics of the barotropic model

The principal of conservation of absolute vorticity is expressed by the relation:

$$\frac{D}{Dt} \zeta_a = 0 \quad (21.2.1)$$

where $D/Dt \equiv \frac{\partial}{\partial t} + \mathbf{V}_H \cdot \nabla$ is a substantial derivative for the horizontal advection and ζ_a is the absolute vorticity, which may be expressed by:

$$\zeta_a = \nabla^2 \psi + f \quad (21.2.2)$$

while $\mathbf{V}_H = \mathbf{K} \times \nabla \psi$ is the rotational part of the motion field, i.e.:

$$\begin{aligned} u &= - \frac{\partial \psi}{\partial y} \\ v &= \frac{\partial \psi}{\partial x} \end{aligned} \quad (21.2.3)$$

where ψ is a stream function. The law of conservation of absolute vorticity may be written as:

$$\frac{\partial}{\partial t} \zeta_a = - u \frac{\partial \zeta}{\partial x} - v \frac{\partial \zeta}{\partial y} - v \frac{\partial f}{\partial y} \quad (21.2.4)$$

which can be simplified to the form:

$$\frac{\partial}{\partial t} \nabla^2 \psi = - J(\psi, \nabla^2 \psi) - \beta \frac{\partial \psi}{\partial x} \quad (21.2.5)$$

where $\beta = \frac{\partial f}{\partial y}$ is the beta parameter. Equation (21.2.5) is the basic framework of the barotropic dynamics and the so-called non-divergent barotropic model. The equation has one unknown ψ .

In the undifferentiated form, this may be expressed by the following three equations for the three unknowns u , v and z ; where u , v are the two horizontal velocity components and z is the height of the pressure surface:

$$\begin{aligned} \frac{\partial u}{\partial t} &= - u \frac{\partial u}{\partial x} - v \frac{\partial u}{\partial y} + fv - g \frac{\partial z}{\partial x} \\ \frac{\partial v}{\partial t} &= - u \frac{\partial v}{\partial x} - v \frac{\partial v}{\partial y} - fu - g \frac{\partial z}{\partial y} \\ \frac{\partial u}{\partial x} + \frac{\partial v}{\partial y} &= 0 \end{aligned} \quad (21.2.6)$$

It should be noted that (21.2.5) and (21.2.6) are equivalent systems. The differentiated form (21.2.5) is not complete if the pressure field is not adequately defined. This may be obtained from the divergence equation from (21.2.6). This comes out as the well-known non-linear balance equation:

$$\nabla^2 g z = \nabla \cdot \mathbf{f} \nabla \psi + 2J \left(\frac{\partial \psi}{\partial x}, \frac{\partial \psi}{\partial y} \right) \quad (21.2.7)$$

The differentiated form of the vorticity equation describes the u , v , and z fields via the system of equations (21.2.5), (21.2.3) and (21.2.7). If these three equations are solved in sequence with appropriate initial and boundary conditions, then one can map the motion and the pressure fields of the barotropic forecast model. This is an interesting system for low latitudes. Equation (21.2.7) is called a reverse balance equation since the pressure field (z) is determined from the motion field. The following simplified versions of the reverse balance equation exist and they are worth examining:

$$\nabla^2 g z = f_0 \nabla^2 \psi \quad (21.2.8)$$

where f_0 is a constant value of the Coriolis parameter, and

$$\nabla^2 g z = \nabla \cdot f \nabla \psi \quad (21.2.9)$$

where equation (21.2.8) describes the pressure (height) distribution from the geostrophic wind law and equation (21.2.9) describes the linear balance pressure-wind law. In the tropics, the problem of the pressure-wind laws is the reverse of that in the middle latitudes. Here the wind is supposed to be given and the pressure field is deduced from it. This is why we call it the "reverse" balance equation.

For a given wind field (i.e., the ψ distribution), if one wishes to compare the three geopotential height fields from equations (21.2.7), (21.2.8) and (21.2.9), it is important that the same boundary conditions be used for z in the three equations.

The barotropic forecast model is defined by equations (21.2.5), (21.2.3) and (21.2.7) and next we shall address the question of the solution of this system.

21.3 Some properties of the barotropic flows

We shall design a closed domain such that there is no net mass flux in or out of the domain and within such a domain we shall be making barotropic forecasts. It is important to recognize some important parcel and domain invariants of the barotropic flows.

21.3.1 Parcel invariants

Following the parcel (two-dimensional flows), absolute vorticity is conserved (equation 21.2.1). In a closed domain, this implies that one should watch the maximum and minimum values of absolute vorticity during the evolution of the barotropic model. A good model will preserve nearly the same value of the maximum and minimum value within the domain. It should be noted that all powers of vorticity are parcel invariants.

21.3.2 Domain invariants

The well known invariants are: $\overline{\zeta_a}$ the mean absolute vorticity, $\overline{\zeta_a^2}$ the mean square absolute vorticity, and \overline{K} , the total kinetic energy where the bar is a domain average. It should be noted that domain averages of all powers of absolute vorticity are also invariants of this system. To show that $\overline{\zeta_a}$ and $\overline{\zeta_a^2}$ are invariants, equation (21.2.1) is written in the advective form, i.e.:

$$\frac{\partial \zeta_a}{\partial t} = -u \frac{\partial \zeta_a}{\partial x} - v \frac{\partial \zeta_a}{\partial y} \quad (21.3.1)$$

Multiply by $\frac{\zeta_a^{n-1}}{n}$ and rewrite:

$$\frac{\partial}{\partial t} \zeta_a^n = -u \frac{\partial}{\partial x} \zeta_a^n - v \frac{\partial}{\partial y} \zeta_a^n \quad (21.3.2)$$

Equation (21.3.2) can be expressed in flux form:

$$\frac{\partial}{\partial t} \zeta_a^n = - \frac{\partial}{\partial x} u \zeta_a^n - \frac{\partial}{\partial y} v \zeta_a^n \quad (21.3.3)$$

upon integration over a closed domain D defined by;

$$D = \int_y \int_x dx dy \quad (21.3.4)$$

we obtain:

$$\frac{\partial}{\partial t} \int_y \int_x \zeta_a^n dx dy = 0 \quad (21.3.5)$$

if the normal wind component is zero at the boundary. We have thus established that all powers of ζ_a are invariants.

To show that the kinetic energy \bar{K} is an invariant, multiply the first equation (21.2.6) by u and the second equation (21.2.6) by v and add. We obtain;

$$\frac{\partial K}{\partial t} = -\mathbb{V} \cdot \nabla K - \mathbb{V} \cdot \nabla gz \quad (21.3.6)$$

In flux form, this can be expressed by:

$$\frac{\partial K}{\partial t} = -\nabla \cdot \mathbb{V} (K + gz) \quad (21.3.7)$$

and over a closed domain D with the previous boundary condition the integration of equation (21.3.7) yields;

$$\frac{\partial}{\partial t} \bar{K} = 0 \quad (21.3.8)$$

which implies a conservation of the domain average kinetic energy. The invariants of ζ_a^2 and \bar{K} are important properties. They are called the quadratic invariants of the barotropic model. If the finite difference analogs of the model do not conserve these properties, then, after some time, the flows in the forecasts look usually very unrealistic.

It is very difficult to design a model that goes beyond the conservation of just the first and second order moments. In designing a barotropic forecasts model for a limited tropical domain, it is better to ensure that at least ζ_a , ζ_a^2 and \bar{K} are conserved for the finite-difference analogs of the system.

21.3.3 Energy exchanges of the barotropic model

The weather map for a given day may contain large-scale motion only. One may see a wave or vortex on the map of the following day. The barotropic model contains an important mechanism for disturbance generation on certain scales. This is the transformation of shear vorticity into curvature vorticity. The absolute vorticity contains the shear, curvature and the Earth's vorticity. Parcels conserving their absolute vorticity can move along their trajectory exchanging shear vorticity into curvature and vice versa. The analogous linear problem is the barotropic instability problem. It is important always to recognize, whenever a development occurs, the extent to which the development could be accounted for by the barotropic process.

Scale analysis shows that large-scale processes in the tropics are quasi-barotropic and the linear stability criterion frequently shows that the fields satisfy the necessary conditions for the existence of barotropic instability. Hence, the use of a barotropic model can be quite meaningful

in this region. The two principle energy exchanges of the barotropic model are:

$$\frac{\partial \overline{\overline{K_E}}}{\partial t} = \langle \overline{K_Z} \cdot K_E \rangle = \overline{[u] \frac{\partial}{\partial y} [u'v']} = - \overline{\frac{\partial [u]}{\partial y} [u'v']} \quad (21.3.9)$$

$$\frac{\partial \overline{\overline{K_Z}}}{\partial t} = \langle K_E \cdot \overline{K_Z} \rangle = - \overline{[u] \frac{\partial}{\partial y} [u'v']} \quad (21.3.10)$$

$$\frac{\partial \overline{\overline{K_T}}}{\partial t} = \frac{\partial}{\partial t} (\overline{\overline{K_E}} + \overline{\overline{K_Z}}) = 0 \quad (21.3.11)$$

where $\overline{\quad}$ is a meridional average, $[\quad]$ is a zonal average, and $\overline{\quad}$ is a time average. $\overline{\overline{K_E}}$, $\overline{\overline{K_Z}}$ and $\overline{\overline{K_T}}$ are, respectively, the total eddy kinetic energy, the total zonal kinetic energy and the total energy. These relations can be derived easily from the equations of motion for a barotropic fluid. The equations merely state that convergence of flux of westerly momentum in a westerly current increases the zonal kinetic energy. These exchanges usually exhibit a quasi-periodic oscillation in time.

21.4 Numerical prediction techniques

21.4.1 The advective term for filtered models

Although there are many ways of expressing an advective term for a filtered model, we shall illustrate the so-called "Arakawa" Jacobian. The advection of a property ζ by the rotational part of the wind ψ may be written as:

$$\Downarrow (\psi, \zeta) = \frac{1}{3} \left\{ \Downarrow_1(\psi, \zeta) + \Downarrow_2(\psi, \zeta) + \Downarrow_3(\psi, \zeta) \right\} \quad (21.4.1)$$

where the three Jacobians on the right-hand side of the above equation are three alternate finite-difference analogs of the advective terms.

Where $\Downarrow_1(\psi, \zeta)$ is a finite difference analog of the term:

$$\frac{\partial \psi}{\partial x} \frac{\partial \zeta}{\partial y} - \frac{\partial \psi}{\partial y} \frac{\partial \zeta}{\partial x} \quad (21.4.2)$$

$\Downarrow_2(\psi, \zeta)$ is a finite difference analog of the term:

$$\frac{\partial}{\partial y} \left(\zeta \frac{\partial \psi}{\partial x} \right) - \frac{\partial}{\partial x} \left(\zeta \frac{\partial \psi}{\partial y} \right) \quad (21.4.3)$$

and $\Downarrow_3(\psi, \zeta)$ is a finite difference analog of the term:

$$\frac{\partial}{\partial x} \left(\psi \frac{\partial \zeta}{\partial y} \right) - \frac{\partial}{\partial y} \left(\psi \frac{\partial \zeta}{\partial x} \right) \quad (21.4.4)$$

It can be shown that this linear combination of the three finite difference Jacobians conserves mean vorticity, mean square vorticity and mean kinetic energy. The following is a final form of the Jacobian for a rectangular mesh of grid points at distance d apart (Arakawa, 1966):

$$\begin{aligned}
 \Psi_{i,j}(\zeta, \psi) = & -\frac{1}{12d^2} [(\psi_{i,j-1} + \psi_{i+1,j-1} - \psi_{i,j+1} - \psi_{i+1,j+1})(\zeta_{i+1,j} - \zeta_{i,j}) \\
 & + (\psi_{i-1,j-1} + \psi_{i,j-1} - \psi_{i-1,j+1} - \psi_{i,j+1})(\zeta_{i,j} - \zeta_{i-1,j}) \\
 & + (\psi_{i+1,j} + \psi_{i+1,j+1} - \psi_{i-1,j} - \psi_{i-1,j+1})(\zeta_{i,j+1} - \zeta_{i,j}) \\
 & + (\psi_{i+1,j-1} + \psi_{i+1,j} - \psi_{i-1,j-1} - \psi_{i-1,j})(\zeta_{i,j} - \zeta_{i,j-1}) \\
 & + (\psi_{i+1,j} - \psi_{i,j+1})(\zeta_{i+1,j+1} - \zeta_{i,j}) \\
 & + (\psi_{i,j-1} - \psi_{i-1,j})(\zeta_{i,j} - \zeta_{i-1,j-1}) \\
 & + (\psi_{i,j+1} - \psi_{i-1,j})(\zeta_{i-1,j+1} - \zeta_{i,j}) \\
 & + (\psi_{i+1,j} - \psi_{i,j-1})(\zeta_{i,j} - \zeta_{i+1,j-1})
 \end{aligned} \tag{21.4.5}$$

where d is a local mean grid distance for a square mesh. In short-range numerical weather prediction it has been stated that a quadratic conserving advection scheme is desirable. There are however, many problems that arise when one uses such a scheme.

Although the weather maps produced by a quadratic conserving scheme appear extremely elegant, they usually exhibit large phase errors. Controlled experiments with idealized systems show that the quadratic conserving schemes are, in fact, not very accurate. The problem, of course, is that one cannot use centred-difference formulae and $\Psi_1(\psi, \zeta)$ alone all the time, since they are known to be non-linearly computationally unstable and can give trouble. The semi-Lagrangian advective scheme has not been used in filtered models; it is described elsewhere in these notes and may be better in some ways.

21.4.2 Time-differencing scheme

In the filtered models we shall use an explicit time-differencing scheme. The schemes we shall use are a slight modification of the Euler backward predictor-corrector technique. For an equation of the type:

$$\frac{\partial P}{\partial t} = Q \tag{21.4.6}$$

The two steps are:

$$P_2^{(1)} = P_1 + Q_1 \Delta t \tag{21.4.7}$$

$$P_2^{(2)} = P_1 + \{\alpha Q_1 + \beta Q_2^{(1)}\} \Delta t \tag{21.4.8}$$

where $P_2^{(1)}$ is the predictor and $Q_2^{(1)}$ is the corresponding value of Q based on the predictor. $P_2^{(2)}$ is the corrector or final value of P . α and β are constants such that $\alpha + \beta = 1$, and if $\alpha = 0$ and $\beta = 1$, it gives the so-called Matsuno scheme. It is necessary to make sure that the linear stability criterion is satisfied by the data set. This is the well-known

Courant-Friederick-Levy criterion and is discussed in standard textbooks on numerical weather prediction (e.g., Haltiner, 1971).

21.4.3 Boundary conditions

In the zonal direction it may be desirable to extend the domain by about 1000 km and add some extra grid points beyond the analysis domain. In this region a smooth cyclic continuity of the map may be assumed to remove east/west boundaries.

In the filtered model, after the stream function is specified at the boundaries by the procedure illustrated in the next section, the stream function is first obtained in the interior of the domain. During the barotropic forecast, a variety of boundary conditions can easily be used at the north/south boundaries:

- (i) $\psi(x, y_B, t) = \psi(x, y_B, t) = 0 \quad t = 0$
- (ii) $\psi(x, y_B, t) = \oint \psi(x, y_B, 0) dx / \oint dx$
- (iii) $\psi(x, y_B, t)$ made to change according to some specifications.

Since there are no problems regarding excitation of gravity-inertial oscillations, the boundaries can be specified relatively easily in this problem.

In general, no smoothing other than that implied by the Arakawa, Jacobian and the time-differencing scheme is necessary. Figure 21.1 illustrates an example of a filtered barotropic forecast in the tropics.

21.5 One-level primitive equation model

This is usually considered next in the hierarchy of the simple models. This model allows for divergence and is known by the following names:

- (i) One-level primitive equation model;
- (ii) Shallow water equations;
- (iii) Laplace's tidal equations; and
- (iv) Divergent barotropic model.

It is described by the following three equations for the three unknowns u , v , and z . The equations of motion are:

$$\frac{\partial u}{\partial t} + u \frac{\partial u}{\partial x} + v \frac{\partial u}{\partial y} - fv = -g \frac{\partial z}{\partial x} \quad (21.5.1)$$

$$\frac{\partial v}{\partial t} + u \frac{\partial v}{\partial x} + v \frac{\partial v}{\partial y} + fu = -g \frac{\partial z}{\partial y} \quad (21.5.2)$$

and the mass continuity equation:

$$\frac{\partial z}{\partial t} + u \frac{\partial z}{\partial x} + v \frac{\partial z}{\partial y} = -z \left(\frac{\partial u}{\partial x} + \frac{\partial v}{\partial y} \right) \quad (21.5.3)$$

where z is the height of a free surface. For our purposes, we shall identify $z = 0$ with the mean sea level. It should be noted that if this model is used to forecast the weather at a level in the troposphere, z should not a priori be assumed to be the height of the pressure surface. The interpretation of

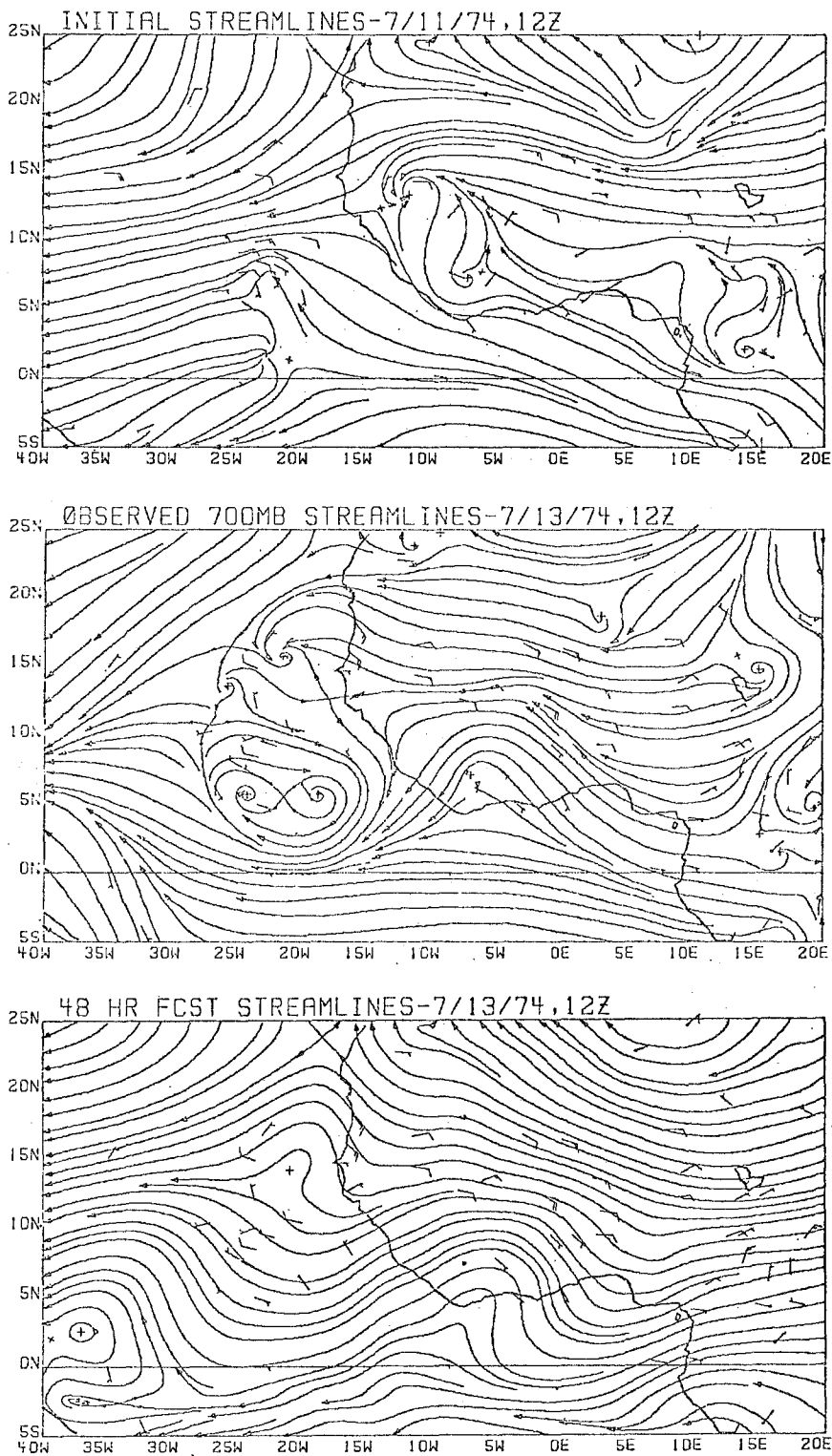


Figure 21.1 — (Top) 700 mb observed winds, time 0; (middle) same at time 48 hours; (bottom) barotropic forecast at time 48 hours

z is an important problem in the application of the shallow-water equations for numerical weather prediction. We shall review this later in this chapter.

This system of equations is very similar to the system described in equation (21.2.6) except for the mass continuity equation. The divergences in the vertical columns are altered by the individual change in the free surface height in the shallow-water equations. This system also permits as solutions external gravity waves. These waves are a part of the physical system and can grow spuriously as a result of certain initial data imbalances. This is another topic which is very important in all primitive-equation prediction models.

21.5.1 Invariants of the shallow-water equations

The parcel invariants of this system are the potential vorticity $\zeta_p = \frac{(\zeta+f)}{z}$ and all its powers. In order to show this, form the usual vorticity equation using (2.1.1) and (2.1.2):

$$\frac{\partial \zeta_a}{\partial t} = -\mathbb{W}_H \cdot \nabla \zeta_a - \zeta_a \nabla \cdot \mathbb{W} \quad (21.5.4)$$

Upon elimination of $\nabla \cdot \mathbb{W}$ from (21.5.3) and (21.5.4), we obtain:

$$\left(\frac{\partial}{\partial t} + \mathbb{W}_H \cdot \nabla \right) \left(\frac{(\zeta + f)}{z} \right) = 0 \quad (21.5.5)$$

or ζ_p is a parcel invariant. Upon multiplication of (21.5.5) by $(\zeta_p)^{n-1/n}$, we show that:

$$\left(\frac{\partial}{\partial t} + \mathbb{W}_H \cdot \nabla \right) \zeta_p^n = 0 \quad (21.5.6)$$

which shows the invariance of all powers of ζ_p . It is easy to see that over a closed domain the mean value of ζ_p is an invariant.

Another important invariant of this system is a total energy parameter. It is given by the integral over a closed domain, i.e.:

$$\frac{\partial}{\partial t} \int_{\sigma} (Kz + gz^2/2) d\sigma = 0 \quad (21.5.7)$$

Equation (21.5.7) shows that the local time change of the total energy of the divergent barotropic model is an invariant. It is worth noting at this point that although the quantity $Kz + gz^2/2$ is often referred to as total energy, the dimensions associated with it (L^3T^{-2}) are different from those of energy (L^2T^{-2}). Here L is a measure of length and T is a measure of time. In MKS units the units of $Kz + gz^2/2$ are $m^3 s^{-2}$. This is to be contrasted with MKS units for energy $m^2 s^{-2}$. Over a closed domain it is easy to see from equation (21.5.3) that z is an invariant and so is also z^2 .

21.5.2 Numerical prediction techniques

Here we shall not try to provide a summary of all existing methods and discuss their relative merits. Instead, we shall describe the details of one good working model.

The two important areas where care must be exercised in the finite-difference aspects are:

- (i) The horizontal advection terms; and
- (ii) The treatment of the pressure gradient, Coriolis and horizontal divergence terms.

The semi-Lagrangian advective scheme used in the Florida State University's primitive equation model is described by Mathur (1970). This scheme is very powerful in conserving parcel and domain invariants of the system. The treatment of the pressure gradient, Coriolis and horizontal divergence term is described by Kanamitsu (1975). The time-differencing scheme used in the present model is an Euler-backward scheme.

21.5.3 The problem of geopotential height in low latitudes

This is really the problem of the wind-pressure laws in low latitudes. The temperature error in the radiosonde element makes it extremely difficult to analyse the pressure field in low latitudes from the hydrostatic law. An error of 1°C corresponds to an error of roughly 20 metres in the geopotential height in the lower troposphere. It turns out that this is intolerable in low latitudes. The synoptic definition of pressure-wind patterns in low latitudes thus has to rely on dynamics and as such must remain model-dependent. This is especially true at present in the equatorial latitudes. How does one go about determining a pressure field in low latitudes? Next we shall discuss several different initialization procedures for numerical weather prediction in low latitudes. These methods yield as a by-product wind-pressure laws of some interest.

21.5.4 Single-level initialization

The starting point here is a given streamline-isotach map over a tropical belt such as West Africa. The pressure field is deduced from the horizontal motion field by a hierarchy of models of increasing complexity.

21.5.5 Static initialization

The single level static initialization techniques are based on the non-linear balance equation and on simplified versions of it. The following laws are relevant to the static initialization problem.

Geostrophic law:

$$\nabla^2 gz = \nabla^2 f_0 \psi \quad (21.5.8)$$

Linear balance law:

$$\nabla^2 gz = \nabla \cdot f \nabla \psi \quad (21.5.9)$$

Non-linear balance law:

$$\nabla^2 gz = \nabla \cdot f \nabla \psi + 2J \left(\frac{\partial \psi}{\partial x}, \frac{\partial \psi}{\partial y} \right) \quad (21.5.10)$$

In these relations the stream function ψ is supposed to be known from the observed wind field (Hawkins and Rosenthal, 1965). The procedure for obtaining the stream function from the wind field has been improved by Mathur

(1970). The relative vorticity of the observed wind is relaxed to obtain the streamfunction with appropriate boundary conditions from the following equation:

$$\nabla^2 \psi = \frac{\partial v}{\partial x} - \frac{\partial u}{\partial y} \quad (21.5.11)$$

where u and v are the velocity components. Around a closed domain, the outward normal velocity v_n at any point is modified to a value v_n^m by the formula:

$$v_n^m = v_n + \epsilon |v_n| \quad (21.5.12)$$

where ϵ is determined from a constraint of zero net mass flux out of the domain, which yields:

$$\epsilon = - \frac{\oint_C v_n ds}{\oint_C |v_n| ds} \quad (21.5.13)$$

where the line integral is taken around the closed domain with line segments ds along the boundary.

In general, for sufficiently large domains $\epsilon \ll 1$. Thus the modification of data implied by equation (21.5.12) is very small. The streamfunction at the boundary is then determined from the relation:

$$\frac{\partial \psi}{\partial s} = v_n^m$$

This equation can be integrated along the boundary to yield ψ with an assigned value at one point.

We now have the right-hand sides of equations (21.5.8), (21.5.9) and (21.5.10). These equations are to be solved for the geopotential height z with appropriate boundary conditions. We could have written (21.5.8) in the form $z = f_0 \psi / g$; however, this is not a suitable form for comparison of the three height fields. For purposes of comparison, it is desirable that the same boundary conditions for z be used. The selection of boundary conditions for z is not an easy matter. If the north/south boundaries are over the middle latitudes, then geostrophic boundary conditions or the observed geopotential (from an analysis) would be appropriate. In the east/west direction, an artificial cyclic continuity is imposed on the initial analysis of the motion field. Thus there are no walls or boundaries in the zonal direction. If the north/south boundaries are within the tropics, i.e. 10°N to 10°S , there is no simple way of assigning boundary conditions. It is desirable to select a sufficiently large-sized domain so that the north/south boundaries are at least 20° away from the Equator.

It is the present feeling that any of these static initialization procedures do not adequately describe the wind-pressure laws for low latitudes. In fact, the feeling is that there exist no diagnostic simple wind-height laws for low latitudes.

21.5.6 Numerical prediction techniques

The single-level dynamic initialization makes use of a one-level NWP model. All of the numerical techniques of the one-level primitive equation model are used in the iterative initialization since it is the backward/forward integration of the same model. Although many versions of the models

exist, we shall here briefly address the model of the Florida State University. For this purpose, the equations are written in the form:

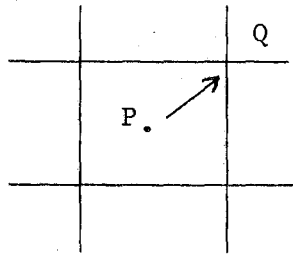
$$\frac{Du}{Dt} = fv - g \frac{\partial z}{\partial x} = A \quad (21.5.14)$$

$$\frac{Dv}{Dt} = -fu - g \frac{\partial z}{\partial y} = B \quad (21.5.15)$$

$$\frac{Dz}{Dt} = -z \left(\frac{\partial u}{\partial x} + \frac{\partial v}{\partial y} \right) = C \quad (21.5.16)$$

21.5.7 Semi-Lagrangian advection

In order to control non-linear computational instability, it is necessary to exercise care in the treatment of horizontal advective terms. We have already stressed the need for this within the context of the filtered models. The semi-Lagrangian advection proposed by Krishnamurti (1962) and Mathur (1970) treats the horizontal motion of the parcels each time-step and no explicit advective terms such as $\mathbf{V} \cdot \nabla Q$ are found in the finite difference analogs of the equations.



In the above diagram, Q denotes a grid point and a parcel which is located at P at time $t - \Delta t$ arrives at location Q in a time Δt . We have to define u , v and z at grid points at the end of each time-step. The first guess on the location of P is:

$$x = -u|_Q \Delta t - 1/2 A|_Q \Delta t^2 \quad (21.5.17)$$

$$y = -v|_Q \Delta t - 1/2 B|_Q \Delta t^2 \quad (21.5.18)$$

The point P falls between the grid points generally and a definition of u , v and z at P at $t - \Delta t$ has to be carried out by a local surface fitting from the information at the various grid points for time $t - \Delta t$.

The second guess on the location of P is next carried out via the relations:

$$x = -u|_P \Delta t - 1/2 A|_P \Delta t^2 \quad (21.5.19)$$

$$y = -v|_P \Delta t - 1/2 B|_P \Delta t^2 \quad (21.5.20)$$

where A and B at time $t - \Delta t$ are interpolated to P from the grid point values at time $t - \Delta t$. The location P, for determining A and B, is the previously guessed value.

The predictor correctors for u and v are constructed as follows:

First guess:

$$u|Q_t = u|P_{t-\Delta t} + A|P_{t-\Delta t} \Delta t \quad (21.5.21)$$

$$v|Q_t = v|P_{t-\Delta t} + B|P_{t-\Delta t} \Delta t \quad (21.5.22)$$

Second guess:

$$u|Q_t = u|P_{t-\Delta t} + A|Q_t \Delta t \quad (21.5.23)$$

$$v|Q_t = v|P_{t-\Delta t} + B|Q_t \Delta t \quad (21.5.24)$$

The above steps are analogous to the predictor corrector of the Euler backward time-differencing scheme used in NWP.

Once u and v are known, the integration of z is carried out with an analogous predictor corrector; the function C is evaluated at $P|_{t-\Delta t}$ and $Q|_t$ for this purpose.

21.5.8 On the treatment of the pressure-gradient force and divergence in the mass-continuity equation

Special care needs to be exercised in the finite-difference formulation of these terms to avoid the excitation of spurious computational gravitational modes (Kanamitsu, 1975). Kanamitsu has shown that a standard centred difference formula for the pressure-gradient force results in a splitting of the solution and resulting spurious divergence. Since this problem is important for one-level and multilevel dynamical initialization, the reader is referred to the original paper.

21.5.9 Boundary conditions for single-level dynamical initialization

The domain has a cyclic continuity in the zonal direction. Along the north/south boundaries we set:

$$\begin{aligned} v &= 0, \\ u &= \text{constant (independent of } x \text{ and } t), \\ z &= \text{constant (independent of } x \text{ and } t). \end{aligned}$$

21.5.10 Single-level dynamic initialization

This dynamic initialization procedure utilizes the shallow-water equations as its basis (see equations (21.5.1), (21.5.2) and (21.5.3)). The procedures entail a forward/backward integration of the one-level primitive equation with the following definition of the pre-initialized u , v , z distributions.

u and v are obtained from the initial analysis of streamlines and isotachs. The pre-initialized z field is obtained from a solution of equation (21.5.10).

The primitive equations are integrated forward and backward utilizing small time steps of a few minutes. The purpose of this exercise is to let the motion and pressure fields adjust to an equilibrium which may depart from the so-called "balance laws." In the process of this forward and backward

integration, gravity-inertial oscillations are excited and the final state of iterative initialization is one which varies very slowly upon forward prediction. The adjusted state does not excite surface-gravity waves. We find from this exercise that the finally adjusted motion field varies very slightly ($\text{rms} \approx 2 \text{ m s}^{-1}$) from the analysed initial analysis. The large changes are in the adjustment of the pressure field in low latitudes. The end product yields a desirable wind-pressure relationship for low latitudes that is consistent with the dynamics of a one-level primitive equation model. It should, however, be recognized that the wind-pressure relationship for a multi-level primitive equation model may be somewhat different.

21.5.11 Multi-level dynamical initialization

The framework here is a multi-level primitive equation prediction model. The first propositions for dynamical initialization were presented by Nitta and Hovermale (1967), Miyakoda and Moyer (1968), Winninghoff (1968), and more recently by Kanamitsu (1975). Our interest here is in the wind-pressure laws for a multi-level primitive equation prediction model in low latitudes.

Florida State University's primitive equation model is the framework here. This model is described elsewhere in these notes. Here again a forward/backward integration of the primitive equation (one hour of forecast time forward and one hour for return) is carried out to obtain a distribution of dependent variables in a "primitive equilibrium". As in the one-level model, the balanced initial state is not accepted by the multi-level primitive equation model. The model excites gravity-inertial oscillations prior to settling down to a slowly varying state. At present the forward/backward integration is carried out with an adiabatic, frictionless version of the model where the influence of mountains is included only in the forecast part which comes after the completion of the iterative initialization. Kiang (1977) used these procedures to illustrate the wind-pressure laws over Africa. The major finding is that the wind-pressure adjustment in low latitudes is quite different from that given by the so-called "balance laws". The validity of the "non-linear balance laws", especially in the equatorial latitudes, is not supported by the dynamical initialization technique.

Experience with a multi-level model shows that the tropical wind-pressure laws depend crucially on the physical processes that are invoked in the model. Convective heating in a cloud-cluster, for instance, gives rise to large horizontal divergence D and on the large scale the departure from the balance laws will be significant. In this context, it is important to keep in mind that the following complete form of the divergence equation is satisfied by the primitive equations:

$$\nabla^2 gz = \nabla \cdot f \nabla \psi + 2J(u, v) + \frac{\partial w}{\partial x} \frac{\partial u}{\partial p} - \frac{\partial w}{\partial y} \frac{\partial v}{\partial p} + D^2 + \frac{\partial D}{\partial t} + \mathbf{V}_H \cdot \nabla D + w \frac{\partial D}{\partial p} \quad (21.5.25)$$

The last six terms are not present in the so-called balance laws. Any physical mechanism that produces large divergence or vertical motion produces a large departure from the balance laws.

21.5.12 One-level primitive equation model with bottom topography

The basic equations of this system are:

$$\frac{\partial u}{\partial t} = -u \frac{\partial u}{\partial x} - v \frac{\partial u}{\partial y} + fv - g \frac{\partial}{\partial x} (z + h) \quad (21.5.26)$$

$$\frac{\partial v}{\partial t} = -u \frac{\partial v}{\partial x} - v \frac{\partial v}{\partial y} - fu - g \frac{\partial}{\partial y} (z + h) \quad (21.5.27)$$

$$\frac{\partial z}{\partial t} = -u \frac{\partial z}{\partial x} - v \frac{\partial z}{\partial y} - z \left(\frac{\partial u}{\partial x} + \frac{\partial v}{\partial y} \right) \quad (21.5.28)$$

where h is a smoothed mountain height. This system has the following three domain invariants:

- (i) potential vorticity, $[\zeta_p]$
- (ii) mean square potential vorticity, $[\zeta_p^2]$
- (iii) a total energy parameter, $E_T = [z(K + 1/2 gz + gh)]$

Parcel invariant (as for the case of no topography) is the potential vorticity ζ_p . This model is a trivial extension of the no-mountain case. No problems arise if straightforward centred difference formulae are used to evaluate the time-independent fields of $\partial h/\partial x$ and $\partial h/\partial y$. A smoothed topography such as that given by Gates and Nelson (1975) is a useful representation of mountains for numerical weather prediction. The finite-difference forms are analogous to the no-mountain case. Figure 21.2 illustrates an example of a forecast made with this model. The mountains used are shown in Figure 21.3.

21.6 Multi-level primitive equation prediction model

This is without doubt the most desirable model for low latitudes. Apart from making forecasts, it is also a very powerful research tool. It will not be possible to go into the details of such a model here. These models include features such as:

- (i) Smoothed mountains;
- (ii) Air/sea interaction;
- (iii) Land/air interaction:
 - (a) heat balance of the Earth's surface,
 - (b) momentum fluxes at the Earth's surface;
- (iv) Dry convective adjustment;
- (v) Moist, shallow and deep convection;
- (vi) Large-scale stable rainfall;
- (vii) Radiative processes in the atmosphere:
 - (a) short-wave radiation, the diurnal change,
 - (b) long-wave radiation,
 - (c) effects of clouds.

Some of the above-mentioned effects are discussed earlier in these notes. However, the student desiring to learn more about applications should spend some time with a group active in this field.

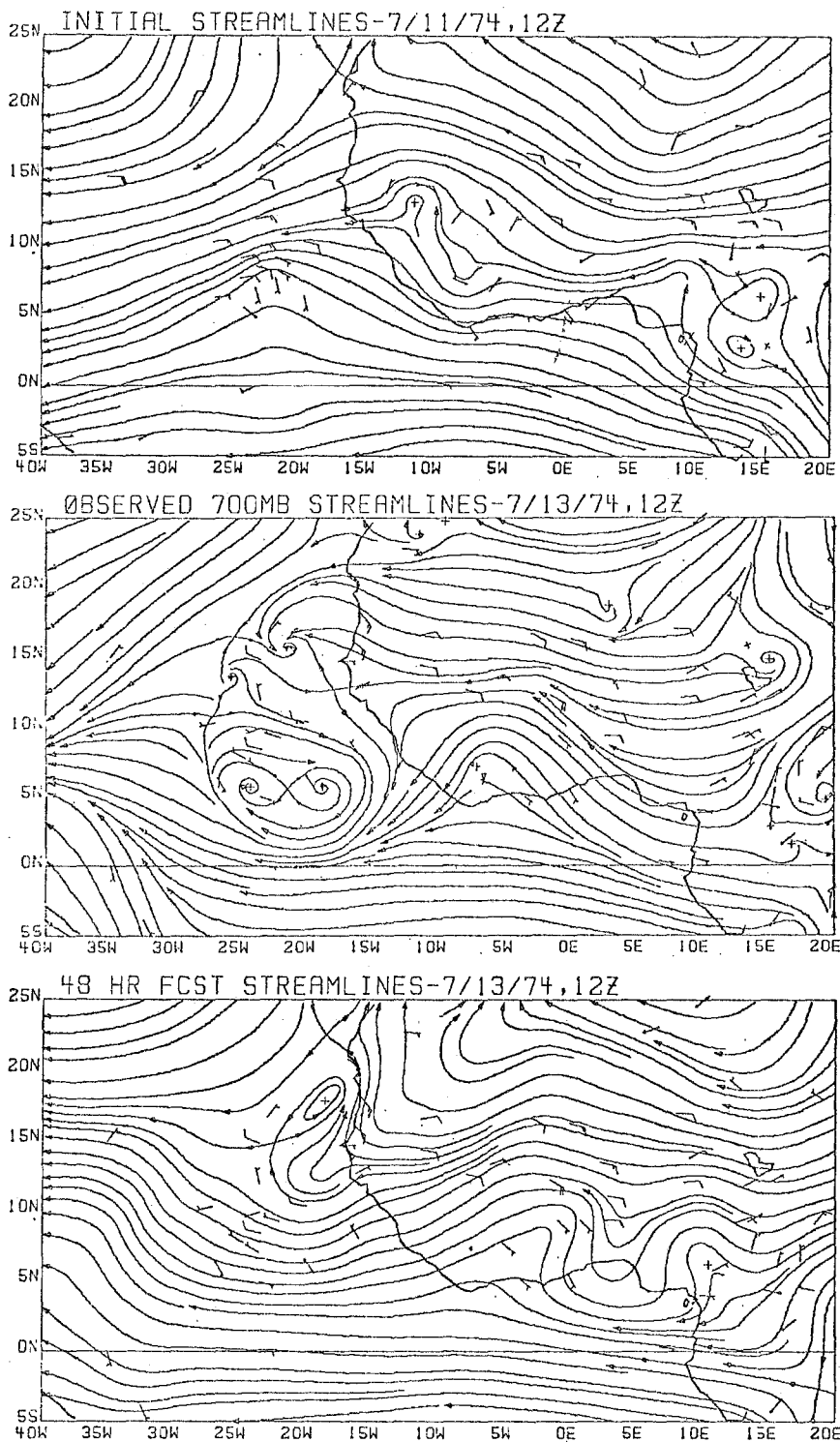


Figure 21.2 - (Top) 700 mb observed wind, time 0; (middle) same at time 48 hours; (bottom) primitive equation forecast at time 48 hours

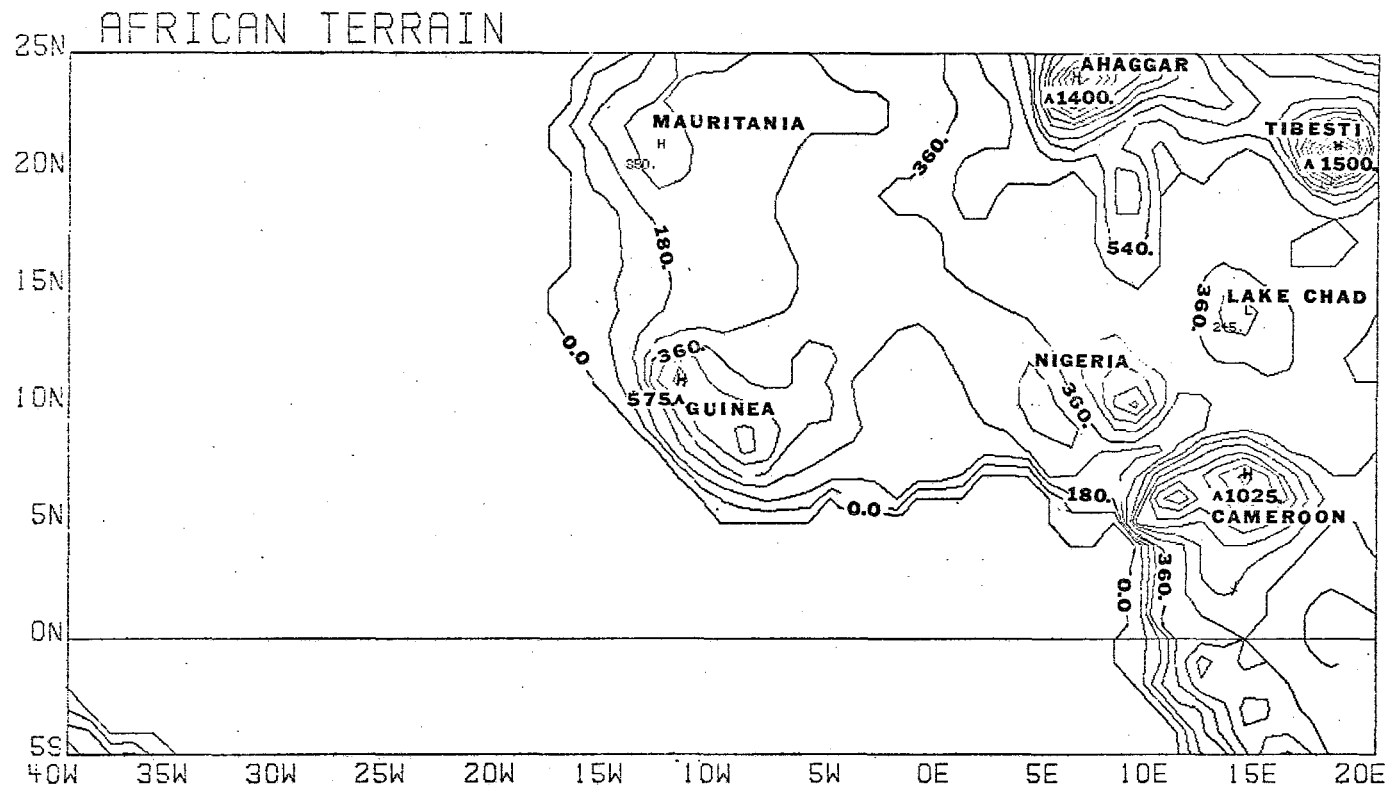


Figure 21.3 — Terrain over West Africa (metres)

LIST OF APPENDICES

The mathematical appendices presented here are no substitute for an appropriate text on dynamical or physical meteorology. The following is a list of appendices cited in the various chapters of this text.

- (i) Moist and dry static-energy equations (Chapter 6);
- (ii) Conditional instability of the first kind (Chapter 6);
- (iii) Arakawa's identity relating saturation specific humidity to the moist static energy (Chapter 6);
- (iv) Necessary conditions for the existence of barotropic instability (Chapter 9);
- (v) Finite-difference methods for studying barotropic instability in the tropics (Chapters 9 & 17);
- (vi) Combined barotropic/baroclinic instability (Chapters 11 & 14);
- (vii) Kinematic vertical velocity for a triangular array (Chapter 12);
- (viii) The Ekman vertical velocity (Chapter 13);
- (ix) Explanation of terms in the energy equations (Chapter 17).

In addition to the topics cited here, this text does assume some knowledge of applied mathematics and elementary statistics. This is no more than that contained in senior level undergraduate programmes in these subjects. Topics such as differential equations (linear), complex variables, time-series analysis, matrix algebra, numerical solution of hyperbolic and elliptic problems are all being increasingly used in the solution of tropical problems. Notes on the topics listed above are presented in sequence.

*
* *

(i) Moist and dry static-energy equations

Here we are interested in presenting a short derivation of the equations governing the time rate of change of $(gz + c_p T)$ the dry static energy and $(gz + c_p T + Lq)$ the moist static energy.

Equations of motion:

$$\frac{\partial u}{\partial t} + u \frac{\partial u}{\partial x} + v \frac{\partial u}{\partial y} + \omega \frac{\partial u}{\partial p} = fv - g \frac{\partial z}{\partial x} + F_x \quad (1)$$

$$\frac{\partial v}{\partial t} + u \frac{\partial v}{\partial x} + v \frac{\partial v}{\partial y} + \omega \frac{\partial v}{\partial p} = -fu - g \frac{\partial z}{\partial y} + F_y \quad (2)$$

Upon multiplication of (1) by u and (2) by v and adding (letting $k = 1/2(u^2 + v^2)$ denote the kinetic energy per unit mass of air) one obtains:

$$\frac{dk}{dt} = -g \mathbb{W} \cdot \nabla z + \mathbb{W} \cdot \mathbb{F} \quad (3)$$

$$= -g \left[\frac{dz}{dt} - \frac{\partial z}{\partial t} - \omega \frac{\partial z}{\partial p} \right] + \mathbb{W} \cdot \mathbb{F} \quad (4)$$

Hydrostatic law:

$$\frac{RT}{p} = -g \frac{\partial z}{\partial p} \quad (5)$$

Upon substitution of (5) in (4) one obtains:

$$\frac{d}{dt} (gz + K) = g \frac{\partial z}{\partial t} - \frac{RT}{p} \omega + \mathbb{W} \cdot \mathbb{F} \quad (6)$$

First law of thermodynamics:

$$c_p \frac{dT}{dt} = \frac{RT}{p} \omega + \sum_i H_i \quad (7)$$

where $\sum_i H_i$ denotes the sum of different heat sources and sinks. Upon substitution of (7) into (6) one obtains:

$$\frac{d}{dt} (gz + c_p T + K) = g \frac{\partial z}{\partial t} + \sum_i H_i + \mathbb{W} \cdot \mathbb{F} \quad (8)$$

Note that $K \ll c_p T$, since $c_p \approx 1000 \text{ metres}^2 \text{ s}^{-2} \text{ deg}^{-1}$; $T \approx 300^\circ$; $c_p T = 3 \times 10^5 \text{ metres}^2 \text{ s}^{-2}$; $K = (u^2 + v^2)/2 \approx 5 \times 10^3 \text{ metres}^2 \text{ s}^{-2}$; then we can neglect K and its dissipation, i.e., $\mathbb{W} \cdot \mathbb{F}$ in equation (8). Furthermore, the pressure tendency term $g \frac{\partial z}{\partial t}$ is also usually neglected on the grounds that it is small compared with the other terms. Thus one obtains:

$$\frac{d}{dt} (gz + c_p T) = \sum_i H_i \quad (9)$$

In the absence of heat sources and sinks:

$$\frac{d}{dt} (gz + c_p T) = 0 \quad (10)$$

which is compatible with the conservation of potential temperature, i.e.:

$$c_p \frac{T}{\theta} \frac{d\theta}{dt} = 0 \quad (11)$$

The student should also derive the familiar dry static-stability relation:

$$- c_p \frac{T}{\theta} \frac{\partial \theta}{\partial p} = - \frac{\partial}{\partial p} (gz + c_p T) \quad (12)$$

Equation (9) is an important energy relation.

Definition of the heating function:

$$\text{We define } H_i = H_{\text{SEN}} + H_{\text{EVC}} + H_{\text{RAD}} + H_{\text{CON}} \quad (13)$$

where

H_{SEN} is the sensible heat flux from the ocean,

H_{EVC} = heating (negative of cooling) due to evaporation of cloud matter,

H_{CON} = condensation heating,

H_{RAD} = rate of radiative heating.

All the above forms of heating refer to unit mass of air. Note that the evaporation from the ocean does not enter equation (8) since the evaporation only cools the ocean and can only affect the temperature of the air when it condenses again.

We shall write:

$$H_{\text{CON}} = - L \frac{dq}{dt} \quad (14)$$

provided that air is saturated (i.e., $q \approx q_s$) and rising.

The conservation of moisture:

$$\frac{dq}{dt} = E_o + E_c - P \quad (15)$$

where

E_o is evaporation from the ocean,

E_c is evaporation of cloud matter,

i.e.,

$$E_c = - H_{\text{EVC}}/L \quad (16)$$

and P is precipitation per unit mass of air.

In energy units we may write (15) in the form:

$$L \frac{dq}{dt} = LE_o - H_{CON} + H_{EVC} \quad (17)$$

Adding equations (17) and (9), we obtain:

$$\frac{d}{dt} (gz + c_p T + Lq) = LE_o + H_{SEN} + H_{RAD} \quad (18)$$

In the absence of heat sources and sinks $gz + c_p T + Lq$ is conserved following a parcel. It can be modified by surface moisture flux LE_o , by flux of sensible heat of the lower boundary H_{SEN} and by radiative processes H_{RAD} .

(ii) Conditional instability of the first kind

In a conditionally unstable atmosphere the prevailing lapse rate of the atmosphere lies between the dry and the moist adiabatic lapse rates. If a parcel of air is lifted from the Earth's surface to the lifting condensation level and then lifted further along the moist adiabat, the parcel will become buoyant and find itself warmer than the environment. Vertical motions and clouds result in these situations. Kuo (1961) and Lilly (1960) have examined the question of what horizontal scales would be most unstable under the above conditions. We present here a very brief outline of this linear analysis.

The basic framework is the so-called Boussinesq system of equations (see Phillips, 1967). These are linearized with respect to a basic state hydrostatic atmosphere whose thermal stratification is stable in the dry sense ($+ d\theta/dz > 0$) and unstable in the moist sense ($d\theta_e/dz < 0$) in the lower troposphere.

The basic state is defined by the following parameters:

(i) Density stratification $\sigma = - \frac{1}{\rho_o} \frac{d\rho_o}{dz}$

(ii) Static stability $\frac{ds}{dz} = \frac{1}{\theta_o} \frac{d\theta_o}{dz}$

(iii) Vertical stratification of specific humidity $\eta = \frac{1}{q_o} \frac{dq_o}{dz}$

Here θ_o, ρ_o, q_o , respectively, are the basic state potential temperature, density and the specific humidity. This base state is conditionally unstable. The moist adiabatic heating in a conditionally unstable atmosphere is usually expressed by:

$$Q = - L_v \frac{dq}{dt}$$

where ($q = q_s$) (i.e., saturated).

In linear problems one frequently writes Q as:

$$Q = - L_v \frac{dq_s}{dt} W$$

where the vertical velocity W is upward, L_v is the latent heat of condensation and q_s is the base state stratification of saturation specific humidity.

The following five equations describe the linear equations for the stability problem:

Horizontal equations:

$$L(u) - fv = - \frac{\partial \pi}{\partial x} \quad (1)$$

$$L(v) + fu = - \frac{\partial \pi}{\partial y} \quad (2)$$

Vertical equation:

$$L(W) = \frac{\partial \pi}{\partial z} + \frac{\partial s'}{\partial z} \quad (3)$$

$$\nabla \cdot \mathbf{V} + \sigma W = 0 \quad (4)$$

First continuity law of thermodynamics:

$$L(S') + \frac{ds}{dz} W = \frac{1}{c_p T_o} Q = - \frac{L}{c_p T_o} \frac{dq_s}{dz} \quad (5)$$

Here

$$L \equiv \frac{\partial}{\partial t} + u_o \frac{\partial}{\partial x} - \nu \nabla^2; \quad s' = c_p \ln \theta'; \quad \pi = (p/p_o)^{R/c_p}$$

From here on, one follows the usual procedure of eliminating variables to obtain a single equation for a single variable. This is usually that for the vertical velocity W , i.e.:

$$L (f^2 + L^2) \frac{\partial}{\partial z} \left(\frac{1}{\rho_o} \frac{\partial \rho_o W}{\partial z} \right) + L \left(g \frac{ds}{dz} + \frac{gL_v}{c_p T_o} \frac{dq_s}{dz} + L^2 \right) \nabla_2^2 W = 0 \quad (6)$$

Kuo next introduced a new variable $\psi = \rho_o W e^{\frac{f\sigma z}{2}}$ and upon substitution in (6) obtained the relation:

$$L (f^2 + L^2) \left(\frac{\partial^2 \psi}{\partial z^2} - \frac{\sigma^2}{4} \psi \right) + L (-gS + L^2) \nabla_2^2 \psi = 0 \quad (7)$$

where

$$S = - \frac{ds}{dz} - \frac{L_v}{c_p T_o} \frac{dq_s}{dz}$$

Next he assumed solutions of the form:

$$\psi = A e^{qt} \sin \frac{k\pi z}{h} F(x,y) \quad (8)$$

where F is a trigonometric function of x and y such that $\nabla_2^2 F = \frac{\alpha^2 \pi^2}{h^2} F$, where q is the frequency, α is the horizontal wave number, and k is the vertical wave number. Substitution of (8) into (7) leads to the relation:

$$q = \left(\frac{g\alpha^2 S - f^2 k^2}{k^2 + \alpha^2} \right)^{1/2} - \frac{\pi}{h} (\alpha^2 \nu - k^2 \nu_z)$$

where ν is the viscosity coefficient. The condition for the existence of an amplifying wave turns out to be:

$$\frac{g\alpha^2 S - f^2}{1 + \alpha^2} > 1$$

Here the maximum value of q , i.e., $k = 1$ (the largest vertical wave in the troposphere) is considered.

This condition is equivalent to requiring that $S > 0$ for growth where $S = 1/T_0 (\gamma - \gamma_m)$ is a measure of the moist static instability (γ and γ_m are the prevailing and the moist adiabatic lapse rates). Kuo next plots q versus α (i.e., growth rate versus scale) for different values of the moist static instability parameter S . The graph clearly shows that for the tropical atmospheric range of values of S , the maximum growth rate (when friction is included) is on horizontal scales of the order of a few km. This is what we understand as the conditional instability of the first kind.

(iii) Arakawa's identity used in Chapter 6

This relates the saturation specific humidity to the moist static energy.

$$\begin{aligned} \text{Let } \gamma &= L/c_p \left(\frac{\partial q^*}{\partial T} \right)_p \\ &= \frac{L}{c_p} \frac{\Delta q^*}{\Delta T}, \text{ expressed in finite difference form} \\ &= \frac{L}{c_p} \frac{(q_{ci} - \tilde{q})}{(T_{ci} - \tilde{T})} \text{ (see Chapter 6 for symbols)} \\ &= L \frac{q_{ci} - \tilde{q}}{s_{ci} - \tilde{s}} \text{ (since } s = gz + c_p T \text{ and } z_{ci} \approx \tilde{z}) \\ 1 + \gamma &= \frac{(Lq_{ci} + s_{ci}) - (L\tilde{q} + \tilde{s})}{(s_{ci} - \tilde{s})} \\ &= \frac{h_{ci} - \tilde{h}^*}{s_{ci} - \tilde{s}}; \quad h = s + Lq \end{aligned}$$

Hence to obtain the relations:

$$s_{ci} - \tilde{s} = \frac{1}{1 + \gamma} (h_{ci} - \tilde{h}^*)$$

and

$$L (q_{ci} - \tilde{q}) = \frac{\gamma}{1 + \gamma} (h_{ci} - \tilde{h}^*)$$

These are very frequently used relations in the formulation of convection. Here * refers to a saturation value.

(iv) Necessary conditions for the existence of barotropic instability

We start from the barotropic vorticity equation:

$$\frac{\partial}{\partial t} \nabla^2 \psi = - J(\psi, \nabla^2 \psi) - \beta \frac{\partial \psi}{\partial x} \quad (1)$$

and express it in linearized form:

$$\frac{\partial}{\partial t} \nabla^2 \psi = -U \frac{\partial}{\partial x} \nabla^2 \psi - \left(\beta - \frac{\partial^2 U}{\partial y^2} \right) \frac{\partial \psi}{\partial x} \quad (2)$$

where U , the basic zonal flow, is a function of y only, and the perturbation stream function ψ is a function of x and t .

We write:

$$\psi = \Psi(y) e^{i\mu(x-ct)} \quad (3)$$

where c is a complex phase velocity. Upon substitution of (3) in (2) we obtain:

$$(U - c) \left[\frac{d^2 \Psi}{dy^2} - \mu^2 \Psi \right] - \left(\frac{d^2 U}{dy^2} - \beta \right) \Psi = 0 \quad (4)$$

We assume a current of finite width centred at $y = 0$ with rigid boundaries at $y = \pm d$, since normal velocities should vanish at these boundaries:

$$v(\pm d) = \frac{\partial \psi}{\partial x}(\pm d) = i\mu \Psi(\pm d) e^{i\mu(x-ct)} = 0 \quad (5)$$

which is the same as:

$$\Psi(d) = \Psi(-d) = 0 \quad (6)$$

Both the phase speed and the amplitude function Ψ considered here are complex.

We may write:

$$c = c_r + i c_i \quad (7)$$

Let Ψ^* be the complex conjugate of Ψ ; multiplying equation (4) we obtain:

$$(U - c) \left[\Psi^* \frac{d^2 \Psi}{dy^2} - \mu^2 \Psi \Psi^* \right] - \left[\frac{d^2 U}{dy^2} - \beta \right] \Psi \Psi^* = 0 \quad (8)$$

Note that:

$$\Psi^* \frac{d^2 \Psi}{dy^2} = \frac{d}{dy} \left(\Psi^* \frac{d\Psi}{dy} \right) - \frac{d\Psi^*}{dy} \frac{d\Psi}{dy} \quad (9)$$

$$\Psi \Psi^* = |\Psi|^2 \quad (10)$$

and

$$\frac{d\Psi}{dy} \frac{d\Psi^*}{dy} = \left| \frac{d\Psi}{dy} \right|^2 \quad (11)$$

Dividing (8) by $(U - c)$ and substituting from (9), (10), and (11) we obtain:

$$\frac{d}{dy} \left(\Psi^* \frac{d\Psi}{dy} \right) - \left| \frac{d\Psi}{dy} \right|^2 - \mu^2 |\Psi|^2 - \frac{\left(\frac{d^2 U}{dy^2} - \beta \right)}{(U - c)} |\Psi|^2 = 0 \quad (12)$$

Integrating (12) from $-d$ to d :

$$\int_{-d}^d \left[\frac{d}{dy} \left(\psi^* \frac{d\psi}{dy} \right) - \mu^2 |\psi|^2 - \left| \frac{d\psi}{dy} \right|^2 \right] dy$$

$$= \int_{-d}^d \left\{ \left[\frac{d^2 U}{dy^2} - \beta \right] / (U - c) \right\} |\psi|^2 dy = 0 \quad (13)$$

Noting that ψ vanishes at $y = \pm d$, its real and imaginary parts should each vanish at $y = \pm d$, hence ψ^* also vanishes at $y = \pm d$, the first term of (13) vanishes, and we thus have:

$$\int_{-d}^d \left\{ \mu^2 |\psi|^2 + \left| \frac{d\psi}{dy} \right|^2 \right\} dy$$

$$= - \int_{-d}^d \left\{ \left[\frac{d^2 U}{dy^2} - \beta \right] / |U - c|^2 \right\} (U - c)^* |\psi|^2 dy \quad (14)$$

where we have multiplied the right-hand side of (13) by the complex conjugate of $(U - c)$.

Note that $(U - c)^* = U - c_r + ic_i$. We can write the real and imaginary parts of equation (14); the imaginary part is:

$$0 = c_i \int_{-d}^d \frac{\left(\frac{d^2 U}{dy^2} - \beta \right) |\psi|^2}{|U - c|^2} dy \quad (15)$$

for amplifying waves $c_i \neq 0$. Thus for the integral to vanish $\left(\frac{d^2 U}{dy^2} - \beta \right)$ must change sign at least once in the interval $y = \pm d$. Thus we write the necessary conditions for barotropic instability as:

$$\left(\frac{d^2 U}{dy^2} - \beta \right)_{y=y_k} = 0 \quad -d < y_k < d \quad (16)$$

which is equivalent to stating that:

$$\frac{d\zeta_a}{dy} = \frac{d}{dy} \left(- \frac{dU}{dy} + f \right) = 0 \quad y = y_k \quad (17)$$

Hence, absolute vorticity ζ_a should be maximum or minimum at some latitude in the basic current.

(v) Finite-difference methods for studying barotropic instability in the tropics

Basic equations:

If the motion is purely horizontal and non-divergent, the vorticity equation can be written as:

$$\frac{d\zeta_a}{dt} = \left(\frac{\partial}{\partial t} + \mathbb{W}_H \cdot \nabla \right) \zeta_a = 0 \quad (1)$$

We may define a stream function for a perturbed motion as:

$$u = - \frac{\partial \psi}{\partial y}, \quad v = \frac{\partial \psi}{\partial x} \quad (2)$$

where ψ is a stream function. Using equation (2), we can write equation (1) in the usual form:

$$\frac{\partial}{\partial t} \nabla^2 \psi + J(\psi, \nabla^2 \psi) + \beta \frac{\partial \psi}{\partial x} = 0 \quad (3)$$

By application of the method of perturbations, (3) can be linearized and written in the form:

$$\left(\frac{\partial}{\partial t} + U \frac{\partial}{\partial x} \right) \nabla^2 \psi + (\beta - U'') \frac{\partial \psi}{\partial x} = 0 \quad (4)$$

where

- (i) a prime denotes a differentiation with respect to y ;
- (ii) $\beta = \frac{\partial f}{\partial y}$ and f is the Coriolis parameter. β is assumed constant for this analysis;
- (iii) U is the zonal current and $U = U(y)$.

We can write down the stream function in the form:

$$\psi(x, y, t) = \phi(y) e^{i\alpha(x-ct)} \quad (5)$$

i.e., assume that this perturbation has a harmonic form.

Substituting for $\psi(x, y, t)$ in equation (4) yields a linear, second-order differential equation in the form:

$$(U - c) (\phi'' - \alpha^2 \phi) + (\beta - U'') \phi = 0 \quad (6)$$

where

α is the wave number

c is the phase speed which may be complex, i.e., $c = c_r + i c_i$

and ϕ denotes the unknown amplitude of the perturbation.

Method of finite differences:

Consider a domain as shown in which the real amplitude functions ϕ vanish at the north and south boundaries, i.e.:

$$\phi(0) = \phi(M) = 0 \quad (7)$$

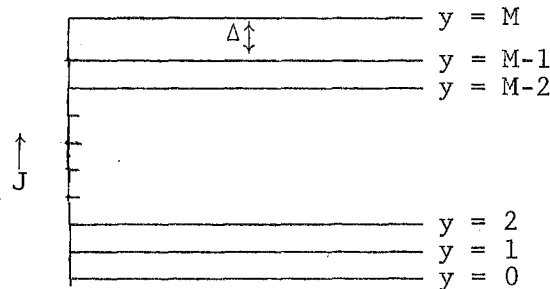


Figure 1 - The domain

The eigenvalue problem, namely the determination of values of c , the phase speed, for which solutions of the systems (5) and (6) exist, is solved here by the use of finite differences.

For a point y_J in the domain, the derivative ϕ'' is approximated by the finite-difference relation:

$$(\phi_{J+1} + \phi_{J-1} - 2 \phi_J) / \Delta^2 \quad (8)$$

Equation (6) can now be expressed in the form:

$$(U_J - c) (\phi_{J+1} + \phi_{J-1} - 2 \phi_J) / \Delta^2 - \alpha^2 \phi_J + [\beta - (U_{J+1} + U_{J-1} - 2 U_J) / \Delta^2] \phi_J = 0 \quad (9)$$

Both the complex phase speed c and the amplitude function ϕ are unknown at this stage. In order that we have an amplifying or non-amplifying wave, we need to know whether c is real or imaginary. This can be done by first collecting all terms involving ϕ in (9), at all points in the interior of the domain between $y = 1$ and $y = (m-1)$, and then writing down a matrix equation for ϕ in the form:

$$(B - cD) (\phi) = 0 \quad (10)$$

where B and D are known functions of U , α , β and Δ . We seek non-zero solutions for the amplitude ϕ . This means $|B - cD| = 0$. The characteristic values of c may now be obtained by imposing the condition for non-trivial solutions for the ϕ . This determines the $M-1$ complex eigenvalues for the phase speed c . The growth rate αc_i for each of the modes determines the scale that has the maximum growth rate. Thus one can construct a stability diagram with a plot of horizontal shear U' as a function of scale α . This approach is due to Haltiner (1963). One can also construct the eigenstructure of the most unstable wave by substituting for c_i in the wave equation.

(vi) Combined barotropic/baroclinic instability

We start from the potential vorticity equation:

$$\left(\frac{\partial}{\partial t} + \mathbb{W}_H \cdot \nabla_p \right) P = 0 \quad (1)$$

where \mathbb{W}_H is the horizontal wind, and P is the potential vorticity defined by:

$$P = \nabla^2 \psi + f + \frac{\partial}{\partial p} \left[\frac{f_0}{\sigma} \frac{\partial \psi}{\partial p} \right] \quad (2)$$

where ψ is the stream function and the dry static stability σ is defined by:

$$\sigma = \frac{\partial \phi}{\partial p} \frac{\partial}{\partial p} \ln \theta ; \phi \text{ is the geopotential and } \theta \text{ the potential}$$

temperature. We shall next carry out a perturbation analysis:

$$\text{Let } P = \bar{P}(y, p) + P'(x, y, p, t)$$

hence

$$\frac{DP}{Dt} = \left\{ \frac{\partial}{\partial t} + (\bar{u} + u') \frac{\partial}{\partial x} + v' \frac{\partial}{\partial y} \right\} P = 0$$

The linearization of the above yields:

$$\left(\frac{\partial}{\partial t} + \bar{u} \frac{\partial}{\partial x} \right) P' + v' \frac{\partial}{\partial y} \bar{P} = 0 \quad (3)$$

where the basic zonal current \bar{u} is a function of both y and p . We define the basic state potential vorticity by the relation:

$$\bar{P} = \nabla^2 \bar{\psi} + f + \frac{\partial}{\partial p} \left[\frac{f_0^2}{\sigma} \frac{\partial \bar{\psi}}{\partial p} \right] \quad (4)$$

The perturbation potential vorticity is defined by:

$$P' = \nabla^2 \psi' + \frac{\partial}{\partial p} \left[\frac{f_0^2}{\sigma} \frac{\partial \psi'}{\partial p} \right] \quad (5)$$

where $v' = \frac{\partial \psi'}{\partial x}$ and $-\bar{u} = \frac{\partial}{\partial y} \bar{\psi}$.

We shall next write:

$$\psi' = \psi(y, p) e^{i(kx-nt)}$$

and obtain:

$$P' = e^{i(kx-nt)} - \left\{ (ik)^2 \psi(y, p) + \frac{\partial^2}{\partial y^2} \psi(y, p) \right\} + e^{i(kx-nt)} \frac{\partial}{\partial p} \left[\frac{f_0^2}{\sigma} \frac{\partial \psi(y, p)}{\partial p} \right] \quad (6)$$

Substituting for P' in equation (3) gives:

$$\begin{aligned} & (-in) \left\{ (ik)^2 \psi + \frac{\partial^2}{\partial y^2} \psi + \frac{\partial}{\partial p} \left[\frac{f_0^2}{\sigma} \frac{\partial \psi}{\partial p} \right] \right\} \\ & + (ik) \bar{u} \left\{ (ik)^2 \psi + \frac{\partial^2}{\partial y^2} \psi + \frac{\partial}{\partial p} \left[\frac{f_0^2}{\sigma} \frac{\partial \psi}{\partial p} \right] \right\} \\ & + (ik) \psi \frac{\partial}{\partial y} \bar{P} = 0 \end{aligned} \quad (7)$$

Division by ik results in:

$$(\bar{u} - c) \left\{ -k^2 \psi + \frac{\partial^2}{\partial y^2} \psi + \frac{\partial}{\partial p} \left[\frac{f_0^2}{\sigma} \frac{\partial \psi}{\partial p} \right] \right\} + \psi \frac{\partial \bar{P}}{\partial y} = 0 \quad (8)$$

where $c = n/k$.

Upon multiplying equation (8) by ψ^* , the complex conjugate of ψ , we obtain:

$$- (\bar{u} - c) k^2 |\psi|^2 + \psi^* \left\{ \frac{\partial^2}{\partial y^2} \psi + \frac{\partial}{\partial p} \frac{f_0^2}{\sigma} \frac{\partial \psi}{\partial p} \right\} (\bar{u} - c) + |\psi|^2 \frac{\partial \bar{P}}{\partial y} = 0 \quad (9)$$

Note that:

$$\psi^* \frac{\partial^2}{\partial y^2} \psi = \frac{\partial}{\partial y} \left(\psi^* \frac{\partial \psi}{\partial y} \right) - \frac{\partial \psi^*}{\partial y} \frac{\partial \psi}{\partial y} \quad (10)$$

Also note that:

$$\psi^* \frac{\partial}{\partial p} \frac{f_o^2}{\sigma} \frac{\partial}{\partial p} \psi = \frac{\partial}{\partial p} \psi^* \frac{f_o^2}{\sigma} \frac{\partial \psi}{\partial p} - \frac{f_o^2}{\sigma} \left| \frac{\partial \psi}{\partial p} \right|^2 \quad (11)$$

Upon substitution of equations (10) and (11) in equation (9), we obtain:

$$\begin{aligned} & - (\bar{u} - c) k^2 |\psi|^2 + \left\{ \frac{\partial}{\partial y} \psi^* \frac{\partial}{\partial y} \psi - \left| \frac{\partial \psi}{\partial y} \right|^2 \right\} (\bar{u} - c) \\ & + (\bar{u} - c) \left\{ \frac{\partial}{\partial p} \psi^* \frac{f_o^2}{\sigma} \frac{\partial \psi}{\partial p} - \frac{f_o^2}{\sigma} \left| \frac{\partial \psi}{\partial p} \right|^2 \right\} + |\psi|^2 \frac{\partial \bar{p}}{\partial y} = 0 \end{aligned} \quad (12)$$

Integration of the above equation over the $y - p$ plane with the assumption of rigid boundaries at $y = \pm d$, i.e., $\psi(\pm d) = \psi^*(\pm d) = 0$ yields:

$$\begin{aligned} & \int_{-d}^d \int_{p_o}^o - (\bar{u} - c) \left\{ k^2 |\psi|^2 + \left| \frac{\partial \psi}{\partial y} \right|^2 + \frac{f_o^2}{\sigma} \left| \frac{\partial \psi}{\partial p} \right|^2 \right\} dy dp \\ & + (\bar{u} - c) \int_{-d}^d \int_{p_o}^o \frac{\partial}{\partial p} \psi^* \frac{f_o^2}{\sigma} \frac{\partial \psi}{\partial p} dy dp + \int_{-d}^d \int_{p_o}^o |\psi|^2 \frac{\partial \bar{p}}{\partial y} dy dp = 0 \end{aligned} \quad (13)$$

The thermodynamic energy equation may be written as:

$$\frac{1}{f_o} \frac{\partial}{\partial t} \frac{\partial \psi}{\partial p} + \frac{1}{f_o} \nabla_g \cdot \nabla \frac{\partial \psi}{\partial p} = - \sigma_o \omega \quad (14)$$

Upon substitution of $\psi = \bar{\psi} + \psi'$, and linearization we obtain:

$$\frac{\partial}{\partial t} \frac{\partial}{\partial p} \psi' + \bar{u} \frac{\partial}{\partial x} \frac{\partial}{\partial p} \psi' + \bar{v} \frac{\partial}{\partial y} \frac{\partial}{\partial p} \bar{\psi} = - f_o \sigma_o \omega \quad (15)$$

We next assume, as above, a solution of the form:

$$\psi' = \psi(y, p) e^{i(kx - nt)} \quad (16)$$

which yields:

$$e^{i(kx - nt)} \left[(-in) \frac{\partial \psi}{\partial p} + \bar{u}(ik) \frac{\partial \psi}{\partial p} - (ik)\psi \frac{\partial \bar{u}}{\partial p} \right] = - f_o \sigma_o \omega \quad (17)$$

If we assume $\omega = 0$ at $p = p_o$, and $p = 0$, then at the top and the bottom of the atmosphere we can set $\psi \frac{\partial}{\partial p} \bar{u} = (\bar{u} - c) \frac{\partial \psi}{\partial p}$, since $n = kc$. It is necessary to assume that $\frac{\partial \bar{u}}{\partial p} = 0$ at $p = p_o$, $p = 0$, in order to proceed to obtain a necessary condition for instability. Such an assumption is consistent with the existence of a jet-like vertical profile of \bar{u} .

Therefore, with the assumption:

$$\int_{-d}^d \int_{p_o}^o \frac{\partial}{\partial p} \psi^* \frac{f_o^2}{\sigma} \frac{\partial}{\partial p} \psi dy dp = 0 \quad (18)$$

Equation (13) can now be written as:

$$\iint \left\{ k^2 |\psi|^2 + \left| \frac{\partial \psi}{\partial y} \right|^2 + \frac{f_0^2}{\sigma} \left| \frac{\partial \psi}{\partial p} \right|^2 \right\} = \iint \frac{|\psi|^2 \frac{\partial \bar{P}}{\partial y}}{(u - c)^2} dy dp \quad (19)$$

We may furthermore write $c = c_r + i c_i$, the sum of real and imaginary parts of the phase velocity, and hence obtain:

$$\begin{aligned} \iint \left(k^2 |\psi|^2 + \left| \frac{\partial \psi}{\partial y} \right|^2 - \frac{f_0^2}{\sigma} \left| \frac{\partial \psi}{\partial p} \right|^2 \right) dy dp = \\ \iint \frac{|\psi|^2 \frac{\partial \bar{P}}{\partial y}}{(u - c)^2} c_r dy dp - i c_i \iint \frac{|\psi|^2 \frac{\partial \bar{P}}{\partial y}}{(u - c)^2} dy dp \end{aligned} \quad (20)$$

Since the left-hand side and the first term on the right-hand side of equation (20) are real,

$$c_i \int_{-d}^d \int_{p_0}^0 \frac{|\psi|^2 \frac{\partial \bar{P}}{\partial y}}{(u - c)^2} dy dp = 0 \quad (21)$$

For amplifying waves we require that $c_i \neq 0$, i.e.:

$$\iint |\psi|^2 \frac{\partial \bar{P}}{\partial y} (u - c)^2 dy dp = 0 \quad (22)$$

which leads to $\left(\frac{\partial \bar{P}}{\partial y} \right)_{y_k} = 0$ for y_k in the range $-d < y_k < d$

Thus the necessary condition for combined barotropic/baroclinic instability is that:

$$\frac{\partial \bar{P}}{\partial y} = \left(\beta - \frac{\partial^2 \bar{u}}{\partial y^2} - \frac{\partial}{\partial p} \frac{f_0^2}{\sigma} \frac{\partial \bar{u}}{\partial p} \right) = 0 \text{ somewhere in the domain,}$$

$$\text{or } \beta - \frac{\partial^2 \bar{u}}{\partial y^2} - \frac{f_0^2}{\sigma} - \frac{\partial^2 \bar{u}}{\partial p^2} - f_0^2 \frac{\partial \bar{u}}{\partial p} \frac{\partial}{\partial p} (\sigma^{-1}) = 0$$

$$\text{or } \beta - \frac{\partial^2 \bar{u}}{\partial y^2} - \frac{f_0^2}{N_s^2} (\rho^2 g^2) \frac{\partial^2 \bar{u}}{\partial p^2} - 2 \frac{\rho g^2}{N_s^2} f_0^2 \frac{\partial \bar{u}}{\partial p} \frac{\partial \rho}{\partial p} = 0$$

where $N_s^2 = g/\theta \frac{\partial \theta}{\partial z}$ and $\sigma = \frac{1}{\rho^2 g^2} N_s^2 \equiv \frac{\partial \phi}{\partial p} \frac{1}{\theta} \frac{\partial \theta}{\partial p}$

(vii) Kinematic vertical velocity for a triangular array

Three weather stations are located at points P, Q, and R whose coordinates, respectively, are $x_1 y_1$, $x_2 y_2$, $x_3 y_3$.

The horizontal motion fields (u, v) are given at these three locations.

We expand u and v as linear functions:

$$\begin{aligned} u &= ax + by + c \\ v &= px + qy + r \end{aligned} \quad (1)$$

Since u and v are known at three locations each, the six constants a, b, c, p, q and r can therefore be expressed as functions of $u_1, v_1, u_2, v_2, u_3, v_3$. The divergence at each level is given by:

$$\frac{\partial u}{\partial x} + \frac{\partial v}{\partial y} = a + q \quad (2)$$

A correction ensuring that the vertically integrated divergence vanishes over the atmospheric depth can easily be made by assuming that the error in divergence is proportional to the magnitude of the divergence.

i.e., $\nabla \cdot \mathbb{V}_{\text{corrected}} = \nabla \cdot \mathbb{V}_{\text{uncorrected}} + \epsilon |\nabla \cdot \mathbb{V}_{\text{uncorrected}}$ such that

$$\int \nabla \cdot \mathbb{V}_{\text{corrected}} dp = 0$$

$$\therefore \epsilon = - \frac{\int (\nabla \cdot \mathbb{V})_{\text{uncorrected}} dp}{\int |\nabla \cdot \mathbb{V}|_{\text{uncorrected}} dp} \quad (3)$$

Vanishing of the vertically integrated mass divergence is essential for budget studies.

It is also important that velocities, i.e. u, v , are accordingly corrected at all levels consistent with the divergence correction. Here it is convenient to assume that the directional error is small and most of the error in the divergence is due to the speed of the wind.

If $\theta = \tan^{-1} v/u$, we state that:

$$\frac{v_{\text{uncorrected}}}{u_{\text{uncorrected}}} = \frac{v_{\text{corrected}}}{u_{\text{corrected}}}$$

Furthermore, the correction in u and v should be made by correcting the coefficients a and q since they define the divergent part of the wind. We have the corrected values of $a + q$, i.e., $a^* + q^* = a$ known quantity. Using the relation:

$$\frac{px + q^*y + r}{a^*x + by + c} = \frac{px + qy + r}{ax + by + c}$$

we have two equations for the two unknowns a^* and q^* which can now be determined. Thus u and v at each level can be corrected. This is very useful for obtaining better estimates of $-\mathbb{V} \cdot \nabla A$ in budget equations.

(viii) The Ekman vertical velocity

The total mass transport along the isobars is to a first approximation proportional to the geostrophic transport, and will therefore be approximately non-divergent. Mass transport across the isobars may be written:

$$D = \frac{H}{f} F |k \times \rho_0 \mathbb{V}_{g0} \quad (\text{Charney and Eliassen, 1949}) \quad (1)$$

where $F = \frac{\sin 2\alpha}{\sqrt{2}} \frac{\sqrt{kf}}{H}$ and \mathbb{V}_{g0} is the geostrophic wind in the friction layer.

Hence, $D = \sin 2\alpha \frac{\sqrt{k}}{2f} |k \times \rho_0 \mathbb{V}_{g0}$ where H is the thickness of the boundary

layer, F is the frictional force per unit mass of air, ρ is the density of air at the surface, f is the Coriolis parameter, K is the coefficient of friction and α is angle of inclination of the flow to the isobars.

Flow across the isobars in the friction layer produces compensating currents across isobars aloft since there is no net accumulation or reduction of mass in the friction layer. So, to a good approximation:

$$\text{div } |D + \rho_0 W_0 = 0$$

where ρ_0 = density at the top of the friction layer; W_0 = vertical velocity at the top of the friction layer.

Thus, from equation (1):

$$W_0 = 1/\rho_0 \text{ div } |D \approx \frac{H}{f} F \zeta_{g0}$$

hence

$$W_B = - \rho g \left(\frac{Ae}{2f_0} \right)^{1/2} (\sin 2\alpha) \zeta_{g0}$$

(ix) Explanation of terms in the energy equations.

In Chapter 17 we presented the energy equations (see equations 17.3 to 17.6). First one notes that in the absence of generation, dissipation or boundary flux terms, the total energy, i.e. $(P + P' + \bar{K} + K')$ is an invariant.

- $\langle \bar{P} \cdot \bar{K} \rangle = - \langle \bar{K} \cdot \bar{P} \rangle$ denotes the generation of zonal kinetic energy by Hadley type overturning. If warm air ascends in certain latitudes and relatively colder air descends over other latitudes, this term would contribute to a generation of zonal kinetic energy.
- $\langle \bar{P} \cdot P' \rangle = - \langle P' \cdot \bar{P} \rangle$ This term denotes a generation of eddy available potential energy. If eddy heat flux is directed down the gradient of the zonally averaged temperature field, then this term is positive and gives rise to a conversion of energy from zonal to eddy available potential energy.
- $\langle P' \cdot K' \rangle = - \langle K' \cdot P' \rangle$ denotes a generation of eddy kinetic energy from eddy available potential energy. If on the scale of the eddies warmer air ascends and relatively colder air descends, a generation of eddy kinetic energy results. This term is important in many convectively driven disturbances over the tropics.
- $\langle \bar{K} \cdot K' \rangle = - \langle K' \cdot \bar{K} \rangle$ generally signifies barotropic generation of eddy kinetic energy from zonal kinetic energy. This is a very important process in the tropics, being generally large when convergence of eddy flux of easterly (or westerly) momentum occurs in a region of westerly (or easterly) jets.

- \bar{G} denotes a generation of zonal available potential energy by heating. This is usually positive when the zonally averaged temperatures are positively correlated with a heating function. The tropical Hadley cell is an example where \bar{G} tends to be positive.
- G' denotes a generation of eddy available potential energy. This again is positive if the heating occurs in regions of warmer anomalies and cooling occurs in relatively cold regions. This term is fairly important in the tropics and heating functions such as convective heating, sensible heating, radiative processes and large-scale condensation can contribute to the increase or decrease of eddy kinetic energy.
-

REFERENCES

- Abbott, D. A., 1977: Hemispheric simulation of the Asian summer monsoon. Monsoon Meteorology, PAGEOPH, Birkhauser Verlag, Basel, October 1977, 1111-1130.
- Alaka, M. A., 1961: The occurrence of anomalous winds and their significance. Mon. Wea. Rev., 89, 482-494.
- Alexander, R. C., and R. L. Mobley, 1974: Monthly average sea-surface temperatures and ice-pack limits on a 1° global grid. Rand Corporation Report, Santa Monica, Calif., pp. 1-30.
- Ananthakrishnan, R., 1977: Some aspects of the monsoon circulation and monsoon rainfall. PAGEOPH, 115, 1209-1249.
- Anthes, R. A., 1972: Development of asymmetries in a three-dimensional numerical model of the tropical cyclone. Mon. Wea. Rev., 100, 461-476.
- Arakawa, A., 1966: Computational design for long-term numerical integration of the equations of fluid motion: Two-dimensional incompressible flow. Part I. J. Comp. Phys., 1, 119-143.
- _____, 1971: A parameterization of cumulus convection and its application to numerical simulation of the tropical general circulation. Paper presented at the 7th Tech. Conf. on Hurricanes and Tropical Meteorology, Barbados, A.M.S.
- Asai, T., 1970: Three-dimensional features of thermal convection in a plane couette flow. J. Met. Soc. Japan, 48, 18-29.
- Atkinson, G. D., 1970: Gradient level wind charts over the tropics. Tech. Rept. No. 215. Air Weather Service (MAC). United States Air Force, 1-360.
- _____, 1971: Forecasters Guide to Tropical Meteorology. Tech. Rept. No. 240, Air Weather Service (MAC). Scott Air Force Base, Illinois, 360 pp.
- Augstein, E., H. Riehl, F. Ostapoff, and V. Wagner, 1973: Mass and energy transports in an undisturbed Atlantic trade-wind flow. Mon. Wea. Rev., 101, 101-111.
- Banerjee, A. K., and C. R. V. Raman, 1976: One hundred years of southwest monsoon rainfall over India. Meteorological Office, Poona 5, 9 pp.
- Baumhefner, D. P., 1968: Application of a diagnostic numerical model to the troposphere atmosphere. Mon. Wea. Rev., 96, 218-228.
- Berlage, H. P., 1966: The southern oscillation and world weather. Mededelingen en Verhandelingen, No. 88, Koninklijk Nederlands Meteorologisch Instituut, 152 pp.
- Betts, A. K., 1973: Non-precipitating cumulus convection and its parameterization. Quart. J. Roy. Meteor. Soc., 99, 178-196.

- Betts, A. K., 1974: Thermodynamic classification of tropical convective soundings. Mon. Wea. Rev., 102, 760-764.
- Bjerknes, J., 1938: Saturated-adiabatic ascent of air through dry-adiabatic descending environment. Quart. J. Roy. Meteor. Soc., 64, 325-330.
- Black, P. G., and R. A. Anthes, 1971: On the asymmetric structure of the tropical cyclone outflow layer. J. Atmos. Sci., 28, 1348-1366.
- Bruce, J. G., 1973: Large-scale variations of the Somali Current during the southwest monsoon, 1970. Deep-Sea Res., 20, 837-846.
- Brummer, B., F. Ostapoff, and H. Schmidt, 1973: The aerological measurements during ATEX. NOAA Tech. Rept.
- Bunker, A. F., 1965: Interaction of the summer monsoon air with the Arabian Sea. Proc. Symp. Meteor. Result. Intern. Ind. Ocean Exp., World Meteorological Organization, Geneva, Switzerland, pp. 3-16.
- Burpee, R. W., 1972: The origin and structure of easterly waves in the lower troposphere of North Africa. J. Atmos. Sci., 29, 77-90.
- Carr, F. H., 1977a: Numerical simulation of a mid-tropospheric cyclone. Dept. of Meteor., Florida State University, 1977.
- _____, 1977b: Tropospheric cyclones of the summer monsoon. Monsoon Meteorology, PAGEOPH, Birkhauser Verlag, Basel, October 1977, 1383-1412.
- Chang, C. B., 1977: On the influence of solar radiation and diurnal variation of surface temperature on North African circulations. Rept. No. 75-2, Dept. of Meteor., Florida State University, Tallahassee, Florida.
- _____, 1978: On radiative interactions in an African disturbance. Ph. D. Dissertation, Florida State University, Tallahassee, Florida, 163 pp.
- Charney, J. G., and A. Eliassen, 1949: A numerical method for predicting the perturbations of the middle latitude westerlies. Tellus, 1, 38-54.
- _____, 1958: On the formation of tropical depressions. Proc. Amer. Meteor. Soc. Tech. Conf. on Hurricanes, Miami Beach, Florida, November, 19-22.
- _____, and A. Eliassen, 1964: On the growth of the hurricane depression. J. Atmos. Sci., 21, 68-75.
- _____, 1969: Proceedings of the WMO/IUGG Symposium on Numerical Weather Prediction in Tokyo. The Intertropical Convergence Zone and the Hadley Circulation of the Atmosphere. Japan Meteorological Agency, Tokyo, 1969.
- Chin, P. C., and M. H. Lai, 1974: Monthly mean upper winds and temperature over southeast Asia and the western North Pacific. Roy. Obser. Tech. Memo, 12, Hong Kong, 1-115.

- Cho, H. R., and Y. Ogura, 1974: A relationship between cloud activity and the low-level convergence as observed in Reed-Recker's composite easterly waves. J. Atmos. Sci., 31, (1974), 2058-2065.
- Chu, J. H., 1981: Vorticity in maritime cumulus clouds and its effects on the large-scale budget of vorticity in the tropics. (To be published.)
- Colon, J., 1961: On the structure of hurricane Daisy 1958. National Hurricane Research Project, Rept. No. 48. U. S. Weather Bureau, 102 pp.
- Crutcher, H. L., and O. M. Davis, 1969: U.S. Navy Marine Climate Atlas of the World. Vol. III, "The World", NAVAIR, 50-1C-54, Naval Weather Service Command, 1 March. pp. 1-110.
- _____, and R. G. Quayle, 1974: Mariner's Worldwide Climatic Guide to Tropical Storms at Sea. Published by Direction of Commander, Naval Weather Service Command. p. 1-114.
- Danard, M. B., 1969: A simple method of including longwave radiation in a tropospheric numerical weather prediction model. Mon. Wea. Rev., 97, 77-85.
- Deacon, E. L., and E. K. Webb, 1962: Small-scale interactions. The Sea, New York, Interscience, 43-87.
- Dean, G. A., 1971: The three-dimensional wind structure over South America and associated rainfall over Brazil. Dept. of Meteorology, Florida State University, Rept. LAFE-164, pp. 1-33.
- _____, 1972: The three-dimensional temperature and wind structure over Africa in 1970. Dept. of Meteorology, Florida State University.
- _____, 1975: The lower tropospheric circulation over the Congo basin in 1958. Dept. of Meteorology, Florida State University, No. 75-1, pp. 1-106.
- Defant, Fr., and H. Taba, 1957: The threefold structure of the atmosphere and the characteristics of the tropopause. Tellus, 9, 259-274.
- Denney, W. J., 1971: Eastern Pacific hurricane season of 1970. Mon. Wea. Rev., 99, 286-301.
- Depradine, C. A., 1978: Energetics of long waves in the tropics during the summer of 1974. Ph. D. Dissertation, Dept. of Meteorology, Florida State University, Tallahassee, Florida. pp. 1-215.
- Dhonneur, G., 1974: Nouvelle approche des réalités météorologiques de l'Afrique occidentale et centrale. ASECNA, Tome I (358 p.), Tome II (470 p.) Université de Dakar, Dakar, Sénégal.
- Doplick, T. G., 1970: Global radiative heating of the Earth's atmosphere. Rept. No. 24, Planetary Circulation Project, Dept. of Meteorology, M.I.T., 128 pp.
- Dvorak, V. F., 1973: A technique for the analysis and forecasting of tropical cyclone intensities from satellite pictures. NOAA Tech. Memo, NESS 45. Published by the U.S. Dept. of Commerce, February.

- Eady, E. T., 1949: Long waves and cyclone waves. Tellus, 1, 33-52.
- Eldridge, R. H., 1957: A synoptic study of West African disturbance lines. Quart. J. Roy. Meteor. Soc., 83, 357.
- Ellingson, R. G., 1972: A new longwave radiation transfer model: calibration and application to the tropical atmosphere. Rept. No. 72-4, Dept. of Meteorology, Florida State University, Tallahassee, Florida.
- Elsasser, W. M., and M. F. Culbertson, 1960: Atmospheric radiation tables. Meteor. Monogr., 4, (29), 43 pp.
- Emmitt, G. D., 1977: Tropical cumulus interaction with and modification of the subcloud region. Ph. D. Dissertation, Dept. of Environmental Sciences, University of Virginia, 1-79.
- Erickson, C., 1969: Diagnostic study of an upper cold low. (Abstract). Trans. Amer. Geophys. U., 50, p. 179.
- Estoque, M. A., 1966a: Land/sea breezes. Published in Thermal convection: a colloquium sponsored by the NCAR Advanced Study Program (5 July - 12 Aug., 1966). NCAR Technical Note 24, pp. 325-346.
- _____, 1966b: Linear sea-breeze models. Published in Thermal convection: a colloquium sponsored by the NCAR Advanced Study Program (5 July - 12 Aug., 1966). NCAR Technical Note 24, pp. 347-367.
- _____, 1966c: Nonlinear theory of sea-breeze. Published in Thermal convection: a colloquium sponsored by the NCAR Advanced Study Program (5 July - 12 Aug., 1966). NCAR Technical Note 24, pp. 369-382.
- _____, 1967: Exchange processes due to penetrative convection. Bull. Amer. Meteor. Soc., 48, p. 624.
- _____, 1971: The planetary boundary layer wind over Christmas Island. Mon. Wea. Rev., 99, 193-201.
- _____, and M. Douglas, 1978: Structure of the intertropical convergence zone over the GATE area. Tellus, 30, 55-61.
- Fein, J. S., 1977: Global vorticity budget over the tropics and subtropics at 200 mb during northern hemisphere summer. Monsoon Meteorology, PAGEOPH, Birkhauser Verlag, Basel, October 1977, 1493-1500.
- Fett, R. W., 1966: Typhoon formation within the zone of the ITCZ. Annual typhoon report. Published by the U.S. Fleet Weather Central/Joint Typhoon Warning Center. Guam, Marianna Islands.
- Findlater, J., 1969: A major low-level air current near the Indian ocean during the northern summer. Quart. J. Roy. Meteor. Soc., 95, 362-380.
- _____, 1971: Mean monthly air flow at low levels over the western Indian ocean. Geophys. Memo. No. 115, Her Majesty's Stationary Office, London, 53 pp.

- Flohn, H., 1965: Studies of the meteorology of tropical Africa. University of Bonn, Bonner Met. Abhandl., Heft 5, pp. 1-58.
- _____, 1968: Contributions to a meteorology of the Tibetan Highlands. Rept. No. 130, Colorado State University, Fort Collins, 120 pp.
- Frank, N., 1970: Energetics of cold lows. Proceedings of the A.M.S. Conference on Hurricanes and Tropical Meteorology. Honolulu, Hawaii. A.M.S., Boston, Massachusetts.
- _____, 1975: Atlantic tropical systems of 1974. Mon. Wea. Rev., 103, 294-300.
- _____, 1976: Atlantic tropical systems of 1975. Mon. Wea. Rev., 104, 466-474.
- Fujita, T. T., K. Watanabe, and T. Izawa, 1969: Formation and structure of equatorial anticyclones caused by large-scale cross-equatorial flows determined by ATS-1 photographs. J. Appl. Meteor., 8, 649-667.
- GATE Rept. No. 4, 1973: The radiation sub-programme for GATE. Published by the World Meteorological Organization, Geneva, Switzerland, 109 pp.
- Gates, L. W., 1973: Global one-degree terrain and bottom tabulations. Rand Corporation Report, Santa Monica, California, pp. 1-132.
- _____, and A. B. Nelson, 1975: A new (revised) tabulation of the Scripps topography on a 1° global grid. Part I. Terrain heights. Rand Corporation Report R-1276-1-ARPA, 132 pp.
- Gilchrist, A., 1977: A simulation of the Asian summer monsoon by general circulation models. Monsoon Meteorology, PAGEOPH, Birkhauser Verlag, Basel, October 1977, 1431-1448.
- Godbole, R. V., 1975: The composite structure of the monsoon depression. Dept. of Meteorology, Florida State University, Rept. No. 75-9, 31 pp.
- _____, 1977: On cumulus-scale transport of horizontal momentum in monsoon depression over India. Monsoon Meteorology, PAGEOPH, Birkhauser Verlag, Basel, October 1977.
- Gray, W. M., 1968: Global view of the origin of tropical disturbances and storms. Mon. Wea. Rev., 96, 669-700.
- _____, and D. J. Novlan, 1974: Hurricane-spawned tornadoes. Mon. Wea. Rev., 12, 476-488.
- _____, and R. W. Jacobson, 1977: Diurnal variation of deep cumulus convection. Mon. Wea. Rev., 105, 1171-1188.
- Graystone, P., 1959: Meteorological Office Discussion. Met. Mag., London, 88, 113-119.
- Griffiths, J. F., 1972: Climate of Africa. Published in World Survey of Climatology, edited by H. A. Landsberg, Elsevier, Amsterdam.

- Griffiths, C. G., W. L. Woodley, P. G. Girube, D. W. Martin, J. Stout, and D. N. Sikdar, 1978: Rain estimation from geosynchronous satellite imagery-visible and infra-red studies. Mon. Wea. Rev., 106, 1153-1171.
- Gruber, A., 1974: The wave number frequency spectra of the 200 mb wind field in the tropics. J. Atmos. Sci., 32, 1615-1625.
- Gunther, E. B., 1977: Eastern north Pacific tropical cyclones of 1976. Mon. Wea. Rev., 105, 508-522.
- Hahn, D. G., and S. Manabe, 1975: The role of mountains in the south Asian monsoon circulation. J. Atmos. Sci., 32, 1515-1541.
- _____, 1976: Reply (to Sadler and Ramage). J. Atmos. Sci., 33, 2258-2262.
- Haltiner, G. J., 1963: Finite difference approximation for the determination of dynamic instability. Tellus, 15, 230-240.
- _____, 1971: Numerical weather prediction. Dept. of Meteorology, Naval Postgraduate School, Monterey, California, John Wiley and Sons, Inc., New York. 317 pp.
- Hamilton, R. A., and J. W. Archibold, 1945: Meteorology of Nigeria and adjacent territories. Quart. J. Roy. Met. Soc., 71, 231.
- Hantel, M., 1970: Monthly charts of surface wind-stress curl over the Indian ocean. Mon. Wea. Rev., 98, 765-773.
- Hawkins, H. F., and S. L. Rosenthal, 1965: On the computation of the stream function from the wind field. Mon. Wea. Rev., 93, 245-252.
- _____, and D. T. Rubsam, 1968: Hurricane Hilda, 1964, II. Structure and budgets of the hurricane on October 1, 1964. Mon. Wea. Rev., 97, 617-636.
- Hayashi, Y., 1970: A theory of large-scale equatorial waves generated by condensation heat and accelerating the zonal wind. J. Meteor. Soc. Japan, 48, 140-160.
- Haydu, K. J., and T. N. Krishnamurti, 1978: Moisture analysis from radiosonde and microwave spectrometer data. Dept. of Meteorology, Florida State University, Rept. No. 78-6, pp. 1-78.
- Holland, J. Z., and E. M. Rasmusson, 1973: Measurements of the atmosphere mass, energy and momentum budgets over a 500 km square of tropical ocean. Mon. Wea. Rev., 101, 44-55.
- Holton, J. R., J. M. Wallace, and J. A. Young, 1971: On boundary layer dynamics and the ITCZ. J. Atmos. Sci., 28, 275-280.
- _____, and D. E. Colton, 1972: A diagnostic study of the vorticity balance at 200 mb in the tropics during the northern summer. J. Atmos. Sci., 29, 1124-1128.

- Holton, J. R., and R. S. Lindzen, 1972: An update theory for the quasi-biennial cycle of the tropical stratosphere. J. Atmos. Sci., 29, 1076-1080.
- Hopewood, J. M., 1972: The quasi-biennial oscillation in the stratosphere. Meteorological Study 22. Bureau of Meteorology, Australia.
- Hsu, S., 1970: Coastal air-circulation system. Observations and empirical model. Mon. Wea. Rev., 98, 487-509.
- Hubert, L. F., A. F. Krueger, and J. S. Winston, 1969: The double inter-tropical convergence zone - fact or fiction? J. Atmos. Sci., 26, 771-773.
- Hudlow, M. D., 1970: Radar echo climatology east of Barbados derived from data collected during BOMEX. Published in reprints of papers presented at the 14th Radar Meteorology Conference, Tuscon, Arizona, 433-437.
- Jaeger, L., 1976: Monatskarten des Niederschlags für die ganze Erde. Berichte des Deutschen Wetterdienstes, Nr. 139, pp. 1-38.
- Jenkins, G. M., and D. G. Watts, 1968: Spectral analysis and its applications, 1968, Holden-Day.
- Johnson, D. H., and H. T. Mörth, 1960: Forecasting research in East Africa. Tropical Meteorology in Africa, Munitalp Foundation, Nairobi, 56-137.
- _____, 1975: The global circulation of the atmosphere. The role of the tropics in the global circulation. Roy. Meteor. Soc., London, England, 113-136.
- Jordan, C. L., 1958: Mean soundings for the West Indies area. J. Meteor. 15, 91-97.
- Joseph, J. H., 1966: Calculation of radiative heating in numerical general circulation models. Tech. Rept. No. 1, Department of Meteorology, University of California, Los Angeles, 60 pp.
- Kanamitsu, M., 1975: On numerical prediction over a global tropical belt. Dept. of Meteorology, Florida State University, Rept. No. 75-1, 282 pp.
- _____, 1977: Monsoonal quasi-stationary ultralong waves of the tropical troposphere predicted by a real data prediction over a global tropical belt. Monsoon Meteorology, PAGEOPH, Birkhauser Verlag, Basel, October 1977, 1187-1208.
- _____, T. N. Krishnamurti, and C. Depradine, 1972. On scale interactions in the tropics during northern summer. J. Atmos. Sci., 29, 698-706.
- _____, and T. N. Krishnamurti, 1978: Northern summer tropical circulations during drought and normal rainfall months. Mon. Wea. Rev., 106, 331-347.

- Katayama, A., 1964: On the heat balance of the troposphere over the northern hemisphere. Ph. D. Dissertation, Tohoku University, Japan.
- _____, 1966: On the radiation budget of the troposphere over the northern hemisphere (I). J. Meteor. Soc. Japan, 44, 381-401.
- _____, 1967a: On the radiation budget of the troposphere over the northern hemisphere (II). J. Meteor. Soc. Japan, 45, 1-25.
- _____, 1967b: On the radiation budget of the troposphere over the northern hemisphere (III). J. Meteor. Soc. Japan, 45, 26-39.
- _____, 1972: A simplified scheme for computing radiative transfer in the troposphere. Tech. Rept. No. 6, Dept. of Meteorology, University of California, Los Angeles, 77 pp.
- Keshavamurthy, R. N., 1972: Certain aspects of monsoon depressions as revealed by satellite pictures. India J. Met. Geophys., 23, 161.
- Kiangi, P. M. R., 1977: Some aspects of dynamic initialization using real tropical wind data. Archiv für Meteorologie, Geophysik und Bioklimatologie, A26, 349-360.
- Kreitzberg, C., R. W. Endlich, and J. R. Sweeney, 1969: Mesoscale and diurnal variations deduced from the Saigon area. Rawinsonde data. Published in Proceedings of the Conference on the Summer Monsoon of Southeast Asia. Navy Weather Research Facility, Norfolk, Va., 271-282.
- Krishnamurti, T. N., 1961: On the role of the subtropical jet stream of winter in the atmospheric general circulation. J. Meteor., 18, 657-670.
- _____, 1961: The subtropical jet stream of winter. J. Meteor., 18, 172-191.
- _____, 1962: Numerical integration of primitive equations by a quasi-Lagrangian advective scheme. J. Appl. Meteor., 1, 508-521.
- _____, 1969: An experiment in numerical prediction in equatorial latitudes. Quart. J. Roy. Meteor. Soc., 95, 594-620.
- _____, 1971a: Observational study of the tropical upper tropospheric motion field during the northern hemisphere summer. J. Appl. Meteor., 10, 1066-1096.
- _____, 1971b: Tropical east-west circulations during the northern summer. J. Atmos. Sci., 28, 1342-1347.
- _____, 1974: Lectures on tropical meteorology in the dynamics of the tropical atmosphere. Published as colloquium notes. National Center for Atmospheric Research, Boulder, Colorado, 105 pp.
- _____, 1977: Monsoon Meteorology. PAGEOPH, 442 pp.
- _____, and R. S. Hawkins, 1970: Mid-tropospheric cyclones of the southwest monsoon. J. Appl. Meteor., 9, 442-458.

- Krishnamurti, T. N., and E. B. Rodgers, 1970: 200 mb wind field June, July, August, 1967. Tech. Rept. No. 70-2, Florida State University, Tallahassee, Florida, 130 pp.
- _____, and W. J. Moxim, 1971: On parameterization of convective and nonconvective latent heat release. J. Appl. Meteor., 10, 3-13.
- _____, and M. Kanamitsu, 1973: A study of a coasting easterly wave. Tellus, 25, 568-585.
- _____, M. Kanamitsu, B. Ceselski, and M. B. Mathur, 1973: Florida State University's Tropical Prediction Model. Tellus, 25, 523-535.
- _____, M. Kanamitsu, W. J. Koss, and J. D. Lee, 1973: Tropical east/west circulations during the northern winter. J. Atmos. Sci., 30, 780-787.
- _____, E. Astling, and M. Kanamitsu, 1975: 200 mb wind field June, July, August 1972: Atlas published by the Department of Meteorology, Florida State University, Tallahassee, Florida, 116 pp.
- _____, M. Kanamitsu, R. Godbole, C. B. Chang, F. Carr, and J. H. Chow, 1975: Study of a monsoon depression (I), synoptic structure. J. Meteor. Soc. Japan, 53, 227-240.
- _____, C. E. Levy, and H. L. Pan, 1975: On simultaneous surges in the trades. J. Atmos. Sci., 32, 2367-2370.
- _____, and H. N. Bhalme, 1976: Oscillations of a monsoon system, Part I. Observational aspects. J. Atmos. Sci., 33, 1937-1954.
- _____, M. Kanamitsu, R. Godbole, C. B. Chang, F. Carr, and J. H. Chow, 1976: Study of a monsoon depression (II), dynamical structure. J. Meteor. Soc. Japan, 54, 208-226.
- _____, J. Molinari, H. L. Pan, and V. Wong, 1977: Numerical weather prediction relevant to the monsoon problem. PAGEOPH, 115, 1357-1372.
- _____, and V. Wong, 1978: A planetary boundary layer model for the Somali jet. Dept. of Meteorology, Florida State University, Rept. No. 78-1, 40 pp.
- Kuettner, J., 1977: Double vortices on either side of the Equator over the eastern Indian ocean. Unpublished manuscript submitted for MONEX planning. National Center for Atmospheric Research, Boulder, Colorado.
- Kuhn, P. M., 1963: Soundings of observed and computed infrared flux. J. Geophys. Res., 68, 1415-1420.
- _____, and D. R. Johnson, 1966: Improved radiometersonde observations of atmospheric infrared irradiance. J. Geophys. Res., 71, 367-373.

- Kuhn, P. M., and L. P. Sterns, 1971: Radiative transfer observations during BOMEX. NOAA Technical Rept. ERL 203-APCL19, 171 pp.
- Kuo, H. L., 1961: Convection in conditionally unstable atmosphere. Tellus, 13, 441-459.
- _____, 1965: On formation and intensification of tropical cyclones through latent heat release by cumulus convection. J. Atmos. Sci., 22, 40-63.
- Kurihara, Y., 1973: Experiments on the seasonal variation of the general circulation in a statistical-dynamical model. J. Atmos. Sci., 12, 25-49.
- LaSeur, N. E., 1963: Synoptic models in the tropics. Proc. of the Symposium on Tropical Meteorology, Rotorua, N. Z., 5-13 November, 1963. New Zealand Meteorological Service, 1964, 319-328.
- Lateef, M. A., 1964: Energy generation and flux processes associated with weakening depression over the Gulf of Mexico. National Hurricane Research Project, Rept. No. 71, Washington, D. C., 1964, 10 pp.
- Lavoie, R. L., 1963: Some aspects of the meteorology of the tropical Pacific viewed from an atoll. Scientific Rept. No. 5, Hawaii Institute of Geophysics. 77 pp.
- Leroux, M., 1976: Processus de formation et d'évolution des lignes de grains d'Afrique tropicale septentrionale. Université de Dakar, Dakar, Sénégal, 159 pp.
- Lilly, D. K., 1960: On the theory of disturbances in a conditionally unstable atmosphere. Mon. Wea. Rev., 88, 1-17.
- _____, 1965: On the computational stability of numerical solutions of time dependent non-linear geophysical fluid dynamics problems. Mon. Wea. Rev., 93, 11-26.
- Lindzen, R. S., 1967: Planetary waves on beta plane. Mon. Wea. Rev., 95, 441-451.
- _____, 1974: Wave-CISK in the tropics. J. Atmos. Sci., 31, 156-179.
- _____, and J. R. Holton, 1968: A theory of the quasi-biennial oscillation. J. Atmos. Sci., 25, 1095-1107.
- Lorenz, E. N., 1967: The nature and theory of the general circulation of the atmosphere. Published by the World Meteorological Organization, WMO-No. 218, 161 pp.
- Madala, R. R., 1973: Numerical simulation of an asymmetric hurricane. Ph. D. Dissertation, Department of Meteorology, Florida State University, Tallahassee, Florida.
- Mahrt, L. J., 1971: A numerical study of advective effects on boundary layer flow at low latitudes. Published in Studies of the Atmosphere Using Aerospace Probing. Space Science and Engineering Center, University of Wisconsin, Annual Report.

- Mahrt, L. J., and J. A. Young, 1972: Some basic theoretical concepts of boundary layer flow at low latitudes. Published in Dynamics of the Tropical Atmosphere, 411-420.
- Mak, M. K., 1975: The monsoonal mid-tropospheric cyclogenesis. J. Atmos. Sci., 32, 2246-2253.
- Manabe, S., and J. Smagorinsky, 1967: Simulated climatology of a general circulation model with a hydrologic cycle II: Analysis of the tropical atmosphere. Mon. Wea. Rev., 95, 155-169.
- Mathur, M. B., 1970: A note on an improved quasi-Lagrangian advective scheme for primitive equations. Mon. Wea. Rev., 98, 214-219.
- _____, 1971: Simulation of an asymmetric hurricane with a fine mesh multiple grid primitive equation model. Ph. D. Dissertation, Dept. of Meteorology, Florida State University, Tallahassee, Florida.
- Matsuno, T., 1966: Numerical integration of primitive equations by a simulated backward difference method. J. Meteor. Soc. Japan, 44, 76-84.
- McGarry, M. M., and R. J. Reed, 1978: Diurnal variations in convective activity and precipitation during phases II and III of GATE. Mon. Wea. Rev., 106, 101-113.
- Mendenhall, B. R., 1967: A statistical study of frictional wind veering in the planetary boundary layer. Dept. of Atmospheric Science, Colorado State University, Fort Collins, Colorado, Paper No. 116, 57 pp.
- Miller, F. R., and R. N. Keshavamurthy, 1968: Structure of an Arabian Sea summer monsoon system. University of Hawaii, East-west Center Press.
- Miyakoda, K., and R. W. Moyer, 1968: A method of initialization for dynamical weather forecasting. Tellus, 20, 113-128.
- Moncrieff, M. W., and M. J. Miller, 1976: The dynamics and simulation of tropical cumulonimbus and squall lines. Quart. J. Roy. Meteor. Soc., 102, 373-394.
- Mower, R. N., 1977: Case study of convection lines during GATE. Atmospheric Science Paper No. 271, Colorado State University, Fort Collins, Colorado, 93 pp.
- Murakami, T., 1977: Regional energetics over the North Pacific, South China Sea and the Indonesian Seas during Winter. Monsoon Meteorology, PAGEOPH, Birkhauser Verlag, Basel, October 1977, 1283-1301.
- _____, 1978: Large-scale aspect of convective activity over the GATE area (submitted for publication to the Monthly Weather Review).
- _____, R. V. Godbole, and R. R. Kelkar, 1970: Numerical simulation of the monsoon along 80°E. In Proceedings of the Conference on the Summer Monsoon of Southeast Asia, C. S. Ramage, ed. Navy Weather Research Facility, Norfolk, Virginia, 39-51.

Petterssen, S., 1956: Weather analysis and forecasting, I, Chapter 9. McGraw-Hill Book Company, New York.

_____, 1956: Weather analysis and forecasting, II, p. 142. McGraw-Hill Book Company, New York.

Phillips, N. A., 1967: The Boussinesq approximation. Published in Thermal Convection: A colloquium. NCAR Tech. Notes, Boulder, Colorado, 23-26.

Pielke, R. A., 1974: A three-dimensional numerical model of the sea breezes over south Florida. Mon. Wea. Rev., 102, 115-139.

Pike, A. C., 1971: Intertropical convergence zone studied with an interacting atmosphere and ocean model. Mon. Wea. Rev., 99, 409-477.

_____, 1972: Response of tropical atmosphere and ocean model to seasonally variable forcing. Mon. Wea. Rev., 100, 424.

Pisharoty, P. R., 1965: Evaporation from the Arabian Sea and the Indian southwest monsoon. Proceedings of the Symposium on Meteorological Results of the International Indian Ocean Expedition. Bombay, 43-54.

Posey, J. W., and P. F. Clapp, 1964: Global distribution of normal surface albedo. Geofisica International, Mexico, 4, 33-48.

Raghavendra, V. K., 1973: A statistical analysis of the number of tropical storms and depressions in the Bay of Bengal during 1890-1969. Indian J. Met. Geophys., 24, 125-130.

Ramage, C. S., 1971: Monsoon Meteorology. New York, Academic Press, 296 pp.

_____, and C. V. R. Raman, 1972: Meteorological atlas of the International Indian Ocean Expedition, Vol. 2. National Science Foundation, Washington, D. C., 121 pp.

Ramamurthy, K., 1969: Some aspects of the break in the Indian southwest monsoon during July and August. Forecasting Manual, No. IV-18.3, India Meteorological Department, Poona, India, 57 pp.

Ramos, R. P., 1974: Precipitation characteristics in the northeast Brazil dry region. Atmos. Science Paper No. 224, Dept. of Atmospheric Science, Colorado State University, Fort Collins, Colorado, 56 pp.

Rao, M. S. V., W. V. Abbott III, and J. S. Theon, 1976: Satellite-derived global oceanic rainfall atlas (1973 and 1974). Published by the National Aeronautics and Space Administration, Washington D.C., 184 pp.

_____, and J. S. Theon, 1977: New features of global climatology revealed by satellite-derived oceanic rainfall maps. Bull. Amer. Meteor. Soc., 58, 1285-1288.

Rao, Y. P., 1976: Southwest Monsoons. Meteor. Monographs, Synoptic Meteorology, June 1976, 367 pp. India Meteorological Department.

- Rasohke, E., and W. R. Bandeen, 1970: The radiation balance of the planet Earth from radiation measurements of the satellite Nimbus II. J. Appl. Meteor., 9, 215-238.
- Reed, R. J., 1964: A tentative model of the 26-month oscillation in tropical latitudes. Quart. J. Roy. Meteor. Soc., 90, 441-466.
- _____, 1965: The quasi-biennial oscillation of the atmosphere between 30 and 50 km over Ascension Island. J. Atmos. Sci., 22, 331-333.
- _____, 1966: Zonal wind behavior in the equatorial stratosphere and lower mesosphere. J. Geophys. Res., 71, 4223-4233.
- _____, W. J. Campbell, L. A. Rasmussen, and D. G. Rogers, 1961: Evidence of a downward propagating annual wind reversal in the equatorial stratosphere. J. Geophys. Res., 66, 813-818.
- _____, and E. E. Recker, 1971: Structure and properties of synoptic scale wave disturbances in the equatorial western Pacific. J. Atmos. Sci., 28, 1117-1133.
- _____, D. C. Norquist, and E. E. Recker, 1977: The structure and properties of African wave disturbances as observed during Phase III of GATE. Mon. Wea. Rev., 105, 317-333.
- Riehl, H., 1945: Tropical Meteorology. McGraw-Hill Book Company, New York, 392 pp.
- _____, and J. S. Malkus, 1958: On the heat balance in the equatorial trough zone. Geophys., 6, 503-538.
- _____, 1961: Some aspects of hurricane Daisy. Tellus, 13, 181-213.
- Robitaille, F. E., and E. J. Zipser, 1970: Atmospheric boundary layer circulations equatorward of the intertropical convergence zone. Symposium on Tropical Meteorology, University of Hawaii, Honolulu, Hawaii.
- Rocha de Aragão, José Oribe, 1975: Um Estudo da estrutura das perturbações sinóticas do nordeste do Brasil. Meteorologia sinótica do nordeste brasileiro, 219 pp.
- Rodgers, C. D., 1967: The radiative heat budget of the troposphere and lower stratosphere. Rept. No. A2, Massachusetts Institute of Technology, Cambridge, Mass., 99 pp.
- Rodhe, H., and H. Virji, 1976: Trends and periodicities in east African rainfall data. Mon. Wea. Rev., 104, 307-315.
- Rogers, R. R., 1976: A short course in cloud physics. Pergamon Press, 40-41.
- Rosenthal, S. L., 1969: Numerical experiments with a multi-level primitive equation model designed to simulate the development of tropical cyclones. Experiment I. U.S. Department of Commerce, ESSA Technical Memorandum No. NHRL-82, 32 pp.

- Warner, J., 1955: The water content of cumuliform cloud. Tellus, 7, 449-457.
- Warsh, K. L., K. L. Echternacht, and M. Garstang, 1971: Structure of near surface currents east of Barbados. J. Phys. Oceanogr., 1, 123-129.
- Washington, W. M., R. M. Chervin, and G. V. Rao, 1977: Effects of a variety in Indian Ocean surface temperature anomaly patterns on a summer monsoon circulation. Experiments with the NCAR general circulation model. Monsoon Meteorology, PAGEOPH, 115, 1335-1357.
- Wernstedt, F. L., 1972: World Climatic Data. Published by Climatic Data Press, Lemont, Pennsylvania, 523 pp.
- Williams, K. T., 1970: A statistical analysis of satellite-observed trade wind cloud clusters in the western North Pacific. Rept. No. 161, Dept. of Atmospheric Sciences, Colorado State University, Fort Collins, 80 pp.
- _____, and W. M. Gray, 1973: A statistical analysis of satellite-observed trade wind cloud clusters in the western North Pacific. Tellus, 25, 313-336.
- Winninghoff, F. J., 1968: On the adjustment toward a geostrophic balance in a simple primitive equation model with application to the problems of initialization and objective analysis. Ph. D. Dissertation, Department of Meteorology, University of California, Los Angeles, California.
- Winston, J. S., 1967: Planetary-scale characteristics of monthly mean long-wave radiation and albedo and some year-to-year variations. Mon. Wea. Rev., 95, 235-256.
- Yamasaki, M., 1968: Detailed analysis of a tropical cyclone simulated with a 13 layer model. Papers in Meteorology and Geophysics, 19, 559-585.
- _____, 1969: Large-scale disturbances in the conditionally unstable atmosphere in low latitude. Papers in Meteorology and Geophysics, 20, 289-336.
- _____, 1971: A further study of wave disturbances in the conditionally unstable model tropics. J. Meteor. Soc. Japan, 49, 391-415.
- Yanai, M., and T. Nitta, 1968: Finite difference approximation for the barotropic instability problem. J. Meteor. Soc. Japan, 46, 389-403.
- _____, S. Esbensen, and J. H. Chu, 1973: Determination of bulk properties of tropical cloud clusters from large-scale heat and moisture budgets. J. Atmos. Sci., 30, 611-627.
- Zipser, E. J., 1969: Structure of a disturbance in the equatorial Pacific Ocean, Sixth Conference Severe Local Storms. American Meteorological Society, Chicago, April, 1969.
- _____, 1969: The role of organized unsaturated convective downdrafts in the structure and rapid decay of an equatorial disturbance. J. Appl. Meteor., 8, 799-814.